NATIONAL CENTER FOR COMPUTATIONAL
HYDROSCIENCE AND ENGINEERING
THE UNIVERSITY OF MISSISSIPPI

Phase II Report for SERRI Project No. 80037:

Investigation of Surge and Wave Reduction by Vegetation (Phase II)

—*Interaction of Hydrodynamics, Vegetation and Soil*

Weiming Wu (PI)

August 2012

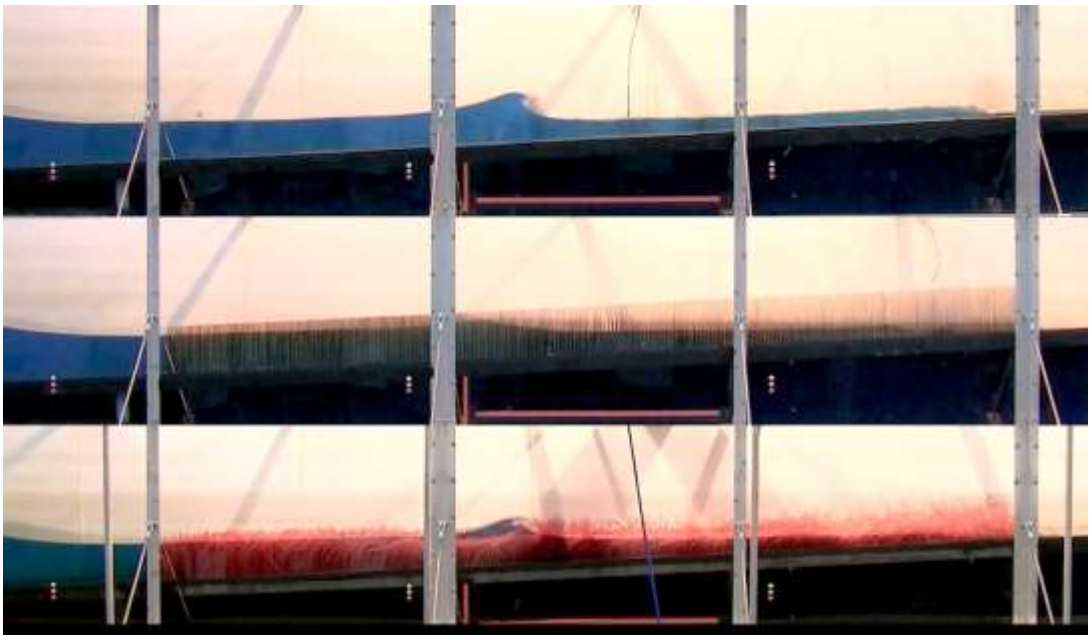

This material is based upon work supported by the U.S. Department of Homeland Security under U.S. Department of Energy Interagency Agreement 43WT10301. The views and conclusions contained in this document are those of the authors and should not be interpreted as necessarily representing the official policies, either expressed or implied, of the U.S. Department of Homeland Security.

SERRI Report 80037-02

SERRI Project: Investigation of Surge and Wave Reduction by Vegetation

FINAL REPORT OF PHASE II

Weiming Wu (PI)
National Center for Computational Hydroscience and Engineering
The University of Mississippi, MS 38677

Yavuz Ozeren (Stationed at UM) and *Daniel Wren* (Co-PI)
National Sedimentation Laboratory, USDA-ARS, Oxford, MS 38655

Qin Chen (Co-PI) and *Guoping Zhang* (Co-PI)
Civil and Environ.Engineering Dept., Louisiana State Univ., Baton Rouge, LA 70803

Marjorie Holland (Co-PI)
Biology Department, The University of Mississippi, MS 38677

Reza Marsooli and Qianru Lin
National Center for Computational Hydroscience and Engineering
The University of Mississippi, MS 38677

Ranjit Jadhav, Kyle R. Parker, Hem Pant and *James Bouanchaud*
Civil and Environ. Engineering Dept., Louisiana State Univ., Baton Rouge, LA 70803

Ying Chen
Biology Department, The University of Mississippi, MS 38677

Date Published:
August 2012

Prepared for
U.S. Department of Homeland Security
under U.S. Department of Energy Interagency Agreement 43WT10301
Southeast Regional Research Initiative (SERRI)
Basic Ordering Agreement 4200000224, Task Order Number 4000075852

Prepared by
OAK RIDGE NATIONAL LABORATORY
Oak Ridge, Tennessee 37831-6283
managed by UT-BATTELLE, LLC
for the U.S. DEPARTMENT OF ENERGY
under contract DE-AC05-00OR22725

ACKNOWLEDGEMENTS

Funding for this project was provided by the Department of Homeland Security-sponsored Southeast Region Research Initiative (SERRI) managed by the Department of Energy's Oak Ridge National Laboratory (ORNL). The program manager Mr. Michael Mathews at the DHS Science and Technology (S&T) Directorate, Mr. Benjamin Thomas, Jr. and Ms. Berky A. Wagner at ORNL are acknowledged for their guidance, insight and timely handling of technical and business affairs related to this project. The present research would not have been so successful without their supervision and support.

Thanks to Dr. Sam Wang, Dr. Mustafa Altinakar, Ms. Kathy McCombs, Mr. Paul Smith and Ms. Natalie Spencer at NCCHE and colleagues at the Office of Research and Sponsored Programs and the Accounting Office of The University of Mississppi for their support for this research.

Assistance from the LUMCON is appreciated for providing boats and personnel for our field work. Special thanks to T. Baker Smith, LLC of Houma, LA for providing boat and personnel during the deployment and recovery of gages for Tropical Storm Lee, and for carrying out the topographic surveys of the marsh site. We greatly appreciate the cooperation of Bobbie Chauvin and Frank Ellender of the Louisiana Land and Exploration Company in granting us permission to access the marsh field site and letting us deploy instrumentation. LSU graduate students Ke Liu, Ling Zhu, Qi Fan, and Qian Zhang assisted in the deployment and measurements of vegetation properties. LSU post-doc researcher Arash Karimpour contributed to the field data collection and analysis.

Jacob Ferguson, Alan Barger, Austin Patton, Weimin Li, Will Simpson, and Glenn Gray are acknowledged for their technical assistance during preparation of the laboratory setup, in field work, and throughout the experiments at the National Sedimentation Laboratory. Glenn Gray served another invaluable role as the agent responsible for arranging the purchasing and delivery of the materials used in the project. Seth Dabney and Lucienne Savell are also acknowledged for their support during this research project.

Thanks to Sam Testa, Lisa Brooks, and Matt Moore at the USDA-ARS National Sedimentation Laboratory for their guidance and insight for the lab analyses carried out by UM-Biology team. Thanks to Dave Ruple and Dr. Mark Woodrey at Grand Bay National Estuarine Research Reserve (GNDNERR), for helping find suitable research sites, obtain data needed and for taking us where we needed to be despite the weather. Gratitude to UM Department of Biology for supporting this study. Thanks to Rani Menon for helping with logistical aspects of our experiment. Thanks to Jeffery Cannon, Mark Winkler, Patrick Hourguettes, Jessica Landrum, Sarah Magee, Melissa Baskin and Steven Nelson for helping us collecting soil and plant samples in the MS field sites.

CONTENTS

LIST OF FIGURES

LIST OF TABLES

NOTATIONS

The most significant parameters and their dimensions used in this report are listed as follows:

A_v	Projected area of vegetation stem [L^2]
C_D	Drag coefficient [-]
C_M	Inertia coefficient [-]
D_v	Stem diameter [L]
d	Water depth [L]
F	Force on vegetation [MLT^{-2}]
F_D	Drag force on vegetation [MLT^{-2}]
F_I	Inertia force on vegetation [MLT^{-2}]
g	Gravitational acceleration [LT^{-2}]
H	Wave height [L]
H_i	Incident wave height [L]
H_{rms}	Root-mean-square wave height [L]
H_s	Significant wave height [L]
h	Still or total water depth [L]
h_v	Vegetation height [L]
K_c	Keulegan-Carpenter number [-]
L	Wave length [L]
l_v	Vegetation span [L]
N_v	Vegetation density [L^{-2}]
Re	Reynolds number [-]
T	Wave period [T]
U and V	Depth-averaged flow velocities in x and y directions [LT^{-1}]
u	Characteristic or local flow velocity [LT^{-1}]
η	Water surface elevation [L]
λ	Spacing between vegetation elements [L]
μ	Dynamic viscosity of water [$ML^{-1}\ T^{-1}$]
ν_t	Turbulent viscosity of water [$L^2\ T^{-1}$]
ρ	Mass density of water [ML^{-3}]

ACRONYMS

CARRI	Community and Regional Resilience Initiative
DHS	Department of Homeland Security
DOE	Department of Energy
LA	Louisiana
LSU	Louisiana State University
MS	Mississippi
NCCHE	National Center for Computational Hydroscience and Engineering
NSL	National Sedimentation Laboratory, USDA-ARS
ORNL	Oak Ridge National Laboratory
SERRI	Southeast Region Research Initiative
UM	The University of Mississippi
VOF	Volume-of-Fluid
1-D	One-dimensional
2-D	Two-dimensional
3-D	Three-dimensional

SOUTHEAST REGION RESEARCH INITIATIVE

In 2006, the U.S. Department of Homeland Security commissioned UT-Battelle at the Oak Ridge National Laboratory (ORNL) to establish and manage a program to develop regional systems and solutions to address homeland security issues that can have national implications. The project, called the Southeast Region Research Initiative (SERRI), is intended to combine science and technology with validated operational approaches to address regionally unique requirements and suggest regional solutions with potential national implications. As a principal activity, SERRI will sponsor university research directed toward important homeland security problems of regional and national interest.

SERRI's regional approach capitalizes on the inherent power resident in the southeastern United States. The project partners, ORNL, the Y-12 National Security Complex, the Savannah River National Laboratory, and a host of regional research universities and industrial partners, are all tightly linked to the full spectrum of regional and national research universities and organizations, thus providing a gateway to cutting-edge science and technology unmatched by any other homeland security organization.

Because of its diverse and representative infrastructure, the state of Mississippi was chosen as a primary location for initial implementation of SERRI programs. Through the Mississippi Research Initiative, SERRI plans to address weaknesses in dissemination and interpretation of data before, during, and after natural disasters and other mass-casualty events with the long-term goal of integrating approaches across the Southeast region.

As part of its mission, SERRI supports technology transfer and implementation of innovations based upon SERRI-sponsored research to ensure research results are transitioned to useful products and services available to homeland security responders and practitioners. Concomitantly, SERRI has a strong interest in supporting the commercialization of university research results that may have a sound impact on homeland security and encourages university principal investigators to submit unsolicited proposals to support the continuation of projects previously funded by SERRI.

For more information on SERRI, go to the SERRI Web site: www.serri.org.

EXECUTIVE SUMMARY

To better understand and quantify the effectiveness of wetland vegetation in mitigating the impact of hurricane and storm surges, this SERRI project (No. 80037) examined surge and wave attenuation by vegetation through laboratory experiments, field observations and computational modeling. It was a collaborative endeavor of the National Center for Computational Hydroscience and Engineering of The University of Mississippi, the USDA-ARS National Sedimentation Laboratory, the Civil and Envionmental Engineering Department of Louisiana State University, and the Biology Department of The University Of Mississippi. In Phase I dated from January 2009 to March 2011, a large amount of measurement data were collected and a series of empirical formulas and numerical models were developed. These efforts have been continued and expanded in Phase II from April 2011 to August 2012.

The laboratory experiments of Phase I considered model and live vegetation at emergent and nearly emergent conditions in a flat-bed wave flume, as well as wave setup with rigid model vegetation on a sloping beach. In Phase II, the team extended the experiments by including the interaction of the regular and irregular waves with rigid and flexible vegetation with higher submergence (i.e., lower ratio of plant height to flow depth). The water levels were measured by both wave gages and video camera. The gage resolution was increased by adding two wave gages in the vegetation zone and a wave runup gage. Additionally, wave setup experiments with rigid model vegetation were extended to flexible model vegetation. The new datasets show that there is no apparent dependency of the drage coefficient on relative plant height for both rigid and flexible model vegetation used in these experiments. The rigid model vegetation had a slightly higher drag coefficient and performed better in reducing wave setup than the flexible one.

As part of the field investigations in Phase II, the team collected wave data in a two-day period (Sept. 3-4, 2011) at a salt marsh wetland in Terrebonne Bay on the Louisiana coast during Tropical Storm Lee, and measured waves and bottom currents near the marsh edge on a vegetated wetland in south Louisiana in April 12–20, 2012 during a cold front passage. These field campaigns provided very useful data of wave attenuation by vegetation in high-energy wave environments, which are sorely needed in the literature. The datasets revealed the presence of bimodal wave spectra in the study site, consisting of low-frequency ocean swell in addition to the wind sea. The bulk drag coefficient was observed to decrease with increasing stem Reynolds number and Keulegan-Carpenter number and to be smaller for the longer-period waves than the shorter-period waves. The data was also used to develop a method to determine the frequency-dependent drag coefficient.

In continued investigation of the vegetation and soil properties in LA and MS marshes, the team conducted vegetation damage testing using a newly designed plant tension testing device and measured the critical shear stress of coastal marshland soils using a cohesive strength meter combined with a laboratory testing program. Two sites in Terrebonne Bay and Barataria Bay of the LA coast were selected. The data collected by eight field visits showed that the tensile damage forces range from 17 to 76 lbs, with an average and standard deviation of 32.41 ± 11.56 lbs. The plants exhibit more failures at the stem in winter and early spring, but damage occurs in both stem and root randomly in summer when the plant reaches its maturity and hence maximum strength. The critical shear stress of the soils at both sites ranges from 0.4 to 1.9 Pa, and the average values are 1.03 to 1.16 Pa. The critical shear stress generally increases with root content, indicating that the roots play an

important role in controlling marshland loss. In addition, the team compared the growth forms and productivities between LA and MS coastal marshes. Three transects in Terrebonne Bay, LA and two transects in Graveline Bayou, MS were selected. The LA site has a higher soil moisture content, organic matter content, clay percentage, live and dead *Spartina alterniflora* standing shoot heights, rhizome thickness and bottom stem diameter, but a lower sediment mean grain size and sand percentage than the MS marsh site. It was found that coastal marshes with low elevation have higher belowground production, which is beneficial for the prolific rhizomes that hold sediments and help vegetation survive and withstand storm waves.

The laboratory and field work was extended in Phase II to marsh edge erosion. A model marsh edge was constructed in the NSL wave flume using the intact marsh edge samples composed of *S. alterniflora* shoots and rhizomes in their native soil that were collected from the Terrebonne Bay area. During the experiments, the detailed progression of waves impacting the marsh, as well as erosion of both the marsh material and the underlying substrate, were observed and recorded. Undercutting and exposure of the plant roots were observed, which is consistent with field observations. The marsh edge erosion was also investigated in LA marshlands. Directional wave measurements were carried out inside a rapidly eroding shallow bay partially protected by barrier islands to quantify the intensity and nature of the wave field. Potential erosion rates were estimated from the measured wave power using methods in the published literature. The GPS system and aerial photographs were successfully employed to determine the short-term and long-term erosion rates in Terrebonne Bay.

Four 1-D and 2-D models were selected in Phase I to demonstrate how to account for the effects of vegetation on surge and wave reduction. In Phase II, a 3-D shallow water flow model coupled with a 2-D wave action model was added in the demonstration model list. It computes current by solving the phase-averaged 3-D shallow water equations with wave radiation stresses and determines the wave characteristics such as wave height, period, angle, and radiation stress by solving the 2-D wave action balance equation. The model considers the effects of vegetation by including the drag and inertia forces of vegetation in the momentum equations and the wave energy loss due to vegetation resistance in the wave action balance equation. The 2-D shallow water model developed in Phase I was enhanced in Phase II with empirical formulas for the vegetation drag coefficient, further tested using laboratory experiments considering vegetation, and then applied to assess the long wave runup reduction by vegetation on a sloping beach and the possible benefits and drawbacks of vegetation in riverine systems. This 2-D model was further enhanced to simulate sediment transport and morphological changes induced by rapidly-varying transient long waves, such as strong storm surge and tsunami waves, near a marsh edge. For more general applications, a 3-D rapidly-varying transient flow model over erodible bed was developed to simulate marsh edge erosion induced by both long and short waves. The model solves the Reynolds-averaged Navier-Stokes equations using a finite volume method on unstructured meshes, and uses the CICSAM-VOF surface-capturing method to trace the changes of the water surface.

In the project period, the research team sought opportunities to participate in relevant communications, meetings, workshops and conferences and worked closely with stakeholders to confirm the value/merits of the results of this research in helping to mitigate the effects of surge and waves caused by hurricanes and severe storms in coastal areas. As one of such efforts, the team implemented the vegetation effect modeling capability in the

Coastal Modeling System (CMS) of the US Army Corps of Engineers Research and Development Center (ERDC), as described in Section 6.2.

The team has completed the planned tasks for Phase II and achieved the goals of this project. The collected laboratory and field measurement data and developed formulas and models are significant contributions and will be widely used in coastal protection and marsh restoration.

1. INTRODUCTION

1.1 General Information

Since 2006, the United States (U. S.) Department of Homeland Security (DHS) has funded UT-Battelle at Oak Ridge National Laboratory to establish a regional pilot program to develop regional systems and solutions to address homeland security issues that can have national implications. The program is called the Southeast Regional Research Initiative (SERRI) and has been established to develop and demonstrate the homeland security benefits of leveraging homeland security-related research, operational and economic development capabilities in the southeast region of the United States. Because of its diverse and representative infrastructure makeup, the state of Mississippi was chosen as a primary location for initial implementation of the SERRI Program. As a principal activity, SERRI has sponsored university research directed toward important homeland security problems of regional and national interest. Technology transfer, commercialization and implementation of innovations based upon SERRI-sponsored research have been pursued to transition research results to useful products and services available to homeland security responders and practitioners.

On July 3, 2008, the University of Mississippi (UM) in collaboration with Louisiana State University (LSU) and National Sedimentation Laboratory (NSL) submitted a research proposal entitled "Investigation of Surge and Wave Reduction by Vegetation" to SERRI, and on December 1, 2008 this proposal was approved. The entire research performed three interrelated technical tasks to address the reduction of surge and waves by wetland vegetation. Successful completion of these tasks helps improve the understanding, estimation and modeling of the effects of vegetation on surge and waves induced by hurricanes and strong storms. Phase I of this project was completed on March 31, 2011. On February 23, 2011, the research team submitted an extension proposal entitled "Investigation of Surge and Wave Reduction by Vegetation (Phase II) — Interaction of Hydrodynamics, Vegetation and Soil", as a continuation of this SERRI project. The Phase II proposal was approved on March 31, 2011. Phase II has lasted from April 1, 2011 to August 31, 2012. This final report documents the research results obtained by the team for Phase II of SERRI project No. 80037. The Phase I report refers to Wu et al. (2011).

1.2 Background and Objectives

As evidenced during Hurricane Katrina, surges and waves generated by hurricanes and other severe storms can cause devastating damage of property and loss of life in coastal areas. Traditional engineering approaches to mitigating these severe impacts include permanent levees, seawalls and gates. Despite considerable advances in these technologies, coastal regions are becoming increasingly and alarmingly vulnerable to natural and man-made disasters due to rapid urbanization, subsidence, wetland loss and potential sea level rise. According to a 1998 statistics, the narrow coastal fringe comprising 17% of the contiguous U.S. land area is inhabited by more than 53% of the nation's population. It is estimated that by the year 2020, 80% of the US population will reside within 200 miles of ocean and lake coastlines, which are potentially subjected to flooding caused by hurricanes and other strong storms. Therefore, more measures to mitigate hurricane and storm surge are needed.

It is generally acknowledged that coastal features such as wetlands, coastal ridges, barrier islands, dunes, reefs, and coastal stream floodplain complexes can reduce surges and waves, complementing those aforementioned traditional engineering approaches. However, little is known regarding the necessary scales and arrangements of these features to maximize surge and wave reduction benefits. These features also provide significant ecological and economic benefits. Therefore, tools are needed to assess trade-offs between ecological and storm mitigation benefits in order to support decisions on the best use of limited resources.

Hence, the main objective of Phase I of this research project was to investigate the effectiveness of wetland vegetation in mitigating hurricane and storm surges. The project examined interactions among surge, wave and vegetation through laboratory experiments and field observations, and developed and validated formulas and models to quantify the reduction of surge and waves by vegetation. The project has made significant progress in field measurements, laboratory experiments and computational modeling for the attenuation of waves and surges by vegetation. Considerable effort was devoted to select sites at Terrebonne Bay, LA, where permission was obtained to access a privately-owned wetland suitable for the project. Eight transects were also established at Graveline Bayou in Gautier, MS and the Grand Bay National Estuarine Research Reserve in Pecan, MS. Measurements of the biomechanical properties of *Spartina alterniflora* and *Juncus roemerianus* and the related soil properties at selected marsh sites were also obtained. An array of instruments were developed and deployed, including 9 wave gages and one water level gage, at a fixed location in Terrebonne Bay to measure wave attenuation over shallow water and over salt marshes in hurricane and cold-front active seasons in 2009 and 2010. In addition to the instrument array at the fixed location, five portable, self-recording wave gages were successfully deployed twice in Breton Sound and Terrebonne Bay in rapid response to the tropical storms Ida in 2009 and Bonnie in 2010, even though no hurricanes made landfall on the Mississippi and Louisiana coasts during the project period of 2009-2010. Laboratory experiments were carried out to investigate wave attenuation by rigid and flexible model vegetation as well as live vegetation under monochromatic and random wave conditions in a flat-bottom wave flume. The live vegetation species include *Spartina alterniflora* (dormant and green) and *Juncus roemerianus* (green). Laboratory experiments were also conducted to assess the effect of rigid model vegetation on the wave setup over a sloped beach. Lastly, computational models were developed to quantify the effects of vegetation on waves and surge. The developed models include a 1-D flow models based on Boussinesq equations, a depth-averaged 2-D shallow water flow model, a vertical 2-D model based on Navier-Stokes equations, and a 2-D spectral wave transformation model.

In Phase II of this project, the team continued to build the capabilities required to understand and model the effects of vegetation on surge and waves induced by hurricanes and severe storms, through expanding data collection and analysis, extending field and laboratory experiments and enhancing computational models. The objectives of Phase II regarding the wave and surge reduction by vegetation are:

- Utilize existing and additional instrumentations to conduct field experiments on wave and surge attenuation under winter storm conditions and surge attenuation under tropical storm conditions.
- Compare the characteristics of vegetation and soils between selected Mississippi and Louisiana marshes.

- Expand laboratory experiments on the effects of vegetation on wave setup and runup over a sloped beach using rigid and flexible model vegetation.
- Expand laboratory investigations to assess the wave energy dissipation and water level changes induced by vegetation in a flat-bottom flume under wider ranges of wave and vegetation conditions, such as varying vegetation submergence (ratio of vegetation height to water depth).
- Expand the laboratory and field data sets to investigate and validate the relationship between surge/wave attenuation and vegetation characteristics.
- Enhance computational models and empirical formulas to quantify the effects of vegetation on waves and surge.

Retaining marshland is an important goal with many benefits such as wave attenuation and preservation of ecological services. However, wave action tends to erode marshlands, particularly at the windward edge, where marsh soils are subjected to direct, repeated impact from waves. The rate of erosion at marsh edge is a key parameter for predicting the longevity of marshlands. The soil and plant types, along with wave characteristics, are the controlling variables for the rate-of-retreat at the marsh edge. According to the literature, there have been only two previous laboratory studies on marsh edge erosion (Feagin et al., 2009; Coops et al., 1996), underlining the need for additional work in this important area. Therefore, in Phase II, the team has also expanded laboratory and field experiments and enhance computational models to address erosion of marshland. We established a model marsh edge in the USDA-ARS National Sedimentation Laboratory (NSL) wave flume and set up a field experiment site at Terrebonne Bay, to evaluate the rate of erosion at marsh edge and examine the mechanisms for wave erosion at the edge of marshes.

1.3 Planned Tasks

To build up the capabilities to understand and model the effects of vegetation on surge and waves induced by hurricanes and severe storms, phase II of the project included three interrelated research tasks: laboratory experiments, field investigations, and computational modeling, as further described below.

Task 1: Expand the field measurements and data collection and analysis activities

In Phase II, from April 2011 to August 2012, we utilized existing and additional instrumentations to conduct wave and surge attenuation field experiments under winter storm conditions and surge attenuation field experiments under tropical storm conditions. We conducted vegetation damage test and measured the critical shear stress for marsh soil erosion, and compared the characteristics of vegetation and soils between selected Mississippi and Louisiana marshes. Data sets previously and newly collected were combined and analyzed to establish relationships between wave/surge attenuation and vegetation characteristics. In addition, we conducted field experiments and collect data leading to better understanding and modeling of marsh edge erosion.

Task 2: Extend laboratory experiments to assess the dissipation of wave energy and water level changes induced by vegetation

Laboratory experiments were continued in the wave flume facility at the USDA-ARS National Sedimentation Laboratory (NSL), Oxford, Mississippi to investigate the effects of

vegetation on wave setup and runup over a sloped beach, as well as wave propagation in a flat-bottom flume. The laboratory investigations aimed to assess the dissipation of wave energy induced by vegetation and to validate the relationship between vegetative elements and wave setup/wave energy reduction. The experiments were expanded to cover a wider range of wave properties and vegetation height/water depth ratio. Rigid and flexible model vegetation was used because of model scaling issues. The attenuation of waves was characterized as a function of vegetation type, density and height. In addition, laboratory experiments were conducted to examine the erosion mechanism of marsh edge by waves.

Task 3: Enhance computational models and empirical formulas for surge and wave reduction by vegetation

We continued and expended efforts to compile the data collected through the laboratory and field experiments, develop computational models and empirical formulas to account for surge and wave attenuation due to vegetation, and enhance the developed models to simulate the erosion process at marsh edges by waves and surge.

In addition, to align this research with well-understood homeland security customer requirements and capability gaps, the PI and other team members sought opportunities to participate in relevant communications, meetings, workshops and conferences organized by homeland security components (e.g., FEMA) and other institutions such as ASCE and IAHR, and assisted these agencies in assessing, articulating and pinpointing the requirements and capability gaps that could be addressed by this research.

To confirm and validate the results of this research with key stakeholders, subject matter experts, and/or an advisory group, we worked closely with stakeholders to confirm the value/merits of the results of this research in helping to mitigate the effects of surge and waves caused by hurricanes and severe storms in coastal areas. Phase I report, the present Phase II report, many articles and presentations were developed to describe the key activities, findings and results of this research. We sent the reports and papers to relevant agencies, peers and experts to seek comments and suggestions, and convince stakeholders to use the developed methods and technologies at the federal, state, and/or local levels. As one of the applications, we implemented the vegetation effect modeling approaches in the Coastal Modeling System (CMS) of the US Army Corps of Engineers Research and Development Center (ERDC).

1.4 Project Team Organization

This project was conducted by a multidisciplinary research team consisting of researchers and professors in the fields of Computational Hydroscience and Engineering, Coastal engineering, Geotechnical engineering, Biology and Ecology, and from universities and government agencies. The institutes participating in this project were the National Center for Computational Hydroscience and Engineering (NCCHE) and the Biology Department, The University of Mississippi (UM); the USDA-ARS National Sedimentation Laboratory (NSL), Oxford, MS; and the Department of Civil and Environmental Engineering, Louisiana State University (LSU), Baton Rouge, LA. The research project was led by Dr. Weiming Wu (PI). Corresponding to the three research tasks mentioned above, three teams were established as follows:

Computational modeling team (NCCHE):
Dr. Weiming Wu (PI), Research Associate Professor
Dr. Yan Ding, Research Associate Professor
Mr. Reza Marsooli, PhD student
Ms. Qianru Lin, PhD Strudent
National Center for Computational Hydroscience and Engineering (NCCHE)
The University of Mississippi, MS 38677

Laboratory experiment team (NSL):
Dr. Daniel Wren (Co-PI), Research Hydraulic Engineer
National Sedimentation Laboratory, USDA-ARS, Oxford, MS 38655
Dr. Yavuz Ozeren, Research Scientist
Stationed at NCCHE, The University of Mississippi, MS 38677

Field investigation team (LSU and UM-Biology):
Dr. Qin Chen (Co-PI), Professor
Dr. Guoping Zhang (Co-PI), Associate Professor
Mr. Ranjit Jadhav, Mr. Kyle R. Parker, PhD Students
Mr. Hem Pant, Mr. James Bouanchaud, MS Students
Civil and Environ. Engineering Dept., Louisiana State University, Baton Rouge, LA 70803

Dr. Marjorie Holland (Co-PI), Professor
Miss Ying Chen, MS Student (Graduated in August 2011)
Biology Department, The University of Mississippi, MS 38677

1.5 Research Approaches

The project was conducted through field investigations, laboratory experiments and computational modeling. These three approaches complemented one other, resulting in a much more successful effort than would be possible using only one of these approaches. The field investigations provide understanding and description of surge and wave attenuation under realistic prototype conditions with winter storm and tropical storm seasons. The laboratory experiments provide systematic physical insight into the problem in a well-controlled environment that reliably covers a wider range of wave and vegetation parameters than the field sites. The field investigations and laboratory experiments provided a large number of data sets for developing and validating formulas and models to quantify surge and wave attenuation by vegetation. The numerical analysis, after validation by experimental data, complements the laboratory and field experiments by extending the range of wave conditions and vegetation properties and by providing more comprehensive understanding and description of the phenomena.

The project was carried out across multidisciplinary research fields, including Computational Hydroscience and Engineering, Civil Engineering, Coastal Engineering, Geotechnical Engineering, Biology and Ecology. Even though we have focused more on the hydrodynamic aspect of the problem, we considered the biomechanical properties of vegetation and geotechnical properties of soils, as well as seasonal growth form of vegetation species under study.

1.6 Technology Innovation and Advantages Gained

This research aims to validate the use of coastal vegetation in mitigating hurricane and storm damage. It addresses several high-priority research needs that can support refinement of existing models and development of new models for quantifying the effects of vegetation on surge and wave attenuation and marsh retreat. Field observation and laboratory experiments were conducted in Phase I of the project and expanded in Phase II to include extensive data sets on wave and surge reduction by vegetation at different depths and at different seasons, as well as soil erosion at marsh edges. The vegetation species under study are *Spartina alterniflora* and *Juncus roemerianus*, which are common to the Gulf Coast where hurricanes often hit. Both species are effective in holding wetland soils because their roots and rhizomes are not easily moved by wave action. The flexibility of aboveground plant parts as well as the resilience and resistance of belowground plant parts to wave effects were investigated. The research generated very valuable datasets and developed models, methods and guidance for use by coastal restoration and disaster mitigation organizations and authorities, such as the U.S. Army Corps of Engineers, Federal Emergency Management Agency, National Oceanic and Atmospheric Administration, Mississippi and Louisiana Departments of Natural Resources, and the U.S. Department of Agriculture, as well as the academic community.

The Phase II tasks of of this project expanded the research scope and strengthen the research findings derived from Phase I. The entire project has the following significant contributions and innovations:

(1) Comprehensive understanding and modeling of surge-wave-vegetation-soil interaction were derived through a multidisciplinary approach in this study.
(2) Extensive field data were collected during winter and tropical storm seasons to characterize and quantify the effects of vegetation on storm surge and waves in different seasons, as well as soil erosion at marsh edges;
(3) These effects were further investigated in a laboratory wave flume in a controlled environment under various wave, vegetation and soil conditions;
(4) The data sets collected in the field and laboratory experiments were used to develop and validate empirical formulas and computational models to better quantify the effects of vegetation on storm surge, waves, and marsh retreat;
(5) The datasets published in the literature by other scientists were also used to augment and generalize the research findings;
(6) Comprehensive numerical analyses complemented the extensive field and laboratory experiments; and
(7) The vegetation species studied are common to the Gulf Coast where hurricanes often land, and the knowledge derived is directly useful for coastal hazard mitigation and marsh restoration in the Gulf Coast and also applicable to other U.S. coasts.

1.7 Outline of the Report

This report is organized into eight chapters. Chapter 1 provides a general introduction of this project. Chapter 2 details the laboratory experiments, including the experimental setup, laboratory measurement technologies, data analysis, and results. Chapter 3 describes the

field investigations of surge and wave attenuation, focusing on hydrodynamics. Chapter 4 presents measurements of coastal vegetation and soils at the field sites located on the Louisiana and Mississippi Gulf coasts. The vegetation species studied are *Spartina alterniflora* and *Juncus roemerianus*. Chapter 5 describes the laboratory experiments and field investigations of marsh edge erosion. Chapter 6 describes the computational models for simulating effects of vegetation on surge and waves. The models include a depth-averaged 2-D shallow water model for breaking and non-breaking long waves, and a 3-D shallow water flow model coupled with a wave-action model for wave energy spectra. Chapter 7 presents the computational models developed for simulating rapidly-varying transient flow and sediment transport, which can be used for marsh edge erosion modeling. A depth-averaged 2-D model and a full 3-D RANS (Reynolds-averaged Navier-Stokes equations) model with volume-of-fluid (VOF) surface tracking method are used. Chapter 8 gives conclusions. Finally, references are listed, and three appendices are included to tabulate the field data sets collected by the LSU field investigation team. Appenix A presents wave and topographic data collected during tropical storms and winter cold fronts, Appendix B includes the field data of marsh soil's critical shear stress. Appendix C covers the field data of vegetation damage resistance.

2. LABORATORY EXPERIMENTS OF WAVE ATTENUATION BY VEGETATION

The energy of coastal waves and storm surges are reduced by vegetation cover, which also helps to maintain wetlands through increased sedimentation and deposition. Coastal regions are becoming more vulnerable to natural disasters due to urbanization and wetland loss. Awareness of the value of wetlands for coastal protection has increased in recent years, resulting in more projects aimed at restoring or creating coastal wetlands. This has created a need for research into the properties of waves passing through wetland vegetation. Numerous experiments examining the interaction between vegetation and flowing water have been undertaken (Wu, 2007). Only a few of these studies had the goal of quantifying the effect of marsh vegetation on waves through experiments (Asano et al., 1988; Gambi et al., 1990; Suzuki, 2011). The mechanism of wave attenuation through vegetation is still not fully understood, partly because of the lack of laboratory and field data.

The first phase of the laboratory work included model and live vegetation experiments at emergent and close to emergent conditions and wave setup experiments with rigid model vegetation. The second phase of the experimental study includes the interaction of the regular and irregular waves with submerged vegetation following the same procedures that were used in the first phase of the project. The vegetation elements were scaled down with a scaling ratio of 1:3 in order to have higher submergence (lower relative plant heights, h_v/h) within the limitations of the wave tank. Therefore, only simulated vegetation with artificial stems was tested during the experimental study. Additionally, wave setup experiments with rigid and flexible vegetation models were carried out.

The experiments resulted in new datasets that allow characterization of wave attenuation through artificial vegetation as a function of relative plant height and stiffness. This chapter includes the description of the new experimental configurations, the procedures followed throughout those experiments, and their results.

2.1 Theory

The interaction between vegetation and waves is complex due to the dynamic nature of the forcing and the spatial variation of both the individual and bulk properties of the plants. Natural wetlands contain a random distribution of plants with variable stem diameter and height. Each plant can be considered as rigid or flexible depending on its deformation under loading. Individual plant characteristics vary along the length of the plant and also change with life cycle stages. Nevertheless, the vegetation zone can be characterized by spatially averaged quantities. Here, the live vegetation elements are considered as an array of circular cylinders with a population density of N_v, which is defined as number vegetation elements per unit horizontal area, average diameter D_v and average stem height h_v.

As waves travel through vegetation, they lose energy by doing work on the vegetation. If vegetation is the only source of energy dissipation, conservation of energy requires that the energy dissipation to be equal to the gradient of the average energy flux i.e.:

$$\varepsilon_D = \frac{\partial (E c_g)}{\partial x} \tag{2.1}$$

where E is the wave energy density, ε_D is the average rate of energy dissipation per unit horizontal area (per wave period) due to vegetation, c_g is the group wave velocity, and x is the spatial coordinate in the direction of wave motion. Assuming linear regular waves where energy dissipation is due only to the drag force:

$$\varepsilon_D = \frac{1}{T} \int_t^{t+T} \int_{-h}^{-h+sh} \mathbf{F_D} \cdot \mathbf{u} dz dt \tag{2.2}$$

where T is the wave period, $s = h_v / h$, where and h is the water depth, $\mathbf{F_D} = F_x \mathbf{i} + F_z \mathbf{k}$ is the total drag force per unit volume where F_x is the force component and u is the velocity component in the x-direction, F_z is the force component and w is the velocity component in the z-direction. Here, z is oriented vertically, $\mathbf{u} = u\mathbf{i} + w\mathbf{k}$ is the flow velocity where $\mathbf{i}$ and $\mathbf{k}$ are the unit vectors in x- and z-directions, and t is time.

The vegetation field considered here consists of vertically oriented stems; therefore, $F_z w$ is very small compared to $F_x u$ and is usually neglected (Dalrymple et al., 1984) where $\mathbf{F_D} \times \mathbf{u} = F_x u + F_z w$, resulting in:

$$\varepsilon_D = \frac{1}{T} \int_t^{t+T} \int_{-h}^{-h+sh} F_x u dz dt \tag{2.3}$$

Total force exerted on a vegetation element is the sum of a drag force and an inertia force, as expressed by the Morison equation (Morison et al., 1950). The inertia force is small compared to the drag force and is typically neglected (Dalrymple et al., 1984 and Mendez and Losada, 2004). The total horizontal time varying force per unit volume can be written as:

$$F_x = \frac{1}{2} C_D \rho a u |u| \tag{2.4}$$

where C_D is the bulk drag coefficient, ρ is the water density, and $a = D_v N_v$, is the total frontal plant area per unit volume projected on a plane normal to u, and D_v is the diameter of single cylinder. The drag coefficient for a single cylinder is related to the Reynolds number, while, for an array of cylinders, other factors like population density and the geometrical arrangement of cylinders can strongly influence the turbulence characteristics of the flow (Nepf, 1999). The turbulence structure is highly affected by the sheltering and wake generated by the neighbouring stems over a vegetation field. The bulk drag coefficient, C_D in Eq. (2.4), is a function of the net mean resisting force exerted against the flow by all of the plants in a vegetation field.

Following Dalrymple et al. (1984), Eqs. (2.1), (2.3) and (2.4) can be combined to establish a relationship between wave parameters and vegetation properties assuming that the bed is flat (constant c_g), linear wave theory is valid, quantities are invariant with depth (constrant a), and rigid vegetation (no swaying motion). For these conditions, the wave height evolution can be written as:

$$\frac{H}{H_i} = \frac{1}{1+\alpha x} \tag{2.5}$$

where H_i is the incident wave height, H is the wave height within the vegetation, and a is the damping factor defined as:

$$\alpha = \frac{4}{9\pi} H_i C_D a k \frac{\sinh^3 sh + 3\sinh sh}{\sinh kh(\sin 2kh + 2kh)} \tag{2.6}$$

where $k = 2\pi/L$ is the wave number and L is the wavelength. The same theory can be extended to irregular waves by assuming that the irregular wave train is a superposition of a series of progressive wave components. Following Mendez and Losada (2004), a similar relation can be established for irregular waves:

$$\frac{H_{rms}}{H_{rmsi}} = \frac{1}{1+\tilde{\alpha} x} \tag{2.7}$$

and

$$\tilde{\alpha} = \frac{1}{3\sqrt{\pi}} H_{rmsi} C_D a k_p \frac{\sinh^3 sh + 3\sinh sh}{\sinh k_p h(\sin 2k_p h + 2k_p h)} \tag{2.8}$$

where H_{rmsi} is the root-mean-square (rms) height of the incident waves and H_{rms} is the rms height of waves inside the vegetation, where $k_p = 2p/L_p$ is the wave number, and L_p is the wavelength associated with peak period. The characteristic velocity acting on the plant, u, is defined as the maximum horizontal velocity at the seaward edge of the vegetation at stem height based on linear wave theory at position $x = 0$ and elevation $z = -h(1-s)$:

$$u = \frac{H_i}{2} \omega \frac{\cosh(kah)}{\sinh(kah)} \tag{2.9}$$

For irregular waves, the water particle velocity can be estimated by replacing H_i with H_{rms} and k with k_p in Eq. (2.9).

2.2 Methods and Materials

Experiments were conducted in a 20.6 m long, 0.69 m wide and 1.22 m deep wave flume (tank) at the USDA-ARS National Sedimentation Laboratory in Oxford, Mississippi (Fig. 2.1). One side and the bottom of the flume are constructed with aluminum sheets coated with epoxy-based paint. The other is made of transparent polycarbonate sheets. The piston type wave generator was located 1.2 m from the upwave end of the tank. The bottom of the wave tank was elevated 0.29 m by a plywood false floor to facilitate the placement of model and live vegetation. A ramp with a slope of 1/7 was built in front of the wave generator to provide a gradual transition up to the false floor. A porous, parabolic wave absorber was constructed at the downwave end of the tank to minimize wave reflection. The effective length of the flume from the paddle to the toe of the absorber was 16.9 m. The test section was placed 11.5 m away from the wave generator and was 3.6 m long. For wave setup experiments a plane beach with 1:21 slope was constructed over the existing false floor,

starting 7.2 m away from the wave generator (Figs. 2.2 and 2.3). Additional details of the wave flume facility can be found in the Phase 1 report for this project (Wu et al., 2011).

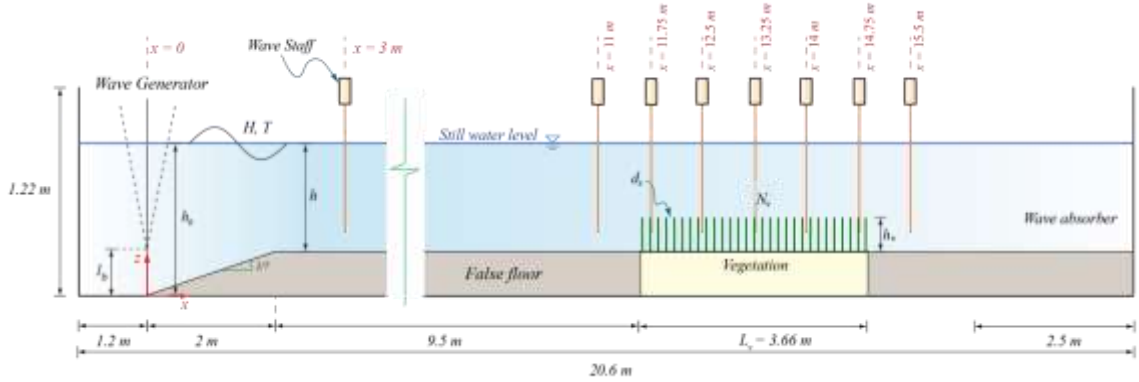

Fig. 2.1. Definition sketch of the wave tank configuration for submerged model vegetation experiments.

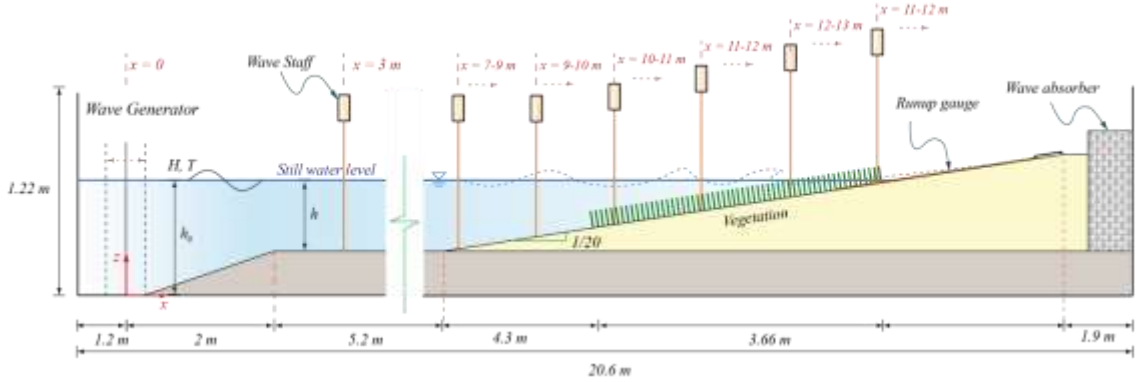

Fig. 2.2. Definition sketch of the wave tank configuration for sloping-beach experiments.

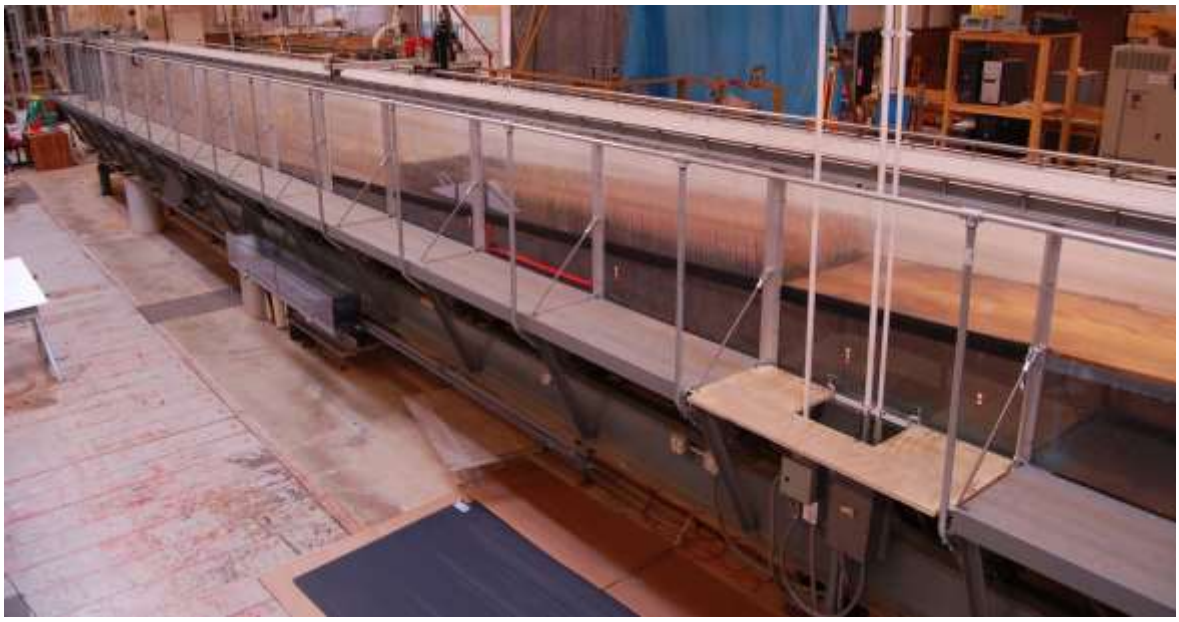

Fig. 2.3. Wave tank with rigid model vegetation over the slopping beach.

2.2.1 Vegetation Models

Two different types of vegetation, rigid and flexible, were used for both submerged and sloping beach experiments in Phase II. The rigid vegetation model was constructed out of 3.1 mm diameter birch dowels. The dowels were cut to 20.3 mm and hammered into the holes of a perforated PVC sheets (Fig. 2.4a).

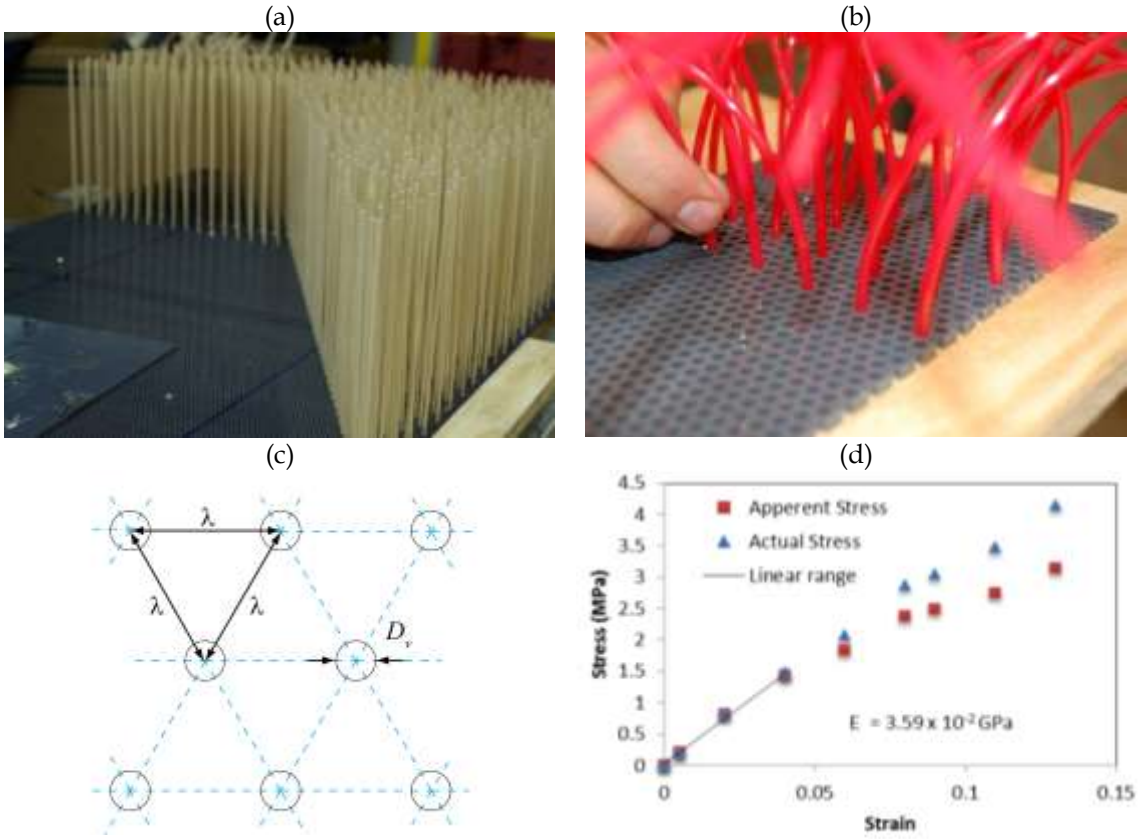

Fig. 2.4. Vegetation models: (a) Rigid and (b) Flexible (c) Stem configuration, where λ is the center-to-center distance between individual stems and D_v is the stem diameter. (d) Stress strain curve of the flexible model vegetation.

The modulus of elasticiy of a *S. alerniflora* is reported to be between 0.01 - 1 GPa in Feagin et. al (2009) and 0.3 GPa in Wu et al. (2011). Polyurethane tubing is the closest match to *S. alterniflora* in terms of elastic properties when the model to prototype ratio is 1:3 (legth scale). Polyurethane tubing was tested at the laboratoy with static loading to measure its elastic properties (Fig. 2.4d). The modulus of elasticity was estimated as 0.04 GPa. The flexible vegetation model was constructed out of 3.1 mm diameter and 20.3 mm long strips of polyurethane tubing. Each strip was glued into the holes of a perforated 3.2 mm thick PVC sheet (Fig. 2.4b). The PVC sheets were attached to the plywood false floor. The top ends of the strips were sealed to increase buoyancy. The staggered arrangement, as shown in Fig. 2.4c, yielded a relationship between the spacing between stems, λ, and the vegetation density:

$$N_v = \frac{2}{\sqrt{3}} \lambda^{-2} \quad (2.10)$$

.

The range of vegetation parameters is shown in Table 2.1. Each experiment is represented by two reference numbers. The wave reference number has eight digits. The first two digits are the water depth in cm, the next three digits are wave height in mm, the sixth and seventh digit are the wave period in 10 x seconds, and last digit is reserved for the repeat index (*hhHHHTT*i). The repeat index appears as one or removed in the following tables and plots since only the averaged values are presented. The values are truncated and leftmost digits are padded with zero when necessary to keep the length of the reference number constant.

Table.2.1. Ranges of vegetation parameters (Mean and standard deviations are given for live vegetation stem height and diameter values)

Ref. #	Vegetation type	Spacing λ (mm)	Density N_v (m^{-2})	Stem height h_v (m)	Stem diameter D_v (mm)	Fractional coverage a = $N_v A_c$
15232001	Rigid model	19.1	3,182	0.20	3.2	0.024
25232001	Flexible model					

2.2.2 Experimental Procedures

Eight capacitance-type wave probes were used to measure water surface displacement. The sampling rate of the wave probes was 30 Hz, and the spatial resolution was 0.24 mm. The probes were calibrated in the wave tank with a point gauge to ensure accurate water level measurements, and the calibrations were checked several times during the study. One of the probes was placed 3 m from the paddle to measure the incident wave height, and the remaining seven were distributed along the test section (Figs. 2.1 and 2.2).

In some of the regular wave experiments, wave heights were measured by a new technique that uses images captured with a consumer grade digital video camera. The camera had a 29.97 Hz frame rate and 1920 x 1080 pixel resolution. It was positioned 6 m away from the wave tank wall, aligned so that the focal plane coincides with the sidewall and leveled relative to the still-water level. The field-of-view was 5.82 m along the wave tank, yielding approximately 3 mm/pixel resolution. Blue dye was added to the water to increase contrast relative to the back wall of the tank. Each video recording began just before the wave generation and continued for 50 seconds. An in-depth discussion of the video frame analysis procedure can be found in Wu et al. (2011).

Wave generation and data collection were controlled by a computer, which enabled automation of multiple experiments. For each vegetation configuration, a range of combinations of wave height, period, and water depth was used. The still water level was measured with a point gauge before each set of experiments and used later for calibration. Regular wave experiments were run for at least 100 wave cycles and each experiment was repeated three times. Control runs without vegetation models were also performed for the same wave properties as used with vegetation. Irregular waves were generated using a set of JONSWAP spectra. Five $100T_p$ long irregular time series signals were generated for each

spectrum, where T_p is the peak wave period. The same time series signals were repeated for each vegetation configuration as well as for the empty flume control runs. A band-pass Butterworth filter was used to remove unwanted frequency components from the wave-height records.

Wave periods were obtained through spectral analysis by using a Fast Fourier Transform (FFT) routine. Peak period, which is the reciprocal of the spectral frequency at the maximum spectral density, was used as the wave period. The wave heights were estimated from the time series signal recorded at each gage by two independent techniques: peak detection and zero-crossing. Peak detection was applied by fitting a quadratic equation to five data points around each peak. The peaks and valleys were found from the zero-points for the first derivative of the fitted equation. Wave height was defined by the difference between two successive peaks and valleys. The zero down-crossing method was used as an alternative method to evaluate the wave heights and wave periods for regular waves. The individual wave heights were defined as the difference between the highest and lowest water surface readings between two zero down-crossing points. Local peak values were discarded in this analysis. Significant wave heights for irregular waves were calculated using spectral analysis.

Regular wave experiments with and without vegetation were repeated three times to minimize uncertainty. The most important sources of uncertainty were reflected waves, mainly from the wave absorber and/or the vegetation models, evanescent waves created during wave generation, and resonance with the longitudinal and lateral seiche period of the wave tank. Evanescent waves decay exponentially as they propagate away from the paddle; hence, their influence is minimal close to the vegetation zone. Resonant seiche periods were avoided during the experiments, and wave reflection was minimized by the wave absorber for a wide range of waves. However, when the wave attenuation through vegetation was low (<5%), reflection became important relative to the amount of dissipation. Higher transmission rates also increased reflected wave height from the absorber. Likewise, for the cases with lower wave transmission, wave reflection through the vegetation created another source of uncertainty that affected the wave height measurements at the first and second gages.

2.3 Results and Discussion

The results are presented in two main sections. The first section presents the summary of the data collected during flat-bed experiments at four different water depths for rigid and flexible vegetation models. The theory summarized in section 2.1 was followed to estimate bulk drag coefficients of the two models. The second section presents the wave height and wave setup data along a sloping beach with rigid and flexible model vegetation.

2.3.1 Submerged Model Vegetation

A typical experiment with submerged rigid and flexible model vegetation at 0.4 m water depth is shown in Fig. 2.5. Blue dye was used to increase the contrast of the free surface for video analysis. For each run with rigid and flexible vegetation, the model defined by Eq. (2.5) for regular and Eq. (2.7) for irregular waves was fitted to the relative wave heights using a nonlinear least squares method and the bulk drag coefficient, C_D , was calculated from Eqs. (2.6) and (2.8). Drag coefficients, C_D are plotted against Reynolds number, Re

and Keulegan-Carpenter number, K_c for regular waves in Figs. 2.6 and 2.7, and irregular waves in Figs. 2.8 and 2.9. Note that the parameter h_v/h in these plots is different than a, since it can be greater than zero. The video data analysis results are also included in these plots when available. Figure 2.10 shows a summary of drag coefficients for the rigid vegetation experiments, and a comparison with data from Phase I. It can be seen that the data collapse along the same line and that the Phase I and Phase II data are well represented by the same regression model as used in the Phase I work. The data are not plotted against Reynolds number, since there was poor collapse of the data. The Keulegan-Carpenter number is a better parameter to use for representing the interaction between waves and vegetation. The list of experiments and the estimated bulk drag coefficients are presented for regular waves in Table 2.2, based on the wave gauge measurements, and Table 2.3 based on video analysis, and Table 2.4 for irregular wave experiments. The models fitted to the data and their confidence intervals are given in Tables 2.5–2.8.

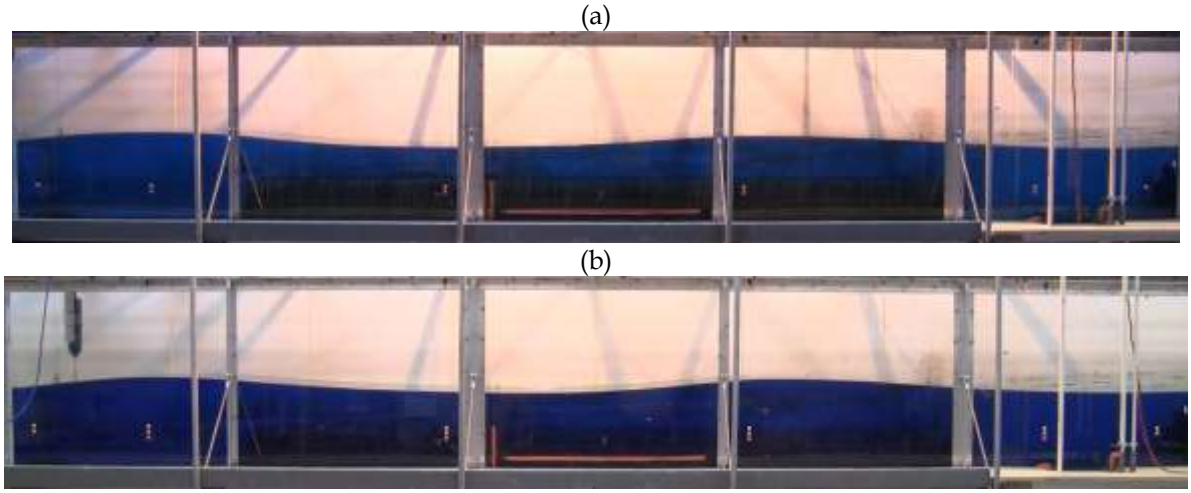

Fig. 2.5. A typical experiment with submerged model vegetation at h = 0.4 m; (a) rigid model and (b) flexible model.

Wave height measurements at eight wave gauges for each flat-bed experiment are presented in Figs. 2.11–2.16. The horizontal axis is normalized by the vegetation span, L_v and vertical axis is normalized by incident wave height (H_i, H_{m0i} if irregular) in these figures. The incident wave heights (H_i or H_{m0}), wave periods (T or T_p), water depths (h), and the estimated drag coefficients are also shown in these plots. Relative regular-wave height distribution along the non-vegetated flat-bed is compared with that of the rigid and flexible vegetation models in Figs. 2.11 and 2.12. Each experiment with a certain H, T, h and vegetation configuration was repeated three times and plotted separately in these figures to show the scale of uncertainty. The uncertainty was higher for smaller wave heights. The wave height distribution estimated by video analysis is compared with the wave gauge measurements for rigid model vegetation in Fig. 2.13 and for flexible model vegetation in Fig. 2.14. The wave gauge data points in these plots correspond to the same experiment recorded with the video camera. The partial standing waves due to reflection from the wave absorber and vegetation models appear as modulations in the wave height profiles and more pronounced for higher wave periods. These standing waves can be clearly seen in Figs. 2.13 and 2.14. The uncertainty introduced by these standing waves was expected to be

low, since for linear waves, incident and reflected wave trains can be separated as the mean and fluctuating component of the wave height distribution. Hence, the fitted lines in these plots are expected to be close to the actual incident wave height profile. When the relative wave heights (H/H_i or H_{m0}/H_{m0i}) in Eqs. (2.5) and (2.7) approach unity, the damping factor (α or $\tilde{\alpha}$) approaches to zero which increases the uncertainty in the estimation of the drag coefficient. In addition, the scattering of the wave heights becomes significant compared to the wave attenuation, which also increases the uncertainty in the drag coefficient estimation.

The relative significant wave height distribution along the non-vegetated flat-bed is compared with that of the rigid and flexible vegetation models in Figs. 2.15 and 2.16. Each irregular wave experiment was repeated for five different random signals with the same spectrum defined by H_{m0}, T_p and the measured data at each gauge were averaged in the spectral domain. The relative significant wave heights in Figs. 2.15 and 2.16 were calculated from the average spectrum.

In general, the correlation was reasonable for both the rigid and flexible models. Video analysis estimates of the bulk drag coefficient (C_D) were consistent with the gauge data estimates. For both types of model vegetation in regular and irregular wave conditions, C_d decreased with increasing Keulegan-Carpenter (K_c) and Reynolds numbers (Re). For larger K_c and Re, C_d approached a constant value. C_d for rigid vegetation is relatively larger then the flexible model vegetation for the larger K_c and Re. There was no apparent dependency of C_d on relative plant height (h_v/h). In general, the relationship with K_c provided a better fit with both of the models used compared to the one with Re.

Table 2.2. Estimated drag coefficients, C_D, from regular wave experiments

Wave ref. No.	H_i (m)	T (s)	L (m)	h (m)	K_C	Re	C_D Rigid model	C_D Flexible model
						Veg. ref. No.	15232001	25232001
						Density - N_v (stems/m^2)	3,182	3,182
						Stem height - h_v (m)	0.2	0.2
						Stem diameter- D_v (mm)	3.2	3.2
200241001	0.0179	1.0	1.212	0.20	22.8	229	2.46	2.32
200270801	0.0232	0.8	0.888	0.20	25.8	325	1.86	2.05
200280601	0.0274	0.6	0.550	0.20	27.7	465	1.80	1.27
200301201	0.0254	1.2	1.523	0.20	37.0	311	1.61	1.53
200320901	0.0250	0.9	1.052	0.20	29.7	333	1.80	1.97
200360701	0.0325	0.7	0.720	0.20	34.2	492	1.99	1.46
200361001	0.0276	1.0	1.212	0.20	35.1	354	2.11	1.75
200371401	0.0247	1.4	1.826	0.20	40.9	295	1.99	1.66
200411101	0.0293	1.1	1.369	0.20	40.0	367	1.70	1.96
200421601	0.0272	1.6	2.123	0.20	50.7	319	1.34	1.16
200440801	0.0393	0.8	0.888	0.20	43.7	551	1.78	1.25
200461201	0.0376	1.2	1.523	0.20	55.0	462	1.67	1.24
200481801	0.0323	1.8	2.416	0.20	67.0	375	1.31	0.93
200530901	0.0439	0.9	1.052	0.20	52.2	585	1.70	1.26
200542001	0.0406	2.0	2.707	0.20	92.6	467	1.49	1.16
200551401	0.0408	1.4	1.826	0.20	67.6	487	1.97	1.36
200602201	0.0415	2.2	2.996	0.20	103.6	475	1.52	1.15
200611001	0.0481	1.0	1.212	0.20	61.3	618	1.71	1.18
200641601	0.0439	1.6	2.123	0.20	81.9	516	1.44	0.98
200662401	0.0392	2.4	3.283	0.20	106.4	447	1.34	0.82
200681101	0.0510	1.1	1.369	0.20	69.6	638	1.65	1.23
200721801	0.0525	1.8	2.416	0.20	108.8	609	1.23	0.86
200761201	0.0635	1.2	1.523	0.20	92.7	779	1.31	0.86
300170601	0.0172	0.6	0.561	0.30	5.6	95	-0.12	0.65
300181201	0.0128	1.2	1.770	0.30	12.6	106	3.65	3.67
300190801	0.0181	0.8	0.961	0.30	10.2	128	2.62	3.55
300200501	0.0195	0.5	0.390	0.30	3.9	78	9.41	9.75
300221401	0.0147	1.4	2.154	0.30	17.3	125	2.01	1.70
300230701	0.0223	0.7	0.755	0.30	10.0	144	2.21	3.98
300230901	0.0202	0.9	1.168	0.30	13.6	152	2.37	3.21
300240551	0.0239	0.6	0.472	0.30	6.3	115	-0.74	-0.29
300251601	0.0207	1.6	2.528	0.30	28.3	178	2.52	1.77
300271001	0.0219	1.0	1.373	0.30	17.0	171	2.26	2.70

Table 2.2. Estimated drag coefficients, C_D, from regular wave experiments

Wave ref. No.	H_i (m)	T (s)	L (m)	h (m)	K_C	Re	C_D Rigid model	C_D Flexible model
300280601	0.0285	0.6	0.561	0.30	9.3	156	-0.45	-0.49
300290801	0.0271	0.8	0.961	0.30	15.2	192	2.77	2.27
300291801	0.0201	1.8	2.895	0.30	31.3	175	1.67	1.35
300310501	0.0208	0.5	0.390	0.30	4.1	83	27.28	19.30
300311101	0.0241	1.1	1.574	0.30	21.2	194	1.85	1.59
300332001	0.0259	2.0	3.257	0.30	45.1	227	2.17	1.59
300350901	0.0301	0.9	1.168	0.30	20.3	227	2.29	2.04
300351201	0.0266	1.2	1.770	0.30	26.1	219	2.24	2.07
300380551	0.0361	0.6	0.472	0.30	9.5	174	3.46	2.89
300380701	0.0376	0.7	0.755	0.30	16.9	243	2.05	1.80
300411001	0.0328	1.0	1.373	0.30	25.5	257	2.47	1.90
300412501	0.0270	2.5	4.150	0.30	59.5	240	1.56	1.08
300431401	0.0310	1.4	2.154	0.30	36.4	262	1.66	1.26
300450601	0.0435	0.6	0.561	0.30	14.2	239	0.44	0.20
300471101	0.0359	1.1	1.574	0.30	31.6	289	2.02	1.45
300480801	0.0460	0.8	0.961	0.30	25.9	326	2.28	1.59
300503001	0.0380	3.0	5.031	0.30	101.3	340	1.90	0.99
300511601	0.0423	1.6	2.528	0.30	57.8	364	2.03	1.30
300531201	0.0407	1.2	1.770	0.30	39.9	335	2.23	1.65
300580901	0.0524	0.9	1.168	0.30	35.2	395	2.09	1.38
300581801	0.0447	1.8	2.895	0.30	69.4	389	1.79	1.19
300600701	0.0591	0.7	0.755	0.30	26.5	382	1.61	0.85
300651401	0.0481	1.4	2.154	0.30	56.4	406	1.69	1.05
300652001	0.0526	2.0	3.257	0.30	91.5	461	1.64	1.06
300691001	0.0580	1.0	1.373	0.30	45.0	454	2.24	1.37
300722201	0.0547	2.2	3.616	0.30	105.4	483	1.85	1.18
300761601	0.0640	1.6	2.528	0.30	87.3	550	1.71	1.02
300770801	0.0720	0.8	0.961	0.30	40.5	511	0.99	0.72
300791101	0.0632	1.1	1.574	0.30	55.5	509	1.88	1.08
300792401	0.0627	2.4	3.973	0.30	132.3	556	1.58	0.95
300871801	0.0723	1.8	2.895	0.30	112.4	629	1.70	1.06
300891201	0.0710	1.2	1.770	0.30	69.4	583	1.86	1.09
300982001	0.0761	2.0	3.257	0.30	132.4	667	1.17	0.56
301081401	0.0839	1.4	2.154	0.30	98.4	709	1.63	0.77
400170601	0.0175	0.6	0.562	0.40	1.9	32	4.04	7.37
400191201	0.0152	1.2	1.936	0.40	10.8	91	5.93	3.36
400200801	0.0196	0.8	0.987	0.40	5.9	74	2.92	6.13

Table 2.2. Estimated drag coefficients, C_D, from regular wave experiments

Wave ref. No.	H_i (m)	T (s)	L (m)	h (m)	K_C	Re	C_D Rigid model	C_D Flexible model
400230701	0.0234	0.7	0.763	0.40	4.6	67	0.71	1.07
400240901	0.0230	0.9	1.224	0.40	9.3	105	2.62	4.08
400241401	0.0186	1.4	2.393	0.40	16.7	120	2.90	1.72
400281601	0.0220	1.6	2.836	0.40	23.8	150	2.52	2.07
400291001	0.0261	1.0	1.464	0.40	13.4	135	2.06	2.34
400300801	0.0296	0.8	0.987	0.40	8.9	112	2.78	4.29
400331801	0.0250	1.8	3.269	0.40	31.5	176	2.43	1.79
400341101	0.0268	1.1	1.702	0.40	16.4	150	2.77	2.85
400370901	0.0350	0.9	1.224	0.40	14.2	159	2.64	3.08
400372001	0.0286	2.0	3.695	0.40	40.8	206	2.34	1.80
400380701	0.0388	0.7	0.763	0.40	7.7	111	-0.15	-0.20
400391201	0.0307	1.2	1.936	0.40	21.9	184	2.40	2.10
400441001	0.0395	1.0	1.464	0.40	20.2	204	2.51	2.00
400472501	0.0319	2.5	4.738	0.40	58.7	237	0.98	0.78
400481401	0.0385	1.4	2.393	0.40	34.6	249	1.95	1.31
400490801	0.0490	0.8	0.987	0.40	14.7	186	2.25	1.86
400511101	0.0412	1.1	1.702	0.40	25.3	232	2.49	2.21
400571601	0.0439	1.6	2.836	0.40	47.4	299	1.74	1.31
400581001	0.0523	1.0	1.464	0.40	26.7	269	2.48	1.74
400581201	0.0472	1.2	1.936	0.40	33.6	282	2.36	1.72
400583001	0.0439	3.0	5.764	0.40	98.8	332	1.43	0.83
400610901	0.0580	0.9	1.224	0.40	23.6	264	2.30	1.91
400651801	0.0541	1.8	3.269	0.40	67.9	380	1.99	1.44
400721401	0.0596	1.4	2.393	0.40	53.6	386	1.81	1.29
400731001	0.0666	1.0	1.464	0.40	34.1	343	2.22	1.62
400742001	0.0568	2.0	3.695	0.40	81.1	409	1.62	1.22
400822201	0.0595	2.2	4.115	0.40	95.0	435	1.30	0.86
400851101	0.0718	1.1	1.702	0.40	44.0	404	1.96	1.53
400851601	0.0643	1.6	2.836	0.40	69.5	438	1.40	0.96
400912401	0.0772	2.4	4.531	0.40	135.9	571	1.84	1.46
400971201	0.0817	1.2	1.936	0.40	58.2	489	1.90	1.21
400981801	0.0841	1.8	3.269	0.40	105.6	591	1.66	1.15
401112001	0.0852	2.0	3.695	0.40	121.6	613	1.30	0.91
401201401	0.1028	1.4	2.393	0.40	92.6	666	1.70	0.95
500170601	0.0178	0.6	0.562	0.50	0.6	11	82.96	209.98
500200801	0.0201	0.8	0.996	0.50	3.2	41	-0.34	1.32
500201201	0.0149	1.2	2.048	0.50	8.0	67	3.87	-0.08

Table 2.2. Estimated drag coefficients, C_D, from regular wave experiments

Wave ref. No.	H_i (m)	T (s)	L (m)	h (m)	K_C	Re	C_D Rigid model	C_D Flexible model
500230701	0.0236	0.7	0.765	0.50	2.1	30	11.13	10.57
500250901	0.0250	0.9	1.248	0.50	6.2	70	0.81	3.33
500261401	0.0214	1.4	2.571	0.50	15.3	110	2.29	2.14
500300801	0.0303	0.8	0.996	0.50	4.9	62	0.68	0.90
500301001	0.0278	1.0	1.513	0.50	9.6	96	2.31	4.63
500311601	0.0242	1.6	3.078	0.50	21.5	136	2.51	2.18
500361801	0.0286	1.8	3.572	0.50	30.1	169	2.74	2.39
500370901	0.0376	0.9	1.248	0.50	9.4	105	1.77	2.30
500380701	0.0391	0.7	0.765	0.50	3.4	49	0.95	1.42
500411201	0.0312	1.2	2.048	0.50	16.7	140	1.74	1.68
500412001	0.0311	2.0	4.056	0.50	37.8	190	2.02	1.95
500451001	0.0423	1.0	1.513	0.50	14.6	147	3.29	4.01
500500801	0.0505	0.8	0.996	0.50	8.1	103	2.06	1.56
500511401	0.0430	1.4	2.571	0.50	30.8	222	1.75	2.01
500522501	0.0434	2.5	5.238	0.50	69.5	280	2.94	2.20
500611201	0.0487	1.2	2.048	0.50	26.1	219	2.03	1.46
500620901	0.0615	0.9	1.248	0.50	15.3	172	1.13	0.99
500621601	0.0492	1.6	3.078	0.50	43.7	276	1.81	1.64
500643001	0.0460	3.0	6.395	0.50	90.8	305	1.34	0.89
500711801	0.0599	1.8	3.572	0.50	63.2	354	2.34	1.78
500761001	0.0709	1.0	1.513	0.50	24.4	246	3.16	2.66
500771401	0.0669	1.4	2.571	0.50	47.9	345	1.86	1.52
500812001	0.0677	2.0	4.056	0.50	82.2	414	2.00	1.57
500891101	0.0786	1.1	1.781	0.50	34.6	317	2.31	1.88
500912201	0.0783	2.2	4.533	0.50	107.4	492	1.87	1.48
500921601	0.0761	1.6	3.078	0.50	67.7	426	1.88	1.51
501002401	0.0811	2.4	5.004	0.50	123.6	519	2.06	1.24
501021201	0.0857	1.2	2.048	0.50	45.8	385	2.24	1.55
501071801	0.0906	1.8	3.572	0.50	95.6	535	1.94	1.22
501222001	0.1009	2.0	4.056	0.50	122.5	618	1.56	1.03

Table 2.3. Estimated drag coefficients, C_D, from regular wave experiments through video analysis

Wave ref. No.	H_i (m)	T (s)	L (m)	h (m)	K_C	Re	C_D Rigid model	C_D Flexible model
						Veg. ref. No.	15232001	25232001
						Density - N_v (stems/m²)	3,182	3,182
						Stem height - h_v (m)	0.2	0.2
						Stem diameter- D_v (mm)	3.2	3.2
300271001	0.0230	1.0	1.373	0.30	17.9	180	2.50	2.30
300411001	0.0335	1.0	1.373	0.30	26.0	262	2.31	1.90
300412501	0.0336	2.5	4.150	0.30	74.1	299	2.71	1.99
300431401	0.0331	1.4	2.154	0.30	38.9	280	2.27	1.37
300480801	0.0461	0.8	0.961	0.30	26.0	327	2.35	1.55
300503001	0.0420	3.0	5.031	0.30	111.7	375	1.73	1.00
300581801	0.0460	1.8	2.895	0.30	71.4	400	1.85	1.21
300600701	0.0632	0.7	0.755	0.30	28.4	409		1.67
300651401	0.0513	1.4	2.154	0.30	60.2	434	1.87	1.00
300652001	0.0571	2.0	3.257	0.30	99.3	501	1.26	0.63
300691001	0.0603	1.0	1.373	0.30	46.8	472	1.96	1.30
300770801	0.0785	0.8	0.961	0.30	44.2	557	2.28	1.22
300792401	0.0723	2.4	3.973	0.30	152.6	641	1.66	1.22
300871801	0.0747	1.8	2.895	0.30	116.1	650	1.50	1.02
300982001	0.0852	2.0	3.257	0.30	148.2	747		0.41
301081401	0.0935	1.4	2.154	0.30	109.7	790	1.68	0.76
400291001	0.0256	1.0	1.464	0.40	13.1	132	3.89	4.02
400372001	0.0274	2.0	3.695	0.40	39.2	197		0.86
400441001	0.0382	1.0	1.464	0.40	19.5	197	2.56	2.43
400472501	0.0373	2.5	4.738	0.40	68.8	277	2.32	1.20
400481401	0.0388	1.4	2.393	0.40	34.9	251	2.25	1.73
400490801	0.0493	0.8	0.987	0.40	14.8	187	2.40	3.22
400583001	0.0517	3.0	5.764	0.40	116.4	391	1.89	1.70
400651801	0.0540	1.8	3.269	0.40	67.8	380	1.95	0.94
400721401	0.0642	1.4	2.393	0.40	57.8	416	2.19	1.34
400731001	0.0639	1.0	1.464	0.40	32.7	329	2.06	1.58
400742001	0.0554	2.0	3.695	0.40	79.1	399	1.15	0.54
400912401	0.0749	2.4	4.531	0.40	131.9	554	1.75	1.15
400981801	0.0828	1.8	3.269	0.40	104.0	582	1.33	0.81
401112001	0.0887	2.0	3.695	0.40	126.6	638	1.11	0.71
401201401	0.1030	1.4	2.393	0.40	92.8	668	1.66	0.83
500301001	0.0302	1.0	1.513	0.50	10.4	105	9.16	5.37
500412001	0.0313	2.0	4.056	0.50	38.0	192	2.98	2.63

Table 2.3. Estimated drag coefficients, C_D, from regular wave experiments through video analysis

Wave ref. No.	H_i (m)	T (s)	L (m)	h (m)	K_C	Re	C_D Rigid model	C_D Flexible model
500451001	0.0420	1.0	1.513	0.50	14.5	146	0.04	1.70
500500801	0.0572	0.8	0.996	0.50	9.2	116	12.01	18.74
500511401	0.0436	1.4	2.571	0.50	31.2	225	0.88	0.76
500522501	0.0394	2.5	5.238	0.50	63.1	254	1.87	1.80
500643001	0.0496	3.0	6.395	0.50	97.8	329	1.55	1.49
500711801	0.0562	1.8	3.572	0.50	59.3	332	1.13	1.04
500761001	0.0725	1.0	1.513	0.50	25.0	252	2.62	2.57
500771401	0.0675	1.4	2.571	0.50	48.4	348	1.75	1.23
500812001	0.0688	2.0	4.056	0.50	83.6	421	1.85	1.54
501002401	0.0756	2.4	5.004	0.50	115.2	484	1.17	0.77
501021201	0.0861	1.2	2.048	0.50	46.1	387	1.85	1.45
501071801	0.0863	1.8	3.572	0.50	90.9	509	0.97	0.46
501222001	0.1077	2.0	4.056	0.50	130.8	659	1.68	1.15

Table 2.4. Estimated drag coefficients, C_D, from irregular wave experiments

Wave ref. No.	H_{m0} (m)	T_p (s)	L_p (m)	h (m)	K_C	Re	C_D Rigid model	C_D Flexible model
						Veg. ref. No.	15232001	25232001
						Density - N_v (stems/m²)	3,182	3,182
						Stem height - h_v (m)	0.2	0.2
						Stem diameter- D_v (mm)	3.2	3.2
20024100	0.0138	1.0	1.212	0.20	17.6	177	2.19	1.99
20027080	0.0177	0.8	0.888	0.20	19.7	248	2.15	1.89
20030120	0.0164	1.2	1.523	0.20	23.9	201	2.20	1.86
20036100	0.0212	1.0	1.212	0.20	27.0	272	1.94	1.66
20037140	0.0191	1.4	1.826	0.20	31.7	229	1.88	1.47
20046120	0.0245	1.2	1.523	0.20	35.8	301	1.58	1.40
20054200	0.0301	2.0	2.707	0.20	68.7	346	1.28	1.11
20055140	0.0274	1.4	1.826	0.20	45.5	328	1.61	1.30
20072180	0.0364	1.8	2.416	0.20	75.4	422	1.42	1.03
20081200	0.0421	2.0	2.707	0.20	96.1	484	1.24	0.91
30014100	0.0090	1.0	1.373	0.30	7.0	70	2.12	2.52
30018120	0.0108	1.2	1.770	0.30	10.5	88	1.98	2.08
30019080	0.0146	0.8	0.961	0.30	8.2	103	2.76	3.65
30022140	0.0123	1.4	2.154	0.30	14.4	104	1.91	1.82
30023070	0.0193	0.7	0.755	0.30	8.7	125	2.40	3.79
30027100	0.0179	1.0	1.373	0.30	13.9	140	1.61	1.69
30029080	0.0218	0.8	0.961	0.30	12.3	155	1.17	2.30
30029180	0.0157	1.8	2.895	0.30	24.4	136	2.07	1.68
30033200	0.0168	2.0	3.257	0.30	29.3	148	1.80	1.33
30035120	0.0201	1.2	1.770	0.30	19.7	165	1.06	1.60
30041100	0.0262	1.0	1.373	0.30	20.3	205	1.45	1.45
30043140	0.0238	1.4	2.154	0.30	27.9	201	1.78	1.45
30053120	0.0303	1.2	1.770	0.30	29.7	249	1.69	1.22
30058180	0.0305	1.8	2.895	0.30	47.4	265	1.87	1.34
30065140	0.0356	1.4	2.154	0.30	41.8	301	1.77	1.22
30065200	0.0346	2.0	3.257	0.30	60.2	304	1.49	1.08
30087180	0.0459	1.8	2.895	0.30	71.4	400	1.54	0.97
30098200	0.0526	2.0	3.257	0.30	91.6	462	1.51	0.93
40019120	0.0119	1.2	1.936	0.40	8.5	71	2.15	1.42
40020080	0.0174	0.8	0.987	0.40	5.2	66	10.81	8.19
40023070	0.0214	0.7	0.763	0.40	4.2	61	16.52	19.01
40024140	0.0141	1.4	2.393	0.40	12.7	92	1.99	1.78
40029100	0.0214	1.0	1.464	0.40	10.9	110	2.77	2.42

Table 2.4. Estimated drag coefficients, C_D, from irregular wave experiments

Wave ref. No.	H_{m0} (m)	T_p (s)	L_p (m)	h (m)	K_C	Re	C_D Rigid model	C_D Flexible model
40030080	0.0245	0.8	0.987	0.40	7.4	93	-19.98	5.30
40033180	0.0177	1.8	3.269	0.40	22.3	125	2.16	1.76
40037200	0.0206	2.0	3.695	0.40	29.3	148	2.34	2.07
40039120	0.0238	1.2	1.936	0.40	16.9	142	2.34	1.93
40044100	0.0319	1.0	1.464	0.40	16.3	164	0.68	1.83
40048140	0.0288	1.4	2.393	0.40	25.9	186	1.99	1.50
40058120	0.0387	1.2	1.936	0.40	27.6	232	1.94	2.06
40065180	0.0377	1.8	3.269	0.40	47.4	265	1.87	1.45
40072140	0.0457	1.4	2.393	0.40	41.2	296	1.30	1.55
40074200	0.0441	2.0	3.695	0.40	62.9	317	2.14	1.71
40098180	0.0595	1.8	3.269	0.40	74.8	419	1.06	1.47
40111200	0.0661	2.0	3.695	0.40	94.3	475	1.32	1.37
50020080	0.0200	0.8	0.996	0.50	3.2	41	74.51	60.41
50020120	0.0139	1.2	2.048	0.50	7.5	63	9.17	8.54
50026140	0.0157	1.4	2.571	0.50	11.3	81	7.95	8.21
50030100	0.0242	1.0	1.513	0.50	8.3	84	6.92	4.78
50036180	0.0193	1.8	3.572	0.50	20.3	114	4.96	0.50
50041120	0.0261	1.2	2.048	0.50	13.9	117	2.83	1.89
50041200	0.0224	2.0	4.056	0.50	27.2	137	3.96	1.95
50051140	0.0318	1.4	2.571	0.50	22.8	164	2.44	1.80
50061120	0.0411	1.2	2.048	0.50	22.0	185	2.22	1.34
50071180	0.0405	1.8	3.572	0.50	42.7	239	2.04	1.40
50077140	0.0488	1.4	2.571	0.50	35.0	252	2.11	1.34
50081200	0.0450	2.0	4.056	0.50	54.7	276	2.18	1.29
50107180	0.0613	1.8	3.572	0.50	64.7	362	1.54	1.15
50122200	0.0665	2.0	4.056	0.50	80.8	407	1.63	1.27

Table 2.5. Parameters and estimated drag coefficients from the regular wave experiments for the model $C_D = a + \left(b/K_c\right)^c$

Ref. No.	Vegetation Type	*a*	*b*	*c*	R^2
15232001	Rigid model	1.26	19.8	1.26	0.88
25232001	Flexible model	0.840	21.0	1.26	0.62

Table 2.6. Parameters and estimated drag coefficients from the irregular wave experiments for the model $C_D = a + \left(b/K_c\right)^c$

Ref. No.	Vegetation Type	*a*	*b*	*c*	R^2
15232001	Rigid model	1.33	14.3	2.61	0.91
25232001	Flexible model	1.14	14.3	2.68	0.94

Table 2.7. Parameters and estimated drag coefficients from the regular wave experiments for the model $C_D = a' + \left(b'/\mathrm{Re}\right)^{c'}$

Ref. No.	Vegetation Type	a'	b'	c'	R^2
15232001	Rigid model	1.26	171	1.62	0.87
25232001	Flexible model	0.840	189	1.78	0.94

Table 2.8. Parameters and estimated drag coefficients from the irregular wave experiments for the model $C_D = a' + \left(b'/\mathrm{Re}\right)^{c'}$

Ref. No.	Vegetation Type	a'	b'	c'	R^2
15232001	Rigid model	1.47	115	2.94	0.49
25232001	Flexible model	1.26	115	2.94	0.57

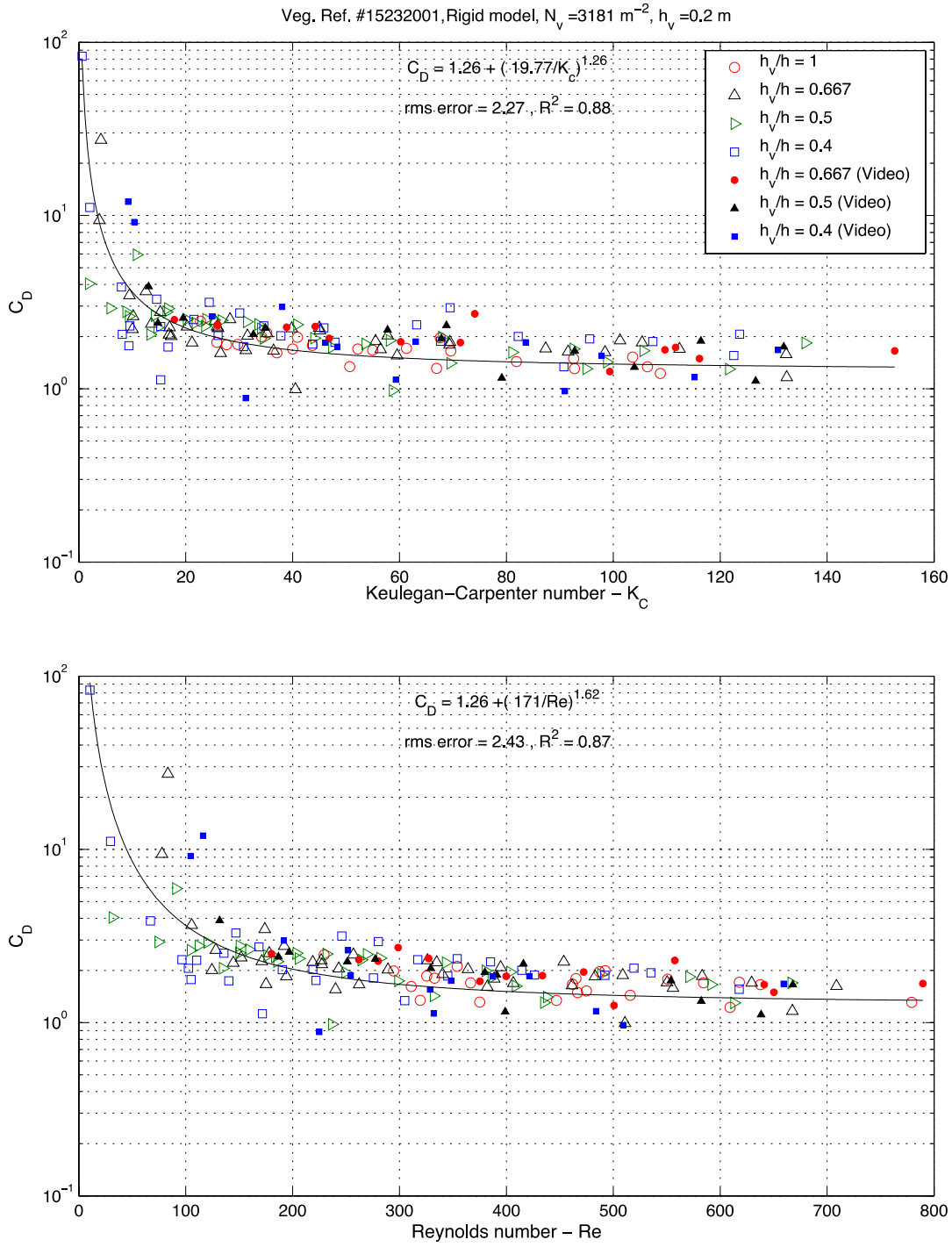

Fig. 2.6. Drag coefficients for rigid model vegetation (regular waves).

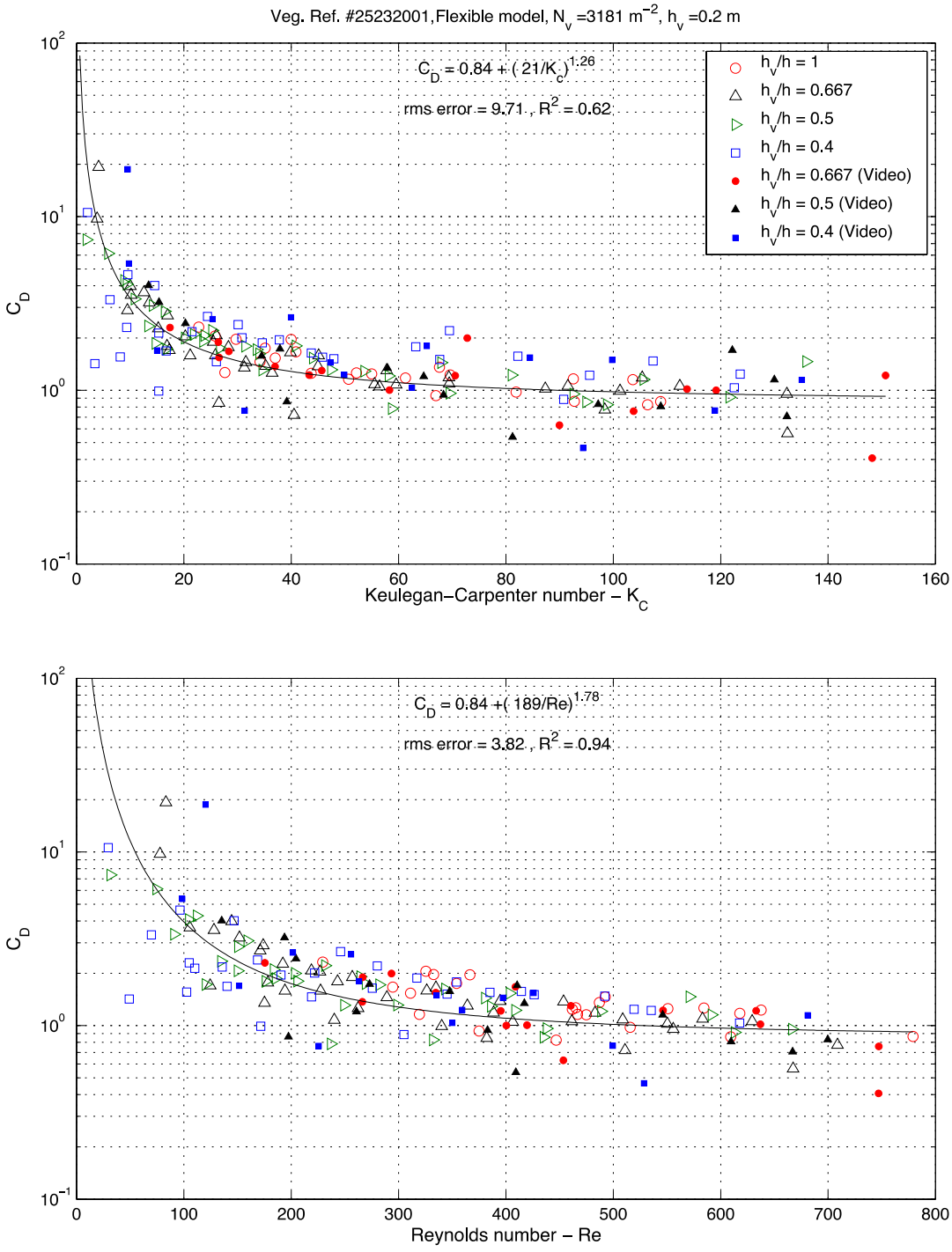

Fig. 2.7. Drag coefficients for flexible model vegetation (regular waves).

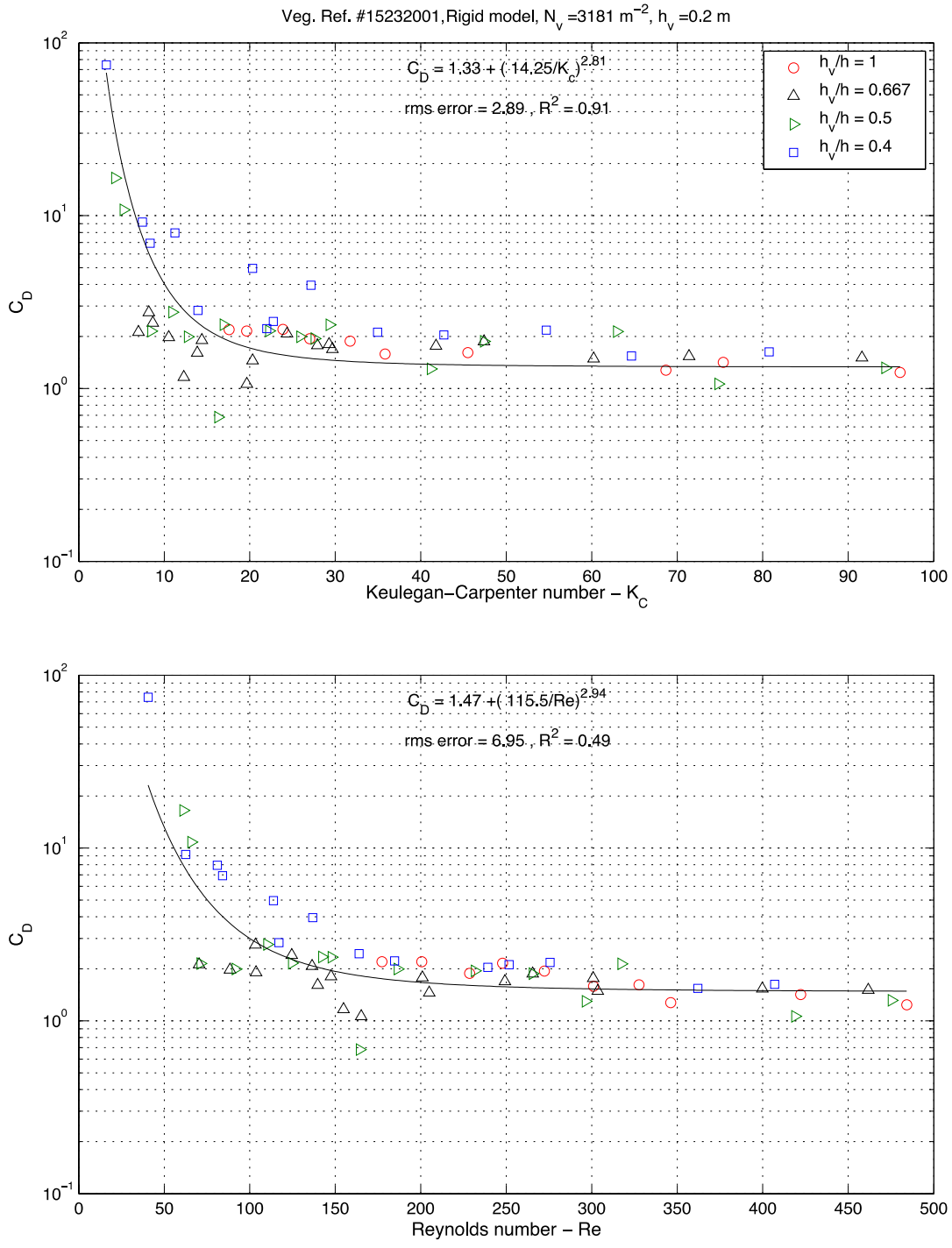

Fig. 2.8. Drag coefficients for rigid model vegetation (irregular waves).

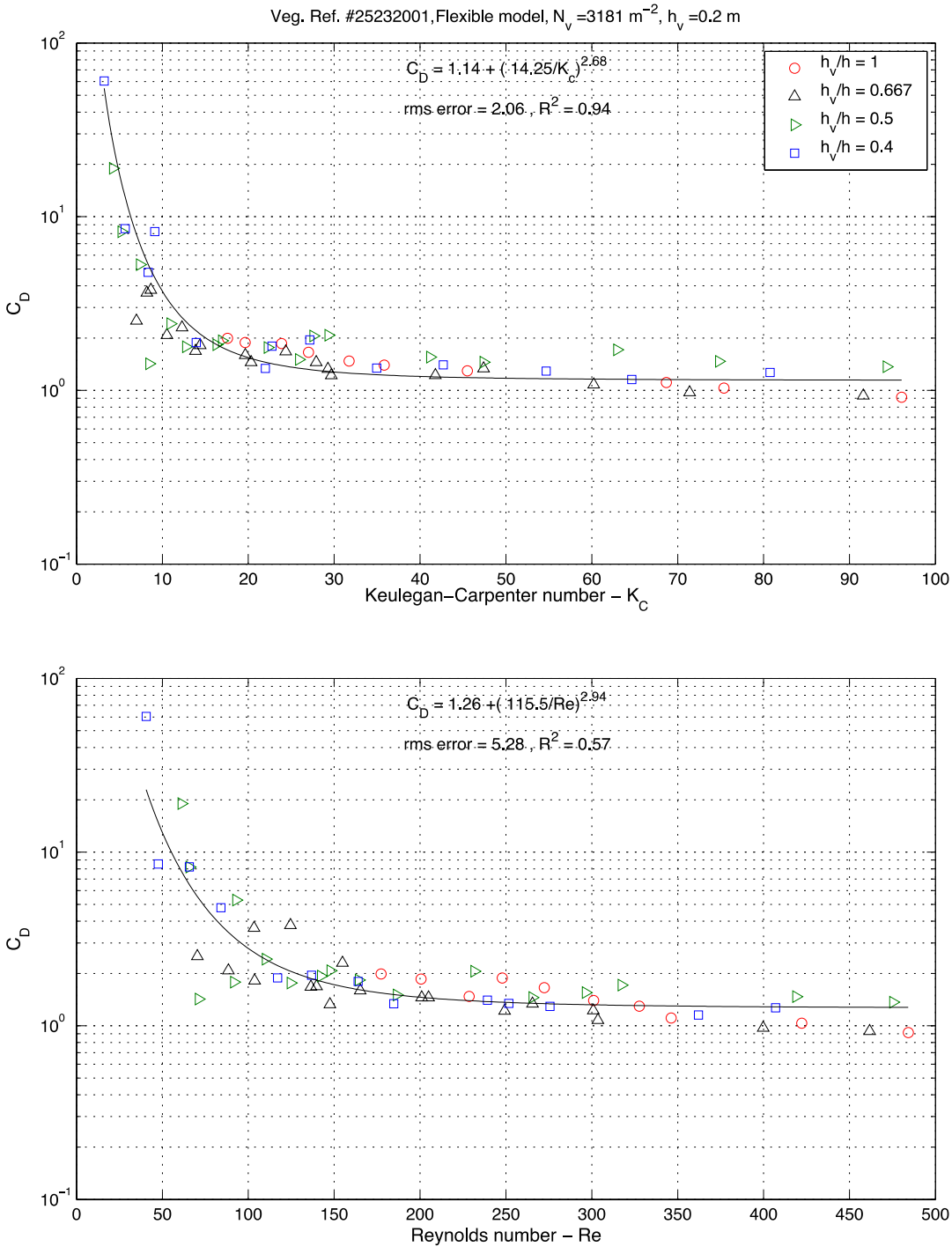

Fig. 2.9. Drag coefficients for flexible model vegetation (irregular waves).

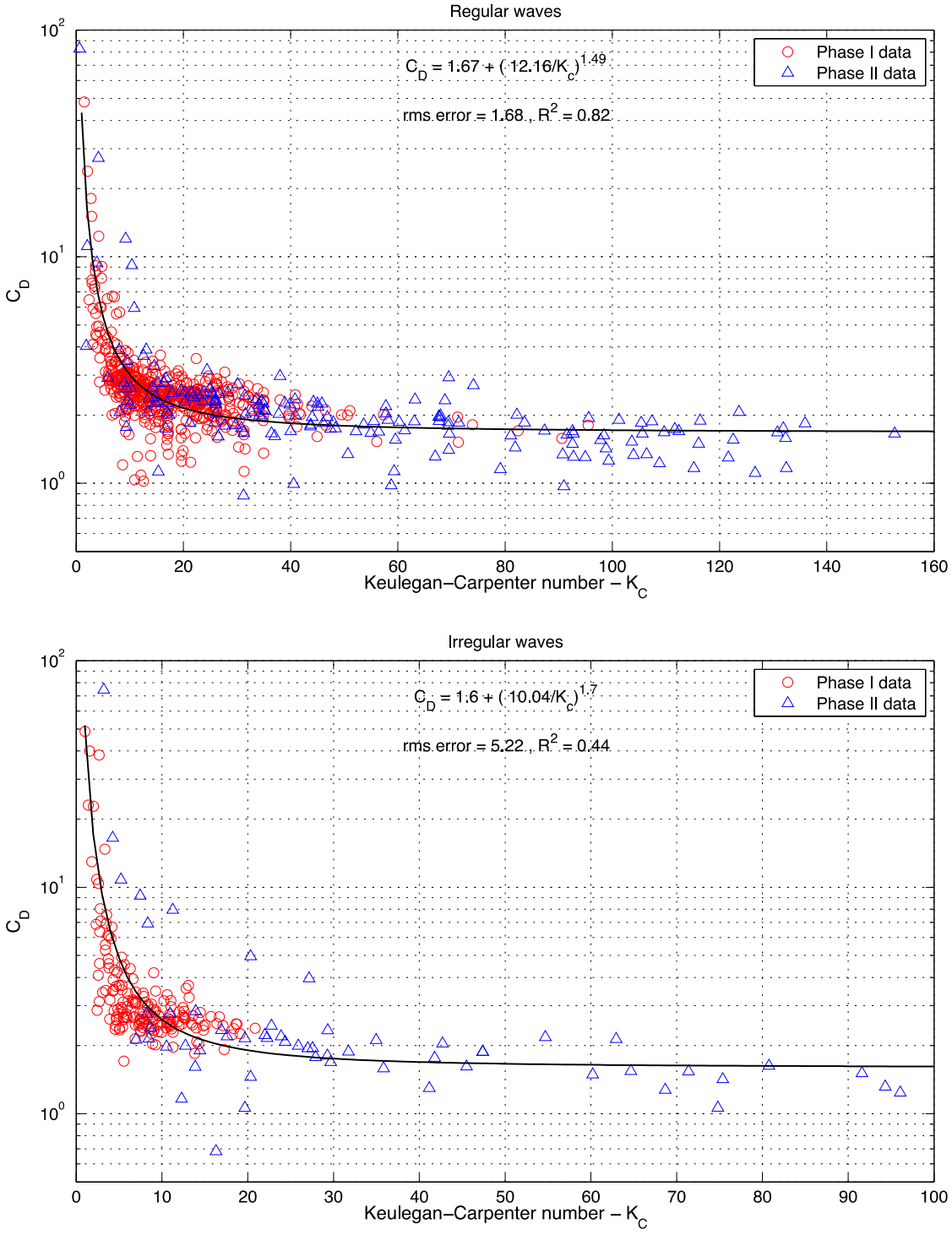

Fig. 2.10. Summary of drag coefficients for rigid vegetation.

Rigid model vegetation – regular waves

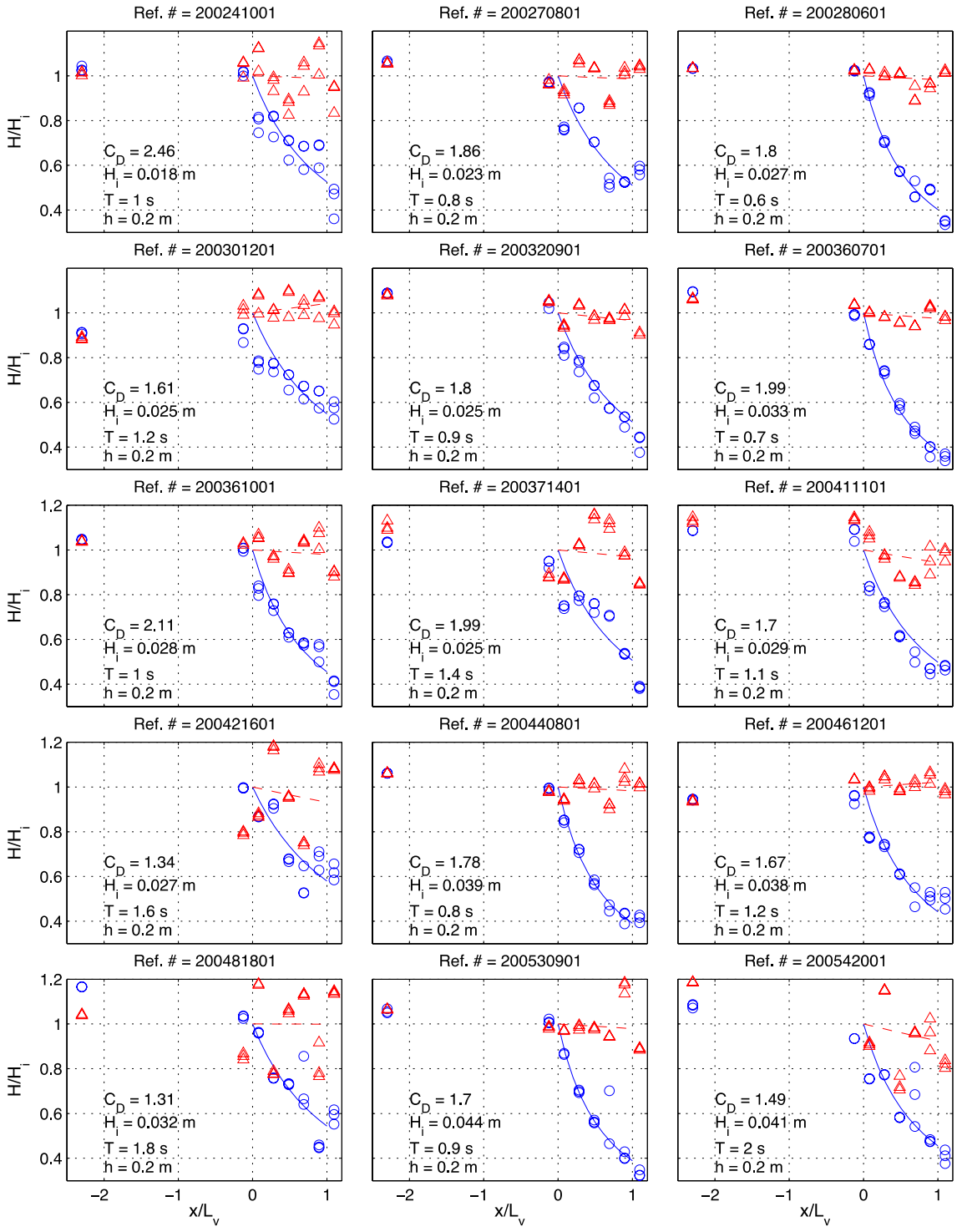

Fig. 2.11. Relative wave height distribution of regular waves along the wave tank for non-vegetated and rigid model vegetation.

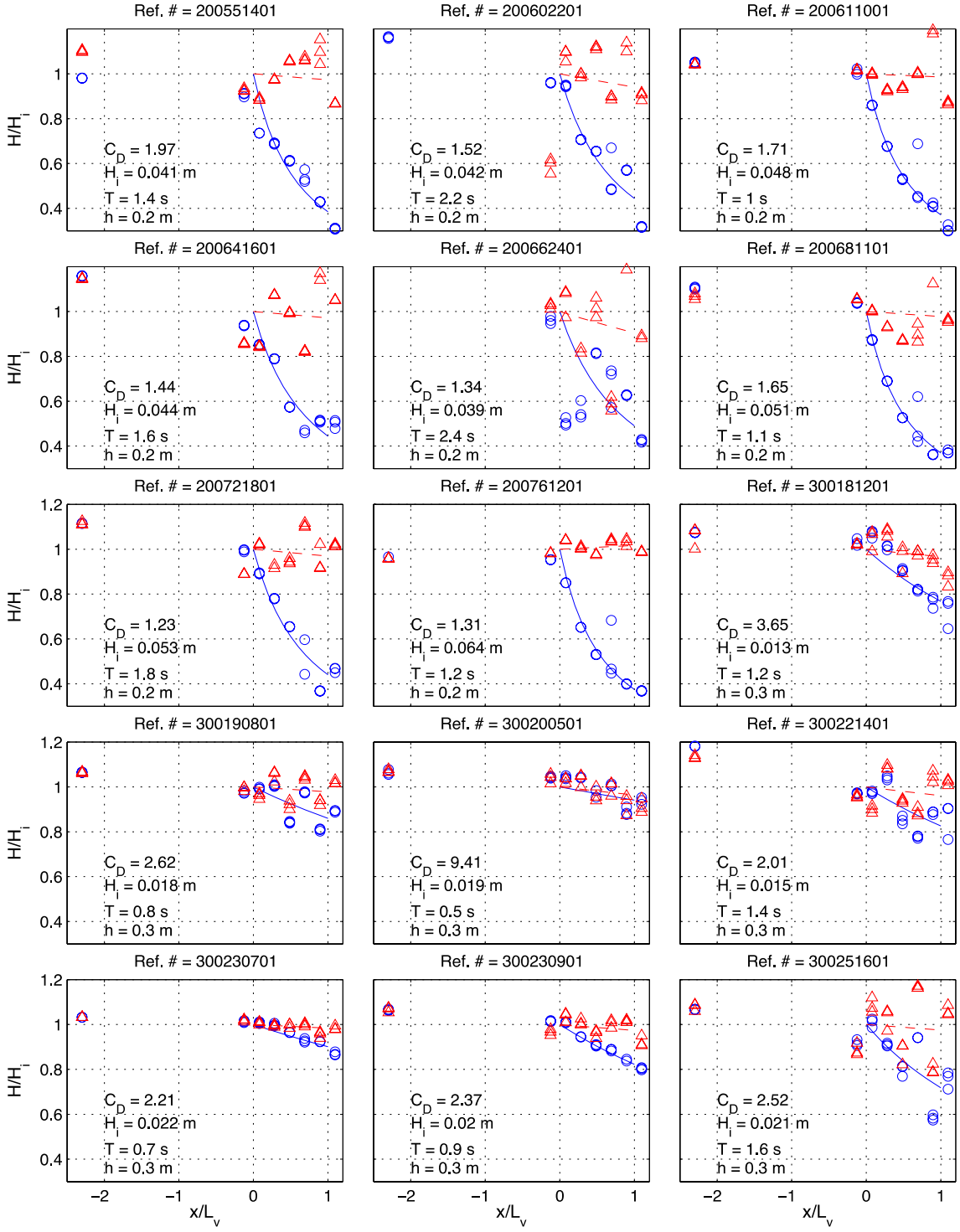

Fig. 2.11. Relative wave height distribution of regular waves along the wave tank for non-vegetated and rigid model vegetation (continued)

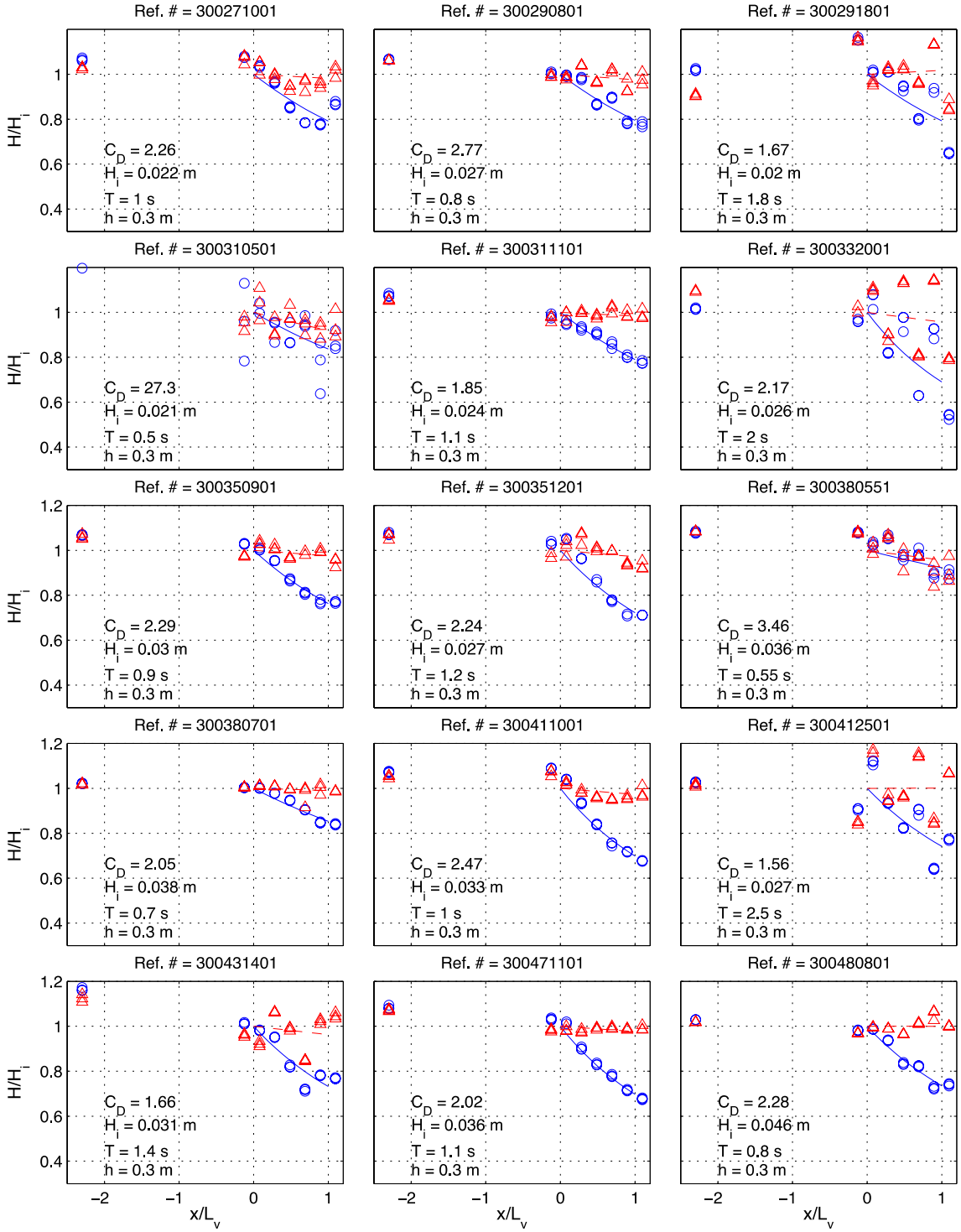

Fig. 2.11. Relative wave height distribution of regular waves along the wave tank for non-vegetated and rigid model vegetation (continued).

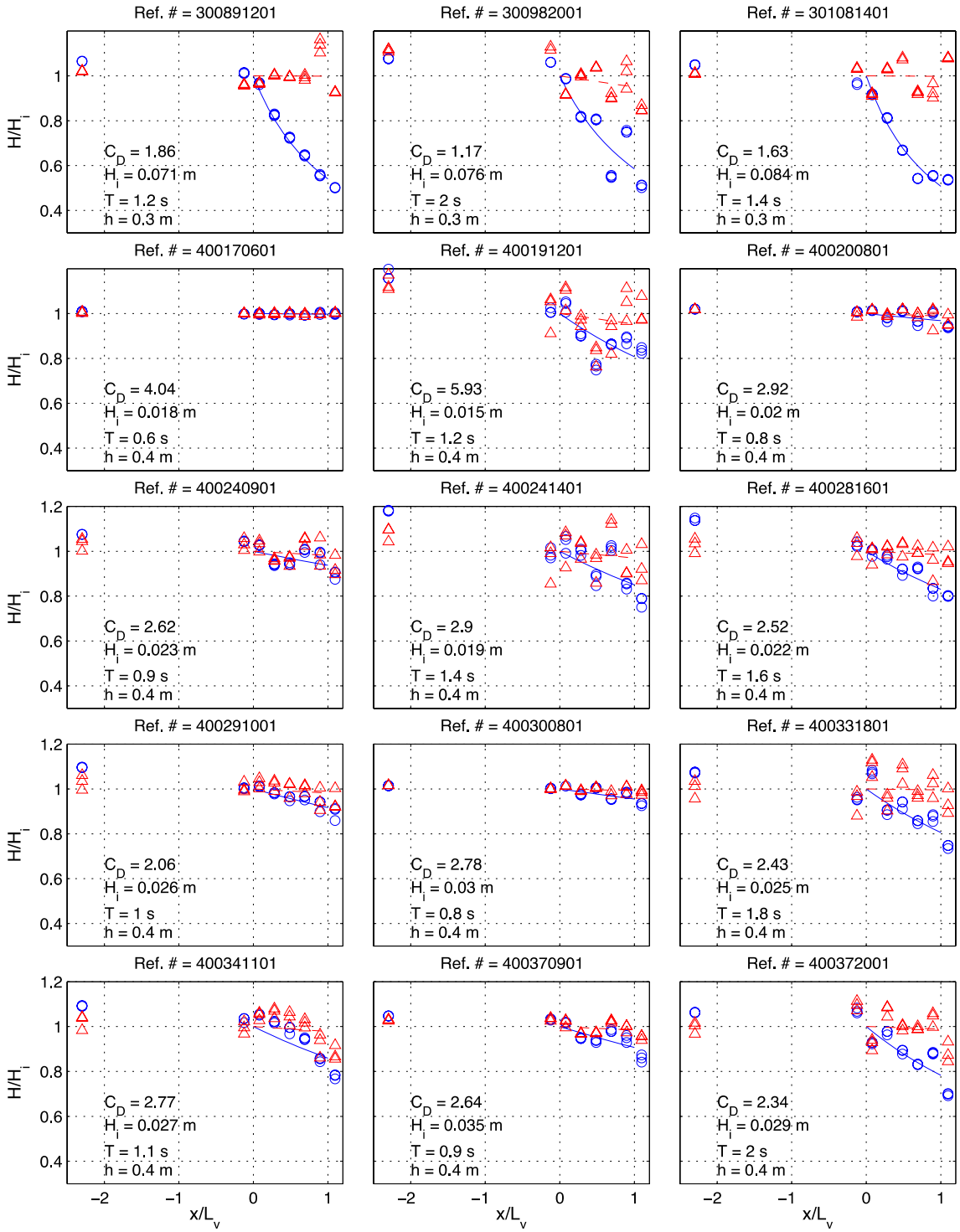

Fig. 2.11. Relative wave height distribution of regular waves along the wave tank for non-vegetated and rigid model vegetation (continued).

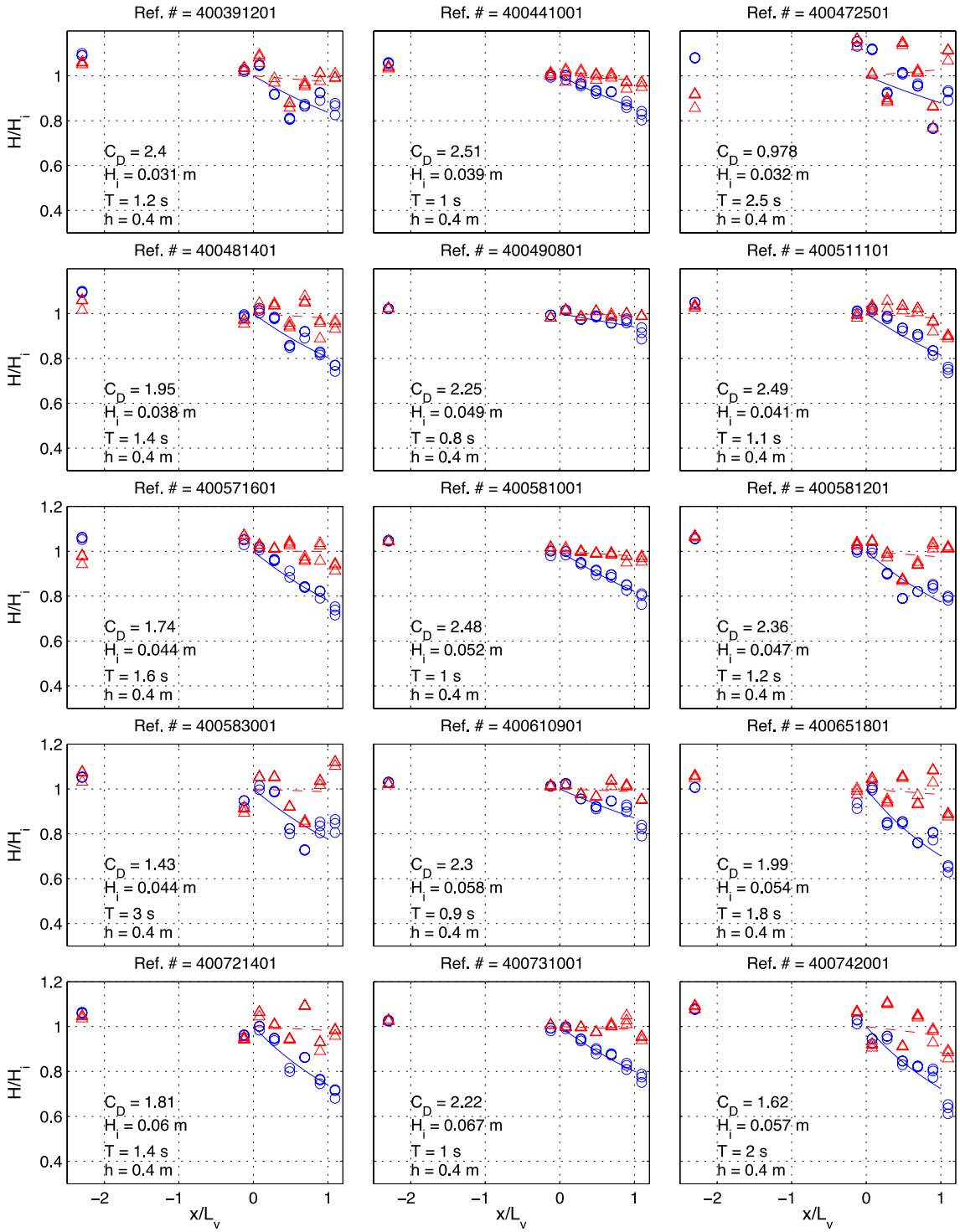

Fig. 2.11. Relative wave height distribution of regular waves along the wave tank for non-vegetated and rigid model vegetation (continued).

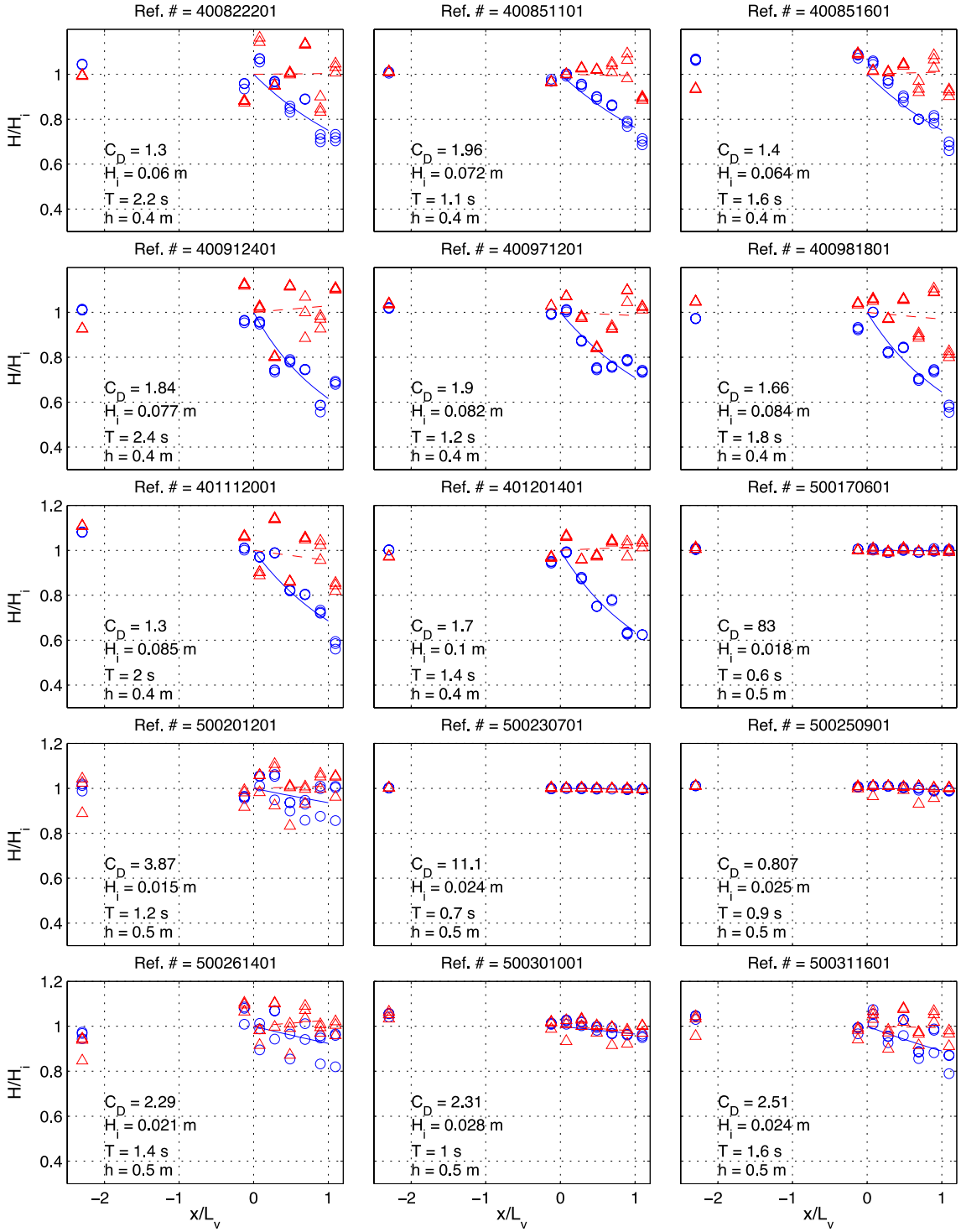

Fig. 2.11. Relative wave height distribution of regular waves along the wave tank for non-vegetated and rigid model vegetation (continued).

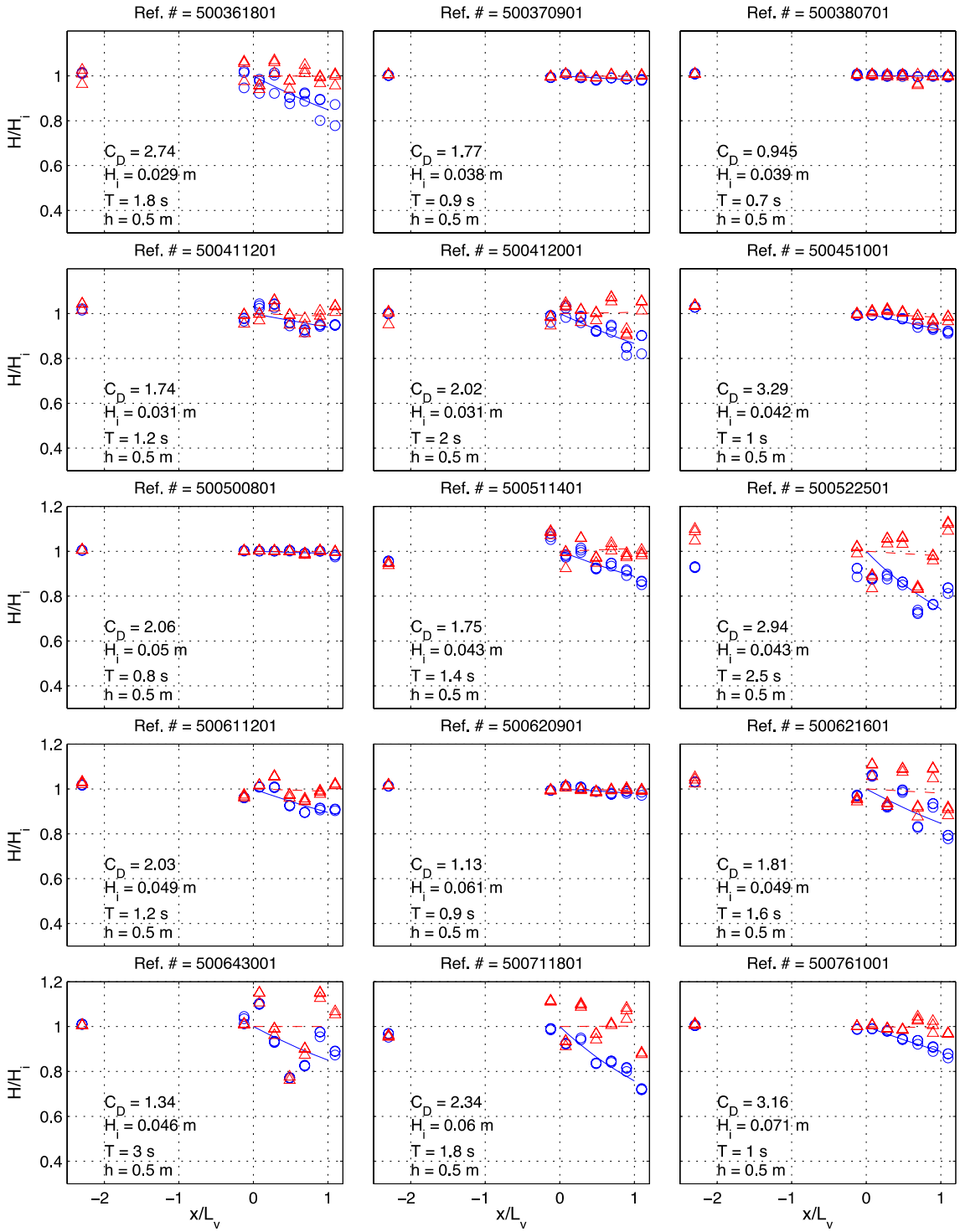

Fig. 2.11. Relative wave height distribution of regular waves along the wave tank for non-vegetated and rigid model vegetation (continued).

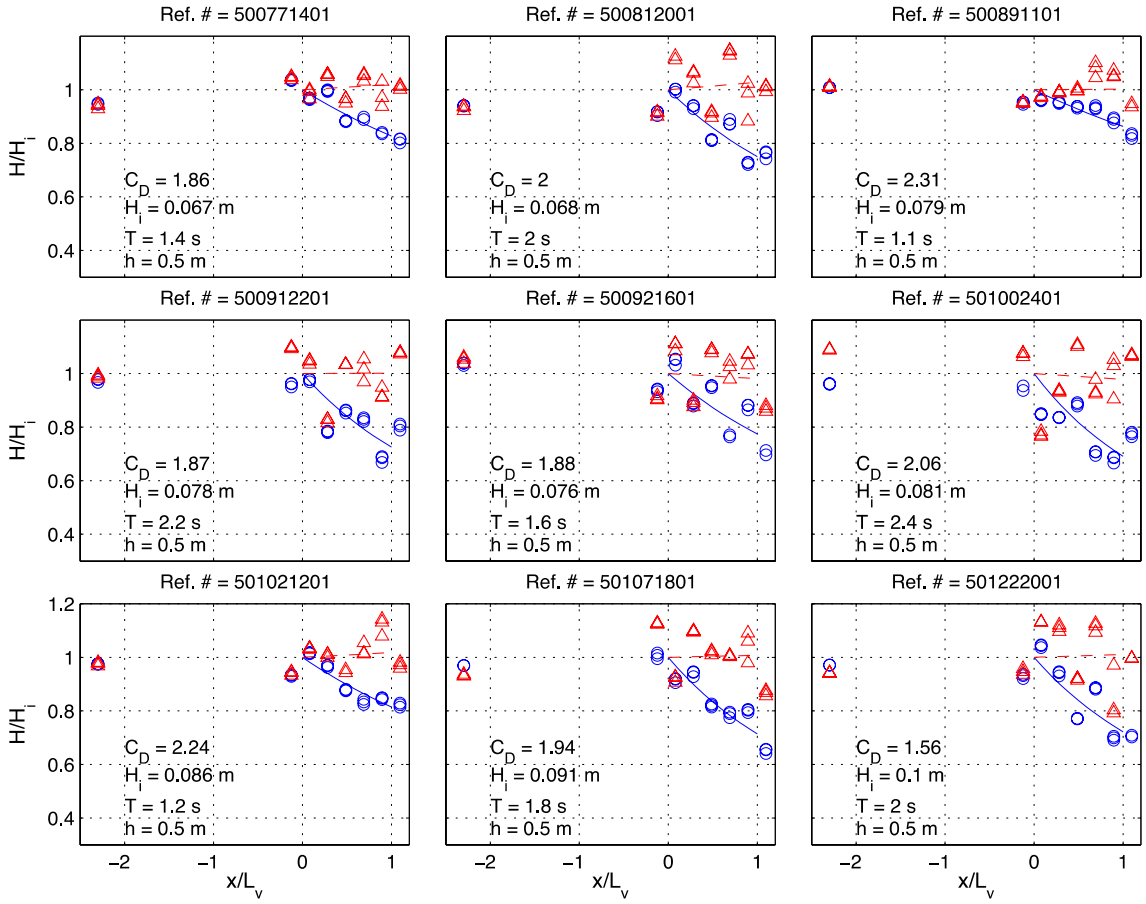

Fig. 2.11. Relative wave height distribution of regular waves along the wave tank for non-vegetated and rigid model vegetation (continued).

Flexible model vegetation–regular waves

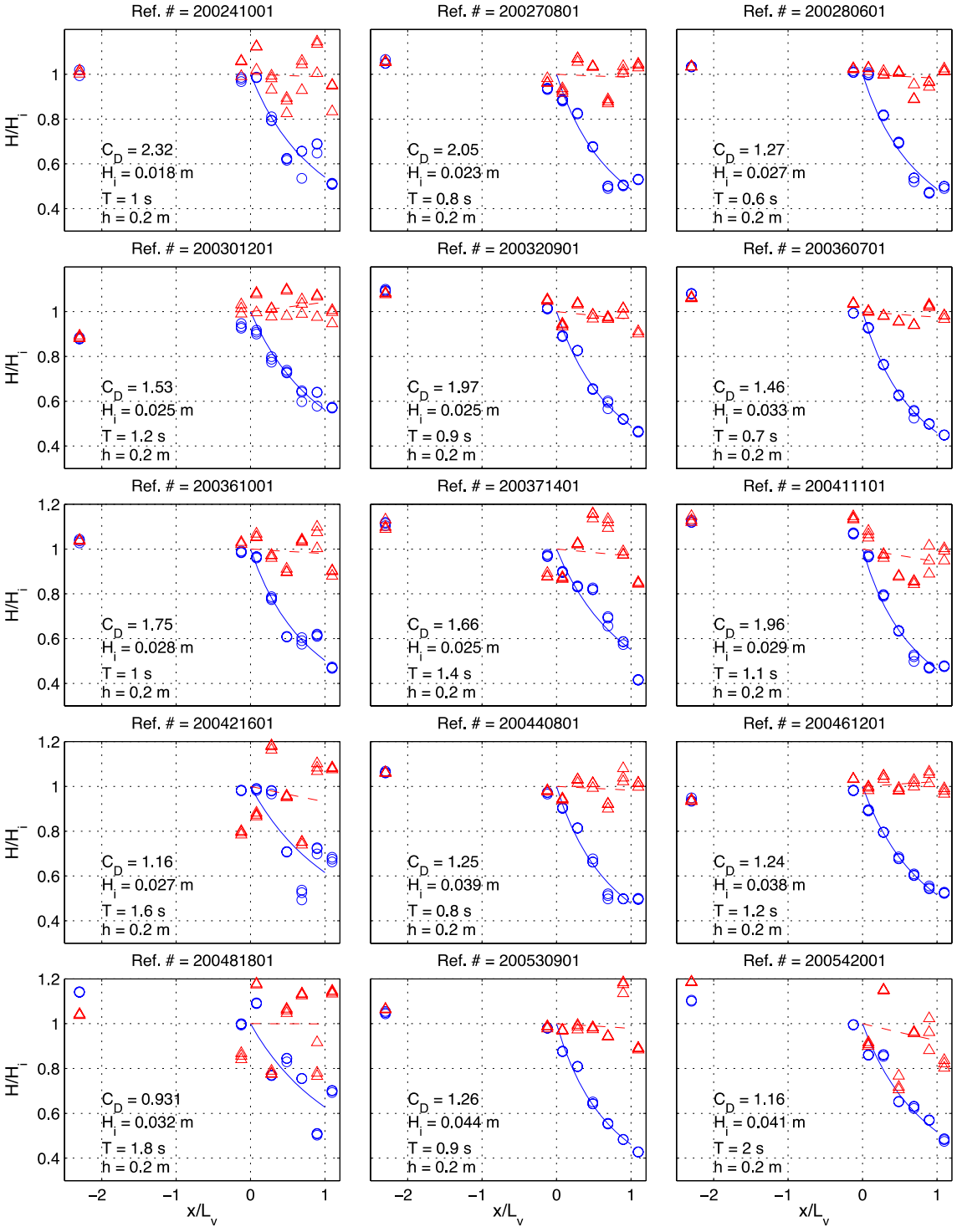

Fig. 2.12. Relative wave height distribution of regular waves along the wave tank for non-vegetated and flexible model vegetation.

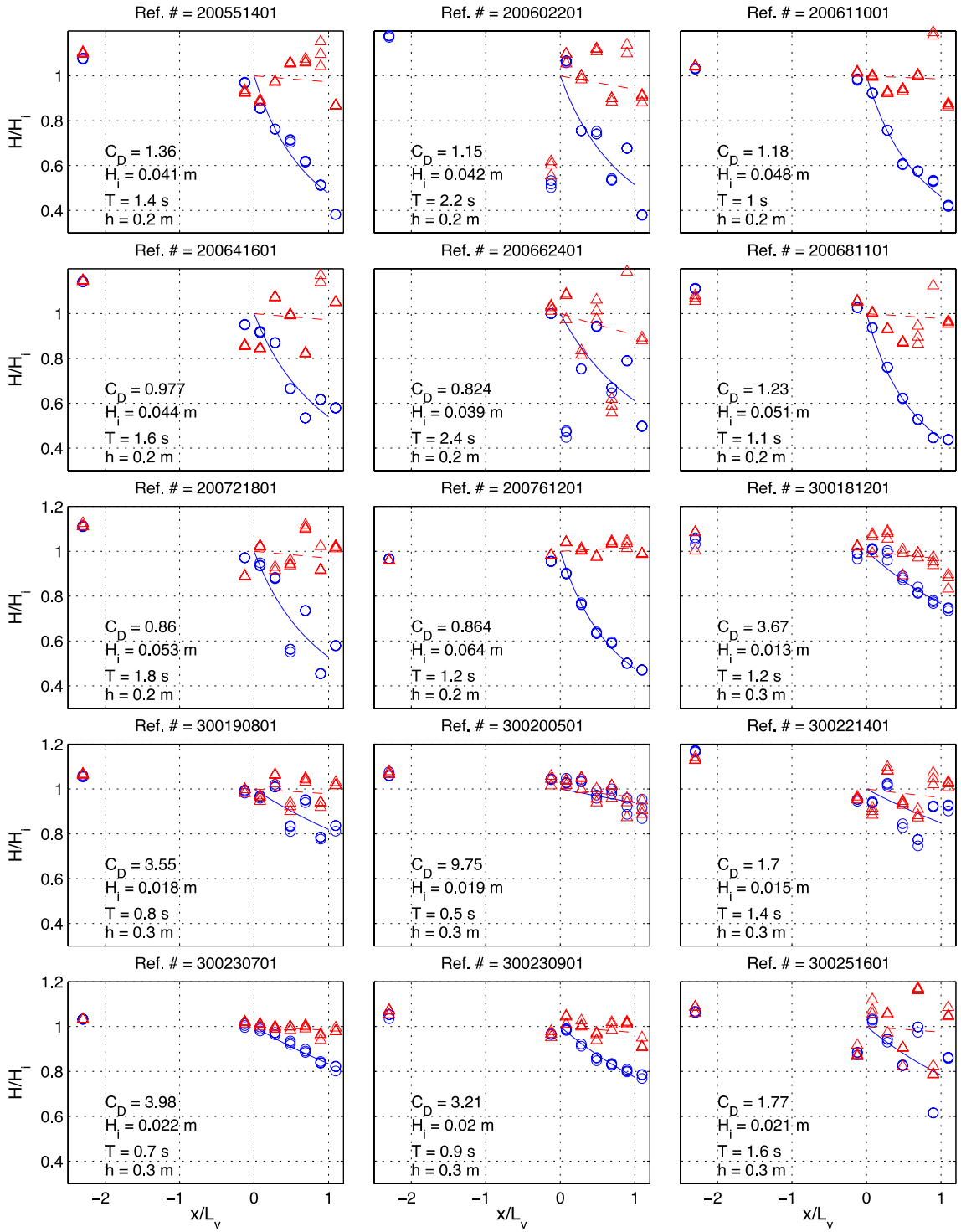

Fig. 2.12. Relative wave height distribution of regular waves along the wave tank for non-vegetated and flexible model vegetation (continued)

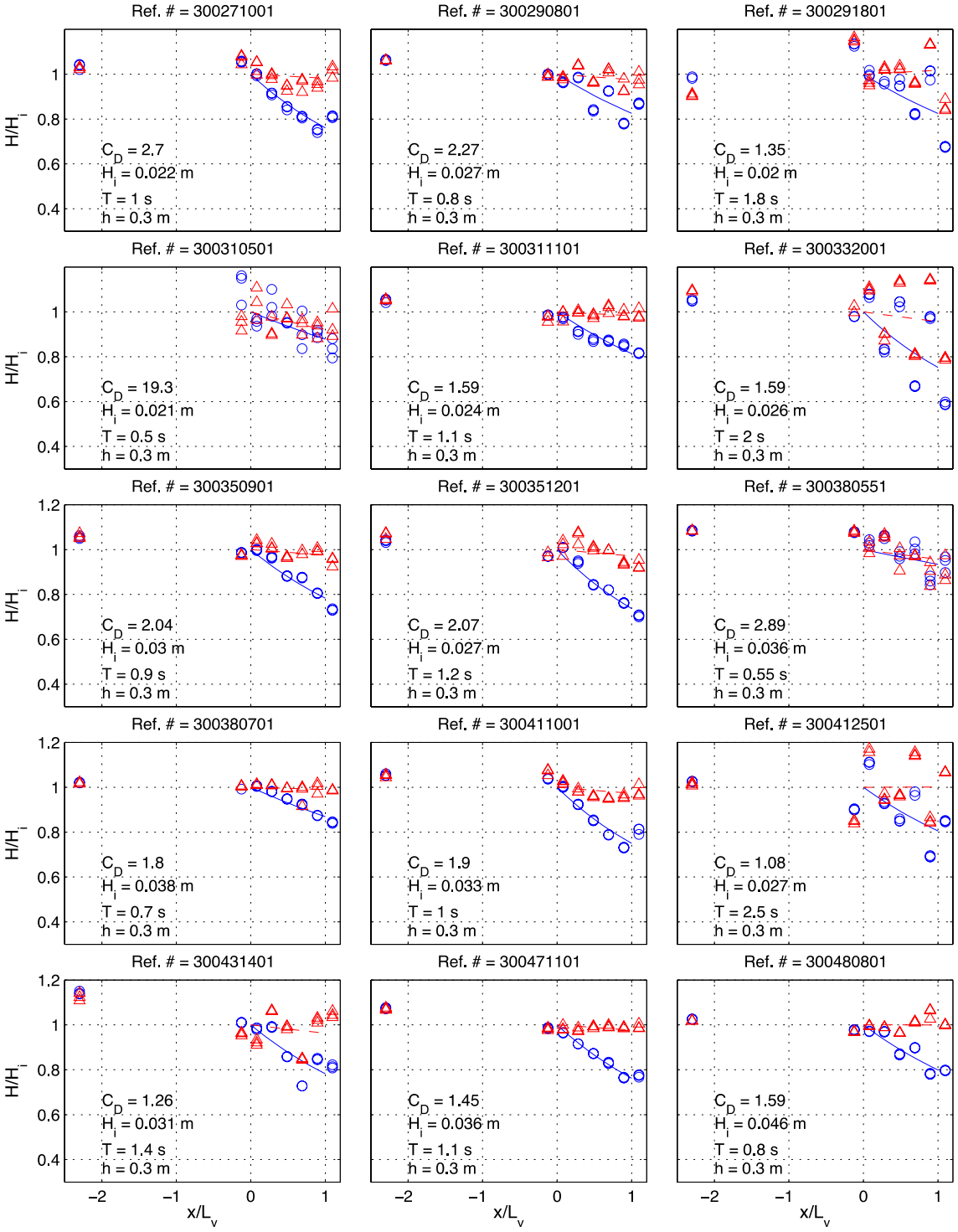

Fig. 2.12. Relative wave height distribution of regular waves along the wave tank for non-vegetated and flexible model vegetation (continued)

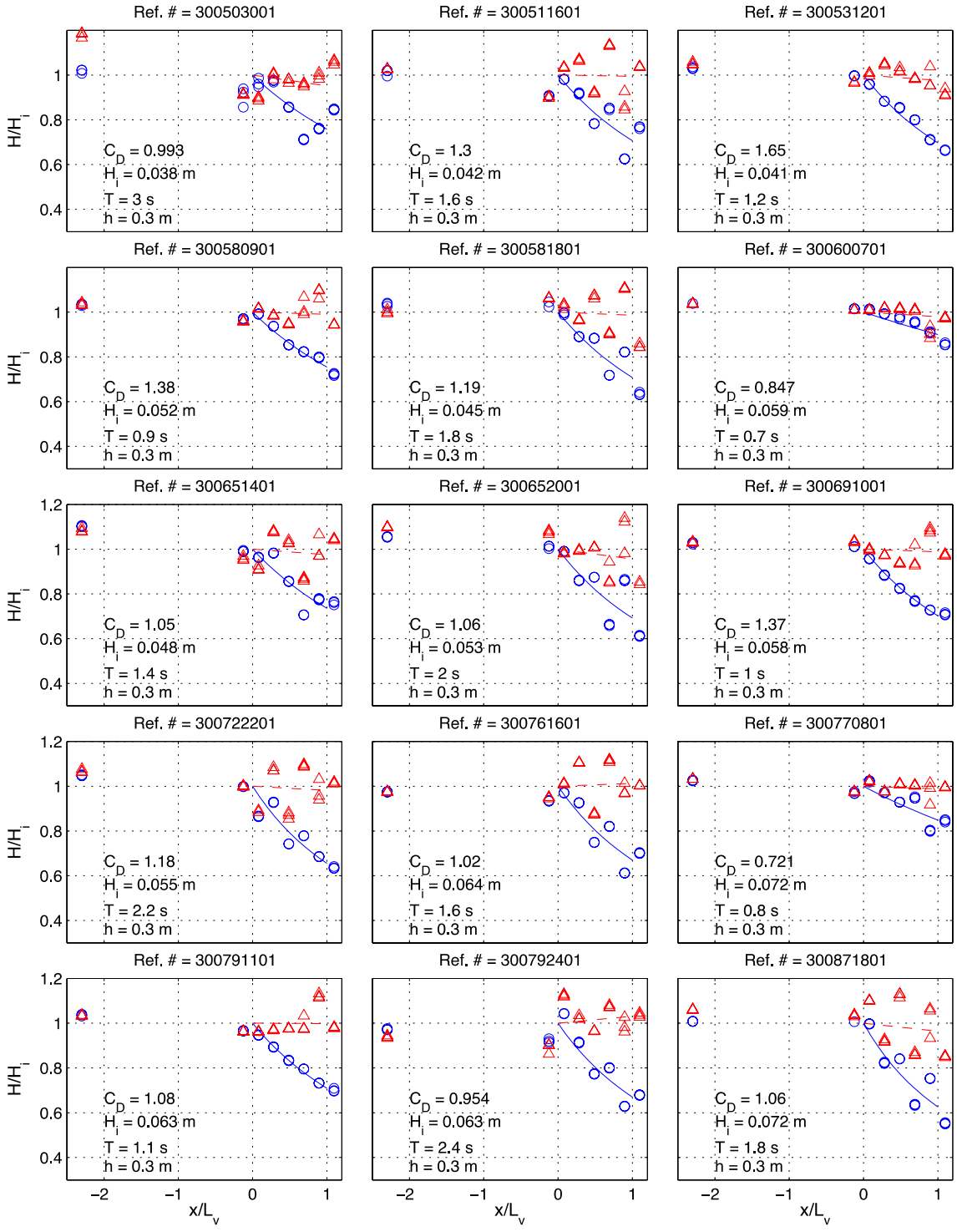

Fig. 2.12. Relative wave height distribution of regular waves along the wave tank for non-vegetated and flexible model vegetation (continued)

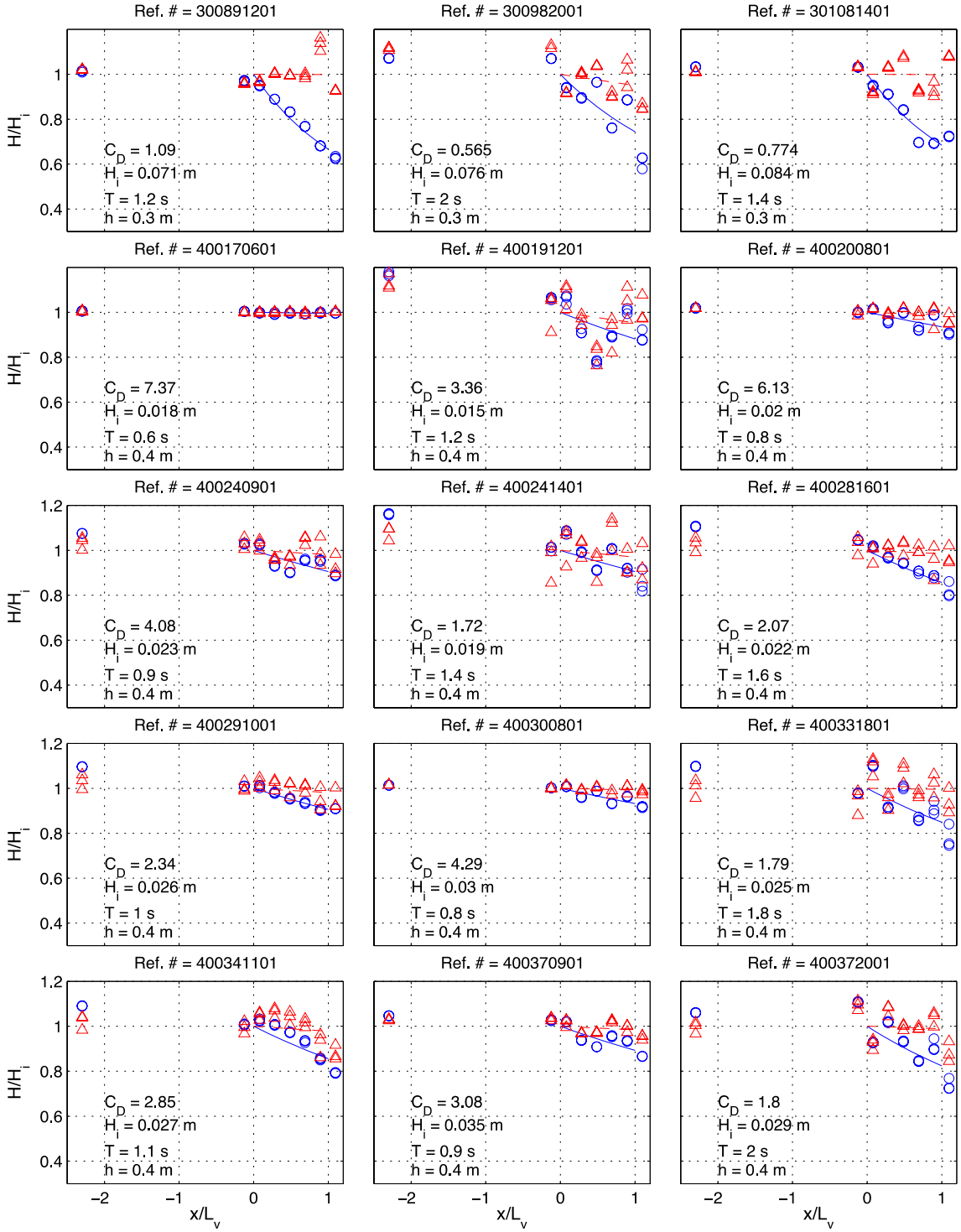

Fig. 2.12. Relative wave height distribution of regular waves along the wave tank for non-vegetated and flexible model vegetation (continued)

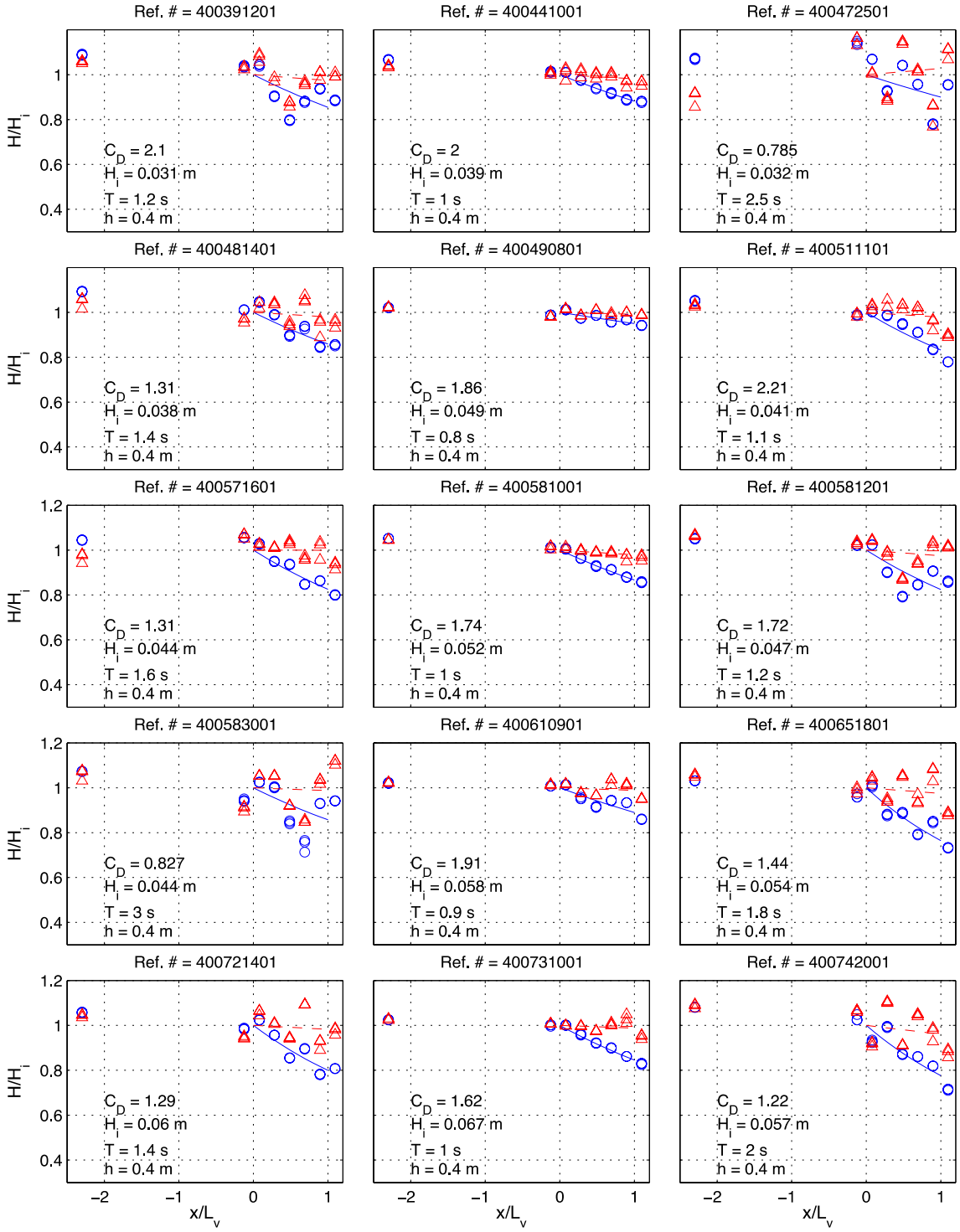

Fig. 2.12. Relative wave height distribution of regular waves along the wave tank for non-vegetated and flexible model vegetation (continued)

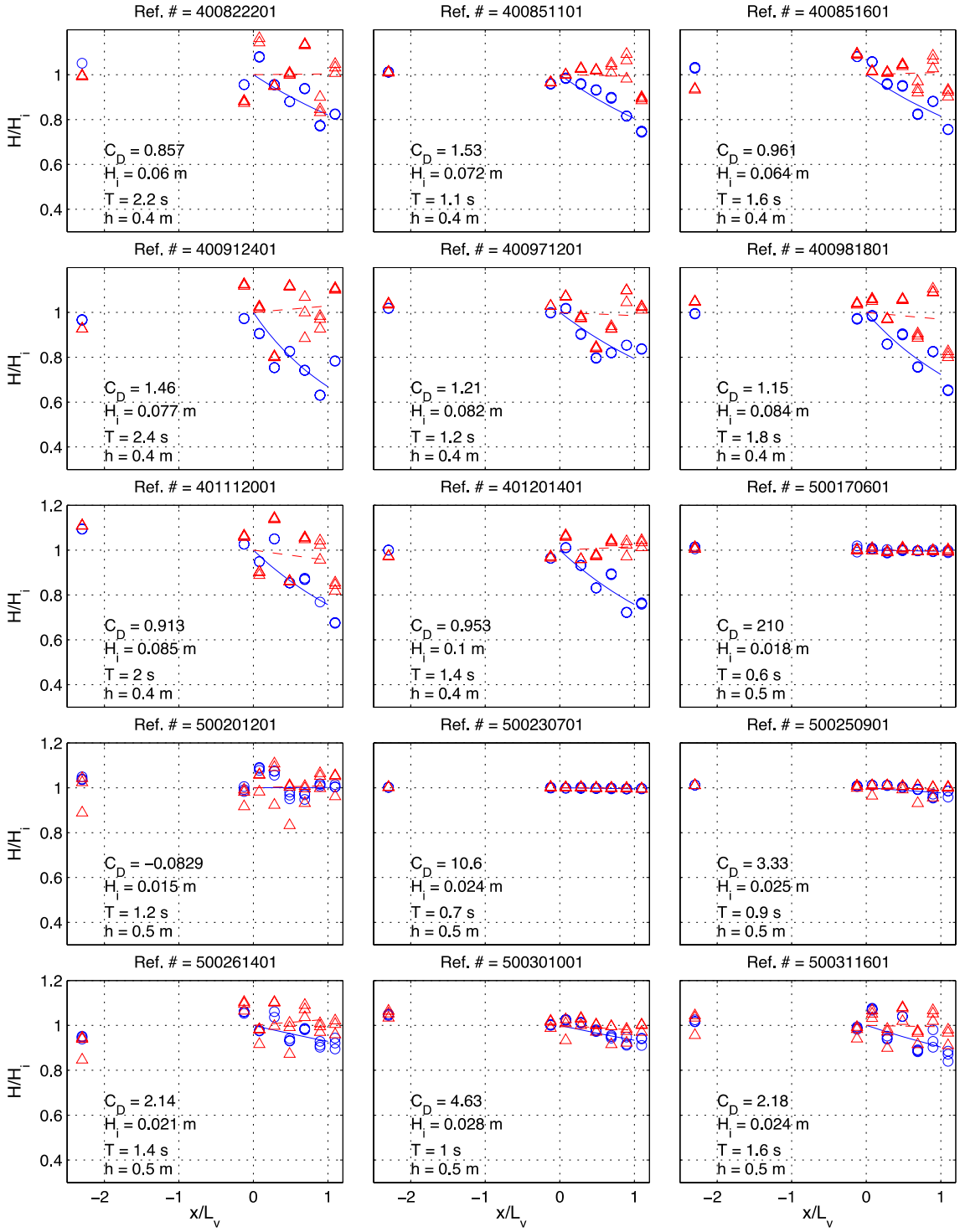

Fig. 2.12. Relative wave height distribution of regular waves along the wave tank for non-vegetated and flexible model vegetation (continued)

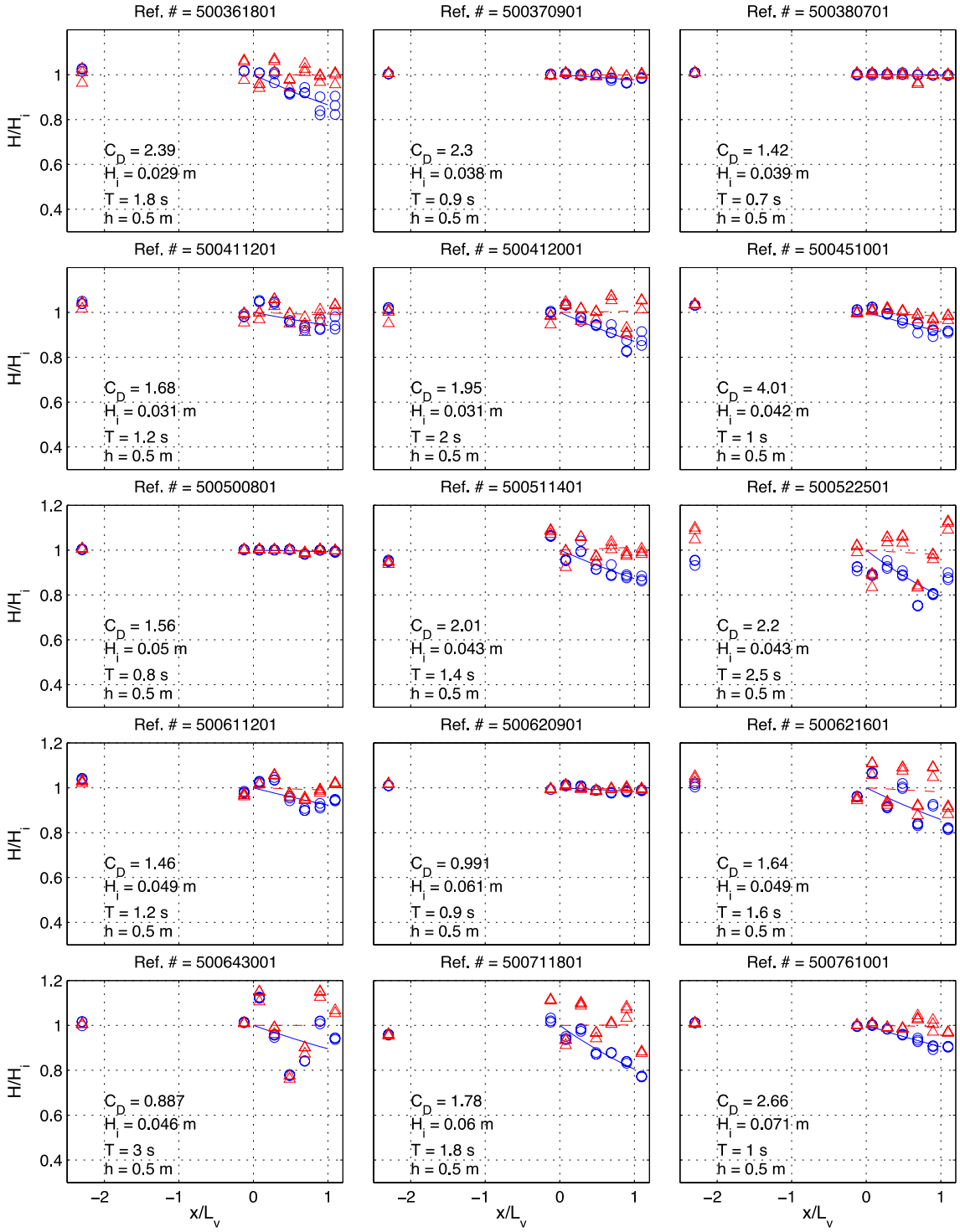

Fig. 2.12. Relative wave height distribution of regular waves along the wave tank for non-vegetated and flexible model vegetation (continued)

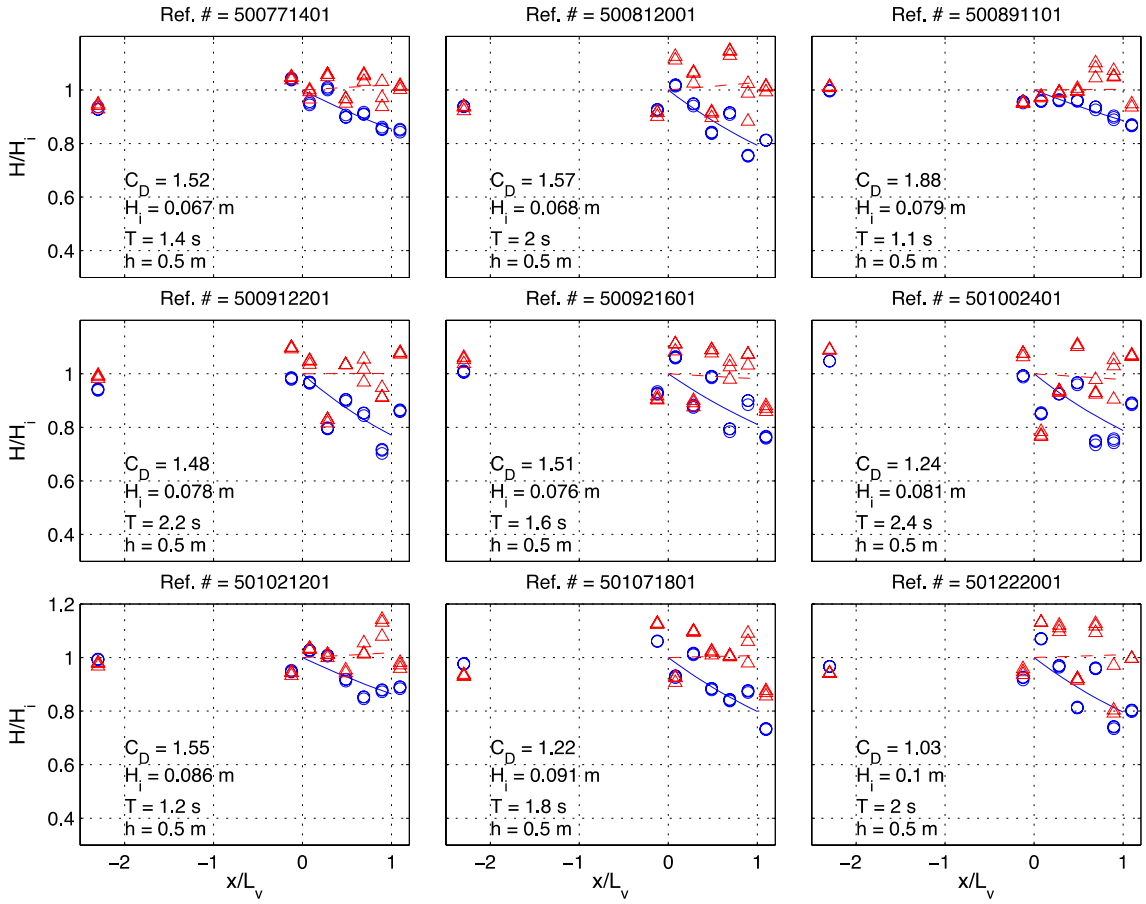

Fig. 2.12. Relative wave height distribution of regular waves of regular waves along the wave tank for non-vegetated and flexible model vegetation (continued)

Video analysis – rigid model vegetation

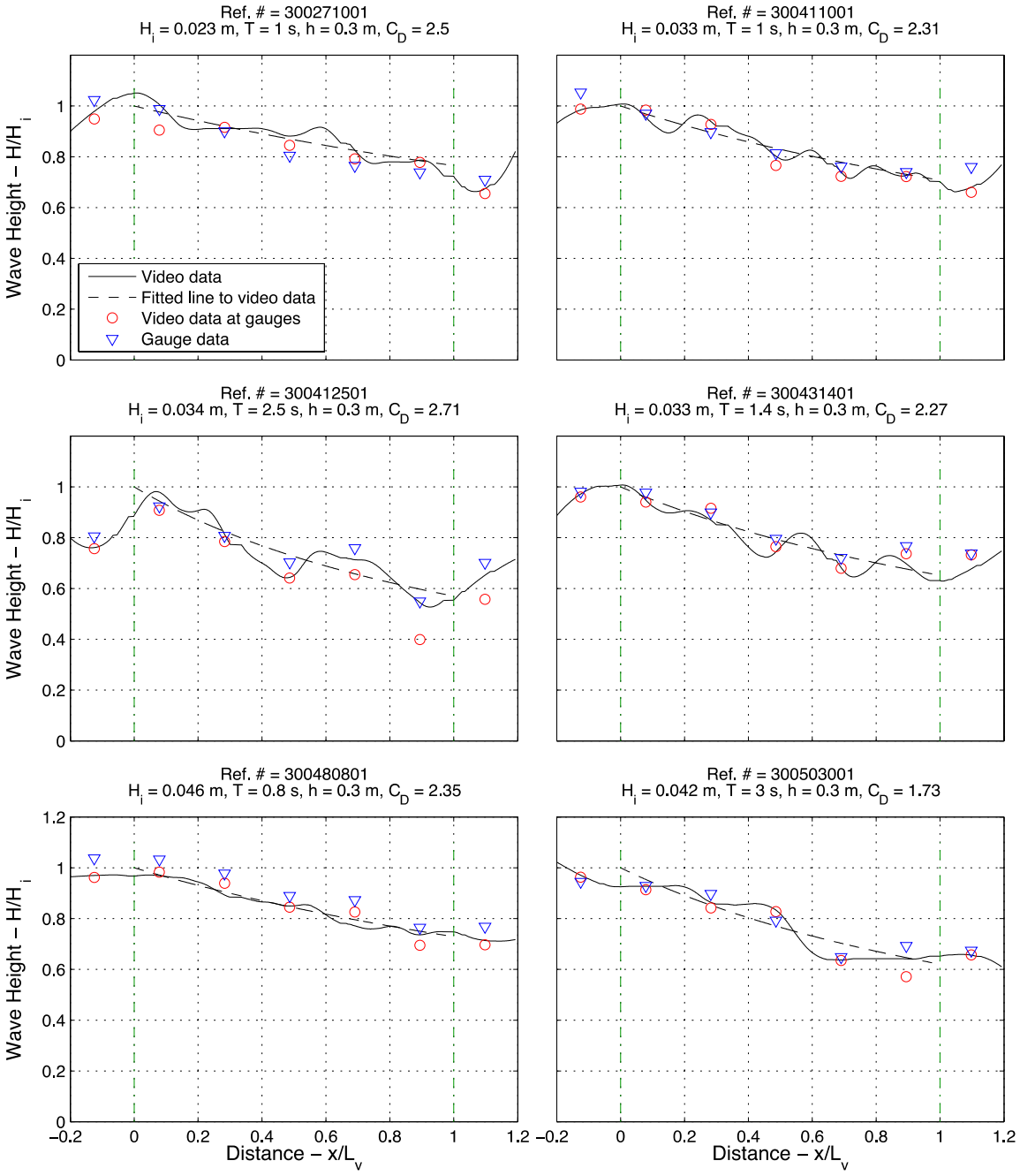

Fig. 2.13. Video and wave gauge measurements of relative wave height distribution of regular waves along the wave tank for rigid model vegetation.

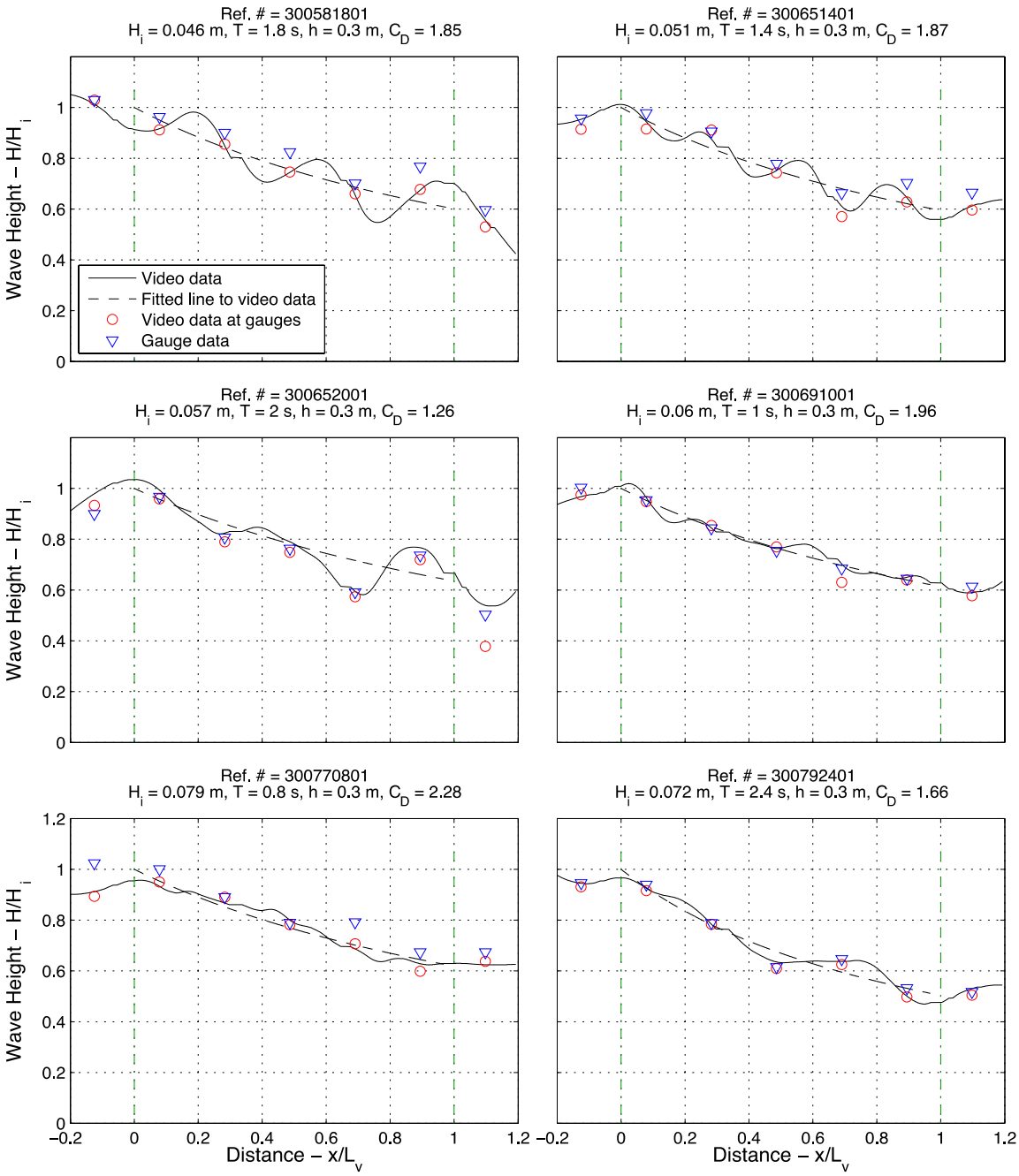

Fig. 2.13. Video and wave gauge measurements of relative wave height distribution of regular waves along the wave tank for rigid model vegetation (continued).

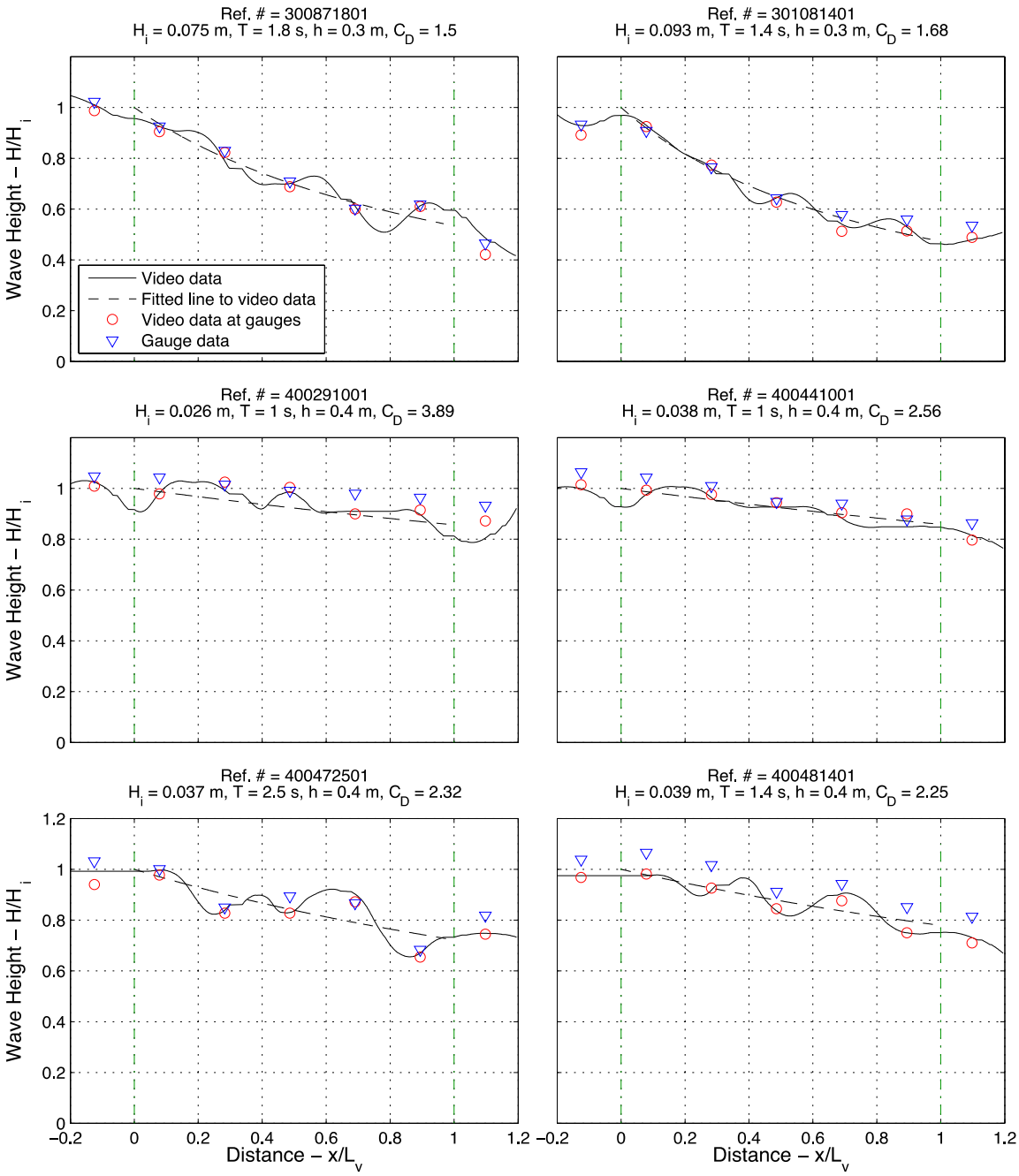

Fig. 2.13. Video and wave gauge measurements of relative wave height distribution of regular waves along the wave tank for rigid model vegetation (continued).

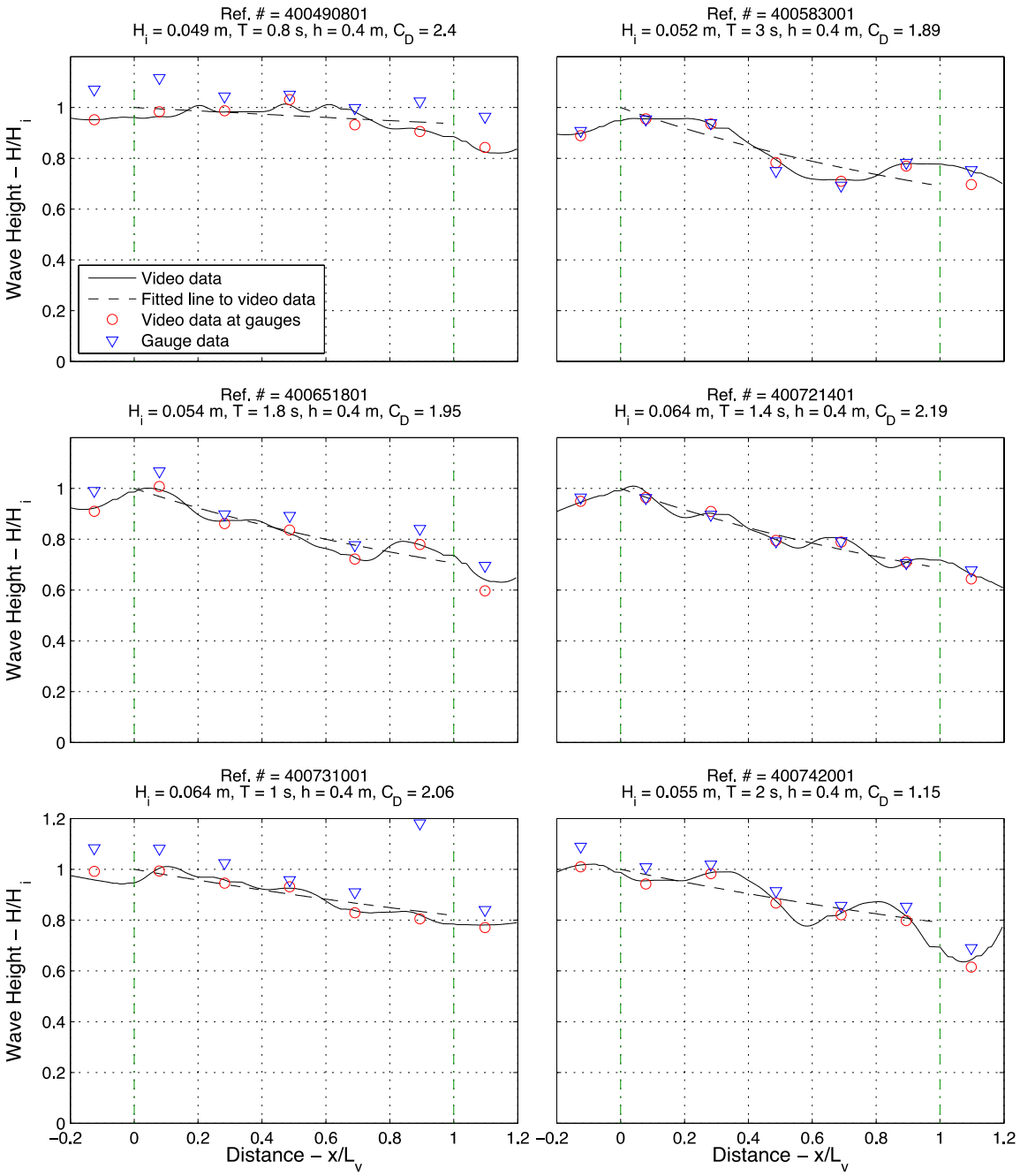

Fig. 2.13. Video and wave gauge measurements of relative wave height distribution of regular waves along the wave tank for rigid model vegetation (continued).

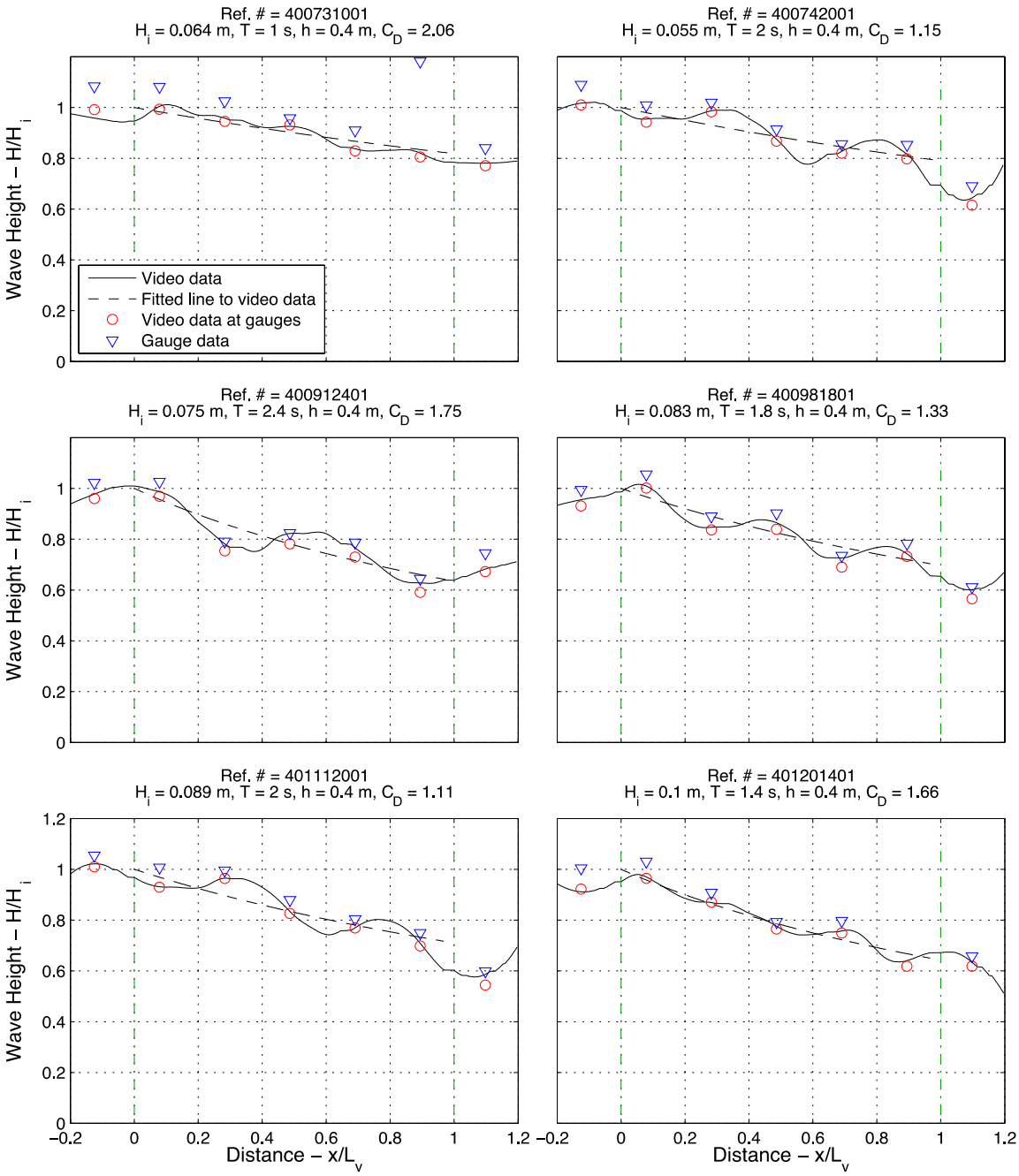

Fig. 2.13. Video and wave gauge measurements of relative wave height distribution of regular waves along the wave tank for rigid model vegetation (continued).

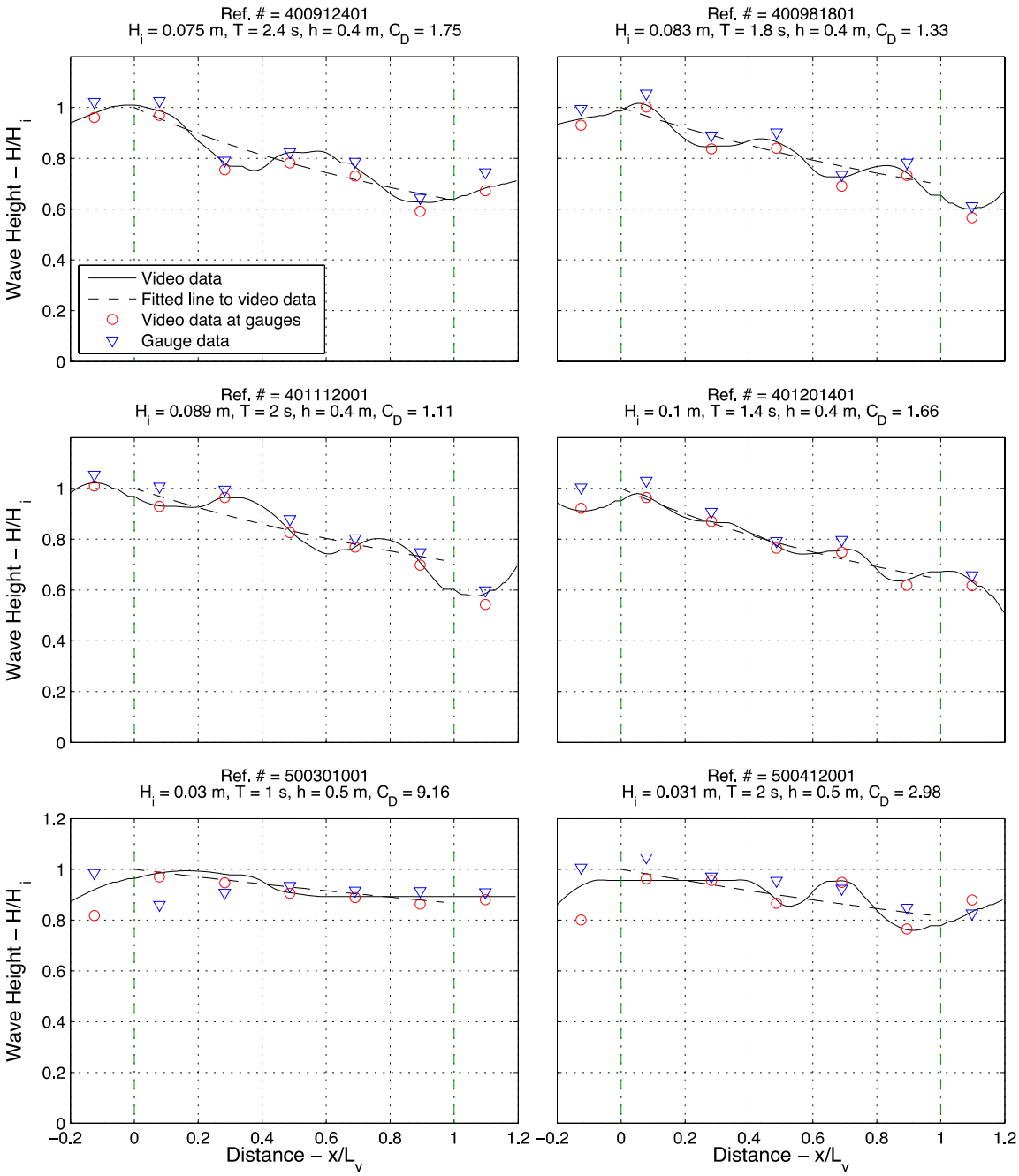

Fig. 2.13. Video and wave gauge measurements of relative wave height distribution of regular waves along the wave tank for rigid model vegetation (continued).

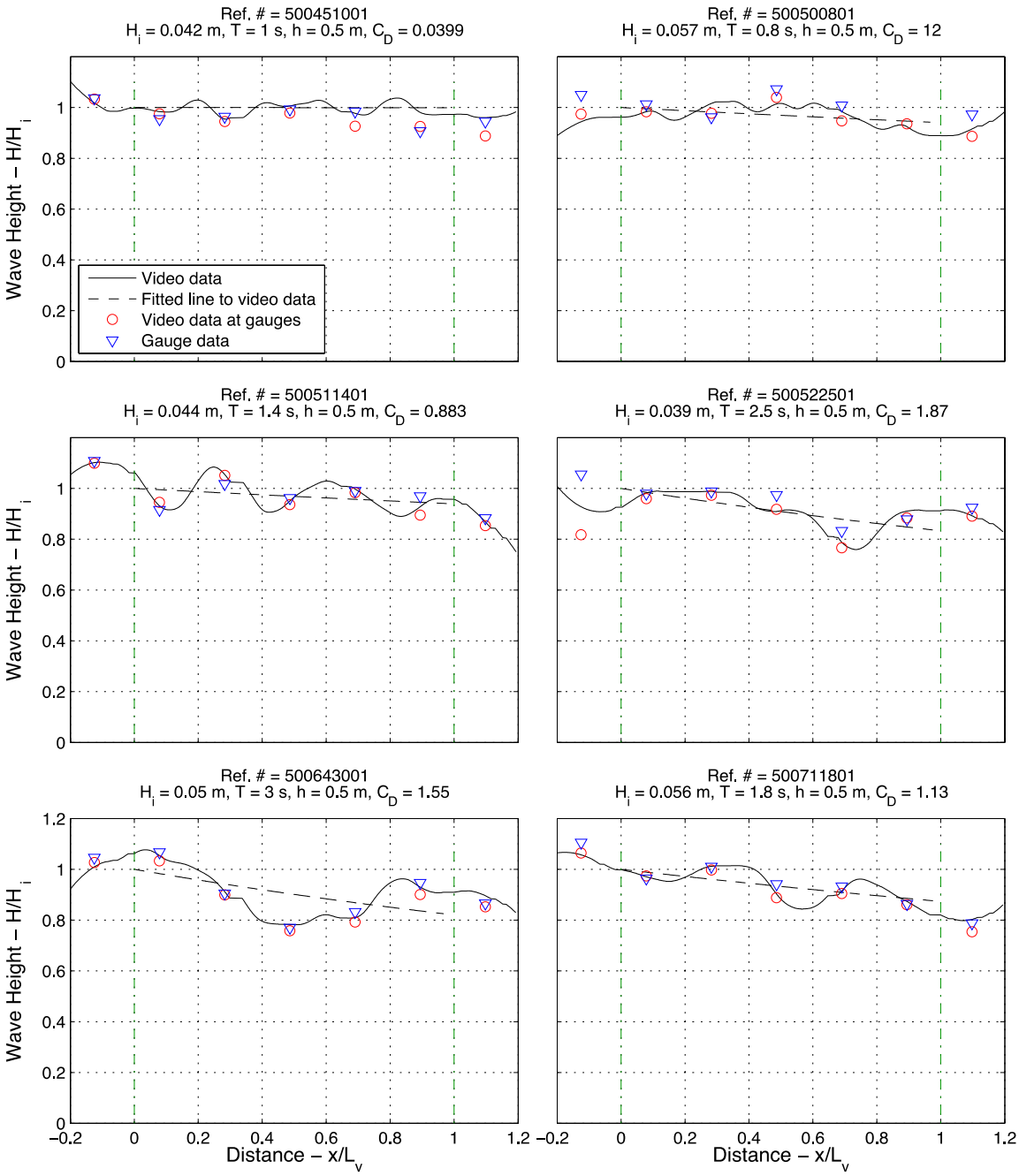

Fig. 2.13. Video and wave gauge measurements of relative wave height distribution of regular waves along the wave tank for rigid model vegetation (continued).

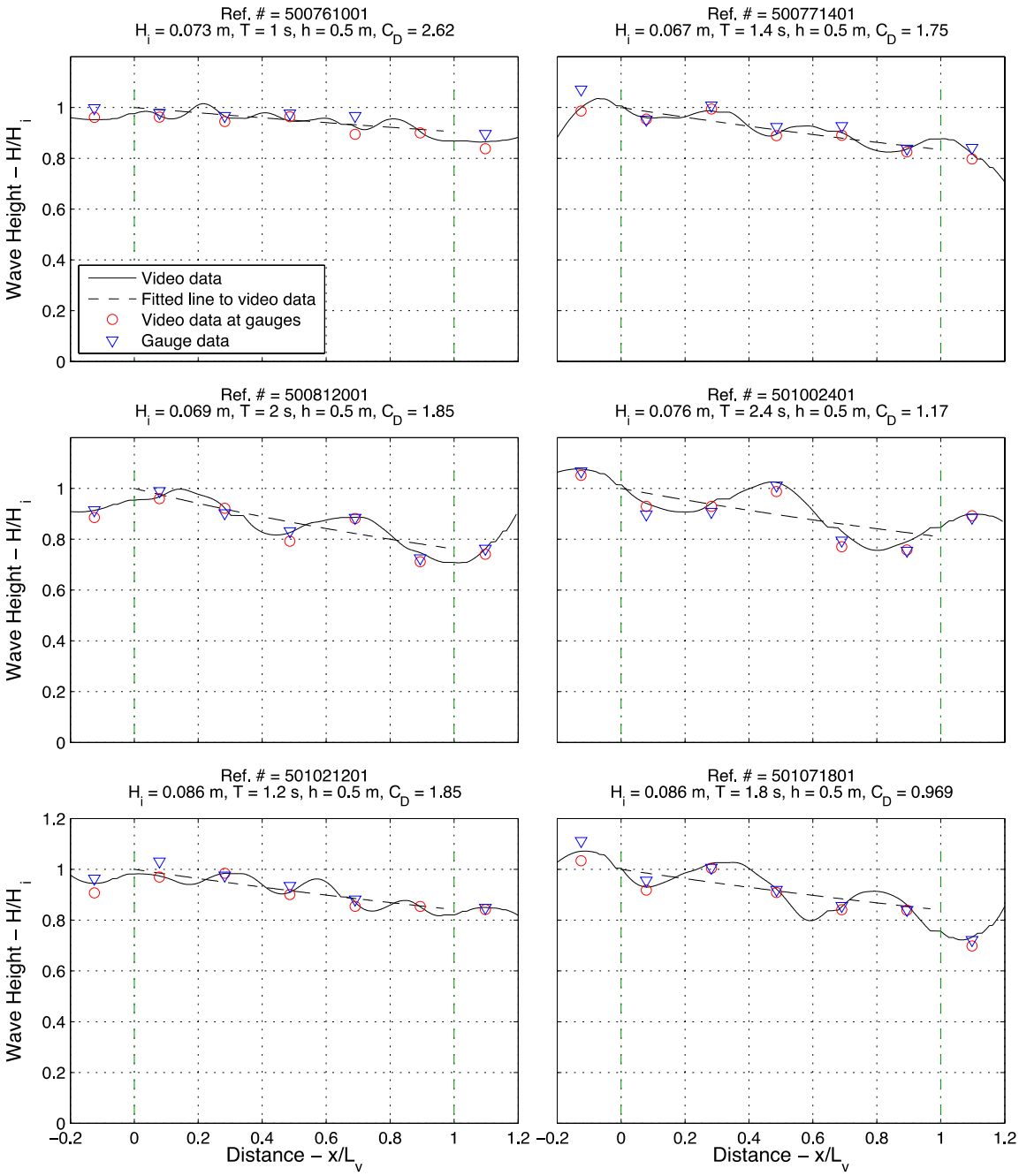

Fig. 2.13. Video and wave gauge measurements of relative wave height distribution of regular waves along the wave tank for rigid model vegetation (continued).

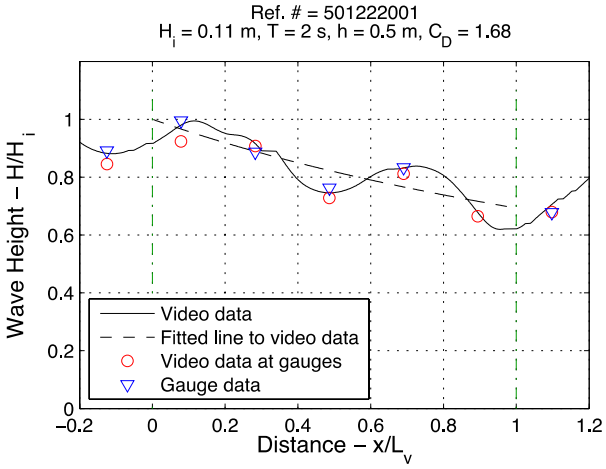

Fig. 2.13. Video and wave gauge measurements of relative wave height distribution of regular waves along the wave tank for rigid model vegetation (continued).

Video analysis - flexible model vegetation

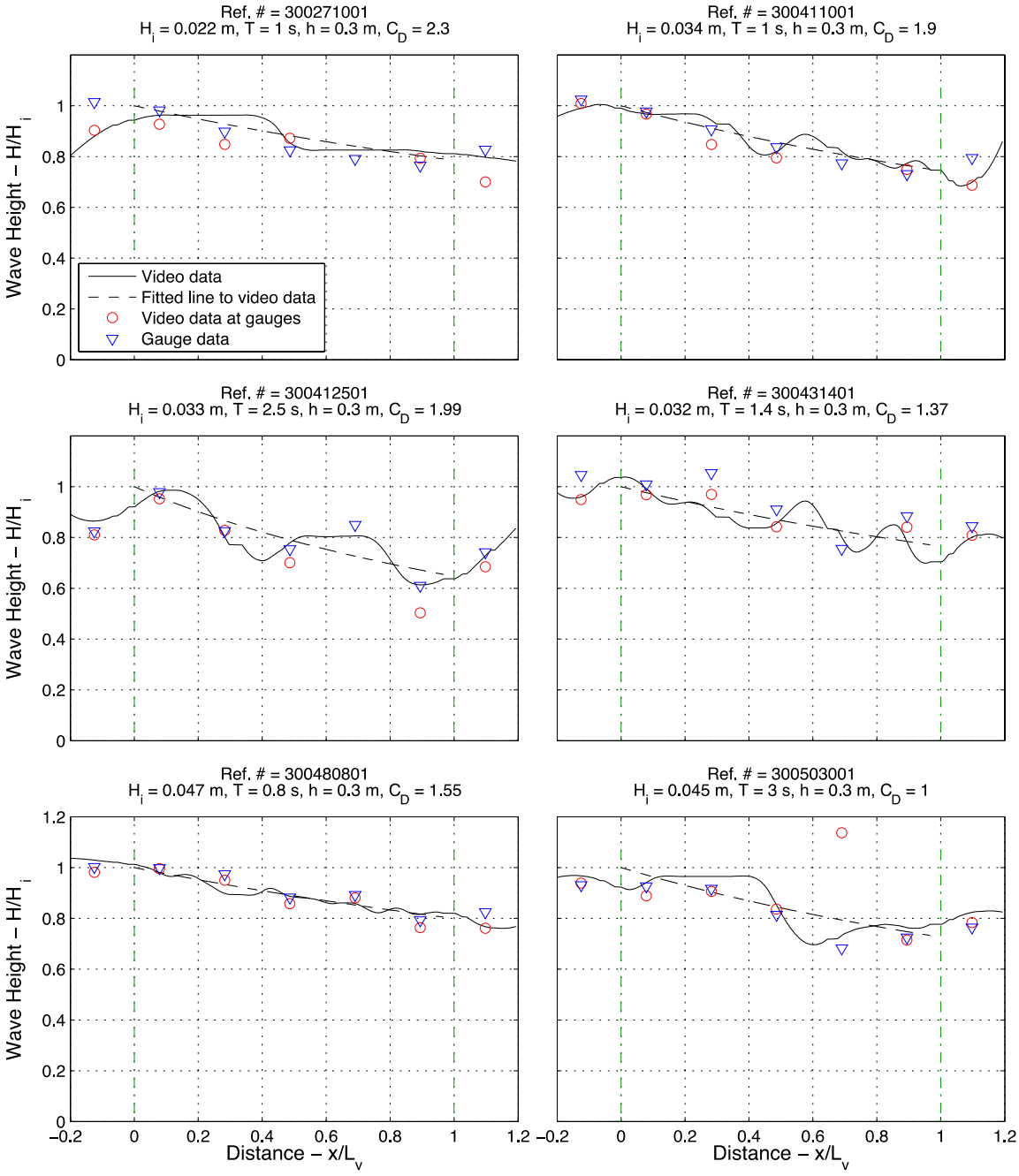

Fig. 2.14. Video and wave gauge measurements of relative wave height distribution of regular waves along the wave tank for flexible model vegetation.

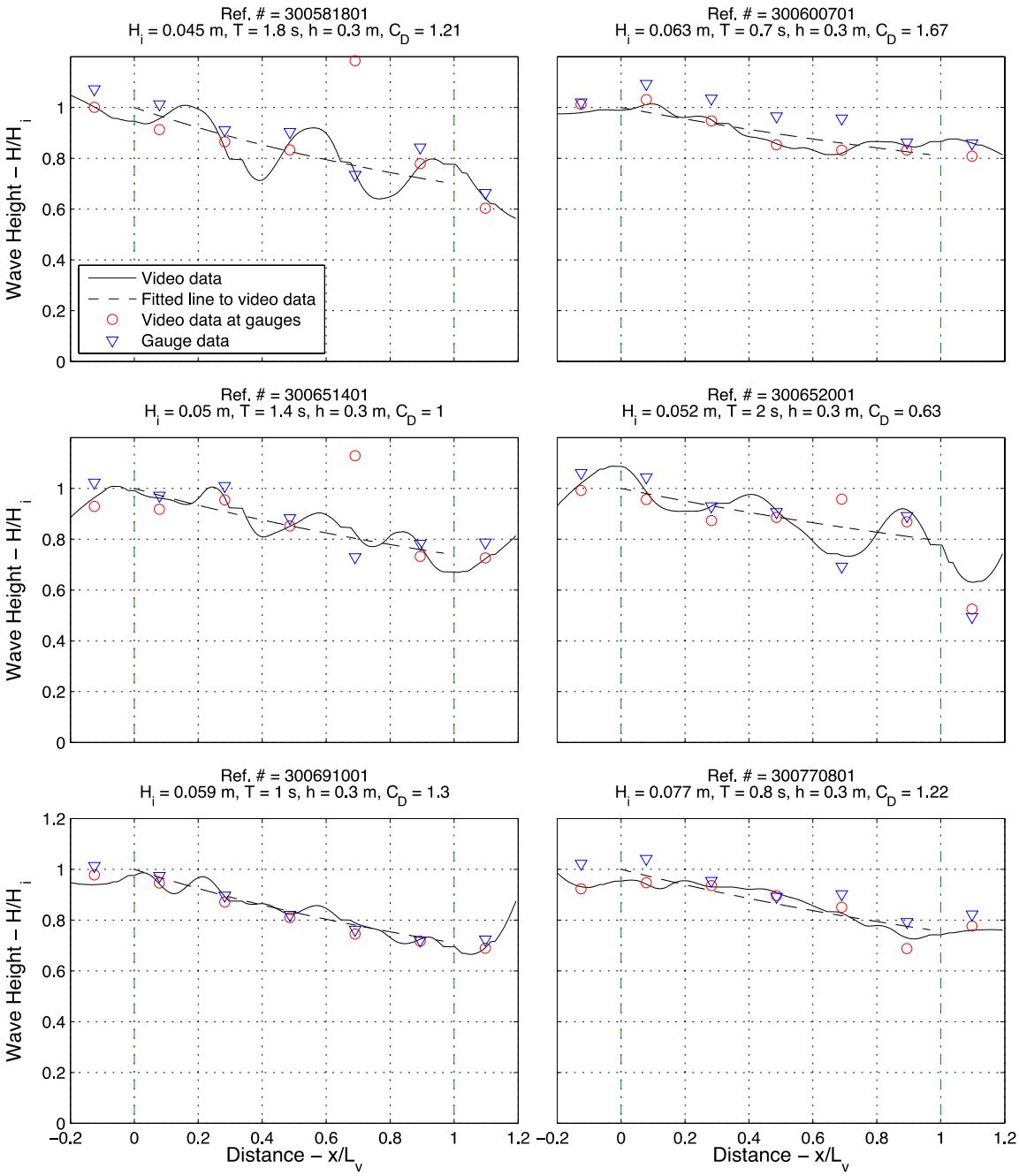

Fig. 2.14. Video and wave gauge measurements of relative wave height distribution of regular waves along the wave tank for flexible model vegetation (continued).

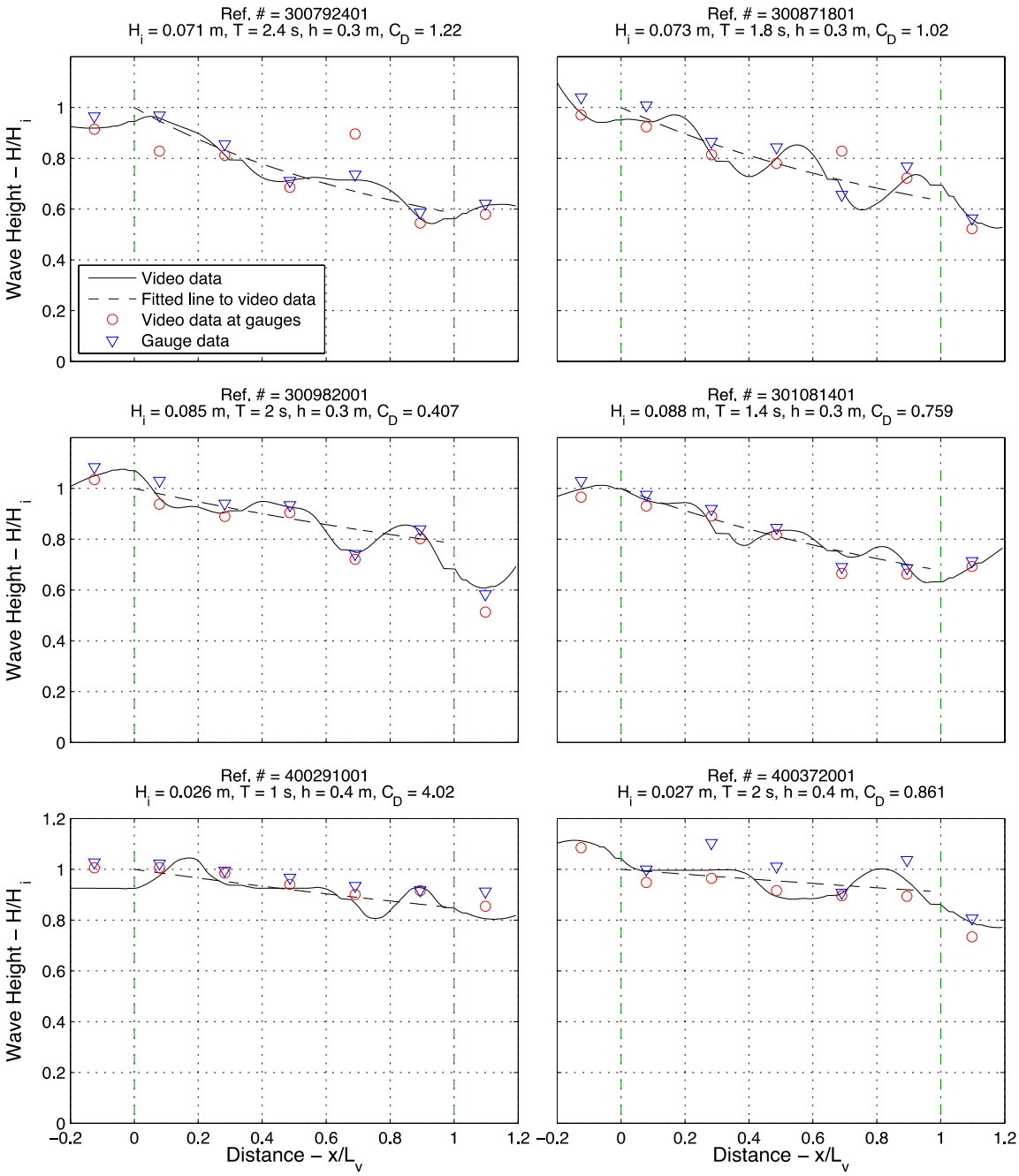

Fig. 2.14. Video and wave gauge measurements of relative wave height distribution of regular waves along the wave tank for flexible model vegetation (continued).

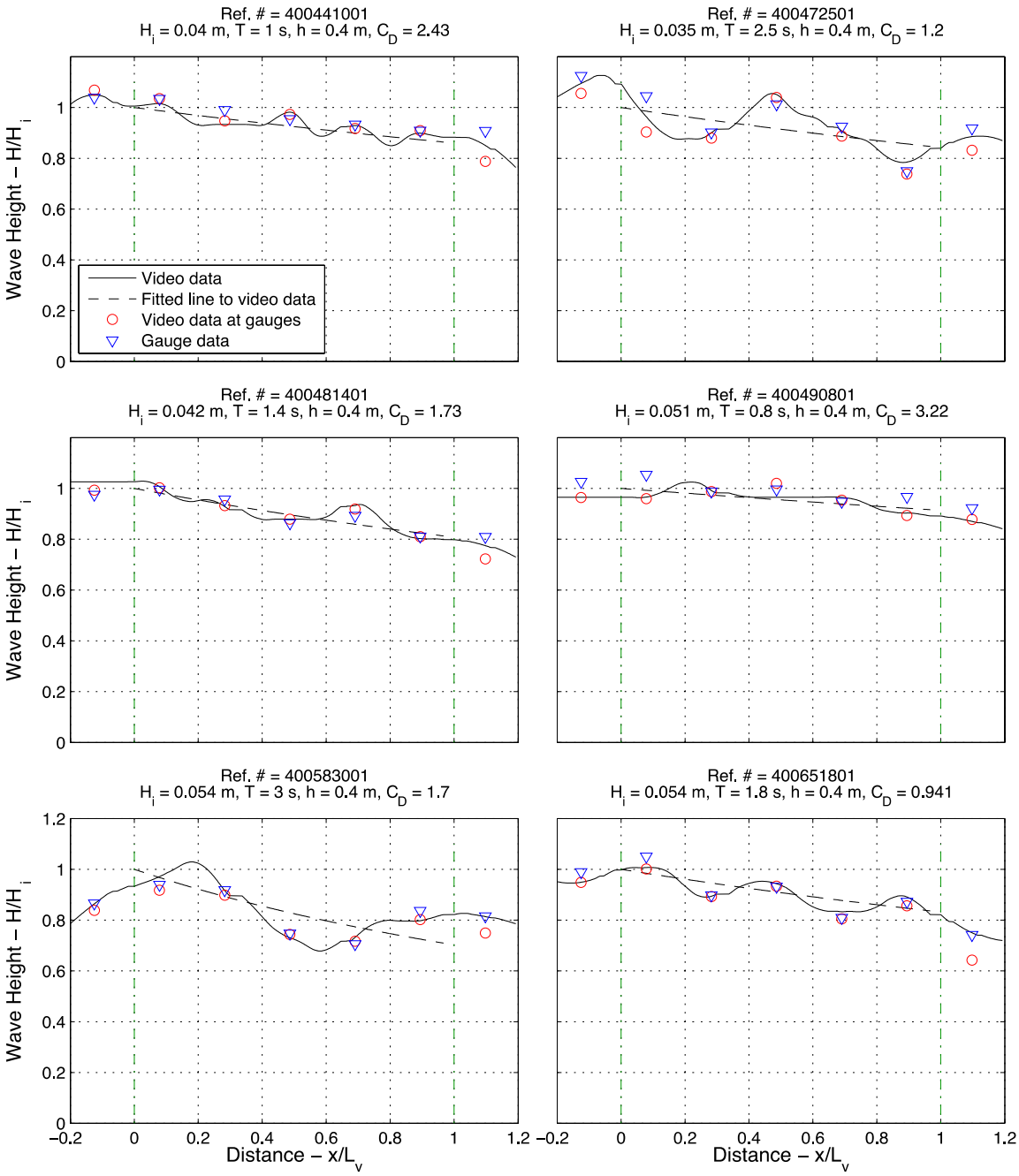

Fig. 2.14. Video and wave gauge measurements of relative wave height distribution of regular waves along the wave tank for flexible model vegetation (continued).

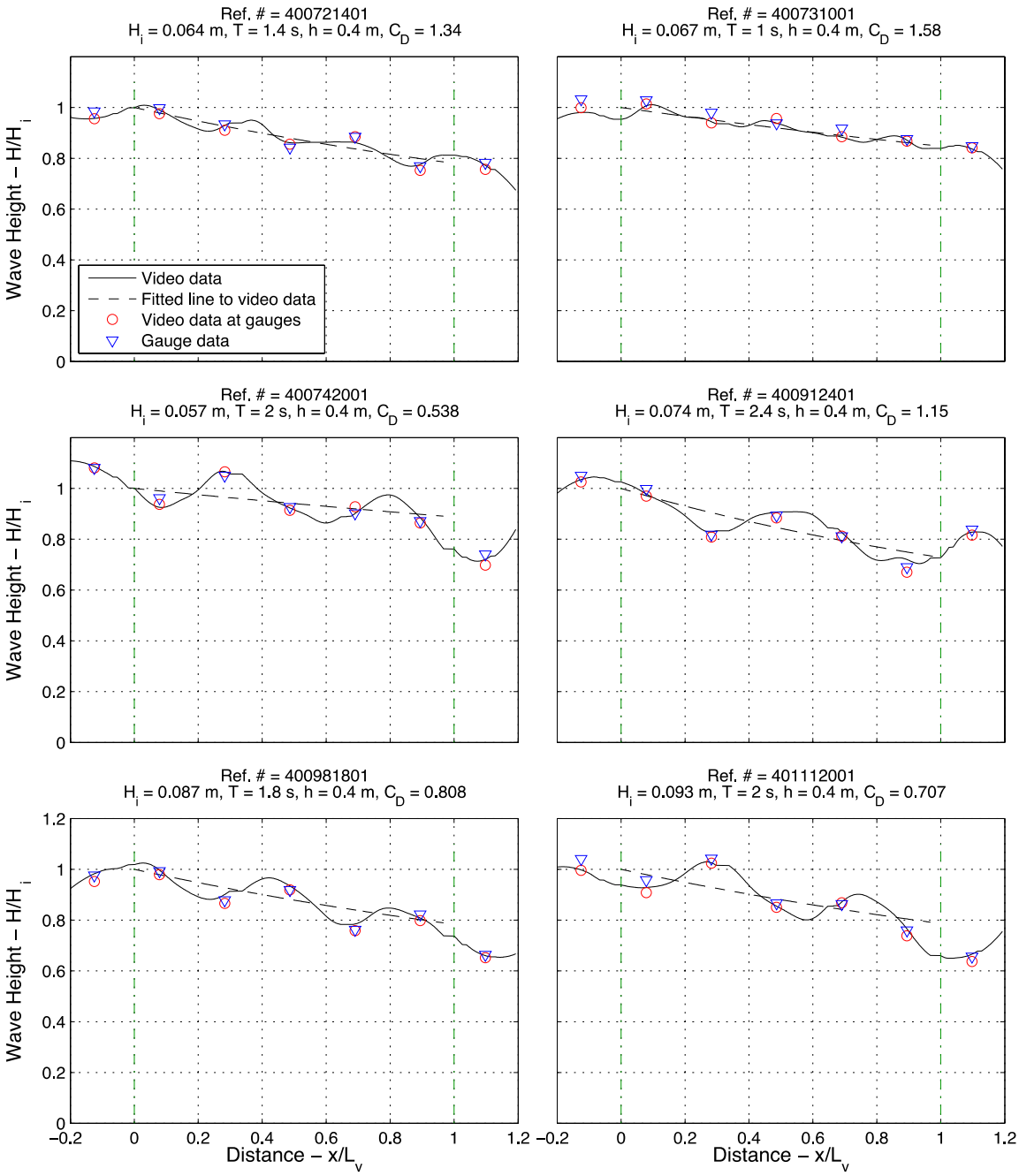

Fig. 2.14. Video and wave gauge measurements of relative wave height distribution of regular waves along the wave tank for flexible model vegetation (continued).

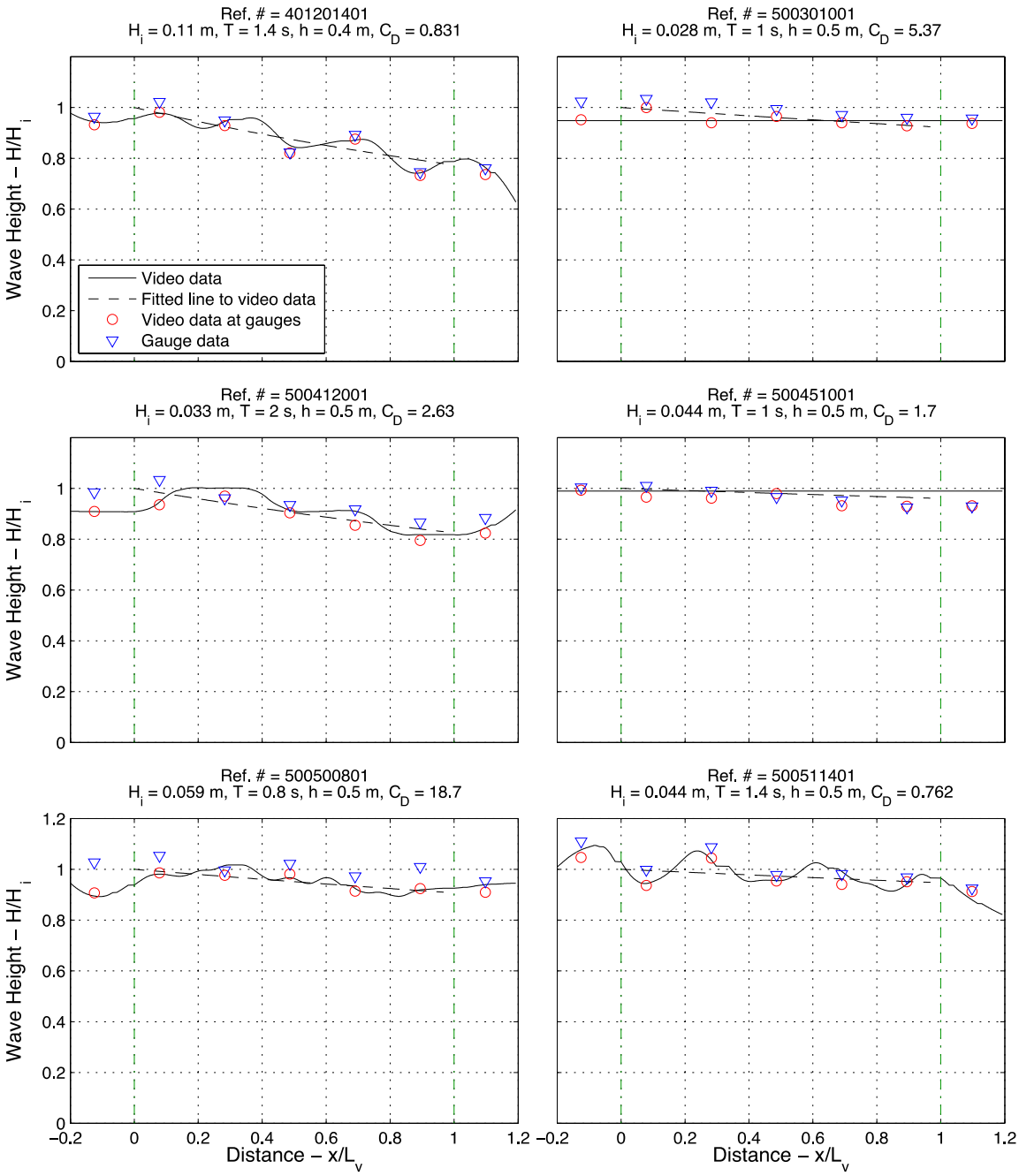

Fig. 2.14. Video and wave gauge measurements of relative wave height distribution of regular waves along the wave tank for flexible model vegetation (continued).

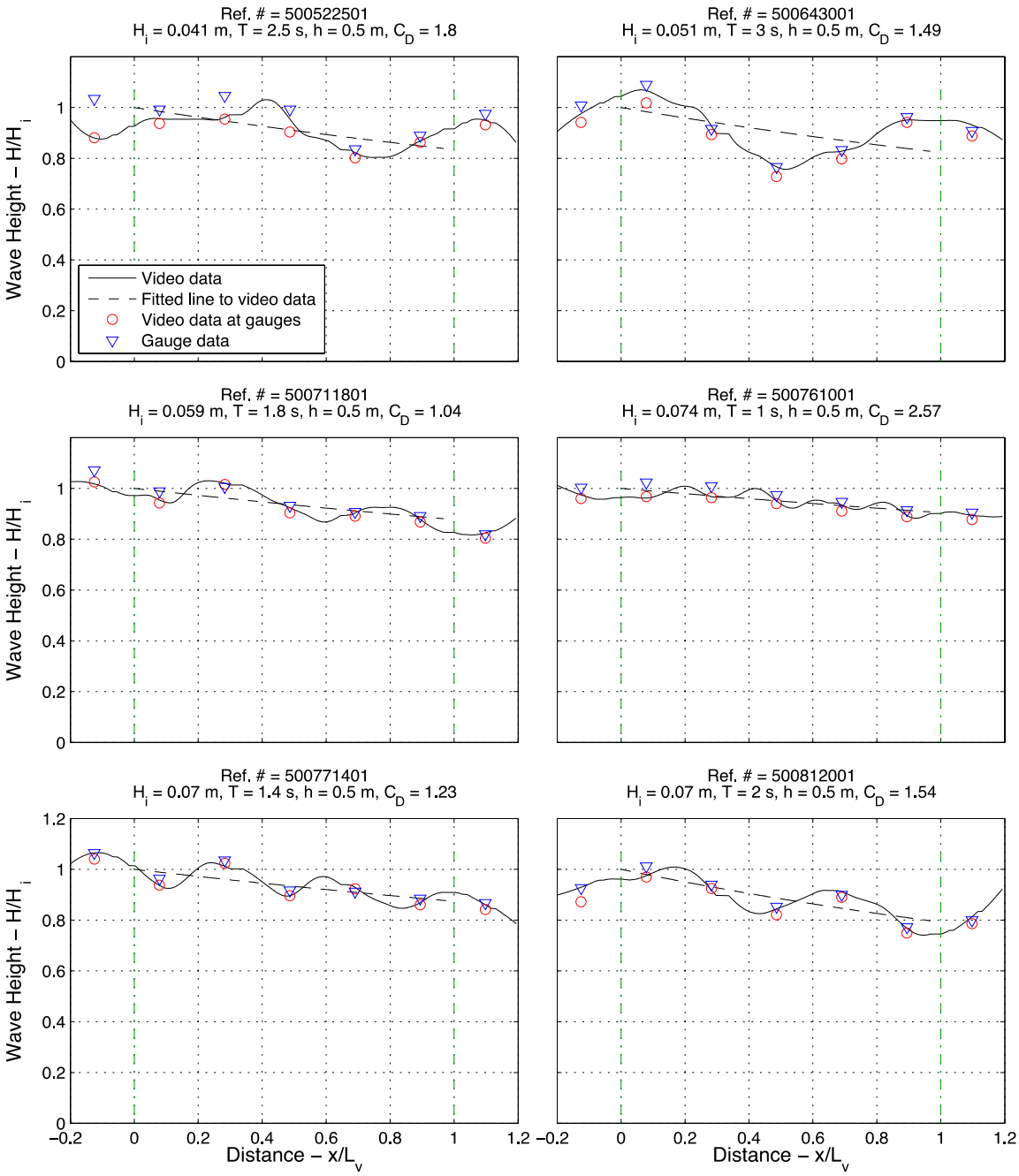

Fig. 2.14. Video and wave gauge measurements of relative wave height distribution of regular waves along the wave tank for flexible model vegetation (continued).

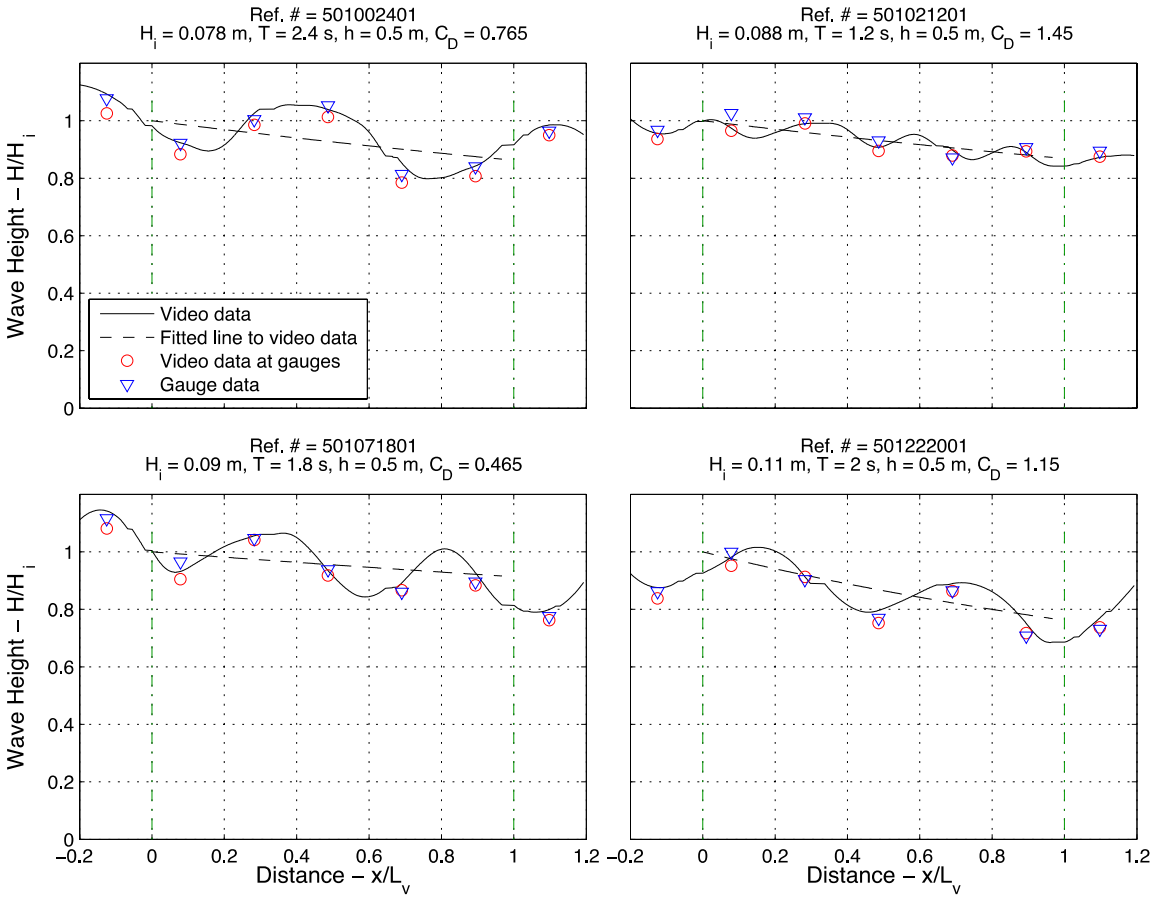

Fig. 2.14. Video and wave gauge measurements of relative wave height distribution of regular waves along the wave tank for flexible model vegetation (continued).

Rigid model vegetation - irregular waves

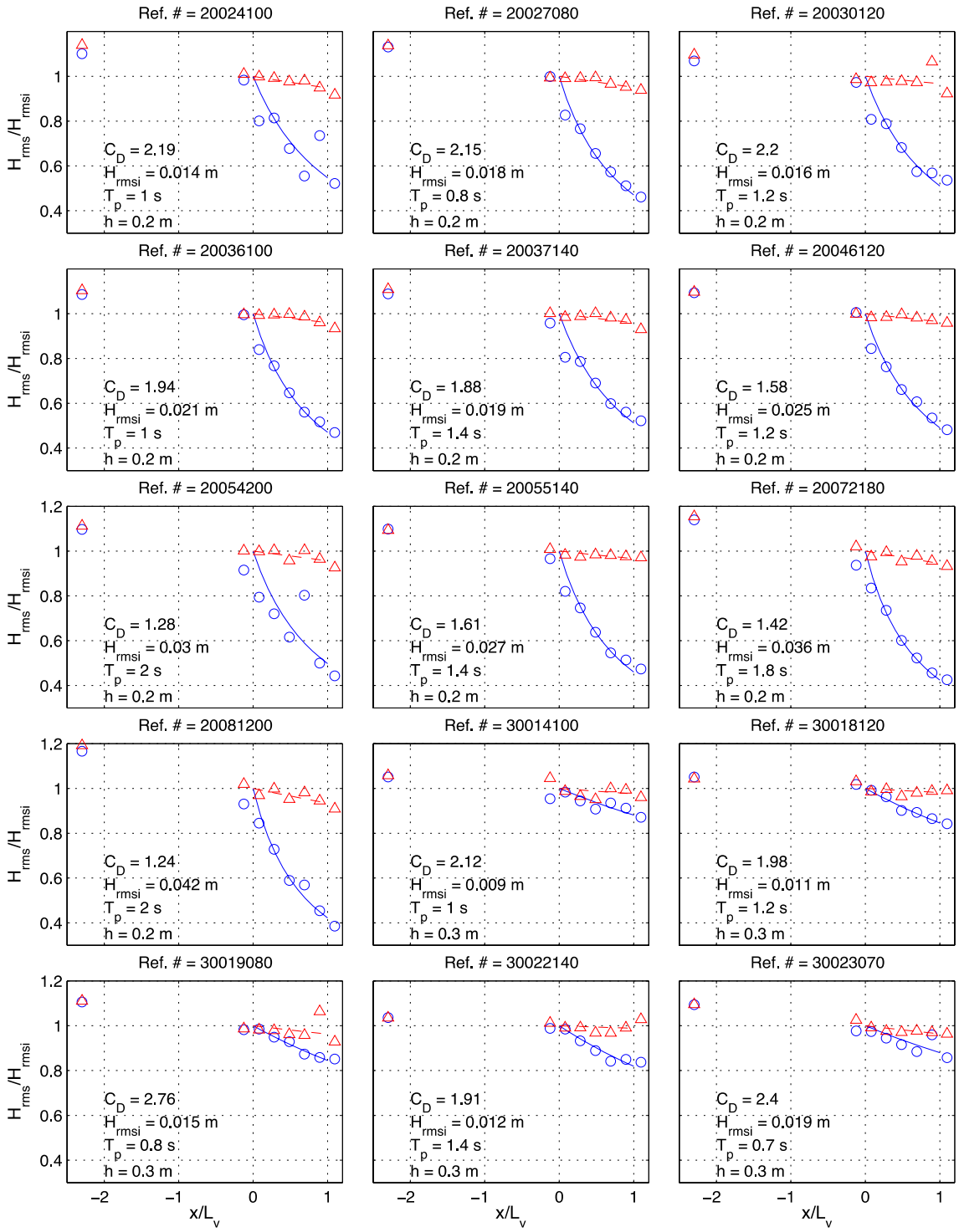

Fig. 2.15. Relative wave height distribution of irregular waves along the wave tank for non-vegetated and rigid model vegetation.

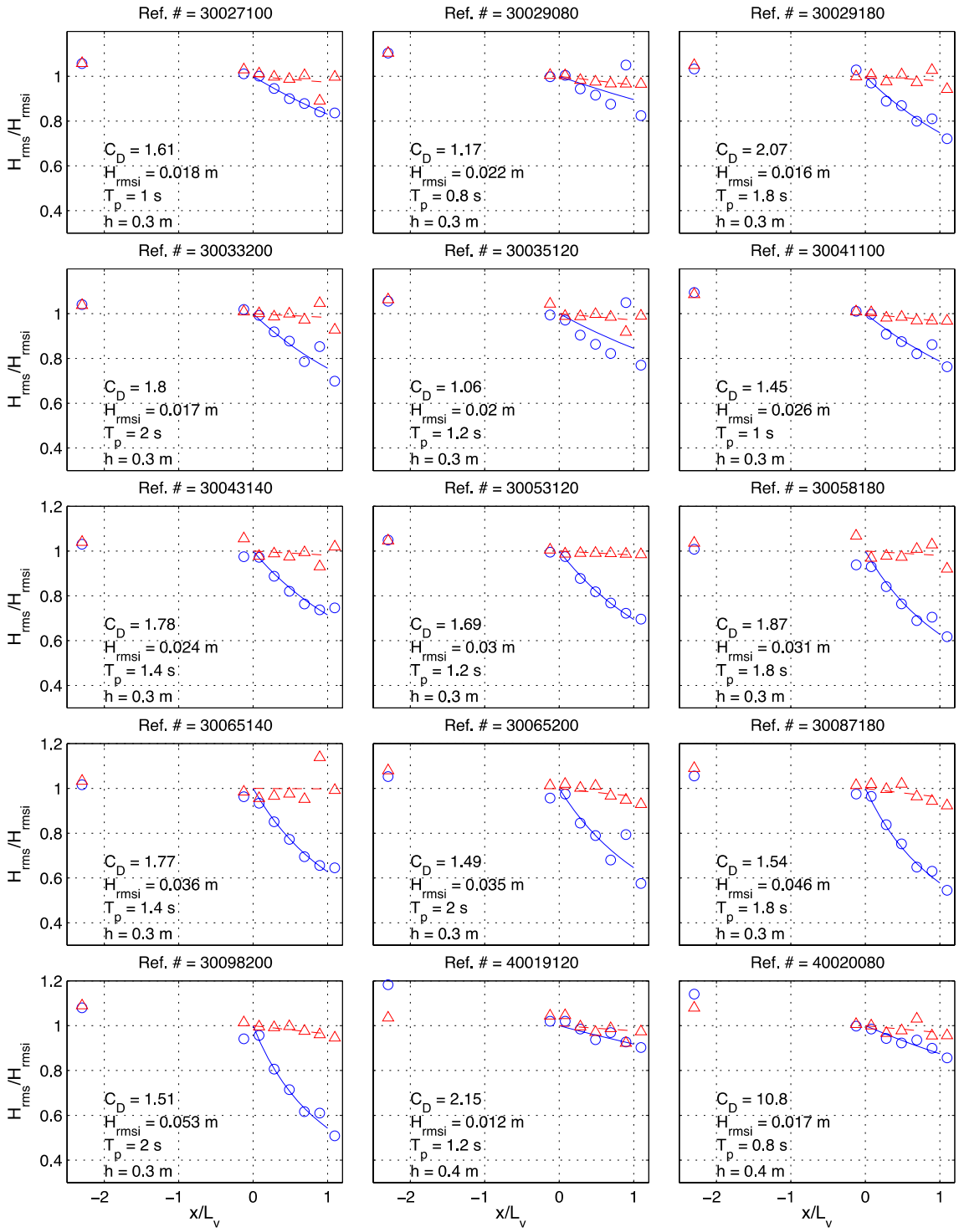

Fig. 2.15. Relative wave height distribution of irregular waves along the wave tank for non-vegetated and rigid model vegetation (continued).

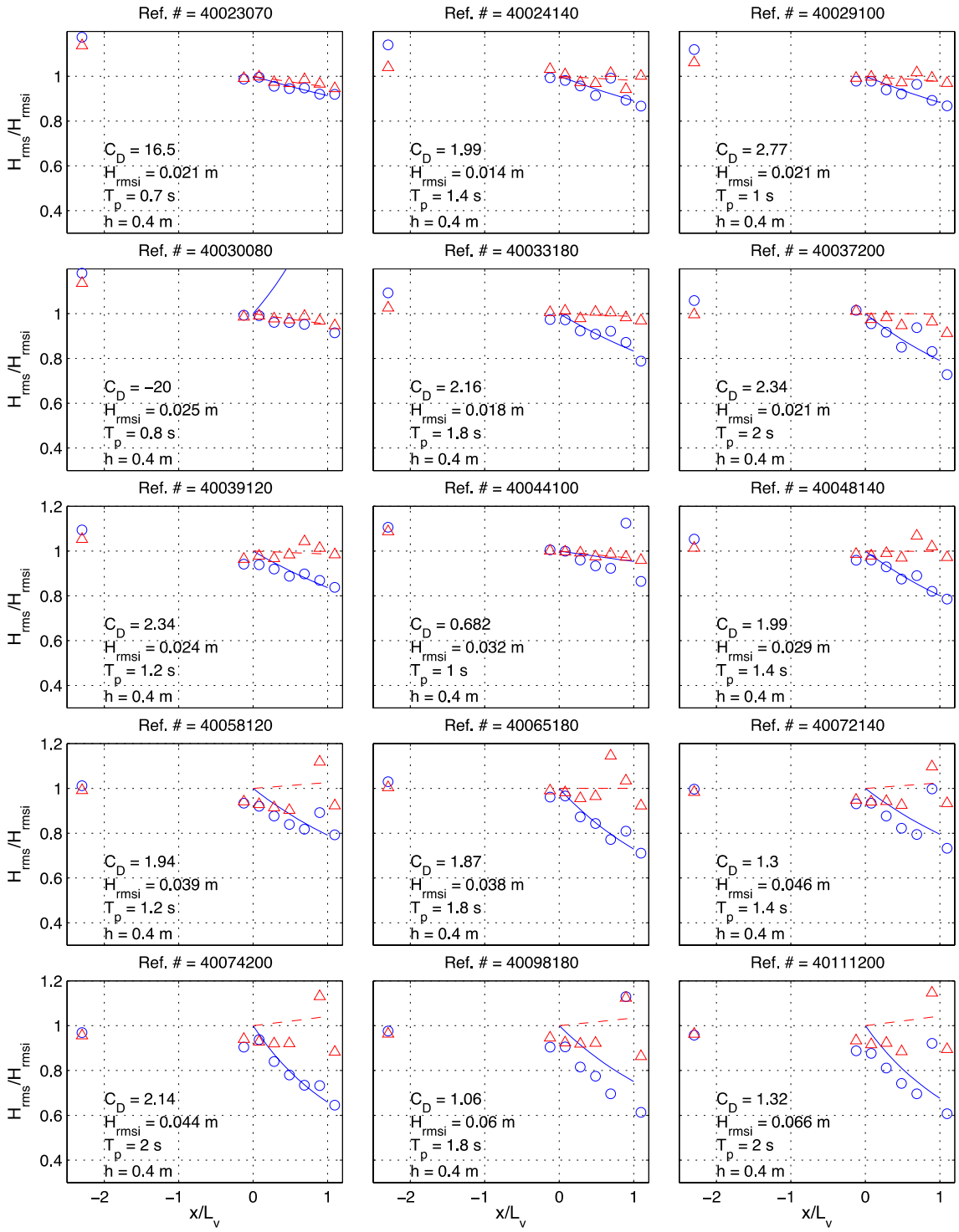

Fig. 2.15. Relative wave height distribution of irregular waves along the wave tank for non-vegetated and rigid model vegetation (continued).

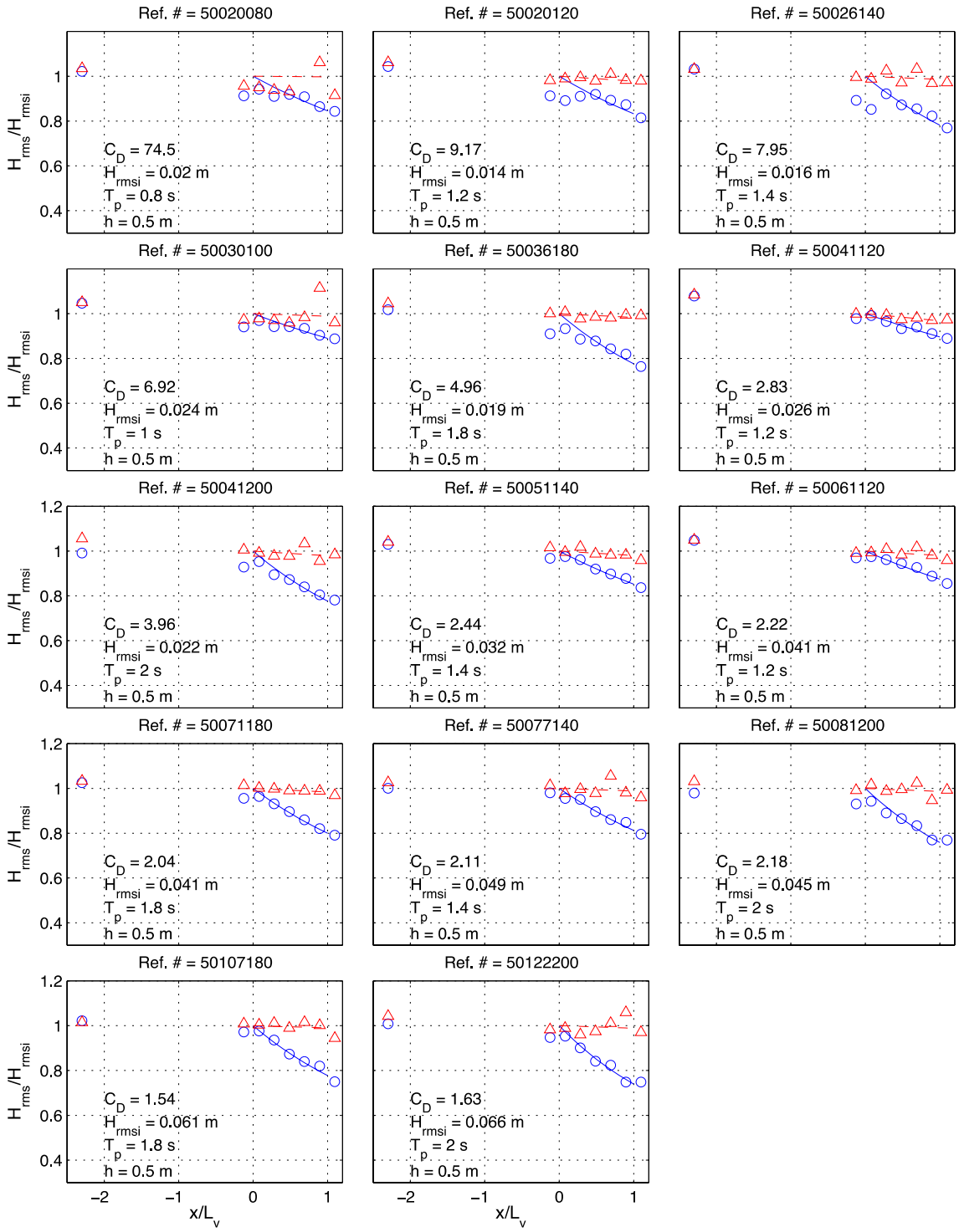

Fig. 2.15. Relative wave height distribution of irregular waves along the wave tank for non-vegetated and rigid model vegetation (continued).

Flexible model vegetation - irregular waves

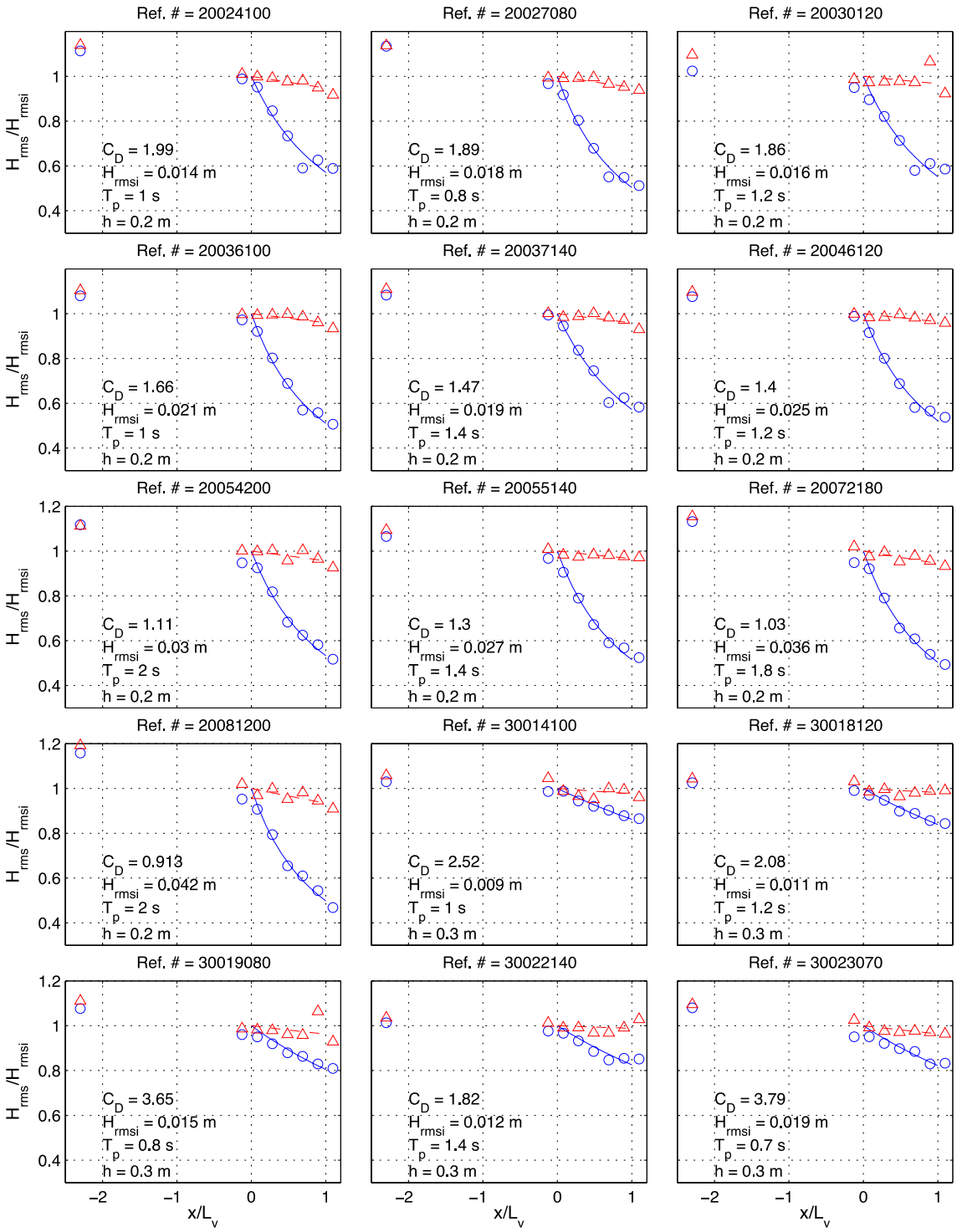

Fig. 2.16. Relative wave height distribution of irregular waves along the wave tank for non-vegetated and flexible model vegetation.

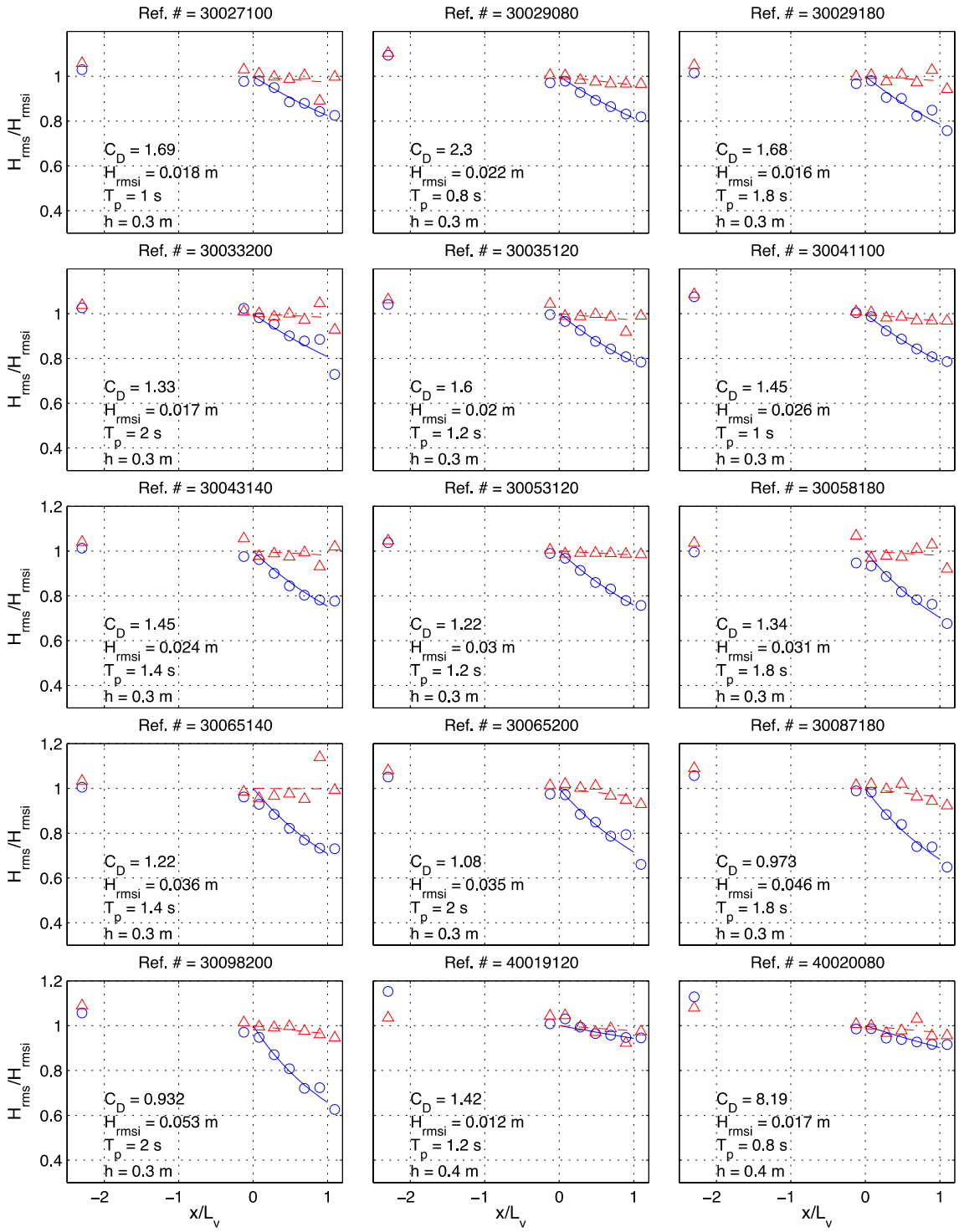

Fig. 2.16. Relative wave height distribution of irregular waves along the wave tank for non-vegetated and flexible model vegetation (continued).

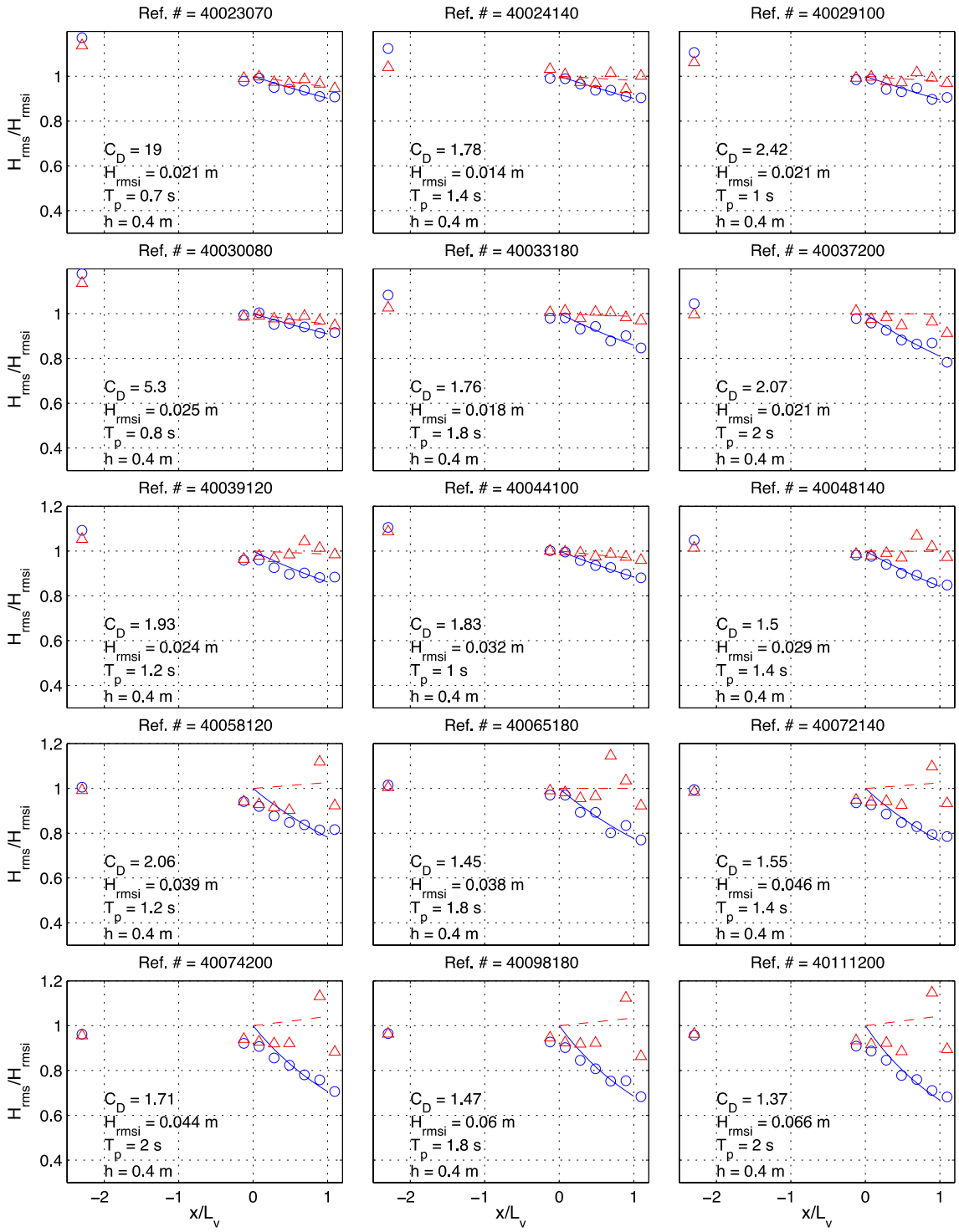

Fig. 2.16. Relative wave height distribution of irregular waves along the wave tank for non-vegetated and flexible model vegetation (continued).

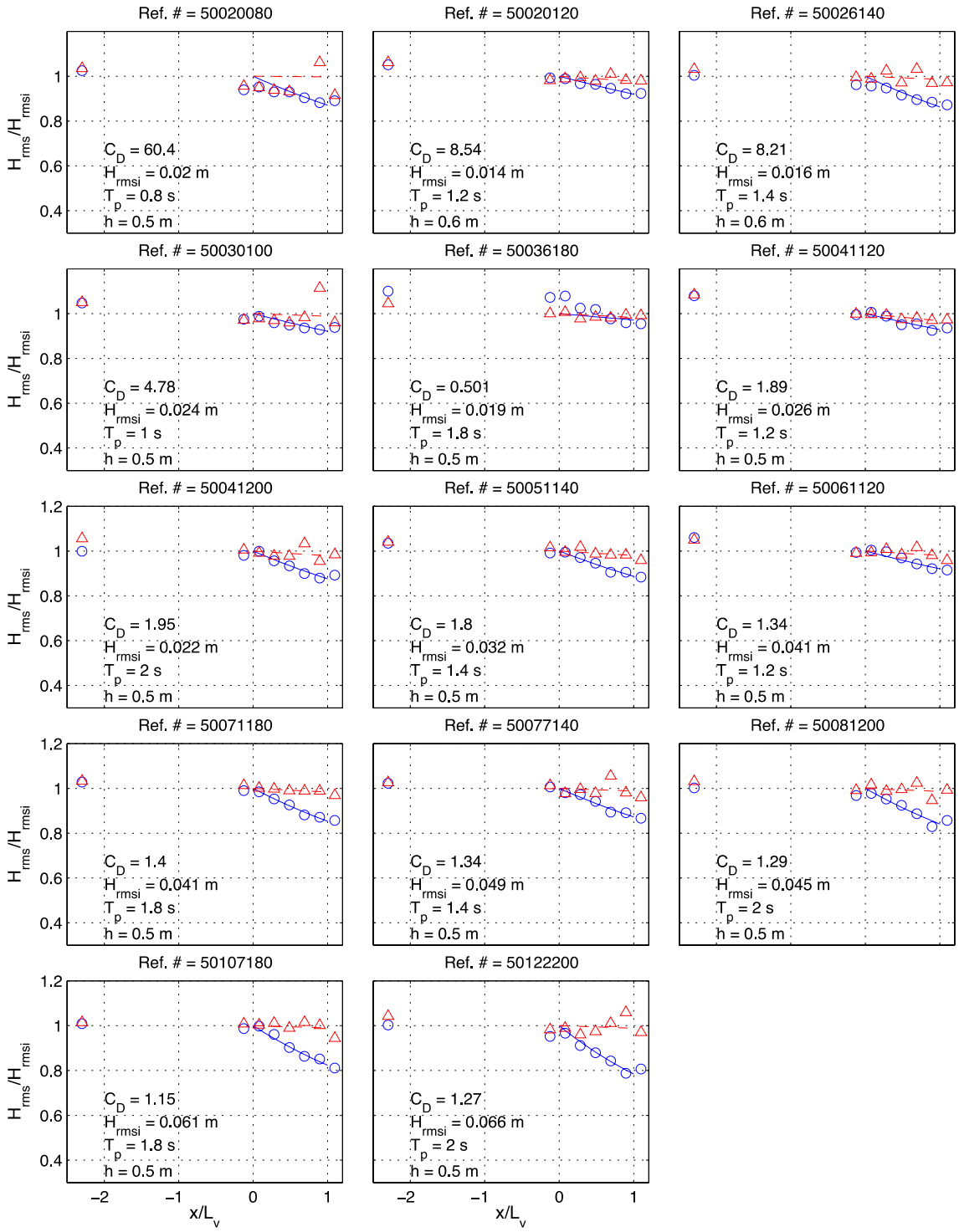

Fig. 2.16. Relative wave height distribution of irregular waves along the wave tank for non-vegetated and flexible model vegetation (continued).

2.3.2 Vegetated Sloping Beach

The waves start breaking as they approach the shoreline and dissipate most of their energy due to the turbulence generated. However, their momentum is transferred to the water column, resulting in a water surface slope. Wave setup is the water level rise due to the momentum transfer to the water column during the wave-breaking process and wave runup is the time varying fluctuation of the water surface elevation at the shoreline due to wave breaking (Fig. 2.17). Wave setup and run-up can contribute to the elevated water levels and almost double the elevation of water at the coast during extreme storm events. Dean and Bender (2006) have theoretically shown that vegetation can substantially reduce wave setup. The phenomenon of wave setup is still not fully understood and laboratory and field experiments are necessary to demonstrate the theory presented in Dean and Bender (2006).

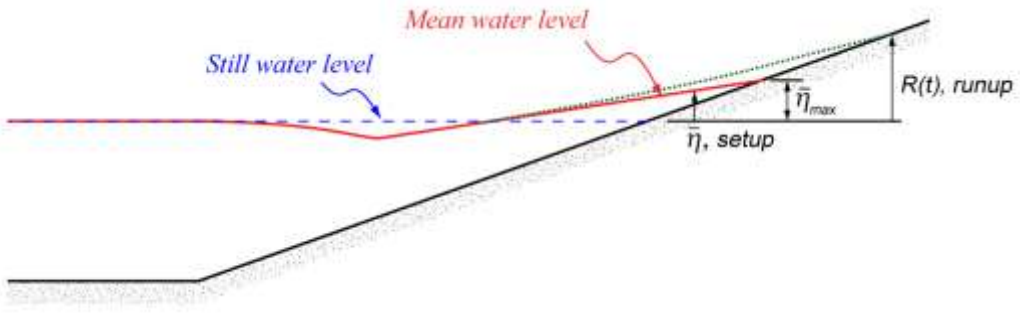

Fig. 2.17. Wave setup and run-up along a typical beach.

Initial wave setup experiments with rigid wooden dowels were based on neglecting plant motion. The results of the experiments with rigid model vegetation during the first phase of the project proved that wave setup can be significantly reduced when vegetation is present. It was also found that vegetation reduced wave heights and the wave breaking process (Fig. 2.6). The second phase of the laboratory work included wave-setup and wave-runup measurements over a plane sloping beach for three different scenarios: non-vegetated, rigid model vegetation and flexible model vegetation (Fig. 2.17).

Wave height transformation and wave setup was be measured by a series of movable capacitance type wave gauges and wave runup was measured by a fixed gauge attached to the sloping beach. The experiments included both regular and irregular waves. Each experiment corresponding to a wave condition (H (H_{m0}) and T (T_p) combination and vegetation configuration) and wave gauge arrangement was repeated three times for regular and five times for irregular waves. Six wave gauges (gauges at 7, 8,9,10,11 and 12 m) were repositioned four times along the wave tank in order to increase the spatial resolution of the wave measurements. The gauge at 3 m and runup gauge was fixed during these experiments for reference. The water depth was kept at 0.4 m for all runs. Fig. 2.18 shows photographs of the sloping beach for the non-vegetated, rigid model, and flexible model cases.

Relative wave height (H/H_i) and relative wave setup (η/H_i) profiles for non-vegetated plane beach, rigid vegetation and flexible vegetation are compared for regular waves in Fig. 2.19 and for irregular waves in Fig. 2.20. The wave heights and mean water levels in these plots are averaged over the repeated experiments. Fig. 2.21 shows the average wave spectra measured at each gauge location compared for three vegetation configurations.

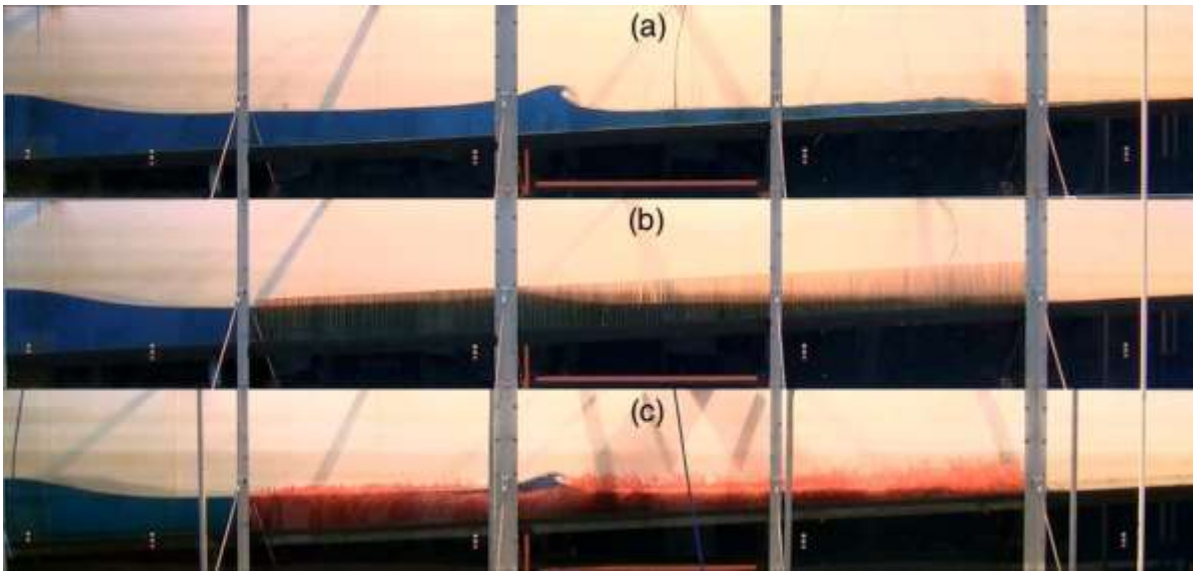

Fig. 2.18. Photograph of the wave flume with a sloping beach; (a) non-vegetated, (b) rigid model vegetation and (c) flexible model vegetation.

Both the rigid and flexible vegetation models significantly mitigated wave breaking and reduced wave setup. For smaller wave heights, no wave breaking was observed. As the waves propagate up a plane beach, they get steeper and steeper until they break. On a vegetated beach, however, wave attenuation avoids wave steepening and prevents wave breaking. The momentum of the wave train was balanced partially with the drag force, which reduced the wave setup. The plots with Ref. no. = 40028160 in Fig 2.21, for instance, clearly shows that waves were considerably attenuated along the vegetation (between 11.5 m and 15.2 m) as opposed to the non-vegetated plane beach. Therefore, no wave setup was observed during these experiments. It can also be seen that there was no significant difference between rigid and flexible vegetation in terms of wave height and mean water level (wave setup) evolution. When the wave steepness was increased, keeping the wave period constant (Ref. no. = 40100160), the wave setup and relative wave heights were higher due to partial wave breaking in the vegetation zone. The wave setup and wave heights were higher over the flexible vegetation than that of the rigid vegetation. This is mainly because flexible vegetation was free to deform with the waves. The flexible vegetation strips tested here were not stiff enough to stand under their own weight above the free surface, which reduced the mean vegetation height. Flat-bed experiments showed that the drag coefficient of the flexible vegetation was less than that of the rigid model vegetation, which is in agreement with the results of the sloping beach experiments. As the wave steepness increased further for the same wave period (Ref. no. 4014216), the wave height profiles of the rigid and flexible vegetation approached that of the plane beach, while the wave setup of the rigid vegetation was nearly zero. The setup in the presence of the flexible vegetation was much less than that of the plane beach experiments. The results of the random wave experiments were also similar, indicating that vegetation can reduce wave setup and run-up considerably even when there is wave breaking.

2.4 Summary

The second phase of the laboratory work included the interaction of the regular and irregular waves with submerged rigid and flexible artificial vegetation. Free surface displacement was measured using eight capacitance type wave gauges and a video camera. Bulk drag coefficients were estimated for rigid and flexible artificial vegetation. Furthermore, wave setup and runup were measured in a laboratory wave flume on a sloping beach profile for non-vegetated, rigid vegetation, and flexible vegetation for both regular and irregular waves.

The main findings can be summarized as follows:

- There was a good correlation between bulk drag coefficient (C_D) and both Reynolds number (Re) and Keulegan-Carpenter number (K_c) for both rigid and flexible vegetation and, in regular and irregular wave conditions.
- K_c provided a better fit for both of the models compared to that of Re. The data for rigid model vegetation in the first and second phases of the project followed the same trend when plotted against K_c.
- Video measurements provided a detailed distribution of wave height through the vegetation models and were consistent with the gauge measurements.
- There was no apparent dependency on of C_D on relative plat height (h_v/h) for both rigid and flexible vegetation models.
- Rigid and flexible vegetation have similar drag coefficients for large values of K_c, although drag coefficient is always slightly higher for the rigid case.
- Both rigid and artificial vegetation significantly dampened wave height and reduced wave setup but in general, rigid vegetation performed better in reducing wave setup.
- On a vegetated sloping beach the momentum of the waves was balanced with the drag force which prevented wave setup even when there was partial wave breaking.

Wave setup experiments – regular waves

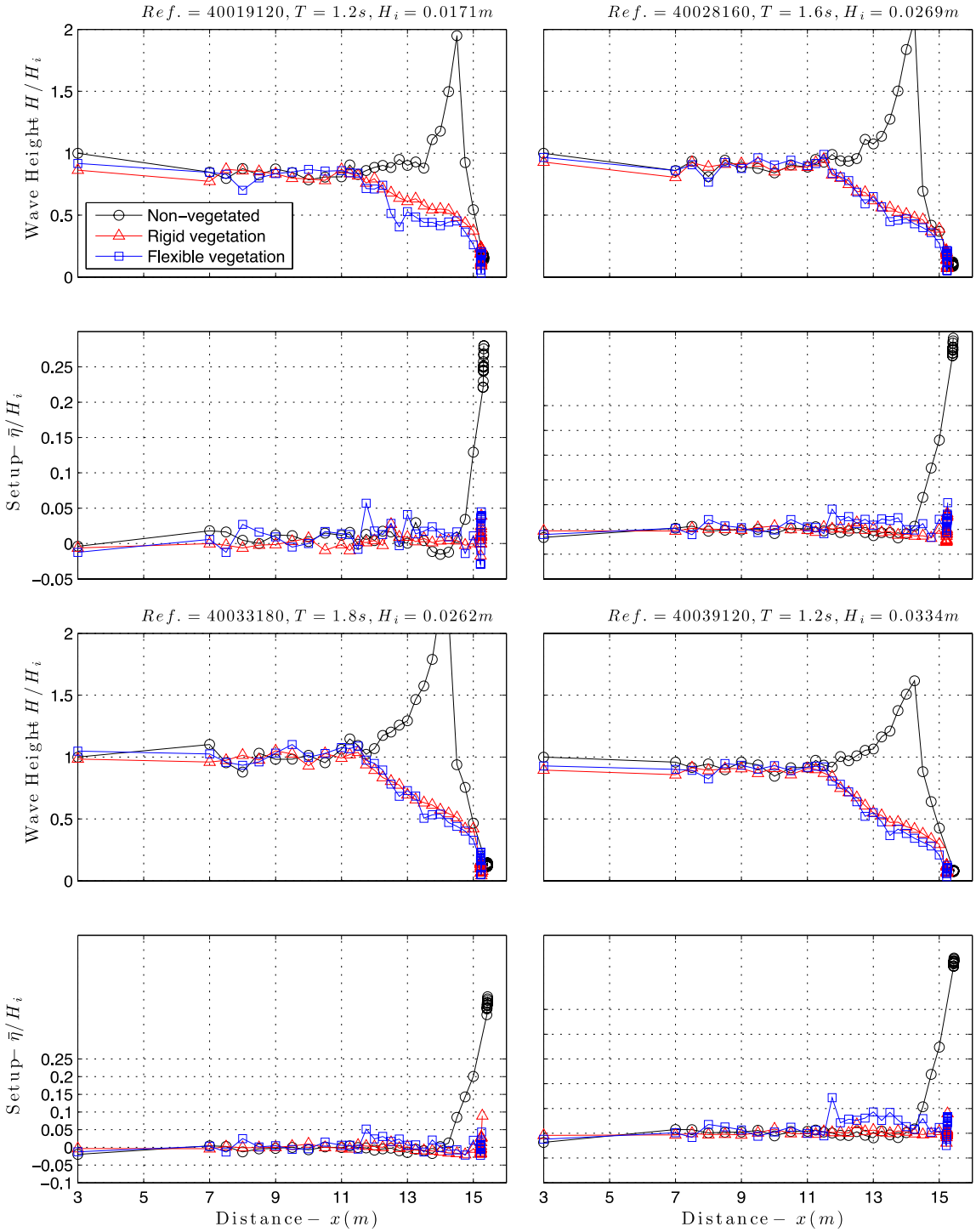

Fig. 2.19. Wave height transformation and mean water level along the plane sloping beach for non-vegetated and rigid model vegetation in regular waves.

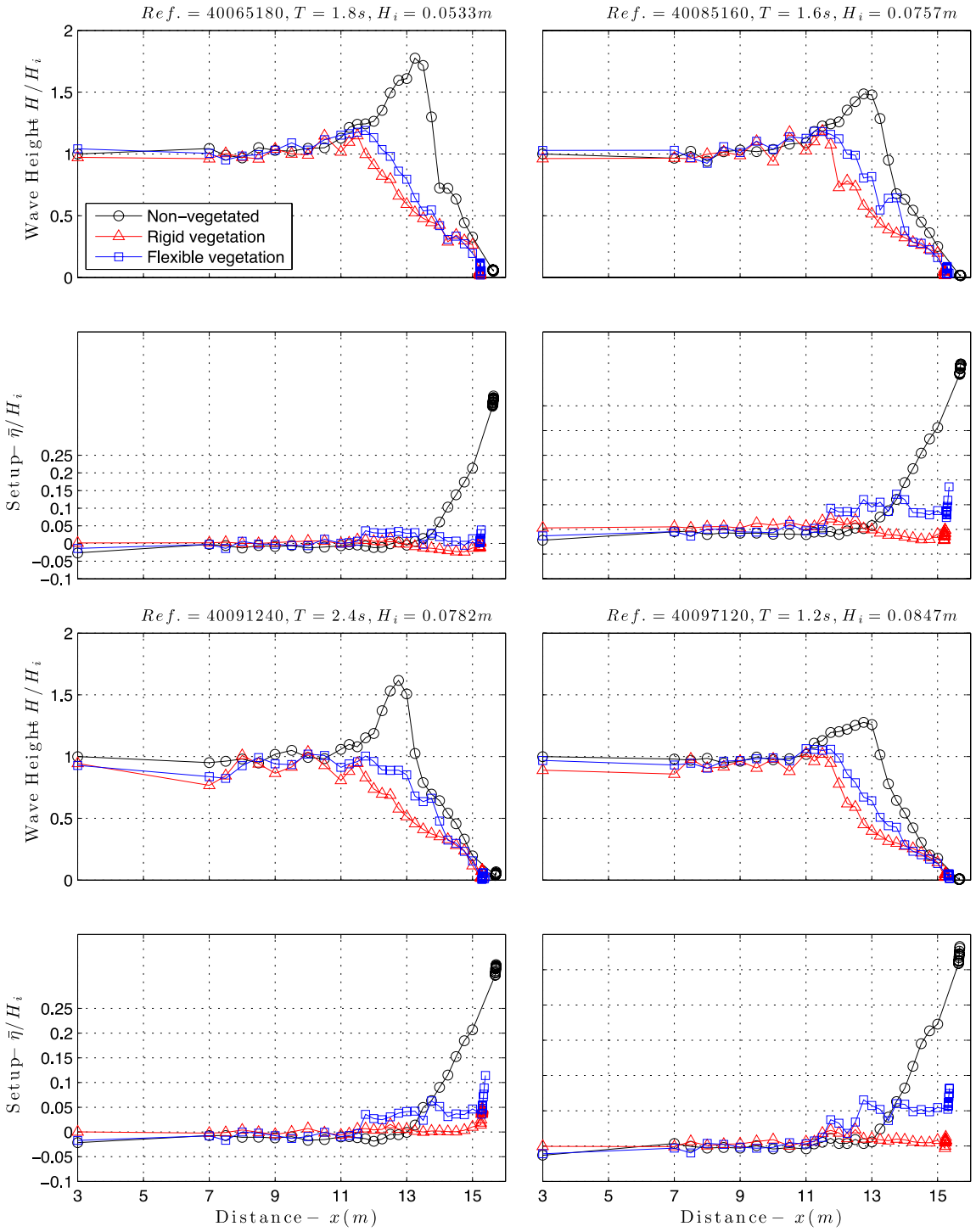

Fig. 2.19. Wave height transformation and mean water level along the plane sloping beach for non-vegetated and rigid model vegetation in regular waves (continued).

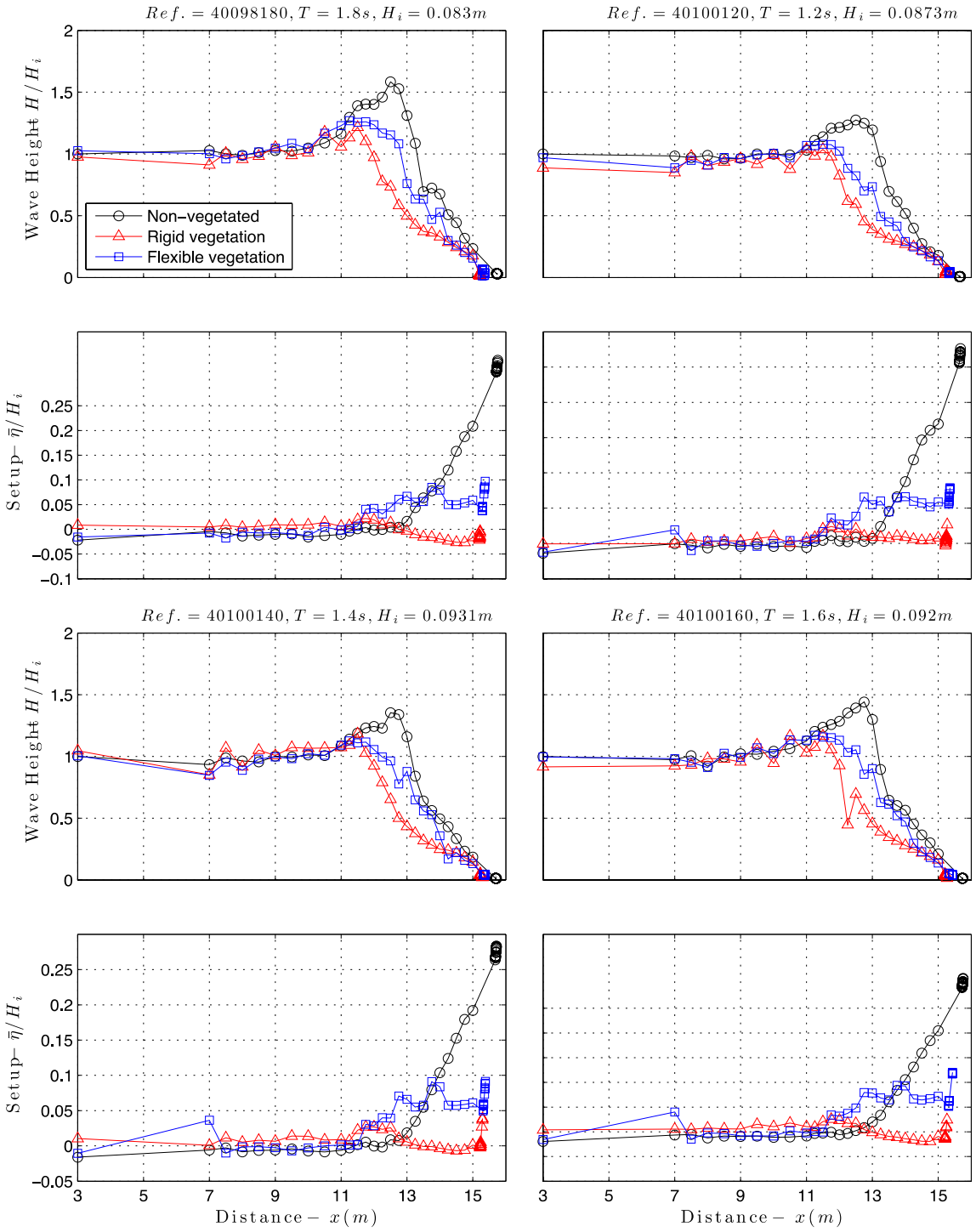

Fig. 2.19. Wave height transformation and mean water level along the plane sloping beach for non-vegetated and rigid model vegetation in regular waves (continued).

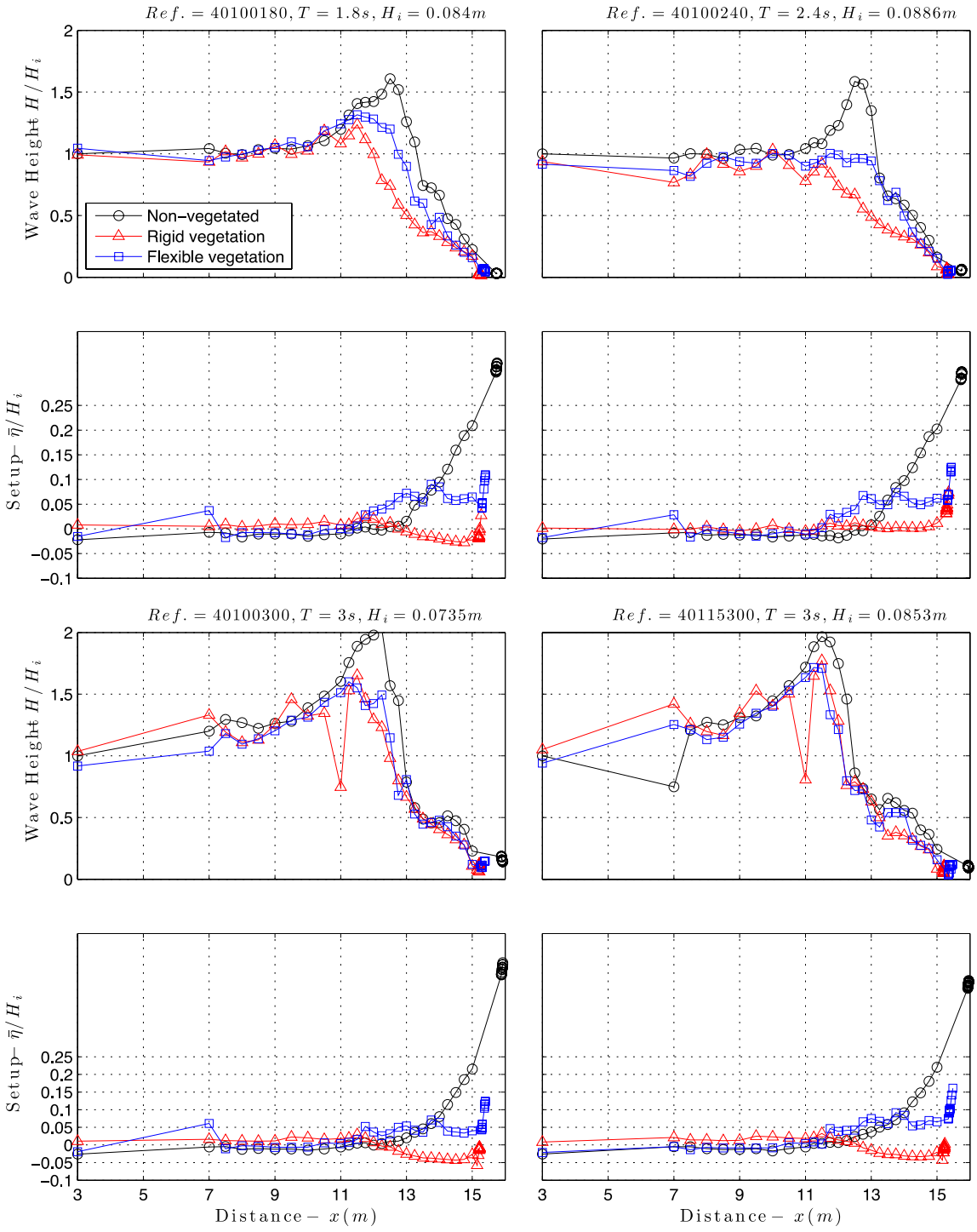

Fig. 2.19. Wave height transformation and mean water level along the plane sloping beach for non-vegetated and rigid model vegetation in regular waves (continued).

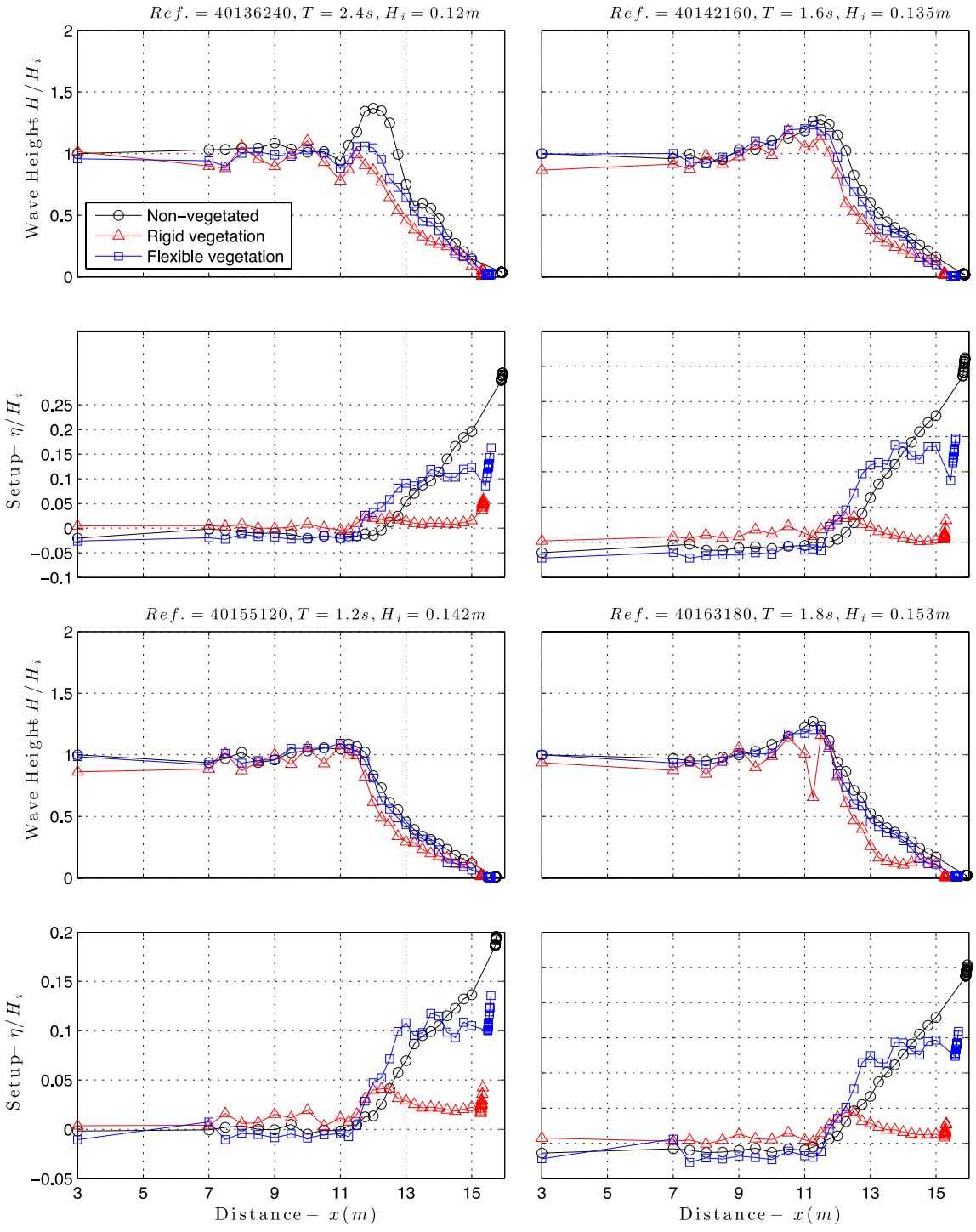

Fig. 2.19. Wave height transformation and mean water level along the plane sloping beach for non-vegetated and rigid model vegetation in regular waves (continued).

Wave setup experiments – irregular waves

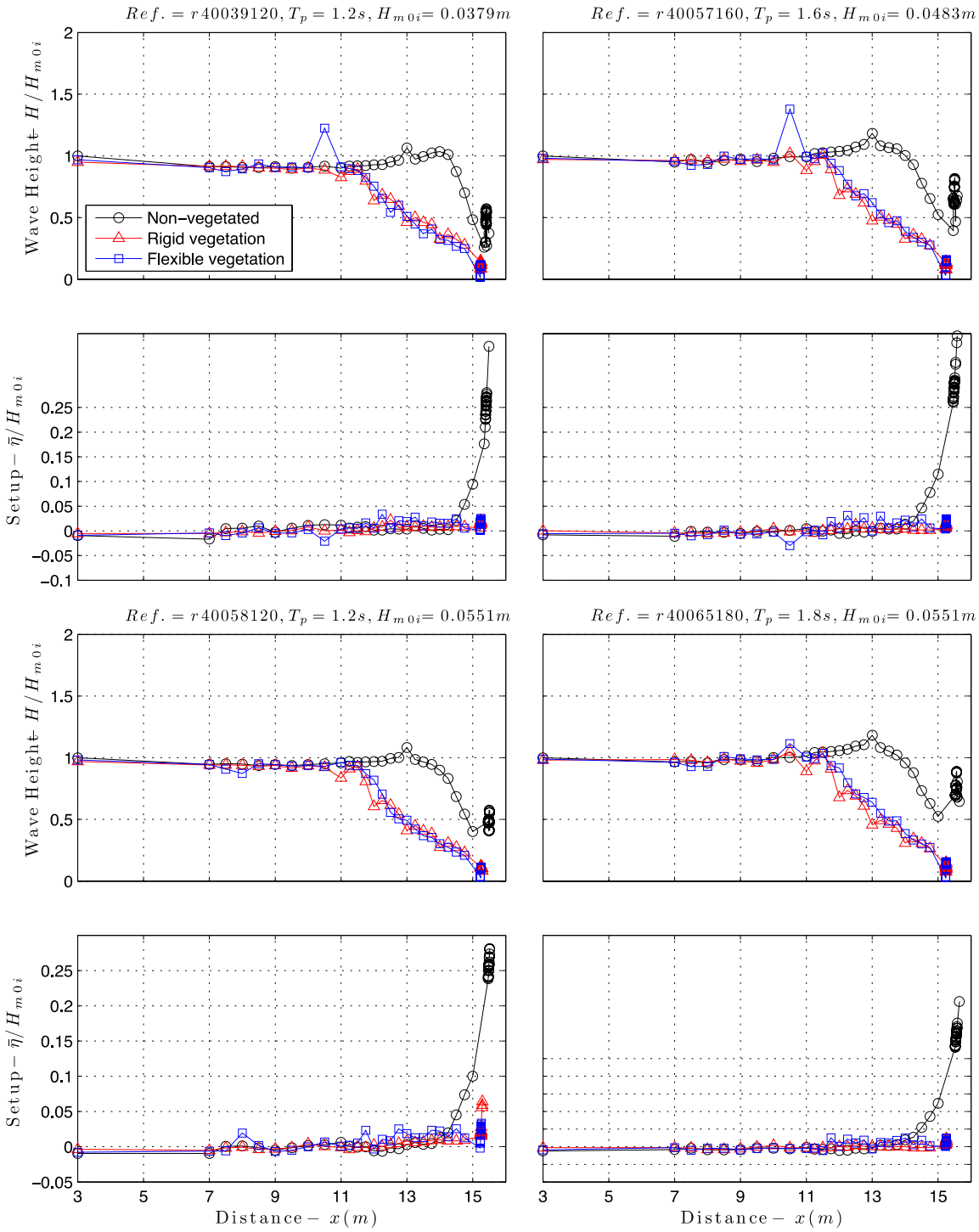

Fig. 2.20. Wave height transformation and mean water level along the plane sloping beach for non-vegetated and rigid model vegetation in irregular waves.

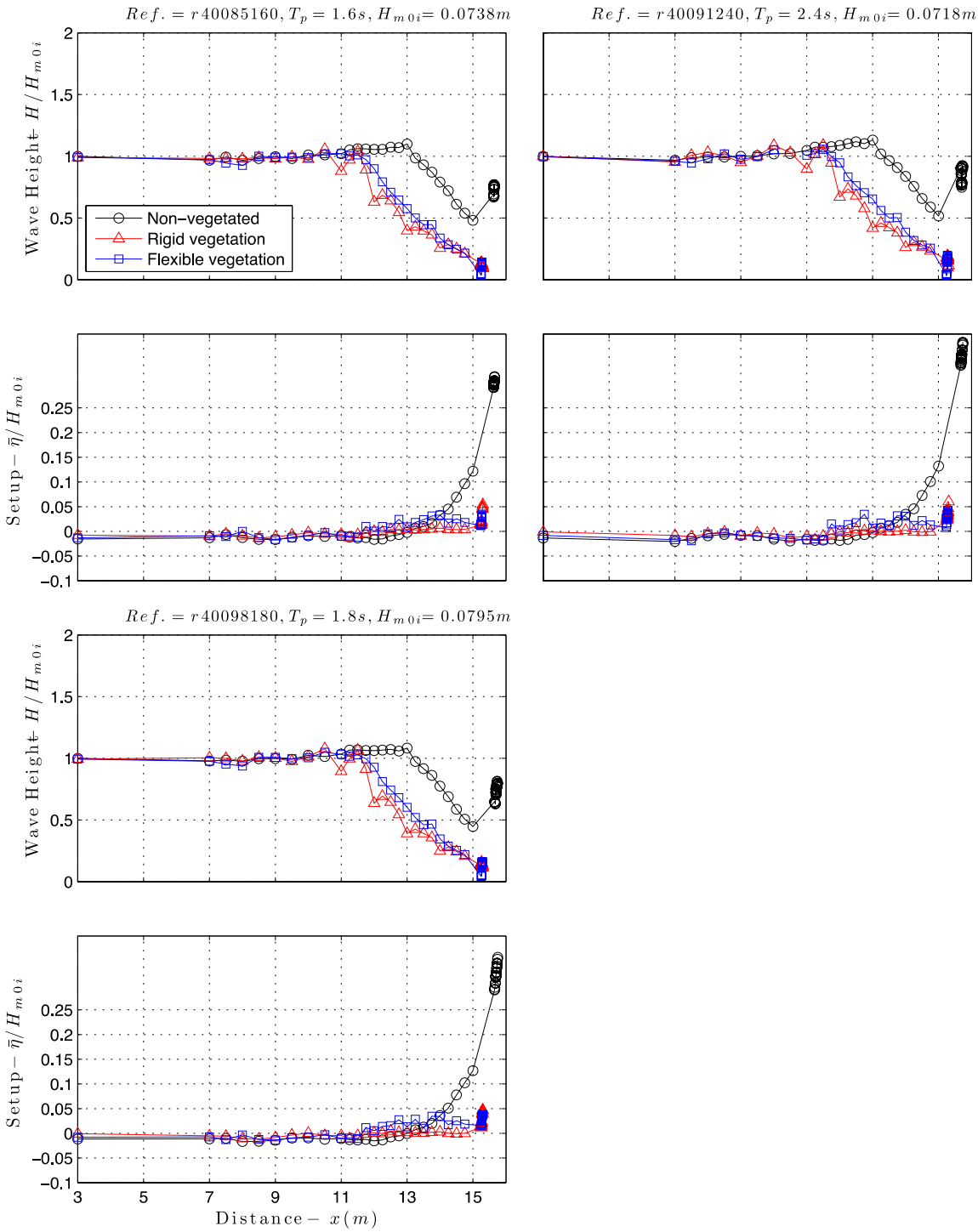

Fig. 2. 20. Wave height transformation and mean water level along the plane sloping beach for non-vegetated and rigid model vegetation in irregular waves (continued).

Wave setup experiments – irregular waves

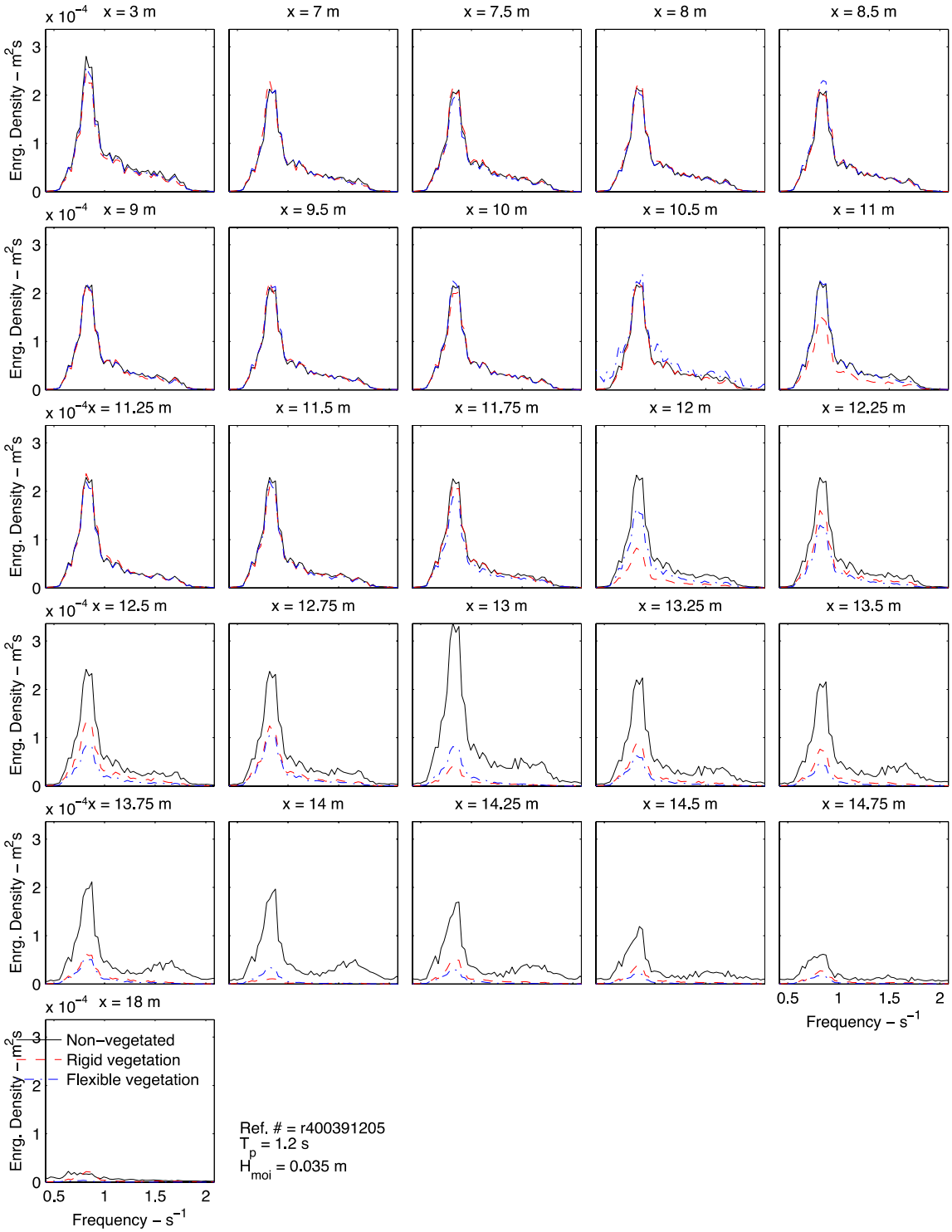

Fig. 2.21. Spectra for irregular waves over the vegetated and non-vegetated sloping beach.

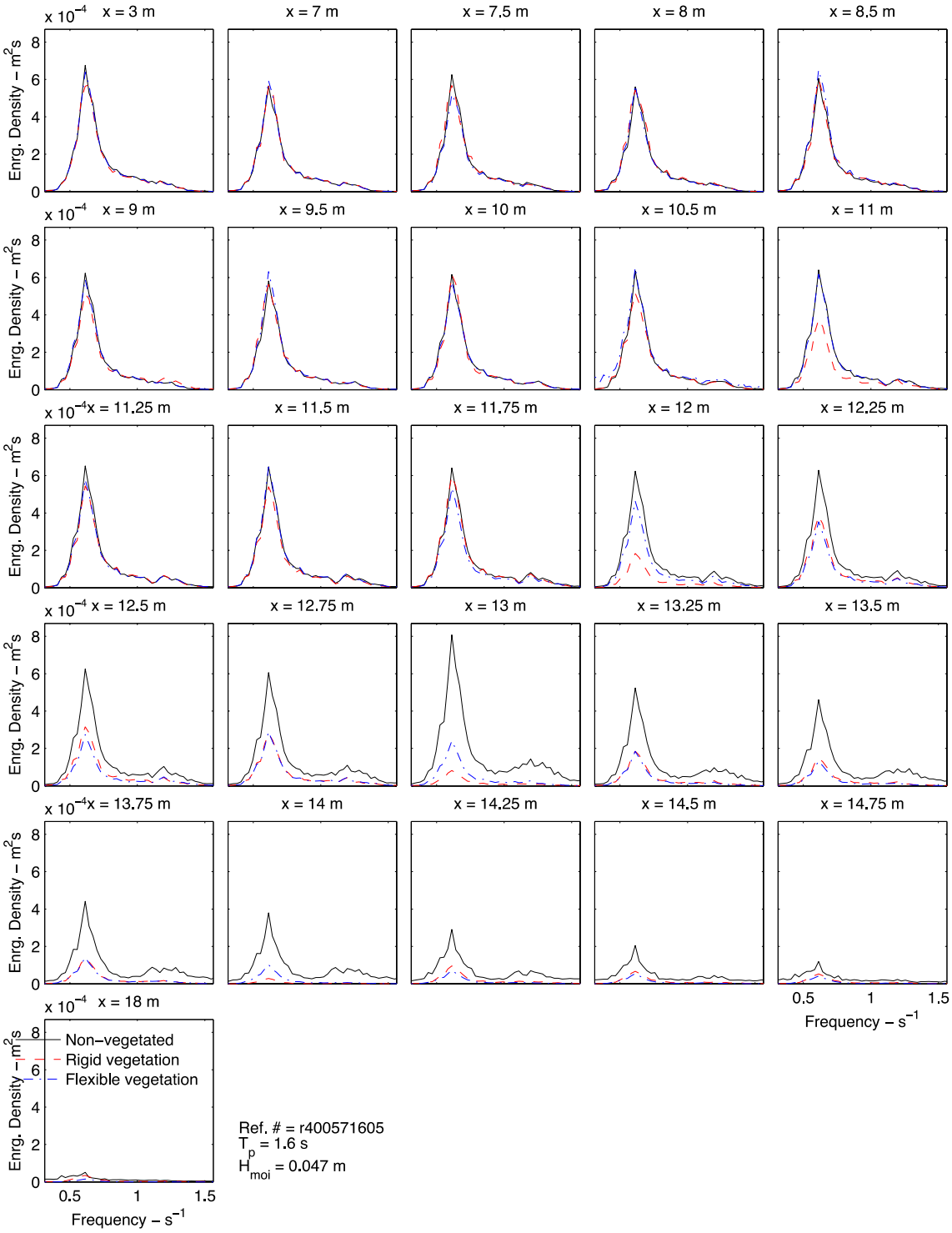

Fig. 2.21. Spectra for irregular waves over the vegetated and non-vegetated sloping beach (Continued).

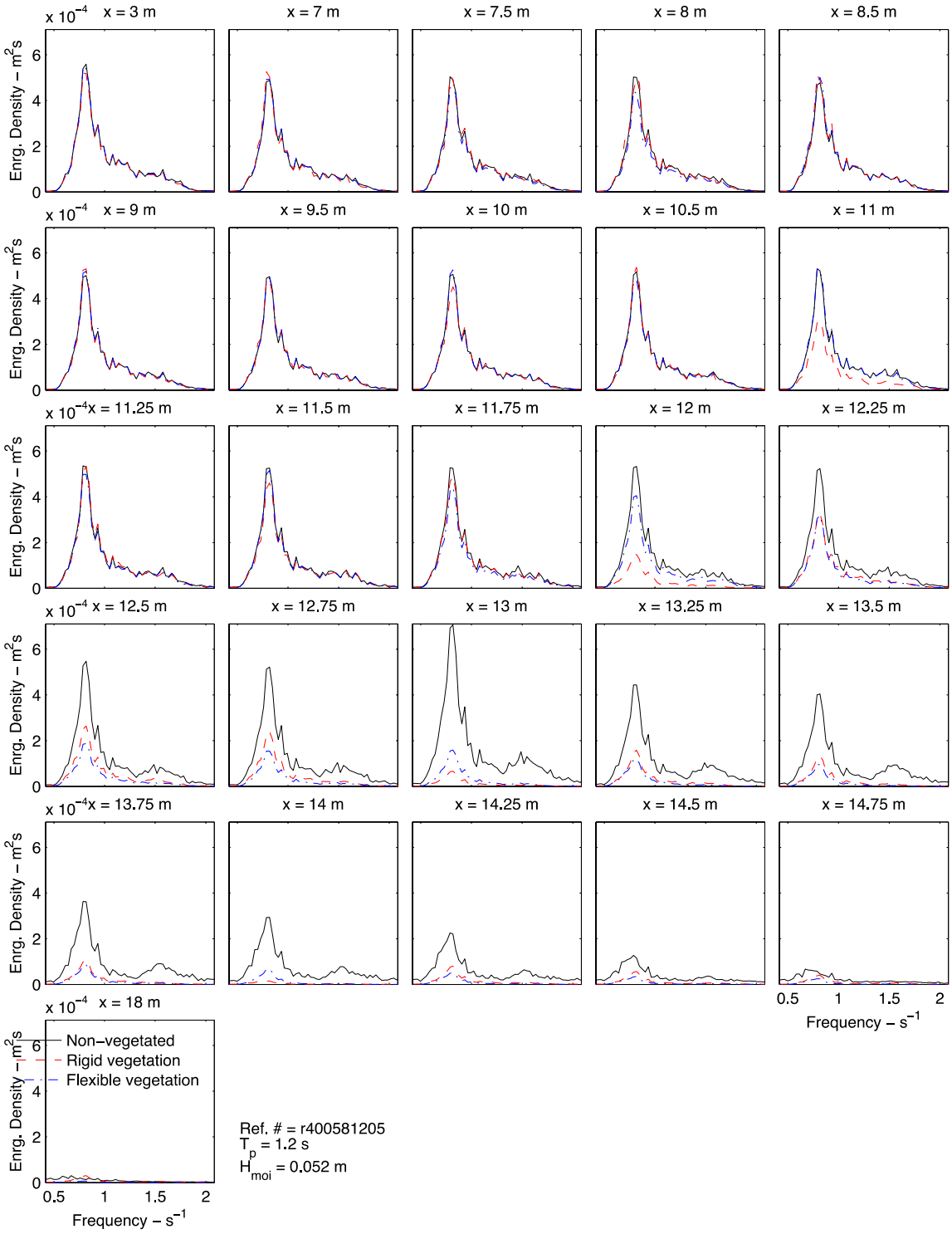

Fig. 2.21. Spectra for irregular waves over the vegetated and non-vegetated sloping beach (Continued).

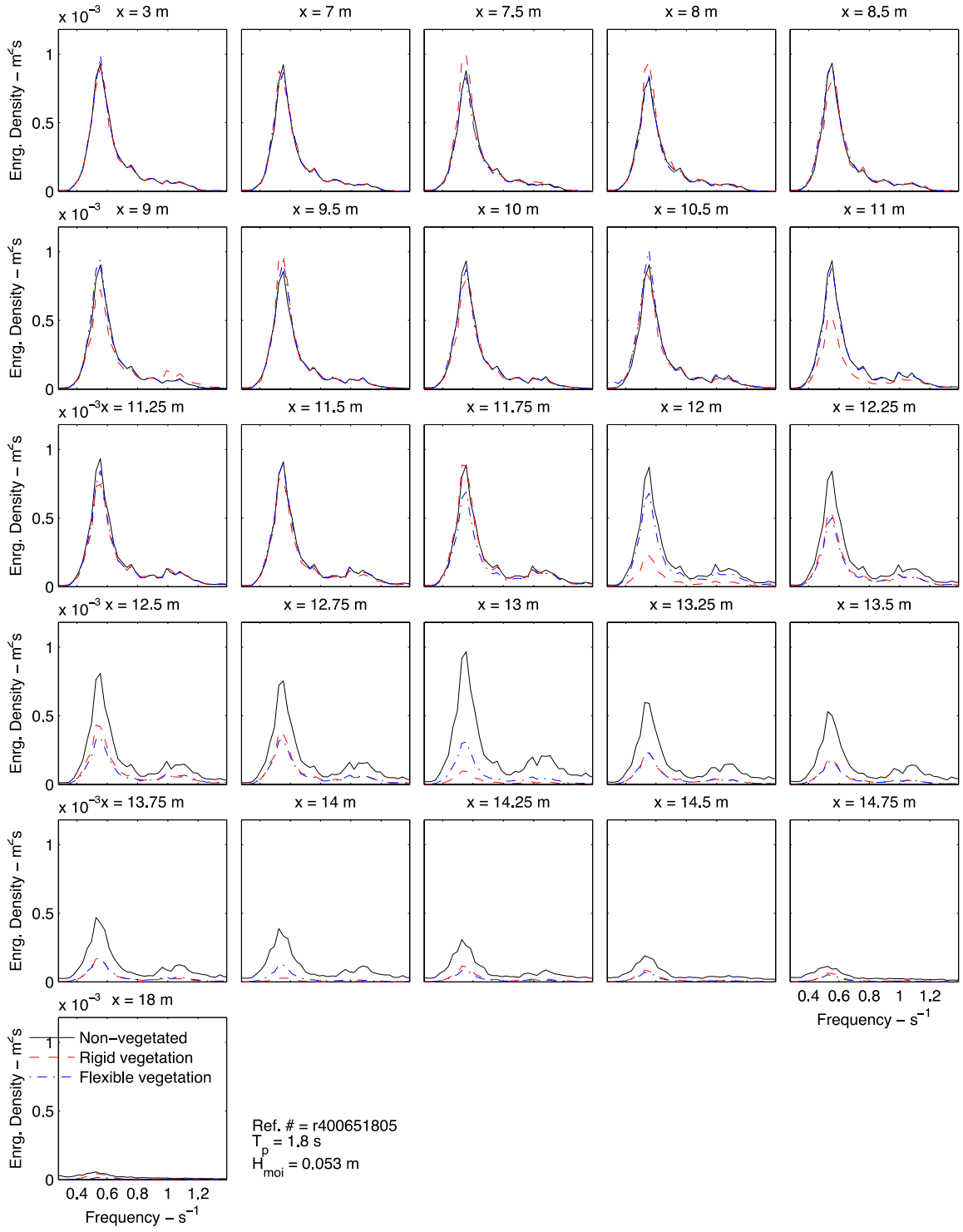

Fig. 2.21. Spectra for irregular waves over the vegetated and non-vegetated sloping beach (Continued).

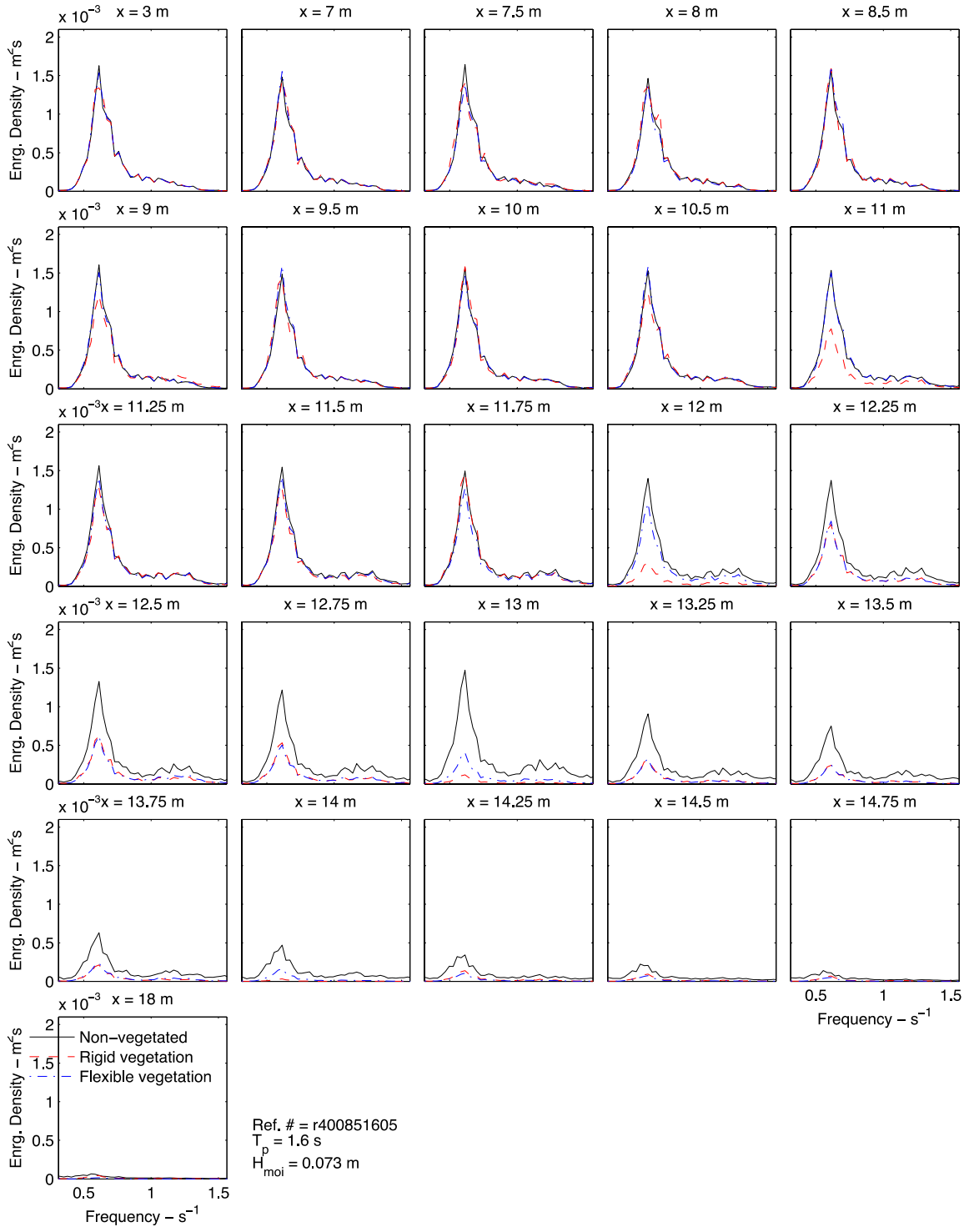

Fig. 2.21. Spectra for irregular waves over the vegetated and non-vegetated sloping beach (Continued).

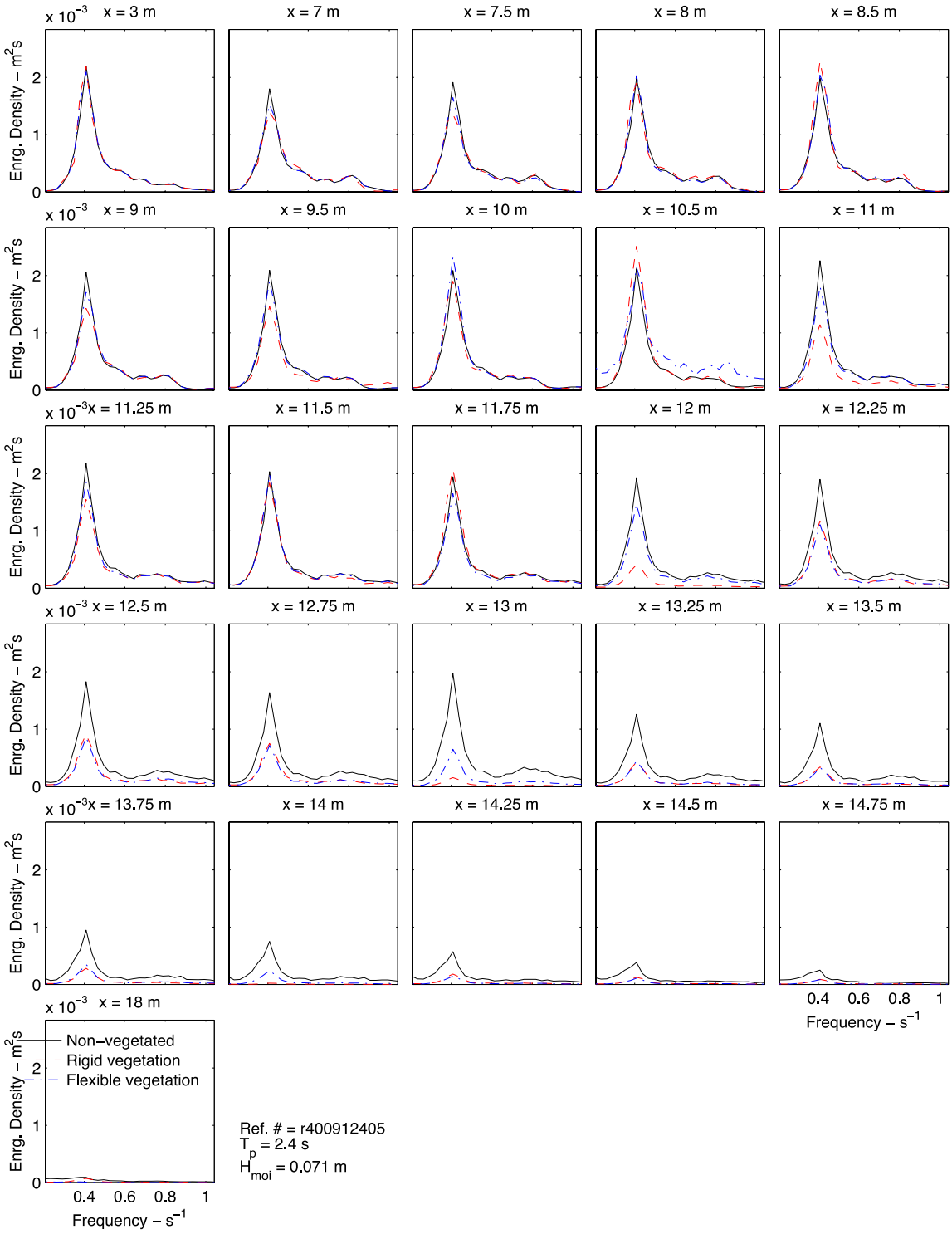

Fig. 2.21 Spectra for irregular waves over the vegetated and non-vegetated sloping beach (Continued).

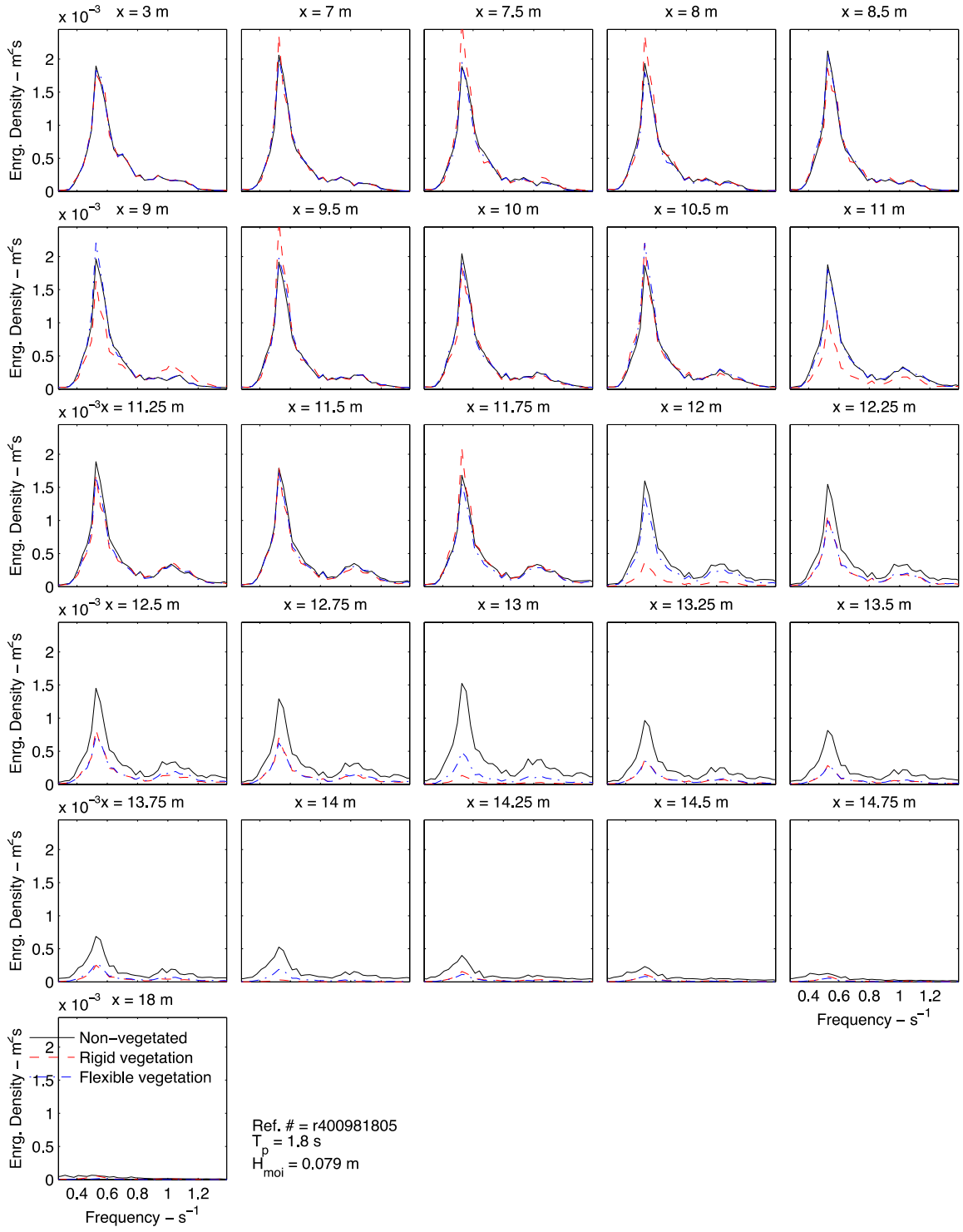

Fig. 2.21. Spectra for irregular waves over the vegetated and non-vegetated sloping beach (Continued).

3. FIELD INVESTIGATIONS OF WAVE AND SURGE ATTENUATION BY VEGETATION

The field investigations conducted by the Louisiana State University (LSU) team in Phase I consisted of two campaigns: (1) measurements of waves and surge using rapidly deployed devices during hurricanes and tropical storms on their landing sites, and (2) measurements of waves using devices installed on fixed sites during winter fronts. In Phase II, the team continued and expanded the efforts and analyzed in-depth the collected data. Wave data were collected over a two-day period (September 3-4, 2011) at a salt marsh wetland in Terrebonne Bay on the Louisiana coast of the Gulf of Mexico during Tropical Storm Lee. A field campaign to measure waves and bottom currents near the marsh edge on a vegetated wetland in south Louisiana was successfully conducted from April 12 to April 20, 2012 during a cold front passage. The collected data were used to assess wave attenuation by vegetation and calibrate the vegetation drag coefficient in two wave energy dissipation models. The field campaigns, collected data, theoretical models and obtained results are presented in this chapter.

3.1 Wave Attenuation by Salt Marsh Vegetation during Tropical Cyclone

3.1.1 Introduction

Coastal wetlands have been recognized as a natural defense against damage from storm surge and waves (e.g., Dixon et al., 1998; Costanza et al., 2008; Lopez, 2009; Gedan et al., 2011). There has been increased interest among scientists, engineers, and policy makers in utilizing coastal wetlands to supplement traditional structural measures used to mitigate coastal flooding from storm surge and waves (e.g., Borsje et al., 2011; CPRA, 2012). To assess the effectiveness of coastal wetlands in wave reduction, an improved understanding of wave transformation over vegetation under storm conditions is needed. Existing literature on wave propagation over wetland vegetation consists of several theoretical and experimental studies. Summaries of these studies can be found in Irish et al. (2008), Anderson et al. (2011) and Wu et al. (2011).

Dalrymple et al. (1984) presented the first theoretical model of wave energy dissipation assuming plants as rigid cylinders that exert drag force on the monochromatic waves. Kobayashi et al. (1993) presented an approach based on continuity and momentum equations demonstrating exponential wave height decay. The Dalrymple et al. (1984) formulation was extended by Mendez et al. (1999) and Mendez and Losada (2004) for irregular waves. Chen and Zhao (2012) examined existing wave energy dissipation formulations and proposed two new models. The first model was based on the model of energy dissipation of random waves by bottom friction developed by Hasselmann and Collins (1968). The second model was based on the joint probability distribution of wave heights and wave periods. Lowe et al. (2005a) developed a theoretical model of monochromatic wave flow structure inside a model canopy of rigid cylinders based on momentum balance, and demonstrated that wave orbital excursion was the single relevant parameter affecting flow attenuation inside the canopy. Lowe et al. (2007) extended this model to random wave conditions, and evaluated its performance in the field by submerging the artificial rigid cylinder canopy on a reef under random waves. They confirmed that the shorter-wave velocity components penetrate the canopy more efficiently,

and result in more energy loss over the same distance, compared with the longer-wave velocity components.

In a controlled laboratory environment, wave propagation through vegetation has been studied by Dubi and Tørum (1996), Løvås and Tørum (2001), Augustin et al. (2009), Chakrabarti et al. (2011), and Stratigaki et al. (2011), among others. Field investigations of waves over vegetation have been carried out in a variety of environments, including salt marshes (Möller et al., 1999; Möller and Spencer, 2002; Cooper, 2005; Möller, 2006; Bradley and Houser, 2009; Mullarney and Henderson, 2010), coastal mangrove forests (Mazda et al., 2006; Quartel et al., 2007), and vegetated lakeshores (Lövstedt and Larson, 2010). All of these studies show varying degrees of wave attenuation, depending on the vegetation types and wave environment. Wave attenuation by salt marshes has been reported to be anywhere from 50% (Möller et al., 1999) to 100% (Cooper, 2005) greater than that over mudflats. In coastal mangroves, wave attenuation has been reported to be 5 times more than that due to bottom friction alone (Quartel et al., 2007). In general, waves over vegetation have been observed to decay exponentially with the distance travelled.

Some of these studies have explored specific mechanisms related to wave-vegetation interaction. For example, Bradley and Houser (2009) examined the role of oscillatory seagrass blade movement in wave attenuation. At lower orbital velocities, blades were observed to sway over the entire wave cycle while at higher orbital velocities, the blades extended in the direction of flow for the longer part of the cycle, becoming streamlined, which resulted in reduced drag and therefore lesser attenuation. Mullarney and Henderson (2010) derived and field-tested an analytical model for the wave-induced movement of single-stem vegetation treated as an Euler-Bernoulli problem for a cantilevered beam. During field tests, vegetation stem motion was observed to lead water motion. The phase difference of motions decreased with increase in wave frequency. For moderately flexible stems, the model predicted total wave energy dissipation equivalent to about 30% of the dissipation for an equivalent rigid stem. Riffe et al. (2011) applied this flexible vegetation model to demonstrate improvement in the predicted wave energy dissipation when vegetation motion is simulated. Lövstedt and Larson (2010) examined wave attenuation and transformation of wave height distribution by reeds in a shallow lake. In their study, a commonly assumed Rayleigh distribution for random variation in wave height was observed to change significantly only under conditions of longer wave propagation distances and higher waves.

Although several field studies have quantified the rate of wave height attenuation and demonstrated the utility of wetlands as a measure for reducing impacts of waves, they have been carried out in low-energy environments with exception of Möller and Spencer (2002). Smith et al. (2011) describe the challenges of measuring storm induced waves in coastal wetlands based on their attempt during Hurricane Gustav (2008), and emphasize the need of such measurements. Table 3.1 shows ranges of wave heights under which some of the more recent field studies were performed. The table also lists some laboratory studies that have developed empirical relationships for drag coefficients. The validity of extrapolating these results to a high-energy environment is uncertain, limiting the utility of the current knowledge. Note that the parameter, drag coefficient, C_D, in Table 3.1 represents the "bulk" value over the measurement transect (vegetation patch) of a given study rather than the drag coefficient of an idealized isolated, cylinder.

Table 3.1. Wave and vegetation parameters and empirical relations of C_D in recent studies

Study and location	Waves (Random unless otherwise stated)	Vegetation	Transect	Empirical relationship
Kobayashi et. al. (1993) based on Asano et al. (1988); Laboratory	Monochromatic h=0.45,0.52 m H=0.036-0.194 m T_p=0.7-2 s	Artificial kelp h_v=25 cm b_v=5.2 cm Thickness=0.003 cm N_v=1100-1490 /m²	6 m (gages 2 m apart)	$C_D = 0.08 + \left(\frac{2200}{R_e}\right)^{2.4}$ 2,000<R_e<18,000 C_D=0.09-1.3
Mendez et al. (1999) based on Asano et al. (1988); Laboratory	Same as above	Same as above	Same as above	Without swaying $C_D = 0.08 + \left(\frac{2200}{R_e}\right)^{2.2}$ 2000<R_e<15,500 C_D=0.1-1.6 With swaying $C_D = 0.40 + \left(\frac{4600}{R_e}\right)^{2.9}$ 2,300<R_e<20,000 C_D=0.3-6.9
Möller et al. (1999); North Norfolk coast, England	h=0.52-1.39 m H_s=0.24 m (mean) T_z =2.8 s	Mixed *Limonium sp., Aster sp., Atriplex sp., Salicornia sp., and Spartina.*	180 m (gage spacing variable)	Not available
Möller and Spencer (2002); East Essex coast, England	h=0.12-1.04 m H_s=0.05-0.30 m (mean) T_z =3.0 s	Seasonal, mixed *Salicornia sp., Suaeda sp., Puccinellia sp.*	10-163 m (gage spacing variable)	Not available
Mendez and Losada (2004) based on Dubi (1995) ; Laboratory	h=0.4-1 m H_{mo}=0.06-0.24 m T_p=1.26-4.42 s	Artificial kelp h_v=20 cm b_v=2.5 cm N_v=1200 /m²	9.3 m (gages 1.15 m apart)	$C_D = 0.47e^{-0.052K_C}$ $3 \le K_C \le 59$ C_D=0.02-0.4 or $C_D = Q^{0.3}e^{-0.013SQ}$ $7 \le Q \le 172$ $Q = K_C\,\alpha^{0.76}$
Möller (2006); East Essex coast, England	h=0.12-0.84 m H_s=0.037-0.28 m (mean) T_z=1.1-3.3 s	Mixed *Salicornia sp., Spartina sp.*	10 m (gages 10 m apart)	Not available
Bradley and Houser (2009); Northwest Florida coast, USA	h=0.95-1.05 m H_{mo}=0.07-0.09 m T_p=1.4 s	*Thalassi testudinum* h_v=25-30 cm b_v=3-3.7 mm N_v=1100 /m²	43 m (gages 5-15 m apart)	$C_D = 0.1 + \left(\frac{925}{R_e}\right)^{3.16}$ 200<R_e<800 C_D=1.7-126.5 $C_D = 126.45\,K_C^{-2.7}$ 1< K_C < 6
Lövstedt and Larson (2010); Lake Krankesjön, Sweden	h=0.36-1.37 m H_{RMS} =0.01-0.06 m T_z=0.5-1.2 s	*Phragmites australis* h_v=h (emergent) b_v=8.4 mm N_v=20-80 /m²	5.3-14.1 m (gages 1-2 m apart)	Not available
Mullarney and Henderson (2010); Puget Sound, Washington, USA	h=0.9 m H= not available T_p=2, 2.13 s	*Schonoplectus americanus* h_v=0.45, 0.81 m b_v=1.6, 2.7 mm 2 stems studied	Not applicable	Not available
Paul and Amos (2011); Isle of Wight, England	h=1 m H_{mo}=0.13-0.18 m T_p=3.1-5.0 s (mean)	*Zostera noltii* h_v=12-16 cm b_v= Not available N_v=1980-4636 /m²	300 m (gages 30-95 m apart)	$C_D = 0.06 + \left(\frac{153}{R_e}\right)^{1.45}$ 100<R_e<1,000 C_D=0.13-1.9
Sánchez-González et al. (2011); Laboratory	h= 0.3-0.8 m H_{mo}= 0.03-0.13 m T_p= 1.25-2.5 s	Artificial *Posidonia sp.* h_v= 10 cm b_v= 3 mm N_v= 40,000 /m²	9 m (gages 3 m apart)	$C_D = 6.7\,K_C^{-0.73}$ 10< K_C < 170 C_D=0.16-1.2
This study; South Louisiana coast; USA	h= 0.2-1.1 m H_{mo}= 0.2-0.4 m T_z= 3-9 s	*Spartina alterniflora* h_v= 20 cm b_v= 8.5 mm N_v= 420 /m²	28 m (gages 12-16 m apart)	$C_D = 2\left(\frac{1300}{R_e} + 0.18\right)$ 600<R_e<3,200 C_D=1.2-4.3 $C_D = 70.0\,K_C^{-0.86}$ 25 < K_C < 135

The objective of the study in this section is to collect and analyze comprehensive field data to investigate wave attenuation over coastal marsh in a high-energy environment, such as that produced by a tropical storm. The wave data are used to quantify the rate of wave attenuation and the vegetation induced bulk drag coefficient. Behavior of the wave height decay rate and the bulk drag coefficient is analyzed with respect to changing wave parameters and surge heights (degree of submergence). The dataset reveals the presence of bimodal spectra, consisting of low-frequency ocean swell in addition to the wind sea, providing an opportunity to examine differences in the bulk drag coefficients associated with these two wave systems.

3.1.2 Modeling Wave Transformation over Vegetation

Waves propagating through vegetation (e.g., seagrass, salt marsh, mangroves) dissipate energy by interacting with the vegetation. Assuming normally incident monochromatic waves that follow linear wave theory, the wave energy balance equation can be written as

$$\frac{\partial EC_g}{\partial x} = -S_v \tag{3.1}$$

where, $E = (1/8)H^2$ is the wave energy density, H is the wave height, $C_g = nc$ is the group velocity, $c = \sqrt{(g/k)\tanh(kh)}$ is the phase speed, k is the wave number, h is the still water depth, g is the acceleration due to gravity, and coefficient n is given by $n = (1/2)[1 + (2kh/\sinh 2kh)]$. The cross-shore coordinate is represented by x, and S_v (m²/s) is the time averaged rate of energy dissipation due to vegetation per unit horizontal area.

This balance equation assumes a rigid bed and neglects all other source terms (local wave generation, white-capping, depth-limited breaking, and bed friction losses) compared to the losses due to vegetation induced drag. For the data analyzed in this section, the magnitudes of these secondary source terms are estimated in Section 3.2.3.

3.1.2.1 Energy Dissipation Models

To estimate wave energy losses caused by vegetation that can be treated as rigid, the stems are represented by rigid obstructing cylindrical elements that impart drag forces on the flow (e.g., Dalrymple et al., 1984; Kobayashi et al., 1993; Mendez and Losada, 2004; Lowe et. al., 2005a; Lowe et. al., 2007; Luhar et al., 2010; Myrhaug and Holmdal, 2011; Chen and Zhao, 2012). The first such formulation was proposed by Dalrymple et al. (1984) for monochromatic waves. In this approach, small-diameter, rigid cylinders obstruct the flow, causing energy dissipation. The forces induced by the vegetation stems are expressed in a manner similar to Morison et al. (1950). For rigid stems, drag forces become dominant compared to the inertial forces due to accelerating fluid. Further, the drag forces due to pressure differences only (form drag) are considered as they are much larger than those arising from friction. The time-averaged (represented by over-bar) rate of energy dissipation per unit horizontal area can then be expressed as

$$S_v = \overline{\int_{-h}^{-(h-sh)} \frac{1}{2g} b_v N_v C_D u_z |u_z| \mathrm{u_z dz}} \tag{3.2}$$

where s is the ratio of vegetation height (h_v) to the still water depth (h), b_v is the stem diameter, N_v is the vegetation density, z is the vertical coordinate with origin at the still water level and pointing upwards, C_D is the bulk drag coefficient, and u_z is the horizontal water velocity at z. More precisely, u_z is the fluid velocity relative to the horizontal velocity of the stem, but the motion of the vegetation is negligible in this analysis (see Section 3.2.3).

Assuming linear wave theory is applicable, integration of the equation above leads to

$$S_v = \frac{2}{3\pi}\frac{C_D b_v N_v}{g}\left(\frac{\sigma}{2}\right)^3 \frac{\sinh^3 ksh + 3\sinh ksh}{3k\sinh^3 kh} H^3 \tag{3.3}$$

where σ is the wave angular frequency.

The monochromatic wave expression above was extended by Mendez and Losada (2004) to random waves, assuming a uni-directional, narrow-banded incident spectrum, as follows,

$$\langle S_v \rangle = \frac{1}{2\sqrt{\pi}}\frac{C_D b_v N_v}{g}\left(\frac{\sigma_r}{2}\right)^3 \frac{\sinh^3 k_r sh + 3\sinh k_r sh}{3k_r\sinh^3 k_r h} H_{rms}^3 \tag{3.4}$$

where the symbol $\langle \quad \rangle$ denotes the expected value of a random variable, subscript r indicates that the parameters are representative and H_{rms} is the root-mean-square wave height based on the Rayleigh probability density function. As representative parameters, Mendez and Losada (2004) used peak values, while implementation of this formulation in the SWAN (Simulation of WAves in Nearshore areas) model uses mean values. SWAN is a third generation wave model that solves the wave action balance equation to describe the evolution of the wave spectrum over time, and geographical and spectral spaces (Booij et al., 2004).

In these integrated formulations of dissipation, as an approximation, it is assumed that the drag coefficient is independent of the wave height and wave period. The uncertainties resulting from this approximation are accounted for by the estimated bulk drag coefficients (Mendez and Losada, 2004).

A more generalized model for energy dissipation of random waves due to rigid vegetation was proposed by Chen and Zhao (2012). According to Chen and Zhao (2012), the expected value of the wave energy dissipation rate is given by,

$$\langle S_v \rangle = \int S_{ds,v}(\sigma) d\sigma \tag{3.5}$$

where,

$$S_{ds,v}(\sigma) = \frac{1}{2}\frac{C_D b_v N_v}{g}\left(\frac{\sigma}{\sinh kh}\right)^2 \left(\int_{-h}^{-(h-sh)} U_{rms}(z)\cosh^2[k(h+z)]dz\right) S_e(\sigma) \tag{3.6}$$

and

$$U_{rms}(z) = \sqrt{2\int \frac{\sigma^2\cosh^2 k(h+z)}{\sinh^2 kh} S_e(\sigma) d\sigma} \tag{3.7}$$

The spectral energy density is denoted by $S_e(\sigma)$.

3.1.2.2 **Wave Height Attenuation**

In the literature, wave height attenuation has been generally quantified as the percentage reduction in the representative wave height as the wave propagates over a vegetated field along a given length (e.g., Möller, 2006; Quartel et al., 2007; Bradley and Hauser, 2009; Lövstedt and Larson, 2010). It is expressed as

$$r = \frac{H_{in} - H_{out}}{H_{in}\ \ (\Delta x)} \cdot\ 100 \tag{3.8}$$

where H_{in} is the wave height entering the measurement transect and H_{out} is the wave height leaving the transect of length Δx along the direction of wave propagation.

Though calculation of the reduction rate, r, offers a compact way of indicating the role and effectiveness of vegetation in wave damping, it is rather inconvenient for universal comparisons because its value depends on several parameters related to vegetation, as well as hydraulic regime. The important parameters affecting the reduction rate are the type of vegetation (grassy, reed-like, leafy, shrubs, or trees), vegetation density, and biomechanical properties (stiffness, height, and stem diameter). All these parameters have seasonal variation. Among the hydraulic parameters, the reduction rate may depend on water depth at the time of measurement and magnitude of the wave heights and wave periods. Thus, to improve the practical utility of the percentage wave height reduction rate, it should be qualified with some of the important parameters mentioned above.

Wave height attenuation has also been characterized as an exponential decay process (Asano et al., 1993; Kobayashi et al., 1993; Möller et al., 1999; Cox et al., 2003) expressed as

$$H_{out} = H_{in} e^{-k_H x} \tag{3.9}$$

where k_H is the decay rate and x is the distance along the direction of wave propagation from the location of the first gage (where H_{in} is measured) to the location where H_{out} is sought. Universal application of k_H suffers from the same drawbacks that apply to the reduction rate parameter, r. However, as shown in Section 3.3.2, some of these dependencies can be quantified. Note that, the reduction rate r in Eq. (3.8) is equivalent to k_H when $k_H x \ll 1$.

Assuming constant water depth and monochromatic waves (Dalrymple et al., 1984) Eq. (3.1) can be integrated to express wave attenuation as

$$H_{out} = \frac{H_{in}}{1 + \beta_1 x} \tag{3.10}$$

where

$$\beta_1 = \frac{4}{9\pi} C_D b_v N_v H_{in} k\ \frac{\sinh^3 ksh + 3\sinh ksh}{(\sinh 2kh + 2kh)\sinh kh} \tag{3.11}$$

Similarly, for random waves over constant depth (Mendez and Losada, 2004), wave attenuation can be expressed as

$$H_{rms,out} = \frac{H_{rms,in}}{1 + \beta_2 x} \tag{3.12}$$

where

$$\beta_2 = \frac{1}{3\sqrt{\pi}} C_D b_v N_v H_{rms,in} k \frac{\sinh^3 ksh + 3\sinh ksh}{(\sinh 2kh + 2kh)\sinh kh} \tag{3.13}$$

When attenuation is low ($\beta_1 x \; or \; \beta_2 x \ll 1$), the exponential decay rate parameter, k_H, in Eq. (3.9) can be shown to be equivalent to β_1 or β_2 by using the approximation $e^{k_H x} \cong 1 + k_H x$ such that $H_{out}/H_{in} = 1/(1 + k_H x)$.

In the analysis presented herein, only k_H in Eq. (3.9) is estimated and examined with respect to wave parameters. Parameter β_2 was not estimated because the presence of slope between our gages violates the assumptions of Eq. (3.12). However, this formulation is presented for completeness.

3.1.2.3 **Determination of Bulk Drag Coefficients and Decay Rates**

The drag coefficient is one of the unknown parameters in the models of wave energy dissipation caused by vegetation. For a single rigid stem in an oscillatory flow, the drag coefficient is a function of orbital velocity at a given depth, which in turn is a function of wave height and wave period. Additionally, in the case of flexible vegetation, stems can sway, reducing the relative velocity between stem and the orbital velocity. In a patch of vegetation, wakes formed by the neighboring stems can interact and affect the magnitude of the drag (Ghisalberti and Nepf, 2002; Folkard, 2011). These factors influence estimates of bulk drag coefficients determined from field measurements.

In most existing experimental studies, the bulk drag coefficients have been estimated from the measurements and then related to non-dimensional parameters such as the Reynolds number, R_e, and the Keulegan-Carpenter number, K_C. Table 3.1 summarizes existing empirical relationships along with relevant features of the studies. The common methods used to estimate C_D are described below as applied to an example set of data from three wave gages deployed along a straight line in the direction of wave propagation.

(1) Using measured wave energy flux between two gauges and inverting Eq. (3.3) to estimate C_D for each burst. In our example with three gages, this gives us two estimates (one each between gage 1 and 2, and between gage 2 and 3) of C_D for each burst. This is similar to the method followed by Bradley and Houser (2009) and Paul and Amos (2011).

(2) Using measured integral wave heights and fitting Eq. (3.10) to the set of synoptic wave heights at all three gages using C_D as the single variable. This results in a single C_D value for each burst. Such approach was utilized by Mendez and Losada (2004). Note that this method assumes horizontal bathymetry.

(3) Using measured wave energy spectra and applying the formulation of Chen and Zhao (2012) (Eq. (3.6)) between consecutive gages. In our example, this results in two estimates of C_D for each burst triplet. This method is adopted in the present study.

Further, to determine a single R_e or K_C for each burst and therefore for each C_D, one can use measurements at the first (windward) gage or use the average of the measurements at all the gages considered. Depending on the distances between the deployed gages, overall length of the measurement transect, and intensity of wave energy and attenuation, different methods of analysis could produce different C_D estimates and empirical relationships. Also, to determine the R_e or K_C for each burst, one can consider time-averaged, maximum orbital velocity at the bed, u_b, or at the canopy height, u_c . The length scale can be the stem diameter (b_v), stem height (h_v) or wave excursion length. Most existing studies have used stem diameter for the length scale.

3.1.3 Data and Methods

3.1.3.1 Study Area and Experimental Setup

Wave data were collected over a two-day period (September 3-4, 2011) at a salt marsh wetland in Terrebonne Bay on the Louisiana coast of the Gulf of Mexico (Fig. 3.1) during Tropical Storm Lee. Situated in the Mississippi River delta, Terrebonne Bay and the coastline extending for about 300 km east and west of Terrebonne Bay is one of the most productive and fragile marsh systems in the world. Due to natural and anthropogenic stressors/forces, between 1956 and 2006, the Louisiana coast has lost land at the rate of approximately 70 km^2/yr. This represents 80% of the total coastal wetland loss in the continental United States (Barras et al., 2003).

Terrebonne Bay is a shallow estuary bounded by the natural levees of Bayou Terrebonne on the east, and the Houma Navigation Canal on the west. Salt marshes line the upper portion of the bay, where vegetation communities include smooth cordgrass (*Spartina alterniflora*) and salt marsh meadow (*Spartina patens*). On the south, the bay is bordered by a series of narrow, low-lying barrier islands, the Isles Dernieres and the Timbalier Islands. The wave environment in the bay is generally comprised of locally generated seas, but offshore swell waves also propagate inwards through the gaps in the barrier island chain, or when the barrier islands are flooded by a tropical storm surge. The region has a micro-tidal environment (tidal range < 0.5 m) and depths in the bay vary from 1 to 3 m. The southern fetch varies from 10 to 24 km. The region experiences annual winter cold weather fronts, and surge and waves from tropical cyclones.

The marsh site selected for the field study is a vegetated platform wetland with a shallow bay on the windward (south) side. On the leeward (north) side the marsh extends for a distance of about 500 m, beyond which lies open water of the bay. A field topographic survey along a north-south transect shows a very low berm near the southern edge from where the marsh floor gently slopes inland.

The southern marsh edge, where the incident waves first landed, has an approximate east-west alignment. The shore-normal direction has a bearing of 20°. Five wave gages (pressure transducers W0 through W4) were deployed along a north-south transect nearly perpendicular to the marsh edge (Fig. 3.2a). Gage W0 was located in the open water on the up-wave (south) side of the marsh about 45 m away at a depth of about 1.4 m below the mean sea level, to measure incoming wave energy. Gage W1 was the first gage on the marsh that encountered incident waves. This gage was placed more than 16 m inwards (north) of the marsh edge to avoid the breaking zone created by waves breaking at the marsh edge. The post-cyclone survey of the site showed vegetation and surface damage within 8 to 10 m of the edge. The remaining

three gages, W2, W3 and W4, were further inland; gage W4 being the farthest north at 43.8 m from the first marsh gage W1. A maximum of 20° error in the alignment would reduce the travel distances between the gages by about 6% $(1 - \cos 20°)$ introducing error by the same amount in the estimates of drag.

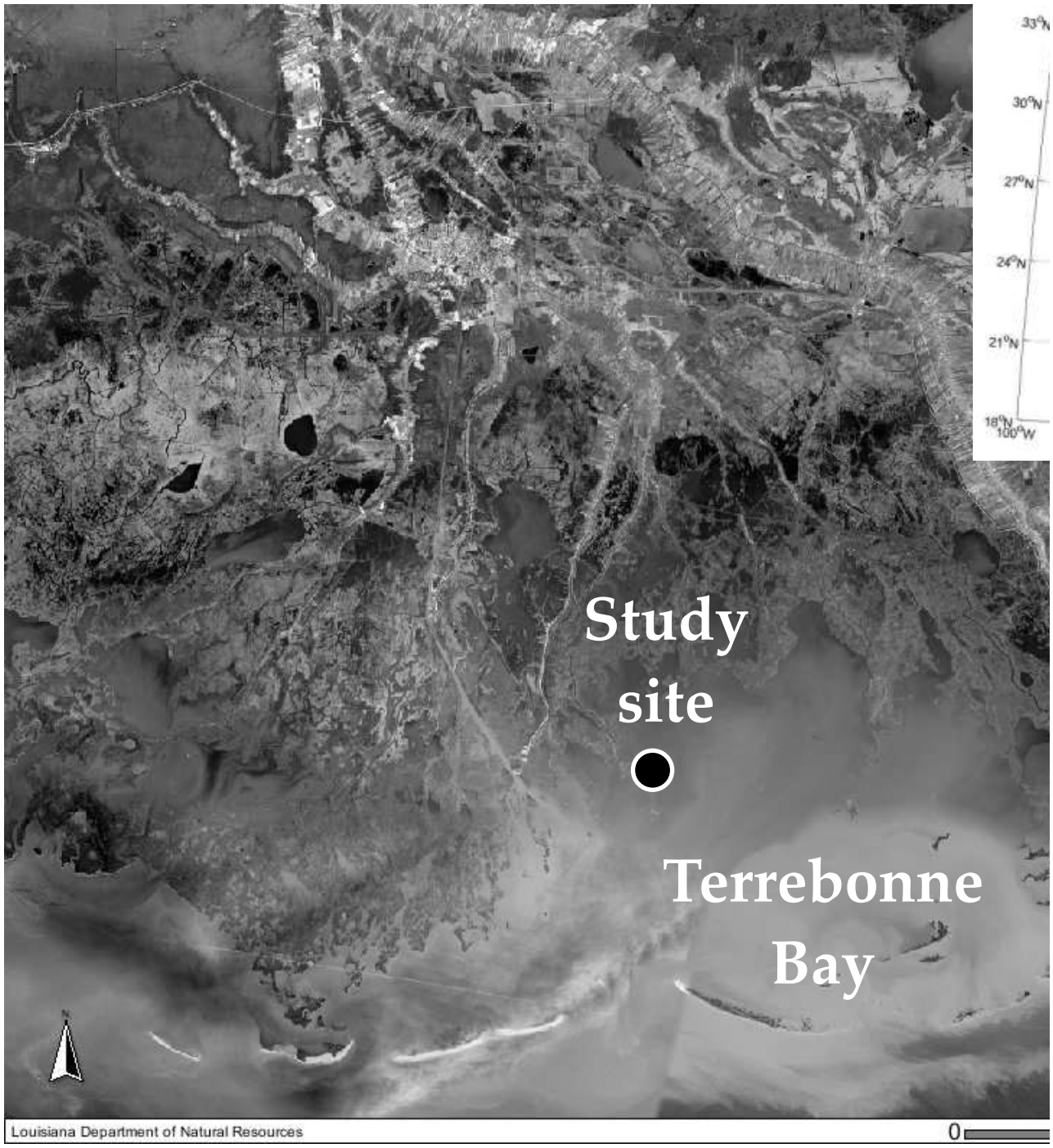

Fig. 3.1. Study area location. Terrebonne Bay, Louisiana.

All gages were self-logging pressure sensors that sampled continuously at 10 Hz over the duration of the storm. The sensors were encased in a heavy metal base to ensure stability under passing waves.

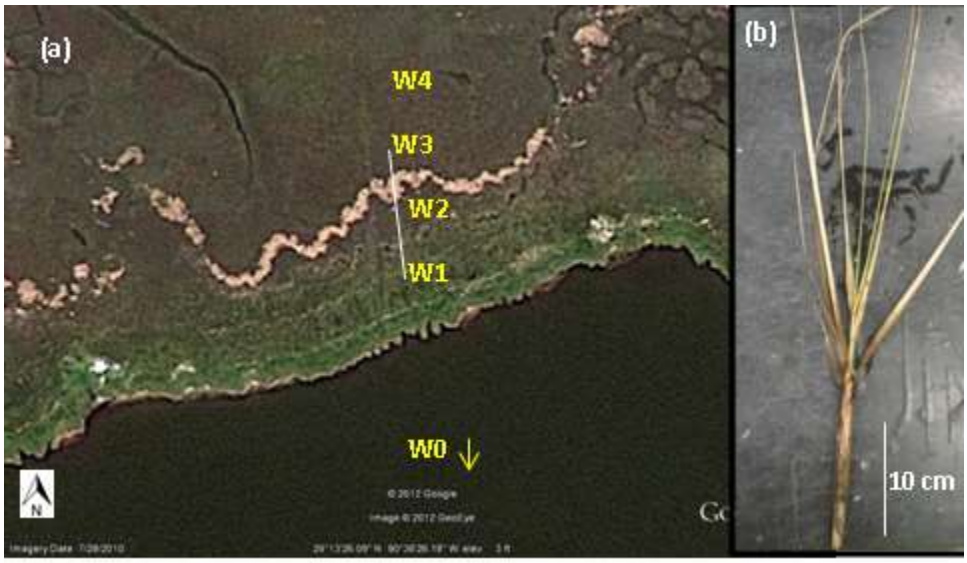

Fig. 3.2. (a) Close up aerial view of the study site showing wave gage configuration, with the line W1-W3 (28m, drawn to scale) showing transect alignment; (b) A *Spartina alterniflora* plant collected from the site for measurements.

3.1.3.2 Vegetation Properties

The dominant vegetation at the site is *Spartina alterniflora*. This plant typically has a thick stem, with tapering flexible narrow blades (Fig. 3.2b). Vegetation properties were measured 11 days after the storm. Stem population density (N_v), stem height (h_v), total plant height (h_{vt}), stem diameter (b_v), and Young's Modulus (E_v) were measured at one location each between gages W1-W2 and W2-W3. The population density is the number of stems in one meter square area. The stem height is defined as the length between the plant base and the location of the topmost blade along the stem. The total plant height is defined as the length between the plant base and the tip of the plant with all blades aligned along the stem. The representative diameter of the plant was measured at one-fourth the stem height. The Young's Modulus was determined from measuring force required to bend the stem in the field from a certain height by a known angle and applying the Euler-Bernoulli beam theory. All above parameters were measured for 14 plants at each location. The mean and standard deviation of the measurements collected from the site between gages W1 and W2 were; N_v =424 m^{-2}, h_v =0.21±0.04 m, h_{vt} =0.62±0.05 m, b_v =8.0±1.1 mm, and E_v =80±27 MPa (E_vI_v =0.017±0.009 N-m^2) where E_vI_v is the flexural rigidity and I_v is the second moment of inertia of a stem. The mean and standard deviation of measurements collected between gages W2 and W3 were; N_v =420 m^{-2}, h_v =0.23±0.06 m, h_{vt} =0.63±0.11 m, b_v =7.5±1.3 mm, and E_v =79±32 MPa (E_vI_v =0.013±0.007 N-m^2).

In the analysis presented in this section, the vegetation is treated as rigid, based on our observations and on the measured biomechanical properties of the vegetation and integral wave

parameters. To ascertain the validity of this treatment, a non-dimensional stiffness parameter, ψ, as defined in Mullarney and Henderson (2010), is calculated using the following expression:

$$\psi = \frac{E_v (B_v/2)^3 T_z}{\rho C_D h_v^4 u_b} \tag{3.14}$$

Using the mean vegetation properties and wave period, the non-dimensional stiffness for our data is in the range of 17 to 38. If the peak wave period is used, then ψ ranges between 32-50. Comparatively, the two stems (*Schoenoplectus americanus*) characterized as moderately flexible by Mullarney and Henderson (2010) to demonstrate effect of stem motion on wave energy dissipation, have non-dimensional stiffness values of 0.27 and 0.71. Also, as seen in Fig. 3.2b, our *Spartina alterniflora* plants have a thick stem with several flat long flexible leaf blades. The blades have been observed to easily align with the flow under even moderate waves, offering no form drag. Streamlined vegetation has been observed to cause little dissipation (e.g., Elwany et al., 1995).

3.1.3.3 **Wave Data Reduction**

As a first step in processing the wave data, all measurements recorded while the water depth was less than 0.4 m were eliminated from further consideration, because the wave energy was found to be negligible at these levels. Thus, the study represents submerged vegetation conditions only.

In the last gage segment, between W3 and W4, the characteristic exponential energy dissipation due to vegetation was observed during only 5 bursts. Therefore, the entire dataset from gage W4 is not used in this analysis.

The wave energy spectra and the integral wave parameters were calculated using standard spectral analysis. The measured continuous pressure time series was first divided into consecutive segments or bursts of 15 minutes. For each burst, the spectral density of pressure, S_p, was calculated using Welch's periodogram method (e.g., Bendat and Piersol, 2000). The pressure spectra were transferred to wave energy spectra, S_e, using linear wave theory. Excessive amplification of noise through the transfer function was generally observed above 0.7 Hz with a distinct local spectral minimum. The amplified portion of the energy spectrum above this minimum was replaced by a f^{-4} spectral tail. The final energy spectrum had a bandwidth of $\Delta f = 0.01$ Hz.

The integral wave parameters are defined in terms of spectral moments calculated as: significant wave height, $H_{mo} = 4\sqrt{\mathrm{m}_0}$; root-mean-squared (RMS) wave height, $H_{rms} = 2\sqrt{2\,\mathrm{m}_0}$; mean wave period, $T_z = \sqrt{\mathrm{m}_0/\mathrm{m}_2}$; and spectral width, $\nu = (m_0 m_2/m_1^2 - 1)$ where m_0, m_1, and m_2 are the zero-th, first and second moment of the wave spectrum (0.03-0.7 Hz), respectively. The spectral energy above 0.7 Hz is generally less than 5% of the total energy, so excluding it does not significantly affect the analysis results.

The wave energy losses due to vegetation were considered dominant compared to the other source terms. To ascertain the validity of this assumption, the relative magnitude of source terms of the local wave generation and the losses due to bottom-friction, white-capping, and depth-limited breaking were evaluated. The wave records with significant potential for these source terms were removed from further analysis as described below.

The existing formulations of wave generation are based on longer fetches than those analyzed in this study (16.5 m between W1 and W2; 11.5 m between W2 and W3). Considering the finite-depth conditions, the magnitude of wind generated wave energy within our study transect was estimated using Young and Verhagen (1996) non-dimensional formulations. This energy was less than 1% on the first day (average wind speed of 16.0 m/s) and less than 10% on the second day (average wind speed of 18.6 m/s). Wave records during which wind generated energy was greater than 7% of the total spectral energy were removed from further analysis.

Following Madsen (1994), energy dissipation of random waves due to bottom friction was computed (see also Lowe et al., 2005b). For the wave records analyzed, this dissipation was less than 7% of the measured energy dissipation.

The magnitude and frequency scale of white-capping is one of the least understood processes. For finite-depth conditions, Babanin et al. (2001) proposed breaking probability as a function of wave parameters based on the extensive Lake George dataset. For our wave records, when the peak spectral steepness exceeded the proposed threshold of 0.055, the breaking probabilities were usually less than 0.03. The few wave records with considerable breaking probabilities (> 0.15) were removed from the analysis.

In the absence of a video documentation, it is reasonable to use $\gamma = H_s/h$=0.6 as the limit for the depth limited breaking (Thornton and Guza, 1982). Due to the down-sloping bathymetry in our case, this limit is likely to be slightly higher (Raubenheimer et al., 1996), reducing the likelihood of breaking even more. In our reach between wave gages W2 and W3, the depth-limited breaking is not a concern because γ is <0.3. At gage W1, there were 6 wave records with γ>0.5, which are removed from the analysis. We chose 0.5 as the breaking limit for γ to be conservative.

Based on above analyses, overall 15 wave records where source terms other than vegetation-induced dissipation were deemed to be of significance, were removed from further analysis.

3.1.4 Observations and Results

3.1.4.1 Characteristics of the Measured Waves

Our study site experiences flooding only during the high tide conditions. Such flooding is generally very shallow, with depths less than 10 cm. However, high winds and associated surge during Tropical Storm Lee on September 3rd and 4th of 2011, caused significant marsh flooding and provided an opportunity to examine wave transformation over vegetation. Tropical Storm Lee made landfall in south-central Louisiana. The slow moving storm produced surge above 1 m at the study site. The greater water depths enabled higher incident waves to propagate over the marsh vegetation. Fig. 3.3 shows the integral wave parameters at the study site during the 2-day sampling period. The magnitude of incident waves to the marsh (gage W0) was related to the water depth (Fig. 3.3a). On the first day, when the depth of water on the marsh steadily rose to about 0.9 m, significant wave heights correspondingly increased to about 0.79 m in the open water and 0.39 m on the marsh. On the second day of the storm, the water on the marsh rose to a slightly lower maximum of about 0.7 m, and the measured significant wave heights were up to 0.65 m in the open water, and 0.22 m on the marsh. The waves reduced sharply in height as they landed on the marsh edge and further reduced in height as they propagated over vegetation. The wave attenuation is quantified and discussed further in Section 3.3.2.

The two series of peak wave periods shown in Fig. 3.3c and 3.3d indicate persistent presence of low-frequency swell in addition to wind-sea. The two wave systems can be clearly identified

in typical energy spectra observed at the four marsh gages at 6:45 AM on September 3, 2011 (Fig. 3.4). The local spectral energy minima (generally found to be around 0.17 Hz) between the peaks of the two wave systems was used to partition the energy into wind-sea and swell. Most incident spectra were bimodal, with a low-frequency swell component and a mid-frequency wind-sea component. In most cases, these spectral signatures were retained as waves propagated over the marsh vegetation.

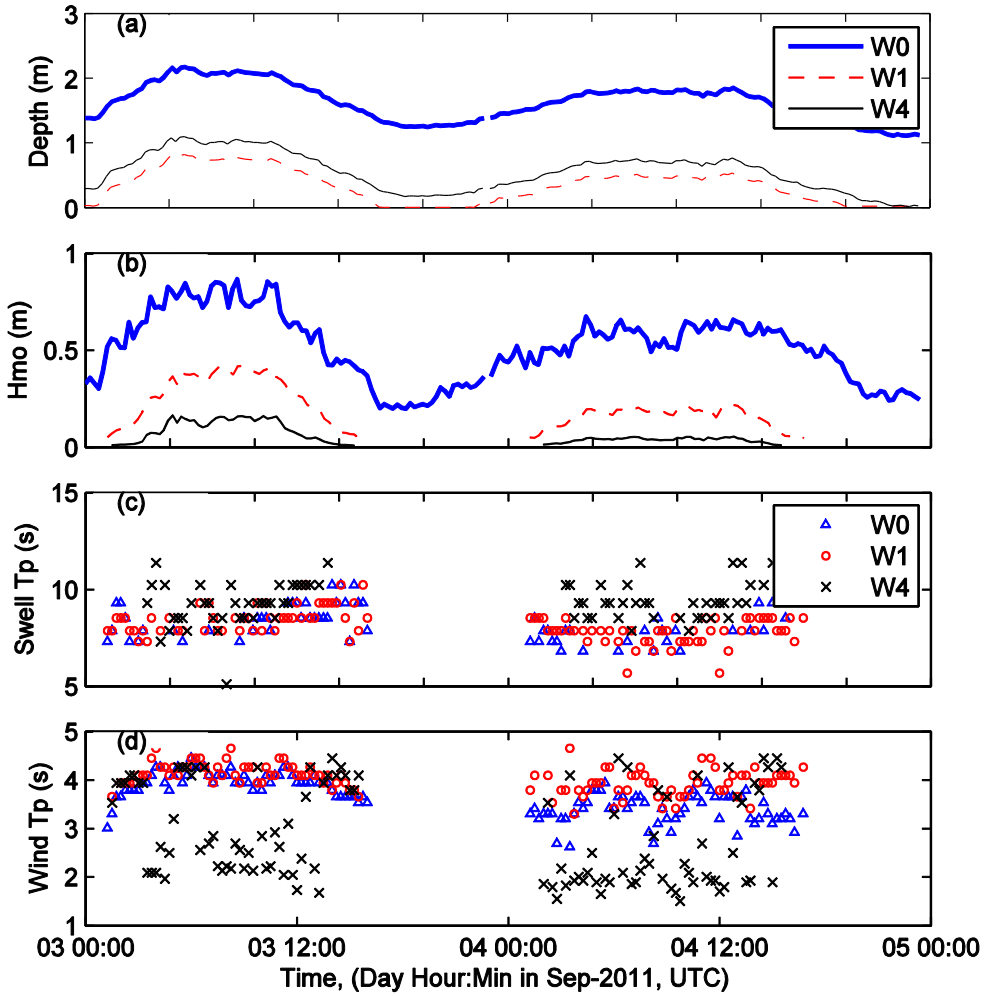

Fig. 3.3. Wave environment at the study site during Tropical Storm Lee: (a) Water depth measured by wave gages (5-min averaged from the continuous record); (b) Spectral significant wave height; (c) Peak period of the low-frequency swell; and (d) Peak period of the wind-sea portion of the spectra.

To understand the characteristics of the wave environment further, the temporal evolution of some of the derived parameters are shown in Fig. 3.5. The parameters are relative wave height, $\gamma = H_{mo}/h$, relative depth, h/L, and Ursell number, $H_{mo}L^2/h^3$, where L is the wave length based on the mean wave period.

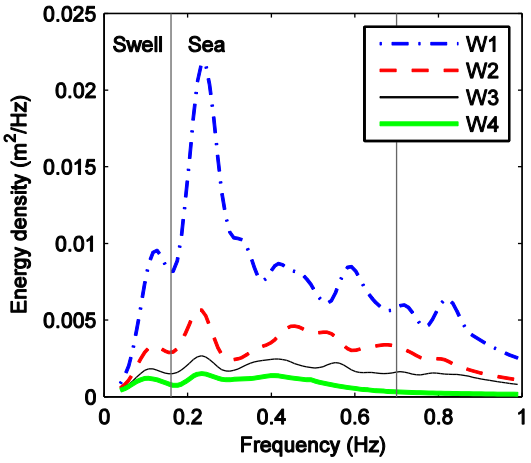

Fig. 3.4. Wave energy spectra recorded at four marsh gages on September 3, 2011 at 6:45 UTC.

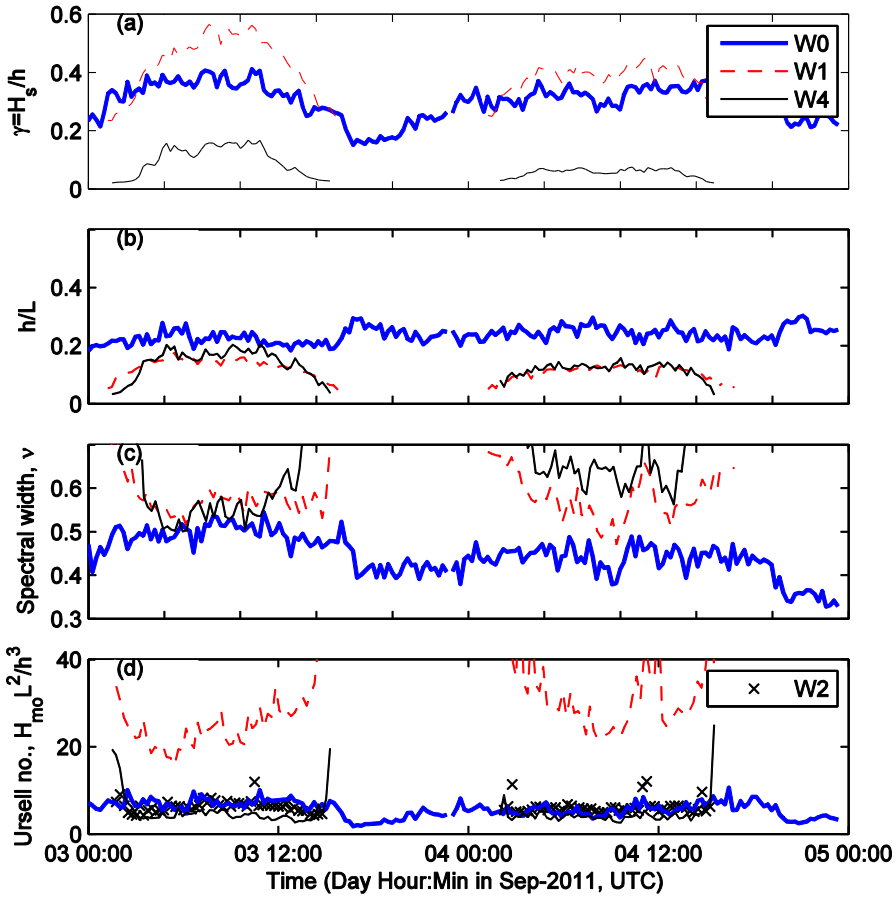

Fig. 3.5. Wave environment at the study site during Tropical Storm Lee: (a) Relative wave height; (b) Relative water depth; (c) Spectral width; and (d) Ursell number.

During the observation period, the relative wave height, γ, was less than 0.6. The ratio, h/L, was less than 0.2, indicating relatively shallow water depths during the observation period.

Energy spectra became broader as waves travelled over vegetation, as indicated by increased spectral width (see Fig. 3.4 also). This tendency to broaden with propagation became stronger on the second day, when water depth was less. Ursell number is a measure of wave non-linearity in shallow water, with higher values indicating higher non-linearity. Waves appear to be rather non-linear at W1, but the non-linearity quickly reduced as the waves propagated into the marsh.

3.1.4.2 Observed Wave Height Attenuation

The vegetation-induced wave energy losses along the wave gage transect result in corresponding attenuation in wave height. Fig. 3.6 shows the spatial variation of observed RMS wave height (H_{rms}) along the study transect for the entire dataset. When computing the mean, the waves are grouped by ranges of plant submergence ratio, $s = h_v/h$ at gage W1. Using the submergence ratio from one gage for a given burst instead of one for each gage, ensures that each s-group consists of the same set of waves as they propagated along the transect.

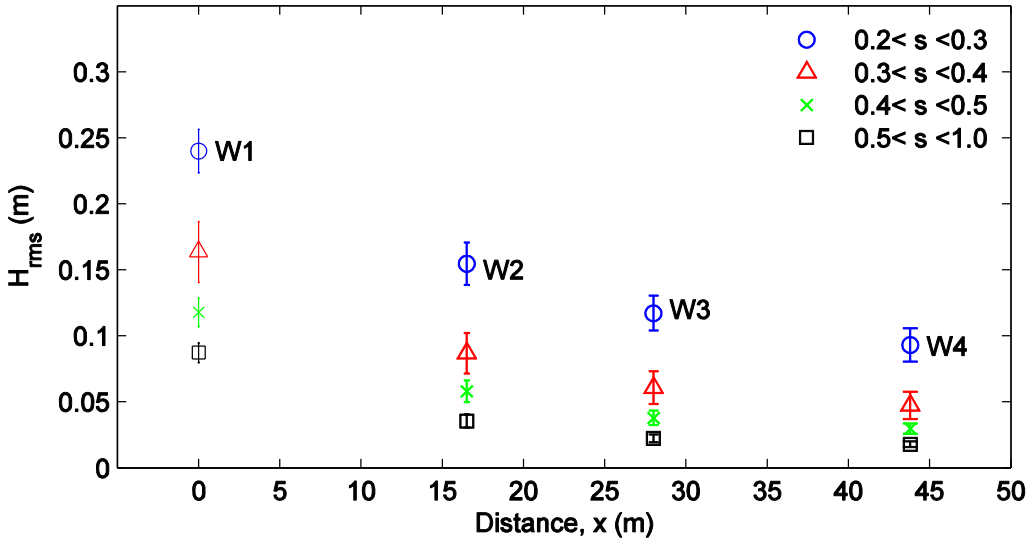

Fig. 3.6. Spatial variation of measured wave heights at four marsh gages for selected ranges of vegetation submergence ratio, $s = h_v/h$, at gage W1. Symbols indicate mean values and vertical bars show ±1 standard deviation.

The data show that the mean incident RMS wave heights varied from 0.09 m to 0.24 m depending on the submergence (or depth). Within about 45 m (the distance to the last gage), mean wave height was reduced to 0.02-0.09 m. The reduction in wave height was sharper in the first reach (W1-W2) compared to the subsequent reach (W2-W3).

Several researchers (Table 3.1) have analyzed wave height attenuation caused by vegetation and evaluated the effect of various parameters on the rate of attenuation. The general observations are that the wave height reduction increased with vegetation patch width and stem density, and decreased with increasing water depth, but no clear relationship to wave period has been reported. Some of these studies (e.g., Möller, 2006) have also presented relationships between wave height attenuation and parameters such as relative wave height, and have identified threshold values beyond which attenuation did not show any increase. In

our study, the wave height attenuation was also calculated in terms of percentage wave height reduction rate (r) within a reach (/m) as defined by Eq. (3.8). The reduction rate varied from 1.5% to 4% /m, depending on the incident wave height (or water depth). The reduction rate decreased with increasing wave height. It should be noted that if the dissipation in the measurement transect is not dominated by vegetation drag (when gage is much farther downwave outside the realm of exponential decay), then the attenuation rate could be skewed by the distance over which it is calculated. The attenuation expressed by Eq. (3.8) implies linear wave height decay, while in reality attenuation is closer to being exponential as stated before. Consequently, reduction rate values may vary depending on the spatial location where they are calculated. This may partly explain the wide ranges of percentage wave height attenuation rates reported in the literature, such as 0.34% /m (Möller et al., 1999), 0.77% /m (Bradley and Houser, 2009) and 4.0-5.0% /m (Lövstedt and Larson, 2010).

To examine the exponential nature of wave height decay, the decay rates (k_H) were obtained by fitting Eq. (3.9) to the data. For each burst, Eq. (3.9) was fitted to the set of RMS wave heights from gages W1, W2, and W3 to obtain a single k_H value. This process was repeated for all bursts, resulting in a set of k_H values that ranged from 0.022 to 0.051 /m, with excellent fit for each burst (lowest R^2=0.98).

For random wave dissipation over artificial kelp in a laboratory flume, Dubi and Tørum (1996) estimated the decay parameters up to 0.011 /m when the depth was 1 m. The range of exponential decay rates reported by Kobayashi et al. (1993) is from 0.015 to 0.101 /m for monochromatic waves over artificial vegetation in a laboratory flume. The decay rates observed by Bradley and Houser (2009) for three wave records were 0.007, 0.015 and 0.008 /m for random waves in the field with incident wave heights of 7 to 10 cm.

To understand the nature of this variation further, the k_H values were plotted against incident wave height, Reynolds number, R_e ($= \rho b_v u_b/\mu$), and Keulegan-Carpenter number, K_C ($= u_b T_z/b_v$) (Fig. 3.7). Here u_b ($= H_{rms}\omega_z/2\sinh k_z h$) is the maximum near-bed orbital velocity in the absence of vegetation given by the linear wave theory, and subscript z indicates the mean value of the parameter, using the measurements at the first (windward) of the two bounding gages. Fig. 3.7 shows that larger waves decayed at a slower rate than smaller waves with similar frequencies. The decay rates for the low-frequency swell were lower than those for the high-frequency wind-sea regardless of wave height. This is consistent with observations of Lowe et al. (2007), who found that, under spectral wave conditions, high-frequency (>0.2 Hz) waves penetrated more effectively into a model canopy and were dissipated at a greater rate.

3.1.4.3 **Bulk Drag Coefficient**

The wave conditions during our study consisted of random waves with broad spectra. This precluded application of the Dalrymple et al. (1984) model, which was developed for monochromatic waves. Therefore, the random wave models by Mendez and Losada (2004) and Chen and Zhao (2012) were used. To apply the Mendez and Losada (2004) model, the left hand side of Eq. (3.4) was calculated by dividing the difference of measured wave energy flux between adjacent pairs of wave gages (i.e., W1-W2 and W2-W3) by the distance between them. The right hand side was calculated by using the average values of integral wave parameters at the same two gages. In applying Chen and Zhao (2012) formulation, the left hand side of Eq. (3.6) was calculated as stated above and the right hand side was calculated by numerical integration along the vertical stem height and along the spectral frequency.

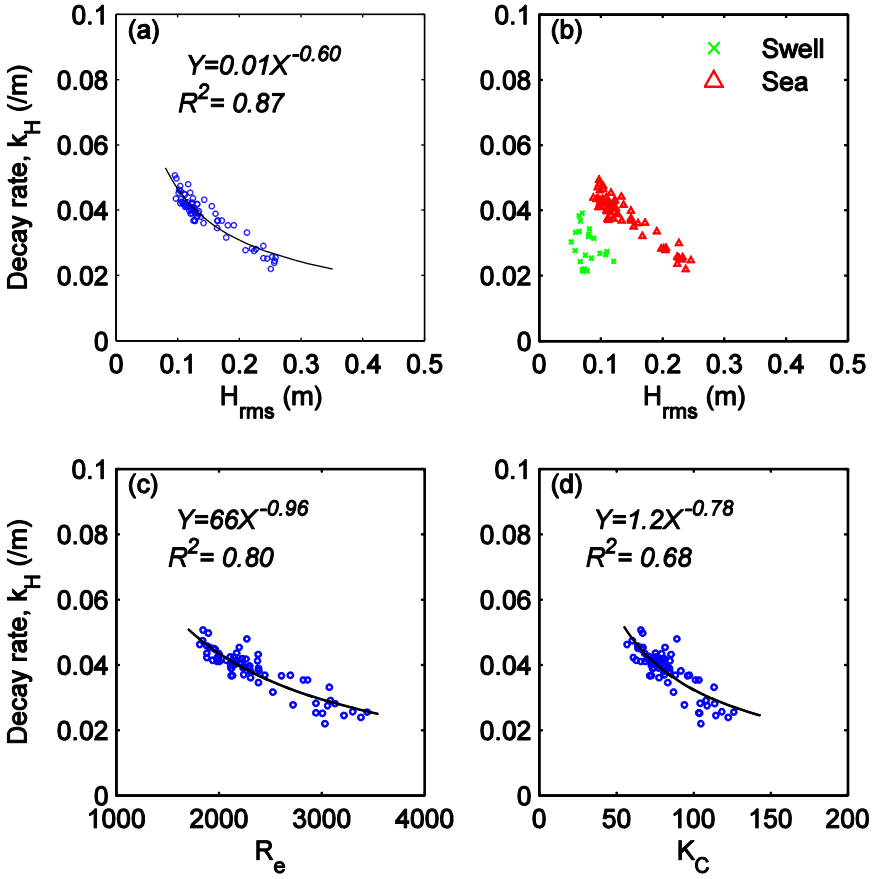

Fig. 3.7. Variation of exponential wave height decay rate with RMS wave height, Reynolds number, and Keulegan-Carpenter number. Independent variables are based on measurements at gage W1.

Fig. 3.8 shows the estimated values of bulk drag coefficients, C_D, using these two methods, plotted against the Reynolds number, R_e. The R_e is calculated based on the velocity at the first of the two bounding gages. The C_D estimates by the two methods are very similar. Note that the relatively low R_e values are due to the small stem diameter (8.0 mm) used as the characteristic length. To derive the empirical relationship between C_D and R_e, the form suggested by Tanino and Nepf (2008) is fitted ($R^2 = 0.93$) to yield,

$$C_D = 2\left(\frac{1300}{R_e} + 0.18\right) \qquad 600 < R_e < 3{,}200 \tag{3.15}$$

The solid volume fraction for our data is $\phi = N_v \pi b_v^2/4 = 0.021$. Considering the range of R_e and ϕ, the coefficients in Eq. (3.15) are of the same order as those listed in Tanino and Nepf (2008). The R_e in Tanino and Nepf's formula is based on pore velocity, but is the same order of magnitude as the R_e in this study.

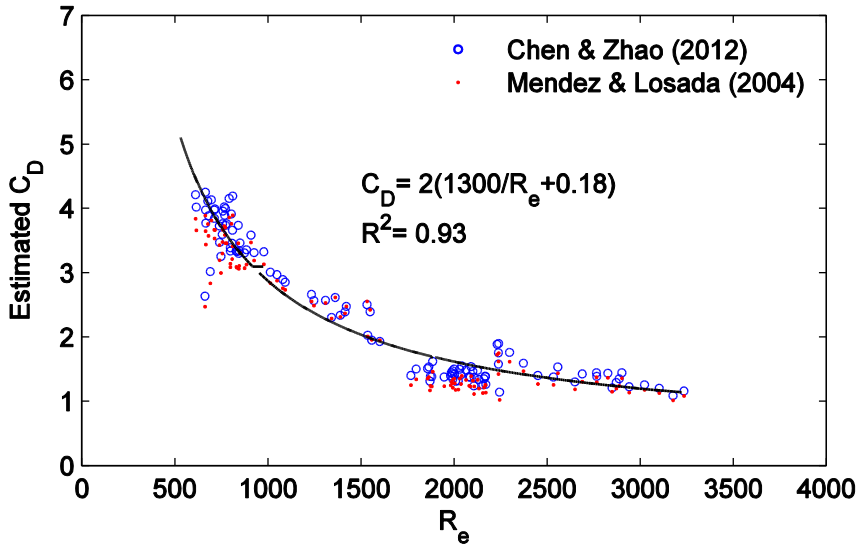

Fig. 3.8. Variation of bulk drag coefficient estimated by two models, with Reynolds number, which is calculated using measurements from the windward gage of each pair and stem diameter.

In Fig. 3.8, the estimated C_D ranges from 1.2 to 4.3. It decreases as R_e increases. The C_D values are larger than those for isolated cylinder, specifically for $R_e < 1500$. This is consistent with the findings of Koch and Ladd (1977) and Tanino and Nepf (2008). Table 3.1 also shows that, in several previous studies, C_D values much larger than 1 have been reported. In Fig. 3.8, smaller C_D values (<2.0) were found in the reach between gages W1 and W2, where $R_e > 1500$.

Variation of C_D with the Keulegan-Carpenter number, K_C, is shown in Fig. 3.9 with the following regression equation,

$$C_D = 70.0\,(K_C)^{-0.86} \qquad 25 < K_c < 135 \tag{3.16}$$

As stated before, the recorded wave spectra showed the presence of low frequency swell in addition to wind-sea. The frequency distributed form of the Chen and Zhao (2012) model (Eq. (3.6)) allows calculation of a band-averaged C_D. Fig. 3.10 shows average C_D values calculated for the swell (0.03-0.17 Hz) and the wind-sea (0.17-0.7 Hz) bands, plotted against the K_C number for the entire spectrum. Each K_C value represents one spectrum.

The estimated C_D for longer-period waves is generally smaller than that for the wind-sea at each spectrum (K_C number). This is consistent with the theoretical analysis proposed by Lowe et al. (2007) for orbital velocity attenuation within a canopy. Our bulk C_D scales as $C_d\alpha^3$, where C_d is the empirical drag coefficient (assumed to be 2.5 in Lowe et al. (2007)) and α is the ratio of the orbital velocity inside the canopy to that outside the canopy. As demonstrated by Lowe et al. (2005b, 2007), the orbital velocity of the longer-period waves inside the canopy is considerably less (smaller α) than that of the shorter-period waves. This results in smaller C_D values for the longer-period waves (swell) compared to the shorter-period wind-sea component of a spectrum. For practical applications of spectral wave modeling, determining yet another $C_D - K_C$ regression equation may be of limited value, while a more detailed investigation into frequency-dependence of C_D is warranted, which is a subject of a separate section.

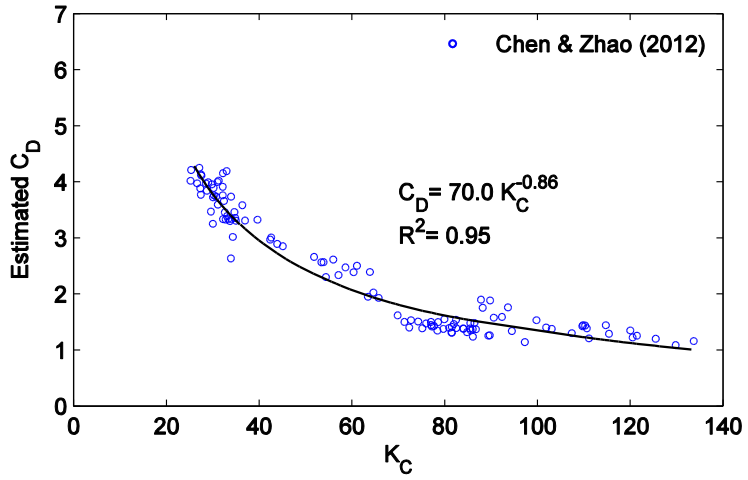

Fig. 3.9. Variation of estimated drag coefficient, with Keulegan-Carpenter number, which is calculated using measurements from the windward gage of each pair and stem diameter.

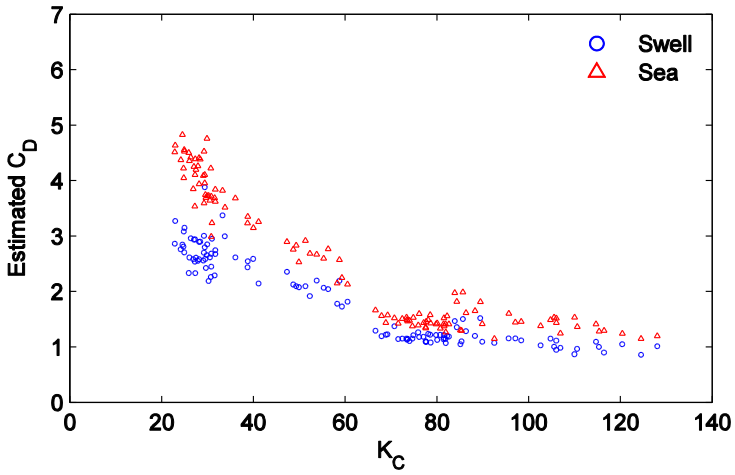

Fig. 3.10. Estimated drag coefficients for the long-period (swell) and the short-period (wind-sea) waves of measured spectra. Each spectrum is represented by a single Keulegan-Carpenter number.

3.1.5 Discussion

The primary objective of this section is to present the unique data and analysis of wave attenuation by vegetation under storm-induced high-energy waves, and review the results in relation to the few past studies, which were mostly conducted under low-energy wave conditions. Based on the published data, a direct comparison of the results, especially the $C_D - K_C$ regression curves, from existing studies (Table 3.1) is not possible. This is due to the different approaches followed in each study. For example, Mendez et al. (1999) estimated C_D as a single calibration parameter fitted to several gages along a transect, while Bradley and Houser (2009) and Paul and Amos (2011) estimated C_D between pairs of gages for each burst. Also, some studies have calculated R_e or K_C based on the maximum orbital velocity at the canopy height, while the others have used near-bed velocity as a reference. Further, this velocity can be either apparent or pore velocity. Some studies have used the average R_e or K_C along the gage

transect, while others have used the value at the first gage. The representative wave period has been selected to be either the peak period or an average period. Among the relationships listed, Mendez et al. (1999) and Kobayashi et al. (1993) were developed under laboratory monochromatic waves, while Bradley and Houser (2009) and Paul and Amos (2011) were developed from field studies of random waves. Moreover, the type of vegetation differs among studies. Nevertheless, the various relationships do show the nature and strength of the dependency on the involved variables.

The results from our study could be extended to reed-like vegetation under similar wave conditions and submergence. In the case of vegetation where above-ground stem is absent or is characterized by significant foliage, our results cannot be applied. The presence of foliage contributes to the drag provided by the plant, especially at lower velocities when it is not streamlined or compressed (Wilson et al., 2008). The vegetation submergence is also important, as the mechanism of turbulence exchange changes from longitudinal to vertical with increasing submergence (Nepf and Vivoni, 2000). Another important factor is the plant flexibility. While empirical results from rigid, reed-like vegetation studies can be used for similar vegetation, for flexible vegetation, models that capture vegetation motion (e.g., Mullarney and Henderson, 2010) must be implemented.

Field data collection of attenuation of storm-induced high-energy waves by salt marsh vegetation poses several challenges which partly explain the lack of such data prior to this study. The first of these challenges is finding a site where a healthy stand of vegetation exists that has a reasonable chance of occurrence of sufficient water depth and waves. This is difficult because, along the coastal locations where high-energy waves are routinely present, salt marsh vegetation does not survive. Therefore, one has to look for a site that has established vegetation, has a fair chance of inundation, and has a favorable fetch to produce high-energy wave conditions when high winds become available. Due to the changing forecast of the storm-track, several candidate salt marsh sites are needed to be considered. The ultimate deployment site can usually be decided only a couple of days prior to cyclone landfall. Our 2011 Tropical Storm Lee field experiment was successful only after failed attempts in 2009 (Tropical Storm Ida) and 2010 (Tropical Storm Bonnie) when our study sites fell on the left side of the storm-track and did not experience either surge or waves along our wave gage transect. Due to the anti-clockwise wind field of the tropical storms in the northern hemisphere, the coastal water is pushed out of the wetlands on the left side of the storm.

Second, the sustained high winds (>20 m/s) and wave forces associated with the storms make it difficult to deploy any upright instrumentation such as video cameras, wave staffs, meteorological stations or acoustic Doppler velocity profilers on wetlands. Therefore, one is limited to the use of bottom-mounted pressure transducers with a short window for rapid deployment prior to cyclone landfall. The presence of high winds also makes it necessary to ascertain that the source terms of wave generation and white-capping (even if the fetch between the gages is short) are negligible compared to the wave energy loses due to vegetation. This is less of a concern in low-energy wave-vegetation studies.

Finally, the relatively rapidly changing (compared to tidally varying) storm-induced hydrodynamic environment results in simultaneous changes in surge, wave heights, and wave periods. The opportunity of controlling one variable to examine others is thus unavailable under storm conditions. Comparatively, when wave attenuation through vegetation is studied during high tide inundation, the depths are relatively stable while wave parameters could be changing.

Though the findings of this study are applicable to any coastal area with Spartina-type salt marsh vegetation, it provides critical wave attenuation and drag information applicable to the vast marshes of the Northern Gulf of Mexico. Due to the catastrophic land-loss and the ensuing navigational, and oil and gas industry impacts of national importance, protection of coastal wetlands in this region to reduce storm damages has become critically important, warranting science based solutions (e.g., Day et al., 2007; CPRA, 2012). Numerical models of wave and surge employed in the design and protection of coastal infrastructure and for resource management will benefit from the improved understanding of vegetation-induced wave attenuation in these wetland systems.

3.1.6 Summary

The phenomenon of wave energy dissipation by salt marsh has been investigated by several laboratory studies but relatively few field studies. Further, the existing field studies were carried out in a low-energy wave environment, limiting their applicability to the high-energy wave field, such as that produced during a tropical cyclone. The present study fills this gap in the knowledge of this important phenomenon by providing analysis of cyclone generated waves over salt marsh consisting of *Spartina alterniflora*. This is the first comprehensive field dataset acquired and analyzed over salt marsh vegetation under tropical storm wave conditions.

The magnitude of the wave height reduction rate, r, commonly expressed by Eq. (3.8) was found to vary considerably (1.5 to 4% /m) depending on the magnitude of incident wave height. Since the incident wave height was different for each pair of gages, r was spatially variable, making it unreliable as a general indicator of the effectiveness of vegetation in wave damping. Also, r values based on observations from different vegetation types or wave conditions cannot be compared.

Consistent with the previous studies, the storm waves were observed to attenuate exponentially over vegetation (decay rates of 0.022-0.051 /m). The larger waves attenuated at a smaller rate than the smaller waves. The wave height attenuation rate was also observed to be dependent on the magnitude of the dominant frequency of the wave systems. The low-frequency waves (swell) attenuated at a lower rate than the high-frequency wind-sea waves. This is consistent with Lowe et al. (2007), who observed efficient attenuation of higher frequency random waves by a rigid model canopy array.

The bulk drag coefficient C_D (1.2-4.3) was estimated along the study transect using two formulations, namely Mendez and Losada (2004) and Chen and Zhao (2012). This coefficient does not represent the drag coefficient of an isolated rigid cylinder but rather a bulk drag coefficient that is temporally and spatially averaged over the vegetation patch. It accounts for uncertainties associated with processes that are not explicitly defined in the equations, such as wake interference due to other vegetation, frictional losses due to vegetation blades in addition to stems, and, most importantly, reduced velocity inside a canopy. Consistent with the previous studies, C_D was observed to decrease with increasing R_e and K_C numbers. The coefficients of the empirical relationship between C_D and R_e developed in this study are consistent with those reported in the literature. For *Spartina* type vegetation, this relationship can be applied within the R_e range of 600-3,200. The *Spartina* spp. is found along the margins of the most continents in the temperate zone (e.g., Chapman, 1960). Comparison of published empirical relationships between C_D and non-dimensional numbers, such as of R_e and K_C requires caution, because the methods employed in various studies to estimate C_D differ, as do the definitions of R_e and K_C.

In a given wave spectrum, the C_D was observed to be smaller for the longer-period waves than for the shorter-period waves. The data presented in this section has been analyzed to quantify variation of the bulk drag coefficient across frequency scales. The results of these analyses are documented in the next section.

3.2 Spectral Distribution of Wave Energy Dissipation by Salt Marsh Vegetation

3.2.1 Introduction

Wave propagation through vegetation is an important physical process along many coastal regions of the world and along the shores of large inland lakes. Waves approaching vegetated shores lose energy due to obstructing vegetation. This reduces shoreline erosion and is of engineering significance for shoreline defense. The role and importance of coastal wetlands as a natural defense system against storm waves is generally acknowledged (e.g., Dixon et al., 1998; Costanza et al., 2008; Lopez, 2009; Gedan et al., 2011). Utilization of coastal wetlands to augment structural measures for coastal flooding mitigation from storm surge and waves is promoted in several regions of the world (e.g., Borsje et al., 2011; CPRA, 2012).

A body of literature exists quantifying reduction rates of integral wave heights due to vegetation (for summary, see Anderson et al., 2011; Jadhav and Chen, 2012). Theoretical models, based on energy conservation, have been proposed that are applicable either for monochromatic waves (Dalrymple et al., 1984) or for narrow-banded random waves (Mendez and Losada, 2004). Kobayashi et al. (1993) presented an approach based on continuity and momentum equations and assuming exponential decay of integral wave height. Chen and Zhao (2012) proposed a vegetation-induced-dissipation model based on the formulation of Hasselmann and Collins (1968) for energy dissipation of random waves by bottom friction. All these models assume rigid vegetation. Recently studies have underscored the importance of accounting for stem and blade motion in case of flexible vegetation and have proposed models that account for it (Bradley and Houser, 2009; Mullarney and Henderson, 2010; Riffe et al., 2011). Wave attenuation has been studied in a controlled laboratory environment (Dubi and Tørum, 1996; Løvås and Tørum, 2001; Augustin et al., 2009; and Stratigaki et al., 2011), in field conditions involving salt marshes (Möller et al., 1999; Möller and Spencer, 2002; Cooper, 2005; Möller, 2006; Bradley and Houser, 2009; Riffe et al., 2011; Jadhav and Chen, 2012), coastal mangrove forests (Mazda et al., 2006; Quartel et al., 2007), and vegetated lakeshores (Lövstedt and Larson, 2010). All the studies to-date are primarily focused on the analysis of attenuation of integral wave heights, energy and estimates of integral bulk vegetation drag coefficients.

As a step beyond integral dissipation characteristics, Lowe et al. (2005) developed an analytical model to predict the magnitude of the in-canopy velocity of waves propagating over model canopy made up of rigid cylindrical cylinders. They parameterized the canopy forces by using a friction coefficient for the shear stress at the top of the canopy, and drag and inertia coefficients. Further, using limited laboratory experiments of monochromatic waves through the artificial canopy they demonstrated that the velocity attenuation inside canopy varied with canopy geometrical properties, various force coefficients and wave excursion length. The velocity attenuation was quantified by a parameter, α_L, which they defined as the ratio of vertically averaged velocity inside canopy to the canopy-independent velocity above the canopy. Lowe et al., (2007) extended this model to wave spectra and predicted that the wave energy would dissipate more efficiently in the high frequency components. The model was

verified by submerging an artificial rigid cylinder canopy on a barrier reef (random wave conditions) for 2 hours and assuming a constant drag coefficient.

In the case of natural vegetation under random waves, there are no published studies that examine in detail the frequency-based characteristics of wave energy dissipation and drag coefficient, though some studies have illustrated such characteristics with an example (Bradley and Houser, 2009; Paul and Amos, 2011). The present study aims to investigate the spectral characteristics of the wave energy dissipation due to natural vegetation and the relationship of the dissipation with the incident wave energy spectrum using comprehensive field data. It also reveals spectral variation of vegetation drag coefficient. We hypothesize that the frequency varying drag coefficient will predict spectral distribution of energy dissipation more accurately than that predicted using an integral drag coefficient. To test the hypothesis, first a consistent method is developed to estimate the spectral drag coefficient over the entire range of measured wave spectra. The spectral and integral drag coefficients are then applied to estimate energy dissipation losses which are compared with the observed dissipation to assess the effectiveness of the proposed approach.

The next subsection describes the spectral energy dissipation model proposed by Chen and Zhao (2012) which is used to estimate drag coefficients and introduces the velocity attenuation factor. It is followed by subsections that describe the field program and the wave data conditions. In the data analysis that follows, spectral characteristics of the observed energy dissipation are examined. Spectral variation of estimated drag coefficient is then demonstrated, and the spectral behavior of the mean velocity attenuation parameter is quantified. The mean velocity attenuation parameter and average drag coefficients are then applied to predict energy dissipation and compared with the existing prediction methods. Finally the results are discussed, followed by summary.

3.2.2 Spectral Energy Dissipation Model

Assuming the linear wave theory holds, evolution of random waves propagating through vegetation can be expressed with the wave energy balance equation as follows,

$$\frac{\Delta(E_j C_{g,j})}{\Delta x} = -S_{ds,j} \tag{3.17}$$

where subscript j represents the j^{th} frequency component of a wave spectrum, E is the spectral wave energy density, $C_g = nc$ is the group velocity, $c = \sqrt{(g/k)\tanh(kh)}$ is the phase speed, k is the wave number, h is the still water depth, g is the acceleration due to gravity and coefficient n is given by $n = (1/2)[1 + (2kh/sinh2kh)]$. The cross-shore coordinate is given by x pointing landward and S_{ds} is the energy dissipation due to vegetation per unit horizontal area. All other source terms are considered negligible compared to the vegetation induced losses.

The spectral wave energy dissipation due to vegetation is obtained by a reorganized form of the model proposed by Chen and Zhao (2012). The model treats vegetation as rigid, cylindrical elements that impart drag forces on the flow. Further, the drag forces due to pressure differences are only considered as they are much larger than those arising from friction in the hydraulic regimes encountered in the field conditions.

According to Chen and Zhao (2012), the spectral energy dissipation due to vegetation can be expressed by,

$$S_{ds,j} = \frac{1}{2}\frac{C_{D,j} b_v N_v}{g}\left(\frac{\sigma_j}{sinh\, k_j h}\right)^2 \left(\sum_{-h}^{-h+sh} U_{z,rms}(z)\cosh^2\left[k_j(h+z)\right]\Delta z\right) E_j \tag{3.18}$$

where $C_{D,j}$ is a bulk drag coefficient, b_v is the stem diameter, N_v is the vegetation population density, σ_j is the wave angular frequency, s is the ratio of vegetation height, h_v, to the still water depth, h, and U_{rms} is the root-mean-squared (RMS) velocity given by,

$$U_{z,rms} = \sqrt{2\sum_{j=1}^{j=N_f} \frac{\sigma_j^2 \cosh^2 k_j(h+z)}{\sinh^2 k_j h} E_j \Delta\sigma} \tag{3.19}$$

where N_f is the total number of frequency components of a spectrum.

Eq. (3.18) is based on the quadratic representation of the shear stress induced by the vegetation. We parameterize the shear stress due to vegetation drag at elevation z (positive downwards with origin at the still water level) due to j^{th} component of the spectrum as,

$$\tau_{z,j} = -\frac{1}{2}\rho b_v N_v C_{D,j}\alpha_j u_{z,j}\left|\alpha_j u_{z,j}\right|\Delta z \tag{3.20}$$

where ρ is the density of water and $\alpha_j u_{z,j}$ is the vegetation-affected velocity at elevation z. The velocity attenuation parameter, α, is defined as the ratio of the vegetation-affected velocity, u_z', to the velocity in the absence of vegetation, u_z, at elevation z inside the canopy.

$$\alpha_{z,j} = \frac{u_{z,j}^{'}}{u_{z,j}} \tag{3.21}$$

This parameter is similar to Lowe et al. (2005) but not exactly the same.

Similar to the definition of α in Eq. (3.21), the ratio of the vegetation-affected RMS velocity at an elevation z, $U'_{z,rms}$, to the RMS velocity in the absence of vegetation, $U_{z,rms}$, at elevation z inside the canopy is defined as,

$$\alpha_{z,r} = \frac{U'_{z,rms}}{U_{z,rms}} \tag{3.22}$$

Using these definitions, Chen and Zhao (2012) formulation is reorganized and the spectral distribution of energy dissipation is expressed as,

$$S_{ds,j} = \frac{1}{2}\frac{\bar{C}_D b_v N_v}{g}\frac{\alpha_{z,j}^2}{\alpha_{z,r}^2}\left(\frac{\sigma_j}{sinh\, k_j h}\right)^2 \left(\sum_{-h}^{-h+sh} U_{z,rms}\cosh^2\left[k_j(h+z)\right]\Delta z\right) E_j \tag{3.23}$$

where $\bar{C}_D$ is the spectrally-averaged drag coefficient. To facilitate solution of Eq. (3.23), α is assumed to be independent of depth and a normalized form of α is introduced as,

$$\alpha_{n,j} = \frac{\alpha_j}{\alpha_r} \tag{3.24}$$

Note that while α_j is always less than 1, $\alpha_{n,j}$ can be greater than 1. Using this parameter, Eq. (3.23) can then be re-written as,

$$S_{ds,j} = \frac{1}{2}\frac{\bar{C}_D b_v N_v}{g}\alpha_{n,j}^2\left(\frac{\sigma_j}{sinh\, k_j h}\right)^2\left(\sum_{-h}^{-h+sh} U_{z,rms}\cosh^2\left[k_j(h+z)\right]\Delta z\right)E_j \tag{3.25}$$

The spectrally variable drag coefficient is then expressed as,

$$C_{D,j} = \bar{C}_D \cdot \alpha_{n,j}^2 \tag{3.26}$$

Integrated over the entire spectrum, the time-averaged rate of energy dissipation per unit area is given by,

$$S_v = \sum_{j=1}^{j=N_f} S_{ds,j}\Delta\sigma \tag{3.27}$$

3.2.3 Study Area and Field Program

The study site was a salt marsh wetland in Terrebonne Bay on the Louisiana coast of the Gulf of Mexico (Fig. 3.11) near the Mississippi River delta. The shallow (depth, 1-3 m), micro-tidal (diurnal tidal range < 0.5 m) bay is bordered with salt marsh in the northern region and with a series of narrow, low-lying barrier islands on the south. The waves in the bay consist of frequent low-energy offshore swell and locally generated seas which intensify during the passages of annual winter cold fronts and tropical cyclones.

During Tropical Storm Lee (September 3-4, 2011), three wave gages (pressure transducers W1 through W3) were deployed on a vegetated platform marsh along a north-south transect (28 m long) approximately perpendicular to the marsh edge (Fig. 3.11). The shore-normal has a bearing of 20°. A maximum of 20° error in the alignment would reduce the travel distances between the gages by about 6% $(1-\cos 20°)$ introducing corresponding error in estimates of energy dissipation. Waves approached from the south and propagated from Gage W1 to W3 through vegetation. Gage W1 was located more than 16 m inwards of the marsh edge to avoid the breaking zone created by waves breaking at the marsh edge. The self-logging pressure sensors sampled continuously at 10 Hz over the 2-day duration of the storm.

The dominant vegetation at the site is *Spartina alterniflora* with thick stem and thin, tapering flexible narrow blades. The average measured vegetation properties were; N_v =422 stems/m^2, h_v =0.22 m, h_{vt} =0.63 m, b_v =8.0 mm, and E_v =80 MPa (E_vI_v =0.015 N-m^2) where E_vI_v is the flexural rigidity and I_v is the second moment of inertia of a stem. Based on our observations and the estimated non-dimensional stiffness parameter (Mullarney and Henderson, 2010), the vegetation is treated as rigid (see analysis in Jadhav and Chen, 2012).

The measured continuous pressure time series was analyzed using standard spectral techniques (e.g., Bendat and Piersol, 2000). The resulting energy spectra had bandwidth, Δf, of 0.01 Hz with 95% of the spectral energy between 0.03 and 0.7 Hz. Thus each spectrum had 69 frequency components (N_f in Eq. (3.27)). The integral wave parameters are defined as: significant wave height, $H_{mo} = 4\sqrt{m_0}$; mean wave period, $T_z = \sqrt{m_0/m_2}$; and spectral width,

$\nu = (m_0 m_2 / m_1^2 - 1)$ where m_0, m_1, and m_2 are the zero-th, first and second moment of the wave spectrum respectively.

The wave energy losses due to vegetation were considered dominant compared to the other source terms. To ascertain the validity of this assumption, the relative magnitude of source terms of the local wave generation and the losses due to bottom-friction, white-capping, and depth-limited breaking were evaluated. The wave records with significant potential for these source terms were removed from further analysis (for details see Jadhav and Chen, 2012).

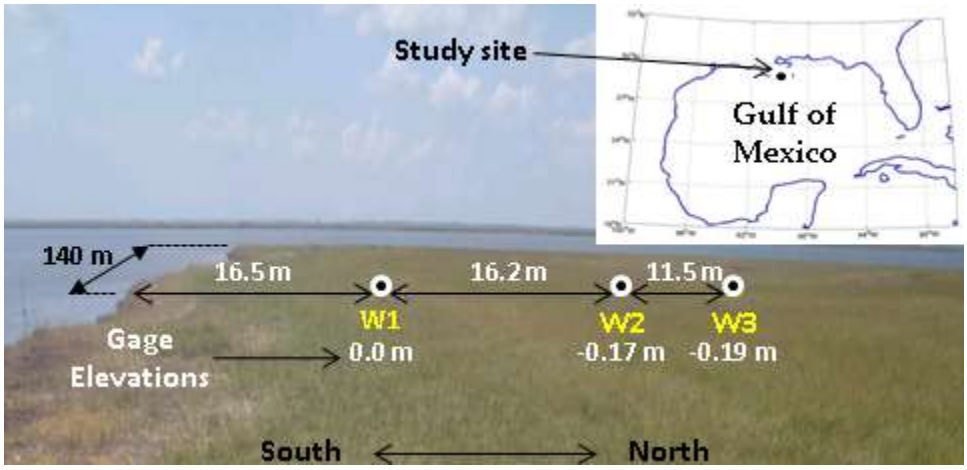

Fig. 3.11. Study area location (Terrebonne Bay, Louisiana) and the schematic of experimental set up showing wave gages (W1-W3). Gage elevations relative to gage W1. Not to scale.

3.2.4 Overview of Wave Conditions

A total of 177 wave records (59 sets of 3 bursts, one at each gage) measured at gages W1,W2 and W3 were analyzed in this study. Table 3.2 lists the ranges and statistics of water depth, zero-moment wave height, mean period and some derived parameters characterizing the wave conditions. The table shows only the analyzed data and not the entire data set. As stated in the previous subsection, the wave records that violated assumptions of Eq. (3.17) were removed from analysis. With the diurnal tide augmented by the storm surge, the water depth rose from about 0.1 m to 0.8 m and then fell along with the tide. However, only the measurements made during water depths greater than 0.4 m are considered in this study because wave energy levels were insignificant during depths smaller than 0.4 m. The incident wave heights (H_{mo}) on the marsh varied from 0.05 to 0.39 m and were directly proportional to the depth of water. The recorded wave spectra were largely bimodal (Fig. 3.12) with distinct low-frequency swell (7-10 s) and wind-sea components (2-4.5 s). The relative depth, h/L_z, was less than 0.2 indicating relatively shallow water depths during the observation period (Wave length L_z is based on the mean wave period). Spectral width, ν, ranged from 0.42 to 0.86, an indicator of broad nature of spectra. Table 3.2 also shows Ursell number, $H_{mo}L_z^2/h^3$, as a measure of non-linearity. Waves were largely non-linear at W1 but the non-linearity quickly reduced as the waves propagated further (beyond W2) into the marsh and dissipated.

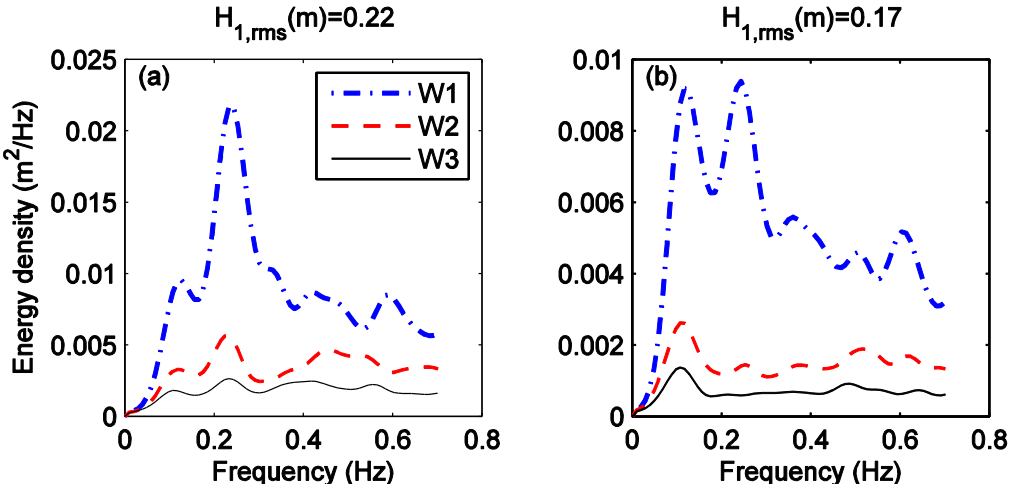

Fig. 3.12. Wave energy spectra recorded on September 3, 2011 at (a) 6:45 UTC and (b) 12:30 UTC.

Table 3.2. Range and mean (in parenthesis) values of analyzed wave parameters

Parameter	Gage W1	Gage W2	Gage W3
Depth, h (m)	0.40-0.82 (0.55)	0.57-1.0 (0.72)	0.57-1.01 (0.72)
Significant wave height, H_{mo} (m)	0.15-0.40 (0.24)	0.07-0.28 (0.14)	0.04-0.21 (0.09)
Peak wave period, T_p (s)	2.5-4.7 (4.0)	1.2-4.5 (2.3)	1.3-4.5 (2.6)
Relative wave height, H_{mo}/h	0.36-0.49 (0.41)	0.12-0.29 (0.18)	0.08-0.22 (0.12)
Relative depth, h/L_z	0.07-0.13 (0.10)	0.09-0.16 (0.13)	0.10-0.16 (0.12)
Spectral width, ν	0.45-0.58 (0.51)	0.44-0.64 (0.5)	0.43-0.65 (0.53)
Ursell number, $H_{mo}L_z^2/h^3$	29-81 (48)	9-16 (11)	6-10 (8)

3.2.5 Observed Spectral Wave Energy Dissipation Characteristics

Measured spectra showed significant wave energy reduction over vegetation as evidenced by the reduction in wave heights (Table 3.2). Energy reduction with respect to frequency was calculated between pairs of wave gages (W1-W2 and W2-W3) based on the measured wave energy density spectra using Eq. (3.17). Ensemble averages of all analyzed energy density spectra, along with the ensemble average of the energy dissipation is shown in Fig. 3.13 for reach W1-W2 (between gages W1 and W2) and W2-W3 (between gages W2 and W3). The energy density and dissipation are normalized by, m_0, the zero-th moment of the individual spectrum measured at the windward gage of the pair of gages bounding the reach. Fig. 3.13 shows that the magnitude of energy dissipation varies with the frequency. Higher dissipation was observed at the frequencies adjacent to the spectral peak in both reaches. Most of the wind-sea energy dissipated in the leading vegetation reach, W1-W2. Significant portions of swell energy propagated beyond the leading reach and dissipated in reach W2-W3.

Fig. 3.13 also shows that the dominant loss near the spectral peak is less pronounced in the second reach W2-W3, where the frequencies higher than the peak contain substantial portion of the total energy loss. This is illustrated in Fig. 3.14 where energy reduction in the dominant wave frequencies, i.e., swell and sea band (0.03-0.36 Hz), as a percentage of the total (0.03-0.7 Hz) energy reduction is plotted as a function of Keulegan-Carpenter number, K_C. The K_C

number is defined as, $K_C = U_{rms}T_z/b_v$, where U_{rms} is the root-mean-square orbital velocity at the bed considering the entire spectrum. In the first reach W1-W2, wave energy reduction in the dominant frequencies accounted for 55 to 70% of the total reduction while in the subsequent reach W2-W3, this percentage was only 40 to 55%. Thus, in reach W2-W3 the energy reduction was more evenly distributed between dominant and higher frequencies. This is partly due to the non-linear transfer of energy to the higher frequencies modifying spectral shape as waves propagated from W1 to W2.

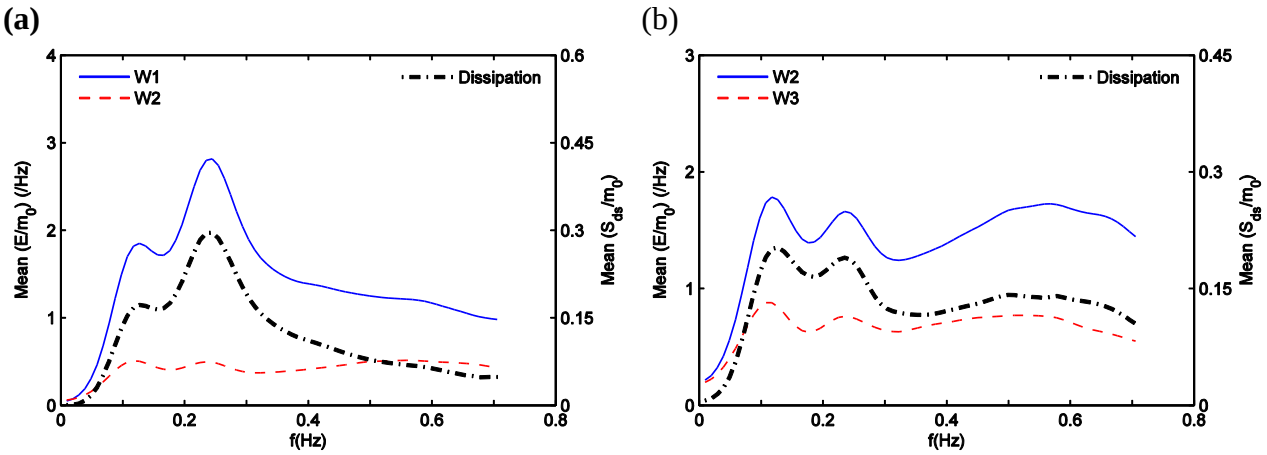

Fig. 3.13. Ensemble average of all normalized energy density and energy dissipation spectra in reach: (a) W1-W2 and (b) reach W2-W3. Spectra normalized by the zero-th moment (m_0) of the energy spectrum measured at the windward gage of the pair of gages.

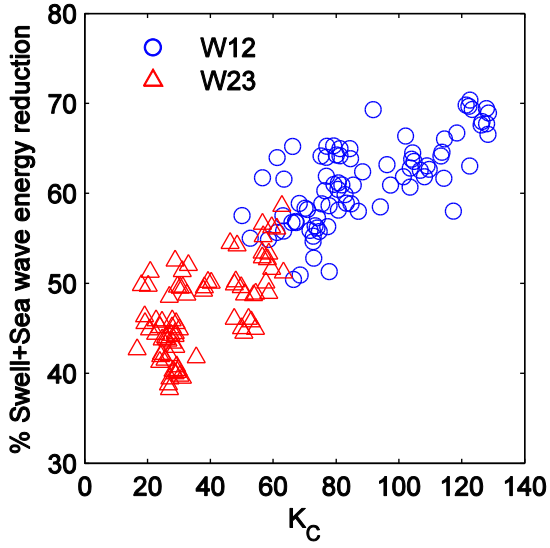

Fig. 3.14. Wave energy reduction in the swell and sea band (0.03-0.36 Hz) as a percentage of the total (0.03-0.7 Hz) energy reduction.

Across the frequencies above peak, the spectral distribution of energy dissipation was observed to gradually taper off. The rate of such tapering with respect to spectral frequency is shown in Fig. 3.15 using normalized dissipation ($S_{ds}(f)/E(f)$) for 3 ranges of Keulegan-Carpenter number, K_C. The choice of the range of K_C for ensemble averaging is inconsequential

and is made for the purpose of creating three ranges of K_C signifying ranges of hydrodynamic conditions.

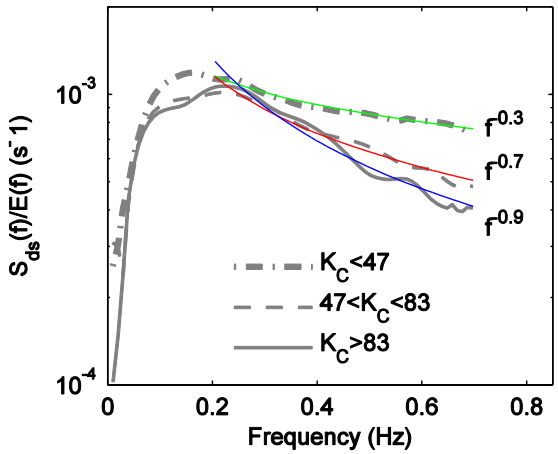

Fig. 3.15. Frequency distribution of the the normalized energy dissipation rate versus frequency. Curves represent ensemble average of all measured spectra in reach W1-W2 and W2-W3. The thin smooth solid lines are obtained by least-square fit to the data points above spectral peaks.

Variation of the frequency exponent over all spectra with respect to K_C is shown in Fig. 3.16. Larger K_C numbers generally represent waves in reach W1-W2. They were more energetic with more peaked spectra and larger concentration of energy in the swell-sea band (0.03-0.36 Hz). On the other hand, the smaller values of K_C numbers represent relatively low energy waves with much broader spectra. Fig. 3.15 shows that at frequencies above the peak, the normalized energy dissipation has a stronger dependence on frequency at higher K_C numbers.

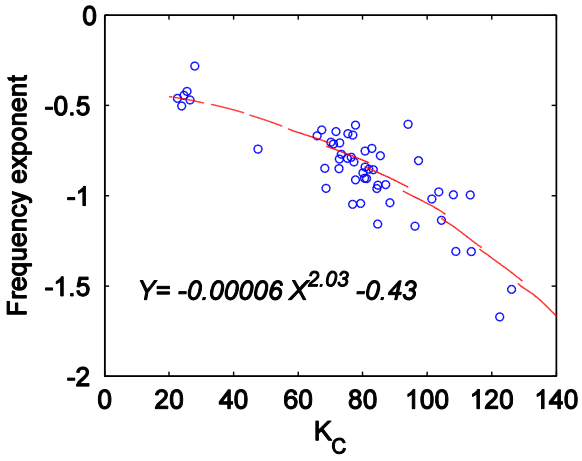

Fig. 3.16. Frequency exponent for all spectra. Only data points with $R^2 > 0.8$ are shown.

The current modeling practice assumes that the distribution of energy dissipation generally follows the incident wave energy density spectrum (e.g., Suzuki et al., 2011). To assess the extent of validity of this assumption, the following hypothesis was tested using measurements:

$$S_{ds}(f) = a \cdot E(f)^b \tag{3.28}$$

where a and b are determined by regression analysis. For a given reach (W1-W2 or W2-W3), each incident energy spectrum, $E(f)$, and the corresponding dissipation spectrum, $S_{ds}(f)$, were divided into three frequency bands of swell (0.03-0.16 Hz), wind-sea (0.16-0.32 Hz) and high frequency (0.32-0.7 Hz). Such division was facilitated by local spectral energy minima observed around 0.16 Hz and 0.32 Hz in the recorded bimodal spectra. For each of these three frequency regions, a coefficient pair (a, b) was determined by fitting Eq. (3.28). Thus for each spectrum (or wave record), three such pairs were obtained. All pairs corresponding to R^2 (coefficient of determination) smaller than 0.8, were discarded from further consideration.

The exponent b is a measure of linearity (linear when b=1) of the relationship between energy dissipation, $S_{ds}(f)$ and incident spectrum, $E(f)$. The probability of occurrence of b is plotted in Fig. 3.17 for the three hydrodynamic ranges based on K_C (based on the entire spectrum). Note that a K_C value of about 60 segregates first pair of gages, W1-W2, and the second pair, W2-W3. Fig. 3.17 shows that the relation between $S_{ds}(f)$ and $E(f)$ is not consistently linear ($b \neq 1$) across the frequency scales. The relation tends to be most linear in the wind-sea band across the entire K_C range with slightly narrow distribution in the middle K_C range. The relationship between the dissipation distribution and spectral shape becomes slightly more nonlinear in the swell band. The coefficient b tends to increase at smaller K_C numbers (second reach). In the high frequency band (f>0.32 Hz) the relationship between $S_{ds}(f)$ and $E(f)$ is linear for waves with K_C<47 and gradually becomes nonlinear with increasing K_C. Note that the energy spectra and hence the dissipation in this high frequency range is also affected by non-linear interactions. Parameter a in Eq. (3.28) was confirmed to be equal to the ratio of the integrated dissipation to the total wave energy, S_v/m_b, where $m_b = \int E^b df$ and $S_v = \int S_{ds}\, df$.

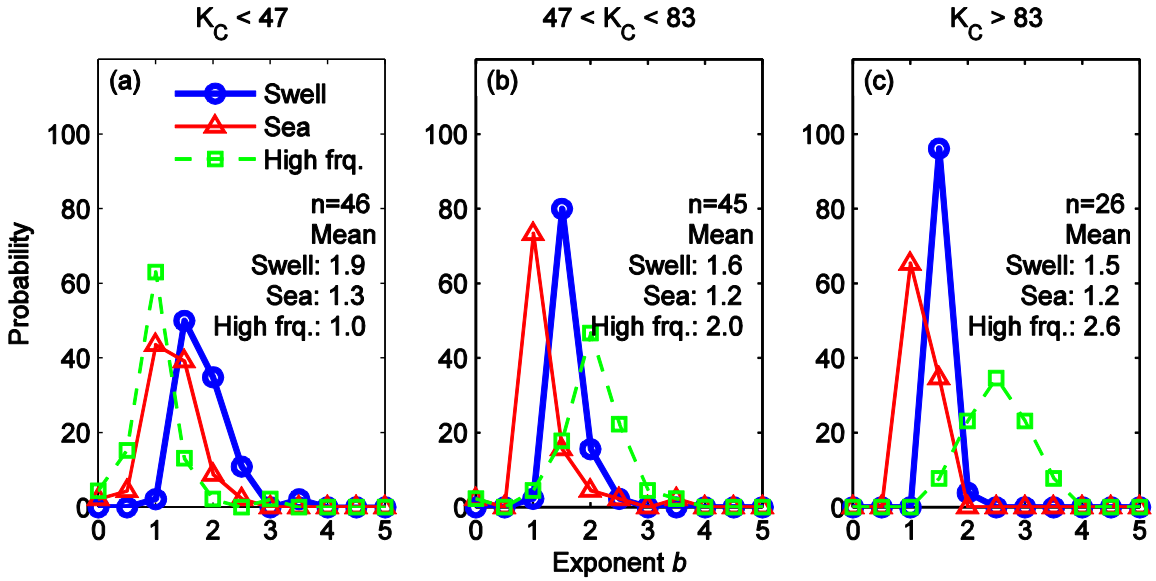

Fig. 3.17. Probability of occurrence of exponent b (Eq. (3.28)) with respect to ranges of Keulegan-Carpenter number.

3.2.6 Estimates of Integral and Frequency –dependent Drag Coefficient

As noted before, the integral energy dissipation formulations (e.g., Mendez and Losada, 2004) assume the drag coefficient is independent of frequency and determine its single value, $\bar{C}_D$, for the entire spectrum, which is assumed to be narrow-banded. The variation of drag coefficient with the hydrodynamics has been typically related to the Reynolds (R_e) and Keulegan-Carpenter (K_C) numbers using empirical forms. Several studies have developed such empirical formulations for integral estimates of $\bar{C}_D$ (Kobayashi et al., 1993; Mendez et al., 1999; Mendez and Losada, 2004; Bradley and Houser, 2009; Paul and Amos, 2011; Sánchez-González et al., 2011; Jadhav and Chen, 2012). The empirical relations provide a valuable tool to use in the models predicting integral wave heights. For the data presented in this section, the integral drag coefficients correlate well to the K_C number ($R^2 = 0.95$) (Fig. 3.18), resulting in the following empirical relation:

$$\bar{C}_D = 70\, K_C{}^{-0.86} \qquad 25 < K_c < 135 \tag{3.29}$$

Note that this drag coefficient represents the "bulk" value over the measurement transect (vegetation patch) rather than the drag coefficient of an idealized isolated, cylinder (e.g., Tanino and Nepf, 2008). The $\bar{C}_D$ in Fig. 3.18 was estimated using Eq. (3.25). Using the same equation and allowing the drag coefficient to vary with frequency for each spectrum produces a frequency distributed drag coefficient. Fig. 3.19 shows such distributions that are ensemble averaged over the three K_C ranges.

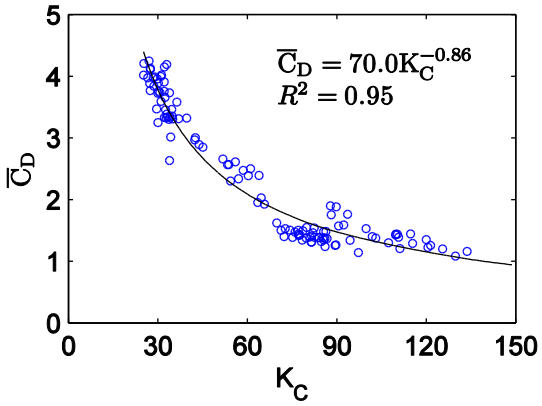

Fig. 3.18. Estimated integral bulk drag coefficient and its variation with the Keulegan-Carpenter number.

It is clear that a single integral drag coefficient over the entire spectral frequency scale will not reflect the spectral distribution of the energy dissipation. This is most notable for the smallest range of K_C, where the drag coefficient varies by a factor of 6. Therefore, in the studies of wave spectral evolution dominated by energy losses due to vegetation, a frequency varying drag coefficient may be more appropriate to predict the dissipation. Eq. (3.29) along with Eq. (3.26) enables computation of the frequency varying drag coefficient, C_D when $\bar{C}_D$ and α_n are known. For a given spectrum (with its K_C), $\bar{C}_D$ can be determined from Eq. (3.29). To determine α_n, the following procedure was followed. Using measured energy spectra, Eq. (3.17) and Eq. (3.25) were numerically solved to compute $\alpha_{n,j}$ for each frequency component of a spectrum.

All $\alpha_{n,j}$ profiles were then the ensemble-averaged to produce a single $\bar{\alpha}_n$ curve shown in Fig. 3.20.

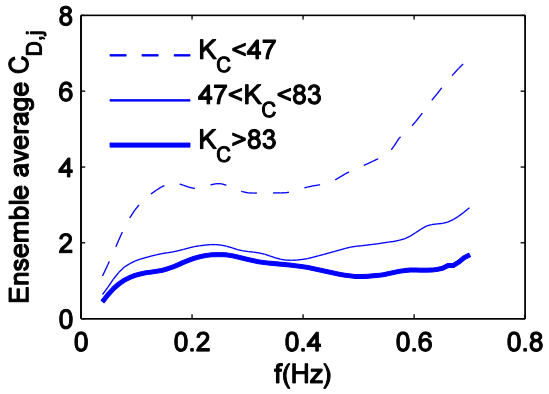

Fig. 3.19. Spectral variation of C_D. All individual spectral distributions ensemble-averaged based on K_C ranges.

Across the spectrum of frequencies, $\bar{\alpha}_n$ gradually increases up to the region of the peak and then slightly decreases. The values above about 0.4 Hz are not considered reliable due to influence of non-linear energy transfer and higher amplification of noise due to pressure response function in that region and are ignored in the further analysis. Parameter $\bar{\alpha}_n$ (Fig. 3.20), when multiplied by integral $\bar{C}_D$ obtained from Eq. (3.29), provides frequency-dependent values of C_D which can be used to predict the frequency-dependent dissipation in wave spectra.

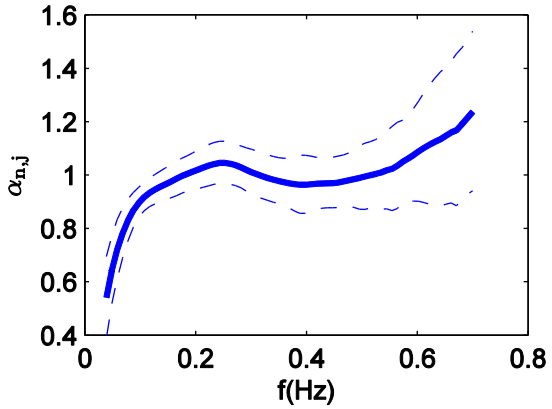

Fig. 3.20. Spectral variation of ensemble-averaged α_n based on all 118 measured prodiles. Dashed lines represent ±1 standard deviation.

3.2.7 Prediction of Energy Dissipation Using Estimated Drag Coefficients

To estimate energy dissipation due to vegetation in practical applications, appropriate selection of the drag coefficient is necessary. This section implements two approaches of selecting drag coefficients with the goal of improving the prediction of wave spectra in fields of vegetation.

In the first, simple approach (existing practice) an integral drag coefficient, $\bar{C}_D$ (e.g., using Eq. (3.29)) is specified and then spectral dissipation is calculated using Eq. (3.18). In the second approach, the frequency-dependent drag coefficient, C_D, is specified (Eq. (3.26)) and then spectral dissipation is calculated using Eq. (3.18). As an illustration, Fig. 3.21 shows the comparison of the measured and predicted energy dissipation for one wave record using these two approaches.

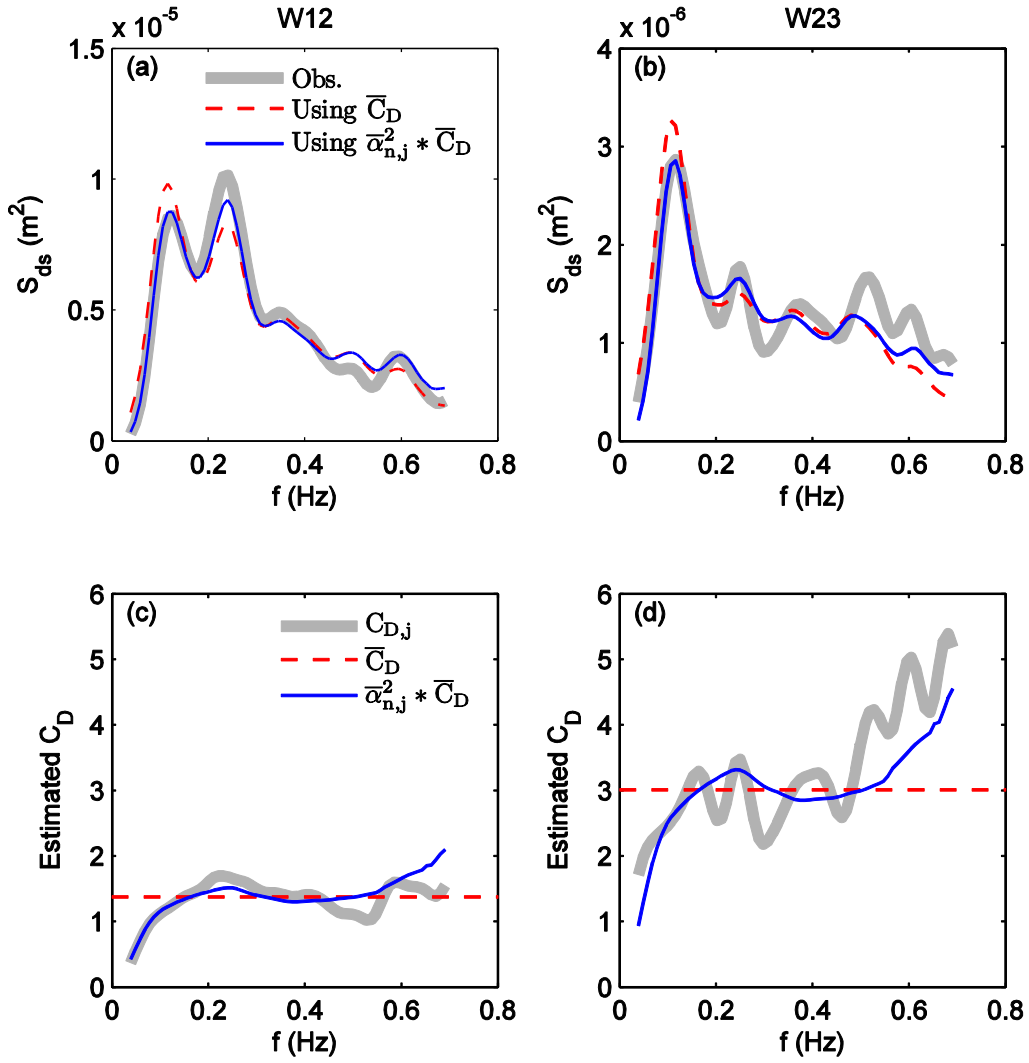

Fig. 3.21. Comparison of observed and predicted spectral energy dissipation using average and spectral drag coefficient for a sample wave record on September 3, 2011 at 12:30 UTC. (a) Dissipation between W1-W2 and (b) W2-W3. Dissipation based on drag coefficient shown in (c) for W1-W2 and (d) for W2-W3.

The frequency-dependent C_D predicts the distribution of energy dissipation with higher accuracy than does the integral $\bar{C}_D$. To assess the predictive skill of spectral C_D over the entire dataset, the error between the measured and the predicted dissipation was calculated for each record and was ensemble averaged as shown in Fig. 3.22a. In the frequency range with the dominant energy (0.03-0.36 Hz), the dissipation predicted by the frequency varying C_D has

much less error than that predicted by the average $\bar{C}_D$. The improvement is especially significant in the vicinity of the spectral peak frequencies where the largest dissipation is encountered. Additionally, Fig. 3.22b shows that by employing frequency-varying C_D, the model is able to predict total dissipation, S_v (Eq. (3.27)) reliably. The error in the prediction of S_v is generally less than 5%. The mean error in the predicted H_{mo} (0.03-0.36 Hz, the dominant frequency range) at gage W2 and W3 by the two methods ($\bar{C}_D$ and frequency-varying C_D) are (6.5% and 8.2%) and (-5.0% and -2.3%) respectively. At W2, the C_D method may appear slightly worse than the $\bar{C}_D$ method, however, the true advantage of the C_D method is in the improved frequency distribution as seen in Figs. 3.22(a) and (b). This is reflected in the much better improvement in the estimate of mean period with errors being (-9.0% and 4.1%) and (-2.6% and 1.5%) at gages W2 and W3, respectively. Likewise the spectral width estimates show improvement by the C_D method compared to the $\bar{C}_D$ method with errors being (-25.1% and -5.4%) and (-9.2% and 2.1%) at gages W2 and W3, respectively.

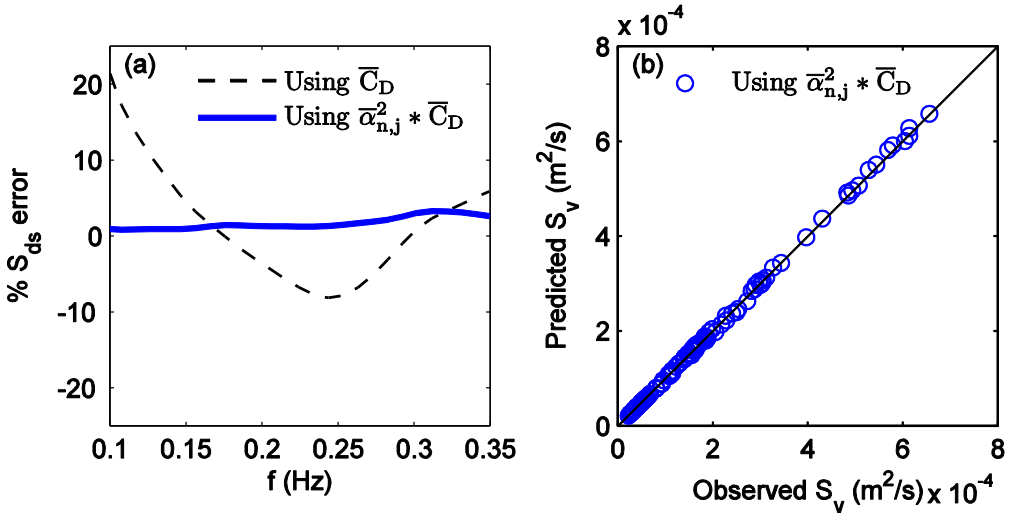

Fig. 3.22. (a) Ensemble average of percentage error between the observed and estimated spectral energy dissipation using average and spectral drag coefficients (b) Comparison of predicted and observed total energy dissipation.

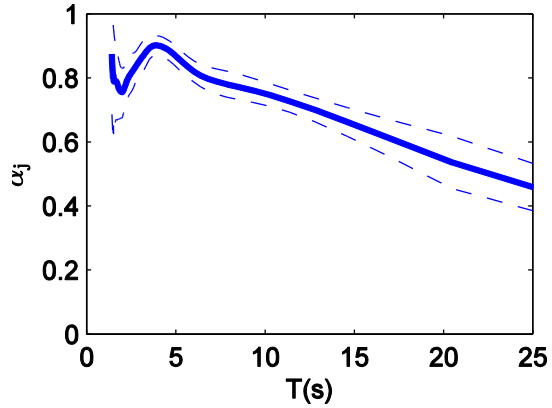

Fig. 3.23. Variation of ensemble-averaged α_j with wave period T_j. Dashed lines represent ±1 standard deviation.

3.2.8 Discussion

The Chen and Zhao (2012) formulation for energy dissipation through rigid vegetation is reorganized by introducing the velocity attenuation parameter, α. It is defined as the ratio of vegetation-attenuated orbital velocity inside the canopy at a given elevation to the orbital velocity in the absence of vegetation at the same elevation. This is similar that of Lowe et al. (2005) who defined it as the ratio of the velocity inside canopy to that outside canopy. The two parameters are related by a factor which results from the decay of orbital velocity with respect to depth. To illustrate the equivalence of the parameter, α was calculated for the Tropical Storm Lee field data and compared with Lowe et al. (2007, Figure 5a). To this end, the integral drag coefficient was set to a fixed value of 2.5 as in Lowe et al. (2007). Fig. 3.18 shows that such relatively stable value of the drag coefficient was observed for wave records with $K_C > 85$, so only those wave records are used for this illustration. Resulting α values are plotted in Fig. 3.23 after ensemble averaging 118 (2 pairs of gags time 59 wave records for each pair) α profiles.

Comparison of Fig. 3.23 with Figure 5a of Lowe et al. (2007) shows that in both cases α reduces gradually for the longer waves and approaches a maximum value near shorter period waves. In Fig. 3.23 from a value of 0.45 at 25 s, α increases to a maximum value of 0.9 at 4 s and then slightly reduces to 0.75 at 2 s. Data for waves shorter than 2 s is unreliable due to observed non-linear energy transfers in that frequency band and possible amplification of noise in the data analysis.

Because the formulation for dissipation given in Eq. (3.25) is based on the velocities at the same elevation inside canopy, the results can be applied to the cases involving shallow water and emergent vegetation. Further, this equation consists of explicit integration over discrete vertical increments and can be conveniently adopted when vertical variations of vegetation properties and hydrodynamics are important (e.g., Neumeier and Amos, 2006).

The velocity attenuation factor α is directly proportional to the normalized energy dissipation ($S_{ds}(f)/E(f)$) as evident from Eq. (3.23). In the special case of shallow water, this equation simplifies to,

$$\alpha_n^2 \propto \frac{S_{ds}}{E} \tag{3.30}$$

This equivalence of α_n^2 and S_{ds}/E is seen in the similarities of Figs. 3.15 and 3.20 in the dominant energy band. As shown in this study and in Lowe et al. (2005, 2007), the magnitude of the velocity attenuation factor is expected to decrease with increasing excursion or K_C number. This decreased α_n, reduces normalized dissipation at the higher K_C numbers in Fig. 3.15, causing steeper decline of the frequency distributions shown.

In the prediction of drag-induced energy dissipation, the specification of the drag coefficient is an important input parameter and attempts to universalize it remain a challenge. Consistent estimates of drag coefficients based on a range of wave and vegetation conditions will improve predictability of C_D as more data become available (Lowe et al., 2007). Several complex processes are involved in the wave energy dissipation induced by vegetation drag. For understanding these mechanisms one is led to the laboratory studies of hydrodynamics around a single rigid circular cylinder in oscillating flows in which force is modeled as a summation of inertial and drag forces by a Morrison type equation (Morrison et al., 1950). Even in this simplest and controlled form, the drag coefficients vary with time, Reynolds number, relative motion of the fluid, relative roughness, variable flow separation, wake interference, ambient

turbulence, etc. (Sarpkaya, 1976). Additionally, in wavy flows (as opposed to the simple oscillatory flows), velocity decays exponentially with depth and the orbital motion induces 3D flow effects and rotating vortices, further complicating processes. Although Stokes' solution exists for force coefficients in un-separated and laminar oscillating flows, such information must be obtained from experimental studies for separated flows which are present in the field conditions (Sarpkaya, 1976). In the case of natural vegetation, the inevitability of deriving drag coefficients from field studies is underscored due to the presence of stem array as opposed to a single cylinder (Tanino and Nepf, 2008).

3.2.9 Summary

Random wave spectra were measured over salt marsh vegetation to study vegetation induced dissipation along two co-linear consecutive reaches. The waves in the leading section of the vegetation were more energetic, highly nonlinear, experienced shallower water and exhibited larger dissipation compared to the subsequent reach where they became less energetic, significantly less nonlinear, and exhibited lesser dissipation. Waves propagating over salt marsh vegetation dissipate energy due to drag induced by the stems. The magnitude of dissipation was observed to vary with the wave frequency. The largest dissipation was observed near the incident spectral peak frequencies and dissipation gradually decreased with frequency above the peak. The rate of this decrease was greater for waves with larger K_C numbers and reduced for waves with decreasing K_C number. Upon entering the vegetation, the low-frequency swell (<0.16 Hz) dissipated less in the leading section of the vegetation than the wind sea (0.16-0.32 Hz), carrying energy further and then dissipating in the subsequent section. On the other hand, the majority of the wind-sea energy dissipated in the leading section of the vegetation. Across a spectrum, dissipation did not linearly follow incident energy density and the extent of non-linearity varied with the frequency scale. The relationship of dissipation to energy (Eq. (3.28)) tended to be less nonlinear in the wind-sea than the swell band, but the relationship became slightly more nonlinear and consistent (across bands) for waves with larger K_C number. In general, the relation was slightly more nonlinear in the swell band than the wind-sea band.

The normalized wave energy dissipation ($S_{ds}(f)/E(f)$) was observed to be the largest near the spectral peak frequencies. The magnitude of the normalized dissipation was directly related to the frequency in the band below the peak and inversely related to the frequency in the band above peak.

The vegetation induced drag coefficient is shown to vary with frequency. The distribution increases gradually up to the spectral peak and then remains generally uniform. The magnitude of the peak of this distribution was directly related to the magnitude of the corresponding K_C number of the waves. The frequency-dependent drag coefficient is parameterized by introducing a normalized velocity attenuation parameter, α_n. The spectral profiles of α_n were ensemble-averaged and a single $\bar{\alpha}_n$ curve was developed. This single curve along with the integral drag coefficient allows prediction of the frequency-dependent drag coefficient. It is demonstrated that the frequency-dependent drag coefficient predicts energy dissipation with better accuracy than the integral drag coefficient.

The methodology and drag coefficient parameterization presented in this section is verified by the same dataset from on which it is based. For a stronger validation, the parameterization needs to be implemented with an independent dataset.

3.3 Field Observations of Current Velocity on Wetland

3.3.1 Study Area, Experimental Method and Measurement Setup

The study area is a vegetated wetland in the upper Terrebonne Bay located at 29° 12' 35.00" N and 90° 34' 12.58" W (Fig. 3.24). This is the southernmost wetland island in the bay where relatively healthy vegetation still exists. The wetland is relatively low-lying compared to the neighboring wetlands to the north and therefore experiences frequent inundation. This makes it a desirable study site for studying wave through wetland vegetation.

Waves approaching from the open water on to the marsh were measured using a bottom-mounted pressure transducer. This was located at a distance of 47 m seaward from the study shoreline and sampled continuously at 10 Hz. As the waves landed on the marsh platform, they travelled through the vegetation along an array (Fig. 3.25) of wave staff gages and Acoustic Doppler Velocimeters (ADV).

Four wave staff gages (Ocean Sensor Systems, OSSI-010-004E) were installed on a 5.5 m long slotted angle steel bar, which penetrated about 3.5 m into the bed and was located one meter apart from each other beginning from the shoreline. The wave staff gages measured the water level for a period of 20 minutes every 30 minutes at a sampling frequency of 10 Hz. The two ADVs (SonTek Triton ADV and SonTek 10-MHz ADV) were buried into the marsh vertically. Each ADV was supported by two $2.5cm \times 10cm \times 1.5m$ lumber underneath to prevent sinking into the soft bottom, and wrapped in the 10cm diameter PVC pipe to ensure lateral stability. ADVs were setup in the upward-looking reading mode, with a 1024-second burst every 30 minutes. Triton ADV and 10-MHz ADV recorded the velocity 14cm above the ground at 4 Hz and 25 Hz sampling frequency, respectively.

Fig. 3.24. The study area is located in Terrebonne Bay on the northern Gulf of Mexico in Louisiana. Top left: Gulf of Mexico, Center: Terrebonne Bay. (Map extracted from ArcGIS Explorer)

Fig. 3.25. Schematic drawing of instruments deployment setup. Left: Wave logger; Right: ADVs

The dominant vegetation at the site was *Spartina alterniflora,* also known as Smooth Cordgrass. Morphological properties of this vegetation were measured at 3 randomly chosen locations at the site. Stem population densities were first measured inside a $0.5m \times 0.5m$ rectangular frame and then the stems were cut from the ground level and brought back to the lab for further measurements. Table 3.3 lists the measured vegetation properties. The definitions of various parameters are shown in Fig. 3.26.

The study was conducted from April 12, 2012 to April 20, 2012. Strong southerly winds with high wave activities were observed in this period, especially during April 14-16, 2012. The southerly winds pushed water into the bay and inundated the study area appreciably, providing an excellent opportunity for the intended measurements.

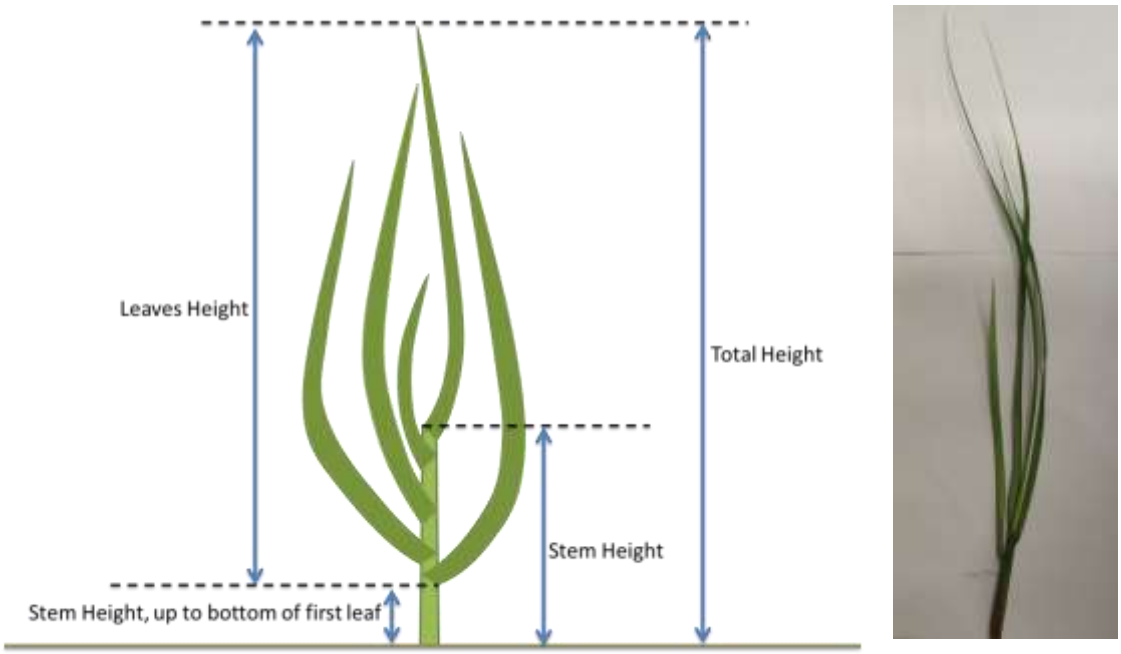

Fig. 3.26. Physical dimension of *Spartina alterniflora* at the deployment site

Table 3.3. Vegetation properties

Physical property	Unit	Mean	Standard deviation
Stem population density	Number of Stems/m^2	454	189
Stem diameter	mm	5	1.6
Stem height up to bottom of first leaf	cm	5.9	2.4
Stem height	cm	8.4	4
Total height	cm	38.3	10.3
Leaves height	cm	34	9.8
Number of leaves	-	5	1.6

3.3.2 Time Series Data and Qualitative Description of Results

Time series of mean water depth, d, and wave properties (i.e. peak wave periods, T_p, significant wave height, H_s and sea/swell wave heights) for the open water measurement, and near bottom current velocity, u_c, and its direction right above the canopy are presented in this section. Measurements were conducted from April 12, 2012 through April 20, 2012. During this period, the wetland (and the wave gage array) became inundated from April 13, 2012 till April 17, 2012 except for a short duration on April 14, 2012. Fig. 3.27 shows the mean water depth on the wetland, one meter from the shoreline, during this period. However, velocity was measured only during the part of this period when the ADVs were inundated. The sampling points for both ADVs were located at 0.14 m above the ground level. Therefore, analysis presented in this section is only based on the period from April 14, 2012 to April 16, 2012 (vertical dashed lines in Fig. 3.27).

The incident wave conditions during the period of analysis are shown in Fig. 3.28. With the diurnal tides, the water depth varied between 1.0 m to 1.2 m at the pressure sensor. Significant wave heights (H_{mo}) varied between 0.3 m to 0.45 m with peak wave periods of 2.6 s to 3.0 s. Fig. 3.29 shows the corresponding depth and wave conditions on the marsh platform. The marsh floor became inundated up to 0.3 m and the wave heights of less than 0.1 m were recorded. The peak period of the waves reduced by a small amount.

The velocities measured by the two ADVs are shown in Fig. 3.30. Velocity direction refers to the direction that current originally comes from with origin from north, which would be 0° from north, 90° from east, 180° from south, and 270° from west.

3.3.3 Summary

A field campaign to measure waves and bottom currents near the marsh edge on a vegetated wetland in south Louisiana was successfully conducted from April 12 to April 20, 2012 during a cold front passage. The wave data recorded from 47 meters seaward from the marsh edge and 1 m landward from the edge show that waves lost considerable energy at the marsh edge due to wave reflection, depth-limited wave breaking and vegetation damping. Two Acoustic Doppler Velocimeters located two meters landward from the edge recorded persistent currents (up to 15 cm/s) generated by wave breaking on the marsh edge. To the authors' knowledge, this is the first comprehensive dataset of vegetation, waves and current velocities ever collected near the edge of an inundated marshland. The dataset can be used to study sediment transport in the wetland and validate numerical models.

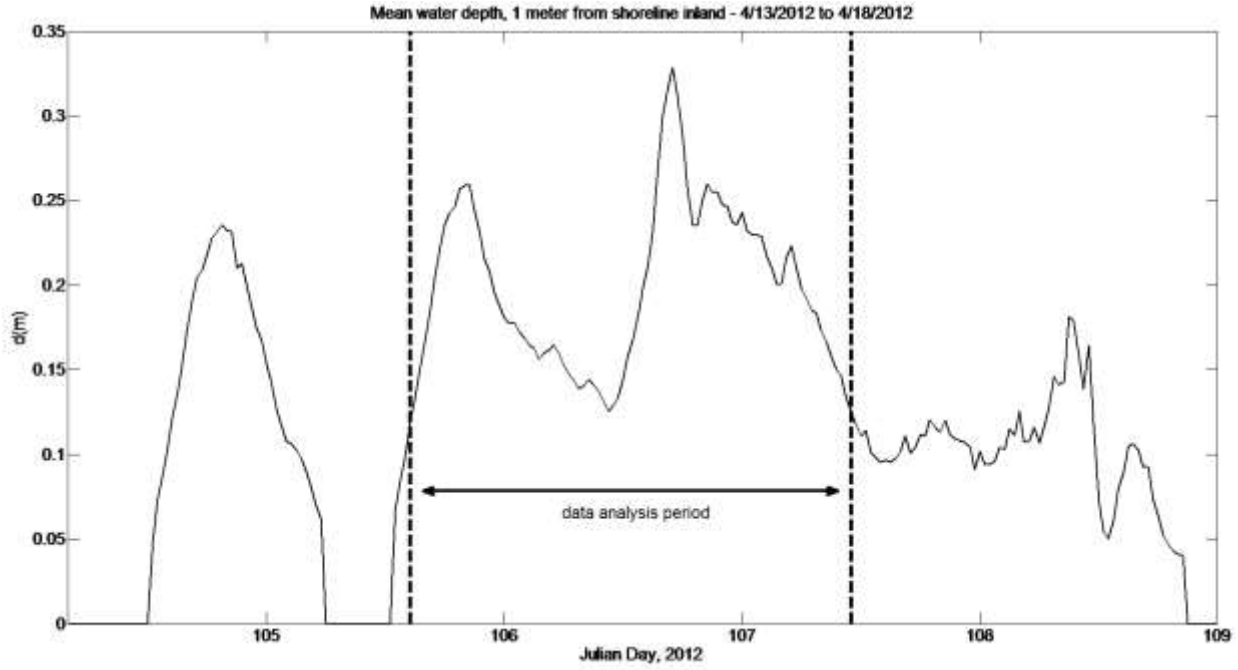

Fig. 3.27. Mean water depth inside wetland, one meter from shoreline, from April 13 to April 18, 2012. The data analysis period is shown by the vertical dashed lines.

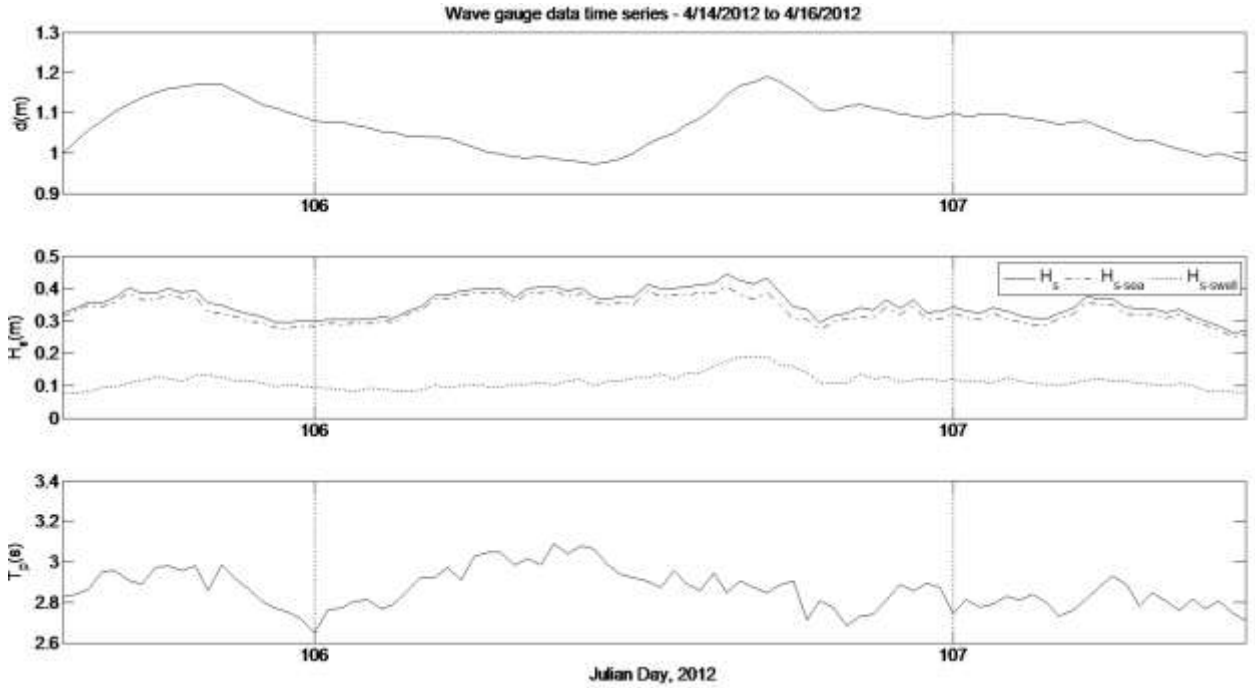

Fig. 3.28. Water depth (top), significant wave height (middle), and peak wave period (bottom) recorded at the open water wave gage (47 m offshore) from April 14 to April 16, 2012.

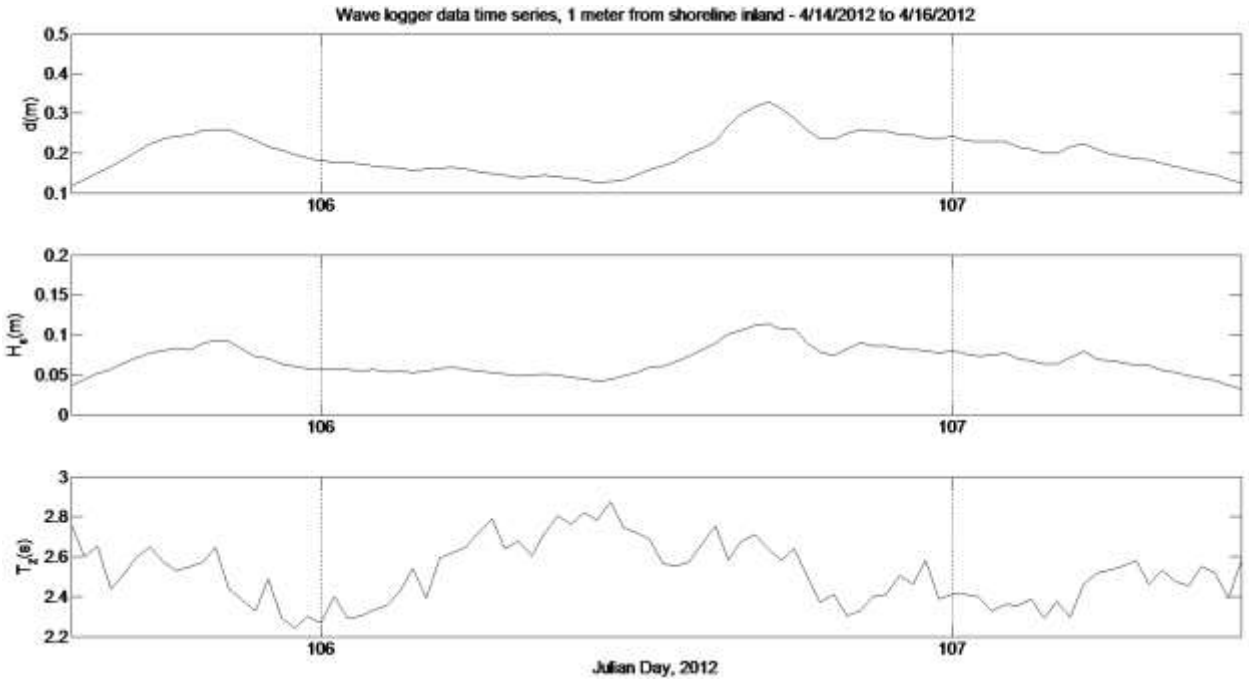

Fig. 3.29. Water depth (top), significant wave height (middle), and peak wave period (bottom) recorded at the wave staff on the marsh (1 m inland) from April 14 to April 16, 2012.

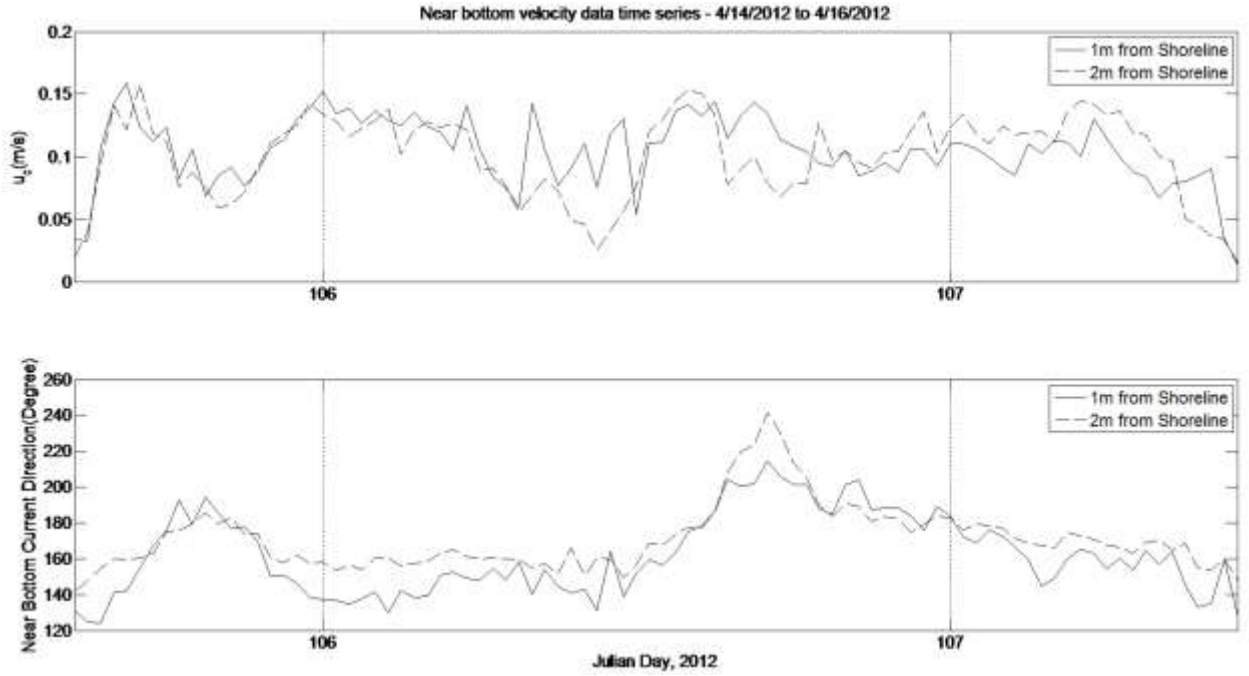

Fig. 3.30. Near bottom current velocity u_c (top) and its direction (bottom) on the wetland, 1m (solid line) and 2m (dashed line) from shoreline, from April 14 to April 16, 2012. Current comes: 0° from north, 90° from east, 180° from south, and 270° from west.

4. FIELD INVESTIGATIONS OF COASTAL MARSH VEGETATION AND SOIL PROPERTIES

To collect field datasets on coastal vegetation and soil properties to improve understanding and quantification of surge and wave attenuation by vegetation, two field campaign programs were carried out by the LSU team and the UM-Biology team in several sites along the Louisiana and Mississippi Gulf Coast. In Phase II, the LSU team conducted vegetation damage testing using a newly designed device and measured the critical shear stress for wetland soil erosion, and the UM-Biology team compared the growth forms and productivities of LA and MS marshes. The experiment sites, devices, field measurement and laboratory analysis methods, collected data and derived results are presented in this chapter.

4.1 Field Testing of Vegetation Damage

4.1.1 Introduction

The Northern Gulf Coast is severely impacted by coastal erosion, relative sea level rise (or subsidence), and the loss and degradation of natural wetlands and habitats. The erosion of coastal wetlands in the Northern Gulf Coast of the United States is a critical issue to the coastal community. At present, these wetlands are being damaged at an alarmingly fast rate. The processes that cause this wetland loss are attributed to both natural and human causes. Examples of natural events that cause erosion of coastal wetlands include strong hydrodynamic forces from waves, strong storms including both tropical and extratropical cyclones, and storm surges. Human actions that contribute to the disappearance of coastal wetlands include wake from heavy marine traffic, creation of river diversions and other control structures such as levees and dams, and pollution discharge. During the period of 1932-2010, the total land loss in coastal Louisiana was 1,883 square miles, and the rate of loss from 1985-2010 was 16.57 square miles per year (Couvillion, 2011). Louisiana is projected to lose an additional 513 square miles by 2050 (Fig. 4.1).

On the other hand, the coastal wetlands are very valuable to the state of Louisiana and the nation. In fact, they serve as protective barriers against powerful storms and surges, and also provide essential habitats for fish and other creatures, which have great commercial values to the nearby coastal community. The protection and restoration of these wetlands are vital to the economy of Louisiana and the security and safety of the coastal infrastructure. Because vegetation prevails in coastal wetlands and serves as a wave energy reducer and damper, studying the native vegetation's ability to resist damages caused by hydrodynamic forces from storms and surges is essentially an important way to understand the health and resilience of coastal wetlands.

The goal of this task is to determine the tensile force required to cause damage to the vegetation, i.e., tensile breakage of the stem or root of individual plants or pullout of vegetation from the ground. The breaking force obtained from individual plants will then be compared to their physical properties, including stem height and stem diameter. Although several types of vegetation are found in Louisiana's coastal wetlands, this study focuses on a specific species, *Spartina Alterniflora*, at two different sites, because it is one of the most abundant plants in saltwater marshes. The main objectives of this task are as follows:

- To determine the tensile force that is required to break a plant or pull it out of the ground;
- To determine if a relationship of stem height or stem diameter to the breaking force exists;
- To compare results from different sites to determine if a universal relationship exists;
- To accumulate vegetation damage data that can be employed for the numerical study of vegetation behavior under various hydrodynamic conditions.

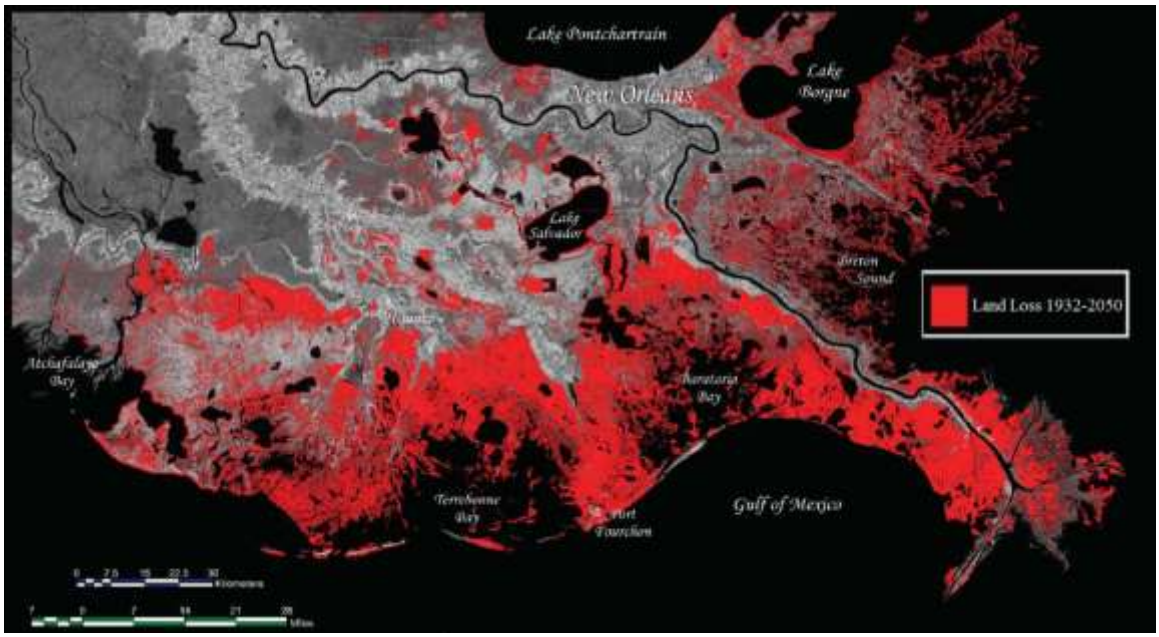

Fig. 4.1. Projected land loss in coastal Louisiana by 2050 (Barras, 2005).

4.1.2 Literature Review

Importance of vegetation to coastal marshes

Vegetation plays an important role in a coastal wetland's ability to resist erosive processes caused by hydrodynamic forces and wind driven forces. Many studies have found that healthy vegetation in coastal wetlands has shown the ability to reduce the height of waves acting upon the marshes (Knutson et. al., 1982; Feagin et. al., 2009; Roland and Douglass, 2005). The reduction in wave height and energy is significant because the erosive turbulent stresses caused by the waves are reduced. Another important contribution from vegetation to the stability of coastal wetlands is its ability to trap sediment. With the reduction in turbulent shear stresses from the flow, some suspended sediment in the water column is removed by settling and trapped by the vegetation (Lopez and Garcia, 1997). Finally, an added benefit of vegetation is the increased soil shear strength in the upper layers due to the rooting systems of the vegetation (Mickovski et. al., 2010; van Eerdt, 1985). In this regard, the roots may function in two ways: they can act as reinforcement to increase soil's shear and tensile strength, and their many rootlets also serve as anchorages to connect and bond soil particles together. Higher soil shear strength means that the soil has a greater ability to resist failure and erosion. The combination

of the stems above the ground and the roots below the ground provides a coastal marsh with the ability to resist erosion and maintain its stability from hydrodynamic forcing.

Biomechanical properties of vegetation

The biomechanical properties of vegetation have recently been studied to gain a better understanding of plants' behavior and response when subjected to external loading. Some of the more commonly studied properties are stiffness, bending strength, and tensile strength. Stiffness is a property that describes the vegetation's capacity to resist deformation when an external load is applied to the plant, typically along the plant's stem direction. The bending strength describes a plant's ability to resist a load causing the plant to bend. The stiffness and bending strength of vegetation are both important properties for determining the vegetation's resistance to fluid flow. These properties are a function of the plant's size, shape, and cellular composition, and may be affected by its biological conditions and climatic factors. The tensile strength of a plant describes the vegetation's resistance to uplifting forces. Tensile strength is important because it reflects vegetation's ability to resist forces that cause plant breakage or uprooting from the soil.

Composition of Stems

A plant's stem consists of tissues and fibers that affect the biomechanical properties of the plant. The mechanical behavior of the cell wall is controlled by the properties of the cellulose materials that mainly make up of wall. Cellulose is a polysaccharide $(C_6H_{10}O_5)_x$ of glucose units that has a high tensile strength and capacity for extension (Niklas, 1992). The plants also possess strong, stiff fibers that are embedded in soft tissues (Schlugasser and Witzum, 1992; Niklas, 1992). These stiff fibers, which are also made of cellulose materials, are considered the main source of strength within the plant stem, and the strength contribution from the soft tissue is negligible except for the fact that it accommodates and fixes the stiff fibers as a soft buffer within the stem (Schlugasser and Witzum, 1997). The arrangement of these fibers within the stem is considered to be anisotropic. This fact allows the plants to achieve higher stability against bending and tension, but not compression or torsion. The plant is also susceptible to local failures in portions of the stem where a smaller amount of stiff tissues are present due to the anisotropic arrangement (Schlugasser and Witzum, 1997).

Because of such arrangement of soft and stiff tissues, a plant's response to loading exhibits very complex behavior. As pointed out by Niklas (1989), the stress-strain behavior of a plant's stem under compression or tension may be subdivided into several stages (Fig. 4.2):

- Linear elasticity: the stress-strain curve is linear and elastic, and the deformation is simply elastic compression or stretching of the plant cell wall. Upon unloading, the deformation is fully recoverable. The slope of the linear elastic response is defined as Young's modulus.
- Nonlinear elasticity: the stress-strain curve is nonlinear and elastic and, upon unloading, the deformation is also fully recoverable. Such deformation mainly comes from the elastic buckling of plant's cell wall.
- Plastic yield and collapse: if the load continues to increase, yield of the plant's cell wall occurs, marking the commencement of plastic deformation. At this stage, the stress-strain curve also behaves nonlinear.
- Densification: this stage is marked by a second rapid increase of stress as strain increases. At the microscale, plant cell walls are crushed if subjected to compression or

fractured if subjected to tension. At the end of this stage, a maximum stress is achieved, marking complete failure or damage to the plant's stem.

As discussed above, a plant's response to loading is very complex. Combined with the geometrical variations of the plant's stem (i.e., the stem has variable diameter along its height) and even daily and seasonal variations of the plant's botanical behavior, it is very challenging to measure the complete stress-strain response of coastal wetland vegetation. However, it may be possible to obtain vegetation's damage force, simply via in-situ testing.

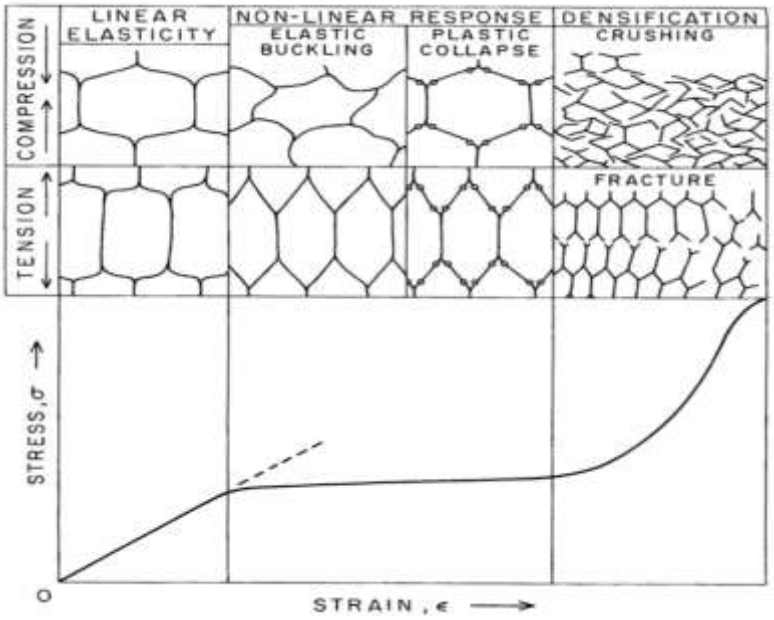

Fig. 4.2. Diagram showing the stress-strain relationship as it applies to plant cells under tension or compression (Niklas, 1989).

Effects of turgor pressure

Turgor pressure is another factor that contributes to plant's stiffness, strength, and other biomechanical properties. "Turgidity" refers to the degree of hydration within cellular protoplasts (Niklas, 1992). A formal definition of "turgor pressure" is the difference between water potential and solute potential. Notice that plant cells are porous and usually are filled with liquid with solute. Turgor pressure does not change stiffness determined from the second moment of area of the plant, but does alter the apparent stiffness of the plant (Niklas, 1989). The effect of turgor pressure is "felt" by the plant when the cells are placed in a state of axial tension, which is similar to pre-stressing a structural element (Niklas, 1992). A higher turgor pressure corresponds to a higher stiffness value for the plant.

It is important to note that, when a plant is dead, the contribution from turgor pressure is negligible when measuring plant stiffness. Fig. 4.3 shows the effect of turgor pressure on plant stiffness. Fig. 4.3A shows an initial plant stem with a stiff wall enclosing soft tissues. When turgor pressure is introduced due to axial tension (Fig. 4.3B), the soft tissue in the stem changes to become a stiff element in Fig. 4.3C. As such, the entire stem is stiffened as a result of increased turgor pressure.

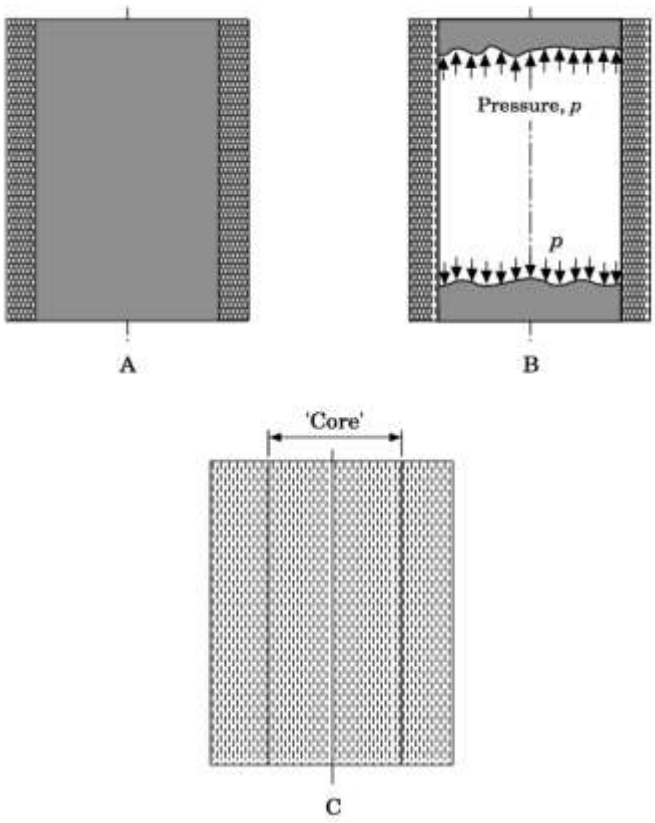

Fig. 4.3. Effects of turgor pressure on plant stem stiffness.

Plant uprooting failures

The use of vegetation as a means of wetland soil stabilization is an inexpensive alternative to more traditional engineering methods. In fact, vegetation has been used as a means to protect against shallow slope failures or to stabilize shallow topsoil. The key mechanism for the slope stabilization is the placement of roots through the soil's potential shear plane to provide additional resistance to circular failure (Fig. 4.4). Here the roots act as a reinforcement just like soil anchors or nails. The problem with the root reinforcement arises when the critical shear plane (or the potential failure surface) occurs below the depth of maximum root penetration. If the slope fails below the depth of roots, the vegetation will be uprooted and be unable to reestablish growth. When the vegetation is subjected to an uplift force, the roots, soil, and plant stem act together to serve as resistance to failure. The plant stem is able to hold a tensile load because of the cellulose, which has a high tensile capacity, in the cell walls, and the turgor pressure that can develop within the stem. The stem also transfers load to the root system, which acts an anchor against pullout from the soil. The ability of the roots to successfully resist the load is determined by the tensile capacity of the roots in conjunction with the frictional interface between the soil and the roots. The amount of friction that exists between the soil and roots depends upon several factors including but not limited to soil composition, soil properties, root composition, root density, root depth, and microbial activity.

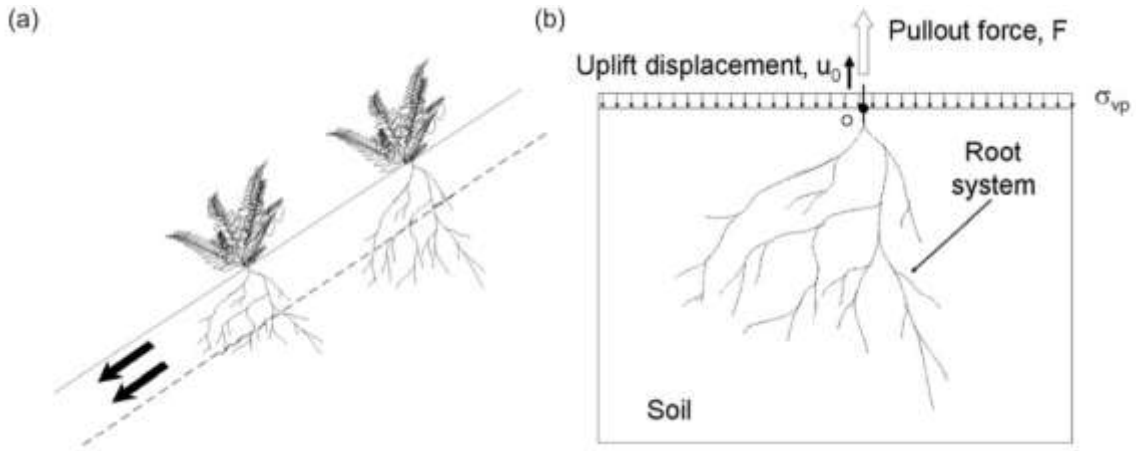

Fig. 4.4. Diagram showing types of uprooting failures in plants: (a) Slope failure and (b) Vertical pullout failure (Mickovski et al., 2010).

Characteristics of *Spartina alterniflora*

Spartina Alterniflora, also known as smooth cordgrass, is the dominant emergent grass species found growing along tidal saltmarshes of the Atlantic and Gulf Coasts (USDA-NRCS, 2005) (Figs. 4.5 and 4.6). This plant has been widely used in the restoration of coastal marshes because of its capacity to absorb wave energy and trap sediments. This plant possesses several characteristics that allow it to survive in many different environments. Smooth cordgrass can grow in the pH range of 3.7 to 7.9 and has a salinity tolerance of up to 35 ppt (parts per thousand) (USDA-NRCS, 2005). *Spartina Alterniflora* is classified as a warm season perennial with the seed head emerging around September or October, and the pollination process is wind driven (USDA-NRCS, 2005). The plant's growth and density along the shore depends on the site conditions such as elevation, shoreline slope, and the site's vulnerability to flooding (USDA-NRCS, 2005). The plant typically grows to a height of two to seven feet with a stem diameter of up to 0.5 inch (USDA-NRCS, 2005).

Fig. 4.5. *Spartina alterniflora* in Terrebonne Bay.

Fig. 4.6. ***Spartina alterniflora*** **during a storm event in Terrebonne Bay.**

4.1.3 Development of a Tension Testing Device for Plant Damage

This task requires the use of a device that is capable of measuring the tensile strength of *Spartina Alterniflora* in the field. Since access to wetland sites is constrained by marine vessels only, the device needs to be portable, light, and easily stored in a boat. A general literature search indicated that no device meeting the required specifications is available commercially. Therefore, a new device was designed and manufactured to meet the requirements necessary to carry out the field tests.

4.1.3.1 Previous Testing Methods

Many studies have been performed to determine the uprooting strength of different plant species. Here are summarized a few exemplary methods developed to test different types of plants. The method used by Mickovski et al. (2005) to test Vetiver grass utilized a 3 mm diameter PVC rope that was attached to the plant with a loop and was connected to a digital force gage. The rope was pulled parallel to the ground surface to apply the load, in order to simulate the condition where a plant is uprooted by surface flow. In a different study performed by Stokes et al. (2007) on bamboo, a similar method was used, but the pulling device was anchored to a nearby tree. Other researchers extracted samples from the field and performed tests in the laboratory (Feagin et. al., 2009; De Baets et. al., 2008).

After reviewing these different methods, a conclusion was reached that none of these existing methods was suitable for the tests required for this project. Laboratory testing is not ideal because this method involves removing plants from their native settings and hence the results may not reflect all factors affecting the process. The method employed by Stokes et al. (2007) for bamboos is not applicable because no vegetation growing in a saltmarsh is capable of sustaining the load from such a pulling device, while Mickovski's method is not ideal either, because the operator may sink in the soft soil while performing the test.

4.1.3.2 A New Device for Testing *Spartina Alterniflora*

The new device that can be used to perform tension tests on vegetation in the field must meet the following performance criteria:

(1) Possess a relatively low weight because the device must be carried on site to different locations on the marsh.
(2) Possess the ability to be stored efficiently because limited space exists while traveling to the site.
(3) Ability to make easy adjustments in the marsh because the availability of tools or other adjustment devices is limited due to the transportation process.
(4) Possess an easily repeatable procedure so that multiple samples or tested can be repeated efficiently.
(5) Possess the ability to resist sinking into the marsh where the surface soil is very weak.

After evaluating several options, the chosen final design includes the following components: a tripod with slight modification, a worm geared winch, 3/16" braided steel wire, in-line tension measuring load cell with a portable data logger, a U-shaped clamp, and wooden bearing plates, as shown in Figs. 4.7–4.9.

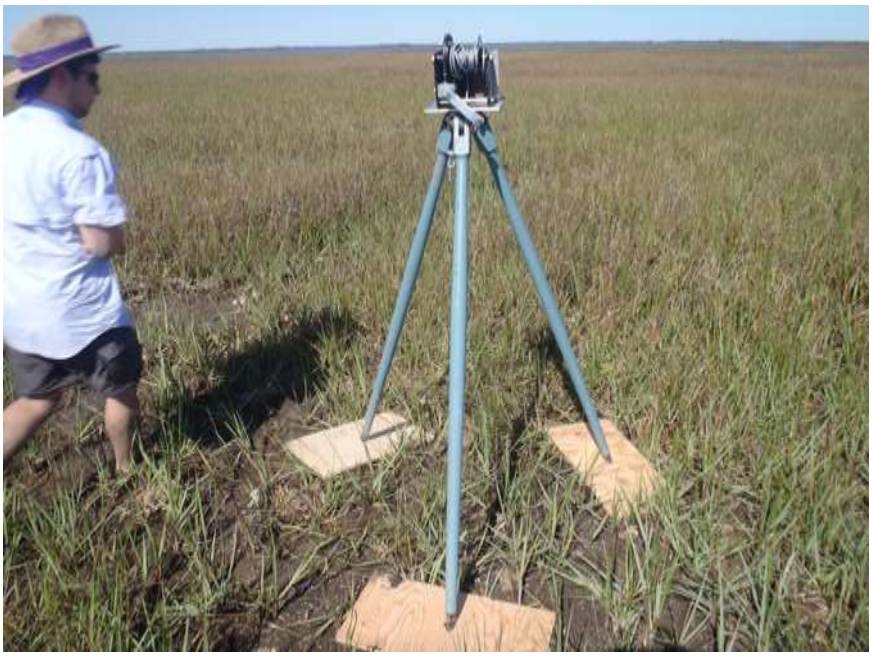

Fig. 4.7. The new testing device fully assembled in the field.

A tripod was chosen as the major structural frame because it was lightweight and can be easily folded so that it could be conveniently stowed. An aluminum mounting plate was added to the head of the tripod so that the winch could be easily attached. A worm geared winch was selected instead of a ratcheting winch because of the ratcheting winch's potential to have a malfunction in the field. Another advantage of the worm geared winch is that its design allows for more consistent spooling of the wire. The loading capacity of the winch is 2,000 lbs. The steel wire, which was included with the purchase of the winch, is very durable and also has the same rating for high capacity load. The load cell has a 500 lbs capacity, and the data logger supplies the voltage to the load cell in addition to recording the digital data from the load cell. The U-shaped clamp is used to connect the plant to the steel wire. The bearing plates have holes drilled in them so that the tripod legs can be placed through the holes to prevent slippage during testing and to reduce the contact pressure. The load applied to the tripod is distributed to each

of the three legs and then to the bearing plates, which are in contact with the surface. The purpose of the wooden bearing plates is to prevent the tripod legs from sinking into the soft to soil in wetlands.

Fig. 4.8. A worm geared winch connected to aluminum mounting bracket atop the tripod.

Fig. 4.9. Photograph of in-line tension load cell.

4.1.4 Methodology

4.1.4.1 Site Selection and Description

During the project period, a total of eight site visits were conducted in two coastal bays, Terrebonne Bay and Barataria Bay, near Southern Louisiana (Table 4.1). The purpose of the initial two site visits was to survey these two areas and hence selected two suitable sites that have appropriate conditions for this study, such as healthy vegetation growth, moderate to severe marsh edge erosion, and suitable hydrodynamic conditions (e.g., waves). The first site selected for this research is located in Terrebonne Bay near Cocodrie, LA, shown in Fig. 4.10. The coordinates for this site are 29° 13′ 25.06″ N, 90° 36′ 21.4″ W. This site is a saltmarsh that consists of mostly *Spartina Alterniflora*, and shows no visible signs of unhealthy vegetation. The second site is located in Bay Jimmy, which is just west of the Mississippi River and near Barataria Bay, shown in Fig. 4.11. The site is located at 29° 26′ 40.23″ N, 89° 53′ 19.93″ W. This site is similar to the Terrebonne Bay location with respect to the fact that it has an abundant population of *Spartina Alterniflora*. The main difference is that the Bay Jimmy location is heavily contaminated with crude oil from the Deepwater Horizon Oil Spill that occurred in 2010.

Fig. 4.10. Satellite image of the Terrebonne Bay site.

Fig. 4.11. Satellite image of the Bay Jimmy site.

Table 4.1. Summary of field visits

Date	Site Location	Description
9/9/2011	Terrebonne Bay	Site Inspection
9/23/2011	Bay Jimmy	Site Inspection
12/13/2011	Terrebonne Bay	15 Pullout Tests
3/5/2012	Terrebonne Bay	15 Pullout Tests
3/26/2012	Bay Jimmy	15 Pullout Tests
4/18/2012	Bay Jimmy	10 Pullout Tests
7/6/2012	Terrebonne Bay	15 Pullout Tests
7/23/2012	Terrebonne Bay	15 Pullout Tests

4.1.4.2 **Field Test Procedures**

A detailed test method developed in consistence with the new tension testing device is provided as follows:

(1) The first step prior to assembling the device for use is to select a test spot that is suitable for testing. The spot should not have any plants that have been damaged by any means of human activity, which means that places where people are walking or placing equipment should be avoided.

(2) Place the bearing plates onto the ground with enough spacing so that the selected plant samples to be tested just lie below the tripod head. Also the distance between the bearing plates and tested plants should be large enough so that the plants will not be affected by the load transmitted to the soil from the bearing plates.
(3) Place the tripod legs through the holes of the bearing plates and make sure that the tripod head is leveled (Fig. 4.7).
(4) Place the worm gear winch on the aluminum mount and secure it using the bolt. Make sure that the steel wire is placed through the center hole of the mount plate atop of the tripod.
(5) Connect the load cell to wire using the eye bolts and make sure that the load cell is zeroed (Fig. 4.12).
(6) Connect the end of the steel wire to the plant using U-bolt clamps. Make sure that the connection is secure by using a wrench to tighten the nuts on the clamp (Fig. 4.13).
(7) Before starting the test, manually inspect the connection to ensure enough friction exists between the clamp and the connected elements.
(8) Begin the test by turning the winch shaft to pull the wire. The pulling should be done at a constant rate and should cease when the plant is removed from the ground. Fig. 4.14 shows a test spot after the plant has been uprooted. It is important that the operator never steps between the legs of the tripod in order to prevent any kind of disturbance that may alter the results of the test.
(9) While the plant is being pulled, record the load from the load cell using the hand-held, portable data logger.
(10) Remove the plant from the clamp and label it. Place the plant in a bucket containing seawater so that the plant can be measured upon returning home.

Fig. 4.12. Photo of U clamp installation before performing the test.

The tested plants should be chosen randomly without any bias. The testing device should be moved to another location after at most 5 tests to ensure that the results are valid and have not

been affected by the previous tests. A total of 15 samples were taken per trip to account for variability.

Fig. 4.13. A plant is clamped while uprooting force is applied to the plant.

Fig. 4.14. Photo of the test spot after the plant has been uprooted.

After testing, the tested plants were brought to the laboratory for further characterization, including the measurement of plant's stem height and stem diameter. The diameter was measured using a caliper at approximately one fourth of the stem height from the bottom of the plant specimen, because the stem diameter typically decreases with increasing stem height. The

stem height was measured from the base of the plant (i.e., typically the connection point between root and stem) to the point where the tallest green leaf coming off the plant.

4.1.5 Analyses of Results

4.1.5.1 Overall Results from the Two Sites

Fig. 4.15 summarizes all results obtained from the two sites: Barataria Bay and Terrebonne Bay, in which the plant damage force is plotted against stem diameter. Totally there are 80 data points obtained from 80 individual plants in two sites. The damage forces range from 17 lbs (minimum) to 76 lbs (maximum), with an average and standard deviation of 32.41 ± 11.56 lbs.

As shown in Fig. 4.15, all data points are scattered in the plot, indicating a very weak dependence of damage force to plant stem diameter. However, an attempt to establish a linear correlation between damage force and stem diameter results in a linear equation shown in the figure, with a coefficient of determination R^2 = 0.112, which is much smaller than 1.0. This equation suggests that the stem diameter has some influence on plant's capacity to resist tensile damage. However, the low R^2 value indicates that the stem diameter is not the sole contributor to the tensile damage resistance. As discussed before, the failure of soil that sorrounds the plant roots and the root failure may not yield good correlations with stem diameter.

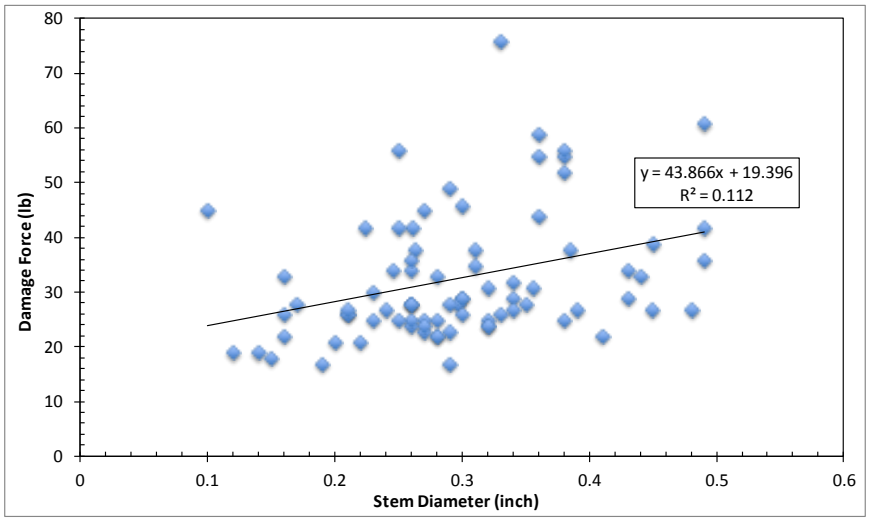

Fig. 4.15. Damage force against stem diameter for all data from the two sites.

Fig. 4.16 shows the relationship between the damage force and plant stem height. Again, this figure contains all data obtained from the tested plants in both locations (Barataria Bay and Terrebonne Bay). As shown in the figure, a very poor linear regression exists between plant damage force and stem height, with a coefficient of determination R^2 = 0.0158. This suggests that the stem height has little or no contribution to plant's tensile resistance to damage.

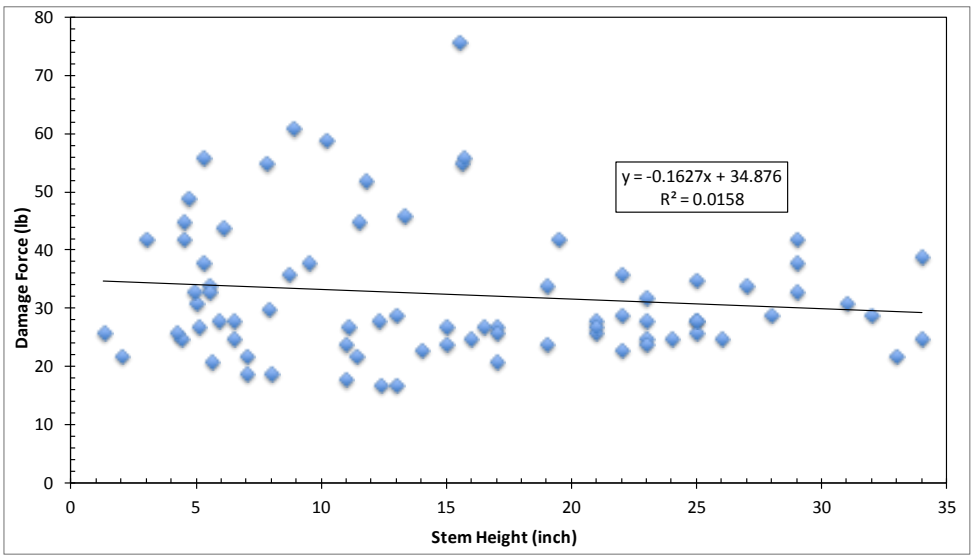

Fig. 4.16. Damage force against stem height.

Fig. 4.17 shows the relationship between stem height and stem diameter for all tested plants in the two locations. Again, significant scattering of the data can be observed. The linear regression shows the coefficient of determination R^2 = 0.1426. This correlation implies that the relationship between stem diameter and stem height is somewhat dependent, but they are not solely dependent upon each other.

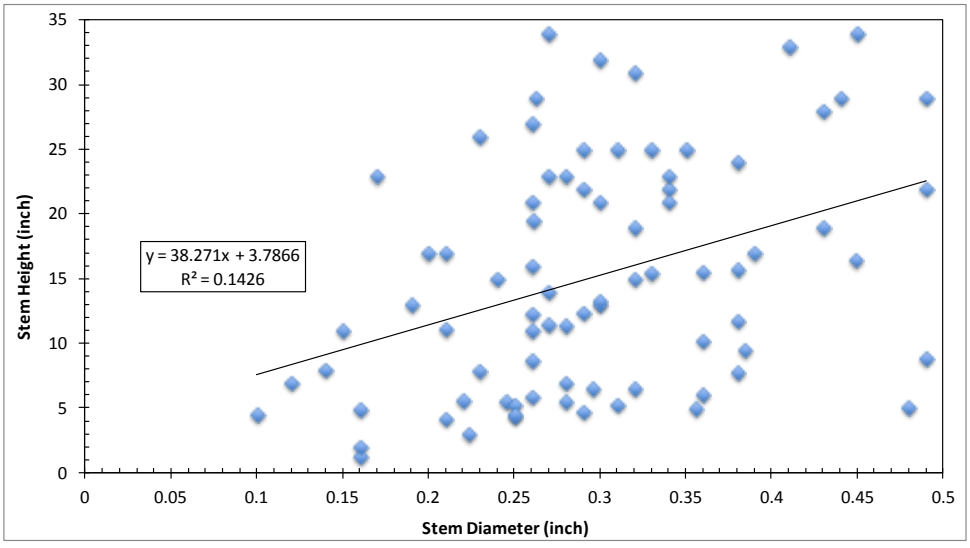

Fig. 4.17. Stem height vs. stem diameter for all plants measured.

4.1.5.2 **Results from Each Individual Site**

In this section, the results from each site are analyzed separately to determine if the stem height or stem diameter has a greater influence on plant damage force at a specific location.

Figs. 4.18 and 4.19 shows the results obtained from the Terrebonne Bay site, while the data from the Barataria Bay site are shown in Figs. 4.20 and 4.21.

As shown in Figs. 4.18 and 4.19, very poor correlations exist between damage force and stem diameter and between damage force and stem height, as indicated by the very small values of the two coefficients of determination R^2 = 0.085 and 0.0032, respectively, for the Terrebonne Bay site. Both figures suggest that the tensile damage resistance of plants in this site is not influenced by the plant dimensions, but mainly by other factors in the environment or factors of other botanical nature and origin, such as salinity, growth seasons, soil strength, and nutrient supply.

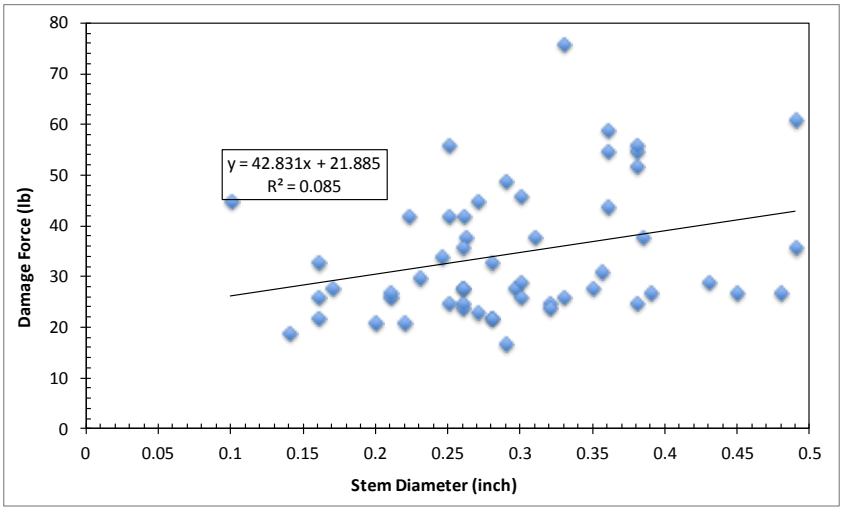

Fig. 4.18. Damage force vs. stem diameter for plants in Terrebonne Bay.

Figs. 4.20 and 4.21 show the testing results from the Barataria Bay site. Interestingly, plant damage force increases, despite the scattering, with both stem diameter and stem height. Attempts are made to obtain linear regressions between plant damage force and plant dimensions. As shown in these two figures, the coefficients of determination for these two regressions are R^2 = 0.5623 and 0.3152, respectively. Given the significant variability of the site conditions and the seasonal variation of the plant growth, these two regressions suggest that the damage resistance of plants in Barataria Bay has a strong dependence on plant dimensions: the damage force increases nearly linearly with stem diameter and stem height. These observations also suggest that the site conditions (e.g., soil strength, pH, salinity) do not exert a significant influence on plant's damage resistance in Barataria Bay.

One possibility for the difference between the two test sites (i.e., Terrebonne Bay vs. Barataria Bay) may be related to oil contamination. The Barataria Bay site has been contaminated by the crude oil, and in some places oil contamination is still present. The presence of the crude oil may minimize the effects of other environmental factors that the plants rely on to gain tensile strength. As a result, the plants may rely more heavily on their physical properties. Another possibility for the difference could be related to the amount of wave and wind forces applied to the two sites. The wave forces could have altered the properties of the supporting soil or even damaged the plants and hence possibly affected their behavior. In other words, the plants in two different sites have adapted themselves to the environments and evolved into different botanical properties.

Some other factors that may contribute to the plant's damage force are root depth, soil properties, soil strength, root density, and root orientation. Root depth, density and orientation all can affect the plants anchorage into the ground. The depth can determine the length and hence magnitude of bonding that the roots have with the soil. The density of roots also can show that plants have more available connections to the soil. The orientation is critical because it can influence the transfer of the applied force to the system. A detailed investigation of these factors is out of the scope of this research, but may be the directions of future research.

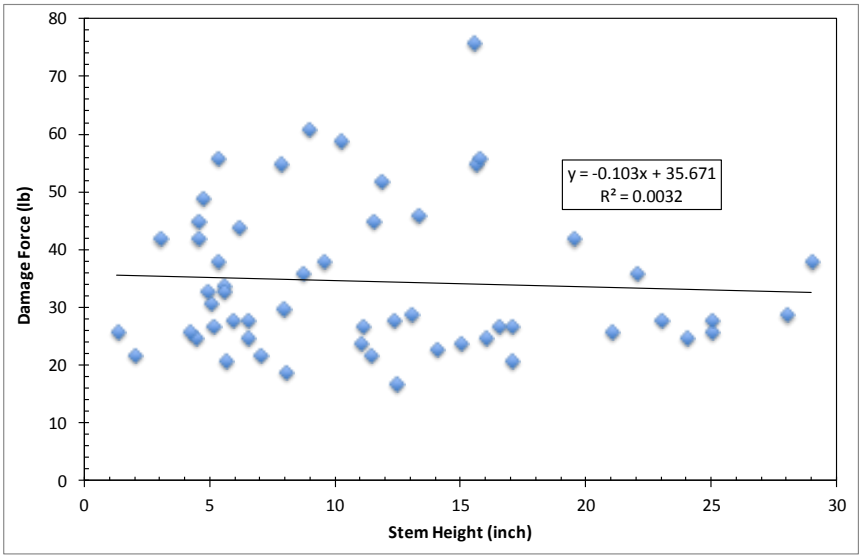

Fig. 4.19. Damage force vs. stem height for plants in Terrebonne Bay.

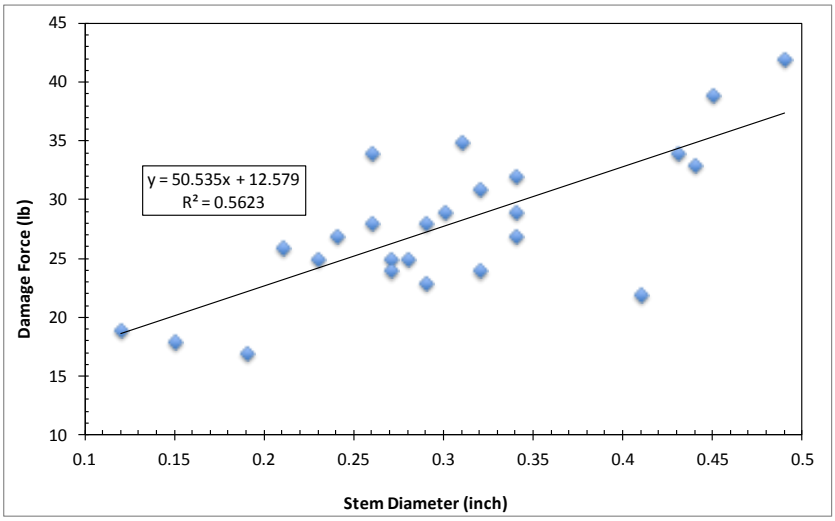

Fig. 4.20. Damage force vs. stem diameter for plants in Barataria Bay.

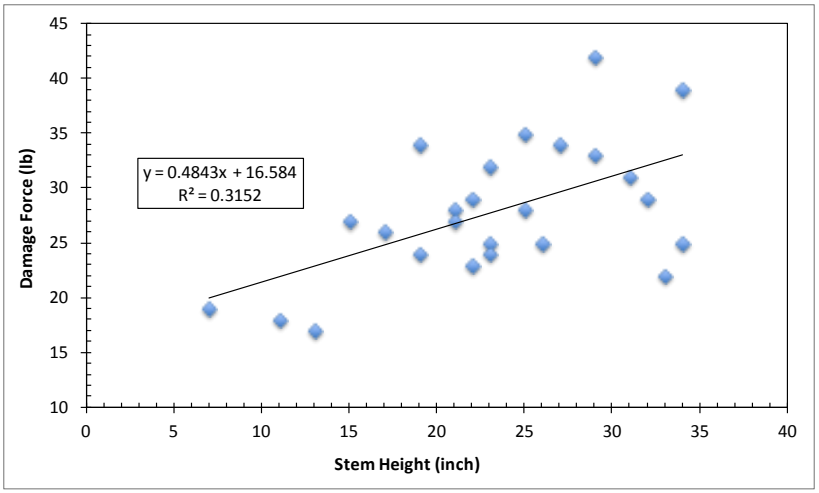

Fig. 4.21. Damage force vs. stem height for plants in Barataria Bay.

It is worth noting further the reason why the plant damage resistance increases with both stem diameter and stem height. As shown in Fig. 4.17, plant stem height has a relatively weak correlation with plant stem diameter. This correlation should be expected if the plant's growth dynamics is considered. In general, during the plant growth season (i.e., not the dying season), a plant gets taller and taller, and at the same time its stem gets thicker and thicker. As a result, the number of plant cells increases per cross-sectional area of the plant stem, leading to increased damage resistance to tensile force.

4.1.5.3 **Failure Modes of Plant under Tension**

As discussed earlier, depending on where the damage occurs, a plant may fail in one of these three modes: damage or breakage in the stem, breakage in the root embedded below the ground, and failure of soil surrounding the root system (where no breakage occurs in stem or major roots). However, during field testing, it was observed that in many cases a plant fails via a combination of soil failure and root damage, which should also be expected. This may be caused by the strong entangling of roots with the soils. Therefore, in this section, only two modes of failure are used to distinguish the observed damage to vegetation: if the damage occurs above the ground without involving soil (i.e., the major roots and soil are still left in the ground), it is classified as "stem failure"; In contrast, if the damage occurs below the ground typically involving soil or roots or both, it is classified as "root failure". In the latter case, a plant is usually displaced out of the ground.

Fig. 4.22 compares the observed failure modes for each field experiment. Clearly, the seasonal variation or plant growth kinetics significantly influences the plant failure mode. In winter, plant roots are still alive, but the stems are dry and dead. As such, the stems are weak, and all failures occur via stem damage. In spring, new stems start to grow but are still weak, and hence stem failure dominates plant damage. In summer, plants nearly reach their maturity and hence both the stem and root are strong. Failure may occur randomly in either stem or root. Another factor is the soil strength. If the soil is very weak (e.g., after an elongated period of flooding), then the failure may occur in the soil, but not in stem or root. In this case, other environmental factors play a major role in controlling plant failure. These findings may find some practical applications for wetland protection.

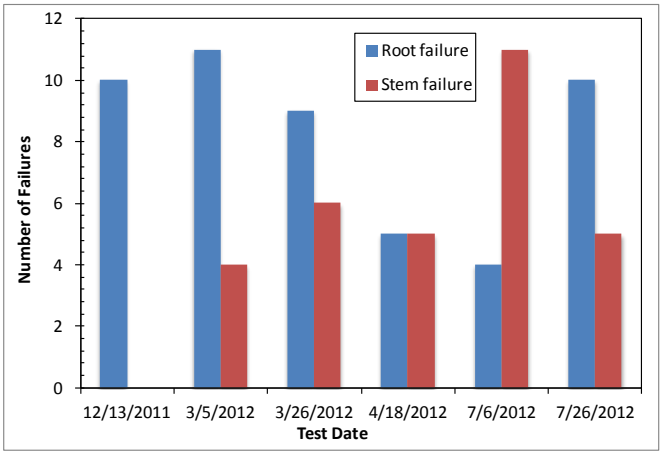

Fig. 4.22. Comparison of the different failure modes of plants during testing.

4.1.6 Summary

In this task, a new plant tension testing device was designed and manufactured to characterize the tensile damage resistance of coastal wetland vegetation. The device was proven to be capable of obtaining quickly and accurately plant's tensile damage resistance in coastal wetlands. It also features ease of operation, high mobility, portability, and enough accuracy. With this new device, a total of eight field visits were conducted to obtain plant damage data in two selected sites located in Terrebonne Bay and Barataria Bay. In both sites, *Spartina alterniflora* is the dominant marsh grass, which is also abundant in the wetlands along the Northern Gulf Coast. During each field visit, a total of 15 plants were tested to obtain their tensile damage resistance.

Based on the obtained results and field observations, the following conclusions can be drawn:

- For the total of 80 tested plants, the tensile damage forces range from 17 lbs (minimum) to 76 lbs (maximum), with an average and standard deviation of 32.41 ± 11.56 lbs. This value may find practical applications for hydraulic and hydrodynamic modeling to predict the survivability of wetland vegetation under waves or storm surges.
- When all tested plants are considered, the plant damage force seems not to be dependent strongly upon plant stem diameter or stem height, indicating other environmental or botanical factors can also affect a plant's damage resistance.
- When the results from different sites are considered separately, the damage force for plants in the Terrebonne Bay site is only slightly affected by plant dimensions, whereas that for the Barataria Bay site can be reasonably correlated with both plant stem diameter and stem height. It is unclear at this point why such observations were obtained, which warrants further investigation.
- The plants in both locations show that they grow in accordance with their natural growing pattern, which is shown by the increased strength and physical properties in spring and summer. The growing trend is further reinforced by the fact that the plants show more failures at the stem in winter and early spring, but failure occurs in both

stem and root randomly in summer when the plant reaches its maturity and hence maximum strength.

- The properties of the soil surrounding plant roots are also important because they affect the stability of the root-soil system. The soil strength is also a key factor influencing the mode of plant failure. In cases where failure occurs in the soil, a true indication of plant damage force cannot be obtained from the conducted experiments.
- The different modes of plant damage failure and soil failure may be used to study the resiliency of coastal wetlands in different seasons and hence to develop corresponding restoration strategies to protect coastal wetlands.

4.2 Field Observation of Critical Shear Stress on Wetland Soils

4.2.1 Introduction

The resilience and functionality of coastal marshlands rely heavily on the stability of the physical foundations of the marshes—wetland soils on which marshes grow and thrive. In other words, the stability of wetland foundation soils directly controls the resilience and health of the coastal ecosystem (Howes et al. 2010). In fact, the inter-dependence between marsh vegetation and soil is well documented, and its importance is reflected in a few recent studies focusing on the sustainability and resiliency of coastal wetlands. Among those are, for example, Howes et al. (2010), Turner (2011), and Day et al. (2000).

Coastal erosion, a huge problem facing all coastal communities around the world, is dominantly controlled by soil stability or strength. In general, soil erosion, the gradual removal of surface material from a soil mass by moving water, depends upon both the energy of the flowing water (i.e., the driving force exerting a flow shear stress to soil surface) and the soil's ability to resist erosive failure (i.e., the resistance of a soil to shear failure). According to the literature, a cohesive soil's erosion resistance is directly related to its undrained shear strength. That is, if the flow-induced shear stress exceeds a cohesive soil's undrained shear strength, erosion or removal of soil particles commences as a result of soil failure. As such, this shear stress is also termed "critical shear stress", an indicator of undrained shear strength of cohesive soils.

Much of the Northern Gulf Coast is underlain by thick cohesive soils. In particular, the fine-grained cohesive sediment brought to the deltaic coast by Mississippi River dominates the central northern part of the Gulf Coast in Southern Louisiana. These cohesive sediments also make up the foundations to the coastal wetlands along the Gulf Coast. Coastal wetlands are the Earth's most energetic, productive ecosystem, and Louisiana covers more than 40% of the tidal wetlands in the 48 conterminous United States.

Over the past several decades, severe land loss, as a result of erosion, subsidence, and sea level rise, has been observed along the Gulf Coast. In fact, this is also a critical issue facing all coastal communities around the world. In the past 200 years, the US has lost more than 50% of its wetlands (Williams, 2001), and nearly 90% of the total wetland loss in the lower 48 states has occurred in Louisiana (USGS, 2003). Moreover, the land loss is ever increasing at an alarming rate. Every year Louisiana is losing 100 square kilometers of wetlands due to both natural and man-made processes, and by 2050 Louisiana is likely to lose 640,000 acres of coastal lands (Fig. 4.23).

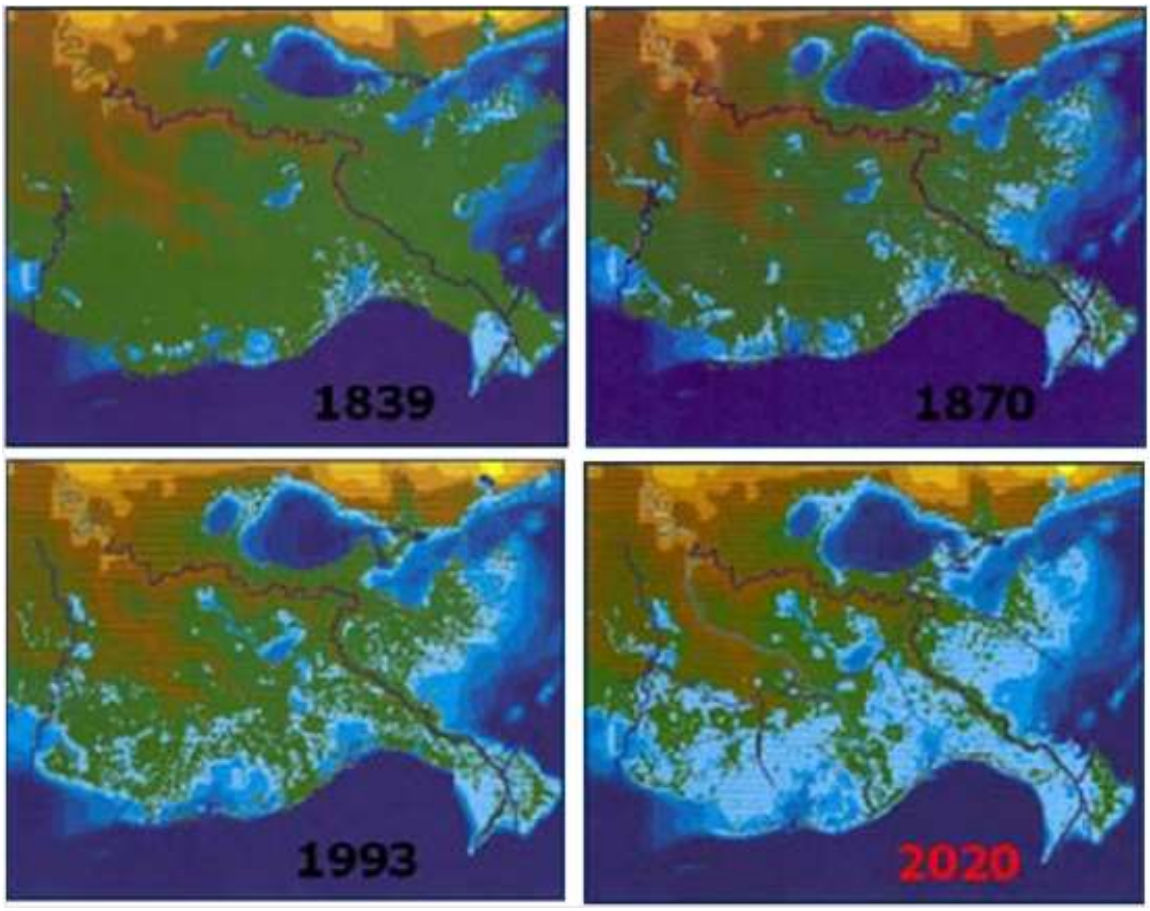

Fig. 4.23. Historic and projected land loss along Louisiana's coast (http://www.restoreorretreat.org/coastal_erosion.php)

The coastal wetlands in Louisiana are of vital importance to the nation's economy, energy, and security. The devastation and death caused by 2005 and 2008 hurricanes further demonstrated the vital importance of sustainable coastal ecosystems to the protection of the coastal civil and energy infrastructure, safety and lives of coastal community, and fisheries and shipping industries. In fact, Louisiana's wetlands are home to many oil and gas pipelines, and a sustainable and stable coastal ecosystem can protect the critical oil and gas infrastructure from storm surges and hurricanes. This infrastructure produces or transports nearly 1/3 of the US's oil and gas supplies and is tied to 50% of the nation's refining capacity. Furthermore, as the most productive ecosystems on Earth, the wetlands in Louisiana provide 26% by weight of the commercial fish in the lower 48 states. Finally, ten major navigation routes are located in Southern Louisiana, and five of the busiest ports in the US, ranked by total tons, are also located there. These facilities handle 19% of the annual US waterborne commerce. Therefore, healthy, sustainable, and stable coastal wetlands in Northern Gulf Coast have great economic, energy, and security importance. To maintain sustainable and resilient coastal wetlands, the cohesive soils as the foundations of the wetlands, must be fully understood to prevent erosion and other land loss. As such, the study of soil erosion and critical shear stress in Louisiana coastal wetlands is deemed timely and necessary.

The overall goal of this task is to study the critical shear stress or erosional resistance of cohesive soils of selected wetlands in Northern Gulf Coast and hence accumulate some

important data for future numerical modeling of coastal erosion and wetland restoration. The knowledge of soil erosional resistance, combined with other hydrodynamic data (e.g., wave measurements, flow shear strength), can be used to analyze and further predict the stability, survivability, and rate of erosion of coastal wetlands. Specifically, the main objectives of this research are:

(1) To conduct field and laboratory measurements of the critical shear stress of cohesive wetland soils using a portable cohesive strength meter.
(2) To further characterize the wetland soils in the laboratory and determine other properties that are expected to affect soil stability.
(3) To understand the erosional resistance of wetland soils by establishing some correlations (if any exists) of critical shear stress with other index and physical properties of the tested soils.
(4) To compare the test results from two different sites and hence understand geographical variability of wetland soils' critical shear stress.

4.2.2 Literature Review

4.2.2.1 Sediment composition

Cohesive sediment is an important component of coastal marshes that play an important role in the stability of coastal marshlands. Since it is a big stakeholder of the coastal ecosystem, its stability against hydrodynamic forcing should be investigated in order to understand the vulnerability of coastal marshlands in Gulf Coast to erosion by waves and storm surges. Understanding coastal soil's erodibility is not easy or simple, because of the complex behavior of coastal cohesive sediment, when compared to relatively clean granular sandy soils. Marshlands that are directly in contact with coastal waters are unstable and fragile due to the continuous attack of water waves. Thus coastal soil is most vulnerable to erosional loss due to frequent hydrodynamic forces and wind forces.

The stability of coastal marshes depends on the hydrodynamic forcing that is responsible for erosion and the resisting forces that the sediment bed offers. When the erosive driving forces overcome the resistive forces (cohesion, gravity, friction, and adhesion), erosion takes place (Grabowski, 2011). Erodibility, which measures the resistance offered by the soil surface, is expressed as a threshold or as an erosion rate (Sanford, 2008). Critical flow velocity or critical erosional shear stress that initiates the erosion is considered as the "erosion threshold", while erosion rate measures the mass of sediment eroded per unit time beyond the erosion threshold. Prediction of erodibility of cohesive sediments that are common in coastal marshes is difficult because the interparticle attraction in cohesive soils is influenced by a number of factors, including those environmental factors such as organic matter content, pH, salinity, water content, and even soil biota or biofilms.

Coastal cohesive sediments typically consist of solid, liquid and gas phases and are a heterogeneous mixture of particulate and porous material (Hillel, 1982; Winterwerp and van Kestern, 2004). In riverine sediment, gases may be present but are not necessarily present in estuarine sediment exposed to air at low tides (Gebert et al., 2006; Sanders et al., 2007). Integrated biofilms produced by microorganisms (e.g., diatoms) are basically found on sediment surface, while extracellular polymeric substances (EPS), a major component of biofilm that is secreted by bacteria may present at depth in the sediment (Fig. 4.24). Structure and

interactions of different subcomponents present in cohesive sediment determines the erodibility of a cohesive soil.

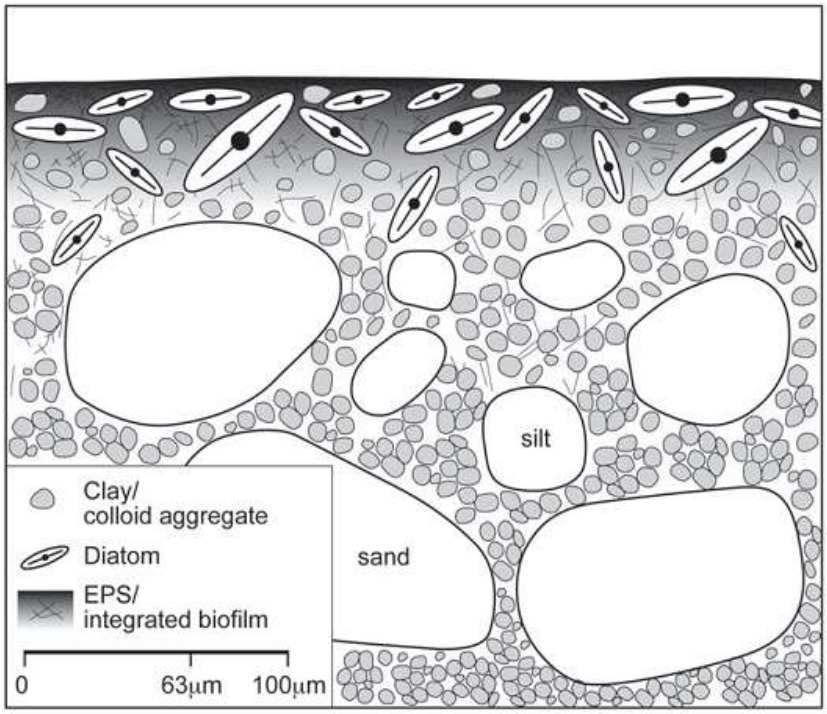

Fig. 4.24. Diagrammatic representation of cohesive sediment microstructure (Grabrowski et al. 2011).

4.2.2.2 **Soil Properties Affecting Erodibility**

Based on the literature, a number of soil properties can affect the erodibility of cohesive sediments. They are divided into physical, geochemical, and biological origins, as summarized in Fig. 4.25. All these properties act together to determine the degree and rate of erosion. Since erodibility depends on a number of factors that are inter-related, a detailed investigation is required in order to gain insight into the erosional threshold of coastal cohesive sediments. To date, many researchers have found that these factors are connected in such a complex manner that the prediction and evaluation of erosional resistance based on only one factor can be very misleading. For instance, when the clay content is low (i.e., 2 wt.% bentonite), the clay can help adhere together sand and silt particles (Lick et al., 2004). However, when the clay content is high (e.g., 4-10 wt.%), the sand or silt grain skeleton framework changes to a clay mineral framework, indicating that a non-cohesive sediment is converted to a cohesive sediment (van Ledden et al., 2004; Winterwerp and van Kesteren, 2004). Furthermore, when the clay content approaches to a pure clay, the mixture exhibits a reduced erosional threshold. In addition, water content plays a more important role in influencing the erodibility of cohesive sediment than the bulk density, because the undrained shear strength and other mechanical properties of a clayey soil are highly dependent upon water content (Gillot, 1987; van Ledden et al., 2004; Winterwerp and van Kesteren, 2004).

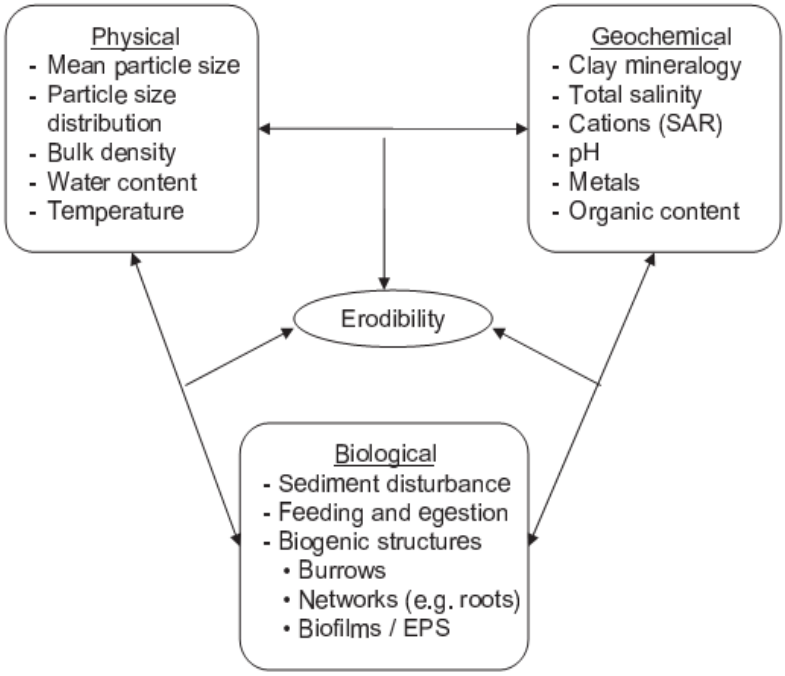

Fig. 4.25. Sediment properties and processes that affect erodibility (Grabrowski et al., 2011).

On the other hand, Amos et al. (2003) described the significance of biogenic stabilization via EPS that act as binding agents to adhere sediment constituent particles together and hence result in an increase in critical shear stress. They found that a critical shear stress of ~0.5 Pa for a lacustrine sediment with a bulk density of less than 1100 kg/m^3 is typically due to the presence of biofilms or EPS, as compared to the negligible shear stress of a stationary fluid mud with a bulk density of 1100 kg/m^3. In addition, organic matter content is also one of the critical factors affecting the erodibility of soils. A positive correlation was reported between organic matter content and erosion threshold for riverine sediments (Aberle et al., 2004; Gerbersdorf et al., 2007). One possible mechanism for this correlation is that organic matter content affects the inter-particle attraction or adhesion. Furthermore, organic matter content is also correlated positively with the water content but negatively with bulk density of a cohesive soil. Finally, cohesive soils contain microorganisms (e.g., bacteria, fungi, diatoms, etc.) and their contribution to bioturbation, biostabilization, and biodestbilization is noteworthy.

A striking feature of coastal wetlands is the abundance of live vegetation and hence the associated root system. In fact, root content can also affect the erosional resistance and the rate of erosion, because roots often provide a net-like structure to encompass soil particles. As such, they reinforce a cohesive soil through such a structural network. In addition, roots can take some of the shear stress applied to the soil through tension (Simon et al., 2006), and hence directly strengthen the soil. This typically results in an increase in erosional threshold. Roots increase the organic content and also help the growth of microbial communities. Soil sample with roots can achieve an increased shear strength by at least 500% in clay and sandy clay soils, and a clayey soil showed an increment of shear strength up to 850% for a root density of 1.8 g/cm^3 (Tengbeh, 1993).

4.2.3 Methodology

4.2.3.1 Site Selection

Two comparable sites in Terrebonne Bay and Barataria Bay were selected for this task (Fig. 4.26), with the following considerations: (1) the two sites should have been subjected to comparable hydrodynamic conditions; (2) the two sites should be currently affected by severe erosion and land loss; and (3) the sites must also be accessible with reasonable costs and time (e.g., close to boat launching sites). Barataria Bay is located between Bayou Lafourche to the west and Mississippi River delta to the east. The exact location for the test site is in Bay Jimmy with a coordinate (29°26'40.23"N, 89°53'19.93"W), as shown in Fig. 4.27. The test site in Terrebonne Bay is close to Cocodrie, Louisiana (Fig. 4.28) and its coordinates are (29°13'25.06"N, 90°36'21.4"W). At both sites, clear signs of severe marsh edge erosion were observed during site visits and field experimentation. In addition, the site in Barataria Bay is also affected by the BP Deepwater Horizon oil spill, while the Terrebonne Bay site is a normal saltmarsh. The vegetation, *Spartina alterniflora* or smooth cord grass, is abundant at both sites.

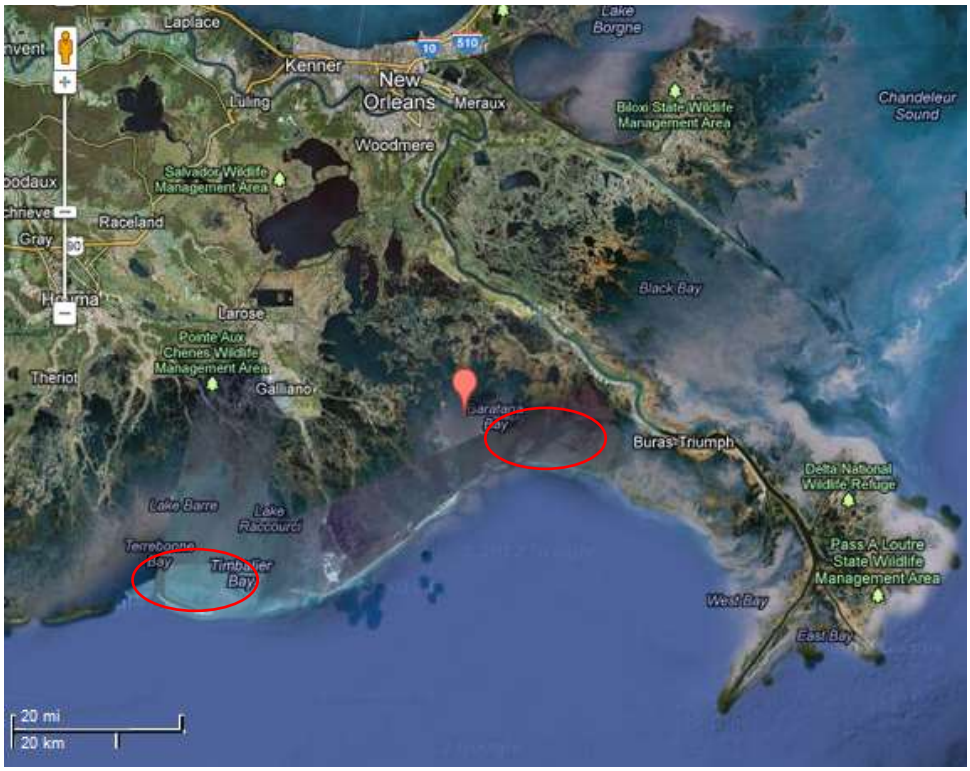

Fig. 4.26. Two selected sites for field testing

Fig. 4.27. Location of the test site in Barataria Bay.

Fig. 4.28. Location of the test site in Terrebonne Bay.

4.2.3.2 Schedule of Site Visits and Field Testing

During the project period, a total of 8 field visits to the two selected test sites were conducted. The activities for each field visit typically include site inspection, visual survey, undisturbed tube soil sampling (using 4 in. diameter aluminum tubes), and critical shear stress measurement by a cohesive strength meter (CSM) (Table 4.2). These field visits were distributed in fall, winter, early spring, spring, and summer. However, usually due to the cold or bad weather (e.g., rains) in winter, only one visit was scheduled in winter. Scheduling of site visits were also affected by other factors, such as availability of boats, weather, budget for field work, and research team's schedule.

Table 4.2. Field visit dates and in-situ activities

Date	Site	In-situ activity
9/9/2011	Terrebonne Bay	Site survey and inspection
9/23/2011	Barataria Bay	Site survey and soil sampling
12/13/2011	Terrebonne Bay	2 CSM tests and soil sampling
3/5/2012	Terrebonne Bay	6 CSM tests and soil sampling
3/26/2012	Barataria Bay	7 CSM tests and soil sampling
4/18/2012	Barataria Bay	6 CSM tests and soil sampling
7/6/2012	Terrebonne bay	7 CSM tests and soil sampling
7/23/2012	Terrebonne bay	2 CSM tests

It is worth noting that six of the seven CSM tests conducted on March 26, 2012 in Barataria Bay were directly performed on the weathered residue of heavy crude oil that was on the top surface of coastal wetland soil. Therefore, these data cannot be used to represent the soil's erosion resistance. From this lesson, it was realized that the top hard layer of weathered oil residue on soil surface needed to be removed before the erosion testing.

4.2.3.3 Measurement of Erosion Resistance

In this task, a high pressure (60 psi) Mike IV cohesive strength meter (CSM) (Partrac, Ltd., UK) was employed to measure the critical shear stress of coastal cohesive soils both in situ and in the laboratory. The CSM was originally designed by Paterson (1989) and is a compact, light and portable device. To date, it has been widely used to measure the stability of cohesive sediments (Fig. 4.29). During testing, the CSM applies a vertical water jet that strikes the sediment surface with a jet of water from a built-in water reservoir by pressurized air contained in an external air tank. The water jet pressure is increased incrementally by the pressurized air inside the tank as the test progresses. Meanwhile, the optical sensor inside the sensor head measures the light transmission through the water cylinder with time. Owing to its unique design, the CSM can measure small-scale spatial and temporal variations in sediment stability quickly.

In addition, this automated and computer controlled CSM is supplied with twenty two pulse programs that can be used for various cohesive soils with different cohesive strength. In fact, the original CSM was developed for the characterization of intertidal mudflats that usually exhibit different critical erosional stress and are susceptible to erosion by waves and tidal

currents in coastal environments, and the shear resistance of the mudflat surface is of great importance to the prediction and modeling of coastal cohesive soils (Tolhurst et al., 1999). Of these various pre-designed testing programs, "Mud 8", "Mud 7", "Mud 17", and "Fine 1" were selected to run the erosional resistance tests. The characteristics of these pulse testing programs are given as follows:

Fig. 4.29. The cohesive strength meter connected to a compressed air tank and the cylindrical sensor head

- **Test Mud 8:**
  - Jet fired for 1.00 s
  - Data logged for 30.00 s
  - Data logged for every 1.00 s
  - Test started at 0.50 psi
  - Incrementing by 0.50 psi per test up to 20.00 psi
- **Test Mud 7:**
  - Jet fired for 1.00 s
  - Data logged for 30.00 s
  - Data logged for every 1.00 s
  - Test started at 0.30 psi
  - Incrementing by 0.30 psi per test up to 12.00 psi
- **Test Mud 17:**
  - Jet fired for 1.00 s
  - Data logged for 30.00 s
  - Data logged for every 1.00 s
  - Test started at 2 psi
  - Incrementing by 2 psi per test up to 60.00 psi
- **Test Fine 1:**
  - Jet fired for 1.00 s
  - Data logged for 3.00 s

- Data logged for every 0.1 s
- Test started at 0.10 psi and incrementing by 0.1 psi up to 2.4 psi
- Incrementing by 0.3 psi from 2.7 psi up to 6.0 psi and by 2.0 psi from 8.0 psi up to 60.0 psi

The critical shear stress (τ_{ocr}) was obtained from the CSM raw data, which describes the dependence of light transmission (at a percentage) on time. On the same plot, the applied water jet pressure or the horizontal applied shear stress was also plotted against time. Values of the horizontal applied shear stress were calculated from vertical water jet pressure using the equation given by Tolhurst et al. (1999):

$$\tau_o\ (Nm^{-2}) = 66.6734 * (1 - e^{\left(-\frac{P}{310.09433}\right)}) - 195.27552 * (1 - e^{\left(-\frac{P}{1622.56738}\right)})$$

where P is the vertical water jet pressure (kPa). As illustrated in Fig. 4.30, a sharp drop of light transmission typically marks the onset of erosion of soil particles that are brought to suspension. Two straight lines can be drawn: the first one through the linear portion of points before the start of erosion and the other through the linear points after erosion. The intersection of these two straight lines represents the starting point of erosion. With the corresponding time of this intersection point, the critical shear stress can be located from the applied shear stress vs. time plot.

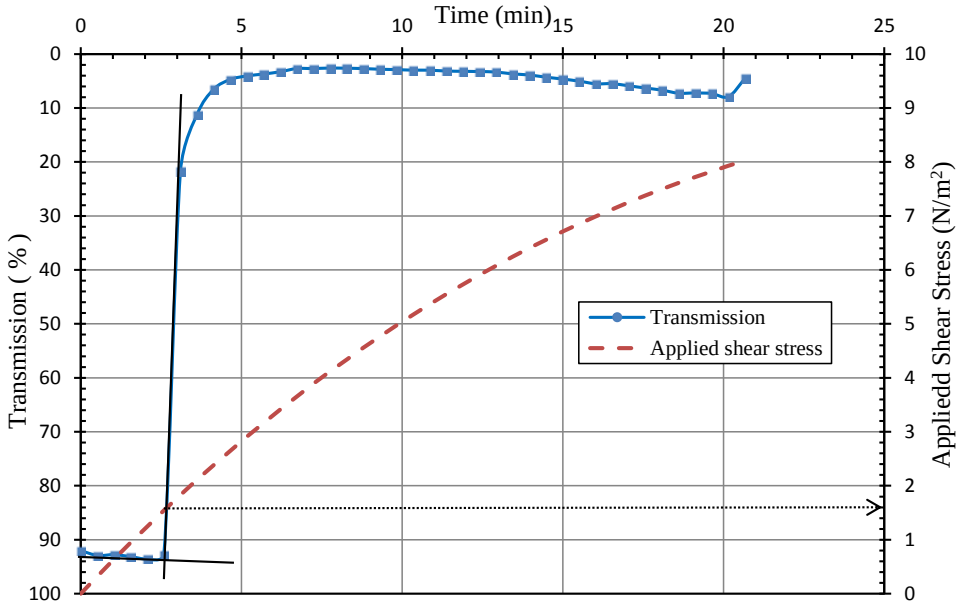

Fig. 4.30. Illustration of the determination of the critical shear stress using the CSM data.

4.2.3.4 In-situ Testing and Sampling

The critical shear stress of the coastal cohesive soils in the two selected test sites was determined by the aforementioned CSM. A brief description of the testing procedures is provided here: first a clean, undisturbed test spot with an area of 4 x 4 inch that is suitable for

the CSM test was located. In general, such a spot should be free of visible shells or other sandy grains, and no vegetation should be present within the selected area; Second, the sediment surface was slightly cleaned very gently and carefully using a spatula or knife to remove disturbed top soil or unwanted freshly deposited organic materials. As such, the cohesive soils or muds were exposed with a relatively flat surface. The sensor head was then pressed and inseted into the ground at the prepared test spot and the CSM was then warmed up for testing. To prevent the change in the critical shear stress caused by water salinity and chemistry, site water was always used in the built-in water reservoir. After the completion of each test, the sensor head is cleaned properly before starting another test. Fig. 4.31 shows an in-situ CSM test being performed in the Terrebonne Bay site.

Fig. 4.31. An in-situ CSM test being performed in the Terrebonne Bay site.

As pointed earlier, the critical shear stress is affected by many different factors of physical, chemical, and biological origins. The in-situ CSM tests can yield the critical shear stress directly. However, other soil properties cannot be obtained. In addition, in-situ CSM tests can only obtain the critical shear stress of the top surface layer of the in-situ soil, but not the soils in the vegetation root zone or other depths. Therefore, undisturbed soil samples (Fig. 4.32) were also obtained using 4 in. diameter and 3 ft long vibrocore, thin-walled aluminum tubes for subsequent laboratory testing.

In addition to the tube samples, other disturbed samples were also obtained for the measurement of organic matter content and/or root content on each in-situ CSM test spot. Soil material adjacent to the test spot was taken to a depth of up to 2 inch and then stored in ziplock bags. On the April 18, 2012 visit to the Barataria Bay site, six CSM tests were performed with two tests near the same test spot and disturbed soil samples were collected from each of the six tested spots to measure the organic matter content, which was expected to examine how sediment stability is affected by organic matter content. On the July 6, 2012 visit to the

Terrebonne Bay site, disturbed samples were also collected for each of the CSM test sites (Table 4.2) for the measurement of water content, organic matter content and root content.

Fig. 4.32. Undisturbed sampling with a vibracore aluminum tube

4.2.3.5 **Laboratory Testing**

Laboratory testing was mainly conducted on the undisturbed tube samples collected from the two test sites. Although the sample tube length was 3 ft, usually the recoverable soil samples extruded from each tube was approximately 2 ft. The tubes were all cut into 3 inch long sections for different types of laboratory testing. Totally three types of tests were performed usually on each tube sample.

- CSM testing: for each sample section cut from the parent tubes, the soil material that was disturbed by cutting (usually with a handsaw) was first removed and saved for water content and organic matter content measurement. Each section is also equivalent to a depth below the ground surface, and thus the vertical critical shear strength profile along the depth can be obtained. For each cut section, two CSM tests were performed and their average was taken to represent the critical shear stress at that depth (Fig. 4.33).
- Physical index testing: In addition to the water content and organic matter content measurements on each cut section, Atterberg limits (including both liquid limit and plastic limit) measurements were also conducted on each sample tube, which usually requires soil material from several cut sections. After CSM testing, soil was extruded from each cut section and mixed to achieve homogenization. Then the composite samples mixed from the entire 3 ft long tube were used for the determination of

Atterberg limits, specific gravity, and particle size distribution. All these physical index tests were performed by following relevant ASTM standard methods.

- Root content measurement: Root content was determined for each 3 in long section cut from the vibracore tubes, which means that root content was measured for different soil layers at a vertical spacing of 3 inch. Since root content measurement is not currently included in the ASTM standards, the following method was adopted: First, a representative portion of soil sample was air dried to obtain the total dry weight of the soil. Then this same material was washed (i.e., wet sieving) through two sieves with a mesh size of #30 and #40 to separate roots from soil (Fig. 4.34). After washing and wet sieving, the roots were air-dried to obtain their dry roots. Finally, the root content (R_C) is calculated via the following formula:

$$\text{Root content } (R_C) = \text{Mass of dry roots } (M_R)/\text{Mass of soil solids } (M_S)$$

In summary, laboratory testing on thin-walled tube samples of 3 ft in length can yield the following soil properties along a depth of 2-3 ft: critical shear stress, water content, organic matter content, and root content along the depth, liquid limit, plastic limit, specific gravity, and particle size distribution for each sampling site.

Fig. 4.33. Running cohesive strength meter test on small 3 inch soil sample tube

Fig. 4.34. Washing in sieves to separate roots from soil

4.2.4 Results and Discussion

4.2.4.1 Terrebonne Bay site

In-situ testing (3/5/2012)

Most in-situ CSM tests were just performed on soil surface, and the results obtained are just the critical shear stress of sediment surface. However, one attempt was also made to run in-situ CSM tests over a limited depth in order to characterize the erosion resistance of marsh soils at different depths (the 3/5/2012 field visit). The results of such an attempt were shown in Fig. 4.35, where the critical shear stress at the Terrebonne Bay site increases from 0.6 Pa at the surface to 1.02 Pa at a depth of 0.15 m, and then decreases to 0.66 Pa at a depth of 0.25-0.30 m. This profile is consistent with the field observation that the eroded marsh edge usually exhibits a stepped pattern. The increased erosion resistance reflects that the soil has a higher undrained shear strength at the depth of 0.15-0.20 m. This depth is typically where the roots of vegetation prevail and grow. The transevaporation of marsh plants needs water from the roots that in turn takes in water from the surrounding soil. As such, the high intake of water by the roots from the soil helps consolidate the soil around the depth, thus the undrained shear strength increases. However, at a depth of below the root zone, the soil is not so much affected by roots' water intake, and as such, the soil is not as consolidated as the soil within the root zone, resulting in a lower shear strength.

In-situ testing (7/23/2012)

During this site visit, two CSM tests were performed, together with subsequent laboratory measurements of water content and organic matter content. Results are shown in Figs. 4.36 and 4.37. The water content at the two tested spots is 55.12% and 58.93%, while the organic matter content is 3.43% and 4.09%. The variation of water content can be considered negligible as compared to the organic matter content, because of the large range of variation in water content. As such the organic matter content increases with water content, and the critical shear stress also increases with organic matter content. A positive correlation between critical shear stress and organic matter content can be observed in Fig. 4.36. Notice that the range of organic matter

content is below 5%, thus supporting the aforementioned idea that an appropriate range of organic matter content can enhance sediment stability.

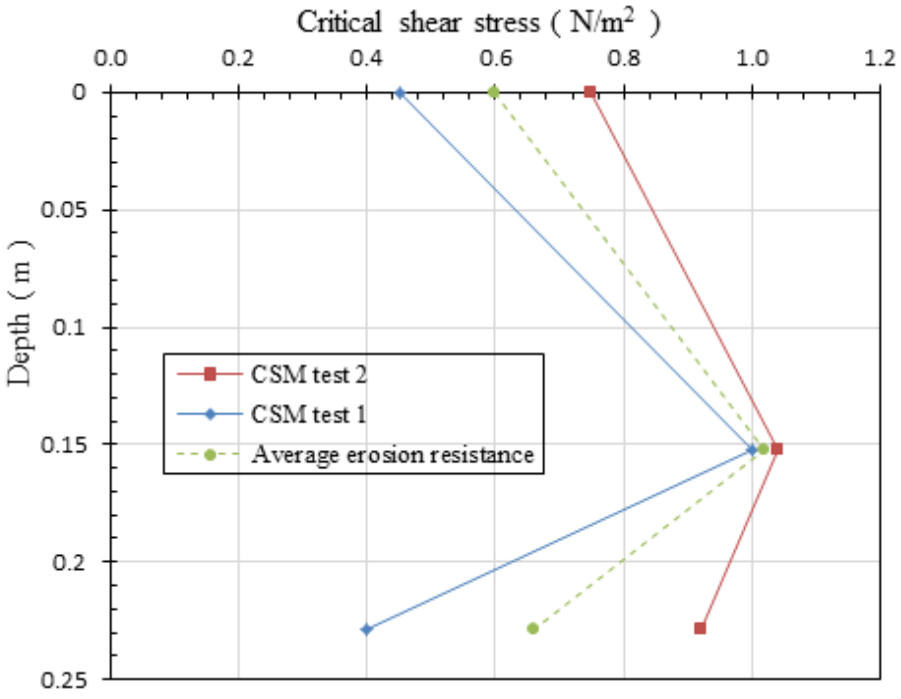

Fig. 4.35. In-situ variation of critical shear stress with depth at Terrebonne Bay

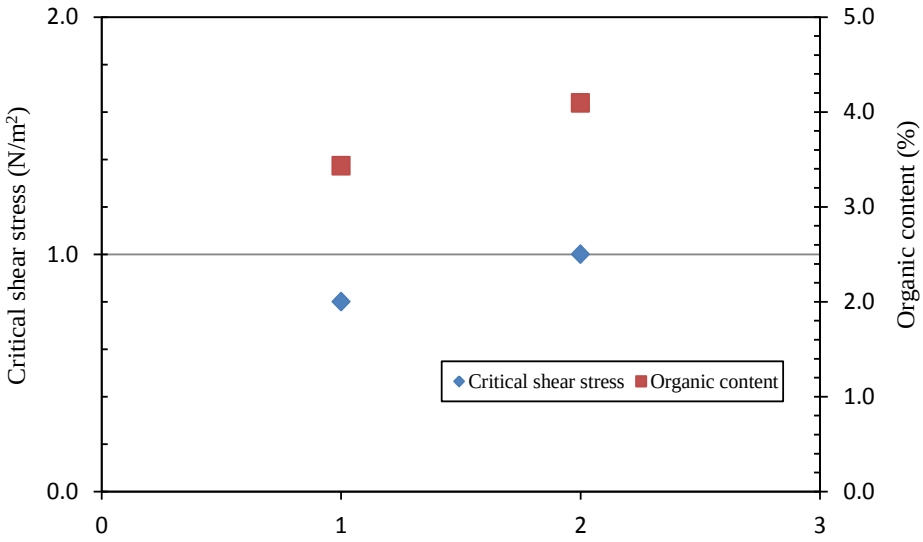

Fig. 4.36. Variation of in-situ critical shear stress with organic content

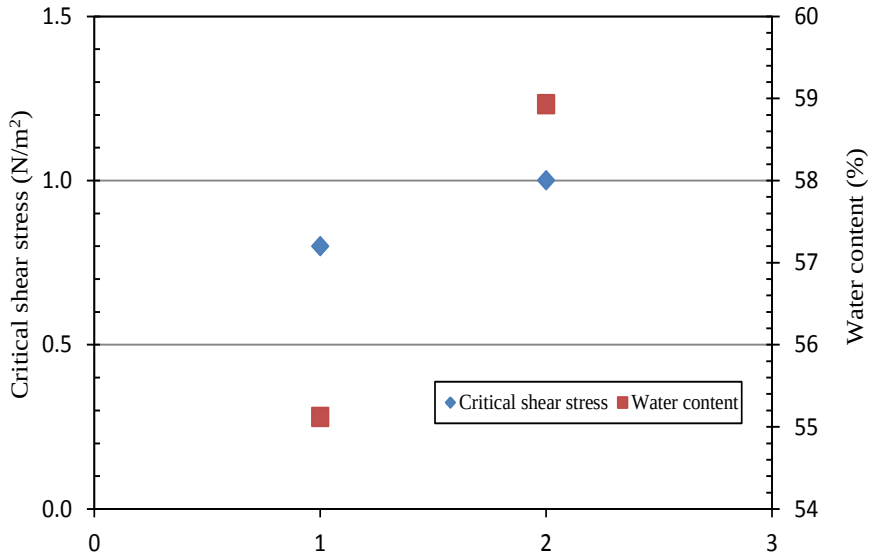

Fig. 4.37. Variation of in-situ critical shear stress with water content

In-situ testing (7/6/2012)

In this site visit, 7 CSM tests were performed at 4 different spots along a transect perpendicular to the shoreline, together with the subsequent laboratory measurements of organic matter content and root content. Results are shown in Figs. 4.38 and 4.39. This visit was in summer, and the vegetation was fully mature and much denser than the previous field visits. Freshly deposited sediment, organic matter and sea shells, probably brought to the site by storms, were observed on sediment surface.

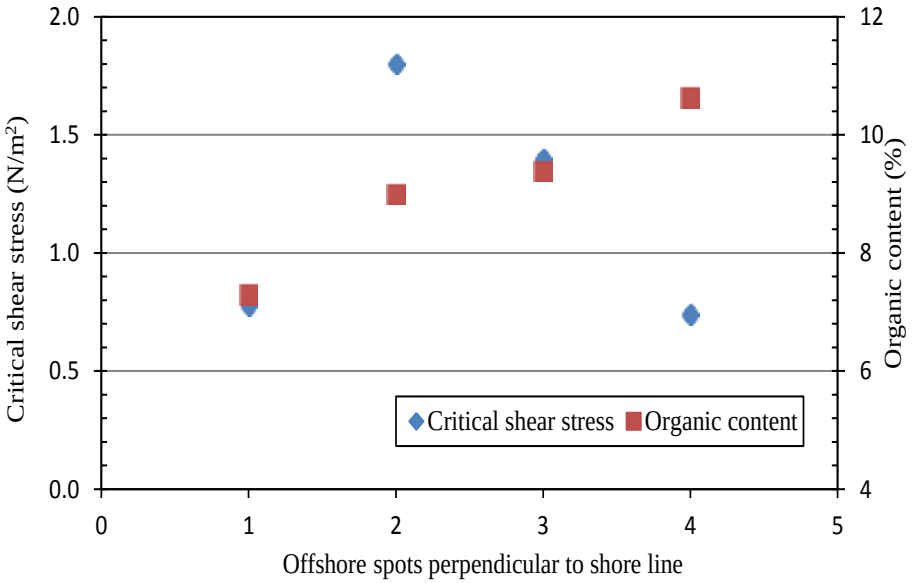

Fig. 4.38. Variation of critical shear stress with organic content at Terrebonne Bay.

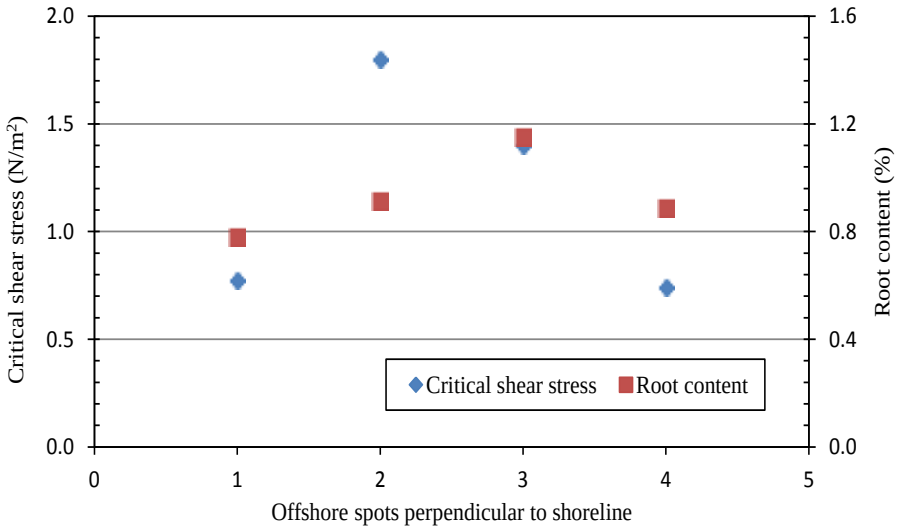

Fig. 4.39. Variation of critical shear stress with root content at Terrebonne Bay.

As stated earlier, a certain range of organic matter content can be positively correlated with the critical shear stress (Fig. 4.36). An organic matter content between 8 to 10% was found to result in a critical shear stress of >1.0 N/m² and beyond 10% it reduces the critical shear stress significantly (Fig. 4.38). This range is quite similar to that observed in the core samples (as discussed later). Overall, there exists a positive correlation between organic matter content and critical shear stress when the organic matter content is <10%. Beyond 10%, the organic matter tends to decrease the stability of marsh soil. Also, for the examined distance (~10 m), the organic matter content is found to increase along the distance away from the shoreline. The critical shear stress was also found to correlate positively with the root content (Fig. 4.39).

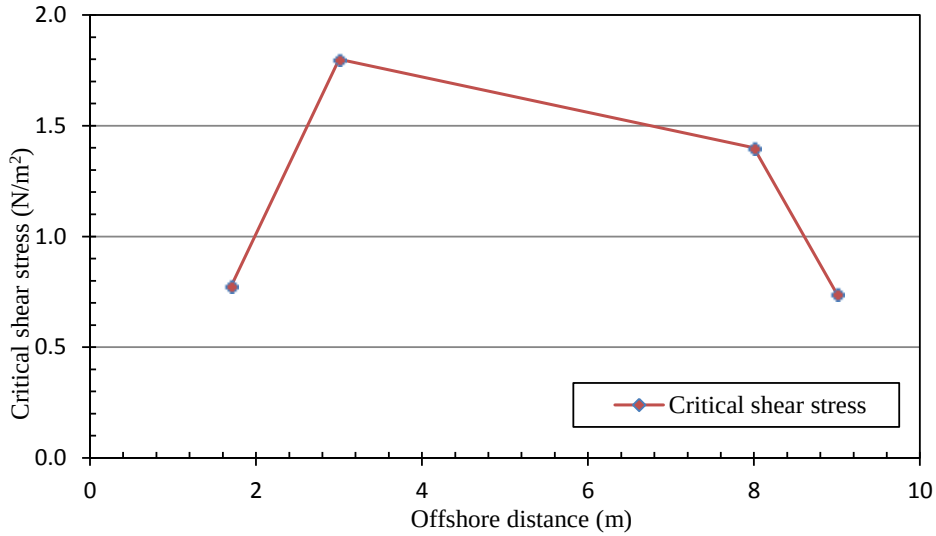

Fig. 4.40. Variation of critical shear stress along the distance to the shoreline

Fig. 4.40 shows the variation of critical shear stress along the distance to the shoreline. Except the first point at a distance of ~2 m, the critical shear stress in general decreases with the

distance from the shoreline. This is possibly true because the area near the shoreline (e.g., within a distance of 0-8 m) has the highest elevation (typically resulted from deposition by vegetation entrapment of sediment).

Summary of in-situ testing results

A total of 15 in-situ CSM tests were conducted in the Terrebonne Bay site, of which 11 were performed on the surface sediment. The results of these 11 tests are plotted in Fig. 4.41. Significant variations can be observed. The critical shear stress ranges from 0.45 Pa to 1.9 Pa, and the average is 1.16 Pa.

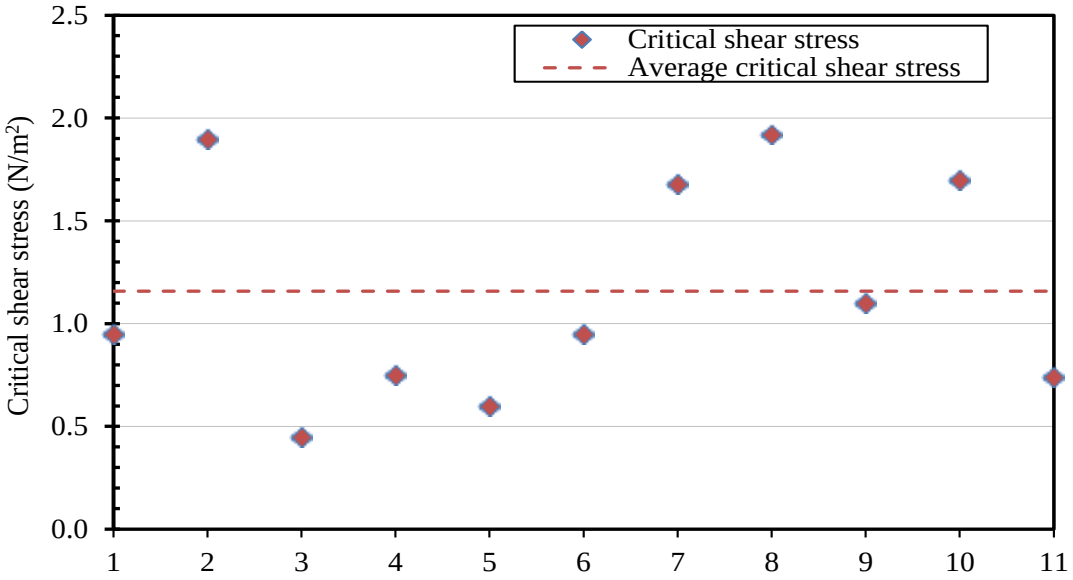

Fig. 4.41. Average of all in-situ critical shear stresses obtained on surface sediment.

Laboratory testing

In this section, the results from laboratory testing on all undisturbed tube samples are averaged and only the averages are presented. Figs. 4.42, 4.43, and 4.44 show the critical shear stress vs. depth along with water content, organic matter content, and root content, respectively.

Basically, the critical shear stress increases slightly with depth, but below the depth of 0.38m, it decreases with depth (Fig. 4.42). This trend was also observed for the in-situ testing results (Fig. 4.35). A similar mechanism can be used to explain the change of critical shear stress with depth. At a depth of <0.3-0.4 m, vegetation roots prevail in this zone, and the transevaporation of vegetation causes roots to intake water from the surrounding soil. The removal of water by roots actually helps consolidate the soil, leading to an increase in shear strength. For the soil at depths below 0.4 m, the roots are usually absent, and thus the soil shear strength is low. The variation of water content with depth does not follow any specific pattern, but generally its value at depths is greater than that at the ground surface. Up to a depth of 0.10 m, there is a dramatic decrease in water content and increase in the erosion resistance of soil. For the next 0.13 m, there is a continuous and significant increase in water content, but the erosion resistance increases just slightly. This is due to the fact that water content is not the only factor affecting the soil's erosion resistance. Furthermore, below the depth of 0.3 m, the water

content is almost constant at ~150 %, but the erosion resistance decreases significantly from 1.2 Pa at a depth of 0.30 m to 0.29 N/m² at a depth of 0.53 m.

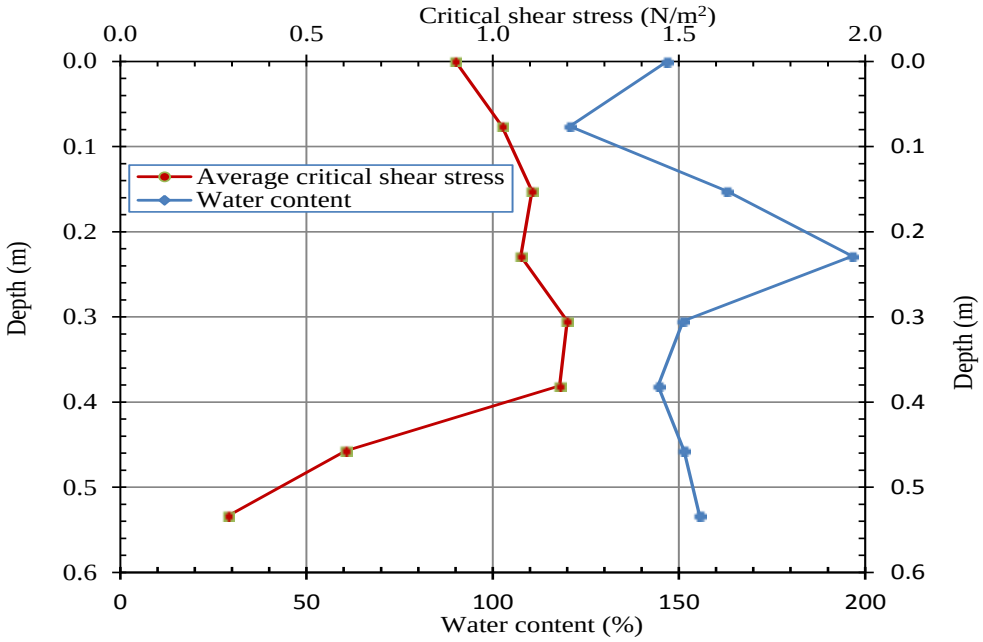

Fig. 4.42. Variation of critical shear stress and water content with depth

As shown in Fig. 4.43, if the entire plot is analyzed, the soil's erosion resistance seems not to be correlated with the organic matter content. According to the literature (e.g., Brady and Weil, 2002; Morgan, 2005), a positive correlation usually exist between a soil's erosion resistance and organic matter content when the latter is from 0 to 10%. For the soils in the Terrebonne Bay site, an organic matter content of 7 to 10% can have positive impact on sediment stability. This range of organic matter content fairly maintained a critical shear stress of > 1.0 Pa. Furthermore, the variation of organic matter content from 7 to 10% does not cause a significant variation in critical shear stress, possibly indicating that this range of organic matter content is optimal range that enhances sediment stability. Finally, the organic matter content is found to depend upon water content and, whenever the water content increases, the organic matter content also increases. Beyond 10% organic matter content, there is a significant decrease in the soil's erosion resistance.

Soil's erosion resistance is also affected by root content. As shown in Fig. 4.44, the critical shear stress increases with root content. However, at the very shallow depth of 0 to 0.1 m, the two parameters seem not to be correlated. Two possible reasons may be responsible for it: (1) the root content at this shallow depth cannot be accurately measured; and (2) the soil is just freshly deposited and hence a coherent integration of soil and roots has not been established (i.e., the roots cannot play its role of reinforcement in the soil). Another possibility is that the water content is the major parameter affecting sediment stability at very shallow depths. Interestingly, at depths of >0.3 m, the critical shear stress line becomes parallel to the root content line, indicating that root content greatly affects sediment stability.

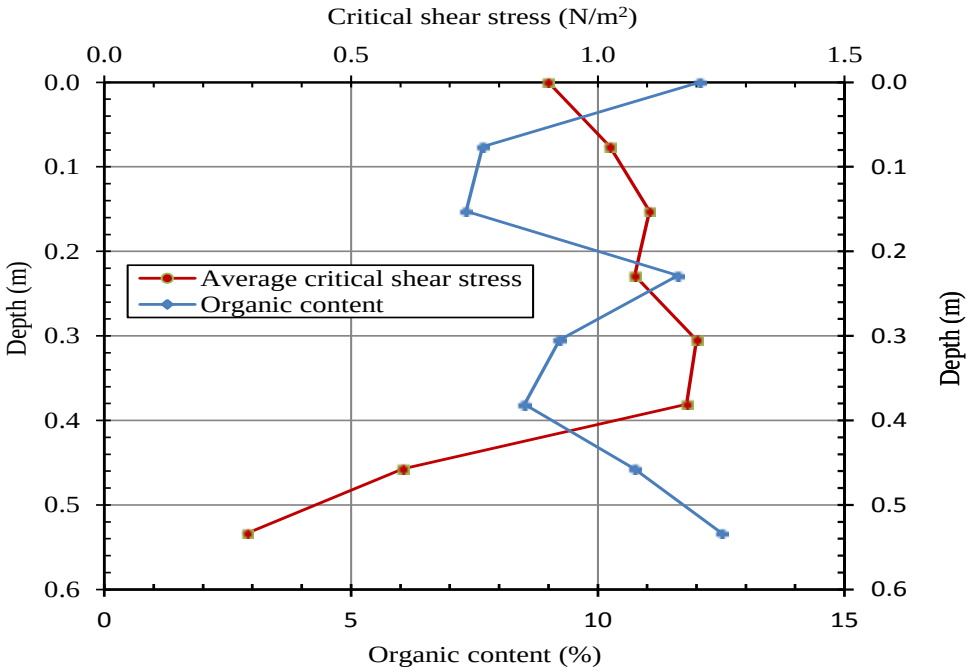

Fig. 4.43. Variation of critical shear stress and organic matter content with depth

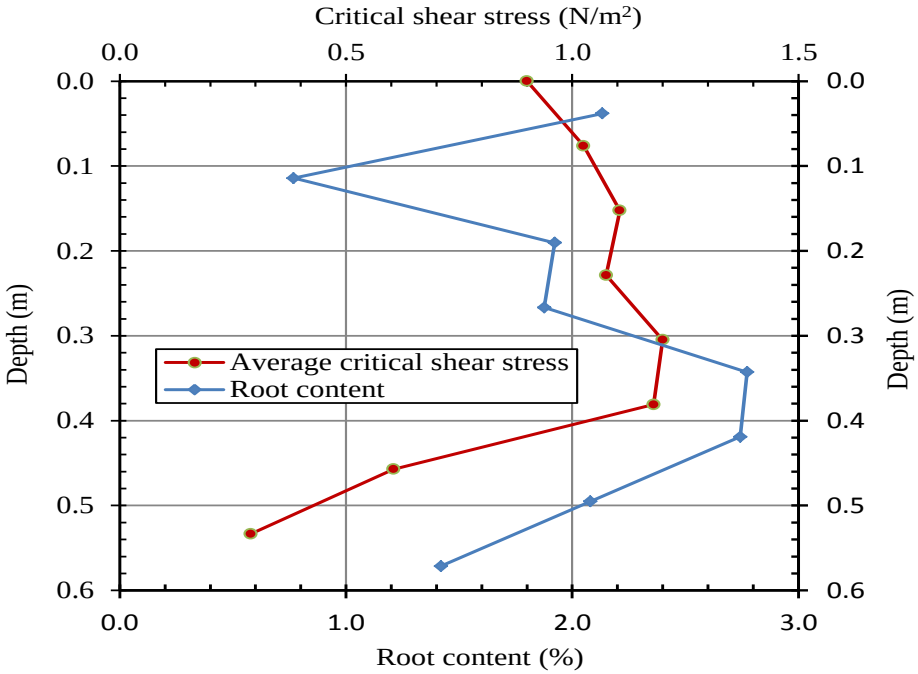

Fig. 4.44. Variation of critical shear stress and root content with depth

4.2.4.2 **Barataria Bay site**

In-situ testing

Results from all in-situ tests conducted at the Barataria Bay site were averaged and only the average data are presented in this section. Totally 8 in-situ CSM tests were performed on the sediment surface at this site, and the obtained critical shear stresses are plotted in Fig. 4.45. The range of these critical shear stresses is 0.4 Pa to 1.6 Pa, with an average of 1.03 Pa. Compared with the results from Terrebonne Bay site, the critical shear stress at the Barataria Bay site shows a smaller variation (e.g., 0.4-1.6 Pa vs. 0.45-1.9 Pa) and a smaller average (e.g., 1.03 Pa vs. 1.16 Pa). Therefore, the marsh soil in the Barataria site may be more vulnerable to erosion than the Terrebonne Bay site.

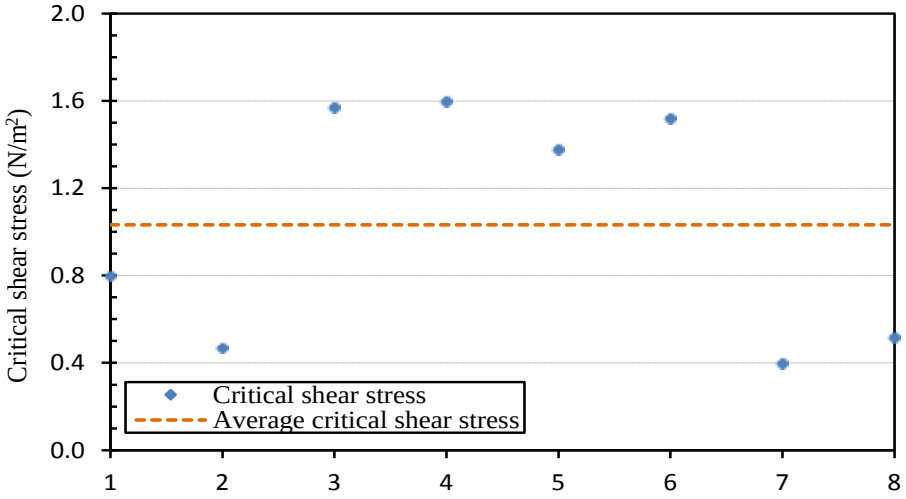

Fig. 4.45. Summary and average of critical shear stresses obtained from in-situ testing

Fig. 4.46 shows the variation of critical shear stress and organic matter content at the tested spots. It appears that the critical shear stress is not always positively correlated with organic matter content. As discussed earlier, there exists a range of organic matter content at which a soil's strength can be increased. Beyond this range, a soil might become more prone to erosion. For this site, the organic matter content ranges from 30% to 40%. As the organic matter content is larger than 35%, the critical erosion stress decreases below its average value (i.e., <1.22 Pa) (Fig. 4.46).

Laboratory testing

Again, this section only presents the average results obtained from all undisturbed tube samples. Figs. 4.47–4.49 shows the variation of critical shear stress with depth together with water content, organic matter content, and root content, respectively. As shown in Fig. 4.47, water content decreases slightly to a depth of 0.23 m. Corresponding to this, there is an increase in critical shear stress. But below this depth, the correlation between critical shear stress and water content is not so clear, although in general the trend is positive. This suggests that other factors may also have a major influence on sediment stability. Also notice that the variation of critical shear stress with depth for this site is very small, which is different from that in the Terrebonne Bay site.

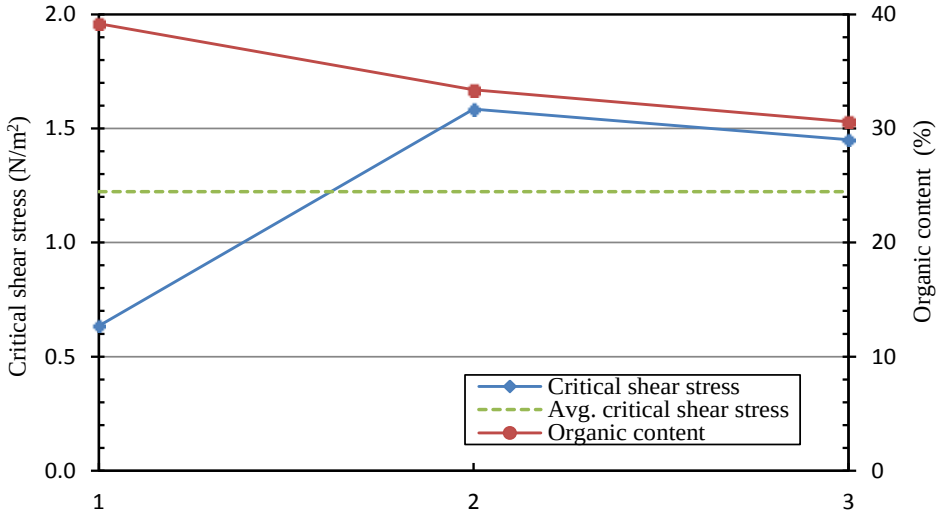

Fig. 4.46. Variation of critical shear stress with organic matter content

Laboratory testing

Again, this section only presents the average results obtained from all undisturbed tube samples. Figs. 4.47–4.49 shows the variation of critical shear stress with depth together with water content, organic matter content, and root content, respectively. As shown in Fig. 4.47, water content decreases slightly to a depth of 0.23 m. Corresponding to this, there is an increase in critical shear stress. But below this depth, the correlation between critical shear stress and water content is not so clear, although in general the trend is positive. This suggests that other factors may also have a major influence on sediment stability. Also notice that the variation of critical shear stress with depth for this site is very small, which is different from that in the Terrebonne Bay site.

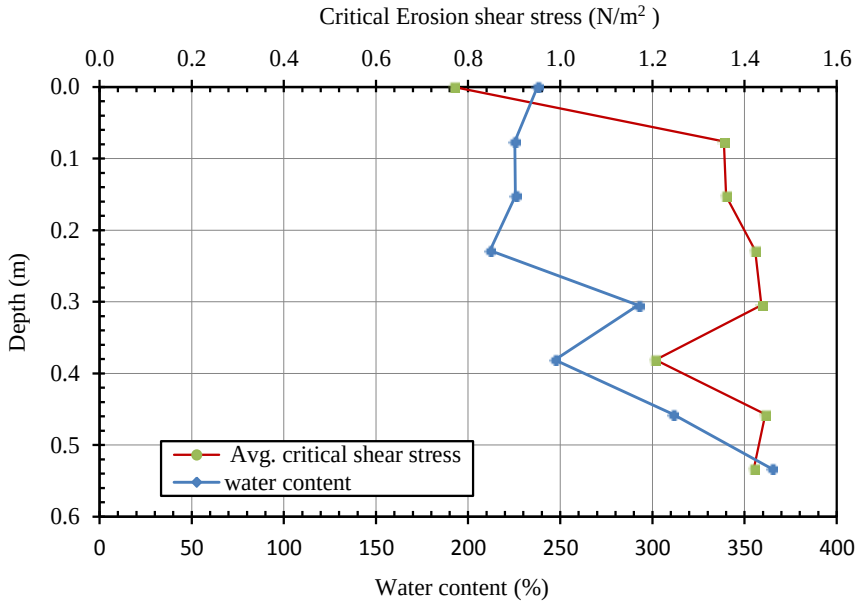

Fig. 4.47. Variation of critical shear stress and water content with depth

Fig. 4.48 shows the variation of critical shear stress and organic matter content with depth. Interestingly, the two curves are nearly parallel to each other. Approximately 20 to 30% of organic matter contents are found in the soils at depths. In addition, the water content also increases with the organic matter content at this site. Such a positive correlation between organic matter content and critical shear stress exists for 20-30% organic matter content, which is contrary to the aforementioned appropriate range of organic matter content (i.e., <10%). One possible reason for such high organic matter contents is that the crude oil spill may have seeped into the sediment at depth and been trapped in the soil pores, and certainly the crude oil was taken into account of the organic matter content during the organic content measurement at 440°C. In addition, the organic matter content for soil at depth was found to be less than that of surface soil (e.g., measured at the in-situ CSM test spot). Again, this is due to the fact that more oil spill (e.g., even weathered oil residue) exists on the sediment surface.

Fig. 4.49 shows the variation of critical shear stress and root content with depth. Except the shallow upper layer of up to 0.1 m in depth, there is a positive correlation between root content and critical shear stress. Furthermore, a root content of 3.5 to 5.5% is likely to improve sediment stability.

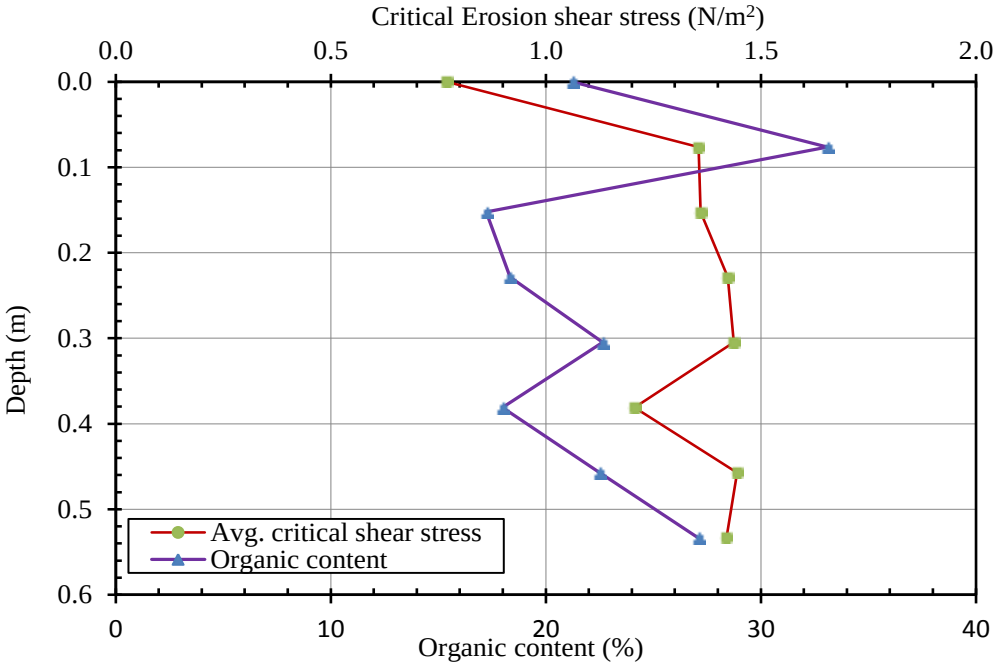

Fig. 4.48. Variation of critical shear stress and organic matter content with depth

4.2.4.3 Comparison of Soil Properties between the Barataria Bay and Terrebonne Bay Sites

Tables 4.3 and 4.4 compare the physical properties and critical shear stresses for the soil from the two sites, respectively. The soil in Barataria Bay has relatively larger mean particle size and smaller specific gravity, but higher plastic and liquid limits, indicating that the soil in this site has more organic matter than the Terrebonne Bay site. The higher organic matter content in Barataria Bay may be caused by the presence of oil spill contamination. The direct organic matter content measurement (Table 4.4) validates this observation.

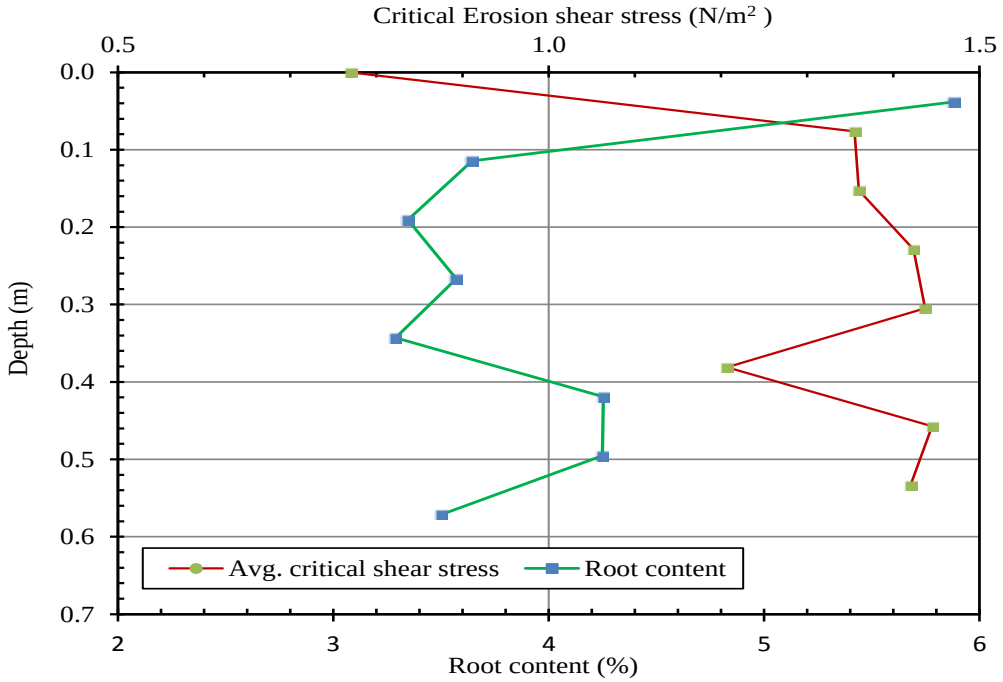

Fig. 4.49. Variation of critical shear stress and root content with depth

As shown in Table 4.4, the surface soil at the Terrebonne Bay site has a slightly greater critical shear stress than the surface soil at the Barataria Bay site, but the deep soil in the former has a much smaller critical shear stress than the latter. These results are also shown in Figs. 4.50 and 4.51. Since wetland erosion usually initiates at sediment surface, the Terrebonne site is more stable than the Barataria Bay site. However, the below-surface soil in Barataria Bay has a higher critical shear stress than that in Terrebonne Bay, suggesting that the latter site is more prone to the undercut-type erosion. In fact, during field visits, it was observed that the Terrebonne Bay site has places where undercut erosion is undergoing. Finally, as mentioned previously, the Barataria Bay site has some very weak spots that are much less stable than the Terrebonne Bay site. These weak spots may be affected by the oil spill, and hence are more prone to erosion. In summary, if the two sites are subjected to the same hydrodynamic erosional driving force, the sequence of erosion will be: 1) surface erosion in the weak area in Barataria Bay; 2) undercut erosion in Terrebonne Bay; 3) surface erosion in the weak area (if any) in Terrebonne Bay; 4) general surface erosion in Barataria Bay; 5) general surface erosion in Terrebonne Bay; and 6) undercut erosion in Barataria Bay.

Table 4.3. Physical properties of soils in the two sites

Site	Mean particle size (mm)	Specific gravity	Liquid limit (%)	Plastic Limit (%)	Plasticity index (%)
Barataria Bay	0.113	2.27	68.2	46.5	21.7
Terrebonne Bay	0.092	2.54	54.4	29.8	24.6

Table 4.4. Critical shear stress, root content, and organic matter content of two sites

Site	Average in-situ critical shear stress (N/m^2)	Average sample tube critical shear stress (N/m^2)	Average sample tube critical shear stress on surface (N/m^2)	Average organic matter content (%)	Average root content (%)
Barataria Bay	1.03	1.28	0.77	21.9	4.0
Terrebonne Bay	1.16	0.82	0.9	9.6	2.1

The root content and organic matter content of the two sites are compared in Fig. 4.52. Both parameters in Barataria Bay are nearly twice greater than those in Terrebonne Bay. Therefore, the higher root content (or dense vegetation) in Barataria Bay is responsible for the overall stability of the site (if no oil spill is present). In contrast, the smaller root content in Terrebonne Bay is responsible for the relatively abundant undercut erosion observed in this site.

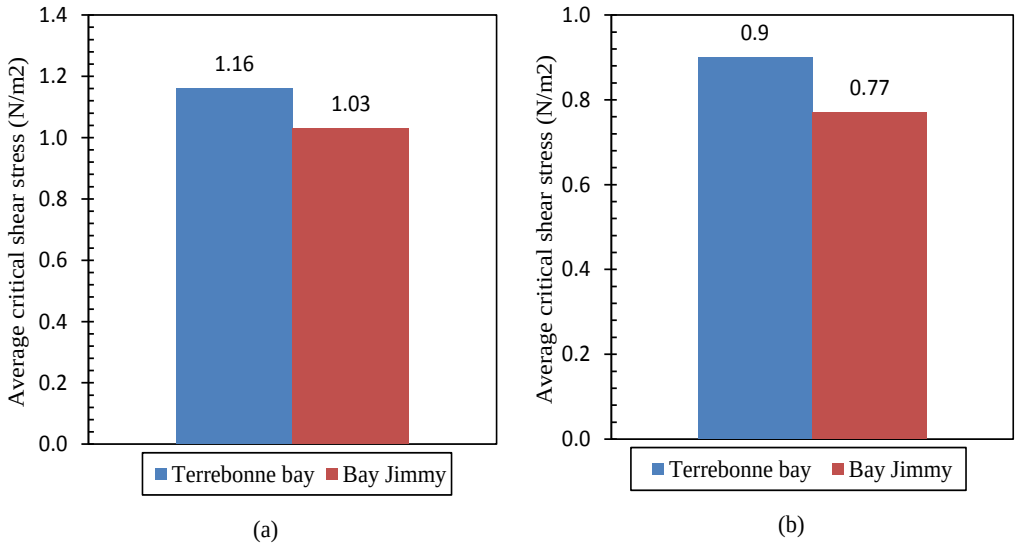

Fig. 4.50. Average critical shear stress of the surface at the two sites: (a) in-situ and (b) laboratory testing.

4.2.5 Summary

This task presents an extensive in-situ and laboratory experimental program designed to determine and understand the critical shear stress of marsh soils in Louisiana's coastal wetlands. Two sites were selected for field testing and sampling, the Terrebonne Bay site and Barataria Bay site. The critical shear stress at the two sites was measured using a cohesive strength meter (CSM): while the surface soil erosion resistance was characterized by in-situ testing, the soil at depth was tested in the laboratory via examining undisturbed tube samples obtained from the site. Laboratory testing consisted of CSM, organic matter content, water content, root content, Atterberg limits, and particle size measurements.

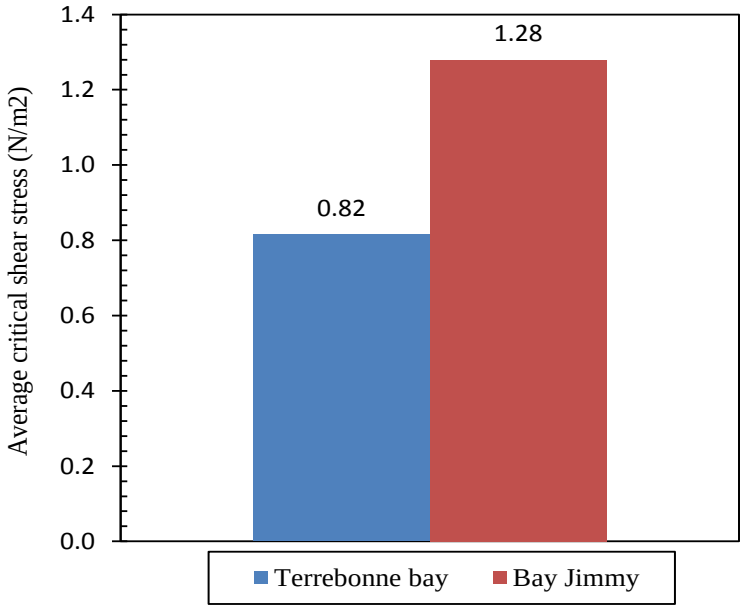

Fig. 4.51. Average critical shear stress of the soil below the surface at the two sites

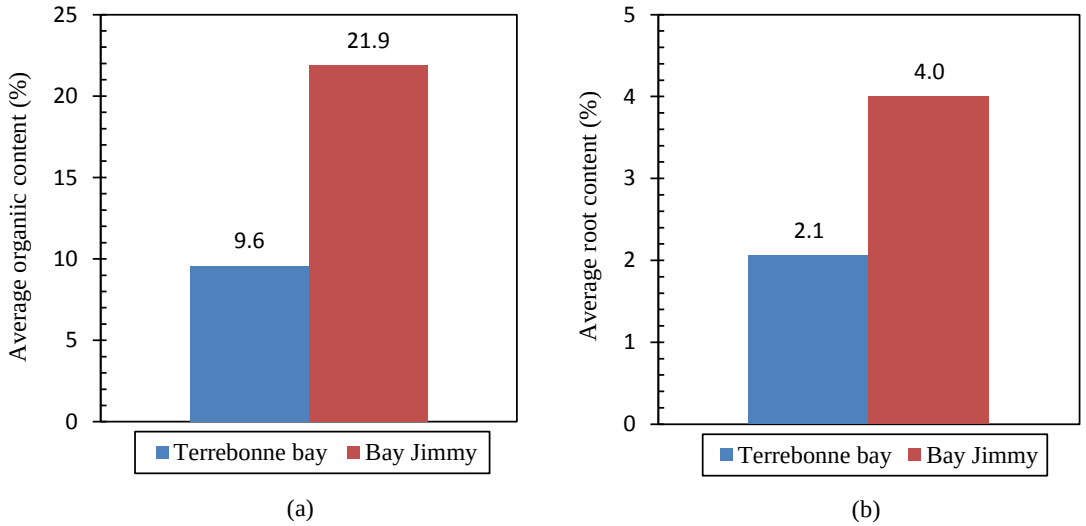

Fig. 4.52. (a) Average organic matter and (b) root content of the two sites

Based on the obtained results, the following conclusions can be drawn:

- For the Terrebonne Bay site, both surface erosion at some weaker areas and undercut erosion are the major causes of marshland loss. For places where the surface soil's critical shear stress is greater than that of soil in depth, undercut erosion will initiate first, leading to the loss of deeper soil layers and hence marsh edge damage.
- For the Barataria Bay site, surface erosion is the major cause for marshland loss, because this site is characterized by a stronger soil below the ground surface.
- For both sites, the critical shear stress ranges from 0.4 to 1.9 Pa, and the average values are 1.03 to 1.16 Pa. These values may provide insight on the initiation of erosion under what hydrodynamic conditions.

- The surface erosion threshold and hence the stability of Terrebonne Bay is greater than Barataria Bay. However, the former is more prone to undercut erosion, most likely due to the less root content or organic matter content in depth.
- Both organic matter and root contents in Barataria Bay are greater than those in Terrebonne Bay.
- In general, certain range of organic matter content can have a positive influence on sediment stability. The organic matter contents of 7-10% for Terrebonne Bay and 20-30% for Barataria Bay were found to enhance sediment stability.
- The critical shear stress increases usually with root content, and thus vegetation roots play an important role in controlling marsh erosion and marshland loss
- Water content and organic matter content affect soil stability at shallower depth, but at a greater depth root content has major impact on sediment stability.
- In-situ CSM tests at Terrebonne Bay showed that the critical shear stress initially increases with depth and then decreases. A similar pattern was also seen from laboratory testing of tube samples obtained from this site.
- Some of the weak spots in Barataria Bay with very low critical shear stress might be caused by oil spill.

4.3 Growth Forms and Productivities of *S. alterniflora* and *J. roemarianus*

The task in this section is to characterize each sampling site by surveying native plants, characterizing associated sediments in both low and high marsh zones, measuring primary production of native vegetation, and assessing elevation and salinity gradients in coastal and inland marshes vegetated by *Spartina alterniflora* and *Juncus roemerianus* along the Mississippi and Louisiana Gulf Coast. In Phase II, the focus was comparison of LA and MS marshes. Graveline Bayou in MS coast and Terrebonne Bay in LA coast were chosen as the research sites. The study would investigate whether there is any significant difference in the soil properties and plant characteristics between LA and MS coastal marshes, as well as whether coastal vegetation produces high aboveground biomass in high marsh zones and high belowground biomass in low marsh zones in both LA and MS coastal marshes in summer.

Presented in this section are also the overall results obtained from the combined data sets collected in both Phases I and II.

4.3.1 Methods

Research sites and transects used in Phase I study were described in Phase I report (Wu et al., 2011). Introdoced below are research sites and transects used in Phase II study, which focused on comparison of LA and MS marshes, as well as field measurement, laboratory test and statistical analysis methods and procedures used in both Phase I and II studies.

4.3.1.1 Research Sites and Experimental Setup

In Phase II, two research sites have been chosen in southeast Mississippi and southern Louisiana in order to compare and contrast coastal marsh development at these two locations. After examining topographic maps and aerial photos, two research locations were chosen: Graveline Bayou and Terrebonne Bay. Graveline Bayou [30° 21.47'N, 88° 41.41'W] (Figs. 4.53

and 4.54) is located between Ocean Springs and Gautier along the Mississippi Gulf Coast. Graveline Bay and Bayou has a wetland reserve boundary of 946 hectares (9,472,950 square meters; Gulf Ecological Management Sites website; GEMS 2010). Graveline Bayou represents one of a few relatively undisturbed estuarine bays and small tidal creeks in Mississippi. The area supports salt marsh, brackish marsh, and several oyster beds. The bay, marsh, adjoining upland forest, and undeveloped beach front near the mouth of Graveline Bayou are an important landing area for neotropical migrant birds. The coastal marsh estuarine system receives only local fresh water runoff and consists largely of mid-level *Juncus roemerianus*-dominated marsh along its entire length. *Spartina alterniflora* occurs largely as narrow (1-3 m) bands along the coast, creeks and bayous. The Louisiana Universities Marine Consortium (LUMCON)'s [29° 15.200'N, 90° 39.800'W] primary facilities are located at the DeFelice Marine Center in Cocodrie, approximately 85 miles southwest of New Orleans (Fig. 4.55). This location, situated within the estuarine wetland complex of the Mississippi River delta plain between the Atchafalaya and Mississippi Rivers, provides ready access to the most productive estuaries in the United States, to a variety of coastal environments, and to the open Gulf of Mexico (LUMCON website). Terrebonne Bay is located on the west side of Barataria Bay. It is bounded by Timbalier Bay on the east and the Houma Navigation canal on the west. Freshwater is delivered into Terrebonne Bay via the Houma Navigation canal, but saltwater intrusion into marshes can be increased by the location of straight and deep canals that connect the coast with the interior marshes (Gosselink 1984). It is bordered on the south by a series of narrow, low-lying barrier islands, called the Isles Dernieres and the Timbalier Islands that are approximately 15 km south of the selected site. The common vegetation communities in these marshes are *Spartina alterniflora* and *Spartina patens*.

Both Graveline Bayou and Terrebonne Bay sites were inundated by Hurricane Katrina in 2005, and no coastal marshes exist in Mississippi and Louisiana which have not been inundated by hurricanes. Hurricane Katrina made landfall and damaged marsh vegetation along the Louisiana and Mississippi coasts on August 29, 2005 as a category 5 storm. Katrina's wind speeds peaked at 282 kph, and, at its largest, the storm had hurricane force winds extending 193 km from its eye. Storm surge heights were 6 to 10 m in some areas along the coast, the effects of which extended as far east as Mobile, AL. At Grand Bay, the maximum sustained wind speed of Hurricane Katrina was stronger than 205 km/hr and the storm surge was 3.97m. Hurricane Rita followed, on September 24, 2005, and made landfall farther to the west, near Sabine Pass, TX, and, consequently, had less of an impact on Graveline Bayou compared to Katrina (McKee and Cherry 2009).

Point Aux Chenes water quality station at Grand Bay is the closest monitoring station to where we sampled at Graveline Bayou and has access to salinity data (Fig. 4.56; MS Gulf Coast Research Lab website; GNDNERR website). Data for the coastal areas at Point Aux Chenes monitoring station showed that the salinity ranged from 11.7 ppt to 17.9 ppt and the average salinity was 15.82 ppt in April. In June, salinity ranged from 16.8 ppt to 21.4 ppt and the average salinity was 19.19 ppt (GNDNERR website). In Terrebonne Bay sites, water salinity ranged from 5.2 ppt to 24.14 ppt and the average salinity was 11.53 ppt in April. In June, water salinity ranged from 10.86 ppt to 30.98 ppt and the average salinity was 15.39 ppt (LUMCON website). There was a significant difference in salinity in both April ($p = 2.59E\text{-}07 < 0.05$) and June ($p = 6.76E\text{-}06 < 0.05$) between Terrebonne Bay and Graveline Bayou (Fig. 4.57). High spring flood flows in the Mississippi River could have lowered salinities at the LUMCON sites.

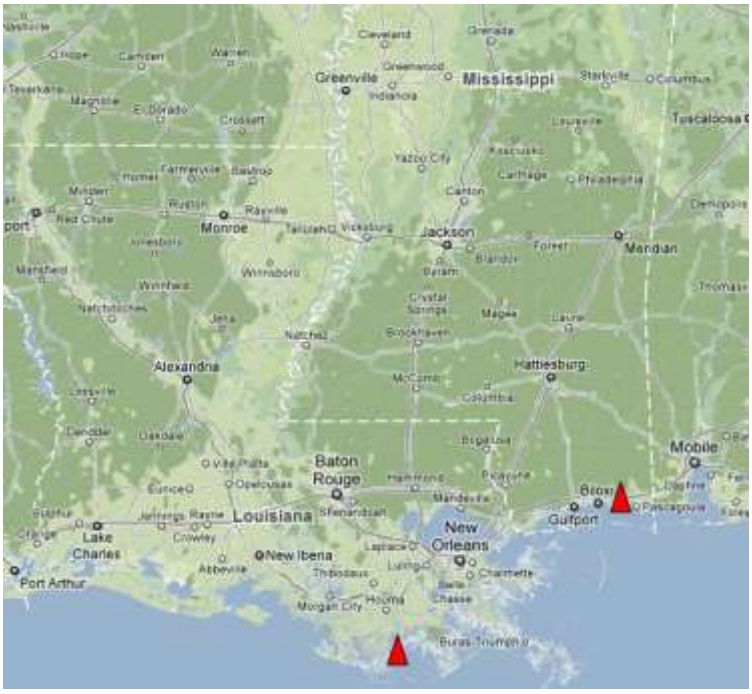

Fig. 4.53. Graveline Bayou and Terrebonne Bay are indicated by red triangles on the Mississippi and Louisiana Coast (Google Map accessed on April 23, 2011).

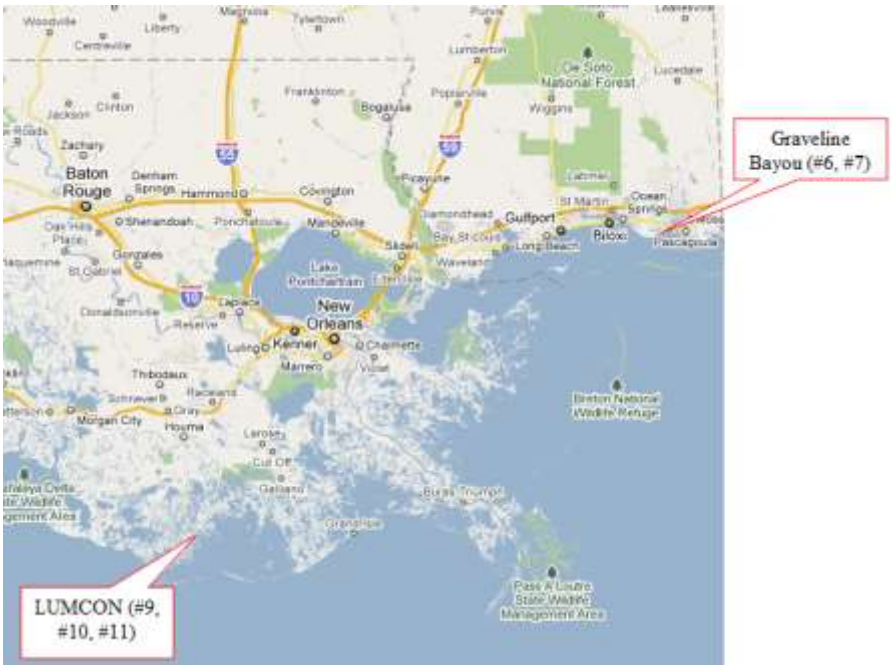

Fig. 4.54. Map of transects sampled at Graveline Bayou and LUMCON (Google Map accessed on April 23, 2011).

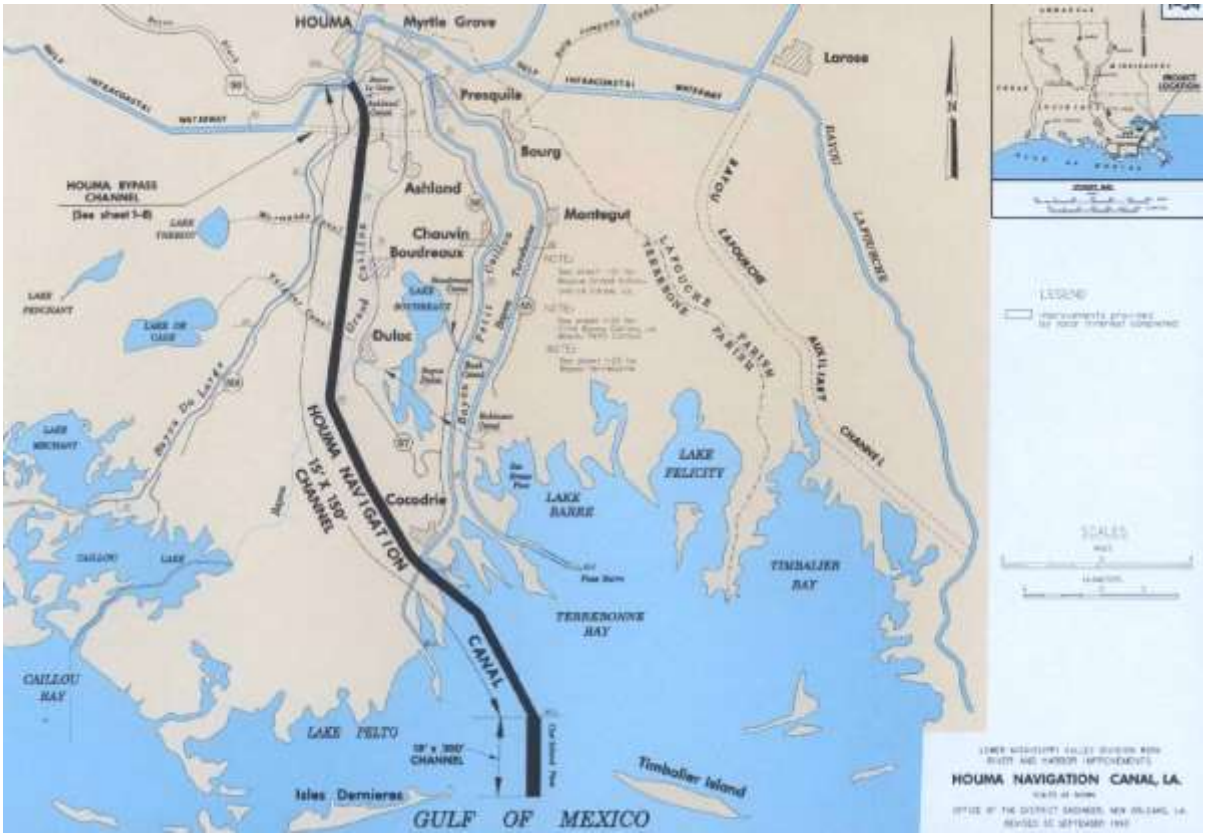

Fig. 4.55. Map of LUMCON and Terrebonne Bay (Google Map, 2011)

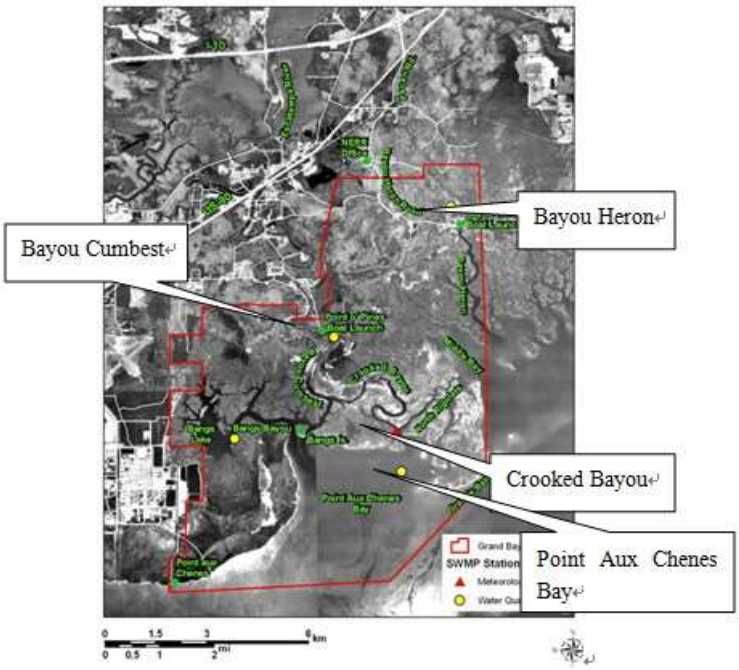

Fig. 4.56. Grand Bay NERR monitoring stations (GNDNERR Website, 2010).

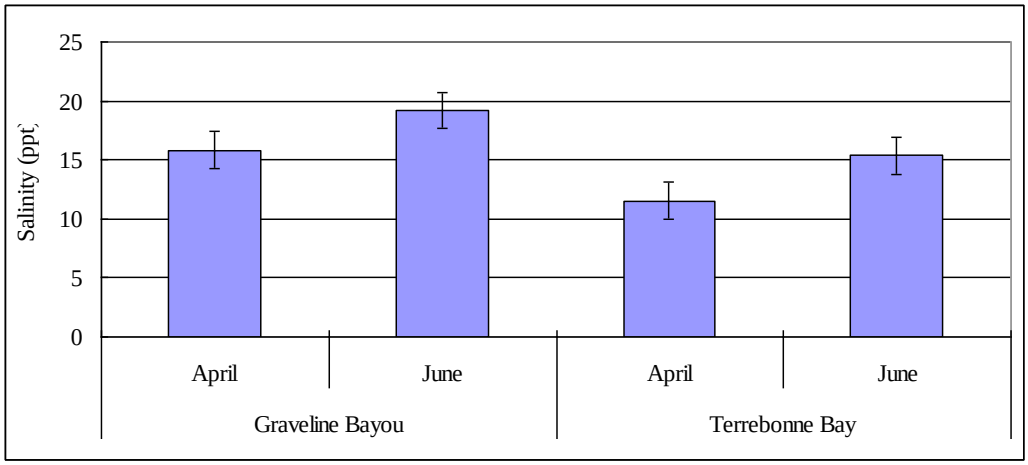

Fig. 4.57. Comparison of salinity data in April and June between Graveline Bayou (GNDNEER, 2011) and Terrebonne Bay (LUMCON, 2011; ±SE, n=66).

4.3.1.2 Field Measurements

Two coastal transect lines were established in each of these two research locations based on the different intensities of the storm surges. Initial samples were obtained at Graveline Bayou along two coastal transects: one was at the south side of Graveline Bayou along the Mississippi Gulf Coast (Transect 6) and the other was also at the south side of Graveline Bayou east of Transect 6 (Transect 7; Figs. 4.58 and 4.59). Both Transects 6 and 7 were located in coastal areas at the Graveline Bayou, which were dominated by *Spartina alterniflora* in low marsh zones and high marsh zones were dominated by *Spartina alterniflora* and *Juncus roemerianus*. Two additional coastal transects were established near the DeFelice Center on the east and west side of Terrebonne Bay in Cocodrie, LA (Transects 9 and 10; Figs. 4.60 and 4.61). The dominant vegetation on both transects was *Spartina alterniflora*. There was no record that Transects 9 and 10 existed before the DeFelice Center was built in 1979. Transect 11 was established at the East Terrebonne Bay along the Gulf Coast, which was dominated by *Spartina alterniflora* in both low and high marsh zones (Fig. 4.62).

Soil samples were collected to observe and measure soil properties from low marsh zones (marsh edge) and at 40 m inland from wave break in high marsh zones of both coastal and inland marshes vegetated by *Spartina alterniflora*. On each transect, ten replicate soil cores were collected in low marsh zones (marsh edge), and another replicate ten soil cores were collected from high marsh zones (40 m inland from the marsh edge). Soil cores were sampled with an 8.5 cm diameter by 30 cm long steel corer device (Art's Manufacturing & Supply; AMS Split Core Sampler). Each soil sample core was removed with a plunger from the top soil layer; thus, the soil sample was extracted from the bottom 5 cm of the soil core. The core samples were each placed in a Freezer Zip-Lock Bag, frozen, and placed in a cooler for transportation to the laboratory. The core samples were kept frozen until processed.

Initial observations were made in April 2011 to characterize the experimental sites as to substrate composition (e.g., classification), plant height (dead and live), and plant growth form (*Spartina alterniflora*, *Juncus roemerianus*, and/ or *Spartina patens*). No evidence of *Spartina patens* was observed during any marsh visits. Both live and dead standing shoot heights of vegetation in each 0.25 m^2 quadrat were recorded in the field. The percent cover occupied by each plant

species in each 0.25 m² quadrat was visually estimated and recorded (Holland and Burk 1990). Aboveground vegetation was clipped within a 0.25 m² quadrat, and rhizomes and roots of vegetation were also collected within a 0.25 m² quadrat to measure above- and belowground biomass from both low and high marsh zones on each transect. The aboveground vegetation and rhizome samples were each placed in carefully labelled 30 gallon sample bags and placed in a cooler for transportation to the laboratory. Then, vegetation samples were refrigerated until sorted by species and measured for above- and belowground biomass. On each transect, elevation was also measured by a total elevation station (electronic level system; Autolaser 300; David White Instruments), which is a theodolite with an electronic distance measurement device (EDM; Anastasiou and Brooks 2003; Warren and Niering 1993) in open water, in low marsh zone (marsh edge), at 20 m and at 40 m from open water along each transect.

Fig. 4.58. Low marsh zone of Transect 6 at south side of Graveline Bayou (6 April 2011).

Fig. 4.59. High marsh zone of Transect 7 at south side of Graveline Bayou (6 April 2011).

Fig. 4.60. High marsh zone of Transect 9 at west side of Terrebonne Bay (southeast to DeFelice Center; 9 June 2011).

Fig. 4.61. Low marsh zone of Transect 10 at west side of Terrebonne Bay (southwest to DeFelice Center; 9 June 2011).

Fig. 4.62. Low marsh zone of Transect 11 at east Terrebonne Bay (8 June 2011).

4.3.1.3 **Laboratory Analyses**

Sediment mean grain size and particle size distribution were analyzed by using standard methods at the USDA-ARS National Sedimentation Lab in Oxford, MS (HORRIBA LA-910 Particle Size Analyzer Dry Sample Analysis Method). Laboratory analyses of the soil samples included measurements of soil bulk density, of soil moisture (105°C for 24 hours) and of soil organic matter content by measuring the loss on ignition (LOI method; 400°C for 1 hour; Black 1965). The soil bulk density was measured by estimating the volume of the samples and measuring the loss of water in soil samples (60 °C for 48 hours; Heuscher et al. 2005; Center for Applied Research and Environmental Systems, CARES website 2010). The volume of void space in the soil sample is equal to the water mass in the fully saturated collected soil sample since one gm H2O is equal to one ml H2O according to the formula: bulk density (g/cm^3) = dry mass (g) / total volume (cm^3); total volume = void volume + solid volume; solid volume (cm^3) = dry mass / 2.65 (g/cm^3); void volume (ml) = wet mass- dry mass = water mass (g) because the exact volume of the sample is hard to measure in the laboratory. The solid particle density is assumed as 2.65 g/cm^3 (CARES website 2010).

Above- and belowground biomass, soil moisture, sediment bulk density and organic matter content were measured in the laboratory in the UM Biology Department in Oxford, MS. Aboveground vegetation and belowground rhizomes were sorted by species, washed and dried at 105°C for 24 hours (or longer) to measure above- and belowground biomass (Cronk and Fennessy 2001; Howes et al. 1986; Whigham and Simpson 1977); formula 1: biomass (g/m^2) = dry weight / quadrat area. Rhizome thickness and stem diameter were also measured with calipers in the laboratory. Measurements of stem diameter included the top (1 cm below top) and bottom of the stem (1 cm above roots and rhizomes). Different plant species were sorted in a 0.25 m^2 quadrat and then translated into standard units (one $meter^2$) by multiplying the number of stems in each 0.25 m^2 quadrat multiplied by four to determine plant density. The formulas for soil moisture and LOI are as follows (Black 1965); formula 2: soil moisture % = (1- dry soil weight / wet weight)×100; formula 3: LOI % = (dry weight – ash weight) / dry weight×100.

4.3.1.4 **Statistical Analyses**

Soil properties (organic matter content, moisture, sediment mean grain size, particle size distribution and sediment bulk density) and plant parameters (live and dead standing shoot heights, rhizome thickness, stem diameter and density) on five transects summarized by "low and high marsh zones" or "Graveline Bayou and Terrebonne Bay" (Graveline Bay sites: Transects 6 and 7; Terrebonne Bay sites: Transects 9, 10 and 11) were used to analyze significant relationships with plant above- and belowground biomass by least square linear regression analyses (Zar 1984) unless non-linear models can explain more of the variance in the dependent variables (based on a higher coefficient of determination, R^2).

An analysis of variance test (ANOVA; Microsoft Office Excel 2003) was used to test if there were any significant differences in soil properties and plant parameters including plant above- and belowground biomass between low and high marsh zones or between Graveline Bayou and Terrebonne Bay. A two-way ANOVA was also used to test if there were any significant differences in plant parameters in spring and summer in low and high marsh zones between Graveline Bayou and Terrebonne Bay categorized as different spatial and time variables. If

ANOVA tests report that a p value < 0.05, there is a significant difference in soil properties and plant parameters between two locations.

4.3.2 Comparosion of LA and MS Marshes Based on Phase II Data

4.3.2.1 Elevation and Zonation

The zonations of the five transects are shown in Fig. 4.63 and the elevation gradients are shown in Table 4.5. In Transect 6 of South Graveline Bayou (West coast), *Spartina alterniflora* was the dominant species in low marsh zones, and high marsh zones was dominated by *Spartina alterniflora* and *Juncus roemerianus*. In transect 7 of South Graveline Bayou (East coast), all the low, middle and high marsh zones were dominated by *Spartina alterniflora* and *Juncus roemerianus*. At Graveline Bayou, the marsh zone between low and middle marsh zones did not grow any plants because of vehicle use. In Transect 9 of Terrebonne Bay (East coast), both low and high marsh zones were dominated by *Spartina alterniflora*. In Transect 10 of Terrebonne Bay (West coast), *Spartina alterniflora* was the dominant species in both low and high marsh zones. Transects 9 and 10 were probably created when the DeFelice Center was built in 1979 because there was no previous record that showed Transects 9 and 10 existed. In Transect 11 of East Terrebonne Bay (East coast), all the low, middle and high marsh zones were dominated by *Spartina alterniflora*.

ANOVA tests showed that there was no significant difference in elevation gradients between low and high marsh zones (p= 0.9846 > 0.05), but the elevation gradients had a significant difference between MS and LA marshes (p= 0.03886 < 0.05; Table 4.5).

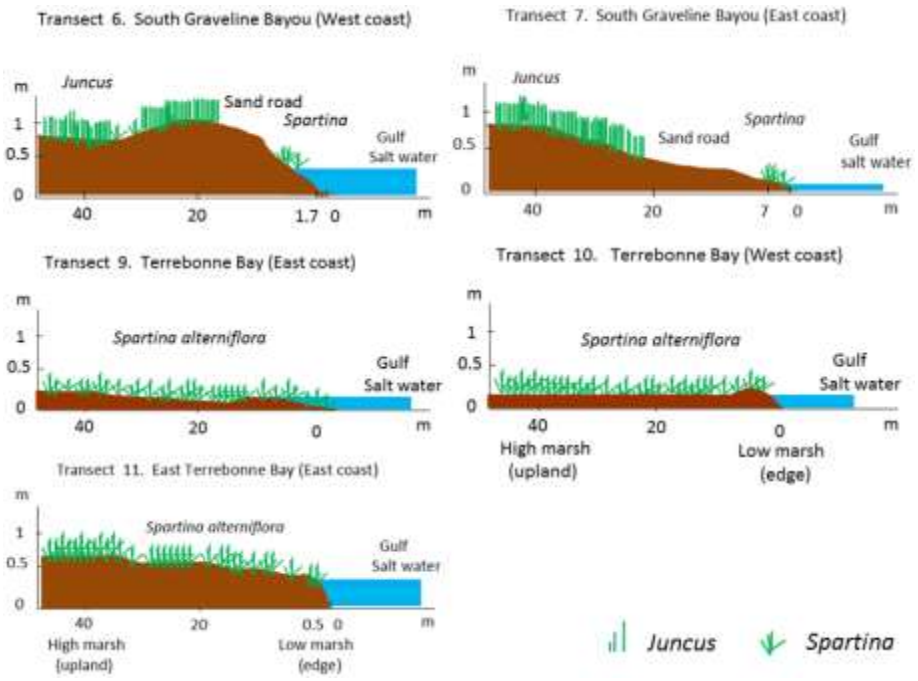

Fig. 4.63. Profile diagrams (bisect) which showed the zonation of salt marshes (Transects 6, 7, 9, 10, and 11) [elevation gradients: std.dev. =0.00283].

Table 4.5. Elevation gradients on five transects

Transect	Elevation (m)			
	Low marsh zones	Middle marsh zones	High marsh zones	Average
Tr.6	0.308	1.045	0.564	0.639
Tr.7	0.134	0.305	0.817	0.419
Tr.9	0.189	0.115	0.201	0.168
Tr.10	0.249	0.195	0.183	0.209
Tr.11	0.46	0.512	0.524	0.499
Average	0.268	0.434	0.458	

4.3.2.2 **Soil Properties**

Fig. 4.64 compares the soil properties between low and high marshes and between LA and MS marshes, and Table 4.6 shows the results of ANOVA tests. Tables 4.7–4.10 lists the average soil moisture, organic matter content, bulk density and sediment size in the five transects. It is found that there was a significant difference in the average soil moisture between low and high marsh zones ($p = 0.0428 < 0.05$) and between LA and MS marshes ($p = 1.04E-08$). The average soil organic matter content in LA marshes was significantly higher than that in MS marshes ($p = 0.00036 < 0.05$). There is no significant difference in soil bulk density between low and high marshes and between LA and MS marshes. The sediment mean grain size in LA marshes was significantly lower than that in MS marshes ($p = 0.000788 < 0.05$).

The soil sand, clay and silt percentages were compared for low and high marsh zones, LA and MS marshes, as shown in Fig. 4.65 and Tables 4.6 and 4.11. There was a significant difference in the soil silt percentage between low and high marsh zones ($p = 0.016 < 0.05$). In addition, there was a significant difference in the soil sand ($p = 0.00268 < 0.05$) and clay percentages ($p = 3.95E-04 < 0.05$) between LA and MS marshes.

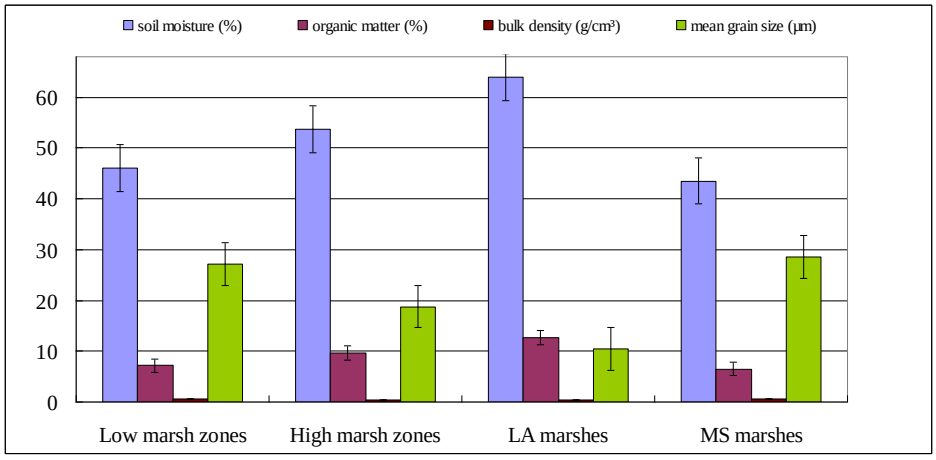

Fig. 4.64. Average soil moisture, organic matter, bulk density and mean grain size compared for low and high marsh zones, LA and MS marshes (±SE, n=30).

Table 4.6. ANOVA test results of significant difference in soil properties

Soil properties	Low vs. high marsh zones	LA vs. MS marshes
Moisture	Yes (p =0.0428 <0.05)	Yes (p =1.04E-08 <0.05)
Organic matter	No (p =0.122 >0.05)	Yes (p =3.6E-04 <0.05)
Bulk density	No (p =0.323 >0.05)	No (p =0.455 >0.05)
Mean grain size	No (p =0.957 >0.05)	Yes (p =7.88E-04<0.05)
Clay percentage	No (p =0.209 >0.05)	Yes (p =3.95E-04<0.05)
Sand percentage	No (p =0.296 >0.05)	Yes (p =2.68E-03<0.05)
Silt percentage	Yes (p =0.016 <0.05)	No (p =0.349 >0.05)

Table 4.7. Average soil moisture in the low and high marsh zones in five transects

Transects	Low marsh zones (%)		High marsh zones (%)	
	Mean	Std.dev.	Mean	Std.dev.
Tr. 6	33.51	12.02	40.38	5.36
Tr. 7	45.72	6.55	54.48	12.27
Tr. 9	54.38	2.79	61.25	6.28
Tr. 10	64.25	2.79	74.17	1.34
Tr. 11	62.75	5.97	67.09	1.08

Table 4.8. Average soil organic matter in the low and high marsh zones in five transects

Transects	Low marsh zones (%)		High marsh zones (%)	
	Mean	Std.dev.	Mean	Std.dev.
Tr. 6	4.87	4.01	5.57	1.54
Tr. 7	5.25	2.35	10.39	6.67
Tr. 9	6.02	1.28	9.03	3.20
Tr. 10	9.03	1.25	19.31	1.68
Tr. 11	20.39	12.50	11.86	1.42

Table 4.9. Average soil bulk density in the low and high marsh zones in five transects

Transects	Low marsh zones (g/cm^3)		High marsh zones (g/cm^3)	
	Mean	Std.dev.	Mean	Std.dev.
Tr. 6	0.27	0.001	0.31	0.02
Tr. 7	0.83	0.16	0.68	0.20
Tr. 9	0.55	0.03	0.48	0.10
Tr. 10	0.39	0.016	0.29	0.02
Tr. 11	0.52	0.06	0.48	0.03

Table 4.10. Soil mean grain size in the low and high marsh zones in five transects

Transects	Low marsh zones (μm)		High marsh zones (μm)	
	Mean	Std.dev.	Mean	Std.dev.
Tr. 6	35.48	28.34	27.13	8.45
Tr. 7	35.08	25.24	16.55	1.27
Tr. 9	8.43	1.21	9.44	0.47
Tr. 10	7.40	3.76	13.19	1.89
Tr. 11	11.05	14.02	13.40	1.55

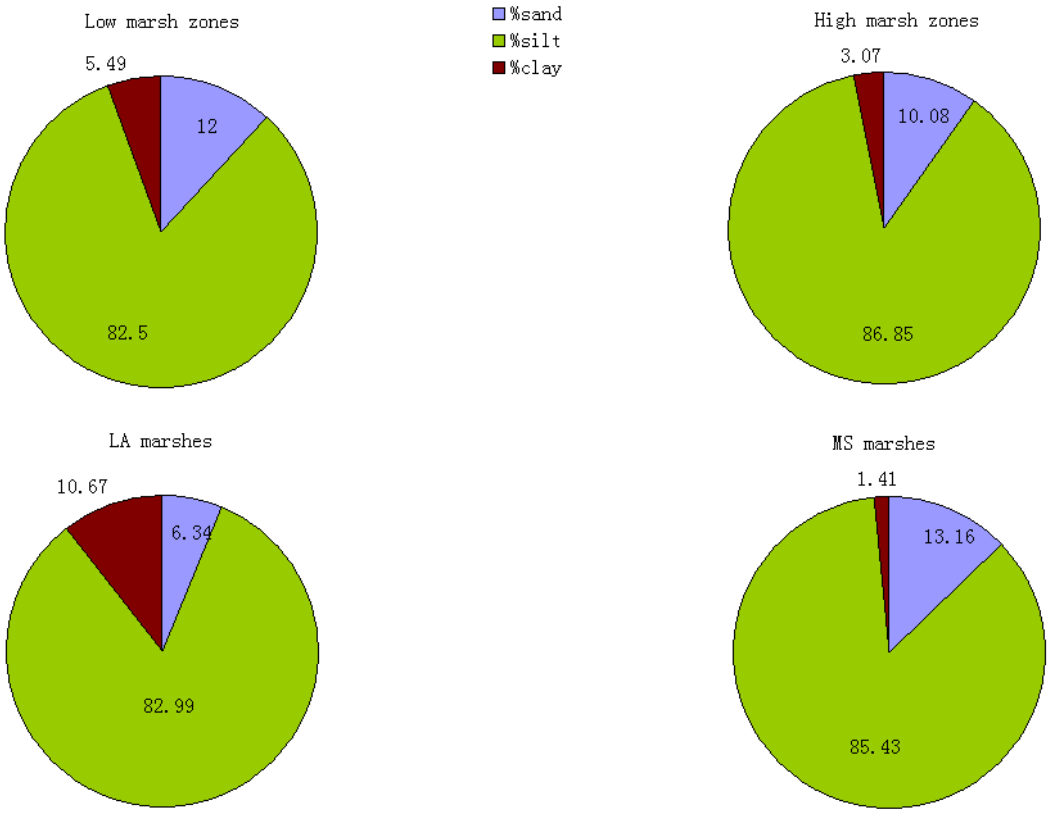

Fig. 4.65. Soil sand, clay and silt percentages compared for low and high marsh zones, LA and MS marshes.

Table 4.11. Soil sand, clay and silt percentages in low and high marsh zones in five transects

Transects	Low marsh zones					
	% sand	Std.dev.	% silt	Std.dev.	% clay	Std.dev.
Tr. 6	14.65	9.80	84.26	9.10	1.09	1.33
Tr. 7	15.24	8.26	84.18	7.66	0.58	0.16
Tr. 9	5.06	2.15	75.15	5.47	19.79	7.26
Tr. 10	5.59	0.45	83.03	3.09	11.38	2.64
Tr. 11	4.57	4.48	86.31	3.37	9.12	1.21
	High marsh zones					
	% sand	Std.dev.	% silt	Std.dev.	% clay	Std.dev.
Tr. 6	13.07	3.17	86.04	2.69	0.89	1.12
Tr. 7	9.67	0.93	87.26	2.29	3.07	1.85
Tr. 9	9.51	4.23	88.59	3.50	1.90	0.97
Tr. 10	6.78	11.74	74.60	14.24	18.63	21.06
Tr. 11	6.54	1.67	90.26	1.43	3.21	0.73

4.3.2.3 **Plant Parameters**

Plant coverage

As in other marsh studies (Holland and Burk 1990), plant percent cover is used here to represent plant density. In Transect 6, the low marsh zone was dominated by *Spartina alterniflora* and the high marsh zone was dominated by *Juncus roemerianus*. The low marsh zone had an average plant cover of 40% *Spartina alterniflora* and 60% open space, whereas the high marsh zone was on average occupied by 85% *Juncus roemerianus* and 15% open space. In Transect 7, the low marsh zone had an average plant cover of 41% *Spartina alterniflora* and 59% open space, and the high marsh zone was on average occupied by 43% *Spartina alterniflora*, 43% *Juncus roemerianus* and 14% open space.

Transects 9, 10 and 11 were dominated by *Spartina alterniflora* with open space. In Transect 9, the low and high marsh zones were on average occupied by 80% and 88% *Spartina alterniflora*, respectively. For Transect 10, the low and high marsh zones had average plant cover of 61% and 72 % *Spartina alterniflora*, respectively. For Transect 11, the low and high marsh zones were on average occupied by 22% and 88% *Spartina alterniflora*, respectively.

The average plant percent cover was compared for low and high marsh zones, and LA and MS marshes. There was no significant difference in the average plant percent cover between low and high marsh zones or between LA and MS marshes (Fig. 4.66; Table 4.12).

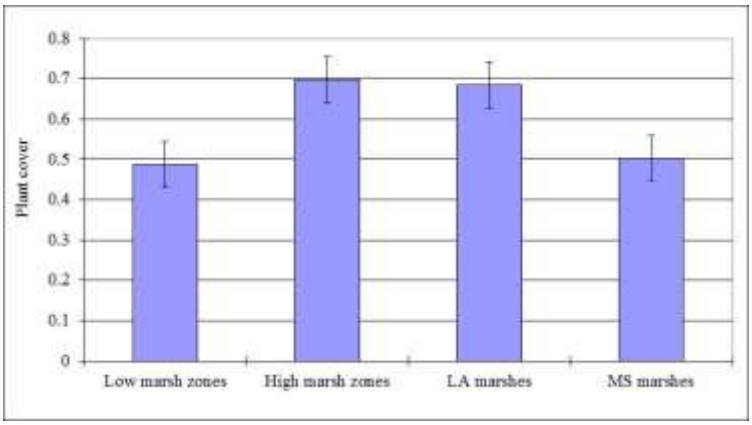

Fig. 4.66. Average plant cover (space occupied) compared for low and high marsh zones, LA and MS marshes (±SE, n=56).

Table 4.12. ANOVA test results of significant difference in plant parameters

Plant parameters	Low vs. high marsh zones	LA vs. MS marshes
Percent cover	No (p =0.198 >0.05)	No (p =0.285 >0.05)
Height (live *Spartina*)	Yes (p =4.8E-05 <0.05)	Yes (p =3.65E-13 <0.05)
Height (dead *Spartina*)	No (p =0.0525 >0.05)	Yes (p =2.37E-11 <0.05)
Rhizome thickness	Yes (p =1.46E-03 <0.05)	Yes (p =3.9E-03 <0.05)
Stem diameter (top)	No (p =0.124 >0.05)	No (p =0.194 >0.05)
Stem diameter (bottom)	No (p =0.061 >0.05)	Yes (p =4.36E-03 <0.05)
Stem density	Yes (p =0.024 <0.05)	No (p =0.287 >0.05)
Aboveground biomass	No (p =0.234 >0.05)	No (p =0.385 >0.05)
Belowground biomass	No (p =0.683 >0.05)	No (p =0.491 >0.05)

Vegetation heights

The results on five transects combined into low and high marsh zones showed that in low marsh zones the standing shoot height of live *Spartina alterniflora* ranged from 0.11 m to 1.98 m with the average value of 0.84 m, whereas that of dead *Spartina alterniflora* ranged from 0.25 m to 1.72 m with the average value of 1.1 m. In high marsh zones, the live *Spartina alterniflora* had standing shoot heights ranging from 0.41 m to 1.83 m with the average value of 1.17 m, and the dead *Spartina alterniflora* had standing shoot heights from 0.43 m to 2.38 m with the average of 1.24 m. *Juncus roemerianus*, which was in high marsh zones, had live standing shoot heights from 0.9 m to 1.72 m with the average value of 1.36 m, and dead standing shoot heights from 0.82 m to 1.79 m with the average value of 1.38 m.

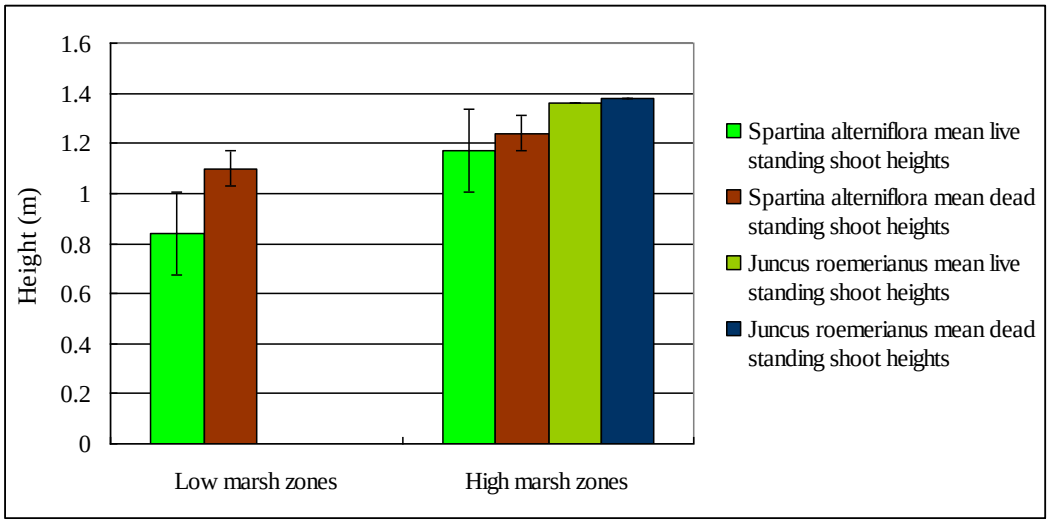

Fig. 4.67. *Spartina alterniflora* and *Juncus roemerianus* mean standing shoot heights compared for low and high marsh zones (±SE, n=120).

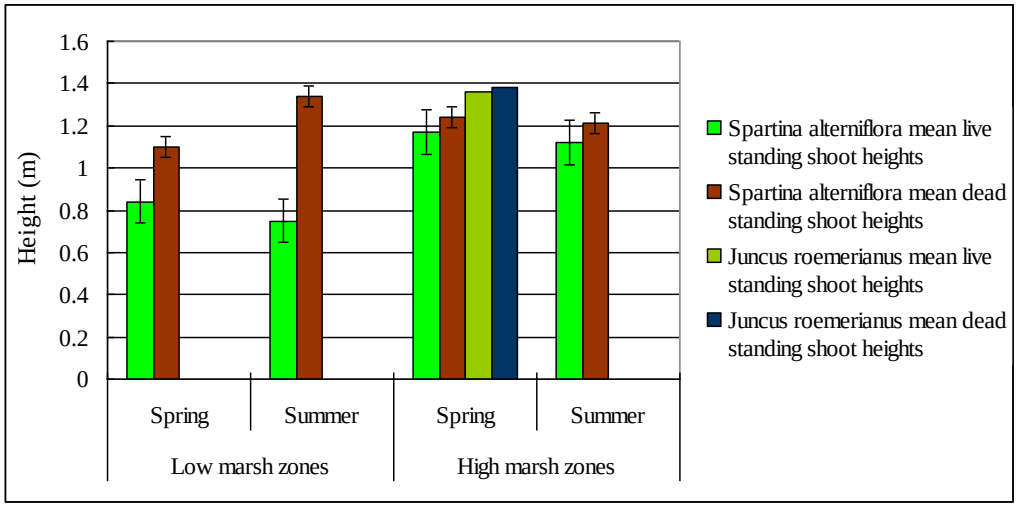

Fig. 4.68. Comparison of mean live and dead standing shoot heights of *Spartina alterniflora* of low and high marsh zones on five transects in spring and summer 2011 (±SE, n=120).

ANOVA tests showed that average live standing shoot heights of *Spartina alterniflora* in low marsh zones were significantly lower than those in high marsh zones (p=4.8E-05 E-07 < 0.05; Fig. 4.67; Table 4.12). Fig. 4.68 shows that there was no significant difference in live or dead *Spartina alterniflora* between spring and summer. Fig. 4.69 shows that the average live (p=3.65 E-13 < 0.05) and dead standing shoot heights of *Spartina alterniflora* (p=2.37E -11 < 0.05; Table 4.12) in LA marshes were significantly higher than those in MS marshes. Fig. 4.70 shows that average live standing shoot heights of *Spartina alterniflora* in MS marshes in spring were significantly higher than those in MS marshes in summer (p=0.0039 < 0.05).

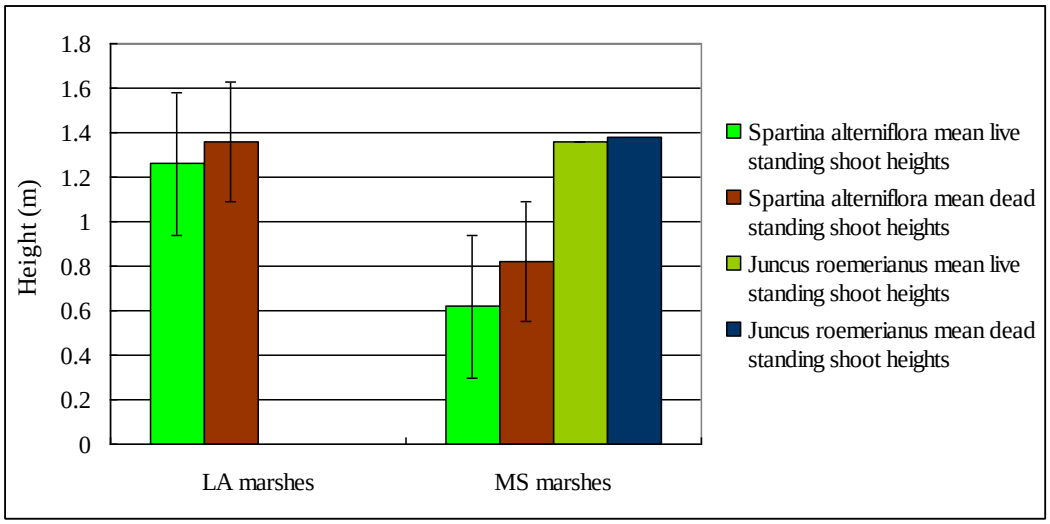

Fig. 4.69. *Spartina alterniflora* and *Juncus roemerianus* mean standing shoot heights compared for LA and MS marshes (±SE, n=120).

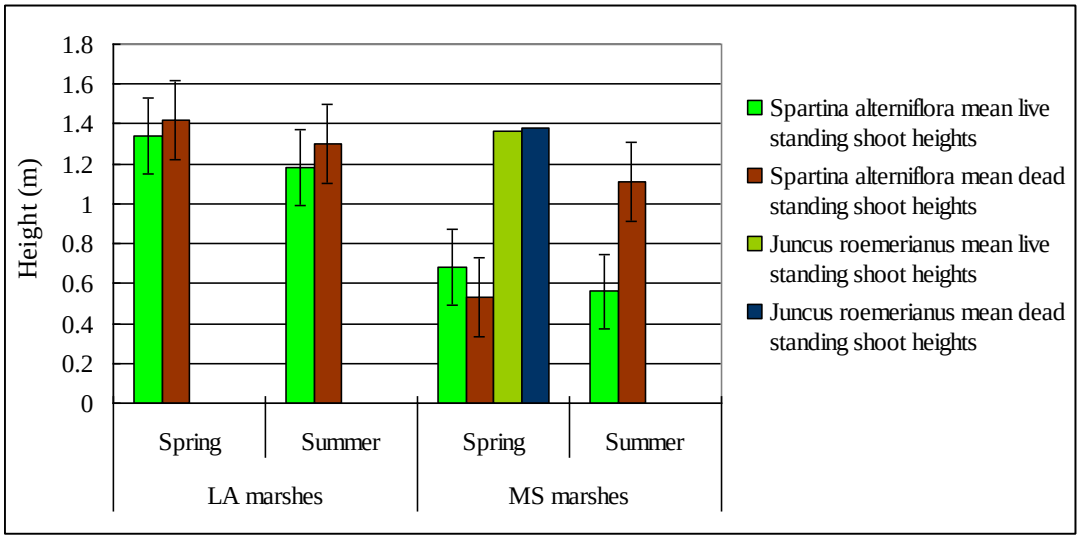

Fig. 4.70. Comparison of mean live and dead standing shoot heights of *Spartina alterniflora* of LA and MS marshes in spring and summer 2011 (±SE, n=120).

Rhizome thickness

Fig. 4.71 shows that mean rhizome thickness of *Spartina alterniflora* in low marsh zones differed significantly from those in high marsh zones (p= 0.0015< 0.05; Table 4.12), and mean rhizome of *Spartina alterniflora* in LA marshes was significantly thicker than that in MS marshes (p= 0.00.9 < 0.05; Table 4.12).

Fig. 4.72 and Table 4.12 show that there was no significant difference in the mean rhizome thickness of *Spartina alterniflora* in low (p= 0.512 > 0.05) or high marsh zones (p= 0.456 > 0.05) between spring and summer. Mean rhizome thickness of *Spartina alterniflora* in LA marshes in spring did not differ significantly from summer (p= 0.447 > 0.05), but there was a significant difference in the mean rhizome thickness of *Spartina alterniflora* in MS marshes between spring and summer (p= 0.0047 < 0.05).

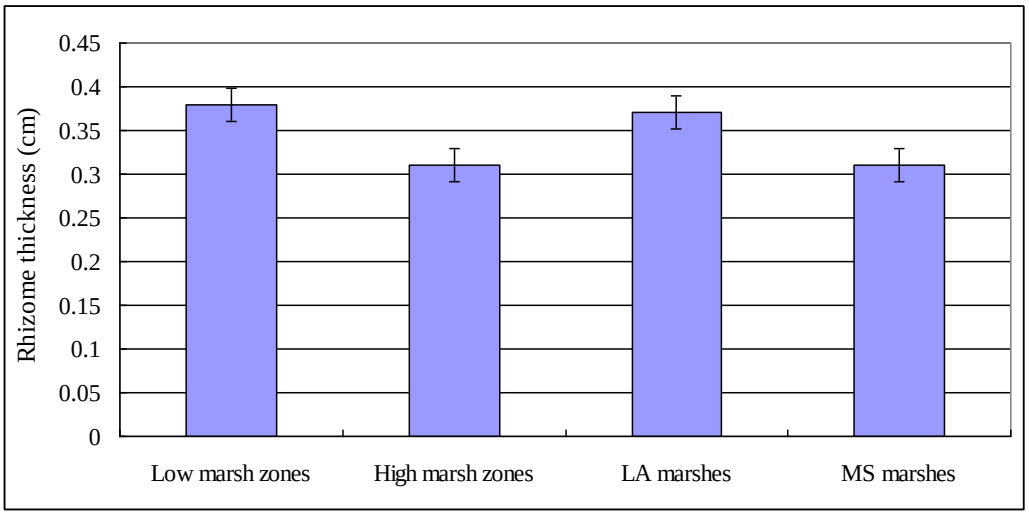

Fig. 4.71. Mean rhizome thickness of *Spartina alterniflora* compared for low and high marsh zones, LA and MS marshes (±SE, n=102).

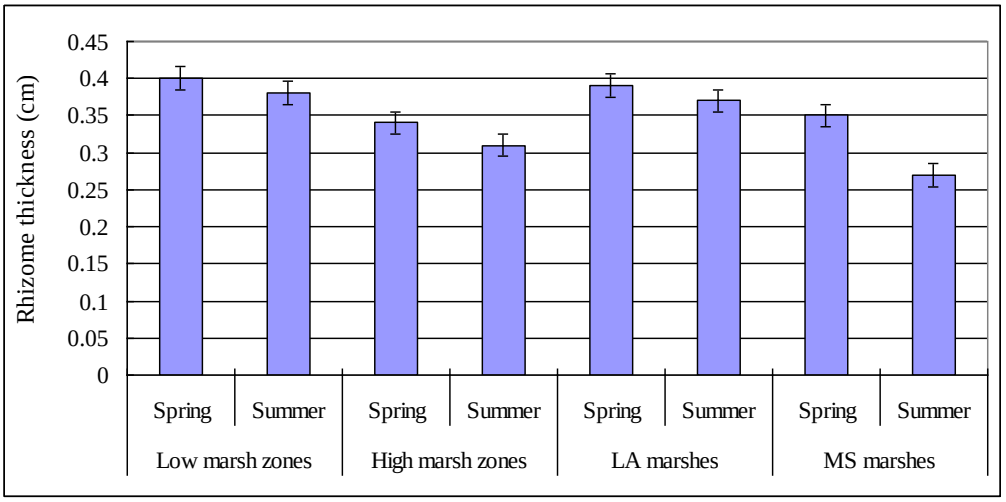

Fig. 4.72. *Spartina alterniflora* mean rhizome thickness compared for low and high marsh zones, LA and MS marshes in spring and summer 2011 (±SE, n=102).

Stem density and stem diameter

Fig. 4.73 shows that average plant stem density in low marsh zones was significantly lower than that in high marsh zones (p=0.024 < 0.05; Table 4.12). Fig. 4.74 shows that there was no significant difference in the average plant stem density in low (p= 0.089 > 0.05) and high marsh zones (p= 0.1 >0.05) between spring and summer. There was no significant difference in the average plant stem density in MS marshes between spring and summer (p= 0.163 >0.05), but the average plant stem density in LA marshes in spring was significantly higher than that in summer (p= 0.03 <0.05).

Fig. 4.75 and Table 4.12 show that there was no significant difference in the mean top stem diameters (1 cm below the top) of *Spartina alterniflora* between low and high marsh zones (p=0.124 > 0.05) or between LA and MS marshes (p=0.194 > 0.05). Fig. 4.76 shows that there was no significant difference in the mean bottom stem diameters (1 cm above the root and rhizome) of *Spartina alterniflora* between low and high marsh zones (p=0.061 > 0.05), but the mean bottom stem diameters of *Spartina alterniflora* in LA marshes were significantly higher than those in MS marshes (p= 4.36E-05 < 0.05). There was no significant difference in the mean top stem diameters in high marsh zones (p= 0.723 >0.05) between spring and summer, but in low marsh zones, the mean top stem diameters in spring was significantly lower than those in summer (p= 0.02 < 0.05). There was no significant difference in the mean top stem diameters in LA (p= 0.069 > 0.05) or MS marshes (p= 0.691 >0.05) between spring and summer. However, there was a significant difference in the mean bottom stem diameters in low marsh zones between spring and summer (Fig. 4.77). In high marsh zones, there was no significant difference in the mean bottom stem diameters between spring and summer (p= 0.75 > 0.05). Fig. 4.77 shows that there was no significant difference in the mean bottom stem diameters in MS marshes (p= 0.518 >0.05) between spring and summer, but there was a significant difference in the mean bottom stem diameters in LA marshes between spring and summer (p= 0.0338 < 0.05).

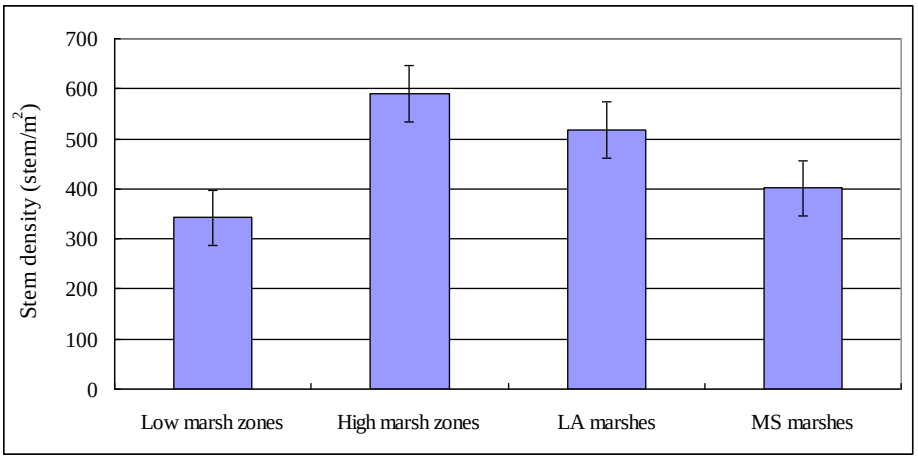

Fig. 4.73. Average plant density compared for low and high marsh zones, LA and MS marshes (±SE, n=40).

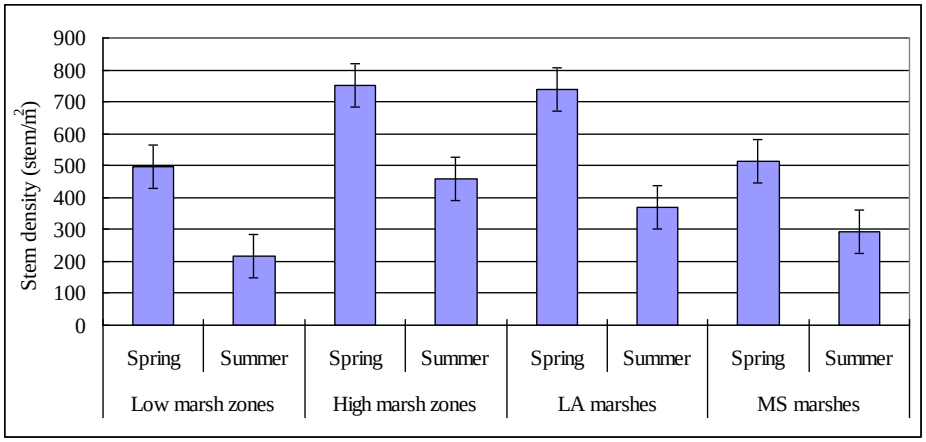

Fig. 4.74. Average plant density compared for low and high marsh zones, LA and MS marshes in spring and summer 2011 (±SE, n=40).

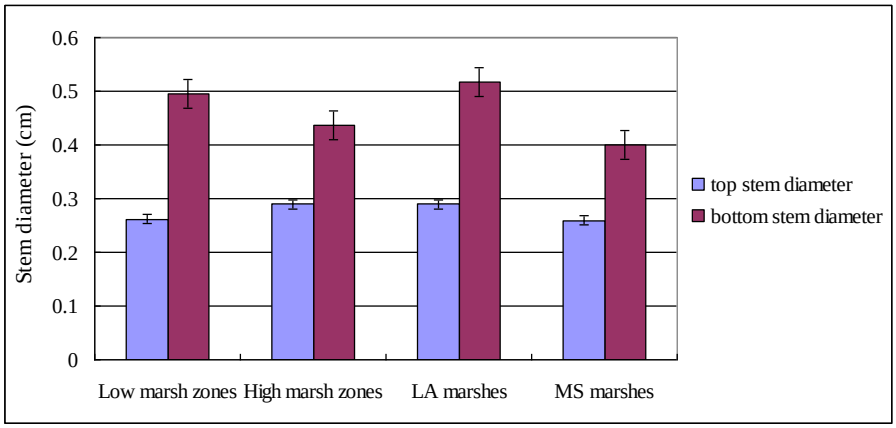

Fig. 4.75. Average top and bottom stem diameter compared for low and high marsh zones, LA and MS marshes (±SE, n=40).

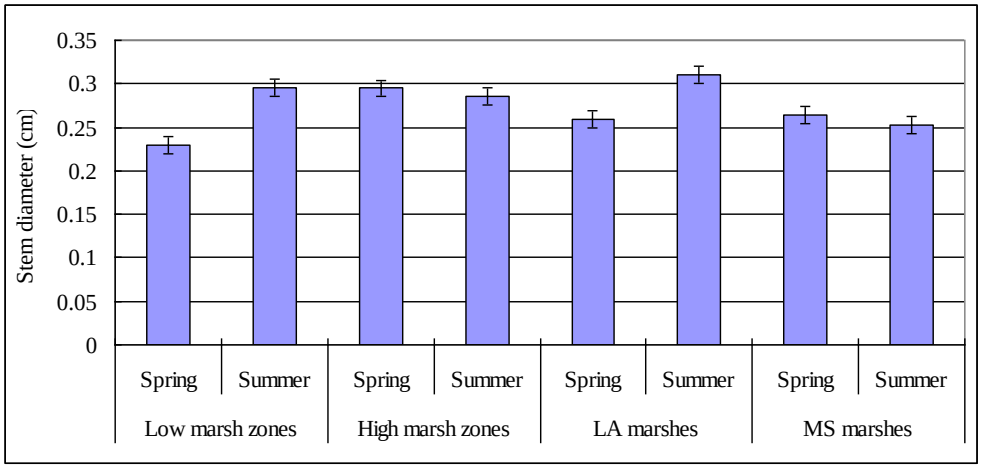

Fig. 4.76. Average top stem diameter compared for low and high marsh zones, LA and MS marshes in spring and summer 2011 (±SE, n=40).

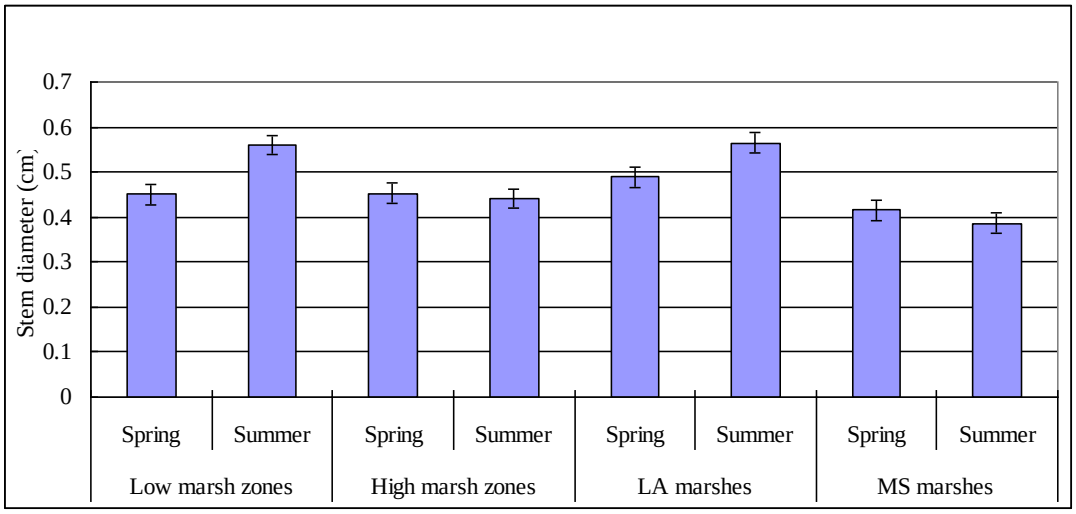

Fig. 4.77. Average bottom stem diameter compared for low and high marsh zones, LA and MS marshes in spring and summer 2011 (±SE, n=40).

Above- and belowground biomass

ANOVA showed that there was no significant difference in the aboveground biomass between low and high marsh zones ($p = 0.234 > 0.05$) or between LA and MS marshes ($p = 0.385 > 0.05$; Fig. 4.78; Table 4.12). Fig. 4.79 shows that there was a significant difference in aboveground biomass in both low ($p = 0.0067 < 0.05$) and high marsh zones ($p = 0.032 < 0.05$) between spring and summer. However, there was no significant difference in aboveground biomass in LA marshes between spring and summer ($p = 0.1 > 0.05$). In MS marshes, aboveground biomass in spring was significantly lower than that in summer ($p = 0.011 < 0.05$).

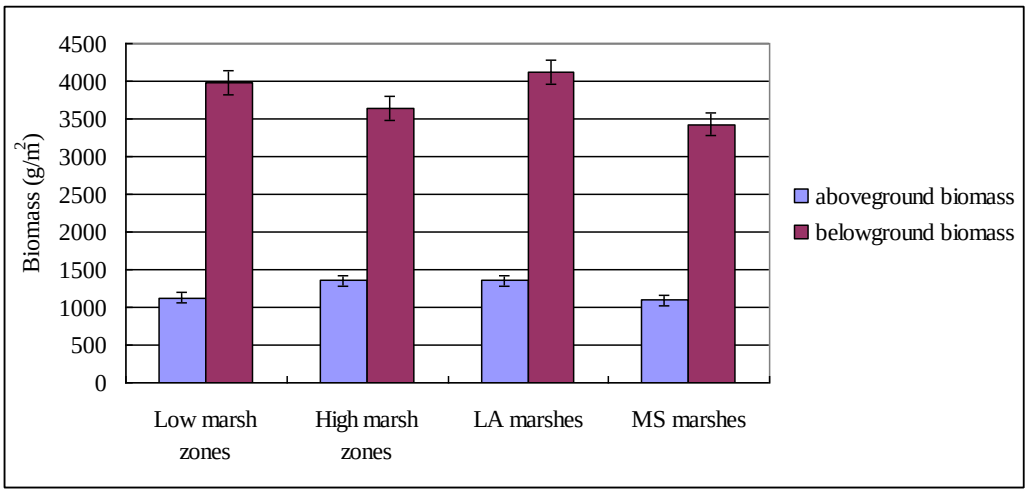

Fig. 4.78. Average plant above- and belowground biomass compared for low and high marsh zones, LA and MS marshes (±SE, n=48).

There was no significant difference in belowground biomass between low and high marsh zones ($p = 0.683 > 0.05$) or between LA and MS marshes ($p = 0.491 > 0.05$; Fig. 4.78; Table 4.12).

Compared for low and high marsh zones on five transects in spring and summer, the results showed that there was a significant difference in belowground biomass in both low ($p = 0.0045 < 0.05$) and high marsh zones ($p = 0.0013 < 0.05$; Fig. 4.79) between spring and summer. In addition, there was also a significant difference in belowground biomass in both LA ($p = 0.0327 < 0.05$) and MS marshes ($p = 6.21E\text{-}04 < 0.05$; Fig. 4.79) between spring and summer.

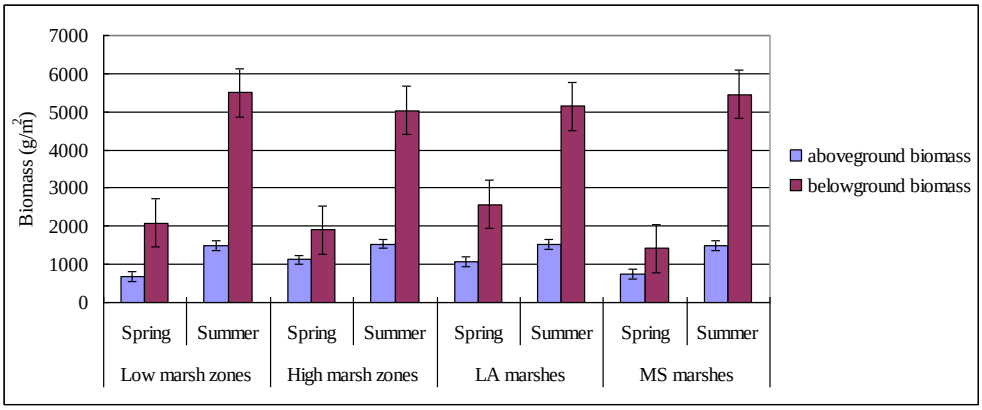

Fig. 4.79. Average plant above- and belowground biomass compared for low and high marsh zones, LA and MS marshes in spring and summer 2011 (±SE, n=48).

4.3.2.4 Regression Relationship

Linear regression analyses were run when data on five transects were combined into low and high marsh zones or LA and MS marshes, the plant above- and belowground biomass as the dependent variables and environmental variables including soil properties, plant parameters and elevation data as the independent variables categorized by low and high marsh zones or LA and MS marshes.

Linear regression analyses based on data on the five transects were combined into low and high marsh zones and showed that plant aboveground biomass in low marsh zones was positively related to *Spartina alterniflora* dead standing shoot heights ($R^2 = 0.30$, $p < 0.05$; Fig. 4.80). Thus, high *Spartina alterniflora* dead standing shoots in low marsh zones indicated high plant aboveground biomass in the last growing season.

Linear regression analyses using data on the five transects were combined into LA and MS marshes and showed that plant belowground biomass in LA marshes was positively related to soil silt percentage ($R^2 = 0.27$, $p < 0.05$; Fig. 4.81). Plant belowground biomass in LA marshes increased as soil silt percentage increased.

In addition, linear regression analyses showed that plant aboveground biomass in MS marshes was positively related to *Spartina alterniflora* live ($R^2 = 0.52$, $p < 0.05$) and dead standing shoot heights ($R^2 = 0.47$, $p < 0.05$; Fig. 4.82). The aboveground biomass in MS marshes increased as *Spartina alterniflora* live and dead standing shoot heights increased. The plant belowground biomass in MS marshes was also positively related to *Spartina alterniflora* live standing shoot heights ($R^2 = 0.55$, $p < 0.05$; Fig. 4.82). Thus, plant belowground biomass in MS marshes increased as *Spartina alterniflora* live standing shoot heights increased.

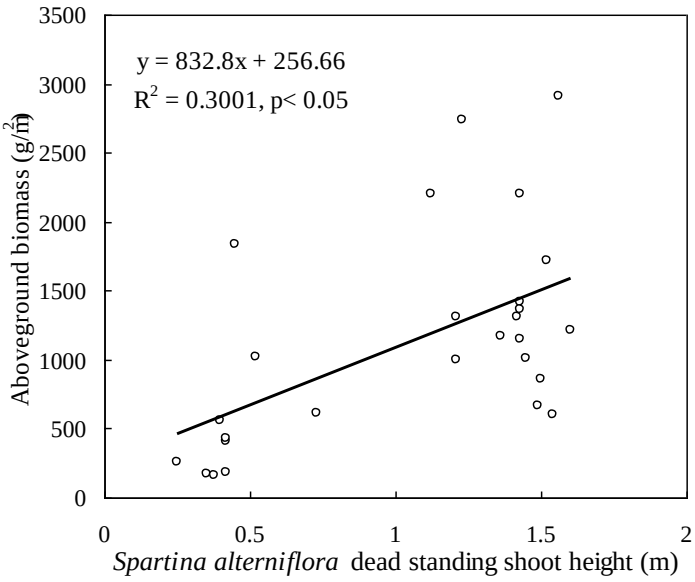

Fig. 4.80. Linear regression of plant aboveground biomass in low marsh against *Spartina alterniflora* dead standing shoot heights (n=27).

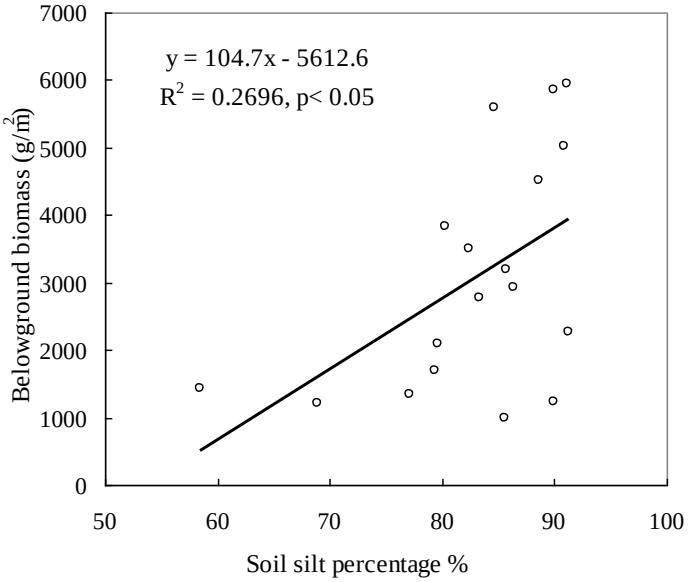

Fig. 4.81. Linear regression of plant belowground biomass in LA marshes against soil silt percentage (n=27).

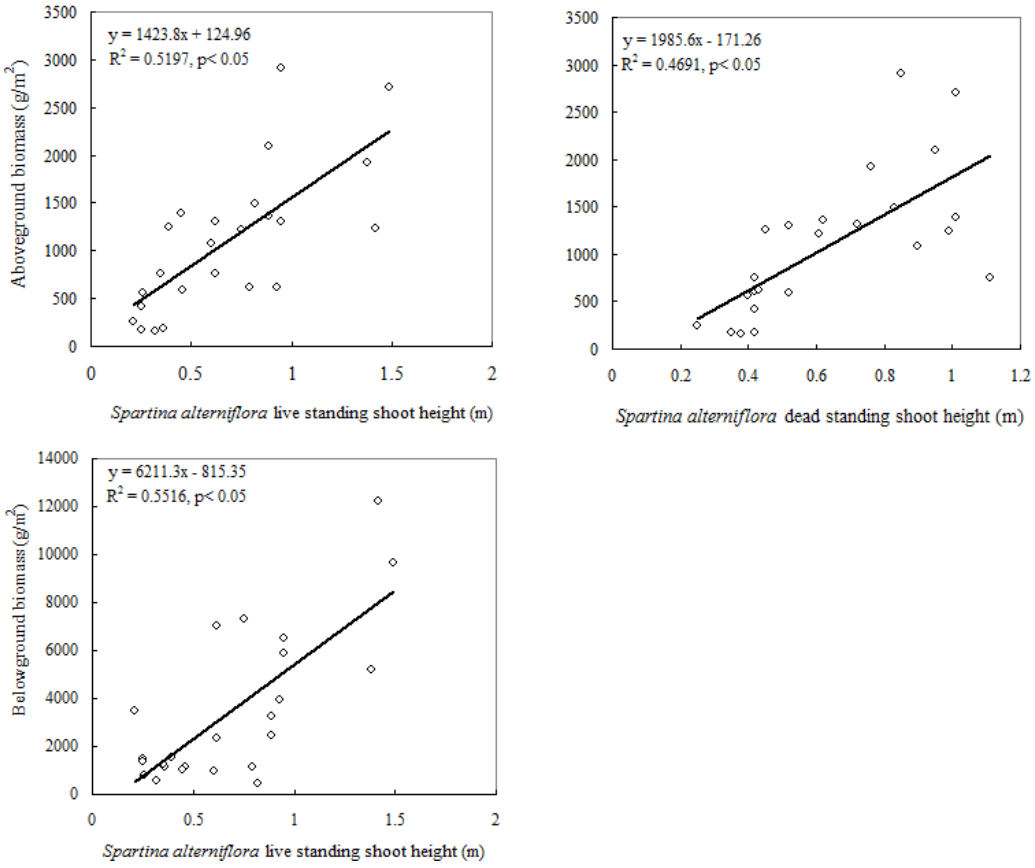

Fig. 4.82. Linear regression of plant above- and belowground biomass in MS marshes against *Spartina alterniflora* live and dead standing shoot heights (n=27).

4.3.2.5 Discussion

Comparison of LA and MS marshes

Although both Graveline Bayou and LUMCON are protected by the respective state (Mississippi and Louisiana) Department of Marine Resources (Figs. 4.53-4.60; GEMS and LUMCON websites), these two sampling locations along the Gulf Coast were inundated by several hurricanes from 2004 to 2010. Along the Gulf of Mexico, two barrier islands, Horn and Petit Bois Islands, are located south of Graveline Bayou. Terrebonne Bay is also located north of several barrier islands, called the Isles Dernieres and the Timbalier Islands. To a great extent, both Graveline Bayou and Terrebonne Bay were affected by hurricanes due to the similarity of the locations (NOAA website). Although there was no statistically significant difference in wave effects between Graveline Bayou and Terrebonne Bay, there was a significant difference in the elevation gradients between LA and MS marsh sites (Fig. 4.63). The profile diagrams of these five transects (Fig. 4.63) showed that a natural levee existed on Transect 6 because the elevation in the middle marsh zone on Transect 6 was significantly higher than that in high marsh zones. A natural levee is probably built by inputs such as waves and storm surges because sediment in coastal areas tends to be redistributed by hurricane and storm surges (Keddy 2010; Redfield 1972).

The soil percentage of organic matter content, particle size distribution, moisture, mean grain size, bulk density, nitrogen and phosphorus are all important factors to consider when comparing erosion rates among sites (Brewer and Grace 1990; Feagin et al. 2009; Howes et al. 1986; Levine et al. 1998; Roberts 2009). The results (Figs. 4.64 and 4.65; Table 4.6) showed that soil moisture, organic matter content, mean grain size, soil clay and sand percentages in LA marshes differed significantly from those in MS marshes. Although Transects 9 and 10 were probably created when the DeFelice Center was built in 1979, there was no significant difference in the soil properties between Transect 11 and Transects 9 and 10. In LA marshes, soil moisture and organic matter were significantly higher than those in MS marshes (Fig. 4.64; Table 4.6). Hurricane and storm surges may have positive effects on accumulation of organic matter through litter deposition or scouring and redeposition of organic marsh substrates in coastal marshes (McKee and Cherry 2009; Guntenspergen et al. 1995).

Sediment mean grain size in MS marshes was significantly higher than that in LA marshes (Fig. 4.64; Table 4.6). Linear regression results showed that plant belowground biomass in LA marshes was positively related to soil silt percentage (Fig. 4.81). Thus, in LA marshes, plant belowground biomass increased as soil silt percentage increased. In addition, soil in LA marshes contained significantly higher clay and lower sand percentages (Fig. 4.65; Table 4.6), which is beneficial for plant growth because small-sized grains can hold more nutrients.

Rhizome thickness of *Spartina alterniflora* in LA marshes was significantly higher than that in MS marshes (Fig. 4.71; Table 4.12). In addition, the bottom stem diameter of *Spartina alterniflora* in LA marshes was also significantly higher than that in MS marshes (Fig. 4.73; Table 4.12), which indicated that thick rhizome systems and high bottom stem diameter could help coastal vegetation withstand waves of storm surges and hurricanes. Both live and dead *Spartina alterniflora* standing shoot heights in LA marshes were higher than those in MS marshes (Fig. 4.69; Table 4.12). Although taller plants could avoid shade and therefore would be expected to provide more energy for growth, there was no significant difference in plant above- and belowground production between LA and MS marshes (Fig. 4.78; Table 4.12). Linear regression results showed that plant aboveground biomass was positively related to both live and dead *Spartina alterniflora* standing shoot heights (Fig. 4.82) in MS marshes, which suggested that *Spartina alterniflora* aboveground production increased as both live and dead *Spartina alterniflora* standing shoot heights. Moreover, plant belowground biomass was also positively related to live *Spartina alterniflora* standing shoot heights in MS marshes (Fig. 4.82). Thus, *Spartina alterniflora* belowground production increased as live standing shoot heights increased.

Changes in production over the growing season

Although there was no significant difference in both live and dead *Spartina alterniflora* in low and high marsh zones between spring and summer 2011 (Fig. 4.68), live *Spartina alterniflora* standing shoot heights in MS marshes in spring 2011 were significantly higher than those in summer 2011 (Fig. 4.70). In MS marshes, rhizome thickness of *Spartina alterniflora* in spring 2011 was significantly higher than that in summer 2011 (Fig. 4.72). However, there was no significant difference in *Spartina alterniflora* rhizome thickness in both low and high marsh zones between spring and summer 2011 (Fig. 4.72). In both 2010 and 2011, the rhizome thickness of *Spartina alterniflora* was significantly higher in spring than summer. However, in spring 2010, the standing shoot heights of both live and dead *Spartina alterniflora* were significantly lower than in summer 2011. In addition, stem density of *Spartina alterniflora* in LA marshes in spring was significantly higher than that in summer (Fig. 4.64). But top stem diameter of *Spartina alterniflora* in low marsh zones in spring was significantly lower than that in summer (Fig. 4.76). Bottom

stem diameter of *Spartina alterniflora* in low marsh zones in spring was significantly lower than that in summer (Fig. 4.77). Moreover, in LA marshes, bottom stem diameter of *Spartina alterniflora* in spring was significantly lower than that in summer (Fig. 4.77).

Therefore, plant aboveground biomass in low and high marsh zones in spring was significantly lower than that in summer (Fig. 4.79), which suggested that *Spartina alterniflora* produced higher top and bottom stem diameter when plant aboveground production was high. In addition, in MS marshes, plant aboveground biomass in spring was significantly lower than that in summer (Fig. 4.79) when photosynthesis is increasing from spring to summer. When comparing low marsh zones, high marsh zones, LA and MS marshes in spring and summer, results showed that plant belowground biomass in low marsh zones, high marsh zones, LA and MS marshes was significantly lower in spring than summer (Fig. 4.79), as carbohydrate reserves are utilized in spring and renewed in summer. Results of this present study showed that *Spartina alterniflora* tended to have high above- and belowground production in summer in coastal marshes (Fig. 4.79). Although *Spartina alterniflora* is peaking in summer (Valiela et al. 1975), marsh edges that are more likely inundated by storm waves may provide vegetation with higher nutrients for primary above- and belowground production in summer since low marsh zones have high organic matter content due to the nutrient loads from wave transportation (Cronk and Fennessy 2001; Keddy 2010; Odum et al. 1995). On the other hand, high belowground production helps vegetation to survive along the marsh edge during hurricane events by holding sediment with roots and rhizomes (Keddy 2010; Redfield 1972).

Eleuterius (1972, 1976 and 1990) and De La Cruz (1973) found that aboveground biomass of a pure stand of *Spartina alterniflora* marsh in the Bay Estuary, LA ranged from 445 to 2883 g/m^2 (Table 2.1 in Phase I report, Wu et al. 2011) and Darby and Turner (2008) found that belowground biomass of a *Spartina alterniflora* marsh located about 0.5 km west of LUMCON in Cocodrie, LA ranged from 370 to 603 g/m^2 with the peak biomass occurring in April (Table 2.2 in Phase I report, Wu et al. 2011). Results of this present study (Fig. 4.78 and 4.27) showed that the plant aboveground biomass in Terrebonne Bay, LA did not differ significantly from the results De La Cruz (1973) found in Bay Estuary marshes. However, the results of this present study (Figs. 4.78 and 4.79) showed that the plant belowground biomass in Terrebonne Bay, LA was significantly higher than the results Darby and Turner (2008) found in Cocodrie, LA possibly because of the higher volume of freshwater moving through the sites in 2011 (LUMCON Website).

Most of hurricanes along the MS and LA Gulf Coast during 2004 to 2010 occurred in late summer and fall (see Phase I report). If this is typical, vegetation may have developed adaptations to increase primary production to survive during storm and hurricane events. Where the natural pulses such as hurricanes, storm surges and flooding are moderate, primary production is highest. In general, net production in most types of wetlands increases with increasing pulse amplitude up to an optimum point beyond which too many pulses reduce production (Odum et al. 1995). On the other hand, increased water inflows to coastal areas can carry additional nutrients and facilitate the exchange of dissolved elements (e.g., oxygen, carbon, phosphorus and nitrogen) by decreasing thickness of the boundary layer at the plant surface, thus enhancing primary production, especially when hydrologic inputs are moderately pulsing (Cronk and Fennessy 2001). Therefore, coastal vegetation in marsh edges can survive during severe hurricanes and storm surges due to high belowground production even though hurricanes and storm surges have a direct negative effect on vegetation standing shoot heights and stem density.

4.3.2.6 Summary

The soil property data demonstrated that in LA marshes, soil moisture, organic matter content, and soil clay percentage were significantly higher than those in MS marshes. However, sediment mean grain size and soil sand percentage in LA marshes were significantly lower than those in MS marshes. On the other hand, there was no significant difference in soil bulk density and silt percentage between LA and MS marshes.

The plant characteristic data showed that in LA marshes, both live and dead *Spartina alterniflora* standing shoot heights were significantly higher than those in MS marshes. *Spartina alterniflora* in LA marshes also had significantly higher rhizome thickness and bottom stem diameter than those in MS marshes. However, there was no significant difference in the plant stem density, percent cover, top stem diameter, above- and belowground production between LA and MS marshes.

Comparing above- and belowground biomass in low and high marsh zones for spring and summer, it was shown that above- and belowground biomass of coastal vegetation was significantly higher in summer than in spring in both low and high marsh zones.

The important findings of this study were that there was significant difference in soil characteristics and plant parameters between LA and MS marshes in different seasons. In southeastern temperate zones, the coastal marshes are dominated by *Spartina alterniflora* because of its high salinity tolerance. *Spartina alterniflora* had thicker rhizomes in spring, but it produced high above- and belowground production in summer when photosynthesis is at its peak. It is shown that *Spartina alterniflora* in coastal areas may have adapted to the coastal environment with high disturbances and stresses by producing high above- and belowground production in summer, usually prior to severe hurricane seasons.

4.3.3 Overall Results Based on Combined Phases I and II Data

4.3.3.1 Soil Properties

The soil properties measured in Phases I and II of this project were combined to derive overall statistics. There were eleven transects (No. 1–11) established during the two phases. Their locations, elevations and other characteristics are described in Phase I report and the previous section. Transects 1, 2, 6, 7, 9, 10 and 11 are grouped as coastal marshes, and Transects 3, 4, 5 and 8 are inland marshes. Each transect is divided into low and high marsh zones. Fig. 4.83 shows the soil moisture, organic matter content, bulk density and sediment mean size on the eleven transects combined into low and high marsh zones, as well as coastal and inland marshes. Tables 4.13–4.16 list the corresponding measured data for convenience use. Similarly, Fig. 4.84 and Table 4.17 show the soil sand, clay and silt percentages measured on the eleven transects.

Table 4.18 shows the ANOVA test results of significant difference in soil properties between low and high marshes, as well as between costal and inland marshes. It was found that there was no significant difference in the average soil moisture, organic matter, bulk density, sediment mean size, clay percentage, and sand percentage between low and high marsh zones or between coastal (Transects 1, 2, 6, 7, 9, 10 and 11) and inland marshes (Transects 3, 4, 5 and 8). However, there was a significant difference in the silt percentage between coastal and inland marshes.

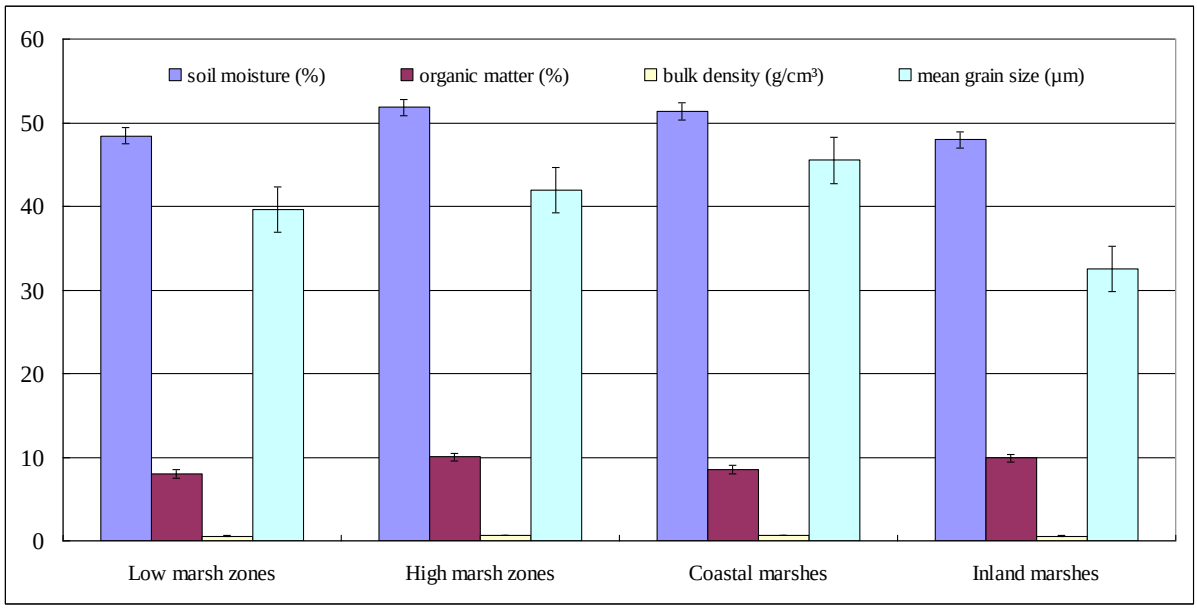

Fig. 4.83. Average soil moisture in the low and high marsh zones in eight transects (±SE, n=150)

Table 4.13. Average soil moisture in the low and high marsh zones in eleven transects

Transects	Low marsh zones (%)		High marsh zones (%)	
	Mean	Std.dev.	Mean	Std.dev.
Tr. 1	52.33	7.31	30.37	8.32
Tr. 2	45.96	6.87	32.61	7.37
Tr. 3	40.11	11.71	57.75	11.25
Tr. 4	37.67	7.59	52.22	12.27
Tr. 5	34.66	9.50	59.51	17.40
Tr. 6	33.51	12.02	40.38	5.36
Tr. 7	45.72	6.55	54.48	12.27
Tr. 8	61.47	5.87	40.12	6.10
Tr. 9	54.37	2.79	61.25	6.28
Tr. 10	64.25	2.79	74.17	1.34
Tr. 11	62.75	5.79	67.09	1.08

Table 4.14. Average soil organic matter in the low and high marsh zones in eleven transects

Transects	Low marsh zones (%)		High marsh zones (%)	
	Mean	Std.dev.	Mean	Std.dev.
Tr. 1	6.85	2.31	2.14	1.50
Tr. 2	5.54	1.69	2.95	1.56
Tr. 3	5.24	3.82	9.97	5.16
Tr. 4	4.16	1.83	9.4	6.56
Tr. 5	5.09	2.47	20.88	13.34
Tr. 6	4.87	4.01	5.57	1.54
Tr. 7	5.25	2.35	10.39	6.67
Tr. 8	15.68	6.92	8.59	10.07
Tr. 9	6.02	1.28	9.03	3.20
Tr. 10	9.03	1.25	19.31	1.68
Tr. 11	20.39	12.50	11.86	1.42

Table 4.15. Average soil bulk density in the low and high marsh zones in eleven transects

Transects	Low marsh zones (g/cm^3)		High marsh zones (g/cm^3)	
	Mean	Std.dev.	Mean	Std.dev.
Tr. 1	0.72	0.10	1.24	0.21
Tr. 2	0.78	0.14	1.2	0.17
Tr. 3	0.69	0.44	0.53	0.29
Tr. 4	0.71	0.46	0.65	0.40
Tr. 5	0.31	0.21	0.23	0.06
Tr. 6	0.27	0.001	0.31	0.02
Tr. 7	0.83	0.16	0.68	0.20
Tr. 8	0.52	0.05	0.92	0.19
Tr. 9	0.55	0.03	0.48	0.10
Tr. 10	0.39	0.016	0.29	0.02
Tr. 11	0.52	0.06	0.48	0.03

Table 4.16. Sediment mean grain size in the low and high marsh zones in eleven transects

Transects	Low marsh zones (μm)		High marsh zones (μm)	
	Mean	Std.dev.	Mean	Std.dev.
Tr. 1	156.9	175.18	105.3	39.68
Tr. 2	75.46	44.12	122.2	76.07
Tr. 3	35.97	43.39	65.68	99.70
Tr. 4	34.97	27.05	56.41	62.70
Tr. 5	10.90	2.30	11.41	1.69
Tr. 6	35.48	28.34	27.13	8.45
Tr. 7	35.08	25.24	16.55	1.27
Tr. 8	24.26	15.85	20.65	5.00
Tr. 9	8.43	1.21	9.44	0.47
Tr. 10	7.40	3.76	16.19	1.89
Tr. 11	11.05	14.02	13.40	1.55

Table 4.17. Soil sand, clay and silt percentage in the low and high marsh zones in eleven transects

Transects	Low marsh zones					
	% sand	Std.dev.	% silt	Std.dev.	% clay	Std.dev.
Tr. 1	56.45	22.58	43.05	22.33	0.50	0.53
Tr. 2	50.72	11.57	49.00	11.41	0.28	0.33
Tr. 3	14.75	16.92	80.10	16.28	5.15	6.06
Tr. 4	23.62	21.11	73.58	19.84	2.80	2.87
Tr. 5	4.87	1.92	82.92	7.01	12.21	8.03
Tr. 6	14.65	9.80	84.26	9.10	1.09	1.33
Tr. 7	15.24	8.26	84.18	7.66	0.58	0.16
Tr. 8	9.20	2.87	91.80	2.87	0	0
Tr. 9	5.06	2.15	75.15	5.47	19.79	7.26
Tr. 10	5.59	0.45	83.03	3.09	11.38	2.64
Tr. 11	4.57	4.48	86.31	3.37	9.12	1.21
	High marsh zones					
	% sand	Std.dev.	% silt	Std.dev.	% clay	Std.dev.
Tr. 1	74.90	14.78	24.92	14.65	0.18	0.24
Tr. 2	68.26	15.86	31.54	15.78	0.20	0.17
Tr. 3	16.90	20.92	80.52	20.06	2.58	4.34
Tr. 4	27.81	25.04	69.40	23.39	2.79	5.16
Tr. 5	4.61	1.43	84.14	5.45	11.25	6.41
Tr. 6	13.07	3.17	86.04	2.69	0.89	1.12
Tr. 7	9.67	0.93	87.26	2.29	3.07	1.85
Tr. 8	9.24	2.18	88.20	6.48	2.56	5.83
Tr. 9	9.51	4.23	88.59	3.50	1.90	0.97
Tr. 10	6.78	11.74	74.60	14.24	18.63	21.06
Tr. 11	6.54	1.67	90.26	1.43	3.21	0.73

Table 4.18. ANOVA test results of significant difference in soil properties

Soil properties	Low vs. high marsh zones	Coastal vs. inland marshes
Moisture	No (p=0.55> 0.05)	No (p=0.25> 0.05)
Organic matter	No (p=0.41> 0.05)	No (p=0.42> 0.05)
Bulk density	No (p=0.59> 0.05)	No (p=0.5> 0.05)
Mean grain size	No (p=0.90> 0.05)	No (p=0.30> 0.05)
Clay percentage	No (p=0.769> 0.05)	No (p=0.959> 0.05)
Sand percentage	No (p=0.52> 0.05)	No (p=0.061> 0.05)
Silt percentage	No (p=0.31> 0.05)	Yes (p=0.036< 0.05)

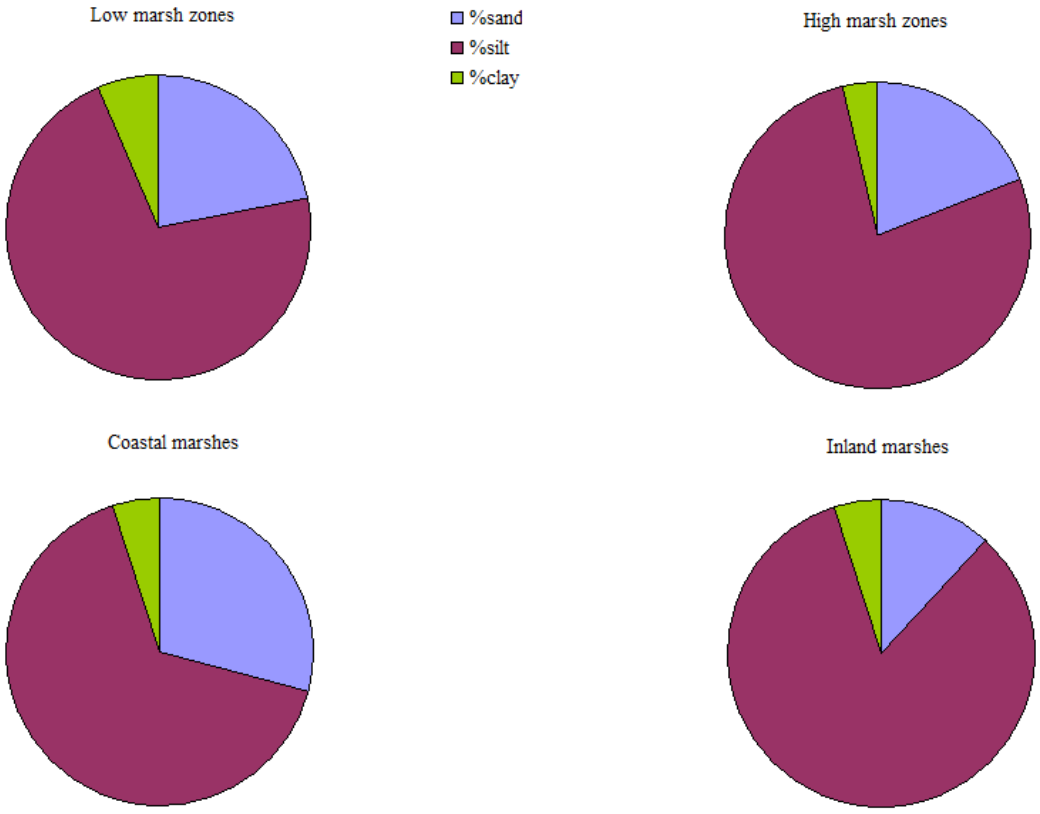

Fig. 4.84. Soil sand, clay and silt percentages compared for low and high marsh zones, coastal and inland marshes.

4.3.3.2 Plant Parameters

The measured plant cover, live and dead vegetation heights, rhizome thickness, stem diameter, plant density, above- and belowground biomass in the eleven transects were analyzed by low and high marsh zones, as well as coastal (Transects 1, 2, 6, 7, 9, 10 and 11) and inland (Transects 3, 4, 5 and 8) marshes. Figs. 4.85–4.91 compare these plant parameters between low and high marsh zones, as well as between coastal and inland marshes. Table 4.19 shows the ANOVA test of significant difference in these plant parameters. The results are described below.

Percent cover

The average plant cover was compared for low and high marsh zones, coastal and inland marshes. There was no significant difference in the average plant percent cover between low and high marsh zones or between coastal and inland marshes (Fig. 4.85; Table 4.19).

Vegetation heights

The average live ($p = 5.1E\text{-}06 < 0.05$) and dead standing shoot heights of *Spartina alterniflora* in low marsh zones were significantly lower than those in the high marsh zones ($p = 0.007 < 0.05$; Fig. 4.86; Table 4.19).

There was no significant difference in the average live or dead standing shoot heights of *Juncus roemerianus* between low and high marsh zones or between coastal and inland marshes (Fig. 4.87).

The live standing shoot heights of *Spartina alterniflora* in coastal marshes were significantly lower than live standing shoot heights of *Juncus roemerianus* (p= 1.39E-10 < 0.05; Fig. 4.87). In addition, the dead standing shoot heights of *Spartina alterniflora* in coastal marshes were significantly lower than dead standing shoot heights of *Juncus roemerianus* (p= 6.61E-10 < 0.05; Fig. 4.87).

Table 4.19. ANOVA test results of significant difference in plant parameters

Plant parameters	Low vs. high marsh zones	Coastal vs. Inland marshes
Percent cover	No (p =0.208 > 0.05)	No (p =0.161 > 0.05)
Height (live *Spartina*)	Yes (p =5.1E-06 < 0.05)	
Height (dead *Spartina*)	Yes (p =0.007 < 0.05)	
Height (live *Juncus*)	No (p =0.429 > 0.05)	
Height (dead *Juncus*)	No (p =0.31 > 0.05)	
Rhizome thickn. (*Spartina*)	Yes (p =0.014 < 0.05)	
Rhizome thickn. (*Juncus*)	No (p =0.786 > 0.05)	
Stem diameter (*Spartina*)	No (p =0.129 > 0.05)	
Stem diameter (*Juncus*)	No (p =0.766 > 0.05)	
Stem Density	Yes (p =0.011 < 0.05)	Yes (p =1.33E-04 < 0.05)
Aboveground biomass	No (p =0.098 > 0.05)	No (p =0.662 > 0.05)
Belowground biomass	No (p =0.843 > 0.05)	Yes (p =0.002 < 0.05)

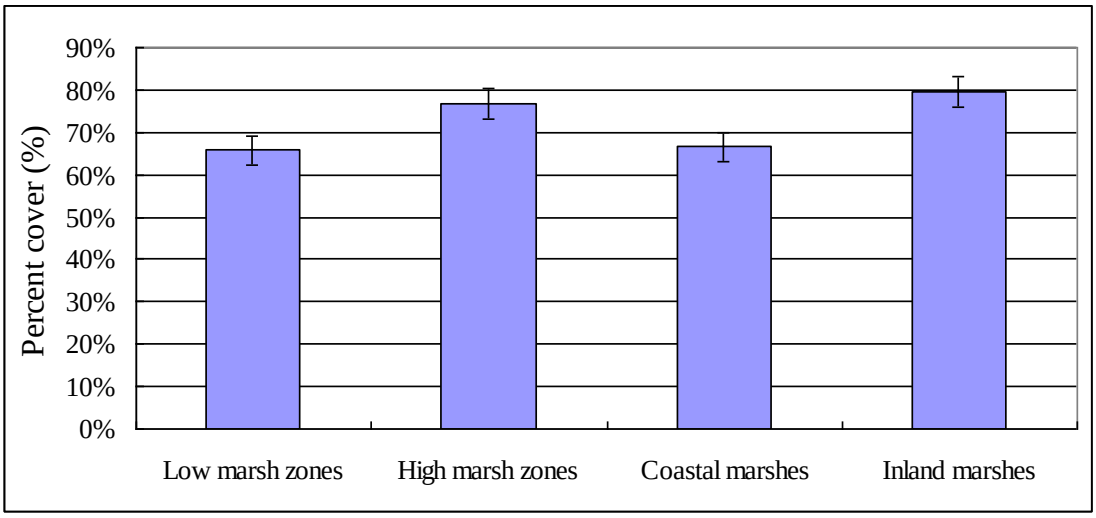

Fig. 4.85. Average percent cover (space occupied) compared for low and high marsh zones, coastal and inland marshes (±SE, n=320).

Rhizome thickness and stem diameter

The mean rhizome thickness of *Spartina alterniflora* in low marsh zones was significantly higher than that in high marsh zones (p= 0.014 < 0.05; Table 4.19, Fig. 4.88). The mean rhizome

thickness of *Juncus roemerianus* in inland marshes was significantly thicker than that of *Spartina alterniflora* in coastal marshes (p= 1.81 E-13 <0.05).

There was no significant difference in the mean stem diameter (bottom) of *Spartina alterniflora* or *Juncus roemerianus* between low and high marsh zones (Fig. 4.89; Table 4.19). However, there was a significant difference in the mean stem diameter between *Spartina alterniflora* in coastal marshes and *Juncus roemerianus* in inland marshes (p= 3.08 E-18 < 0.05; Fig. 4.89).

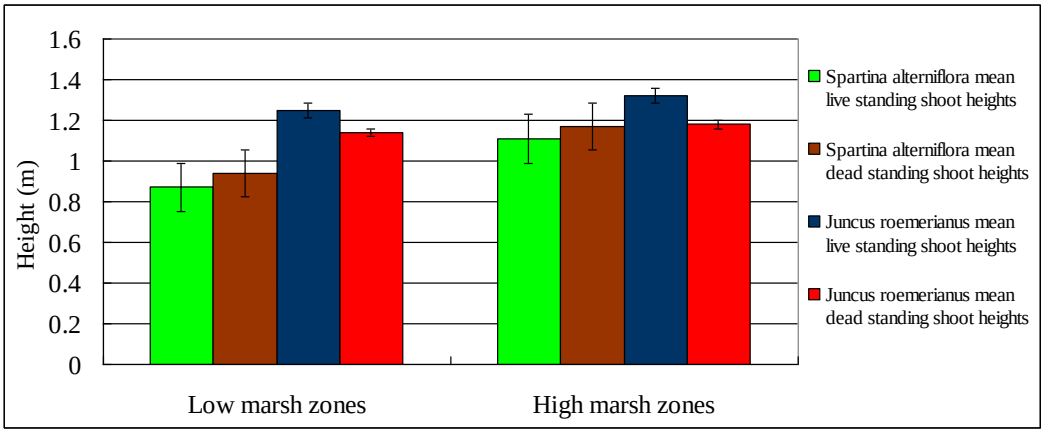

Fig. 4.86. *S. alterniflora* and *Juncus roemerianus* mean standing shoot heights compared between the low and high marsh zones (±SE, n=320)

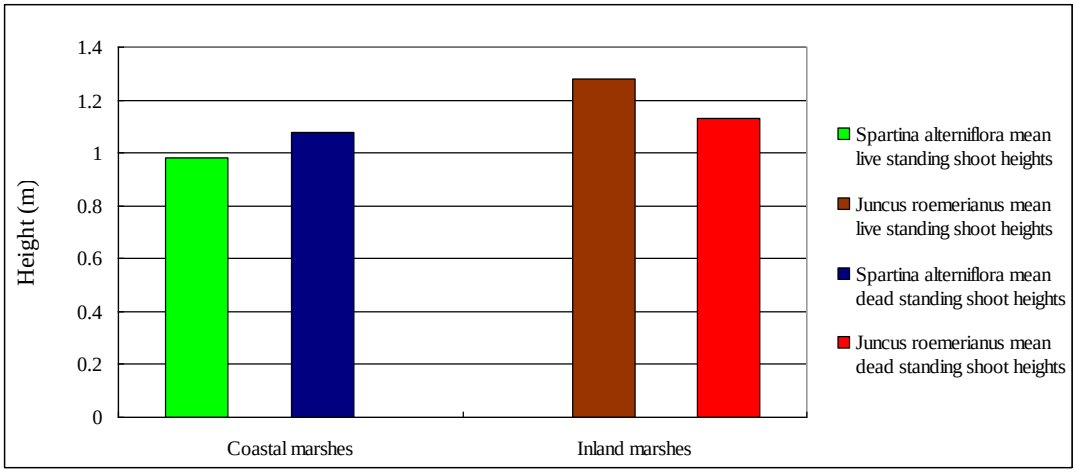

Fig. 4.87. *S. alterniflora* and *Juncus roemerianus* mean standing shoot heights compared between the coastal and inland marshes (n=320).

Plant density

Average plant density (units / m^2) was estimated by measuring the stem diameter of different plant species and then calculating the number of plant stems by dividing each percent cover by the appropriate stem diameter in each 0.25 m^2 quadrat. A repeated ANOVA measures showed that the average plant density in low marsh zones was significantly lower than that in high marsh zones (p=0.011 <0.05; Fig. 4.90; Tables 4.19 and 4.20). There is also a significant

difference in average plant density between coastal and inland marshes (p=1.33 E-04 <0.05; Fig. 4.90; Tables 4.19 and 4.20).

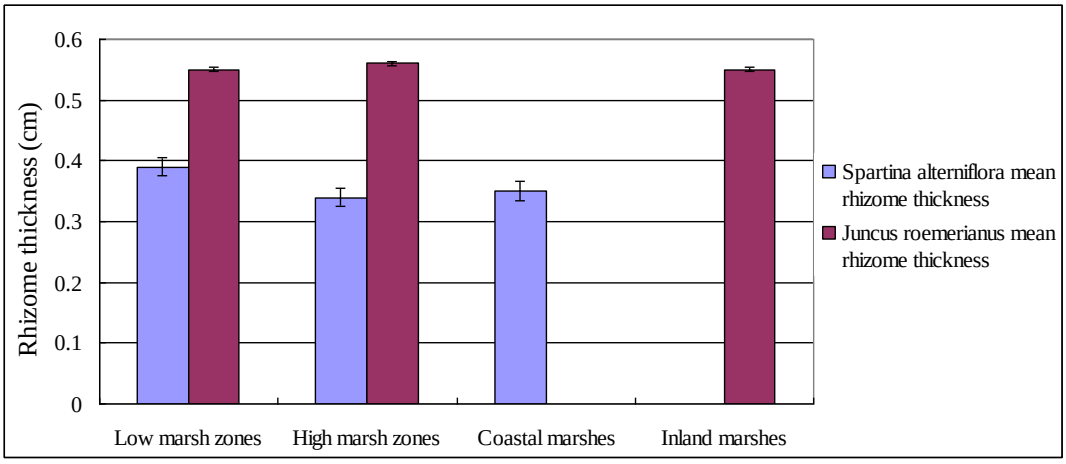

Fig. 4.88. Mean rhizome thickness of *Spartina alterniflora* and *Juncus roemerianus* compared for low and high marsh zones, coastal and inland marshes (±SE, n=132)

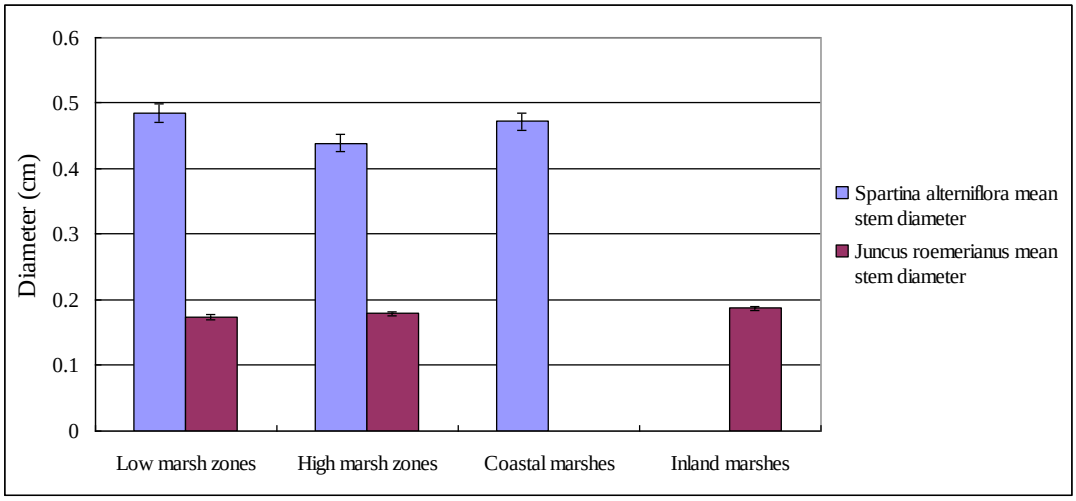

Fig. 4.89. Mean stem diameter of *Spartina alterniflora* and *Juncus roemerianus* compared for low and high marsh zones, coastal and inland marshes (±SE, n=100).

Above- and belowground biomass

Both average plant above- and belowground biomass in low marsh zones combined on Transects 1-11 in spring and summer from 2010 to 2011 did not differ significantly from that in high marsh zones (Fig. 4.91; Table 4.19). In addition, there was no significant difference in plant aboveground biomass between coastal and inland marshes (Fig. 4.91; Table 4.19). However, plant belowground biomass in coastal marshes was significantly higher than that in inland marshes (p= 0.001 < 0.05; Fig. 4.91; Table 4.19).

Table 4.20. Average stem density in the low and high marsh zones in eleven transects

Transects	Low marsh zones (units/m²)		High marsh zones (units/m²)	
	Mean	Std.dev.	Mean	Std.dev.
Tr. 1	204	14.93	677	15.27
Tr. 2	213	5.46	618	30.50
Tr. 3	644	14.79	896	6.92
Tr. 4	720	54.99	964	30.28
Tr. 5	743	51.47	889	26.90
Tr. 6	245	12.14	550	1497
Tr. 7	187	16.26	655	19.82
Tr. 8	865	47.77	834	24.50
Tr. 9	765	74.26	803	26.88
Tr. 10	259	21.63	365	35.96
Tr. 11	200	18.66	596	30.22

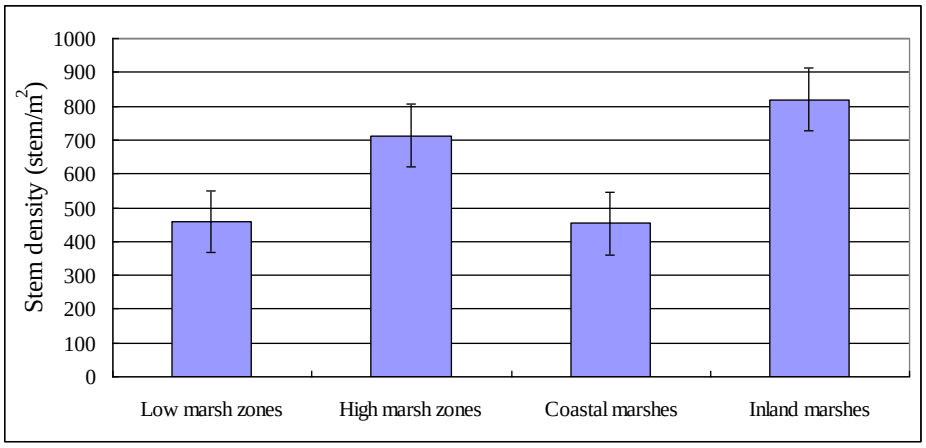

Fig. 4.90. Average plant density compared for low and high marsh zones, coastal and inland marshes (±SE, n=70).

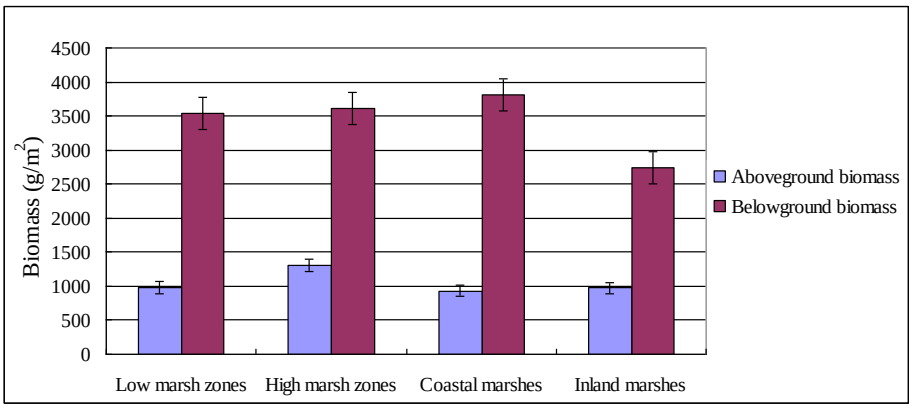

Fig. 4.91. Mean above- and belowground biomass sampled in spring and summer (2010-2011) compared for low and high marsh zones, coastal and inland marshes (±SE, n=200).

4.3.3.3 **Regression Relationship**

Linear regression analyses were conducted based on the data on the eleven transects categorized by low and high marsh zones or coastal and inland marshes, using the plant above- and belowground biomass as dependent variables and environmental variables including soil properties, plant parameters and elevation data as independent variables.

Fig. 4.92 shows that plant aboveground biomass in low marsh zones was negatively related to *Spartina alterniflora* live standing shoot heights (R^2= 0.30, p< 0.05), which suggests that plant aboveground biomass decreased as *Spartina alterniflora* live standing shoots in low marsh zones increased. In addition, plant belowground biomass in low marsh zones was positively related to *Juncus roemerianus* dead standing shoots (R^2= 0.34, p< 0.05). Thus, high *Juncus roemerianus* dead standing shoots in low marsh zones indicated high plant belowground biomass in the last growing season.

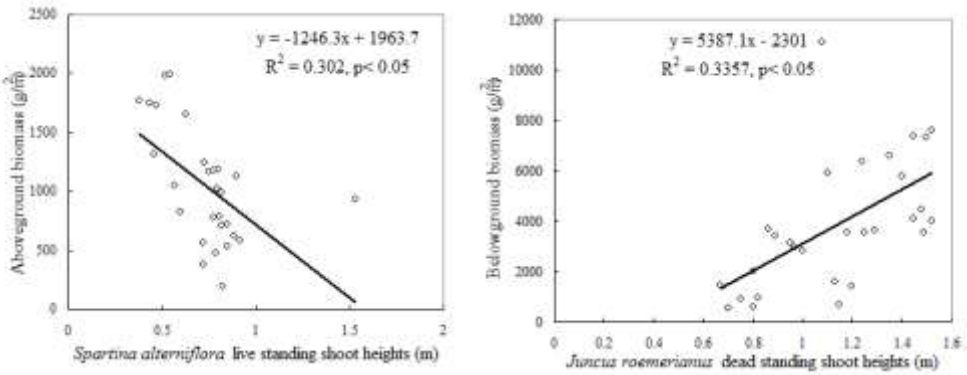

Fig. 4.92. Linear regressions of plant aboveground biomass in low marsh zones against *Spartina alterniflora* live standing shoot heights and belowground biomass in low marsh zones against *Juncus roemerianus* dead standing shoot heights (n=30).

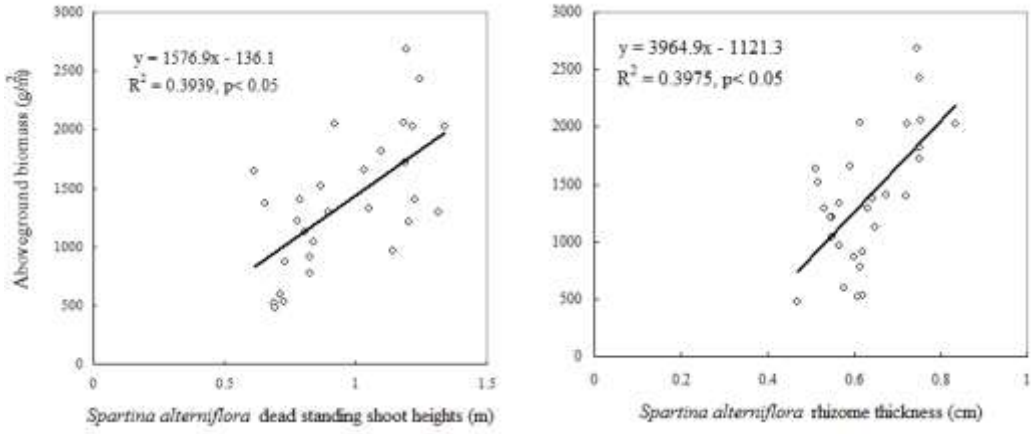

Fig. 4.93. Linear regressions of plant aboveground biomass in coastal marshes against *Spartina alterniflora* dead standing shoot heights and rhizome thickness (n=30).

Fig. 4.93 shows that plant aboveground biomass in coastal marshes was positively related to *Spartina alterniflora* dead standing shoot heights (R^2= 0.39, p< 0.05), which suggests high *Spartina*

alterniflora dead standing shoot heights indicated high plant aboveground biomass in coastal marshes in the last growing season. Plant aboveground biomass in coastal marshes was also positively related to *Spartina alterniflora* rhizome thickness (R^2= 0.40, p< 0.05). Thus, plant aboveground biomass increased as *Spartina alterniflora* rhizome thickness increased.

4.3.3.4 **Discussion**

Comparison of low and high marsh zones

When all the soil data results were combined from eleven transects (Grand Bay: Transects 1, 2, 5 and 8; Graveline Bayou: Transects 3, 4, 6 and 7; Terrebonne Bay: Transects 9, 10 and 11) from 2009 to 2011 into low and high marsh zones, there was no significant difference in soil properties (e.g., soil moisture, organic matter content, bulk density, mean grain size and soil distribution) between low and high marsh zones (Figs. 4.83 and 4.84; Tables 4.13–4.18). On the other hand, both *Spartina alterniflora* live and dead standing shoot heights in high marsh zones were significantly higher than those in low marsh zones (Fig. 4.86; Table 4.19). Linear regression analyses showed that plant aboveground biomass in low marsh zones was negatively related to *Spartina alterniflora* live standing shoot heights (Fig. 4.92). The plant aboveground production decreased as *Spartina alterniflora* live standing shoot heights increased, which suggested that *Spartina alterniflora* growth (especially the plant height) would utilize energy, thus, decreasing plant aboveground production in low marsh zones. Moreover, stem density in low marsh zones may be a better indicator of production than heights because coastal plant percent cover tends to be low in low marsh zones where organisms are more likely to be inundated by flood and storm surges (Bannister 1976; Chapman 1976; Keddy 2010; Weis and Butler 2009). In low marsh zones, plant belowground biomass was positively related to *Juncus roemerianus* dead standing shoot heights (Fig. 4.92). Thus, high *Juncus roemerianus* dead standing shoots in low marsh zones indicated high plant belowground biomass in the last growing season, which suggests that higher plant belowground production could produce higher standing shoot heights for *Juncus roemerianus* or higher standing shoot heights could contribute to higher plant belowground production because taller plants could avoid shade and therefore would be expected to provide more energy for growth. Although there was no significant difference in the plant above- and belowground biomass between low and high marsh zones (Fig. 4.91; Table 4.19), rhizome thickness of *Spartina alterniflora* in low marsh zones was significantly higher than that in high marsh zones (Fig. 4.88; Table 4.19) which suggested that healthy rhizome systems could help coastal vegetation to consolidate sediment in low marsh zones and survive during storm surges and hurricane events.

Comparison of coastal and inland marshes

In coastal marshes, soil silt percentage was significantly lower than that in inland marshes (Fig. 4.84; Tables 4.17 and 4.18). Higher soil silt percentage in inland marshes can be beneficial for plant growth because small-sized grains made up of silt and clay can hold more nutrients than coarse sandy soil due to their greater surface-to-volume ratio (Weis and Butler 2009).

Although there was no significant difference in plant aboveground biomass between coastal and inland marshes (Fig. 4.91; Table 4.19), linear regression results showed that plant aboveground biomass in coastal marshes was positively related to *Spartina alterniflora* dead standing shoot heights (Fig. 4.93), which means high *Spartina alterniflora* dead standing shoot heights indicated high plant aboveground biomass in coastal marshes in the last growing season. In addition, plant aboveground biomass in coastal marshes was positively related to

Spartina alterniflora rhizome thickness (Fig. 4.93). Thus, plant aboveground biomass increased as *Spartina alterniflora* rhizome thickness increased. On the other hand, plant belowground biomass in coastal marshes was significantly higher than that in inland marshes (Fig. 4.91; Table 4.19), which suggests that *Spartina alterniflora* produces higher belowground production in coastal marshes than *Juncus roemerianus* produces in inland marshes. High plant belowground production in coastal areas indicated coastal vegetation produced healthy root and rhizome systems which could help coastal vegetation to hold sediments and store carbohydrates during hurricanes and storm surges for regrowth in the next growing season.

Seasonal changes in coastal vegetation structures

Results of our studies suggested that in brackish marshes, *Juncus roemerianus* invested most carbohydrates into aboveground production when photosynthesis is high in summer. In fall, *Juncus roemerianus* began to move carbohydrates from aboveground to belowground, but *Juncus roemerianus* had thinnest rhizomes during this time, which suggests that belowground parts of *Juncus roemerianus* produced an abundance of extensive rhizomes (Fig. 4.94). In winter, rhizomes of *Juncus roemerianus* were enlarging so *Juncus* had the thickest rhizomes in spring. In addition, *Juncus* began to produce aboveground plant tissue including standing shoot heights when temperatures warmed up in spring.

On the other hand, in coastal marshes, plants produced both high above- and belowground production in summer, which suggests that *Spartina alterniflora* could adapt to coastal disturbances such as hurricanes by producing high belowground production to withstand the storm waves (Fig. 4.95). *Spartina alterniflora* had high standing shoot heights when photosynthesis was high in summer. Although *Spartina alterniflora* did not have the thickest rhizomes in summer, the high belowground production is likely caused by the large numbers of rhizomes which possibly helped vegetation to consolidate sediments in coastal areas. Results in Figs. 4.94 and 4.95 showed that there was a significant difference in belowground production between inland (brackish) and coastal (salt) marshes. In brackish marshes, vegetation produced high aboveground production in summer and high belowground production in fall; however, in coastal marshes, vegetation produced both high above- and belowground production in summer.

The important findings of this study were that there was a significant difference in the seasonal changes of vegetation belowground production between coastal and inland marsh species. In southeastern temperate zones, the inland marshes are dominated by *Juncus roemerianus*, and *Spartina alterniflora* always dominates the coastal marshes because of its high salinity tolerance. Both *Juncus roemerianus* and *Spartina alterniflora* had thinnest rhizomes in fall. The rhizomes of both *Juncus roemerianus* and *Spartina alterniflora* were enlarging during winter, and then were thickest in spring. However, *Juncus roemerianus* produced high aboveground production in summer in inland marshes, and then moved carbohydrates from the aboveground to the belowground parts when photosynthesis was decreasing prior to winter months. On the other hand, *Spartina alterniflora* exhibited both high above- and belowground production in summer in coastal marshes. The findings showed that *Spartina alterniflora* in coastal areas may have adapted to the coastal environment by producing high above- and belowground production in summer in advance of hurricane seasons when high disturbances and stresses are common. Although the different physical plant growth form of these two dominant plant species between coastal and inland marshes could result in the significant difference in plant belowground production, plant adaptation and environmental variables including physical stresses are most likely to account for these significant differences between

coastal and inland marshes. In coastal marshes and in low marshes, the greater belowground biomass allocation can help *Spartina alterniflora* survive during the hurricane seasons by stabilizing the sediments and providing nutrient storage for the next growing season.

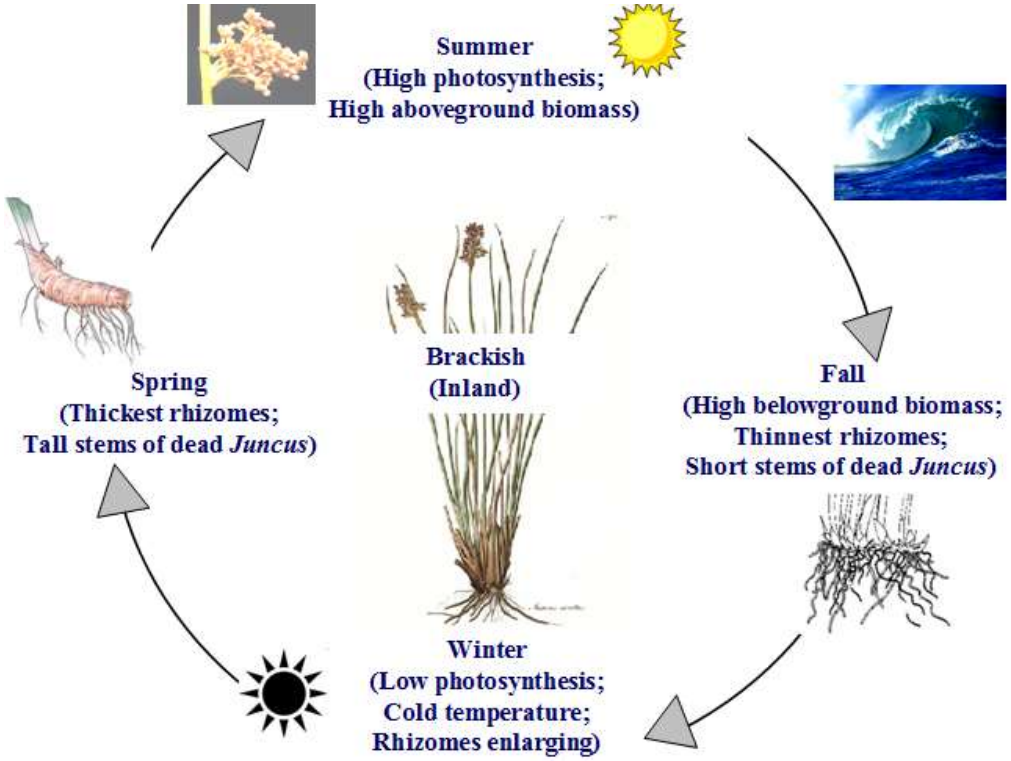

Fig. 4.94. Seasonal changes in *Juncus roemerianus* dominating inland marshes (brackish).

4.3.3.5 Summary and Future Recommendation

Results of this study showed that coastal marshes had high belowground production. Although native coastal vegetation tended to have lower heights and lower density in low marsh zones in coastal areas where coastal plants tend to be inundated by storm surges and waves, vegetation could survive and withstand the storm waves in these coastal areas by increasing belowground primary production which may be beneficial for the prolific rhizomes to hold sediments. On the other hand, hurricanes and storm surges have a direct negative effect on the native vegetation in coastal marshes with lower elevations by decreasing standing shoot heights and stem density. However, coastal marshes have higher vegetation percent cover in high marsh zones, but have higher belowground production in low marsh zones in coastal areas which could provide sediment stabilization during storm surges and hurricane events.

In order to learn more about how coastal plants are affected by storm surges and waves in different marsh zones and at different marsh sites, this experiment, or one similar to it, is recommended to be conducted in different seasons at these sampling sites or some additional marsh locations which have similar vegetation growth patterns. For example, a study could be conducted to compare above- and belowground biomass in different seasons at other marsh sites which have the same plant growth pattern. Another experiment could also be conducted to

compare *Spartina alterniflora* and *Juncus roemerianus* rhizome thickness in winter, fall, spring and summer in low and high marsh zones in coastal LA and Florida as photosynthesis is increasing. It would be interesting to see how plant rhizome thickness changed in different seasons between these different locations which have similar vegetation growth patterns.

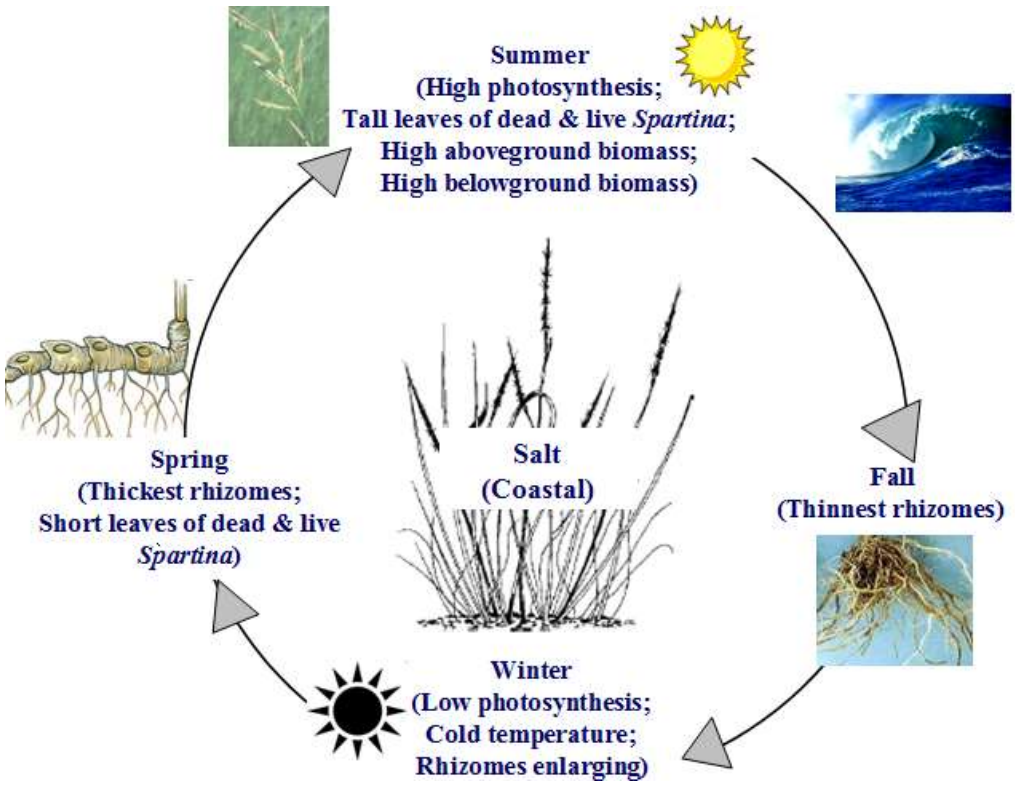

Fig. 4.95. Seasonal changes in *Spartina alterniflora* dominating coastal marshes (salt).

5. LABORATORY AND FIELD INVESTIGATIONS OF MARSH EDGE EROSION

This chapter presents the laboratory experiments and field observations of marsh edge erosion. The marsh retreat rate in a field site in Terrebonne Bay, LA was measured using GPS systems and aerial photographs, and the wave environment was also measured to correlate the marsh edge retreat rate and wave conditions. A model marsh edge was constructed in laboratory using the intact marsh edge samples collected from the field, and its erosion process by wave undercutting was recorded.

5.1 Introduction

Coastal ecosystems are some of the most productive and threatened ecosystems in the world (Lotze et al. 2006; Halpern et al. 2008). They comprise of salt marshes, coral reefs, mangroves, and seagrasses, and provide important ecological and economic values (e.g. Costanza et al., 1997). An estimated 50% of salt marshes, 35% of mangroves, 30% of coral reefs, and 29% of seagrasses are either lost or degraded worldwide (Barbier et al., 2011 and references therein). The loss has resulted in 33% decline in the number of viable fisheries; 69% decline in the provision of nursery habitats such as oyster reefs, seagrass beds, and wetlands; and 63% decline in filtering and detoxification services provided by suspension feeders, submerged vegetation, and wetlands (Worm et al., 2006).

In the world's major deltaic plains, land loss has been estimated to be 95 km^2/yr over the past 14 years (Coleman et al., 2008). Mississippi River delta in Louisiana has particularly experienced dramatic wetland loss. Between 1956 and 2006, annual land loss rates ranged from 34 to 104 km^2/yr with an average annual land loss rate over that time period was approximately 70 km^2/yr (Barras et al., 2003). This loss represents 80% of the coastal wetland loss in the entire continental United States. The public use value of this loss is estimated to be in excess of $37 billion by 2050 (LCWCRTF, 1998).

On the Louisiana coast, the reasons for wetland loss are complex and both natural and anthropogenic (Day et al., 2000; Gagliano, 2003; Morton et al., 2006). One of the important causes of erosion is the constant wave action along the marsh edges. Analysis by Penland et al. (2000) showed that 26% of the wetland loss in the Mississippi river delta from 1932 to 1990 can be attributed to erosion due to wind waves.

Wind waves also influence sediment re-suspension in the nearshore area (Sanford, 1994; Sheremet et al., 2005; Kineke et al., 2006; Jaramillo et al., 2009). Wind waves have been shown to play an important role in the morphological evolution of intertidal regions (Defina et al., 2007; Fagherazzi et al., 2007; Fagherazzi and Wiberg, 2009). Kirby (2000) noted that the shape of the mudshore profile is controlled by tidal currents and particularly by wave climate. Importantly, wind waves degrade salt marsh through scarp erosion (Tonelli et al., 2010). The role of wave attack on coastal marshes is compounded by the conversion of marsh platforms to open-water, thereby increasing the fetch and wave forces on exposed marsh edges.

On the Louisiana-Mississippi coast, the marshes are typically protected by barrier islands. When the barrier islands disappear, so do the marshes mainly because of the wave-induced damage and erosion. Studies have found a strong correlation between the level of wave energy and the survival of wetland marshes (e.g. Roland and Douglass, 2005).

The Northern Gulf of Mexico annually experiences tropical storms and hurricanes, and the coastal wetlands provide a natural first line of defense against approaching storm surge and

waves (e.g. Lopez, 2009). By one estimate, in the US, the coastal wetlands were estimated to provide $23.2 billion in storm protection services annually (Costanza et al., 2008).

Therefore, retaining marshland is an important goal with many benefits. The rate of erosion at the marsh edge is a key parameter for predicting the longevity of a given vegetated marsh. The soil and plant types, along with wave characteristics, are the controlling variables for the rate-of-retreat at the marsh edge. In general, marsh edge sediments are characterized by the presence of extensive, well-developed root systems, which act as fibrous reinforcement and provide cohesion that enhances sediment strength. Laboratory testing that utilizes relatively undisturbed samples taken from the field can better control the boundary conditions and perform more sophisticated and longer duration experiments than what is possible in the field. There have been only a few previous laboratory studies on marsh edge erosion (Feagin et al., 2009 and Coops et al., 1996), underlining the need for additional work.

In this study, we investigated the marsh edge erosion via laboratory experiment and field observation. We measured the shoreline retreat rate and investigated its relation to the wave climate in Terrebonne Bay, a rapidly eroding shallow estuary on the fragile Gulf coast of Louisiana. Analyzing directional wave gage data collected over a period of 7 months, we examined the extent of wave energy affecting the fringing eroding salt marshes. Using wave power calculations, we estimated marsh retreat rates and compared them with the rates obtained from our topographic surveys (short term) and those estimated from the aerial photography (decadal). In order to further understand the marsh edge erosion mechanisms, a model marsh edge was constructed in laboratory and the erosion process under a regular wave action was recorded.

5.2 Field Observations of Wetland Erosion

5.2.1 Study Area

Terrebonne Bay is a shallow estuary on the Louisiana coast of Northern Gulf of Mexico on the west side of the mouth of Mississippi River (Fig. 5.1). As part of the abandoned deltaic lobes, currently the basin receives no major fluvial discharge. The bay is bounded by the natural levees of Bayou Terrebonne on the east and the Houma Navigation Canal on the west. Salt marshes line the upper portions of the bay with vegetation communities of smooth cordgrass (*Spartina alterniflora*) and saltmarsh meadow (*Spartina patens*). On the south, the bay is bordered a series of narrow, low-lying barrier islands of the Isles Dernieres and the Timbalier Islands. The wave environment in the bay comprised of generally locally generated seas but offshore swell waves do propagate inwards through the gaps in the barrier island chain. The region has a microtidal environment (tide < 0.5 m) and depths in the bay vary from 1 to 3 m. Fetch mainly exists in the southeast quadrant and varies between 10 to 24 km. Every year from October to April about 30 cold weather fronts pass through the region (Moeller et al., 1993). A typical front lasts from 3-7 days when winds build up from the southerly quadrants and then turn clockwise to strong northerly winds. The dominant wind directions are southeast and northwest. The region also experiences tropical storms and hurricanes annually.

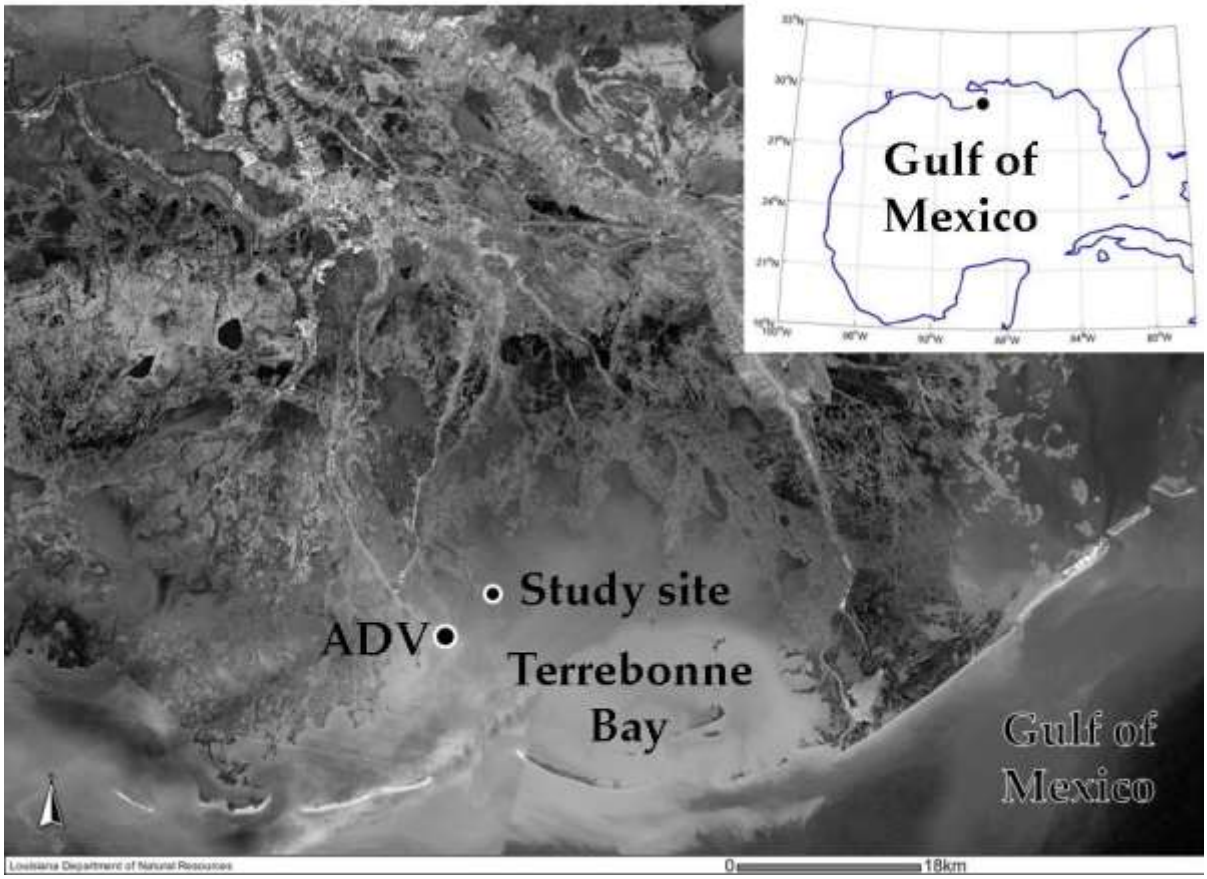

Fig. 5.1. Marsh erosion study site and the location of the ADV monitoring station.

5.2.2 Data and Methods

The field investigations involved collection of wave data affecting the marsh edge and topographic surveys to quantify shoreline retreat. Our wave data collection period did not always coincide with the topographic surveys. The marsh retreat rates in the area were also determined from historical aerial photos and a set of measurements of shoreline retreat in the area completed previously by LDNR.

The directional wave data was collected using an acoustic doppler velocimeter, Sontek Triton-ADV Wave/ Tide/ Current Gauge (ADV) deployed at 4 km seaward of the study area. The ADV was deployed at 29°11'13.20"N 90°36'33.59"W, approximately 10 km north of the Timbalier Isalnds (ADV in Figs. 5.1 and 5.2). The ADV location has a limited fetch from northwest to southwest. However, it is directly to the north of Cat Island Pass which provides a break in the barrier island chain allowing low energy swell to propagate northwards in the bay. Over the periods from February 23, 2010 through April 29, 2010 and from July 24, 2010 through February 14, 2011, 17 min bursts were sampled at 4 Hz frequency every 30 minutes to record puv (pressure, x-component of velocity and y-component of velocity) time series. The wave records were analyzed using standard spectral methods to produce integral parameters of (zero moment) wave height, H_{mo}, and peak period, T_p. For the analysis presented in this section, wave heights exceeding 0.05 m were only considered. This subset represents about 40% of the 7 month dataset.

Non-directional pressure transducers were also deployed in conjunction with the shoreline survey from June 2011 to July 2012. All the wave gages were successfully retrieved and data were examined for quality controlled. Only a subset of the raw data was processed. More time is needed to fully process and analyze all the wave data. Thus, the wave power estimated in this section is only based on the directional wave data.

Fig. 5.2. ADV being retrieved for monthly data acquisition and maintenance.

To estimate the rate of shoreline retreat two methods were followed. First, historical trends of shoreline retreat were estimated using aerial photographs from the year 1998 and 2010 obtained from the LDNR. Second, topographic surveys of the marsh edge were carried out using Trimble RTK GPS Survey system on 5 different occasions at the interval of 1 to 3 months (June 8, 2011; September 9, 2011; December 13, 2011; March 5, 2012; July 6, 2012).

Fig. 5.3. Graduate students performing topographic surveys at the study site.

5.2.3 Results

5.2.3.1 Shoreline Retreat Rates

The historical trends of shoreline retreat at the study site were estimated from the aerial photographs. Fig. 5.4 compares an aerial photograph of the study area from 1998 (top panel) to that from 2010 (bottom panel). During these 12 years, the southerly facing, main marsh edge is estimated to have retreated approximately 18 to 28 m.

Fig. 5.4. Aerial photographs of the study site from 1998 (top panel) and 2010 (bottom panel) with arrows indicating shoreline retreat.

The five topographic surveys of the marsh edge that were carried out during 2011-2012 provided short term estimates of the shoreline retreat. Fig. 5.5 shows topographic survey lines. A close-up view of the main east-west marsh edge is shown in Fig. 5.6.

Table 5.1 summarizes the retreat rates computed from the aerial photos and the five shoreline surveys. Note that a large number of hurricanes and tropical storms impacted south Louisiana between 1998 and 2010. Among the short term measurements, the rates during the period from June 8, 2011 to September 9, 2011 are larger due to the forcing resulting from about 1 m surge over the study area and incident waves of up to 0.8 m significant wave height (H_{mo}) during Tropical Storm Lee.

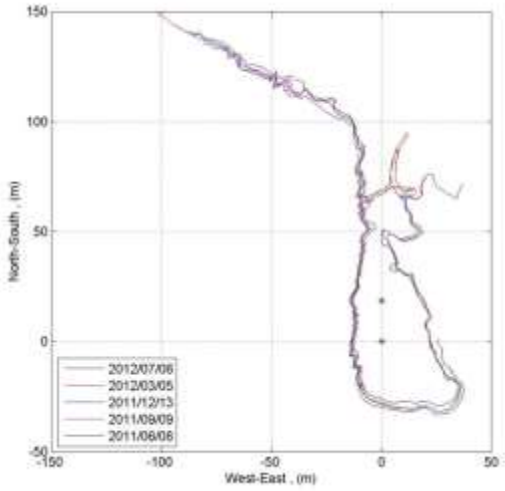

Fig. 5.5. Plot of the five topographic survey lines marking shoreline at various times. Two asterisks show local temporary benchmarks.

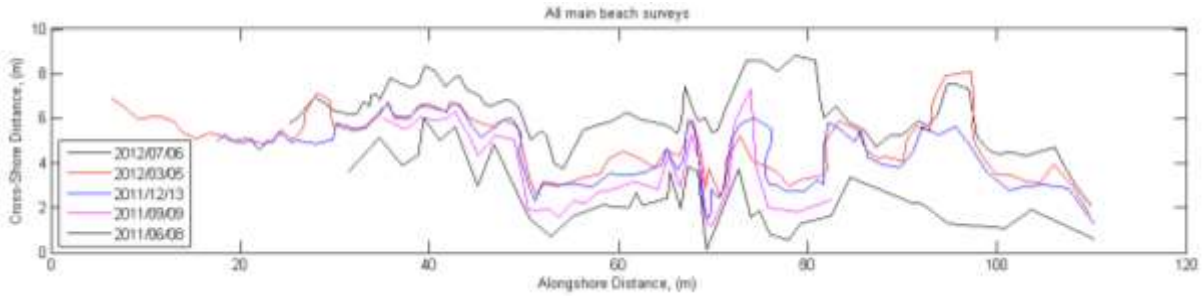

Fig. 5.6. Close-up (main east-west edge) of the five shoreline surveys shown in Fig. 5.5.

Table 5.1. Estimated long-term and short-term shoreline retreat rates

Time Period	Measured Retreat (m)	Retreat Rate (m/year)
1998 – 2010	27 (in 12 years)	2.3
June 8, 2011 - September 9, 2011	1.04 (in 93 days)	4.08
September 9, 2011 – December 13, 2011	0.67 (in 95 days)	2.57
December 13, 2011 – March 5, 2012	0.22 (in 83 days)	0.97
March 5, 2012 – July 6, 2012	2.16 (in 123 days)	6.41
June 8, 2011 – July 6, 2012	4.09 (in 394 days)	3.79

5.2.3.2 **Wave Power and Shoreline Retreat Rates**

Using the directional wave data obtained from the ADV, we examined potential for the landward retreat of the marsh edge caused by attacking waves. Wave power, $P_w = E.C_g$, where E is the wave energy and C_g is the group velocity, was computed for each directional wave record. Wave power in a given direction was then summed over the entire data set. Following

Schwimmer (2001) the wave power was related to marsh edge retreat rate as shown in Fig. 5.7. Although the wave power estimates are based on measurements about 4 km away from the marsh edge and the possibility of differing retreat rate relation from that proposed by Schwimmer (2001), the estimates indicate grave retreat potential. At three sites in the northern marsh edges of the bay, during the period from 1998 to 2005, the retreat rate averaged 3-6 m/yr (CPRA, 2012) which agrees well with our estimates. In addition to the relentless wind wave action, the marsh edge is also subject to persistent swell as captured by our data. Studies have shown that the long waves produce strong swash currents resulting in marsh substrate detachment (Priestas and Fagherazzi, 2011)

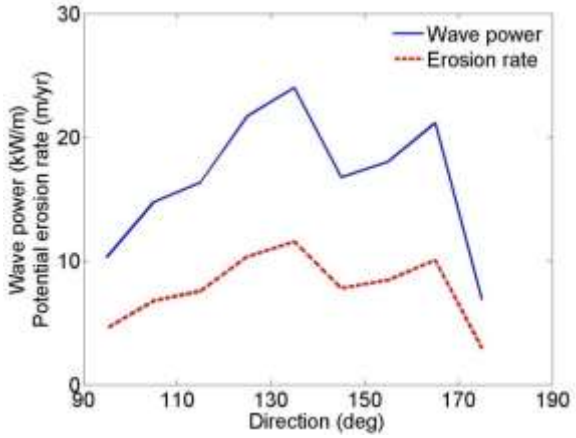

Fig. 5.7. Wave power and estimated erosion rate for waves coming from southeast quadrant (meteorological directions).

5.3 Laboratory Experiments of Marsh Edge Erosion

A model marsh edge was established in the National Sedimentation Laboratory wave flume in order to evaluate the rate of erosion of a marsh edge with a mature stand of *Spartina alterniflora* and to examine the mechanisms for wave erosion at the edge of marshes. The soil types and marsh-front slopes were chosen to be representative of marsh soils in the Louisiana Mississippi coasts of the Gulf of Mexico.

5.3.1 Field Sampling of Marsh Edge

In order to understand the natural phenomenon of marsh edge erosion and obtain the representative marsh samples, we made four field trips during Phase II in support of the laboratory testing. In April 2011, a fied trip to Terrebonne Bay was made by the laboratory experiment team. The purpose was to investigate the dynamics of wave impact on marsh edges and to collect *S. alterniflora* samples. Wave action on a marsh edge was photographed and recorded by a video camera, as shown in Figs. 5.8 and 5.9. In addition, many field trips were made and the marsh edge erosion mechanisms were studied by the field investigation team, as described in Chapters 3 and 4.

In June 2011 a field trip was made by the laboratory team to Terrebonne Bay and Grand Bay, followed by two additional trips to Terrebonne Bay in March and July 2012. The purpose of the three trips was to collect intact marsh edge samples to be tested at the laboratory. Several

14" wide, 24" long and 6" thick *S. alterniflora* sections were cut and carefully placed into trays, shown in Fig. 5.10. The trays were filled with seawater and transferred to the laboratory. The section was thicker than the root layer to have some native soil below the root layer, so that disturbance of the marsh soil-root system could be minimized. After the samples were transported to the laboratory, the grass was cut to grow new grass and recover the root-soil system somehow (Fig. 5.11).

Fig. 5.8. Inspection of marsh edge erosion.

Fig. 5.9. Marsh edge impacted by waves.

Fig. 5.10. Marsh edge sampling in Terrebonne Bay, LA.

Fig. 5.11. Marsh edge samples with new growth after they were transported to the laboratory.

5.3.2 Experimental Setup

The existing wave tank used in the wave experiments reported in Chapter 2 was modified for the second test of marsh edge erosion as shown in Fig. 5.12. The wave tank was divided longitudinally into two channels with a temporary wall starting at 13.6 m away from the wave paddle. The 0.35 m wide channel on the glass wall side of the wave tank was used as the test section (Fig. 5.12). The test section was located 13.6 m away from the wave paddle and extended 1.8 m. Capacitive water level sensors were positioned at 3, 11.5, 12.5, and 13.5 m away from the wave paddle. A digital camera was positioned 6 m away from the wave tank, and its optical axis was aligned normal to the sidewall. A digital video camera was also set up to record individual waves during the experiments.

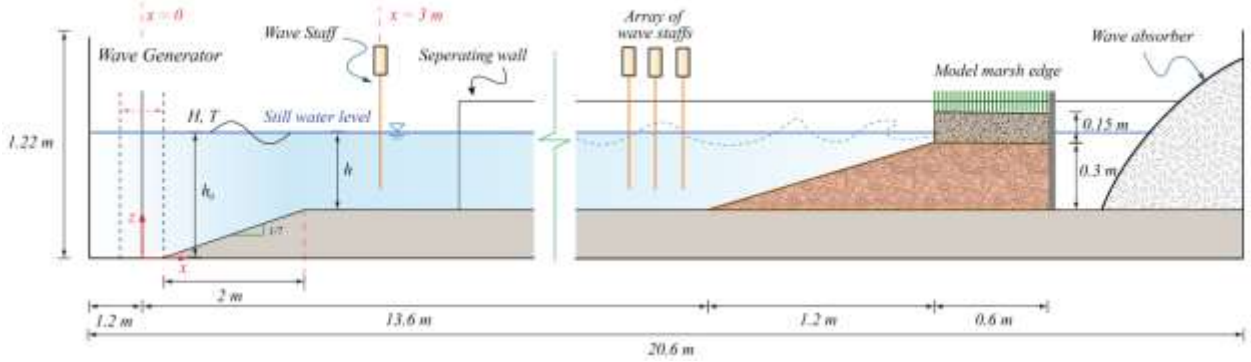

Fig. 5.12. Schematics of the wave tank setup for marsh edge erosion experiments.

Two different marsh edge configurations were tested at the laboratory wave tank. For the first test, a model marsh edge with a vertical front was established. During the first set of experiments, no wave breaking was observed and most of the wave energy was reflected back from the vertical edge. Also, upon removal of the wall supporting model marsh edge, the underlying soil failed to a slope under gravity and wave action. Therefore, for the second test, a sloping beach was constructed in front of the marsh edge. Considering the second test was more realistic, it is reported here.

The model marsh edge was composed of two layers: a layer of packed soil, which was prepared at the laboratory, and the *S. alterniflora* turf, which was collected during the field trips. A mixture of sand, silt, and clay was prepared at the laboratory with the grain size distribution shown in Fig. 5.13. The soil consisted of 40.7% clay, 53.9% silt and 5.4% sand. The prepared soil was packed in the test section in twelve 2.54 cm tick layers. The soil was supported by walls at the ends of the test section. For each layer, the soil mixture was spread evenly along the test section and leveled with an aluminum plate attached to the measurement cart. Then, an aluminum plate was placed on the soil layer and vibration was applied to the aluminum plate for at least 50 s (Fig. 5.14). The density of the packed soil was approximately 1.5 kg/m^3. The marsh edge samples were then placed over the packed soil. The top rhizome layer was 0.15 m thick, and the packed soil layer is 0.3 m thick and had a front slope of 1:4.

The wave tank was filled with fresh water, and the model marsh edge was left for at least two weeks to recover and grow roots under growing lights in the laboratory. The supporting wall on the up-wave end of the test section was removed prior to initiation of the experiments, while the down-wave end of the test section was separated by a vertical supporting wall.

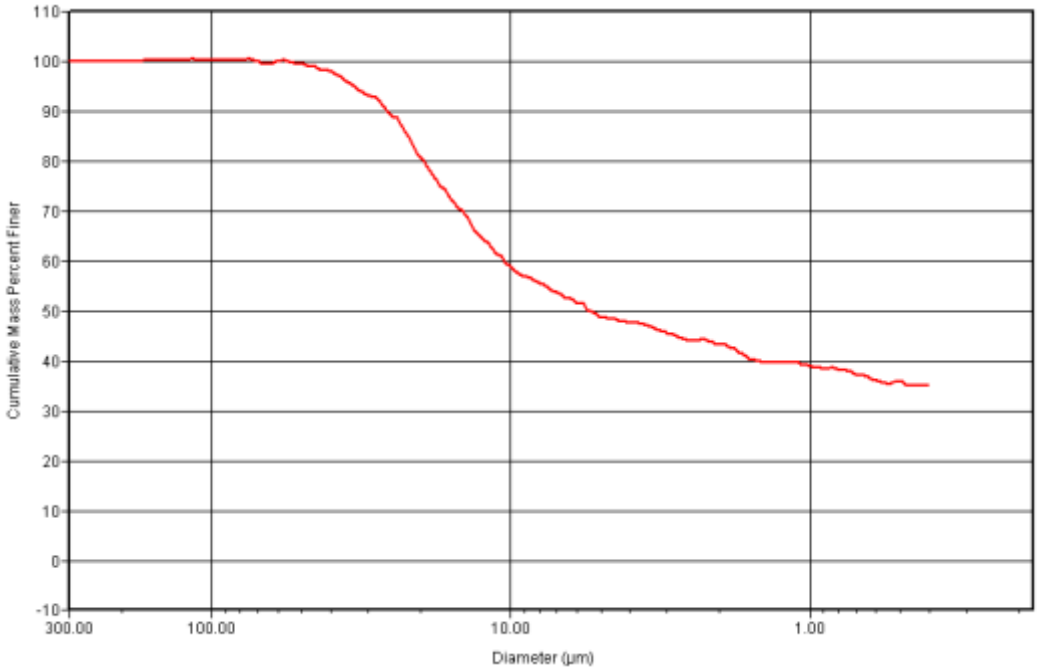

Fig. 5.13. Particle size distribution of the model marsh edge.

5.3.3 Experimental Procedures and Results

The experiment used only regular waves. Waves of H_i = 0.2 m and T = 2.0 s at h = 0.4 m were generated for 60 seconds, and then the wave paddle was stopped until the water surface was still again. This procedure was repeated 12 times. A typical recording at four wave gauges is shown in Fig. 5.15. No significant difference was observed between repeated measurements of water surface displacement during experiments, indicating that the change in beach profile had minor influence on the wave train.

As the waves propagate over a sloping beach, they get steeper and steeper and collapse. This is called shoaling and wave breaking. A large amount of energy is converted to turbulent kinetic energy during wave breaking and transferred to the breach. Some of the wave energy is reflected back during wave breaking depending on the beach profile and morphology. In Fig. 5.16, a single wave breaking over the model marsh edge is shown. The surf similarity parameter, $\xi_0 = (H_0 / L_0)^{-1/2}$ where the subscript "0" indicates deepwater conditions, was approximately 8 and collapsing breaking waves were present. Followed by wave breaking, the waves swashed up the slope and hit the marsh edge. Some of the wave energy was reflected back and interacted with the incident waves. The experiment was divided into a series of 1-minute intervals and the wave paddle was stopped between the intervals, in order to minimize the effects of such reflective waves traveling back and forward between the wave paddle and the marsh edge. Fig. 5.16 also shows that a significant amount of sediment on the beach slope was entrained by wave breaking and swashing. The sediment concentration increased as the wave moved up the slope, as indicated by darker and darker color of the water in the onshore direction.

Fig. 5.17 shows the progress of undercutting and retreat during 10 60-second-runs. Erosion was observed on the upper part of the beach slope in the front of the marsh edge. Undercutting

occurred at the toe of the marsh edge, due to the direct impact of waves and transport of sediment by the offshore waves. The sediment transported by the offshore waves was deposited on the lower part of the beach slope. Erosion and undercutting generated a scour hole at or near the toe of the marsh edge, and the marsh root layer hung over the edge. The experiment period was too short to observe the death of the marsh, but it is expected that the undermined marsh would die and retreat because its soil-root system was damaged by wave impact and the underlying soil was removed. This experiment test demonstrated that undercutting is one of the marsh edge erosion mechanisms.

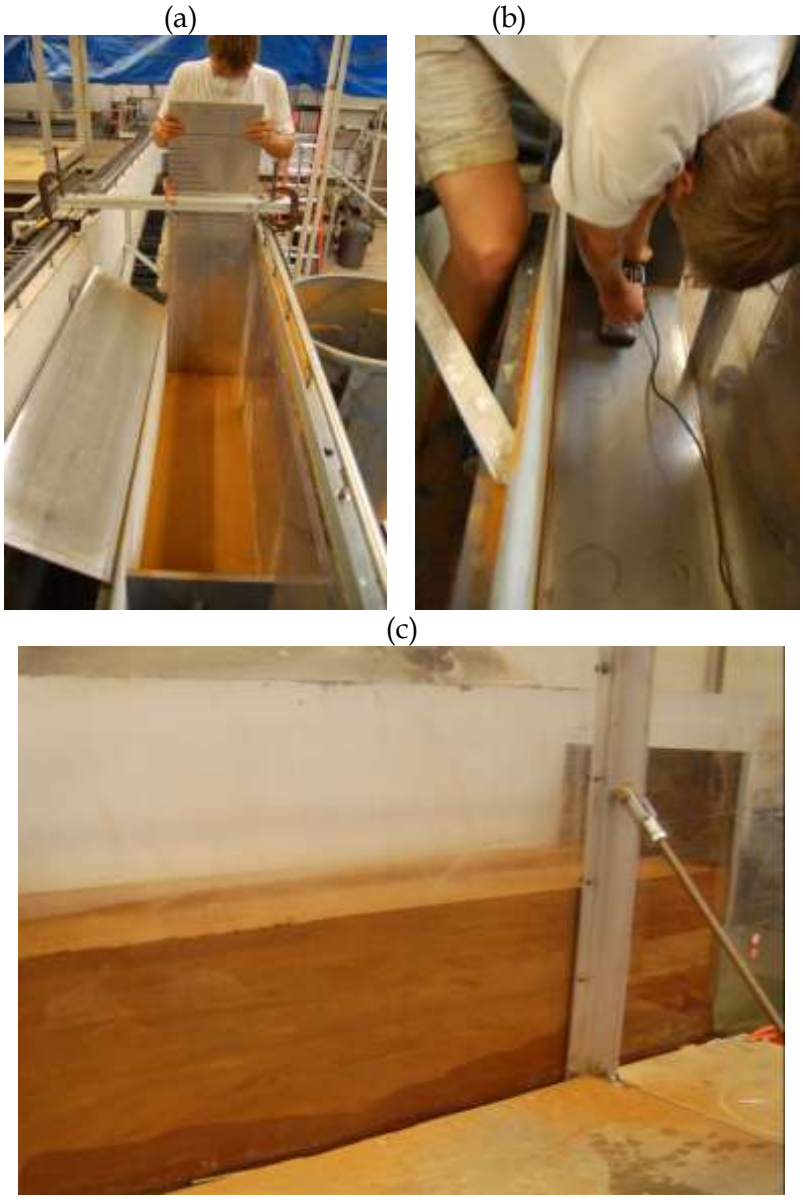

Fig. 5.14. Model marsh edge preparation at the laboratory wave tank: (a) leveling of the soil layer; (b) compaction of the soil layer; and (c) the packed soil.

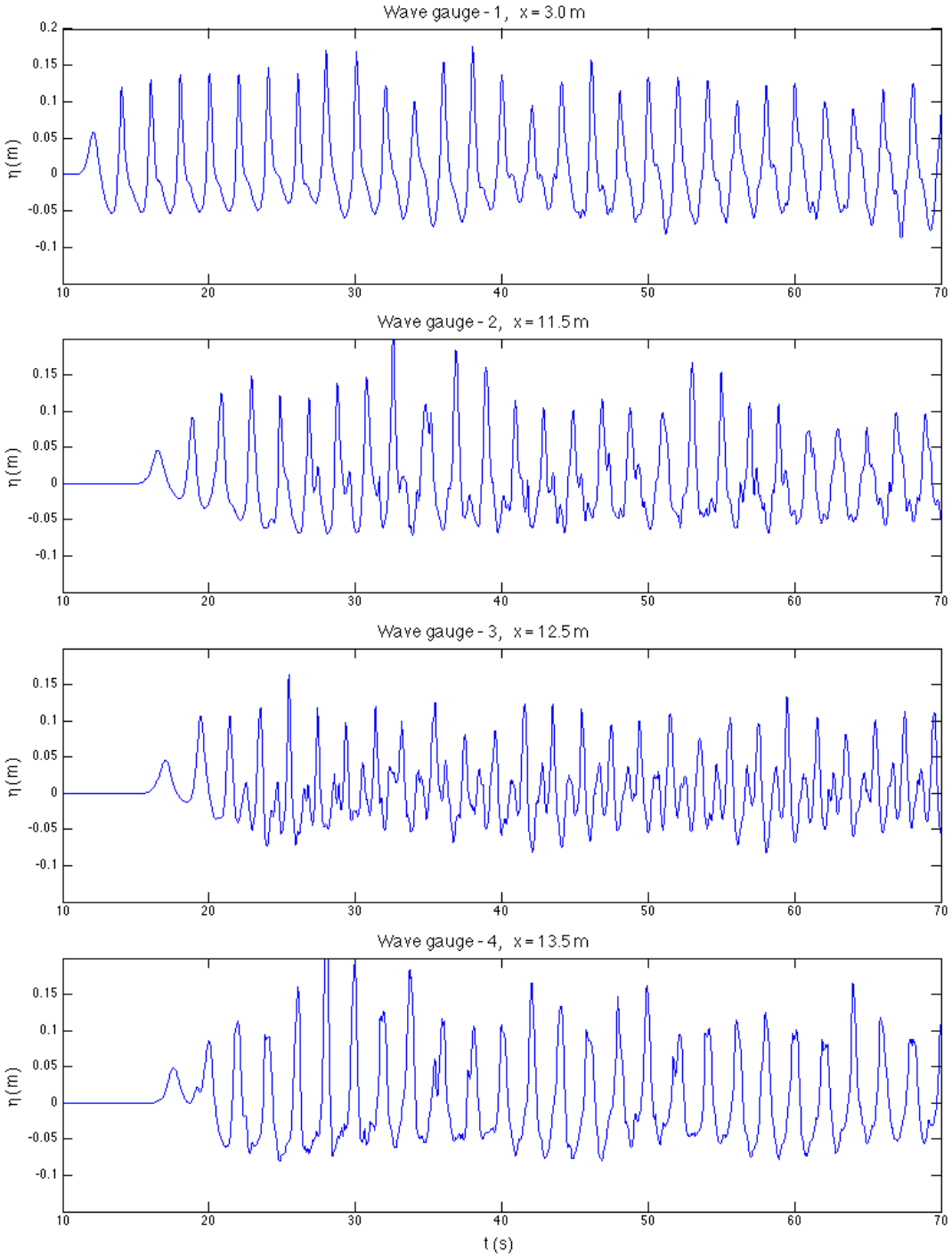

Fig. 5.15. Water surface displacement measurements at four gauges (H_i = 0.2 m, T = 2.0 s and h = 0.4 m).

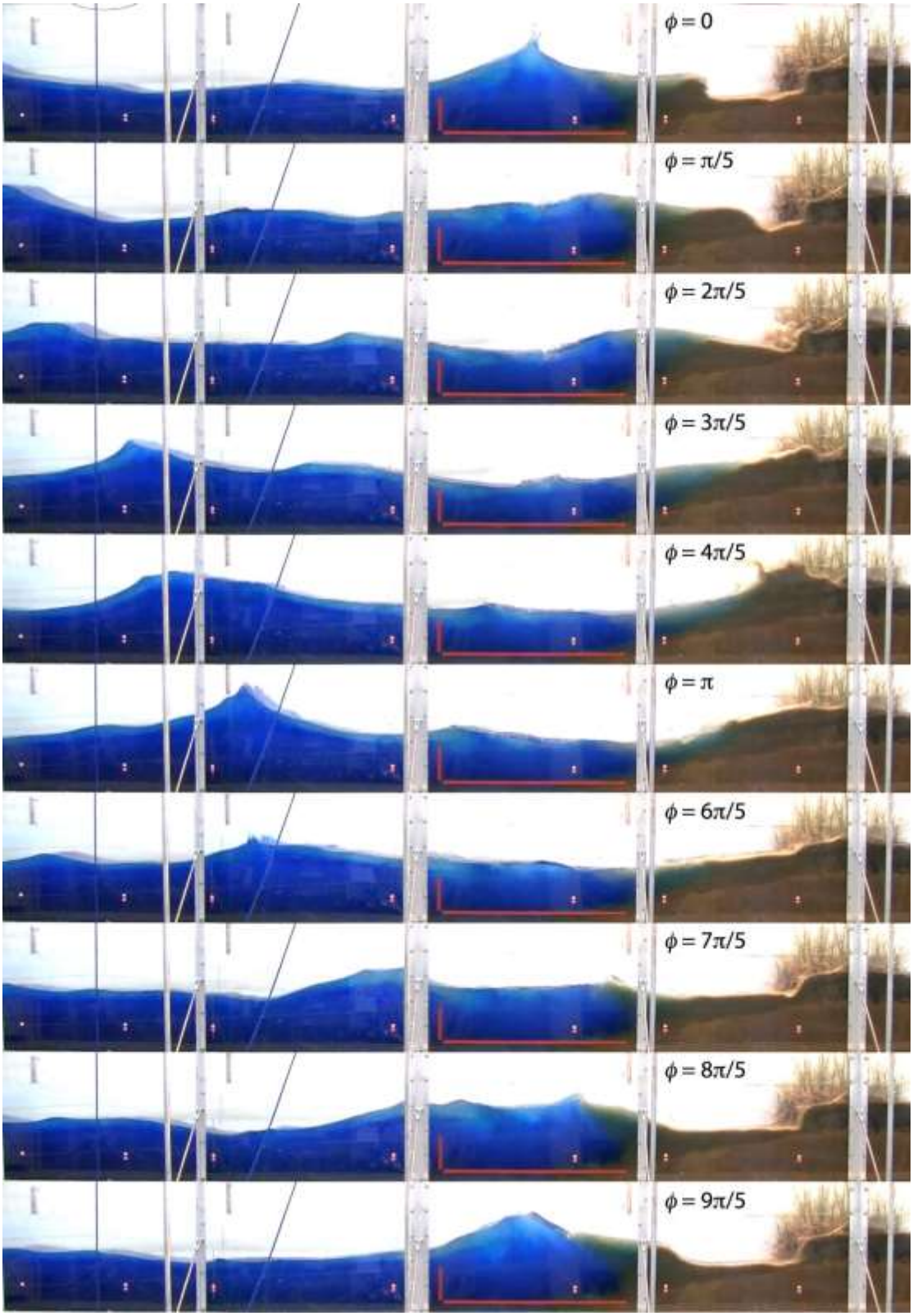

Fig. 5.16. Propagation and breaking of a single wave along the model marsh edge at the laboratory wave tank (h = 0.4 m, H_i = 0.18 m T = 2 s)

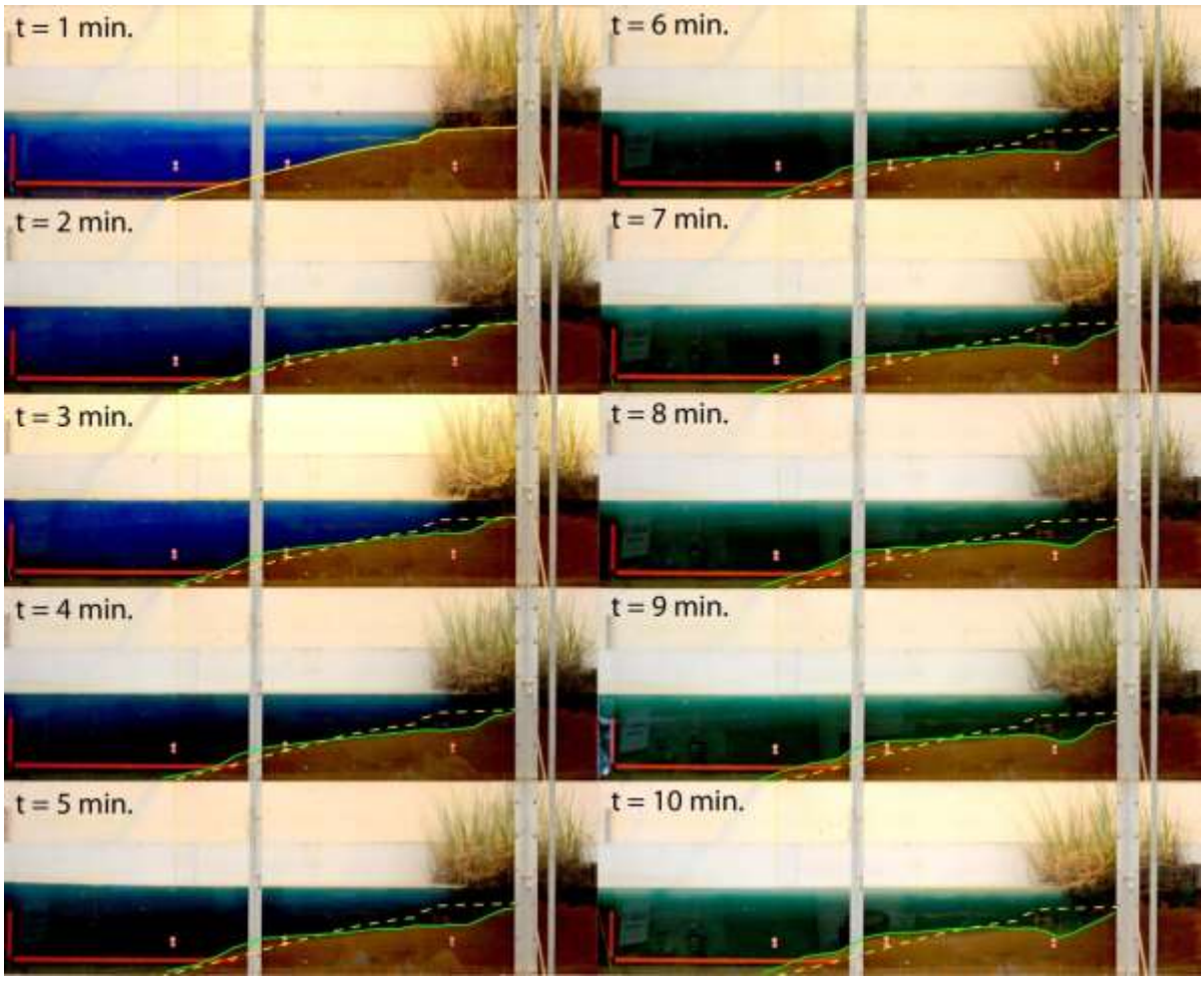

Fig. 5.17. Model marsh edge undercutting and retreat (dashed lines indicate the initial beach profile and solid lines show the deformed beach profiles at different elapsed times; red strips are reference frame)

5.4 Summary

GPS system and aerial photographs were successfully employed to determine the short-term and long-term erosion rates in Terrebonne Bay, a rapidly eroding shallow bay partially protected by barrier islands. Both methods utilized the unique technology and resources available at LSU. The GPS system utilized the LSU GULFNet Real-Time Network that provided accurate GPS data for rapid short-term survey, while the aerial photographs provided a long-term and large spatial coverage.

Directional wave measurements were carried out to quantify the intensity and nature of the wave field. Potential erosion rates were estimated from the measured wave power using methods in the published literature. The rates were found to be comparable with the short term measurements of shoreline retreat obtained from the topographic surveys and long term measurements estimated from the aerial photographs.

A model marsh edge is constructed in the laboratory using the intact marsh edge samples composed of *S. alterniflora* shoots and rhizomes in their native soil that were collected from

Terribonne Bay area. The erosion process under regular wave conditions was measured. Undercutting was observed as the erosion mechanism in the test case. The measured wave and soil conditions and beach profile evolutions are useful to validate numerical models and provide insights into marsh edge retreat due to wave action.

6. COMPUTATIONAL MODELING OF SURGE AND WAVES IN VEGETATED WATERS

In Phase I, four models were selected to demonstrate how to account for the effect of vegetation on surge and waves. The four models include a depth-averaged 2-D shallow water model used for long waves such as tsunami wave propagation, a 1-D Boussinesq-type model primarily used for short waves, a vertical 2-D model based on the Reynolds-averaged Navier-Stokes (RANS) equations with the Volume-of-Fluid (VOF) method which is able to handle both long and short waves, and a wave-action model for wave spectra. In Phase II, the depth-averaged 2-D shallow water flow model was applied to assess the long wave runup reduction by vegetation on a sloping beach and the possible benefits and drawbacks of vegetation in a riverine system. A 3-D shallow water flow model coupled with a 2-D wave action model was added in the demonstration model list and implemented with vegetation effect modeling capability. Presented in this chapter are the depth-averaged 2-D and 3-D shallow water flow models.

6.1 A Depth-Averaged 2-D Shallow Water Model for Breaking and Non-breaking Long Waves Affected by Vegetation

A depth-averaged 2-D shallow water model has been developed to simulate long waves in vegetated water bodies under breaking and non-breaking conditions. The effects of vegetation are modeled in the form of drag and inertia forces as sink terms in the momentum equations. The drag coefficient is treated as a calibrated bulk constant and also determined using two empirical formulas as functions of stem Reynolds number, Froude number, and vegetation volume fraction. The governing equations are solved using an explicit finite-volume method based on rectangular mesh with the HLL approximate Riemann solver with second-order piecewise linear reconstruction for the streamwise convection fluxes, a second-order upwind scheme for the lateral convection fluxes, and a stable centered difference scheme for the water surface gradient terms. The model was tested using several laboratory experiments and then applied to assess the hydrodynamic effectiveness and limitations of vegetation in coastal and river protection. It is shown that vegetation along coastal shoreline has positive benefit in reducing wave runup on sloping beach, whereas vegetation in open channel causes conflicting impacts: reducing inundation in the downstream areas but increasing flood risk in a certain distance upstream.

6.1.1 Introduction

Traditional coastal and river protection typically involved construction of hard structures, such as levees, jetties, breakwaters, spur-dikes and bank revetments. These measures may alter regional and local hydrodynamic and morphodynamic processes and cause unintended ecosystem consequences. The latest trend in coastal and river engineering focuses more and more on sustainable, non-intrusive forms of protection measures, such as wetland and floodplain vegetation. Vegetation can help to dissipate incoming wave energy, regulate water levels, increase bank stability, improve water quality, provide important fish and wildlife habitats, and support recreational activities, whereas vegetation may reduce channel

conveyance capacity. Therefore, it is useful to quantitatively assess the effectiveness and limitations of vegetation in coastal and river protection.

A considerable number of research efforts have been devoted to conduct laboratory experiments and field measurements and develop numerical models to understand and simulate waves through vegetated water bodies. A detailed literature review on such efforts can be found in Wu et al. (2011). The often used modeling approaches include the phase-averaged wave spectral models (e.g., Dalrymple et al. 1984; Mendez and Losada 2004), and phase-resolved models that directly simulate dynamic wave shape deformations using the Navier-Stokes equations (e.g., Naot et al. 1996; Li and Yan 2007), the Boussinesq wave equations (Augustin et al. 2009; Kuiry et al. 2011), or the shallow water equations (e.g., Wolanski et al. 1980; Thuy et al. 2009 & 2010). Normally, the wave spectral models are only for short waves, and the Navier-Stokes equations and Boussinesq wave equations are mainly used for dispersive short waves even though they can be applied to a broader range of waves. The shallow water equations are valid for non-dispersive long waves. For examples, Wolanski et al. (1980), Wu et al. (2001), Wu and Wang (2004), Teo et al. (2009), and Thuy et al. (2010) developed or applied two-dimensional (2-D) shallow water flow models to study the impact of mangroves, coastal forests and instream vegetation on tsunami waves, tidal current and river flow, which are typical long waves. However, these 2-D shallow water models are not designed for wave breaking conditions.

As a long wave approaches shallow water, its wavelength and energy are compressed and its amplitude increases. In this region nonlinearities lead to steepening waves, propagating bores or even breaking waves. Flood waves caused by dam break exhibit steep gradients, mixed flow regimes, and discontinuities. Considering accuracy, wave breaking and dam-break wave front are dispersive, non-hydrostatic and should be simulated using the Navier-Stokes equations with free surface tracking techniques. However, such models are very time-consuming and the wave breaking is only in a small portion of the domain, so that computationally more efficient long wave models widely used in practice are based on the shallow water equations (Brocchini and Dodd 2008). The shallow water models tolerate wave breaking and approximate it as shock moving with estimated speed. To simulate this, shock-capturing schemes, such as approximate Riemann solvers, TVD (Total Variation Diminishing) schemes and discontinuous Galerkin method, are usually required (Toro 2001). Dodd (1998) investigated wave runup, overtopping and regeneration problem using the approximate Riemann solver of Roe (1981) and resolved the moving boundary value problem by imposing a minimum water depth criteria in the dry area. Hu et al. (2000) presented a similar model based on the Harten, Lax and van Leer (HLL) approximate Riemann solver (Harten et al. 1983). Wei et al. (2006) presented a 2-D long wave runup model using an exact Riemann solver. Delis et al. (2008) developed 1-D and 2-D models for propagation, runup and rundown of long surface waves based on Roe's Riemann solver and improved wet/dry algorithm. Brufau et al. (2002), Valiani et al. (2002), Begnudelli and Sanders (2006), Ying and Wang (2008), and Liang and Marche (2009) used approximate Riemann solvers and Schwanenberg and Harms (2004) and Lai and Khan (2012) used discontinuous Galerkin method to solve the shallow water equations for dam-break flows.

In this study, a depth-averaged 2-D shallow water flow model has been developed to simulate the long wave propagation in vegetated water bodies, with the focus on long wave runup over vegetated beaches and dam-break wave in vegetated channels. To handle the breaking and non-breaking cases, the HLL approximate Riemann solver is used within the finite volume method based on rectangular mesh. The model considers the effects of vegetation by

adding the drag and inertia forces in the momentum equations. The governing equations, numerical methods, validations, and applications of the developed model are presented in the following sections.

6.1.2 Model Formulations

6.1.2.1 Governing Equations

Flow through vegetation or other large-scale bed roughness usually is unsteady and turbulent, but the mostly considered flow properties in practice are the time- and space-averaged behaviors rather than the detailed instantaneous flow features around individual vegetation or roughness elements. Nikora et al. (2007) derived the governing equations of free-surface flow through general large-scale bed roughness by double-averaging (in time and space) the Navier-Stokes equations, and Lopez and Garcia (2001) specifically derived such equations for flow through vegetation. Based on the hydrostatic pressure assumption, further depth-averaging the double-averaged 3-D Navier-Stokes equations leads to the shallow water equations for long waves through vegetation. In general, vegetation density (or porosity) appears in the continuity and momentum equations, and the drag and inertia forces of vegetation are included in the momentum equations (Wu 2007). In the case of low vegetation density, the terms related to vegetation density are ignored, so that the depth-averaged 2-D shallow equations with vegetation effects are simplified as

$$\frac{\partial h}{\partial t}+\frac{\partial (Uh)}{\partial x}+\frac{\partial (Vh)}{\partial y}=0 \tag{6.1}$$

$$\frac{\partial}{\partial t}(Uh)+\frac{\partial}{\partial x}\left(U^2h\right)+\frac{\partial}{\partial y}(UVh)=-\frac{1}{\rho}F_x-gh\frac{\partial \eta}{\partial x}+\frac{\partial}{\partial x}\left(\nu_t h\frac{\partial U}{\partial x}\right)+\frac{\partial}{\partial y}\left(\nu_t h\frac{\partial U}{\partial y}\right)-g\frac{n^2 m_b U\bar{U}}{h^{1/3}} \tag{6.2}$$

$$\frac{\partial}{\partial t}(Vh)+\frac{\partial}{\partial x}(UVh)+\frac{\partial}{\partial y}\left(V^2h\right)=-\frac{1}{\rho}F_y-gh\frac{\partial \eta}{\partial y}+\frac{\partial}{\partial x}\left(\nu_t h\frac{\partial V}{\partial x}\right)+\frac{\partial}{\partial y}\left(\nu_t h\frac{\partial V}{\partial y}\right)-g\frac{n^2 m_b V\bar{U}}{h^{1/3}} \tag{6.3}$$

where t is the time, x and y are the horizontal (horizontal and lateral) coordinates, h is the total flow depth, U and V are the flow velocities in x and y directions, $\bar{U}=\sqrt{U^2+V^2}$, η is the water level above the still water, n is the Manning roughness coefficient, g is the gravitational acceleration, F_x and F_y are the components of forces acting on vegetation in x and y directions, ρ is the density of water, ν_t is the turbulent or eddy viscosity, and $m_b=\sqrt{1+\left(\partial z_b/\partial x\right)^2+\left(\partial z_b/\partial y\right)^2}$ considering the bed slope with z_b being the bed level (Wu 2007).

6.1.2.2 Forces on Vegetation

Consider a group of rigid vegetation elements (stems) conceptualized as cylinders, as shown in Fig. 6.1. The forces acting on vegetation include the drag and inertia forces. The drag force is due to viscous effect and form drag around the stems, and the inertia force is due to the acceleration of surrounding fluid. These two forces can be expressed using the Morison equation (Morison et al. 1950):

$$F_i=\frac{1}{2}\rho C_D N_v A_v U_{vi}\sqrt{U_{vj}U_{vj}}+\rho C_M N_v V_v\frac{\partial U_{vi}}{\partial t} \tag{6.4}$$

where U_{vi} is the apparent velocity acting on the vegetation elements in the ith direction, C_D is the drag coefficient, C_M is the inertia coefficient, N_v is the vegetation density defined as number of vegetation elements per unit horizontal (bed) area, A_v is the projected area defined as the frontal area of a vegetation element projected to the plane normal to the stream-wise flow direction, and V_v is the volume of a vegetation element. The first term on the right-hand side of Eq. (6.4) denotes the drag force and the second term denotes the inertia force. The inertia force is usually much smaller than the drag force for vegetation under long waves, but it is still kept in the present model for general application. A constant value of 2.0 is used for C_M in this study.

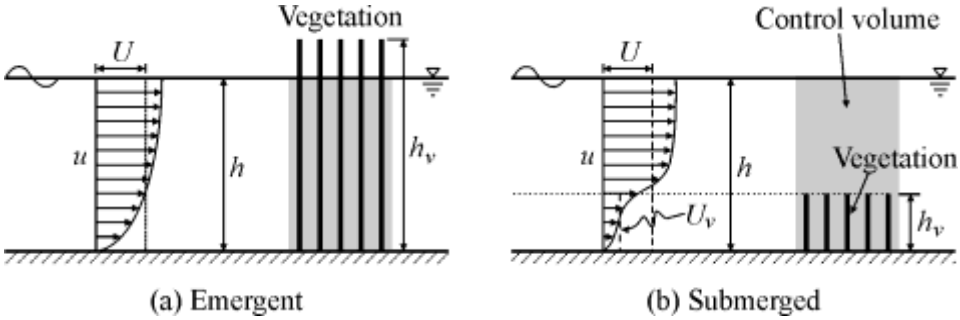

Fig. 6.1. Sketch of emergent and submerged vegetation elements.

The drag coefficient C_D is the key parameter in Eq. (6.4). Petryk and Bosmajan (1975) incorporated the drag force effect into the Manning bed roughness coefficient, but most of the later models separate the drag coefficient from the Manning coefficient. The drag coefficient for a single cylinder in an ideal two-dimensional flow is related to the Reynolds number. Li and Shen (1973) investigated the drag coefficient for a group of cylinders with various setups. They identified four factors that need to be considered to determine the drag coefficient: (1) turbulence of the flow, (2) non-uniform velocity profile, (3) free surface, and (4) blockage. Lindner (1982) suggested that in densely vegetated channels, the first two of these factors are of minor importance and can be neglected. Lindner extended the work of Li and Shen, and established a method to compute the drag coefficient C_D for a single rigid plant in a group. Based on Lindner's approach and further experiments, Pasche and Rouve (1985) presented a semi-empirical iterative process to determine C_D. Bokaian and Geoola (1984) and Nepf (1999) explored the drag of vegetation on steady currents using arrays of rigid cylinders and concluded that the bulk drag coefficient is a function of vegetation density as represented by the occupied fractional volume. Ghisalberti and Nepf (2004) considered the effects of canopy submergence on flow, turbulence and drag. They observed significant reduction in drag relative to the Nepf (1999) expression when the top of the canopy was submerged, attributed to vortex shedding by the free end of the submerged grass blades. Järvelä (2002) suggested the drag coefficient for the leafless willows equal to 1.5 based on his experimental results. Struve et al. (2003) conducted experiments in a laboratory flume and validated the drag coefficient of mangrove trees as 0–4.5.

According to Stone and Shen (2002), the drag coefficient C_{Dm} based on the constricted cross-sectional velocity U_{vmi} is more appropriate than C_D, which is based on the apparent velocity U_{vi}. This is because C_{Dm} is closer to the drag coefficient of single cylinder and has less variation for a wide range of values for vegetation density, stem size, and cylinder Reynolds number in comparison with C_D. C_D is related to C_{Dm} as

$$C_D = C_{Dm} U_{vmi}^2 / U_{vi}^2 \tag{6.5}$$

Because U_{vmi} and U_{vi} are related by $U_{vi} = U_{vmi}(1 - D/l_n)$ based on flow continuity, Eq. (6.5) becomes

$$C_D = C_{Dm}(1 - D/l_n)^2 \tag{6.6}$$

where D is the diameter of vegetation stem and l_n is the lateral spacing of vegetation stems.

Tanino and Nepf (2008) formulated the drag coefficient of emergent rigid circular cylinders based on their experimental data as follows:

$$C_D = 2\left(\frac{\alpha_0}{\mathrm{Re}_p} + \alpha_1\right) \tag{6.7}$$

where Re_p is the cylinder Reynolds number $Re_p = U_{vi}D/\nu$, and a_0 and a_1 are functions of the vegetation volume fraction φ, which is the volume occupied by vegetation over the volume of the water and vegetation mixture and is related to the vegetation density by $\varphi = N_v \pi D^2/4$. Based on a set of experiments, Tanino and Nepf established a linear regression between a_1 and φ as $a_1 = 0.46 + 3.8\varphi$. They also established a graphical relationship between a_0 and φ, from which we derive a linear regression equation as $a_0 = 5 + 313.17\varphi$, with R^2 of 0.80. The data used to develop Eq. (6.7) are in the range $O(30) \le Re_p \le O(700)$.

Kothyari et al. (2009) proposed the following equation for the drag coefficient of emergent rigid cylindrical stems based on a set of fluid force measurements in sub- and supercritical flows:

$$C_D = 1.8\xi \,\mathrm{Re}_p^{-0.06}\left[1 + 0.45\ln(1 + 100\varphi)\right] \times \left(0.8 + 0.2F - 0.15F^2\right) \tag{6.8}$$

where ξ is a constant equal to 0.8, and F is the Froude number.

Eqs. (6.7) and (6.8) were established under steady (or quasi-steady), uniform (or quasi-uniform) flow conditions. Huang et al. (2011) also established a formula for C_D, but it is independent of the stem Reynolds number and valid for only turbulent flow regime. Eqs. (6.7) and (6.8) are selected in this study because the data used to develop them are relatively wide. They are herein assumed to be applicable for unsteady flows and waves with varying stem Reynolds number and Froude number.

Because vegetation may be emergent or submerged, as shown in Fig. 6.1, the projected area and volume of the wetted portion should be used in Eq. (6.4). For emergent vegetation, the acting flow velocity U_{vi} used in Eq. (6.4) is the depth-averaged flow velocity U_i (i.e. U and V). For submerged vegetation, U_{vi} is the velocity averaged over the height of the vegetation layer, as shown in Fig. 6.1. Stone and Shen (2002) and Huthoff et al. (2007) derived analytical relations of U_{vi} in the submerged vegetation layer. In this study the method of Stone and Shen is used to determine U_{vi}:

$$U_{vi} = \eta_v U_i \left(\frac{h_v}{h}\right)^{1/2} \tag{6.9}$$

where h_v is the vegetation height, and η_v is a coefficient whose formulation can be found in Stone and Shen (2002).

6.1.2.3 Turbulence Closure

The often-used turbulence closure models for Eqs. (6.1)–(6.3) with vegetation effects include zero-equation and *k*-ε models (e.g. Lopez and Garcia, 2001; Wu and Wang 2004), as discussed in detail by Wu (2007). Because the *k*-ε model needs improvement to consider wave breaking, the modified mixing-length turbulence model, which is a zero-equation turbulence model, is used to determine the eddy viscosity ν_t (Wu 2007)

$$\nu_t = \sqrt{\left(\alpha_0 U_* h\right)^2 + \left(l_h^2 \left|\bar{S}\right|\right)^2} \tag{6.10}$$

where $\left|\bar{S}\right| = \left[2\left(\partial U/\partial x\right)^2 + 2\left(\partial V/\partial y\right)^2 + \left(\partial U/\partial y + \partial V/\partial x\right)^2\right]^{1/2}$; α_0 is an empirical coefficient, set as $\kappa/6$ with κ being the von Karman constant; U_* is the bed shear velocity; and l_h is the horizontal mixing length, determined by $l_h = \kappa \min\left(c_l h, y\right)$, with y being the distance to the nearest wall and c_l an empirical coefficient. The parameter c_l has values between 0.4–1.2 for common open channel flows (Wu 2007), whereas it is estimated as 0.2–0.3 for the test cases of this study.

6.1.3 Numerical Solution Methods

6.1.3.1 Finite Volume Discretization

Eqs. (6.1)–(6.3) are written in the following vector form:

$$\frac{\partial \mathbf{\Phi}}{\partial t} + \frac{\partial \mathbf{F}\left(\mathbf{\Phi}\right)}{\partial x} + \frac{\partial \mathbf{G}\left(\mathbf{\Phi}\right)}{\partial y} = \mathbf{S}\left(\mathbf{\Phi}\right) \tag{6.11}$$

where $\mathbf{\Phi}$, $\mathbf{F}\left(\mathbf{\Phi}\right)$, and $\mathbf{G}\left(\mathbf{\Phi}\right)$ represent the vectors of unknown variables and fluxes:

$$\mathbf{\Phi} = \begin{bmatrix} h \\ Uh \\ Vh \end{bmatrix}, \quad \mathbf{F}\left(\mathbf{\Phi}\right) = \begin{bmatrix} Uh \\ U^2 h \\ UVh \end{bmatrix}, \quad \mathbf{G}\left(\mathbf{\Phi}\right) = \begin{bmatrix} Vh \\ UVh \\ V^2 h \end{bmatrix} \tag{6.12}$$

and $\mathbf{S}\left(\mathbf{\Phi}\right)$ includes the remaining terms in each equation.

Consider the finite volume mesh shown in Fig. 6.2. Each control volume (cell) is a rectangle embraced by four faces. Non-staggered (collocated) grid system is used. The primary variables *d*, *U,* and *V* are defined at cell centers and represent the average values over each cell, while the fluxes are calculated at cell faces.

Integrating Eq. (6.11) over the (*i*, *j*) control volume, applying the Green theorem, and using the Euler scheme for the time derivative, one can derive the following discretized equation:

$$\mathbf{\Phi}_{i,j}^{n+1} = \mathbf{\Phi}_{i,j}^{n} - \frac{\Delta t}{\Delta x_{i,j}}\left(\mathbf{F}_{i+1/2,j}^{n} - \mathbf{F}_{i-1/2,j}^{n}\right) - \frac{\Delta t}{\Delta y_{i,j}}\left(\mathbf{G}_{i,j+1/2}^{n} - \mathbf{G}_{i,j-1/2}^{n}\right) + \Delta t \mathbf{S}_{i,j} \tag{6.13}$$

where Δt is the time step length, $\Delta x_{i,j}$ and $\Delta y_{i,j}$ are the cell lengths in *x* and *y* directions, $\mathbf{F}_{i+1/2,j}^{n}$ is the flux at face (*i*+1/2, *j*), and $\mathbf{G}_{i,j+1/2}^{n}$ is the flux at face (*i*, *j*+1/2).

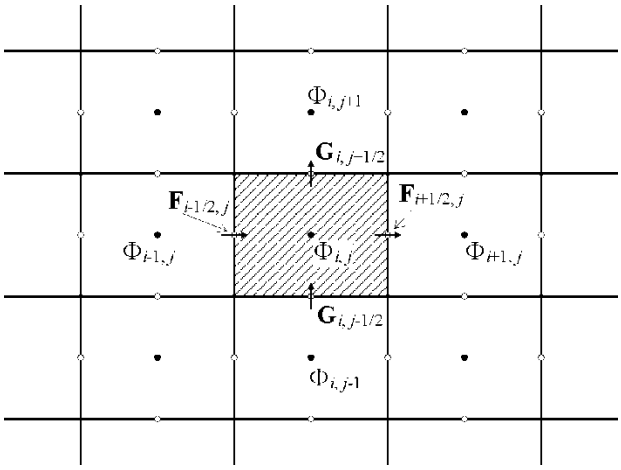

Fig. 6.2. 2-D finite-volume mesh.

The discretized equation (6.13) has first-order accuracy in time, but its accuracy in space is determined by how to approximate the fluxes at cell faces and the source terms. The diffusion terms on the right-hand sides of Eqs. (6.2) and (6.3) are discretized using the central difference scheme at time level *n*. The bed friction and vegetation drag force terms are approximated by a semi-implicit scheme, and the intercell convective fluxes and the water surface gradient terms are approximated by second-order accurate methods, which are described in the next subsections. The present model has an overall accuracy of second order in space.

Because the developed solution procedure is explicit, the computational time step should be limited by the Courant-Friedrichs-Lewy (CFL) stability condition (see Wu 2007).

6.1.3.2 HLL Approximate Riemann Solver and MUSCL Reconstruction

The HLL approximate Riemann solver (Harten et al. 1983) is used to determine the fluid mass and momentum fluxes at cell faces as

$$\mathbf{F}_{\mathrm{HLL}} = \begin{cases} \mathbf{F}_L & \text{if } S_L \geq 0 \\ \dfrac{S_R\mathbf{F}_L - S_L\mathbf{F}_R + S_L S_R\left(\boldsymbol{\Phi}_R - \boldsymbol{\Phi}_L\right)}{S_R - S_L} & \text{if } S_L < 0 < S_R \\ \mathbf{F}_R & \text{if } S_R \leq 0 \end{cases} \tag{6.14}$$

where subscripts *L* and *R* denote the quantities evaluated at the left- and right-hand sides of each cell face, respectively; and S_L and S_R represent the wave speeds, separating constant states of the local Riemann problem solution at cell faces. As suggested by Toro (2001), the wave speeds are estimated as

$$S_L = U_L - a_L\lambda_L, \quad S_R = U_R + a_R\lambda_R \tag{6.15}$$

where U_K (K = L, R) is the velocity, a_K is the wave celerity $\sqrt{gh_K}$, and λ_K is given as

$$\lambda_K = \begin{cases} \sqrt{\dfrac{1}{2}\dfrac{\left(h_* + h_K\right)d_*}{h_K^2}} & \text{if } h_* > h_K \\ 1 & \text{if } h_* \leq h_K \end{cases} \tag{6.16}$$

with h_* being an estimate for the exact solution of h in the star region, evaluated as

$$h_* = \frac{1}{2}(h_L + h_R) - \frac{1}{4}(U_R - U_L)(h_L + h_R)/(a_L + a_R) \tag{6.17}$$

If the left and right fluxes in Eq. (6.14) are determined by setting the intermediate states $\mathbf{\Phi}_L$ and $\mathbf{\Phi}_R$ as the cell-centered values, the scheme has first-order accuracy in space. A second-order accurate approximation can be obtained by reconstructing the left and right states using the Monotonic Upstream Scheme for Conservation Laws (MUSCL) (van Leer 1979). A piecewise linear reconstruction is used, e.g. at face i+1/2,

$$f_L = f_i + \frac{\Delta x_i}{2}\left(\frac{\partial f}{\partial x}\right)_i, \qquad f_R = f_{i+1} - \frac{\Delta x_{i+1}}{2}\left(\frac{\partial f}{\partial x}\right)_{i+1} \tag{6.18}$$

where f is a state variable or flux. The gradient across cell i can be determined using the values in the neighboring cells $i \pm 1$. However, such gradient calculation often results in spurious oscillations in the solution. To eliminate such oscillations, the following slope limiter is used to determine the gradient (Toro 2001):

$$\left(\frac{\partial f}{\partial x}\right)_i = \begin{cases} \max\left[0, \min\left(\beta\Delta_{i-1/2}, \Delta_{i+1/2}\right), \min\left(\Delta_{i-1/2}, \beta\Delta_{i+1/2}\right)\right], & \text{if } \Delta_{i+1/2} > 0 \\ \min\left[0, \max\left(\beta\Delta_{i-1/2}, \Delta_{i+1/2}\right), \max\left(\Delta_{i-1/2}, \beta\Delta_{i+1/2}\right)\right], & \text{if } \Delta_{i+1/2} < 0 \end{cases} \tag{6.19}$$

where $\Delta_{i-1/2} = (f_i - f_{i-1})/(x_i - x_{i-1})$ and $\Delta_{i+1/2} = (f_{i+1} - f_i)/(x_{i+1} - x_i)$. The parameter β =1 reproduces the MINBEE (or MINMOD) flux limiter, and β =2 reproduces the SUPERBEE flux limiter. β =1 is used in this study.

The HLL approximate Riemann solver (14) was derived for the 1-D shallow water problem. Several approaches have been developed in literature to extend it to the 2-D shallow water problem (Toro 2001). These approaches treat the x- and y-direction convection terms as two 1-D Riemann problems and apply the HLL flux in the x- and y-direction convection terms separately. Such treatments may experience strong numerical diffusion. In most dam-break flow cases, the convection terms are dominant and the diffusion terms in Eqs. (6.2) and (6.3) are usually omitted, so that the numerical diffusion does not cause significant errors. However, for general flows, the numerical diffusion may overwhelm the physical diffusion. A hybrid approach is used here to improve the accuracy. The HLL flux is applied to determine only the streamwise convection fluxes, i.e. the x convection flux in the U momentum equation and the y convection flux in the V momentum equation, whereas the lateral convection fluxes, such as the y convection flux in the U momentum equation and the x convection flux in the V momentum equation, are determined using a second-order upwind scheme called HLPA (Hybrid Linear/Parabolic Approach) proposed by Zhu (1991, also see Wu 2007). This hybrid approach can significantly reduce the numerical diffusion in the lateral direction.

6.1.3.3 **Treatment of Water Surface Gradient Term**

In many dam-break flow models the water surface gradient term in the momentum equation is split into the depth gradient and bed slope terms, and the depth gradient term is added to the convection flux term (Toro 2001). To handle an uneven bed, the bed slope term needs to be specially treated; otherwise physically unrealistic flow motions will be generated under still water conditions (Zhou et al. 2001). The recent dam-break flow models of Ying and

Wang (2008) and Lai and Khan (2012) suggest an alternative method, in which the water surface gradient term is treated as a single term on the right-hand side of the momentum equation, as shown in Eqs. (6.2) and (6.3). Even though the eigenvalues change, the single-term approach has been proven to be as efficient as the splitting approach in many case studies of dam-break flow, if the original wave speeds are used in the HLL approximate Riemann solver as expressed in Eq. (6.15). The single-term approach is adopted here to treat the water surface gradient term as

$$gh\frac{\partial \eta}{\partial x} = gh_i^{n+1}\frac{\eta_{i+1/2}^{n+1} - \eta_{i-1/2}^{n+1}}{\Delta x_i} \tag{6.20}$$

where $\eta_{i+1/2}^{n+1} = \left(\eta_{i+1/2,L}^{n+1} + \eta_{i+1/2,R}^{n+1}\right)/2$, with $\eta_{i+1/2,L}^{n+1}$ and $\eta_{i+1/2,R}^{n+1}$ being the left and right water surface elevations at cell face $i+1/2$ determined using the MUSCL reconstruction method expressed in Eq. (6.18). A similar treatment applies to $\eta_{i-1/2}^{n+1}$. Eq. (6.20) has second-order accuracy in space. It is similar to but more stable than the center difference scheme.

Note that the water surface elevation of the new time level (n+1) is used in Eq. (6.20). This is achieved by solving the continuity equation first and then the momentum equations at each time step. This implicit treatment is found to be more stable.

In addition, to handle an uneven bed, the water level rather than the water depth is used for the state variables $\mathbf{\Phi}_L$ and $\mathbf{\Phi}_R$ in Eq. (6.14) when determining the mass flux for solution of the flow continuity equation.

6.1.3.4 **Treatment of Bed Friction and Vegetation Force Terms**

The bed friction term, i.e. the last term on the right-hand side of Eqs. (6.2) and (6.3), is approximated by the following semi-implicit scheme:

$$g\frac{n^2 m_b \bar{U}}{h^{1/3}}(U,V) = g\left(\frac{n^2 m_b \bar{U}}{h^{1/3}}\right)^n \left(U_{i,j}^{n+1}, V_{i,j}^{n+1}\right) \tag{6.21}$$

The drag force, i.e. the first term in Eq. (6.4), can be rewritten in terms of depth-averaged flow velocities U and V by using Eq. (6.9), and then treated semi-implicitly as follows:

$$\frac{1}{2}\rho C_D N_v A_v \frac{h_v}{h}\bar{U}(U,V) = \frac{1}{2}\rho C_D N_v A_v h_v \left(\frac{\bar{U}}{h}\right)^n (U_{i,j}^{n+1}, V_{i,j}^{n+1}) \tag{6.22}$$

The bed friction and drag force terms are moved to the left-hand side of Eq. (6.11) for $U_{i,j}^{n+1}$ and $V_{i,j}^{n+1}$. This semi-implicit scheme is more stable than the fully explicit scheme for these two terms.

The time derivative of velocity in the inertia force term of Eq. (6.4) is discretized using the Euler scheme as used for the time derivative in Eq. (6.13). Thus, the inertia force term can be combined with the temporal terms in the momentum equations (6.2) and (6.3).

The coefficient m_b accounts for the effect of a sloping bed or bank, but it becomes indefinite in the case of a vertical bank. In such a case, the velocity normal to the bank is set as zero, and the bank friction is added with the bed friction by multiplying Eq. (6.21) with a factor of $1+(n_w/n_b)^2 h_b/\Delta y'$. Here, n_w and n_b are Manning's coefficients for bank and bed respectively, h_b is the flow depth at the bank, and $\Delta y'$ is the near-bank grid spacing in the direction normal to the bank line. This factor was derived by determining the bed and bank friction forces using the last

terms in Eqs. (6.2) and (6.3) and considering the flow depth d_b and grid spacing $\Delta y'$ as the corresponding near-bank wetted perimeters which the two friction forces act on.

6.1.3.5 Wetting and Drying Technique

During the long wave propagation over sloping beaches or banks, the water edges change with time and the computational nodes may become wet or dry at different time steps. In the present model, a threshold flow depth (a small value such as 0.0001 m), denoted as d_{tol}, is used to judge drying and wetting. If the flow depth on a node is larger than the threshold value, this node is considered to be wet; otherwise, this node is dry. The dry nodes are assigned zero velocity and the threshold flow depth. At the wet/dry front, if a wet cell's water level is lower than the neighboring dry cell's bed elevation, the water surface gradient across the front is set as zero. This treatment can help to avoid the negative depth caused by pumping of the dry areas.

The HLL approximate Riemann solver usually needs to specially treat the wave speed estimates in Eq. (6.15) at the edge between dry and wet nodes (Valiani et al. 2002; Ying and Wang 2008). However, it is found that Eq. (6.16) can handle the problem at the water edge as well as inside the wet domain.

6.1.4 Model Testing

The developed model is tested using five laboratory experiments, including steady flow in a flume with alternate vegetation zones, solitary wave over a vegetated flat bed, long wave over a partially-vegetated sloping beach, dam-break wave overtopping a barrier, and breaking solitary wave over a sloping beach. The first three cases are used to validate the vegetation effect model. The last two cases do not consider vegetation, but they demonstrate the developed model's capability of simulating dam-break wave in open channels and breaking wave on sloping beaches before the model is applied to assess the effects of vegetation on these waves as presented in the next section.

Case 1: Steady flow in a flume with alternate vegetation zones

Laboratory experiments on steady flow around alternate vegetation zones were performed by Bennett et al. (2002) using a tilting recirculating flume that was 16.5 m long and 0.6 m wide. Six semi-circular vegetation zones with equal spacing of 2.4 m were distributed alternately in the flume to achieve a meandering pattern, as shown in Fig. 6.3. The diameter of each vegetation zone was 0.6 m. The model vegetation was emergent rigid wooden dowels with a diameter of 3.2 mm, laid out in a staggered pattern. In the selected case, the vegetation density was 10% by volume. The flow discharge was 0.0043 m^3/s, and the pre-vegetation initial flow depth was 0.027 m. The slope of the flume was 0.0004. The surface flow velocity was measured using the Particle Image Velocimetry (PIV) technique. The computational mesh consists of 900× 60 nodes, uniformly distributed over the domain. The drag coefficient C_D is set as a bulk constant of 3.0 as used by Wu and Wang (2004), and also determined using the formulas of Tanino and Nepf (2008) and Kothyari et al. (2009) expressed in Eqs. (6.7) and (6.8). The formulated C_D varies in the domain as functions of the local flow conditions and vegetation characteristics, and the average values of C_D calculated by Eqs. (6.7) and (6.8) are 2.3 and 1.8, respectively. The average Re_p is 200, which is in the applicable range of the Tanino and Nepf formula. The coefficient c_l in the mixing-length turbulence model is calibrated as 0.3, and the Manning roughness coefficient n is set as 0.01 $m^{-1/3}s$ for the smooth flume floor. The Manning n

of flume walls is set as 0.007 $m^{-1/3}s$ in this case and kept the same in other test cases in this study considering the flume walls are mostly glassed. The simulation starts from a still water field imposed with a constant flow discharge at the inlet and finishes when a steady flow in the domain is obtained. The computational time step is set as variable according to the CFL stability condition.

Fig. 6.4 compares the measured streamline pattern near the fourth and fifth vegetation zones and the final steady one calculated using the bulk constant C_D of 3.0. Similar flow patterns are obtained using the drag coefficients determined with Eqs. (6.7) and (6.8), but not presented here. It can be seen that the flow was curved due to vegetation zones. Recirculation occurs downstream of each vegetation zone. The locations and sizes of the recirculation eddies observed in the experiment were not stable due to vortex shedding. The sizes of simulated recirculation zones match the small one observed in the experiment. Fig. 6.5 compares the measured and calculated flow velocities along several cross-sections. It should be noted that the measured data are the velocities at water surface taken by PIV, whereas the calculated results are the depth-averaged flow velocities. The qualitative agreement between the simulation and measurement is generally reasonable. The calculation results using three drag coefficients do not differ significantly.

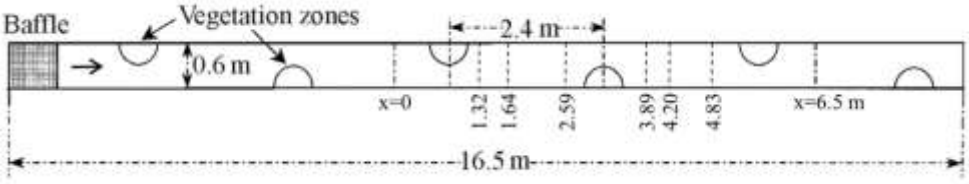

Fig. 6.3. Plan view of experiments of Bennett et al. (2002)

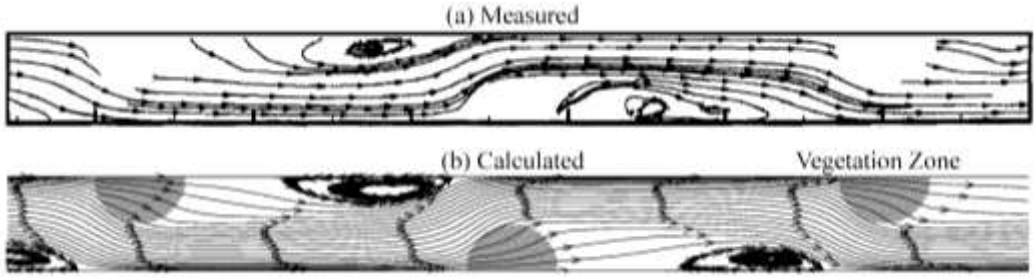

Fig. 6.4. Measured and calculated flow patterns around alternate vegetation zones.

Case 2: Solitary wave on a flat bed with emergent vegetation

Laboratory experiments on solitary wave interaction with emergent rigid vegetation were conducted by Huang et al. (2011) in a 32 m long and 0.55 m wide glass-walled wave flume. The model vegetation was made of Perspex tubes with a uniform outer diameter of 0.01 m, and each vegetation block was 0.545 m in width. Experiments A1 and B2 simulated by the present model had a vegetation volume fraction φ equal to 0.175 with a staggered vegetation distribution pattern and 0.087 with a parallel pattern, respectively. Several resistance-type wave probes were used to record the surface elevations at the selected locations shown in Fig. 6.6. The initial water depth was 0.15 m. The computational domain is represented with a mesh consisting of 3200×25 cells in the longitudinal and lateral directions. The time step is variable and determined using the CFL stability condition. The coefficient c_l in the mixing-length turbulence model is set as 0.3,

which is less important in this 1-D case with negligible horizontal turbulent diffusion of momentum. The Manning coefficient n is estimated as 0.01 $m^{-1/3}s$ for the flume bed. The drag coefficient C_D in experiments A1 and B2 is calibrated as bulk constants of 2.0 and 1.0, respectively. The drag coefficient C_D is also determined using the formulas of Tanino and Nepf (2008) and Kothyari et al. (2009), and the average C_D values calculated by Eqs. (6.7) and (6.8) are 2.6 and 2.2 for experiment A1 and 1.86 and 1.94 for experiment B2, respectively. The average Re_p is 180.

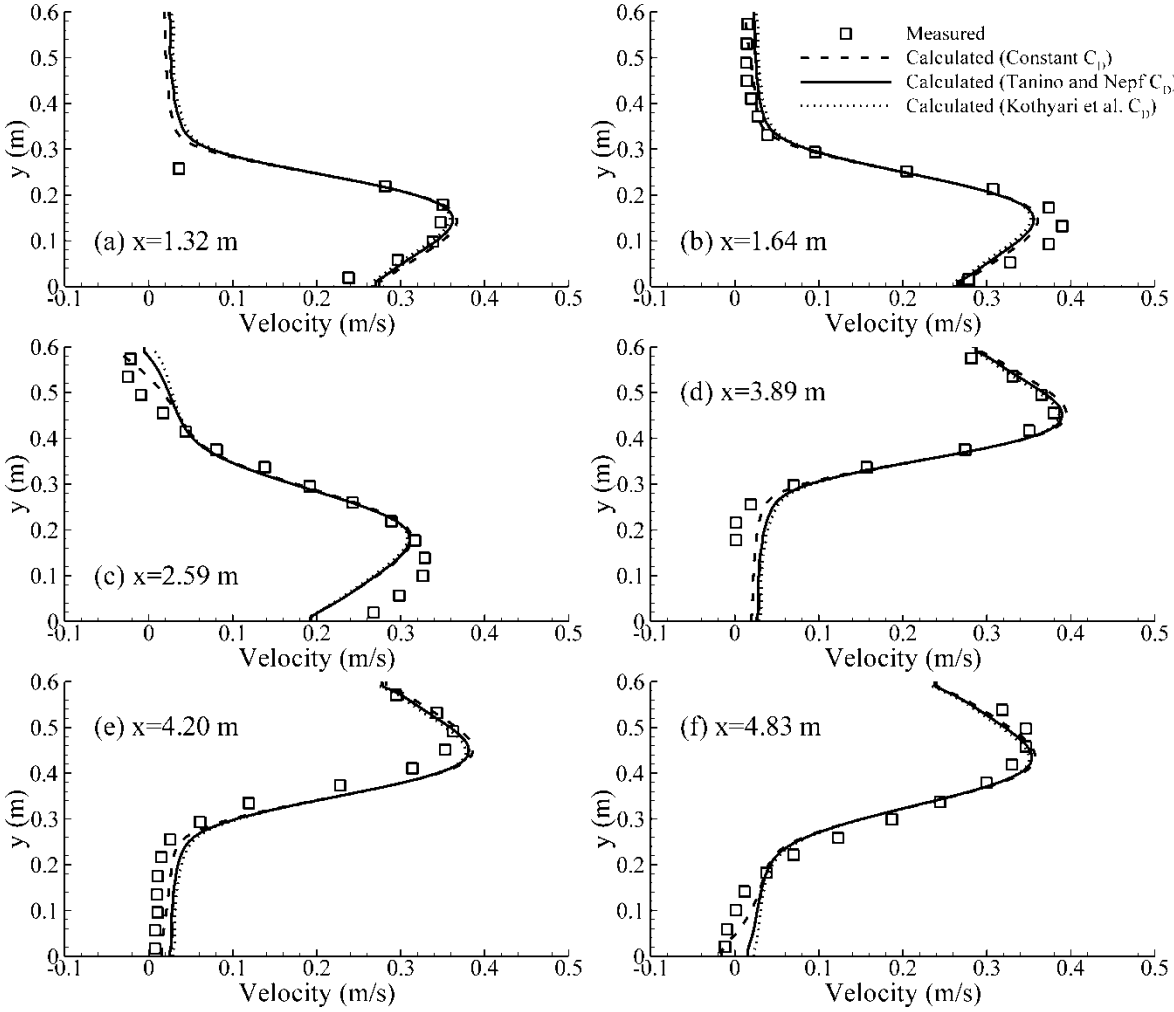

Fig. 6.5. Measured and calculated velocities around alternate vegetation zones (Measurement by Bennett et al. 2002).

Figs. 6.7(a)–(d) indicate that the predicted wave heights in front of the vegetation block, at probe G1, and behind the vegetation block, at probe G5, are in a good agreement with the measured ones for both cases A1 and B2. Similar waveforms are obtained by the model using the calibrated bulk constant C_D and the variable C_D determined with the two formulas. Three methods reproduce well the waves in case A1, whereas the two formulas overdamp the waves in case B2. Note that the simulated transmitted wave has a steeper rising limb and a gentler falling limb, due to the errors of the shallow water equations in cases of short and intermediate waves.

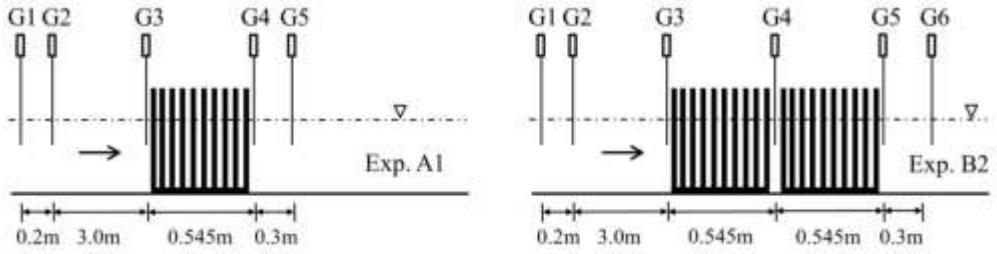

Fig. 6.6. Location of wave probes and vegetation blocks (Huang et al. 2011).

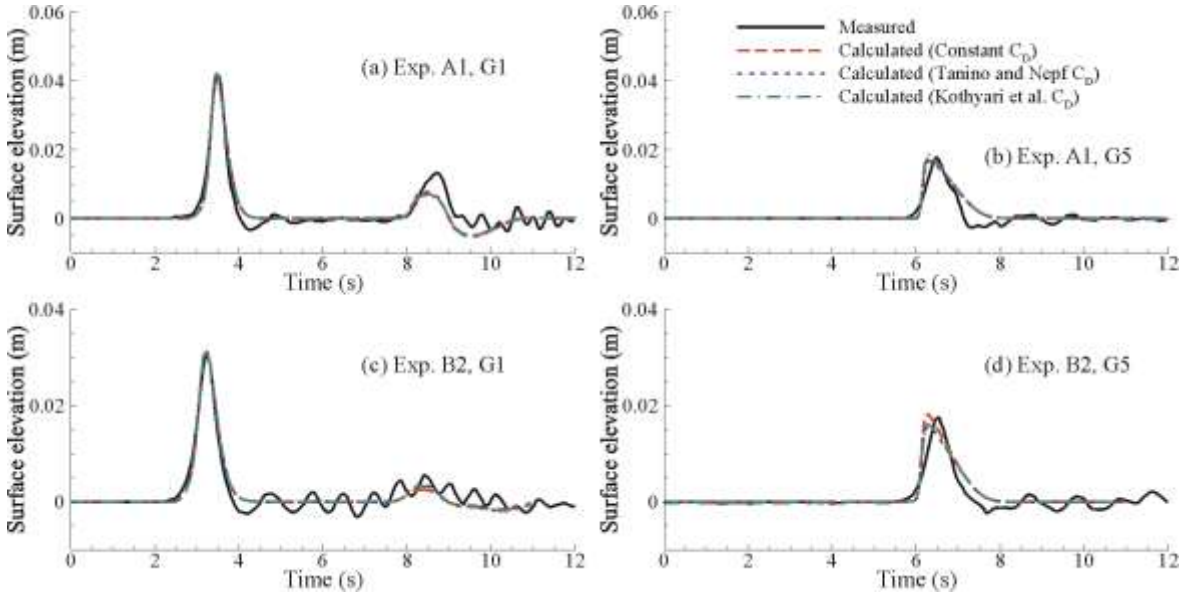

Fig. 6.7. Water surface elevation: (a) incident and reflected waves at G1, experiment A1; (b) transmitted wave at G5, experiment A1; (c) incident and reflected waves at G1, experiment B2; (d) transmitted wave at G5, experiment B2 (Measurement by Huang et al. 2011).

Case 3: Long wave over a partially-vegetated sloping beach

A laboratory experiment of long waves on a partially-vegetated sloping beach was conducted by Thuy et al. (2009 and 2010). The wave flume was 15 m long and 0.4 m wide. The beach profile consisted of segments with various slopes, and the main slope was 1:20.5, as shown in Fig. 6.8. The vegetation zone started at x = 10.36 m and ended at x = 11.36 m, and partially or fully occupied the flume width. The vegetation was modeled with wooden cylinders with a diameter of 5 mm in a staggered arrangement, and the cases with a density of 2,200 units/m2 are considered in the present study. The incident sinusoidal waves with a period of 20 s were generated on the offshore side, and the still water depth was 0.44 m.

The simulation domain is represented with a uniform mesh consisting of 750×40 nodes in longitudinal and lateral directions, respectively. The time step is set by means of a Courant number of 0.25. After trial and error, it is found that an incident wave height of 1.6 cm gives the best fit between measured and calculated results at Gage 1. The drag coefficient C_D is calibrated as a bulk constant of 2.5 and also determined using the formulas of Tanino and Nepf (2008) and Kothyari et al. (2009). The Manning bed roughness coefficient n is set as 0.012 $m^{-1/3}s$ as used by Thuy et al. (2009), and the coefficient c_l in the mixing-length turbulence model is estimated as

0.2. Fig. 6.9 compares the measured and calculated wave characteristics in the case of full-width vegetation with no gap. Figs. 6.10 and 6.11 show the temporal evolutions of measured and calculated velocities at the centers (y = 0.035 and 0.235 m) of gap and vegetation zone and the transverse distributions of maximum velocities along the cross-section at Gage 6 in the case of a 0.07 m wide gap existed. Since the flow dominates in the x direction, the velocity signs (+ and -) in Fig. 6.10 are defined by its longitudinal component. The maximum velocities in Fig. 6.11 are averaged from the maximum velocities of five wave periods at the final developed stage. The comparisons between the calculated and measured velocities indicate that the present model with the formulated drag coefficients underpredicts the flow velocity in the gap zone, but the results in the vegetated zone are accurate.

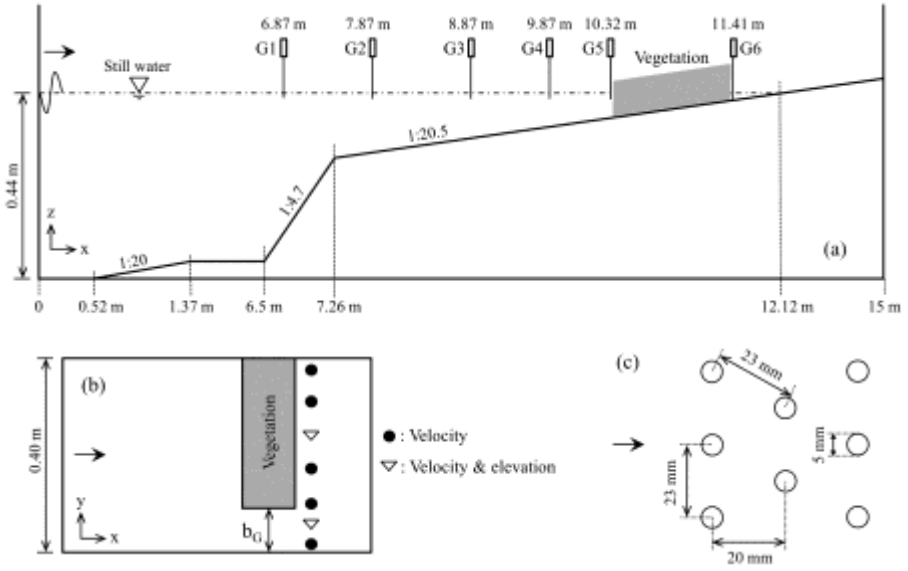

Fig. 6.8. Experimental setup of wave flume: (a) longitudinal section; (b) plan view of vegetation zone and measurement points; and (c) vegetation arrangement (Thuy et al. 2009).

6.1.5 Model Applications

The developed model was applied to simulate long wave runup on vegetated sloping beach and dam-break wave in open channel with vegetated floodplains. Effectiveness and limitations of vegetation in these two typical applications in coastal and river protection are quantitatively assessed.

Reduction of wave runup by vegetation on sloping beach

Before application to assess wave runup reduction by vegetation, the model was tested using experiments of solitary wave runup on a sloping beach conducted by Synolakis (1986). The topography consisted of a plane beach with a slope of 1:19.85 adjacent to a constant depth region, as shown in Fig. 6.12. The initial condition was still water of h=1 m in depth. Solitary waves of various height H were specified at the seaside (left) boundary, but only the experimental run with H/h=0.3 is presented here to demonstrate the developed model's capability of simulating breaking waves. The computational domain is represented by a uniform mesh with the longitudinal grid spacing of 0.02 m. The time step varies according to the CFL stability condition. The threshold water depth for dry bed definition is 0.0001 m. The

Manning's bed roughness coefficient is set as 0.01 $m^{-1/3}s$ for the glassed flume, and the parameter c_l is 0.3, similar to cases 1 and 2.

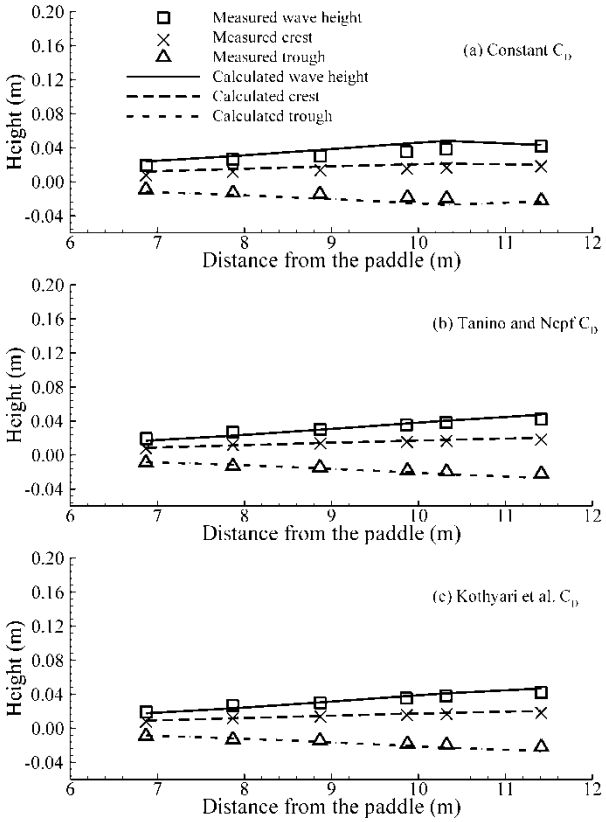

Fig. 6.9. Comparison of measured (Thuy et al. 2009) and calculated wave crests, heights, and troughs (no gap, N_v=2,200 units/m²).

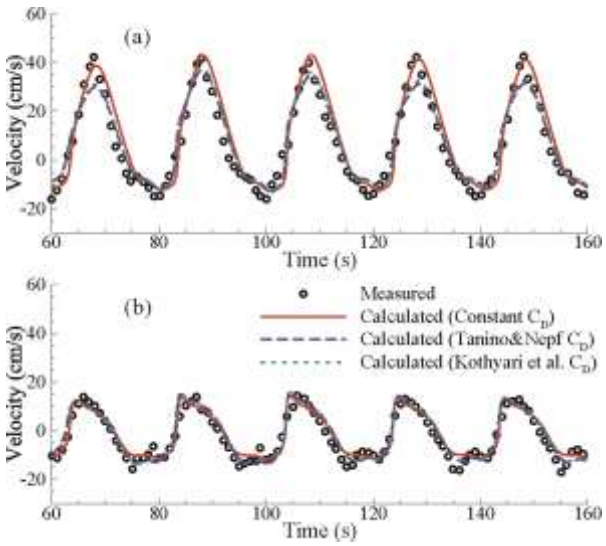

Fig. 6.10. Temporal variations of velocities: (a) at the gap center (y = 0.035 m); and (b) at the vegetation zone center (y = 0.235 m) in cross-section of Gage 6 (N_v=2,200 units/m²).

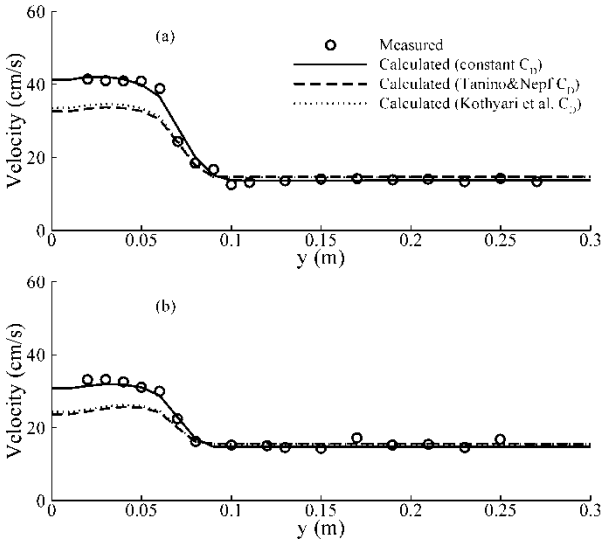

Fig. 6.11. Cross-sectional distributions of maximum velocity at Gage 6: (a) N_v=2,200 units/m²; and (b) N_v=1,000 units/m² (Measurement by Thuy et al. 2010).

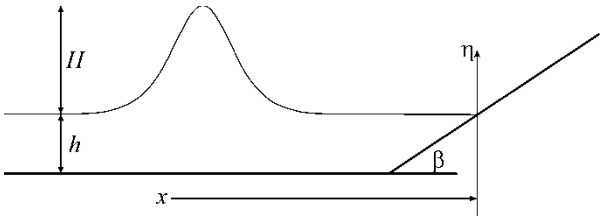

Fig.6.12. Sketch for solitary wave runup on sloping beach.

Figs. 6.13(a)–(e) show the calculated and measured water surface profiles. For convenience, the results are reported in non-dimensional forms: $x^* = x/h$, $\eta^* = \eta/h$, and $t^* = t\sqrt{g/h}$. At the early stage (t^* = 15) shown in Fig. 6.13(a), the wave shoals and its front face becomes a bore type structure. The computed bore is steeper and slightly earlier than the experimental wave, perhaps due to that the wave dispersion effect is not well considered in the shallow water flow equations. Wave breaking is represented by the model as collapse of the bore near the shoreline approximately at t^* = 25. Thereafter, the attenuated wave forms a tongue propagating up the sloping beach as shown in Fig. 6.13(c). After the wave reaches the highest point around t^* = 45, rundown takes place, in which a thin layer of water accelerates down the beach and impacts the wave tail near the still water shoreline. Finally, a hydraulic jump is formed near the shoreline as shown in Fig. 6.13(e). The measured and calculated water surface profiles exhibit discrepancy in the receding period, but the wave propagation, runup and rundown processes are generally well reproduced by the model.

To evaluate wave attenuation on a vegetated sloping beach, case 5 in the previous section is re-calculated by adding vegetation in the beach front from x = -4 to -2 m. The model vegetation is conceptualized from coastal marsh vegetation such as *Spartina alterniflora* (Wu et al. 2011) and has a diameter of 0.01 m but various vegetation densities from 100 to 1,000 units/m². The inertia coefficient C_M is specified as 2.0. Since this hypothetical test does not have any measurement data, the drag coefficient C_D is determined using three methods: Eqs. (6.6)–(6.8). The bulk C_D values for different vegetation densities determined with Eq. (6.6) by assuming C_{dm}=1.0 are

given in the second column of Table 6.1. Figs. 6.14(a)–(h) compare the water surface profiles without and with vegetation effects (N_v = 1,000 units/m²). During t^* = 15 and 20 the wave shoals and the front face becomes steep, but thereafter the wave is partially reflected and the wave height and runup are significantly reduced due to the presence of vegetation.

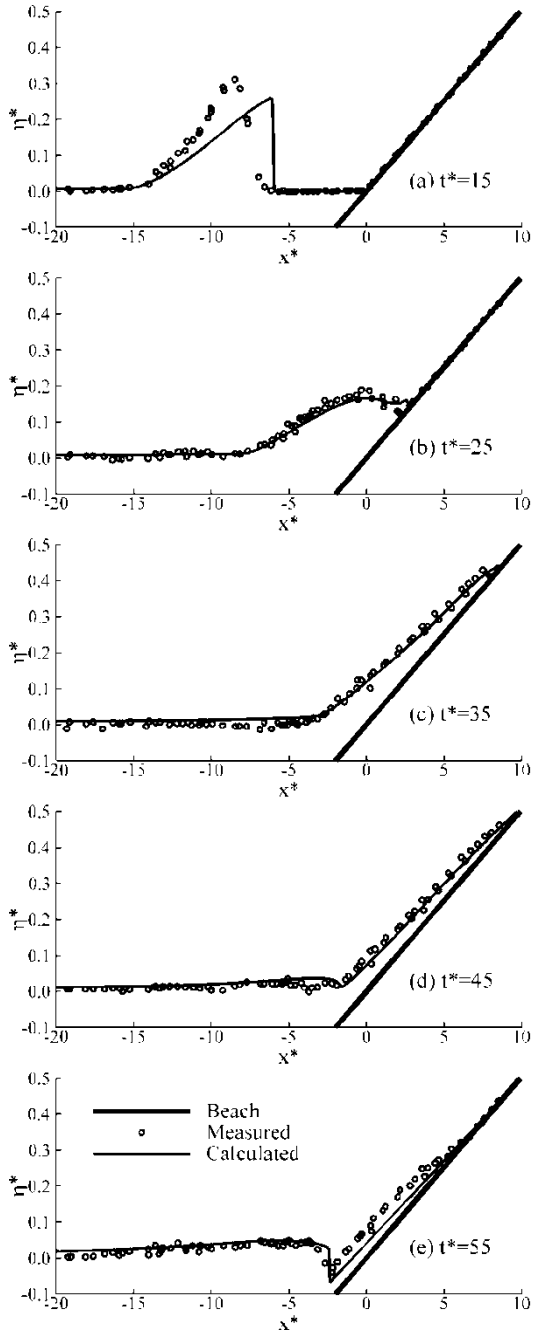

Fig. 6.13. Runup of *H/h* = 0.3 breaking solitary wave on a 1:19.85 sloping beach.

Table 6.1 summarizes the calculated maximum wave runup reductions for various vegetation densities and using three methods for C_D. The results show that the higher the vegetation density, the larger the wave runup reduction. Comparable wave runup reductions

are predicted using the two empirical C_D formulas of Tanino and Nepf (2008) and Kothyari et al. (2009). Certainly, the wave runup reduction may be smaller in reality, because vegetation may be damaged or bended by waves and surge and many other factors also affect the effectiveness of vegetation in wave attenuation.

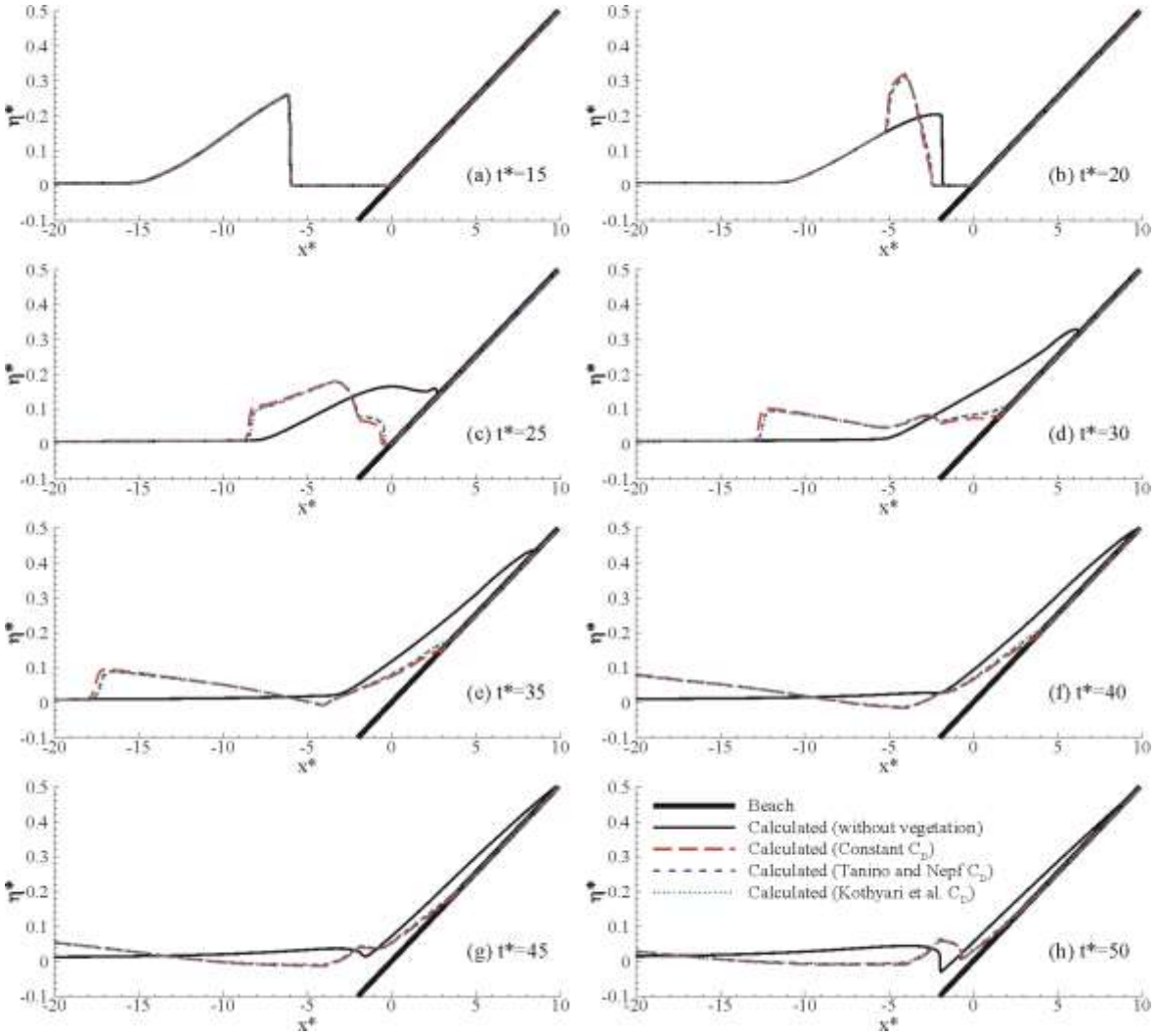

Fig. 6.14. Comparison of calculated runups of H/h = 0.3 breaking solitary wave on a 1:19.85 sloping beach without and with vegetation (N_v = 1,000 units/m²).

Table 6.1. Calculated maximum wave runup reduction on vegetated sloping beach

Vegetation density (units/m²)	Bulk constant C_D	Calculated maximum runup (m)			Calculated runup reduction (%)		
		with Constant C_D	Tanino & Nepf C_D	Kothyari et al. C_D	with Constant C_D	Tanino & Nepf C_D	Kothyari et al. C_D
0	-	10.30	10.30	10.30	-	-	-
100	1.2	8.38	8.64	8.74	19	16	15
250	1.4	6.80	7.24	7.22	34	30	30
500	1.7	5.26	5.84	5.80	49	43	44
1000	2.1	3.74	4.26	4.36	64	59	58

Effects of vegetation on dam-break wave in open channel

The model is applied to a hypothetical case to investigate the effects of floodplain vegetation on the flood inundation level during a dam break event. Fig. 6.15 shows the plan view and cross-section setup of the study channel. The channel is 7,000 m long, and a 5,000 m long reservoir is placed upstream of it. The channel (and reservoir) cross-section consists of a main channel and two symmetric floodplains. The main channel is 100 m wide and has bank slopes of 30 degree. The floodplains are 3 m higher than the main channel bed. The total channel width is 400 m and the longitudinal bed slope is 0.001. The initial reservoir water level is 20 m referenced to the main channel bed in the downstream end, which implies 13 and 8 m water heights above the main channel bed at the dam site and the upper end of the reservoir, respectively. The channel downstream of the dam is dry initially. Forests are placed over the floodplains in a 2,000 m long reach starting 1,000 m downstream of the dam. The type of trees is Ponderosa pine, which is one of the most widely distributed trees in North America, assumed to have a diameter of 1 m and a density of 1 tree per 4 m^2. The computational domain is represented by a mesh of 1,200 and 80 cells in the longitudinal and lateral directions, respectively. The Tanino and Nepf formula is chosen to estimate the drag coefficient, and the Manning roughness coefficient is 0.02 $m^{-1/3}s$. The turbulence model is not used in this application, similar to test case 4. A full-width dam break event is considered, and the time step is set as variable according to the CFL condition.

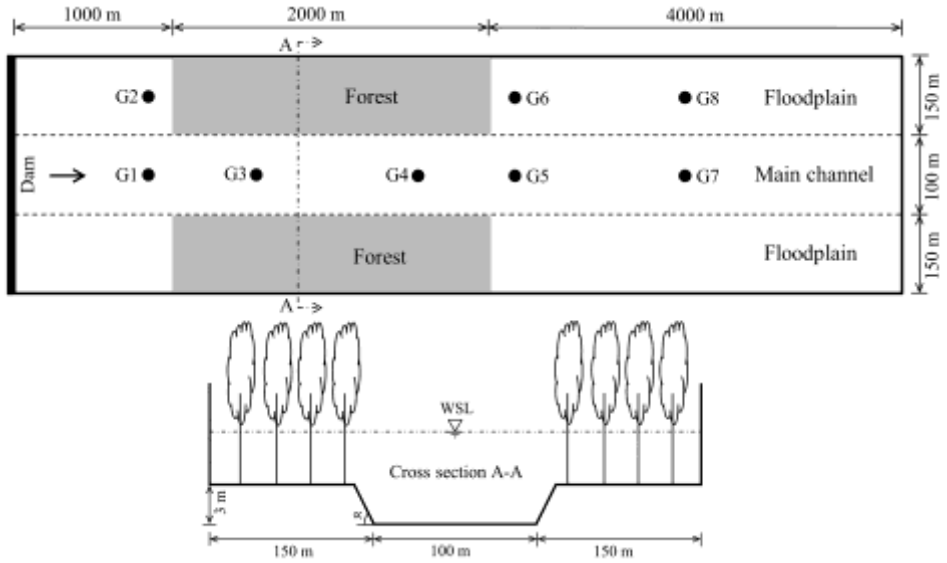

Fig. 6.15. Plan view and cross-section of the channel.

Fig. 6.16 shows the calculated time series of water levels in eight stations. Stations G1, G3, G4, G5, and G7 are located 950, 1500, 2500, 3050, and 5000 m downstream of the dam site, respectively, along the center line of the main channel, while stations G2, G6, and G8 are located 950, 3050, and 5000 m downstream of the dam site, respectively, along the center line of the left floodplain. The results show that the maximum water levels at stations G1 and G2 in the case with the forest are significantly higher than those without the forest, but lower at stations G7 and G8 downstream of the forest. Vegetation on floodplains reduces the inundation risk in the

downstream areas but increases the risk in the upstream certain areas. It is also recognizable that vegetation causes the reach to be drained slower. For instance, station G2 is drained after 60 minutes in the case without forest, but takes about 100 minutes in the case with forest. Therefore, planting vegetation in open channels can be both beneficial and harmful for flood control.

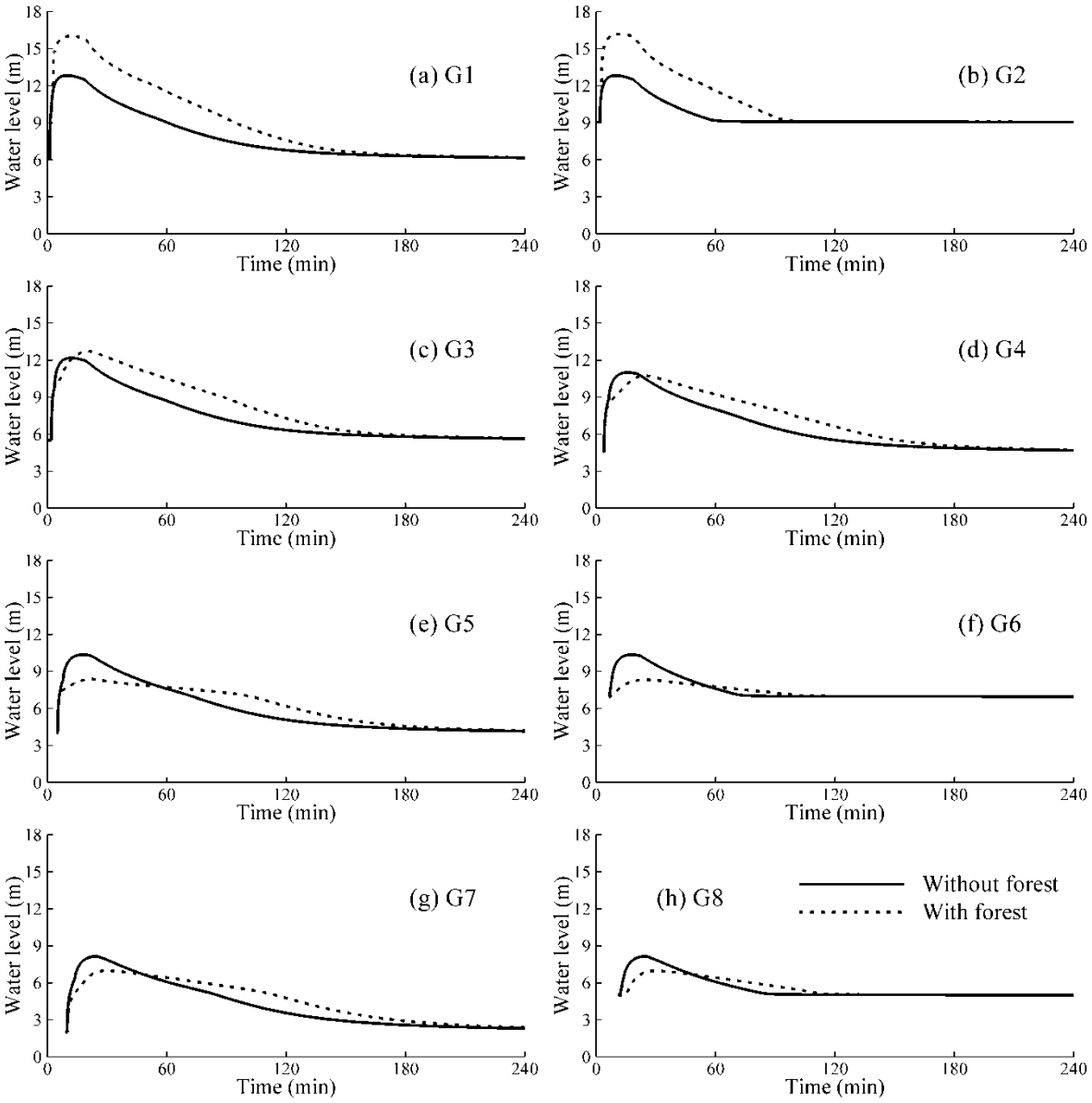

Fig. 6.16. Comparison of calculated time series of water levels at different stations.

6.1.6 Summary

A depth-averaged two-dimensional shallow water model has been developed to simulate the dynamic deformation processes of long waves such as tsunami and dam-break waves in

vegetated water bodies. The effects of vegetation are taken into account by adding the drag and/or inertia forces in the momentum equations. The model adopts an explicit finite-volume method based on rectangular mesh, which is first-order accurate in time and second-order accurate in space. The model uses the Euler scheme to discretize the temporal terms, a stable central difference scheme for the water surface gradient terms, and the central difference scheme for the diffusion fluxes. A novel hybrid approach is established for the convection fluxes at cell faces, which evaluates the streamwise convection fluxes using the HLL approximate Riemann solver with second-order MUSCL reconstruction and the lateral convection fluxes using the second-order upwind scheme HLPA. This hybrid approach can significantly reduce the numerical diffusion in the lateral direction. The drag force and bed resistance terms are treated semi-implicitly for better numerical stability.

The developed model was tested using three sets of laboratory experiments considering vegetation: steady flow around alternate vegetation zones, solitary wave through vegetation zone in a flat-bed flume, and long wave on a partially vegetated sloping beach, as well as two cases without vegetation effects: solitary wave runup on a sloping beach and dam-break wave over a triangular hump. The drag coefficient was calibrated as a bulk constant and also determined using the formulas of Tanino and Nepf (2008) and Kothyari et al. (2009) as functions of stem Reynolds number, Froude number, and vegetation volume fraction. The calculated flow patterns, velocity distributions and wave heights were in good agreement with experimental observations when the calibrated bulk constant drag coefficient was used. The model with the drag coefficient determined using the two formulas provided similar reliable results in the first two cases, but less accurate results in the third case. This indicates that in the absence of measured data one may use these formulas to estimate the drag coefficient, but caution needs to be taken for possible errors. The two cases without vegetation effects demonstrated the developed model is capable of approximately handling breaking waves. The tests also show the wave shape is distorted near the breaking and when the wave is short, due to the limitation of the shallow water model.

The model was then applied to assess the effectiveness and limitations of vegetation in coastal and river protection in the aspect of hydrodynamics. The simulated wave runups on the beach with and without vegetation were compared, showing that it is beneficial to plant vegetation along coastal shoreline to reduce wave runup. However, comparison of the simulated dam-break flows in the open channel with and without vegetation on the floodplains shows that vegetation reduces the flood level in the downstream areas but increases the inundation risk in the upstream certain distance. Thus, planting vegetation on floodplains in open channel may cause conflicting impacts on the upstream and downstream areas.

6.2 A 3-D Phase-Averaged Model for Shallow Water Flow with Waves in Vegetated Water

An implicit 3-D shallow water flow model, called CMS3D (Coastal Modeling System - Three-Dimensional), has been developed to simulate the flow in coastal vegetated waters with short waves. The model adopts the 3-D phase-averaged shallow water flow equations with radiation stresses induced by short waves and vegetation drag and inertia forces. It solves the governing equations using a finite volume method based on quadtree rectangular mesh in the horizontal plane and stretching mesh in the vertical direction. The flow model is coupled with a spectral wave deformation model called CMS-Wave. The wave model solves the spectral wave

action balance equation and provides wave characteristics to the flow model. The model considers the effects of vegetation on current and waves by including the drag and inertia forces of vegetation in the momentum equations and the wave energy loss due to vegetation resistance in the wave action balance equation. The model was tested using several sets of laboratory and field measurement data. The model formulations, numerical solution methods, and model testing are presented in this section.

6.2.1 Introduction

Three-dimensional current and wave features significantly affect the mass transport in coastal surface water systems. Even though many 1-D and depth-averaged 2-D models have been widely used with certain success, realistic simulation of these complex features requires a 3-D model, which can be based on the full 3-D Navier-Stokes equations or the 3-D shallow water equations that are simplified from the Navier-Stokes equations by assuming hydrostatic pressure. Solving the 3-D Navier-Stokes equations to compute the long and short waves or current and waves together in detail is very time-consuming. The often used approach is the phase-averaged model in which only the long wave or current is simulated using a phase-averaged 3-D shallow water flow equations that include the radiation stresses generated by short waves. The short wave characteristics and radiation stresses are determined by a spectral wave model that solves the wave action balance equation. This phase-averaged modeling approach can be much cheaper than the full 3-D model solving the Navier-Stokes equations.

A 3-D phase-averaged shallow water flow model is developed in this study to simulate the current induced by short waves in coastal water. The wave radiation stresses are obtained by coupling with CMS-Wave model which solves the spectral wave action balance equation. The model is also able to account for vegetation effects by adding the drag and inertia forces term in the momentum equations and the wave energy loss due to vegetation resistance in the wave action balance equation. The governing equations are solved using the finite volume method based on non-staggered grid. The SIMPLEC algorithm (van Doormal and Raithby, 1984) and the Rhie and Chow's (1983) momentum interpolation method are used to handle the coupling of water level and velocity. The model uses the sigma coordinate in the vertical direction and the quadtree rectangular mesh on the horizontal plane.

The developed 3-D model and the CMS-Wave model enhanced with the vegetation effect modeling capability are part of the Coastal Modeling System (CMS), which is a official software of the US Army's Corps of Engineers Research and Development Center (ERDC). CMS is a research area of the Coastal Inlets Research Program (CIRP) at ERDC's Coastal and Hydraulics Laboratory, and a coordinated system of 2-D and 3-D numerical models integrated to simulate waves, currents, water level, sediment transport, and morphology change in the coastal zone. Emphasis is on navigation channel performance and sediment exchanges between the inlet and adjacent beaches in the coastal zone. The CMS is verified with field and laboratory data and provided within a user-friendly interface running in the Surface-Water Modeling System (SMS).

The vegetation effect modeling capability has also been implemented in CMS2D model, but it is not described here because of similarity to other depth-averaged 2-D models in the reports. Only mathematical formulations, numerical solution methods and validations of the developed 3-D model coupled with the CMS-Wave model are described below.

6.2.2 Model Formulations

6.2.2.1 3-D Phase-Averaged Shallow Water Flow Equations

The 3-D shallow water equations in the Cartesian coordinate system are written as

$$\frac{\partial u}{\partial x}+\frac{\partial v}{\partial y}+\frac{\partial w}{\partial z}=0 \tag{6.23}$$

$$\begin{aligned}&\frac{\partial u}{\partial t}+\frac{\partial (uu)}{\partial x}+\frac{\partial (vu)}{\partial y}+\frac{\partial (wu)}{\partial z}=-\frac{1}{\rho}\frac{\partial p_a}{\partial x}-\frac{1}{\rho}\left(\rho_0 g\frac{\partial \eta}{\partial x}+g\int_z^\eta \frac{\partial \rho}{\partial x}dz\right)\\&+\frac{\partial}{\partial x}\left(\nu_{tH}\frac{\partial u}{\partial x}\right)+\frac{\partial}{\partial y}\left(\nu_{tH}\frac{\partial u}{\partial y}\right)+\frac{\partial}{\partial z}\left(\nu_{tV}\frac{\partial u}{\partial z}\right)-\frac{1}{\rho}\frac{\partial S_{xx}}{\partial x}-\frac{1}{\rho}\frac{\partial S_{xy}}{\partial y}-\frac{1}{\rho}f_x+f_c v\end{aligned} \tag{6.24}$$

$$\begin{aligned}&\frac{\partial v}{\partial t}+\frac{\partial (uv)}{\partial x}+\frac{\partial (vv)}{\partial y}+\frac{\partial (wv)}{\partial z}=-\frac{1}{\rho}\frac{\partial p_a}{\partial y}-\frac{1}{\rho}\left(\rho_0 g\frac{\partial \eta}{\partial y}+g\int_z^\eta \frac{\partial \rho}{\partial y}dz\right)\\&+\frac{\partial}{\partial x}\left(\nu_{tH}\frac{\partial v}{\partial x}\right)+\frac{\partial}{\partial y}\left(\nu_{tH}\frac{\partial v}{\partial y}\right)+\frac{\partial}{\partial z}\left(\nu_{tV}\frac{\partial v}{\partial z}\right)-\frac{1}{\rho}\frac{\partial S_{yx}}{\partial x}-\frac{1}{\rho}\frac{\partial S_{yy}}{\partial y}-\frac{1}{\rho}f_y-f_c u\end{aligned} \tag{6.25}$$

where t is the time; x and y are the horizontal coordinates; z is the vertical coordinate pointing upward; u, v, and w are the velocities in x-, y-, and z-directions; η is the water surface elevation above the reference (still) sea level; p_a is the atmospheric pressure; g is the gravitational acceleration; ρ is the density of flow; ρ_0 is the flow density at the water surface; S_{xx}, S_{xy}, S_{yx}, and S_{yy} are wave radiation stress terms; f_x and f_y are the forces acting on vegetation in x and y-directions; f_c is the Coriolis force coefficient; and ν_{tH} and ν_{tV} are the eddy viscosities in horizontal and vertical directions.

6.2.2.2 Eddy Viscosity

The vertical eddy viscosity is determined using either of the mixing- length model or parabolic model. The mixing-length model reads

$$\nu_{tV}=l_m^2\left|\bar{S}\right| \tag{6.26}$$

where $\left|\bar{S}\right|=\left[\left(\partial u_i/\partial x_j+\partial u_j/\partial x_i\right)\partial u_i/\partial x_j\right]^{1/2}$, with u_i being the velocity in i-direction (i=1, 2, 3 or x, y, z); and l_m is the mixing length determined by $l_m=\kappa l\sqrt{1-l/h}$, in which l is the distance to the nearest solid wall with a upper limit of $2h/3$, h is the flow depth, and κ is the von Karman constant.

Van Rijn (1984) suggested that the eddy viscosity has a parabolic distribution in the lower half water depth and is constant in the upper half water depth, i.e.

$$\nu_{tV}=\begin{cases}\alpha_\nu \kappa u_* z\left(1-z/h\right) & z<0.5h\\ 0.25\alpha_\nu \kappa u_* h & z\geq 0.5h\end{cases} \tag{6.27}$$

where u_* is the bed shear velocity, and a_ν is an empirical coefficient. a_ν is 1.0 for a 2-D uniform flow, and here set as a calibrated parameter for general situations.

The horizontal eddy viscosity is assumed proportional to the vertical eddy viscosity in the case of current only, i.e. $\nu_{tH}=A_v\nu_{tV}$. Here, A_v is an empirical coefficient and depends on specific cases. When waves appear, the horizontal eddy viscosity includes the effect of waves and wave breaking. A simple linear combination of these contributions is used in this study, as described below:

$$\nu_{tH} = A_v\nu_{tV} + \nu_{tw} + \nu_{tb} \tag{6.28}$$

where ν_{tw} and ν_{tb} are eddy viscosities due to waves and wave breaking, respectively.

Waves contribute significantly to lateral mixing, particularly in the surf zone. The eddy viscosity due to waves is determined using the Kraus and Larson (1991) formula:

$$\nu_{tw} = \Lambda U_{wm} H \tag{6.29}$$

where Λ is an empirical coefficient representing the lateral mixing strength, U_{wm} is the maximum orbital bottom velocity of wave, and H is the wave height.

Wave breaking also generates a significant amount of turbulent eddies in the surf zone. Its contribution to eddy viscosity is determined with

$$\nu_{tb} = k_b \left(\frac{D_b}{\rho} \right)^{1/3} h \tag{6.30}$$

where D_b is the energy dissipation rate due to wave breaking, and k_b is an empirical coefficient.

6.2.2.3 **Forces on Vegetation**

The forces acting on vegetation per unit volume are determined as

$$f_i = \frac{1}{2}\rho C_{D(i)} N_v D_v u_i \sqrt{u_j u_j} + \rho C_M N_v a_v \frac{\partial u_i}{\partial t} \tag{6.31}$$

where D_v is the vegetation stem diameter or width normal to the flow direction, a_v is the horizontal coverage area (or volume per unit height) of the stem, and $C_{D(i)}$ is the drag coefficient in i-th direction. Because the vegetation elements usually stand vertically, the resistance force in the horizontal direction is composed of form drag (pressure gradient force) and skin friction, whereas the resistance force in the vertical direction is due to only skin friction. In the case of high Reynolds number, the form drag is dominant, so that the horizontal resistance is larger than the vertical resistance. Therefore, the drag coefficient $C_{D(i)}$ should be anisotropic and have different values for horizontal and vertical directions. The vertical component is usually much smaller than the horizontal component and thus ignored in this study.

6.2.2.4 **Flow Boundary Conditions**

For Eqs. (6.23)-(6.25), the flow discharge or velocity is needed at inflow boundaries, while the water level is usually given at outflow boundaries for a subcritical flow or at inflow boundaries for a supercritical flow. At the water surface, the free-surface kinematic condition is applied:

$$\frac{\partial \eta}{\partial t} + u_h \frac{\partial \eta}{\partial x} + v_h \frac{\partial \eta}{\partial y} = w_h \tag{6.32}$$

where u_h, v_h, and w_h are the flow velocities at the water surface.

Near rigid wall boundaries, such as beaches and islands, the wall-function approach is employed. By applying the log-law of velocity, the resultant wall shear stress, $\vec{\tau}_w$, is related to the flow velocity, $\vec{V}_P$, at the center, P, of the control volume close to the wall by the following relation:

$$\vec{\tau}_w = -\lambda \vec{V}_P \tag{6.33}$$

where λ is a coefficient determined as $\lambda = \rho u_* \kappa / \ln\left(E y_P^+\right)$ with $y_P^+ = u_* y_P / \nu$, in which y_P is the distance from cell center P to the wall, and E is a coefficient related to wall roughness (Wu, 2007). Since λ is related to u_*, iteration is needed to solve Eq. (6.33).

The bed shear stress can be determined using Eq. (6.33) by treating the bed as a solid wall, or an alternative method as follows:

$$\tau_{bx} = \rho c_f u_b \sqrt{u_b^2 + v_b^2 + 0.5 U_{wm}^2}, \quad \tau_{by} = \rho c_f v_b \sqrt{u_b^2 + v_b^2 + 0.5 U_{wm}^2} \tag{6.34}$$

where τ_{bx} and τ_{bx} are the bed shear stresses in x- and y-directions; u_b and v_b are the x- and y-velocities on the first node above the bed; and c_f is the bed friction coefficient.

6.2.2.5 **Spectral Wave-Action Balance Equation**

The wave model, CMS-Wave, is used here to simulate variations of wave-action density in time, space, wave directions, and frequency. CMS-Wave is a spectral wave transformation model and solves the wave-action balance equation using a forward marching finite difference method (Mase et al. 2005; Lin et al. 2008). CMS-Wave includes physical processes such as wave shoaling, refraction, diffraction, reflection, wave-current interaction, wave breaking, wind wave generation, white capping of waves, and the influence of coastal structures. The vegetation effect is added in this study. The wave-action balance equation of the wave-action density N is written as

$$\frac{\partial N}{\partial t} + \frac{\partial (c_x N)}{\partial x} + \frac{\partial (c_y N)}{\partial y} + \frac{\partial (c_\theta N)}{\partial \theta} = \frac{\kappa}{2\sigma}\left[\frac{\partial}{\partial y}\left(CC_g \cos^2\theta \frac{\partial N}{\partial y}\right) - \frac{1}{2} CC_g \cos^2\theta \frac{\partial^2 N}{\partial y^2}\right] - \varepsilon_b N - Q_v + Q \tag{6.35}$$

where $N = E(x,y,\sigma,\theta,t)/\sigma$; E is the spectral wave density representing the wave energy per unit water surface area per frequency interval; σ is the wave angular frequency (or intrinsic frequency); t is the time; x and y are coordinates in two horizontal directions; θ is the wave angle relative to the positive x-direction; C and C_g are wave celerity and group velocity, respectively; c_x, c_y, and c_θ are the characteristic velocities with respect to x, y and θ, respectively; κ is an empirical coefficient; ε_b is a parameter for wave breaking energy dissipation; Q_v represents the wave energy loss due to vegetation resistance; and Q includes source/sink terms of wave energy due to wind forcing, bottom friction loss, nonlinear wave-wave interaction, etc.

The first term on the left-hand side of Eq. (6.35) represents the local rate of change of action density in time and is dropped in CMS-Wave which considers a steady wave field at each time interval based on a quasi-steady approach. The second and third terms represent propagation of wave action density in a horizontal x-y plane. The fourth term represents depth-induced and current-induced refraction (with propagation velocity c_θ in θ space). The expressions for these propagation speeds are given as

$$c_x = C_g \cos\theta + U$$
$$c_y = C_g \sin\theta + V \tag{6.36}$$

$$c_\theta = \frac{\sigma}{\sinh 2kh}\left(\sin\theta\frac{\partial h}{\partial x} - \cos\theta\frac{\partial h}{\partial y}\right) + \cos\theta\sin\theta\frac{\partial U}{\partial x} - \cos^2\theta\frac{\partial U}{\partial y} + \sin^2\theta\frac{\partial V}{\partial x} - \sin\theta\cos\theta\frac{\partial V}{\partial y} \tag{6.37}$$

where U and V are the depth-averaged velocities in x and y directions, k is the wave number, and h is the water depth.

The first term on the right-hand side of Eq. (6.35), introduced by Mase (2001), represents the energy dissipation due to the diffraction effect in the alongshore y-direction, which is implicitly perpendicular to wave direction. Mase (2001) suggested the coefficient κ has a possible value between 2.0–3.0. The second, third and fourth terms on the right-hand side represent wave energy loss due to wave breaking and vegetation resistance and other sources/sinks of wave energy.

6.2.2.6 **Wave Energy Loss due to Vegetation Resistance**

Based on the linear wave theory and an assumption of impermeable bottom proposed by Dalrymple et al. (1984), Mendez and Losada (2004) established a relationship between the wave energy loss and vegetation parameters in the case of random waves that are assumed to have the Rayleigh probability density distribution function (Thornton and Guza 1983) as follows:

$$Q_v = \frac{1}{\sigma 2\sqrt{\pi}}\rho C_{Dw} b_v N_v \left(\frac{kg}{2\sigma}\right)^3 \frac{\sinh^3(kh_v) + 3\sinh(kh_v)}{3k\cosh^3(kh)} H_{rms}^3 \tag{6.38}$$

where ρ is the water density (kg/m^3), b_v is the plant area per unit height of each vegetation stand normal to horizontal velocity (m), C_{Dw} is the drag coefficient of vegetation under waves, h_v is the vegetation height, and H_{rms} is the root-mean-square wave height (m).

Eq. (6.38) was derived in the case without current. When current and waves coexist, the interaction between current and waves leads to more complex situations. The total energy loss due to vegetation resistance, Q_{tv}, is then expressed as

$$Q_{tv} = \frac{1}{T}\int_0^T\int_0^{h_v} F_i u_i dz dt \approx \frac{1}{T}\int_0^T\int_0^{h_v} F_x u dz dt = \frac{1}{T}\int_0^T\int_0^{h_v}\frac{1}{2}\rho C_D a_v u^3 dz dt \tag{6.39}$$

Since $u=u_c+u_w$, where u_c is the current velocity and u_w is the wave velocity, one can have $u^3=u_c^3+3u_c^2u_w+3u_cu_w^2+u_w^3$, and then the following relation:

$$Q_{tv} = \frac{1}{T}\int_0^T\int_0^{h_v}\frac{1}{2}\rho C_D a_v u_c^3 dz dt + \frac{1}{T}\int_0^T\int_0^{h_v}\frac{3}{2}\rho C_D a_v u_c u_w^2 dz dt + \frac{1}{T}\int_0^T\int_0^{h_v}\frac{1}{2}\rho C_D a_v u_w^3 dz dt \tag{6.40}$$

The first and last terms on the right-hand side of Eq. (6.40) represent the energy loss due to current and waves acting on vegetation, respectively, whereas the second term is energy loss related to the interaction of waves and currents. If the current velocity is zero, the last term leads to Eq. (6.38) as derived by Mendez and Losada (2004). In the present phase-averaged model, the first term in Eq. (6.40) is taken into account through the vegetation drag force term in the momentum equations (6.24) and (6.25), whereas the last term in Eq. (6.40) is considered through the Q_v term in the wave action balance equation (6.35). The second term can be split into two parts corresponding to current and waves and is modeled by modifying the drag force term in Eq. (6.24)-(6.25) and the Q_v term in Eq. (6.35). Modification of the drag force term can be

done by recalibrating the drag coefficient C_D under current and waves coexisting conditions. Modification of the Q_v term in Eq. (6.35) can be achieved by using the same drag coefficient C_D under current and waves coexisting conditions as the flow model and introducing a correction factor ϕ in Eq. (6.38) as

$$Q_v = \frac{1}{\sigma 2\sqrt{\pi}} \rho C_D \phi b_v N_v \left(\frac{kg}{2\sigma}\right)^3 \frac{\sinh^3(kh_v) + 3\sinh(kh_v)}{3k\cosh^3(kh)} H_{rms}^3 \tag{6.41}$$

Based on Li and Yan's (2007) measurement data and numerical results shown in Fig. 6.17, the correction function ϕ can be approximated as

$$\phi = 1 + a\left(\frac{U_c}{U_{wm}}\right)^m \tag{6.42}$$

where U_c is the current velocity magnitude, and U_{wm} is the maximum orbital bottom velocity of wave. m=1.25 and a=0.63, which are approximated using Li and Yan's (2007) data.

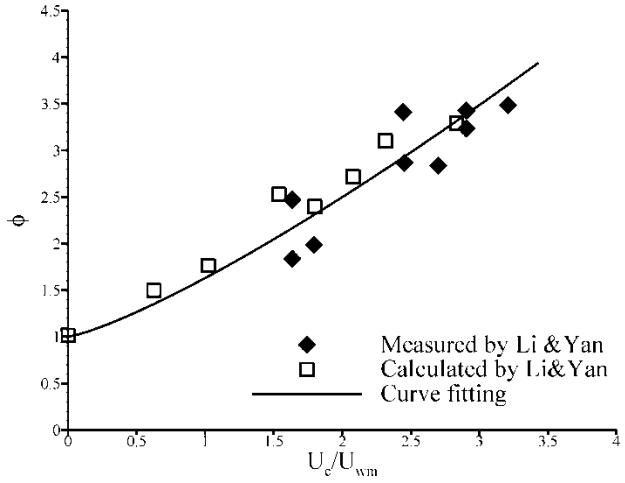

Fig. 6.17. Wave energy attenuation as function of current-waves velocity magnitude ratio (Data courtesy to Li and Yan, 2007).

Because the random wave energy can be defined as $E = \frac{1}{8}\rho g H_{rms}^2$, the Q_v term can be written as the local linear form of the wave action density, i.e., $Q_v = \varepsilon_v N$, in which ε_v is given as

$$\varepsilon_v = \frac{4}{g\sqrt{\pi}} C_D \phi b_v N_v \left(\frac{kg}{2\sigma}\right)^3 \frac{\sinh^3(kh_v) + 3\sinh(kh_v)}{3k\cosh^3(kh)} H_{rms} \tag{6.43}$$

6.2.2.7 **Wave Radiation Stress**

The wave radiation stresses are calculated using the formula of Mellor (2008):

$$S_{ij} = \int_0^\infty \int_{-\pi}^{\pi} \left\{ k(f)E(f,\theta)\left[\frac{k_i(f)k_j(f)}{k(f)^2}\frac{\cosh^2 k(h+z')}{\sinh kD\cosh kD} - \delta_{ij}\frac{\sinh^2 k(h+z')}{\sinh kD\cosh kD}\right] + \delta_{ij}E_D(f,\theta)\right\} d\theta df \tag{6.44}$$

where E is the wave energy, k is the wave number, θ is the angle of wave propagation to the onshore direction, f is the wave frequency, h is the still water depth, D is the total water depth, z' is the vertical coordinate referred to the still water level, and E_D is a modified Dirac delta function which is 0 if $z \neq \eta$ and has the following quantity:

$$\int_{-h}^{\eta+} E_D = E/2 \tag{6.45}$$

6.2.3 Numerical Solution Methods

6.2.3.1 Computational Mesh and Data Structure

To handle the complex computational domain, grid flexibility is often an issue in numerical modeling of surface water flows. A simple rectangular mesh is hard to conform to the irregular boundaries and locally refine the mesh around the structures or high-gradient regions. A structured quadrilateral (curvilinear) grid can serve this purpose by stretching or shrinking the mesh lines, but it is less flexible for a very large, complex domain than the triangular mesh. On the other hand, the rectangular or quadrilateral mesh is more convenient than the triangular mesh for establishing high-order (e.g., second and third) schemes or for discretizing second or higher order spatial derivatives. Therefore, quadtree rectangular or quadrilateral mesh has been recently used for local refinement of computational mesh (Ferziger and Peric, 1995; Nabi, 2008; Wu et al., 2011). On the quadtree mesh, a coarse cell is split into four child cells, and as many levels of refinement as necessary can be used.

The present model uses the multiple-level quadtree rectangular mesh on the horizontal plane and the sigma coordinate in the vertical direction. An example of the mesh is shown in Fig. 6.18. The horizontal quadtree mesh system is exactly the same as that used in the CMS2D model (Wu et al., 2011). For simplifying the mesh, a cell is refined by splitting into four equal child cells on the horizontal plane. Corresponding to this refining, any cell has one or two faces on each of its south, north, west, and east sides. For further simplification, we eliminate those isolated single refined or coarse cells. This means that a cell should be refined if all of its adjacent cells on either x or y direction are refined, and on the other hand, a cell should not be refined if all of its adjacent cells are not refined. Through this handling, each cell has only four to six faces even though its each side may have one or two faces, as shown in Figs. 6.18 and 6.19, so that the computational mesh will be less complicated. Fig. 6.19 shows the connectivity of the mesh on the horizontal plane. The 3-D cell includes a face on each of the top and bottom sides.

In combination with the vertical sigma coordinate, the nodes on the quadtree mesh at all horizontal layers are numbered in a fully unstructured approach, in which all cells are numbered in a one-dimensional sequence and pointers are used to determine the connectivity of neighboring cells for each cell. In addition, in order to take advantage of the CMS2D model's Graphical User Interface (GUI) for pre- and post-processing, the developed 3-D model also uses the numbering system of the CMS2D model on the horizontal plane and numbers the nodes in each vertical line with an index. This means the 3-D model also has a two-dimensional numbering system. The global one-dimensional index and the two-dimensional numbering system can be converted.

One may use staggered or non-staggered approach to arrange the primary variables u, v, w and η. The staggered approach uses a different grid system for each of these variables, while the non-staggered grid uses only one grid system for all of them. The 3-D shallow water equations inherit the weakness of the Navier-Stokes equations, in which the velocity is linked to the

pressure (water level) gradient by the momentum equations but not the continuity equation. The continuity equation is just an additional constraint on the velocity field without directly linking to the pressure. Because of such a weak linkage, potential checkerboard oscillations may appear when the linear interpolation method is used with non-staggered (collocated) grid arrangement (Patankar, 1980). Staggered grid arrangement, often used with MAC (Marker and Cell) method (Harlow and Welch, 1965), projection method (Chorin, 1968), SIMPLE (Semi-Implicit Method for Pressure-Linked Equations) algorithm (Patankar and Spalding, 1972) and SIMPLEC (SIMPLE Consistent) algorithm (van Doormal and Raithby, 1984), can eliminate the potential oscillations, but it is convenient only in simple rectangular mesh system (Casulli and Cheng, 1992). Since successful application of the Rhie and Chow's (1983) momentum interpolation method to eliminate the potential checkerboard oscillations, non-staggered grid has been used more and more in 3-D models, especially in curvilinear or other complicated meshes (Wu et al., 2000; Wu, 2007). Considering the staggered approach is more complicated than the non-staggered approach near the interface between coarse and fine meshes, as shown in Fig. 6.19, the non-staggered grid is used in this study. All the primary variables are arranged at cell centers, and the fluxes are stored at cell faces.

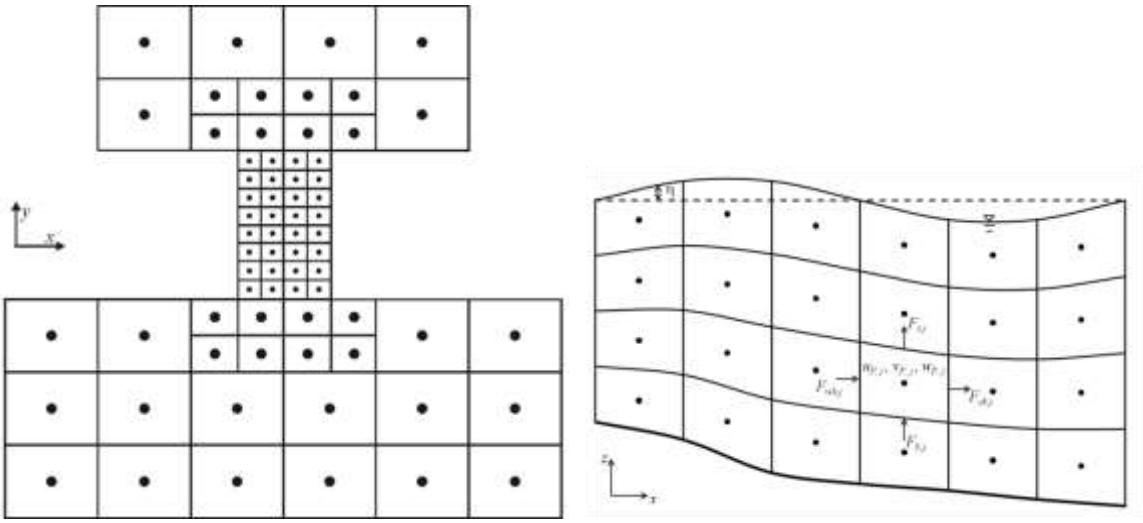

Fig. 6.18. Example of the mesh: (left) horizontal quadtree mesh and (right) vertical sigma coordinate.

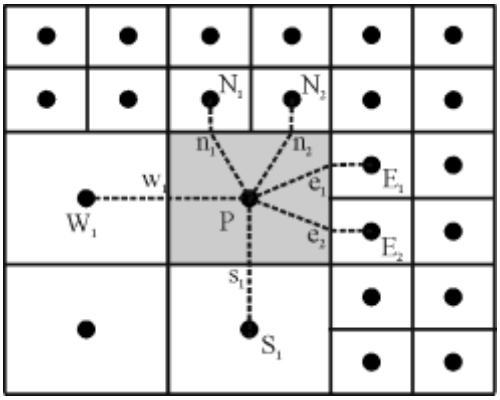

Fig. 6.19. Control volume in the horizontal quadtree mesh.

6.2.3.2 **Numerical Discretization**

Integrating the continuity equation (6.23) over the 3-D control volume (whose side and top views are shown in Figs. 6.18 and 6.19, respectively), applying Green's theorem and discretizing the temporal derivative by the backward difference scheme, one can derive the following equation:

$$\frac{\Delta V_{P,j}^{n+1} - \Delta V_{P,j}^{n}}{\Delta t} + \sum_{k=1}^{m_e} F_{ek,j} - \sum_{k=1}^{m_w} F_{wk,j} + \sum_{k=1}^{m_n} F_{nk,j} - \sum_{k=1}^{m_s} F_{sk,j} + F_{t,j} - F_{b,j} = 0 \tag{6.46}$$

where Δt is the time step length; $\Delta V_{p,j}$ is the volume of the control volume (cell) at node P with vertical cell index j; the superscript n denotes time level; F denotes the convective fluxes across cell faces; the subscripts w, e, s, n, b and t denote the west (negative x), east (positive x), south (negative y), north (positive y), bottom (negative z) and top (positive z) sides of the control volume; the subscript k is the index of the horizontal faces, with a value of 1 or 2; and m_w, m_e, m_s and m_n are the numbers of cell faces at west, east, south and north sides of the cell. For the control volume shown in Fig. 6.19, m_w=1, m_e=2, m_s=1 and m_n=2. For simplicity, m_w, m_e, m_s, m_n, and the superscript n+1 will be omitted in the following notations.

The convective fluxes at cell faces are defined as

$$\begin{aligned} F_{wk,j} &= u_{wk,j}\Delta A_{wk,j}, \quad F_{ek,j} = u_{ek,j}\Delta A_{ek,j} \\ F_{sk,j} &= v_{sk,j}\Delta A_{sk,j}, \quad F_{nk,j} = v_{nk,j}\Delta A_{nk,j} \\ F_{b,j} &= \tilde{w}_{b,j}\Delta A_{b,j}, \qquad F_{t,j} = \tilde{w}_{t,j}\Delta A_{t,j} \end{aligned} \tag{6.47}$$

where ΔA denotes the areas of cell faces, and $\tilde{w}$ denotes the velocity normal to the bottom and top faces of the cell. $\tilde{w}$ is related to the vertical velocity w as well as the horizontal velocities.

Eq. (6.46) is rearranged as

$$F_{t,j} = F_{b,j} - \frac{\Delta V_{P,j}^{n+1} - \Delta V_{P,j}^{n}}{\Delta t} - \left(\sum_k F_{ek,j} - \sum_k F_{wk,j} + \sum_k F_{nk,j} - \sum_k F_{sk,j} \right) \tag{6.48}$$

Because the vertical flux at the bed is zero, Eq. (6.48) is used to determine the vertical flux and in turn the vertical velocity at the top face of each cell by sweeping from the bed to water surface in each vertical line.

Integration of the momentum equations (6.24) and (6.25) over the 3-D control volume and discretization of the temporal derivative using the backward difference scheme, the convective terms using an upwinding scheme and the diffusion terms using the central difference scheme leads to

$$u_{P,j}^{n+1} = \frac{1}{a_{P,j}^{u}} \left(\sum_l a_{l,j}^{u} u_{l,j}^{n+1} + S_u \right) - \sum_k D_{ek,j}^{1} \eta_{ek} + \sum_k D_{wk,j}^{1} \eta_{wk} \tag{6.49}$$

$$v_{P,j}^{n+1} = \frac{1}{a_{P,j}^{v}} \left(\sum_l a_{l,j}^{v} v_{l,j}^{n+1} + S_v \right) - \sum_k D_{nk,j}^{2} \eta_{nk} + \sum_k D_{sk,j}^{2} \eta_{sk} \tag{6.50}$$

where a^u and a^v denote the coefficients for the discretized u and v momentum equations, $D_{wk,j}^{1} = g\Delta A_{wk,j} / a_{P.j}^{u}$, $D_{ek,j}^{1} = g\Delta A_{ek,j} / a_{P,j}^{u}$, $D_{sk,j}^{2} = g\Delta A_{sk,j} / a_{P,j}^{v}$, $D_{nk,j}^{2} = g\Delta A_{nk,j} / a_{P,j}^{v}$, and S_u, S_v include the source terms and the variables at time level n generated from discretization of the temporal derivative terms. Note that the first summation in Eqs. (6.49) and (6.50) is applied with

the index, *l*, sweeping over all the neighboring cells of cell P. The convection terms can be discretized using several numerical schemes with upwinding capability, such as the hybrid upwind/central scheme (Spalding, 1972), exponential scheme (Spalding, 1972) and HLPA scheme (Zhu, 1991). The HLPA scheme is approximately second-order accurate, while the hybrid and exponential schemes have accuracy between first and second orders. Details of these schemes can be found in Wu (2007).

6.2.3.3 **Coupling of Velocity and Water level**

Eq. (6.49) is used to compute the *u* velocity for an assumed water level field in an iterative manner. Application of under-relaxation (Majumdar, 1988) leads to

$$u^*_{P,j} = \alpha_u \left(H^*_{1P,j} - \sum_k D^1_{ek,j} \eta^*_{ek} + \sum_k D^1_{wk,j} \eta^*_{wk} \right) + (1-\alpha_u) u^o_{P,j} \tag{6.51}$$

where η^* is the guessed water level, $u^*_{P,j}$ is the approximate solution of *u*-velocity, $u^o_{P,j}$ is the *u*-velocity in the previous iteration step, $H^*_{1P,j}$ denotes the first term on the right-hand side of Eq. (6.49) and α_u is the relaxation factor that is set as about 0.8 in this study.

There are several approaches to conduct the iteration and couple the flow velocity and water level, including the SIMPLE (Patankar and Spalding, 1972), SIMPLEC (van Doormal and Raithby, 1984), and IDEAL (Sun et al., 2009) algorithms. The SIMPLEC algorithm is used here. One can derive the relation between the water level and velocity corrections from Eq. (6.51):

$$u^{n+1}_{P,j} = u^*_{P,j} + \alpha_u \left(\sum_k \tilde{D}^1_{wk,j} \eta'_{wk} - \sum_k \tilde{D}^1_{ek,j} \eta'_{ek} \right) \tag{6.52}$$

where η' is the water level correction $\eta' = \eta - \eta^*$. In the SIMPLEC algorithm, $\tilde{D}^1_{wk,j} = D^1_{wk,j} \Big/ \left(1 - \alpha_u \sum_l a^u_{l,j} \Big/ a^u_{P,j} \right)$ and $\tilde{D}^1_{ek,j} = D^1_{ek,j} \Big/ \left(1 - \alpha_u \sum_l a^u_{l,j} \Big/ a^u_{P.j} \right)$. The relation of water level and velocity corrections for the SIMPLE algorithm is similar to Equation (6.52), with $\tilde{D}^1_{wk,j}$ and $\tilde{D}^1_{ek,j}$ replaced by $D^1_{wk,j}$ and $D^1_{ek,j}$.

Similarly, one can have the *v*-equation and the corresponding correction equation:

$$v^*_{P,j} = \alpha_v \left(H^*_{2P,j} - \sum_k D^2_{nk,j} \eta^*_{nk} + \sum_k D^2_{sk,j} \eta^*_{sk} \right) + (1-\alpha_v) v^o_{P,j} \tag{6.53}$$

$$v^{n+1}_{P,j} = v^*_{P,j} + \alpha_v \left(\sum_k \tilde{D}^2_{sk,j} \eta'_{sk} - \sum_k \tilde{D}^2_{nk,j} \eta'_{nk} \right) \tag{6.54}$$

where $H^*_{2P,j}$ denotes the first term on the right-hand side of Eq. (6.50), $\tilde{D}^2_{sk,j} = D^2_{sk,j} \Big/ \left(1 - \alpha_v \sum_l a^v_{l,j} \Big/ a^v_{P,j} \right)$ and $\tilde{D}^2_{nk,j} = D^2_{nk,j} \Big/ \left(1 - \alpha_v \sum_l a^v_{l,j} \Big/ a^v_{P,j} \right)$. Here, a_v is the relaxation factor for the *v*-equation.

In order to avoid the checkerboard splitting for the collocated arrangement (Patankar, 1980), the momentum interpolation technique proposed by Rhie and Chow (1983) is adopted to

evaluate the variable values at cell faces from the quantities at cell centers. For example, the *u*-velocity at w-face and the *v*-velocity at s-face are determined as

$$u^*_{wk,j} = \alpha_u\left[\left(1-f_{x,p}\right)H^*_{1PWk,j} + f_{x,p}H^*_{1P,j}\right] + \alpha_u\left[\left(1-f_{x,p}\right)/a^u_{PWk,j} + f_{x,p}/a^u_{P,j}\right]g\Delta A_{wk,j}\left(\eta^*_{Wk}-\eta^*_P\right) + (1-\alpha_u)\left[\left(1-f_{x,p}\right)u^o_{Wk,j} + f_{x,p}u^o_{P,j}\right] \tag{6.55}$$

$$v^*_{sk,j} = \alpha_v\left[\left(1-f_{y,p}\right)H^*_{2PSk,j} + f_{y,p}H^*_{2P,j}\right] + \alpha_v\left[\left(1-f_{y,p}\right)/a^v_{PSk,j} + f_{y,p}/a^v_{P,j}\right]g\Delta A_{sk,j}\left(\eta^*_{Sk}-\eta^*_P\right) + (1-\alpha_v)\left[\left(1-f_{y,p}\right)v^o_{Sk,j} + f_{y,p}v^o_{P,j}\right] \tag{6.56}$$

in which $f_{x,p}$ and $f_{y,p}$ are the weighting factors used to interpolate the values of a variable at cell faces w and s from the values at two adjoining cell centers P and W or P and S, respectively; $H^*_{1PWk,j}$ and $H^*_{2PSk,j}$ stand for $H^*_{1P,j}$ and $H^*_{2P,j}$ when applying Eqs. (6.51) and (6.53) on the cells centered by W and S, respectively. The velocity corrections corresponding to Eqs. (6.55) and (6.56) for the SIMPLEC algorithm are derived as

$$u^{n+1}_{wk,j} = u^*_{wk,j} + \alpha_u\tilde{Q}^1_{wk,j}\left(\eta'_{Wk}-\eta'_P\right) \tag{6.57}$$

$$v^{n+1}_{sk,j} = v^*_{sk,j} + \alpha_v\tilde{Q}^2_{sk,j}\left(\eta'_{Sk}-\eta'_P\right) \tag{6.58}$$

where $\tilde{Q}^1_{wk,j} = \left[\left(1-f_{x,p}\right)/a^u_{PWk,j} + f_{x,p}/a^u_{P,j}\right]g\Delta A_{wk,j}\Big/\left[1-\alpha_u\left(1-f_{x,p}\right)\left(\sum_l a^u_l/a^u_P\right)_{PWk,j} - \alpha_u f_{x,p}\left(\sum_l a^u_l/a^u_P\right)_{P,j}\right]$

$\tilde{Q}^2_{sk,j} = \left[\left(1-f_{y,p}\right)/a^v_{PSk,j} + f_{y,p}/a^v_{P,j}\right]g\Delta A_{sk,j}\Big/\left[1-\alpha_v\left(1-f_{y,p}\right)\left(\sum_l a^v_l/a^v_P\right)_{PSk,j} - \alpha_v f_{y,p}\left(\sum_l a^v_l/a^v_P\right)_{P,j}\right]$

With the definition of fluxes at cell faces and Eqs. (6.57) and (6.58), one can derive the flux corrections at w and s faces:

$$F_{wk,j} = F^*_{wk,j} + a^\eta_{Wk,j}\left(\eta'_{Wk}-\eta'_P\right) \tag{6.59}$$

$$F_{sk,j} = F^*_{sk,j} + a^\eta_{Sk,j}\left(\eta'_{Sk}-\eta'_P\right) \tag{6.60}$$

where $a^\eta_{Wk,j} = \alpha_u\tilde{Q}^1_{wk,j}\Delta A_{wk,j}$, $a^\eta_{Sk,j} = \alpha_v\tilde{Q}^2_{sk,j}\Delta A_{sk,j}$, and $F^*_{wk,j}$ and $F^*_{sk,j}$ are the fluxes at faces w and s in terms of the velocities $u^*_{wk,j}$ and $v^*_{sk,j}$ evaluated using Eqs. (6.57) and (6.58).

Summation of Eq. (6.48) over each vertical line and application of the free-surface kinematic condition (6.32) leads to the depth-integrated continuity equation:

$$\frac{\eta^{n+1}_P-\eta^n_P}{\Delta t}\Delta A_P + \sum_k\sum_{j=1}^J F_{ek,j} - \sum_k\sum_{j=1}^J F_{wk,j} + \sum_k\sum_{j=1}^J F_{nk,j} - \sum_k\sum_{j=1}^J F_{sk,j} = 0 \tag{6.61}$$

where *J* is the number of cells at the vertical line, and ΔA_P is the area of the cell projected onto the horizontal plane.

Inserting Eqs. (6.59) and (6.60) into (6.61) leads to the following equation for water level correction:

$$a^\eta_P\eta'_P = \sum_k a^\eta_{Wk}\eta'_{Wk} + \sum_k a^\eta_{Ek}\eta'_{Ek} + \sum_k a^\eta_{Sk}\eta'_{Sk} + \sum_k a^\eta_{Nk}\eta'_{Nk} + S_\eta \tag{6.62}$$

where $a_{Wk}^{\eta} = \sum_{j=1}^{J} a_{Wk,j}^{\eta}$, $a_{Ek}^{\eta} = \sum_{j=1}^{J} a_{Ek,j}^{\eta}$, $a_{Sk}^{\eta} = \sum_{j=1}^{J} a_{Sk,j}^{\eta}$, $a_{Nk}^{\eta} = \sum_{j=1}^{J} a_{Nk,j}^{\eta}$, $a_P^{\eta} = \sum_l a_l^{\eta} + \frac{\Delta A_P}{\Delta t}$, and $S_{\eta} = -\frac{\eta_P^* - \eta_P^n}{\Delta t}\Delta A_P - \left(\sum_k \sum_{j=1}^{J} F_{ek,j}^* - \sum_k \sum_{j=1}^{J} F_{wk,j}^* + \sum_k \sum_{j=1}^{J} F_{nk,j}^* - \sum_k \sum_{j=1}^{J} F_{sk,j}^* \right)$.

6.2.3.4 **Solution of Discretized Equations**

The set of non-linear dicretized equations are solved iteratively. The iteration process consists of inner and outer iteration loops. The inner iteration is designed for iteratively solving each of the discretized momentum equations (6.49) and (6.50) and the water-level-correction equation (6.62). Because all computational cells are numbered in an unstructured form, the coefficient matrices in the discretized equations are sparse. A variant of the GMRES (generalized minimum residual) method (Saad, 1993) is chosen to solve the algebraic equations. The original GMRES method (Saad and Schultz, 1986) uses the Arnoldi process to reduce the coefficient matrix to the Hessenburg form and minimizes at every step the norm of the residual vector over a Krylov subspace. The variant of the GMRES method recommended by Saad (1993) allows changes in the preconditioning at every iteration step. To speed up the convergence, the ILUT (Incomplete LU Factorization; Saad, 1994) is used as the preconditioner. The details of this iteration solver can be found in the above references.

The outer iteration loop visits the discretized equations in the following sequence in each time step as required by the SIMPLEC algorithm:

(1) Guess the water level field η^*;
(2) Solve the momentum equations (6.51) and (6.53) to obtain $u_{P,j}^*$ and $v_{P,j}^*$;
(3) Use the Rhie and Chow's momentum interpolation to determine the horizontal velocities and fluxes at cell faces;
(4) Calculate η' using Eq. (6.62);
(5) Correct η by $\eta = \eta^* + \eta'$, and update $u_{P,j}$ and $v_{P,j}$ using Eqs. (6.52) and (6.54) and horizontal fluxes using Eqs. (6.59) and (6.60);
(6) Determine the vertical fluxes at top and bottom faces using the discretized continuity equation (6.46) by sweeping from the bottom to the water surface along each vertical line, and then the vertical velocity $w_{P,j}$ at cell centers using the derived vertical fluxes;
(7) Treat the corrected water level, η, as a new guess η^*, and repeat the procedure from steps 2 to 6 until a converged solution is obtained.

Because the solution of each of the variables u, v, w, and η needs the updated intermediate values of other variables through the outer loop, it is not necessary to reach a convergent solution in each inner loop. However, an approximately convergent solution for Eq. (6.62) will ensure mass conservation at each iteration step.

6.2.3.5 **Wetting and Drying Techniques**

Handling the wetting and drying processes is one of the key issues for surface water flow simulation. The present model uses a threshold flow depth (a small value such as 0.02 m in field cases) to judge drying and wetting. If the flow depth at a vertical line is larger than the

threshold value, the vertical line is considered to be wet; otherwise, the vertical line is dry. For the convenience of solution algorithm, each dry vertical line is represented by the same number of nodes as the neighboring wet vertical line. Because a fully implicit solver is used in the present model, all the wet and dry nodes participate in the solution. The nodes on all dry vertical lines are assigned a zero velocity. On the water edges between the dry and wet nodes, the wall-function approach is applied.

6.2.3.6 Coupling of Flow and Wave Models

The developed 3-D flow model and the CMS-Wave model are coupled together using a process called steering. The variables passed from CMS-Wave to the flow model are the significant wave height, peak wave period, wave direction, wave breaking dissipation, and radiation stress gradients. CMS-Wave uses the updated bathymetry (if sediment transport is on), water levels, and currents from CMS-Flow. The time interval at which CMS-Wave is run is called the steering interval. The steering process is described as follows:

(1) CMS-Wave model is run the first two time steps and the wave information is passed to the flow model.
(2) The wave height, period, dissipation, radiation stress gradients, and wave unit vectors are interpolated spatially from the wave grid to the flow grid.
(3) The 3-D flow model is run until the next steering interval and wave variables are linearly interpolated in time during the steering interval. At each flow time step, variables such as wave length and bottom orbital velocities are updated for wave-current interaction.
(4) Water levels, current velocities and bed elevations are estimated for the next wave time step and are interpolated from the flow grid to the wave grid.
(5) CMS-Wave is run again for the next time step.
(6) Steps (2)–(5) are repeated until the end of the simulation.

6.2.4 Model Testing

The developed model was tested in the two cases of tidal flows in estuaries, through which the stability, efficiency and reliability of the model for unsteady flows are quantitatively validated. The coupling between the flow and wave models was tested using an experiment of undertow flow generated by waves on a sloping beach. The capability of simulating effects of vegetation on current and waves was demonstrated using experiments of flow and waves though vegetation.

Case 1: Tidal flow in San Francisco Bay

San Francisco Bay is the largest estuary on the west coast of the U.S.A. It includes four bays: Suisun Bay, San Pablo Bay, Central Bay and South Bay, as shown in Fig. 6.20. The simulation domain includes the full bay and the open sea. Because the domain is very irregular, the used mesh consists of 72081 quadtree rectangular cells on the horizontal plane and 6 layers in the vertical direction. Fig. 6.21 shows the computational mesh, with dots representing locations of cell centers. The coarsest cell size is 3200×3200 m near the offshore ocean boundary, and the finest cell size is 25×25 m near the southern shoreline of Pacific coast. The bathymetry data covering the full bay area was downloaded from USGS's San Francisco Bay Bathymetry Web

Site (http://sfbay.wr.usgs.gov/sediment/sfbay/index.html). The measured tidal levels are used at the offshore boundary. The simulation period is 120 hours long in April 25–30, 2003. The simulation starts from a static condition (zero flow velocity), but with a two-day ramp period to get reasonable initial tidal flow field. The Coriolis coefficient is 0.000089. The bed friction coefficient c_f is set as 0.002. The computational time step is 15 minutes.

Figs. 6.22 and 6.23 show the computed flow patterns near the Golden Gate Bridge and Port Chicago in flood and ebb tides. One can see that the wetting and drying processes on the flood plain are handled well. Fig. 6.24 compares the measured and simulated water levels at four stations: Alameda, Golden Gate Bridge, Richmond, and Mallard Island. The amplitudes and phases of the tidal levels are well predicted. There is no significant phase difference between the measurement and simulation. Fig. 6.25 compares the measured and simulated flow velocities at the upper, middle and bottom layers of water in station Richmond. The general trend of the temporal variation of velocity is reasonably well obtained.

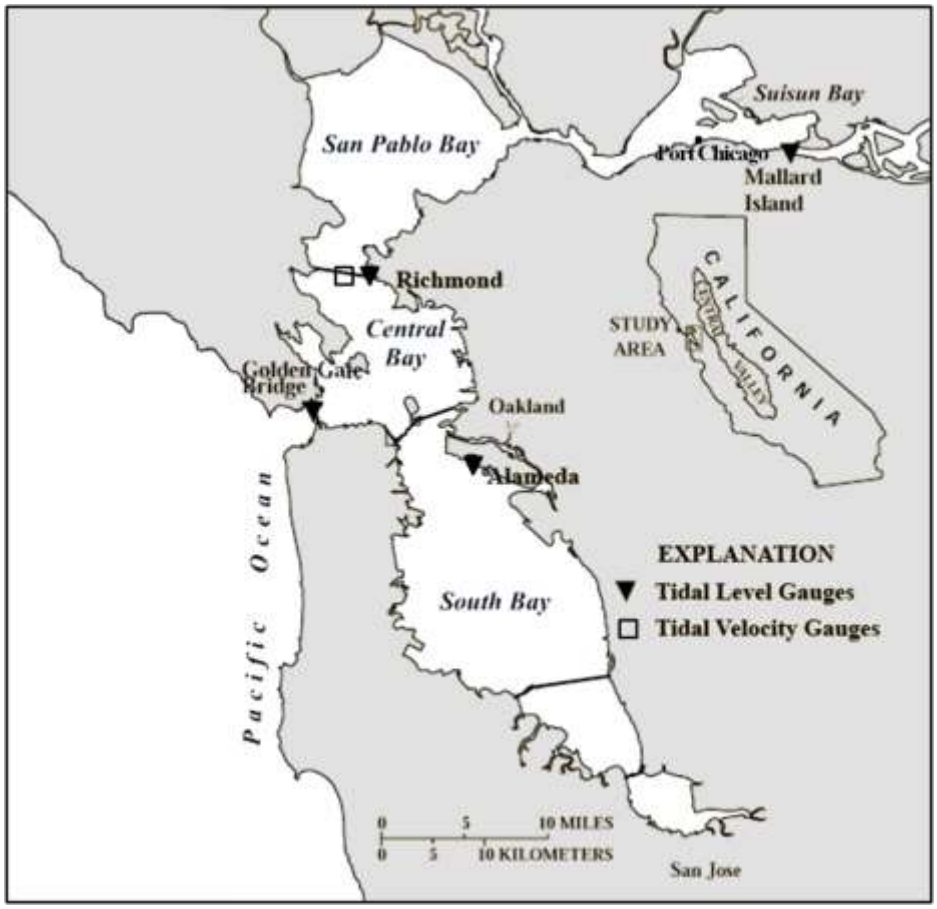

Fig. 6.20. Computational domain and measurement stations in San Francisco Bay, CA.

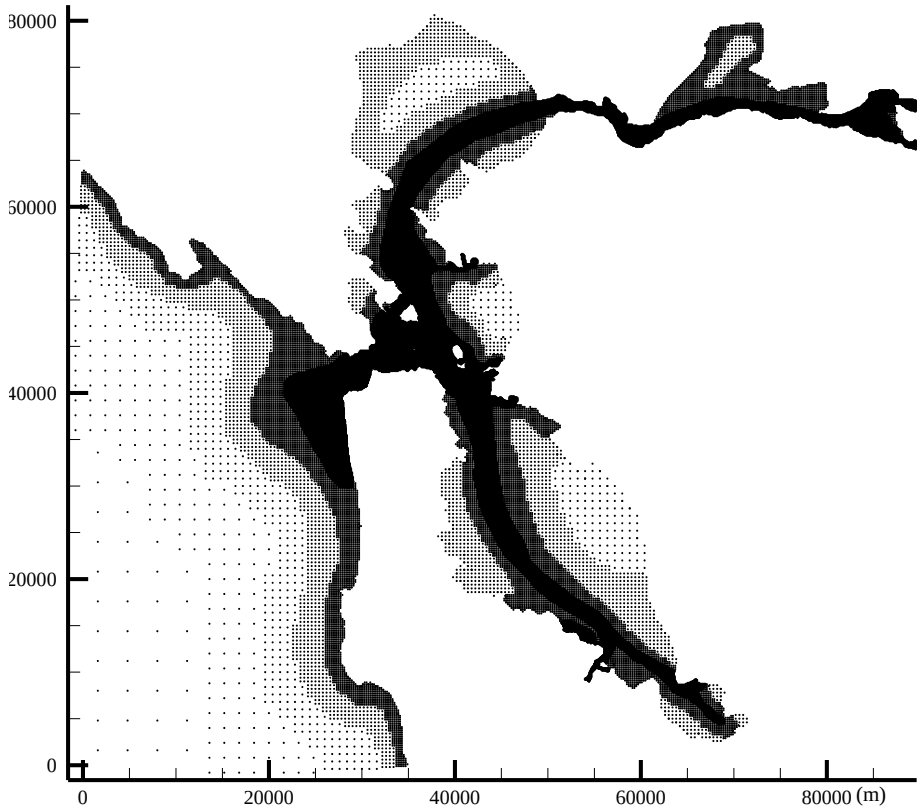

Fig. 6.21. Computational mesh for San Francisco Bay (dots: cell centers).

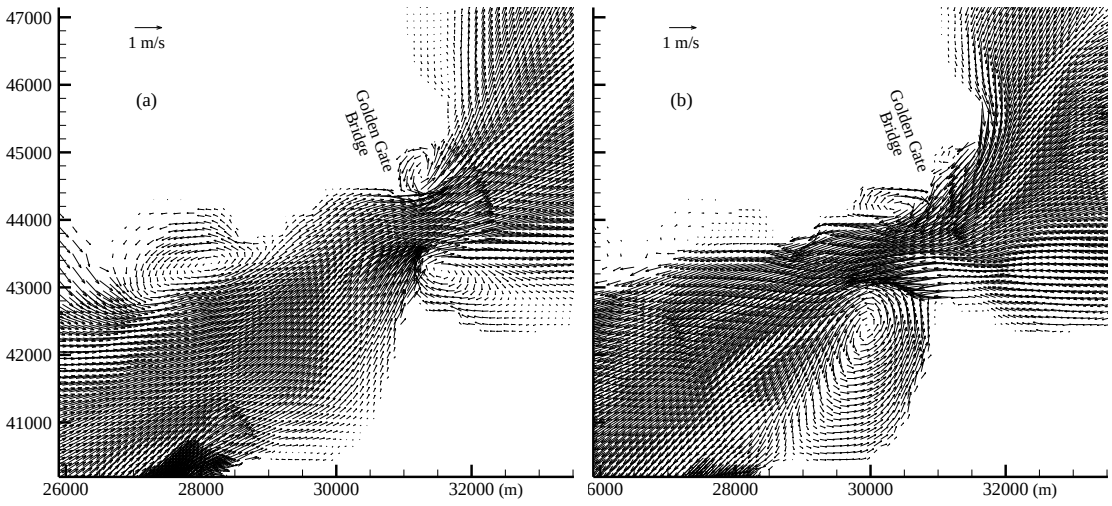

Fig. 6.22. Computed depth-average flow patterns near Golden Gate Bridge: (a) flood tide and (b) ebb tide.

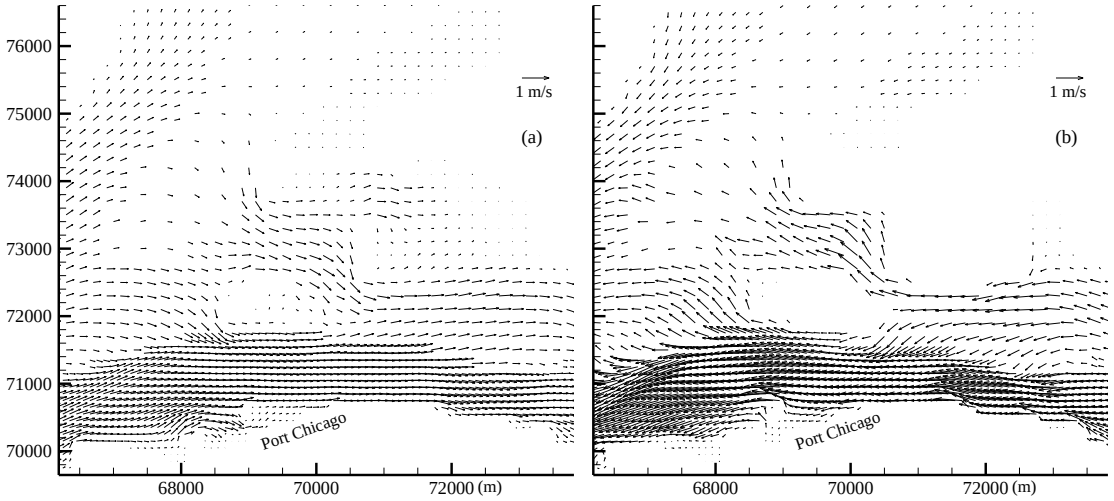

Fig. 6.23. Computed depth-average flow patterns near Port Chicago: (a) flood tide and (b) ebb tide.

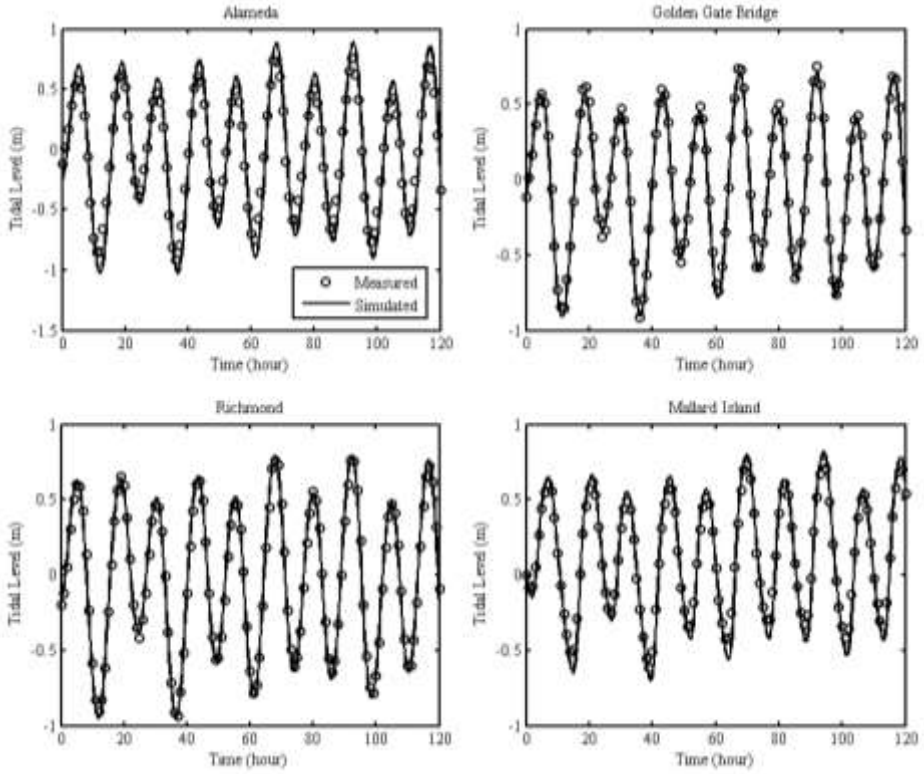

Fig. 6.24. Measured and simulated tide levels in San Francisco Bay.

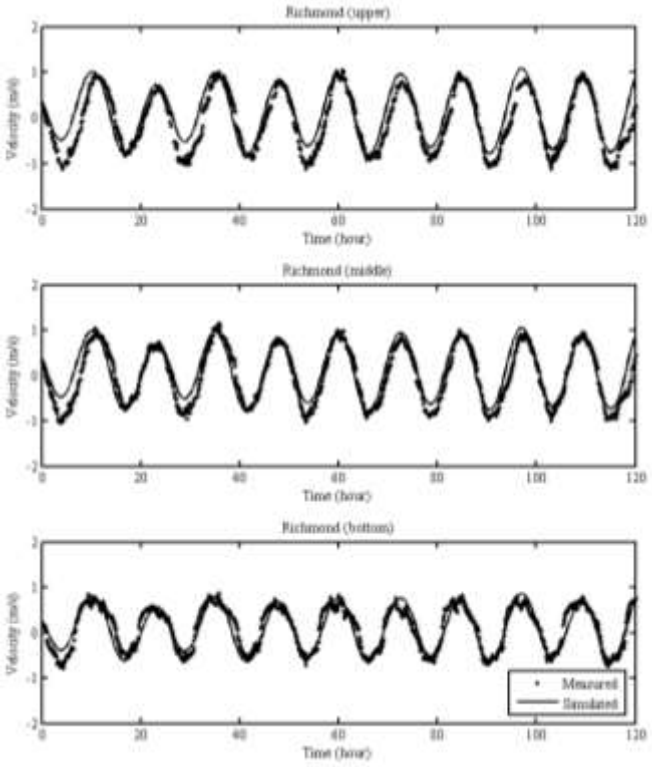

Fig. 6.25. Measured and simulated velocities at station Richmond, San Francisco Bay.

Case 2: Tidal flow in Gironde Estuary

The Gironde Estuary, located in southwestern France, is the passage of the Garonne River and the Dordogne River into the Atlantic Ocean, as shown in Fig. 6.26. The water body is about 2–14 km wide, and the navigation channel is about 6–30 m deep. The estuary is partially mixed and macrotidal, with a 12 hour and 25 minutes tidal lunar period and a tidal amplitude of 1.5–5 m at the mouth (Li et al., 1994). The simulation domain is about 80 km long, starting from the mouth to the Garonne River and the Dordogne River. The horizontal domain is represented by a uniform mesh with a size of 250 m × 125 m for each cell, and each vertical line is divided to 6 layers. The data measured from May 19–25, 1975 is used to validate the developed model. The computational time step is 15 minutes. At the estuary mouth, the tidal elevation is given by the recorded time series at station "Pointe de Grave". At the two upstream ends, the flow discharges of the Garonne River and the Dordogne River are specified according to the measured data at La Réole and Pessac. The bed friction coefficient c_f is estimated as 0.002.

Fig. 6.27 compares the measured and simulated water levels at stations Richard and Ile Verte. The amplitude and phase are well predicted by the numerical model. No obvious phase difference exists between the measured and simulated tidal levels. Fig. 6.28 shows the comparison of the measured and simulated flow velocities at 1 m under the water surface and 1 m above the bed in stations Blaye and PK68. The agreement is reasonably good.

Fig. 6.26. Sketch of Gironde Estuary, France.

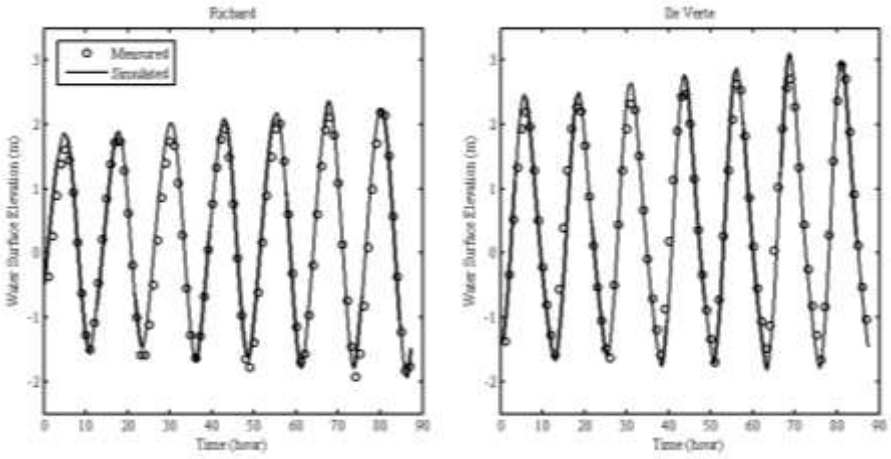

Fig. 6.27. Measured and calculated water levels at selected stations in Gironde Estuary.

Case 3: Undertow flow induced by waves on a slopped beach

The undertow is a near-bottom compensating cross-shore flow for mass transport and Stokes drift in the surf zone. The developed 3-D shallow water flow model coupled with the CMS-Wave model was applied to simulate the undertow flow in this case. The experiment was conducted by Ting and Kirby (1994) in a two-dimensional wave tank, 40 m long, 0.6 m wide and 1.0 m deep, as shown in Fig. 6.29. The bottom slope was 1:35, and the water depth in the horizontal region was 0.4 m. The experimental data were obtained with a wave height of 0.128 m in the horizontal region and a wave period of 5 sec.

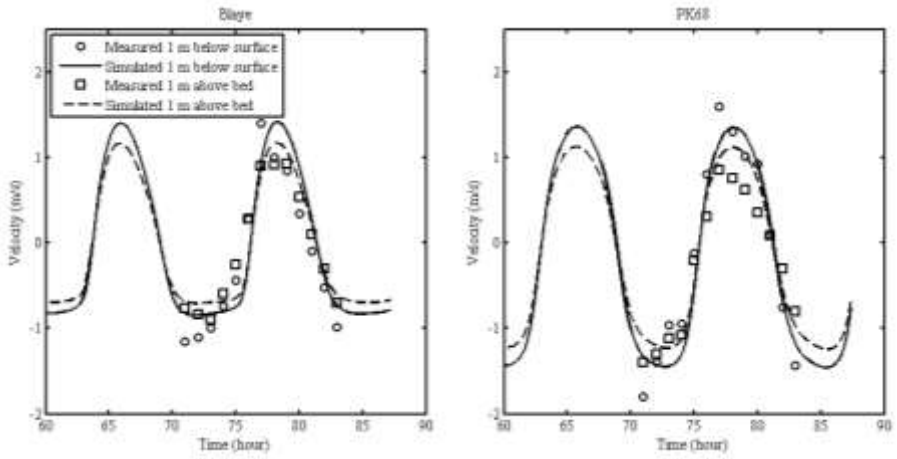

Fig. 6.28. Measured and calculated flow velocities at selected stations in Gironde Estuary.

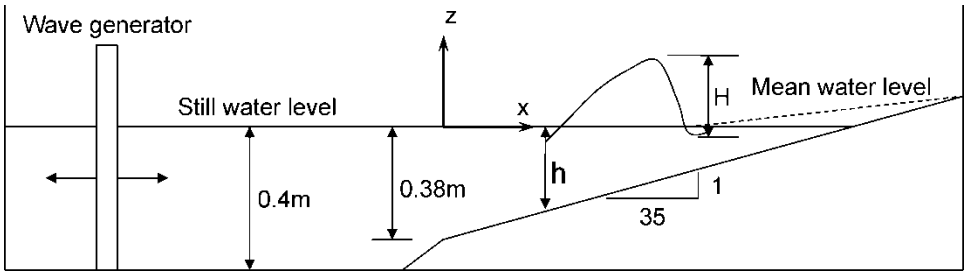

Fig. 6.29. Cross-shore Plan of Ting and Kirby (1994) Undertow Flow Experiment Setup.

The computational domain included the horizontal region and the beach. The cross-shore grid spacing was 0.5 m, and 16 layers with a uniform spacing were used in the vertical direction. The time step was 60 sec. The total simulation period was 3 hours, which was much longer than the time required to reach a steady flow state. Fig. 6.30 shows the calculated undertow flow pattern in a cross-shore vertical plane. The results are obtained using the Mellor (2008) vertical profile of wave radiation stresses and the mixing length and modified parabolic models for eddy viscosity. The calculated undertow offshore flow and upper onshore flow are qualitatively reasonable. Fig. 6.31 shows the calculated and measured phase-averaged flow velocities in seven stations at x=7.295, 7.795, 8.345, 8.795, 9.295, 9.795, and 10.395 m. In this experiment, the wave breaks at the location x=7.795 m. The calculated and measured values agree generally well. However, the model predicts gentle gradients of velocity between the upper onshore and lower offshore flows, whereas the measurements show very sharp gradients there. Because the model predicts a steady flow state, the calculated onshore and offshore fluxes are almost equal because of mass balance ensured by the numerical model; however, the onshore flux is smaller than the offshore flux in the experiment, which is questionable. This leads to that the calculated dividing point between the upper and lower zones is lower than the measured one for all the stations.

Comparison of the velocity profiles calculated using the mixing length model and the parabolic eddy viscosity model shows that the mixing length model gives an almost linear velocity profile in the upper layer, whereas the parabolic eddy viscosity model gives more curved profiles. Because the wave radiation stress by the Mellor formula is almost constant except near the water surface in shallow water, the mixing length model includes the velocity

gradient which self-adjusts and leads to an almost linear velocity profile in the calculation. Nevertheless, both eddy viscosity models give the similar magnitude of the undertow flow.

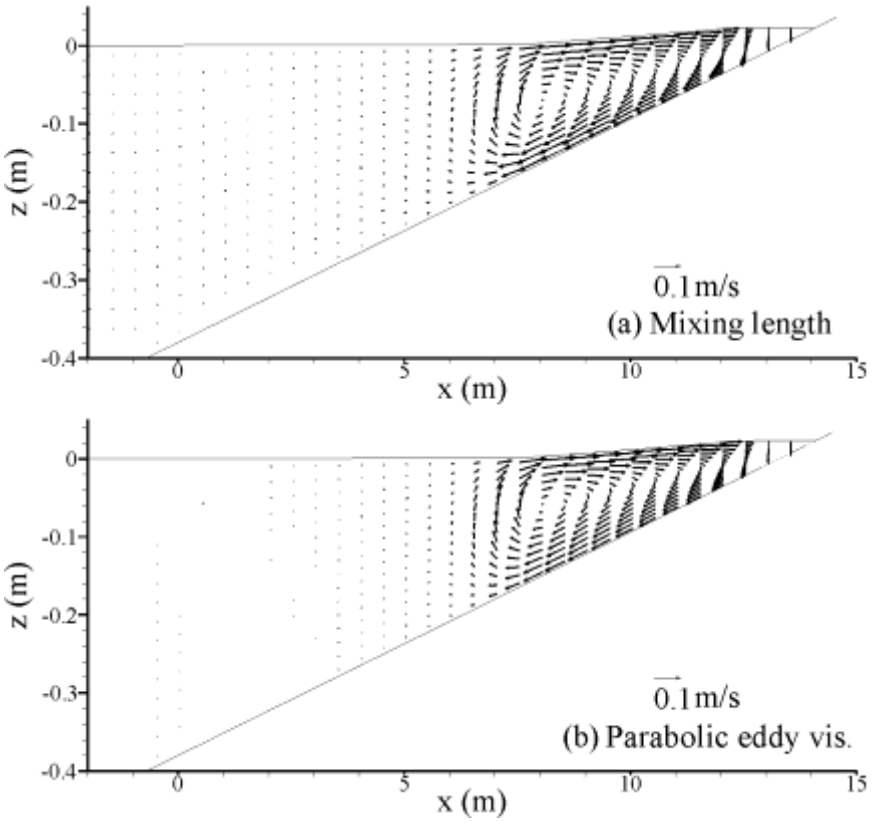

Fig. 6.30. Calculated cross-shore currents: (a) using mixing length model and (b) modified parabolic eddy viscosity model.

Case 4: Flow in a flume with submerged vegetation

In this case the model is tested to simulate the flow in an open channel with submerged vegetation. The experiments were carried out by Lopez and Garcia (1997) in a 19.5 m long, 0.91 m wide and 0.61 m deep tilting flume under unidirectional flow conditions. Vegetation was simulated by rigid wooden cylinders and flexible plastic commercial drinking straws. Velocity measurements were taken with a Sontek acoustic Doppler velocimeter at a sampling frequency of 25 Hz, at four different plan-locations with 10 measuring points in each vertical. Four experimental runs were selected to test the developed model, as shown in Table 6.2. The first two runs used rigid wooden dowels, and the last two runs used the drinking straws. The bulk drag coefficient was calibrated to be about 1.1–1.3.

The computational domain was 19.5 m long, 0.91 m wide and a flow depth in the vertical. A uniform mesh is used in the horizontal plane, with grid spacing of 0.1 and 0.07 m in the streamwise and lateral directions, respectively. Ten layers of stretching grids were used in the vertical direction, with a finer resolution near the flume bottom. Fig. 6.32 shows the comparisons of measured and calculated velocity profiles in the vertical direction for the four test cases. The vegetation resistance produces a velocity defect at the vegetation region, while the upper layer without vegetation has higher velocity. The agreement between measurements

and simulations is good. This demonstrates that the developed model can reproduce the velocity distribution for flow through submerged vegetation.

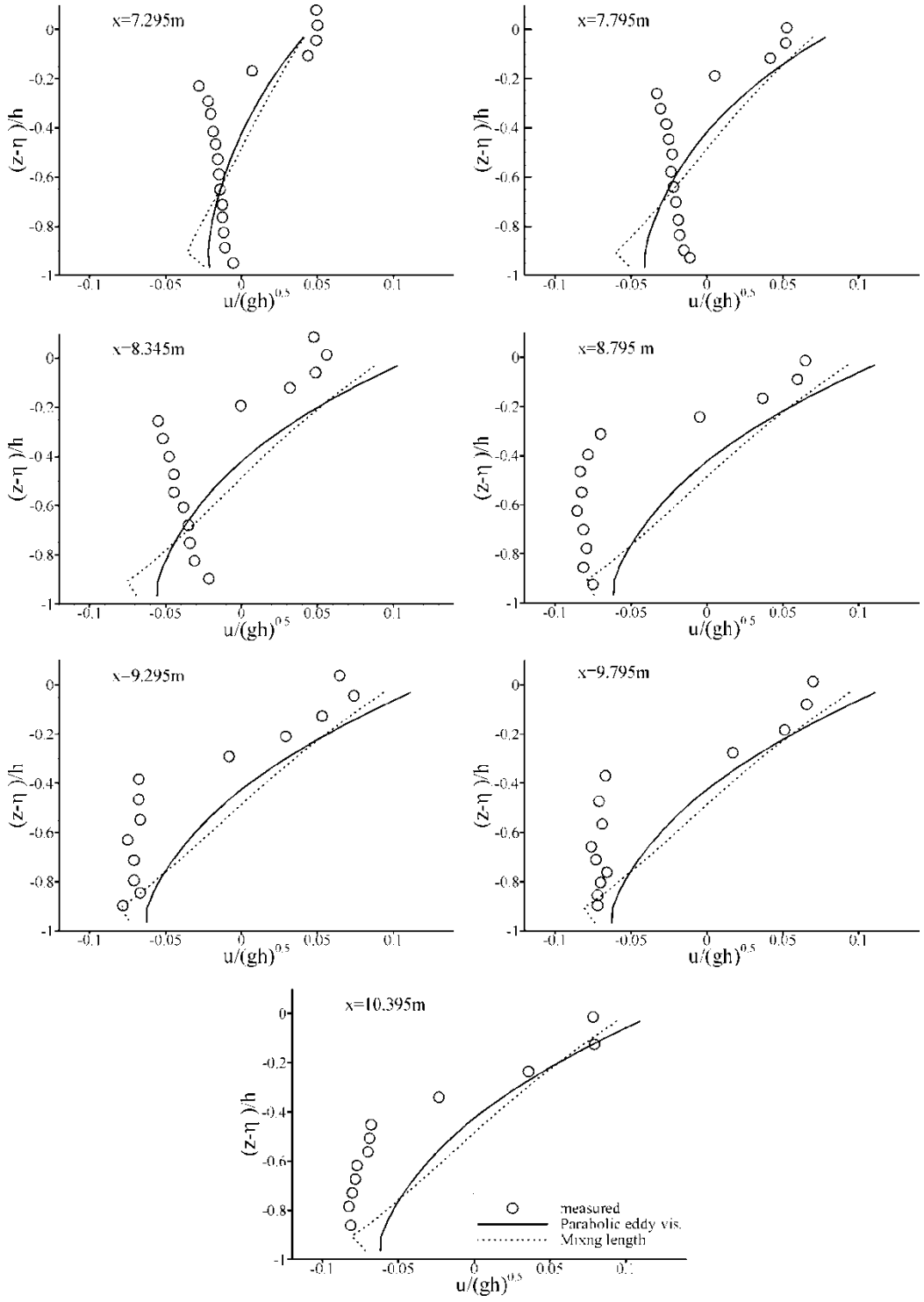

Fig. 6.31. Comparison of measured and calculated vertical profiles of velocities at Gages x=7.295, 7.795, 8.345, 8.795, 9.295, 9.795, and 10.395 m.

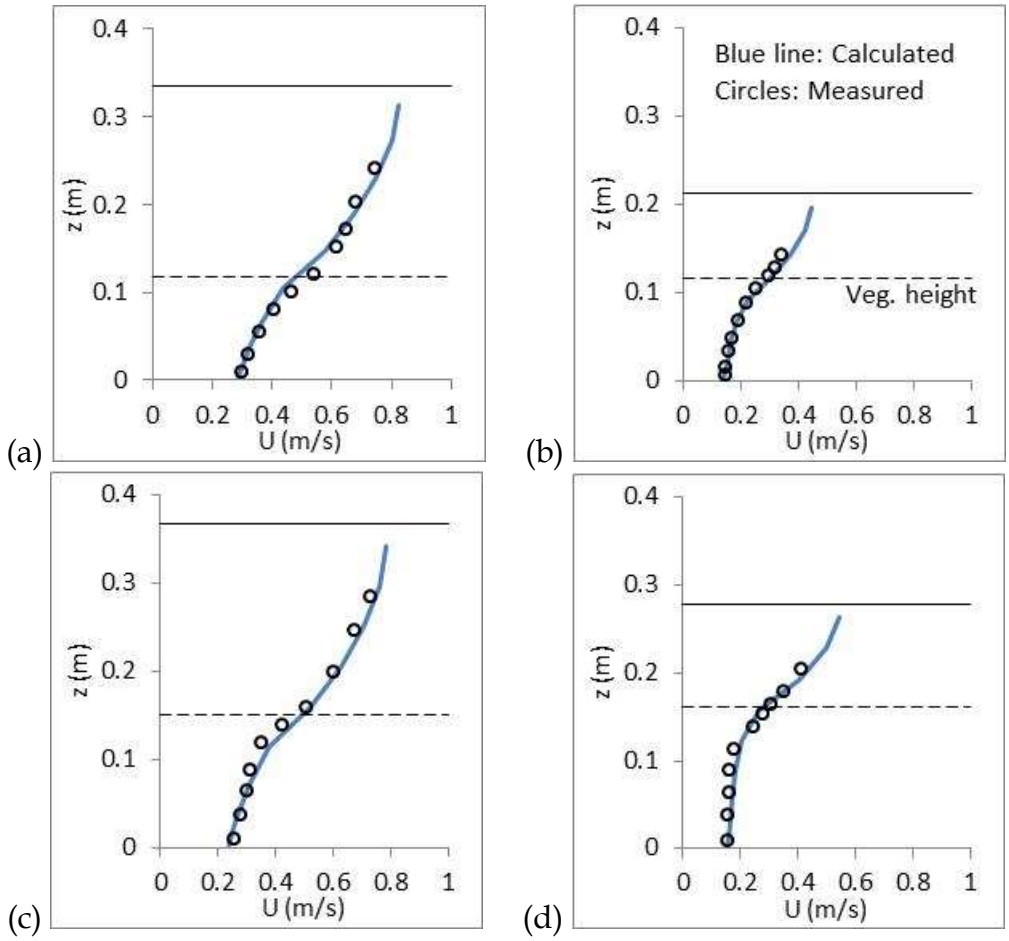

Fig. 6.32. Comparison of measured and calculated velocities in a flume with submerged vegetation: (a) Experiment No. 1, (b) No. 9, (c) No. 13, and (d) No. 17 (Horizontal dashed lines indicate vegetation tip, horizontal solid lines for water surface, blue lines for the calculated results, and circles for the measured data).

Table 6.2. Conditions of Lopez and Garcia (1997) experiments

Exp. No.	Discharge (m^3/s)	Flow depth (m)	Bed slope	Vegetation type	N_vD_v (1/m)	Vegetation height (m)	Drag coefficient
1	0.179	0.335	0.0036	Rigid	1.09	0.1175	1.1
9	0.058	0.214	0.0036	Rigid	2.46	0.1175	1.1
13	0.179	0.368	0.0036	Flexible	1.09	0.152	1.2
17	0.078	0.279	0.0036	Flexible	2.46	0.16	1.3

Case 5: Waves in a flume with submerged vegetation

The CMS-Wave model enhanced with vegetation effect modeling capability has been tested using the experimental results for random wave through an artificial kelp field provided by

Dubi and Torum (1997). The artificial kelp models were *L. hyperborea* with b_v=0.025 m and h_v=0.2 m. The vegetation field was 9.3 m long, located at the center of the flume. The vegetation density was N_v = 1,200 units/m^2. Two experimental runs (IR5WD63 and IR7WD68) were used for validating the wave model. The water depth was 0.6 m for both runs, and the other parameters are described in Fig. 6.33. The input irregular waves had the JONSWAP (Joint North Sea Wave Project) spectrum with a shape parameter of 3.3. Fig. 6.33 compares the computed results and measured data for root-mean-square wave height along the channel. The drag force was determined with the bulk C_D equal to 0.3 and 0.18 for the two cases. The agreement is pretty good and shows that the model can correctly predict the root-mean-square height of random waves with vegetation effect.

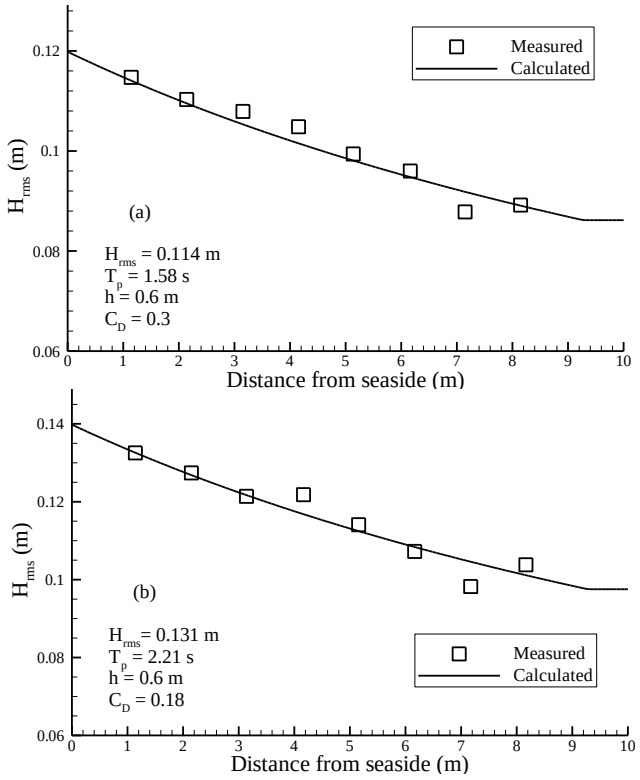

Fig. 6.33. Calculated and measured random wave heights in a vegetated channel.

6.2.5 Summary

An implicit 3-D shallow water flow model has been developed to simulate the flow in coastal vegetated waters. The model splits the water motion into current and waves. The current is phase-averaged water motion, which is governed by the phase-averaged 3-D shallow water equations with wave radiation stresses as the action of waves on current. The flow model is coupled with the CMS-Wave model, which provides the wave characteristics such as wave height, period, angle, and radiation stress for the simulation of phase-averaged current generated by waves using the flow model. The vertical profile of wave radiation stresses is determined using the Mellor (2008) method. The model is thus able to simulate the 3-D longshore and cross-shore currents induced by waves. The model considers the effects of vegetation on current and waves by including the drag and inertia forces of vegetation in the

momentum equations and the wave energy loss due to vegetation resistance in the wave action balance equation.

An implicit finite volume method with several advanced techniques has been applied to solve the 3-D shallow water flow equations. The developed model uses a multiple-level quadtree rectangular mesh on the horizontal plane for the convenience of local refinement around structures or in high-gradient regions, and the sigma coordinate in the vertical direction to efficiently track the water and bed surface changes. The computational nodes in the 3-D domain are numbered by means of an unstructured one-dimensional index system to ensure the grid flexibility. The vertical lines are also numbered using the index system of the CMS2D model on the horizontal plane, so that the developed 3-D model can use the CMS2D model's GUI for pre- and post-processing.

The developed model discretizes the diffusion terms with the central difference scheme and the convective terms with several upwinding schemes, such as the hybrid upwind/central difference, exponential difference and HLPA schemes. The primary variables *u*-, *v*-, *w*-velocities and water level are arranged in a non-staggered (collocated) system. Fluxes at cell faces are determined using the Rhie and Chow's momentum interpolation method, which eliminates spurious oscillations that can occur with linear interpolation on non-staggered grid. The discretized momentum equations and water-level-correction equation are solved in a procedure consisting of inner and outer iteration loops. Each discretized equation is solved iteratively using the flexible GMRES method with ILUT preconditioning in an inner iteration loop, while the water level and velocity are coupled using the SIMPLEC algorithm with under-relaxation in the outer iteration loop.

The model was tested using measurement data of tidal flows in San Francisco Bay, USA and Gironde Estuary, France. The used time step was 15 minutes in simulation of tidal flows with a 12-hr period in both cases, showing that the model is quite stable and efficient and handles the wetting and drying problem well. The simulated tidal levels and velocities are in good agreement with the measured data. The model was also tested using experiments of undertow flow generated by waves on a sloping beach, and flow and waves through vegetation zones. The calculated undertow flow velocities and flow velocity and wave properties attenuated by vegetation agree generally well with the experimental data.

7. COMPUTATIONAL MODELING OF MARSH EDGE EROSION

The morphodynamic processes near marsh edge under actions of strong storm surge and waves involve mixed supercritical/subcritical flows, hydraulic jump, strong non-equilibrium sediment transport, and rapid bed erosion. Therefore, understanding and prediction of flow, sediment transport and morphology development during such events are crucial but very challenging. To accurately simulate these processes, the flow model is required to have shock-capturing capabilities. For example, the 1-D and depth-averaged 2-D models often adopt approximate Riemann solvers and TVD (Total Variation Diminishing) schemes (Toro 2001), while the vertical 2-D and 3-D models use the VOF (volume-of-fluid) method and smooth particle hydrodynamics method to handle the rapidly varying unsteady flows. In this chapter, the depth-averaged 2-D model developed in Chapter 6 is enhanced with sediment transport modeling capability to compute the morphology change near marsh edge caused by long waves such as storm surge and tsunami waves. A 3-D model based on the RANS equations and the VOF technique is developed in Section 7.2 for more general applications.

7.1 A Depth-Averaged 2-D Model of Storm-Surge Induced Morphodynamic Processes near Marsh Edge

7.1.1 Model Formulations

Flow and sediment transport near marsh edge induced by strong storm surges and tsunami waves are very complex. The flow may exhibit shock waves and discontinuity, and the sediment transport is strong and the bed changes rapidly. The interaction between flow, sediment transport and bed change become significant and cannot be ignored. In the depth-averaged 2-D model, the flow is approximately governed by the generalized shallow water equations, which are derived by depth-integration of the Navier-Stokes equations based on the hydrostatic pressure assumption but considering the effects of sediment transport, bed changes and vegetation resistance:

$$\frac{\partial(\rho h)}{\partial t}+\frac{\partial(\rho uh)}{\partial x}+\frac{\partial(\rho vh)}{\partial y}+\rho_b\frac{\partial z_b}{\partial t}=(\rho_s-\rho_w)\left[\frac{\partial}{\partial x}\left(\varepsilon_s h\frac{\partial C_t}{\partial x}\right)+\frac{\partial}{\partial y}\left(\varepsilon_s h\frac{\partial C_t}{\partial y}\right)\right] \tag{7.1}$$

$$\begin{aligned}&\frac{\partial}{\partial t}(\rho uh)+\frac{\partial}{\partial x}\left(\rho u^2h\right)+\frac{\partial}{\partial y}(\rho uvh)\\&=\frac{\partial}{\partial x}\left(\mu_t h\frac{\partial u}{\partial x}\right)+\frac{\partial}{\partial y}\left(\mu_t h\frac{\partial u}{\partial y}\right)-F_x-\rho gh\frac{\partial z_s}{\partial x}-\frac{1}{2}gh^2\frac{\partial\rho}{\partial x}-\rho g\frac{n^2m_bUu}{h^{1/3}}\end{aligned} \tag{7.2}$$

$$\begin{aligned}&\frac{\partial}{\partial t}(\rho vh)+\frac{\partial}{\partial x}(\rho uvh)+\frac{\partial}{\partial y}\left(\rho v^2h\right)\\&=\frac{\partial}{\partial x}\left(\mu_t h\frac{\partial v}{\partial x}\right)+\frac{\partial}{\partial y}\left(\mu_t h\frac{\partial v}{\partial y}\right)-F_y-\rho gh\frac{\partial z_s}{\partial y}-\frac{1}{2}gh^2\frac{\partial\rho}{\partial y}-\rho g\frac{n^2m_bUv}{h^{1/3}}\end{aligned} \tag{7.3}$$

where t is the time, x and y are the longitudinal and lateral coordinates, h is the flow depth, u and v are the depth-averaged flow velocities in x and y directions, $U=\sqrt{u^2+v^2}$, $\partial z_b/\partial t$

denotes the rate of change in bed surface elevation, z_b is the bed surface elevation above a reference datum, z_s is the water level, n is the Manning roughness coefficient, g is the gravitational acceleration, C_t is the volumetric concentration of total-load sediment, ρ_w and ρ_s being the water and sediment densities, ρ is the density of the water and sediment mixture in the water column determined by $\rho = \rho_w(1-C_t) + \rho_s C_t$, ρ_b is the density of the water and sediment mixture in the bed surface layer determined by $\rho_b = \rho_w p'_m + \rho_s(1-p'_m)$ with p'_m being the porosity of the surface-layer bed material, F_x and F_y are the components of forces acting on vegetation in x and y directions, μ_t is the turbulent or eddy viscosity, and $m_b = \sqrt{1+(\partial z_b/\partial x)^2 + (\partial z_b/\partial y)^2}$ considering the curved bed (bank) surface or perimeter. Note that this symmetrical treatment of x and y in the term m_b allows it to be applied to the entire flow domain without the need of explicitly defining the bank slope.

Because Eq. (7.1) governs the continuity of the water and sediment mixture, it accounts for the effect of sediment turbulent diffusion by including the term on its right-hand side. This term can be derived by time-averaging the 3-D flow continuity equation with variable flow density which is a function of sediment concentration and fluctuates due to turbulence and using the eddy-diffusivity concept to model the correlation of the fluctuating velocity and sediment concentration.

The forces acting on vegetation, including the drag and inertia forces, are determined using Eq. (6.4), and the drag coefficient is given by methods described in Eqs. (6.5)-(6.8). The turbulence closure model (6.10) is used to determine the eddy viscosity.

Simulation of the non-cohesive sediment transport processes can be achieved by computing bed load and suspended load separately or the total load directly (Wu 2007). The latter approach is used herein, so that the sediment transport and bed change equations are

$$\frac{\partial(hC_t)}{\partial t} + \frac{\partial(huC_t)}{\partial x} + \frac{\partial(hvC_t)}{\partial y} = \frac{\partial}{\partial x}\left(\varepsilon_s h \frac{\partial C_t}{\partial x}\right) + \frac{\partial}{\partial y}\left(\varepsilon_s h \frac{\partial C_t}{\partial y}\right) - \frac{1}{L}\left(UhC_t - m_b q_{t*}\right) \quad (7.4)$$

$$(1-p'_m)\frac{\partial z_b}{\partial t} = \frac{1}{L}\left(UhC_t - m_b q_{t*}\right) \quad (7.5)$$

where q_{t*} is the total-load sediment transport capacity or the so-called equilibrium transport rate per unit channel width, and L is the non-equilibrium adaptation length that is a characteristic distance for sediment to adjust from a non-equilibrium state to the equilibrium state under given flow and sediment conditions. The adaptation length L is determined by (Wu and Wang 2007, Wu 2007)

$$L = \max\left\{L_b, \frac{Uh}{\alpha\omega_s}\right\} \quad (7.6)$$

where ω_s is the settling velocity of sediment particles, L_b is the adaptation length of bed load, and a is the adaptation coefficient of suspended load. Wu (2007) describes various methods published in the literature to evaluate L_b and a in cases of common open-channel flows. In general, the bed load adaptation length L_b is related to the dominant bed form or sediment transport scale, while a has a wide range of values, mostly between 0.25-5.0. These two parameters (or the total-load adaptation length L) are usually treated as calibrated parameters.

Like in Eqs. (7.2) and (7.3), the coefficient m_b used in Eq. (6.55) considers sediment entrainment along the curved bed and bank surfaces. It is close to 1 and is often omitted in the case of gentle bed slope, but it is important along the steep bed or bank slope. In addition, the effect of steep bed or bank slope on sediment entrainment is considered by adding the tangential component of gravity along the slope to the bed shear stress as suggested by Wu (2004, 2007) when determining the capacity q_{t^*} using the formula of Wu et al. (2000).

In addition, to consider the effect of sediment concentration, the settling velocity ω_s is determined using Richardson and Zaki's (1954) method: $\omega_s = \omega_{s0}(1-C_t)^m$, with m ≈ 4.0 and ω_{s0} being the settling velocity of single sediment particles in quiescent, distilled water.

7.1.2 Numerical Methods

7.1.2.1 Solution of Hydrodynamic Equations

As explained in the introduction, an approximate Riemann solver based on finite volume method is one of the often used methods to solve the flow problem that involves mixed flow regimes and hydraulic jump. Because the existing approximate Riemann solvers are usually developed for clear-water flow, Eqs. (7.1)–(7.3) are reformulated by moving the flow density from their left-hand sides to right-hand sides using the relation of $\rho = \rho_w(1-C_t)+\rho_s C_t$ and Eqs. (7.4) and (7.5). The derived continuity and momentum equations are:

$$\frac{\partial h}{\partial t}+\frac{\partial (uh)}{\partial x}+\frac{\partial (vh)}{\partial y}=-\frac{1}{1-p'_m}\frac{UhC_t-m_b q_{t*}}{L} \tag{7.7}$$

$$\begin{aligned}&\frac{\partial (uh)}{\partial t}+\frac{\partial \left(u^2h\right)}{\partial x}+\frac{\partial (uvh)}{\partial y}\\&=\frac{1}{\rho}\left[\frac{\partial}{\partial x}\left(\mu_t h\frac{\partial u}{\partial x}\right)+\frac{\partial}{\partial y}\left(\mu_t h\frac{\partial u}{\partial y}\right)\right]-\frac{1}{\rho}F_x-gh\frac{\partial z_s}{\partial x}-\frac{1}{2}gh^2\frac{1}{\rho}\frac{\partial \rho}{\partial x}-g\frac{n^2 m_b U u}{h^{1/3}}\\&+u\frac{\rho_s-\rho_w}{\rho}\left[-\frac{\partial}{\partial x}\left(\varepsilon_s h\frac{\partial C_t}{\partial x}\right)-\frac{\partial}{\partial y}\left(\varepsilon_s h\frac{\partial C_t}{\partial y}\right)+\left(1-\frac{C_t}{1-p'_m}\right)\frac{UhC_t-m_b q_{t*}}{L}\right]\end{aligned} \tag{7.8}$$

$$\begin{aligned}&\frac{\partial (vh)}{\partial t}+\frac{\partial (uvh)}{\partial x}+\frac{\partial \left(v^2h\right)}{\partial y}\\&=\frac{1}{\rho}\left[\frac{\partial}{\partial x}\left(\mu_t h\frac{\partial v}{\partial x}\right)+\frac{\partial}{\partial y}\left(\mu_t h\frac{\partial v}{\partial y}\right)\right]-\frac{1}{\rho}F_y-gh\frac{\partial z_s}{\partial y}-\frac{1}{2}gh^2\frac{1}{\rho}\frac{\partial \rho}{\partial y}-g\frac{n^2 m_b U v}{h^{1/3}}\\&+v\frac{\rho_s-\rho_w}{\rho}\left[-\frac{\partial}{\partial x}\left(\varepsilon_s h\frac{\partial C_t}{\partial x}\right)-\frac{\partial}{\partial y}\left(\varepsilon_s h\frac{\partial C_t}{\partial y}\right)+\left(1-\frac{C_t}{1-p'_m}\right)\frac{UhC_t-m_b q_{t*}}{L}\right]\end{aligned} \tag{7.9}$$

Note that the last terms on the right-hand sides of Eqs. (7.7)–(7.9) are derived due to the flow density and bed change terms in Eqs. (7.1)–(7.3).

Eqs. (7.7)–(7.9) and (7.4) are written as Eq. (6.11). The numerical solution methdods for the flow model are the same as that used in Section 6.1.3. The governing equation is integrated over the control volume shown in Fig. 6.2. The HLL approximate Riemann solver (Harten et al. 1983)

is used to determine the fluid mass and momentum fluxes at cell faces. A second-order accurate approximation can be obtained by reconstructing the left and right states or fluxes using the Monotonic Upstream Scheme for Conservation Laws (MUSCL) (van Leer 1979). A piecewise linear reconstruction is used, with the slope limit method (5.19) for the gradient of state variable or flux. The water surface gradient term is treated using Eq. (6.20). The bed friction and drag force terms are approximated with Eqs. (6.21) and (6.22).

7.1.2.2 **Sediment Transport Calculations**

When Eq. (6.13) is applied to sediment transport equation (7.4), the convective flux of sediment at cell faces is determined using the HLPA (Hybrid Linear/Parabolic Approximation) scheme (Zhu 1991), which has approximately second-order accuracy in space. The quantities in the exchange term are evaluated using the values at cell centers at time level *n*.

The bed deformation equation (7.5) is discretized as

$$\Delta z_b = \frac{\Delta t}{1-p'_m}\left(\frac{UhC_t - m_b q_{t*}}{L}\right)^n \tag{7.10}$$

It should be noted that the HLL approximate Riemann solver may provide a discontinuous solution of flow discharge near hydraulic jumps (Ying and Wang 2008). This may cause instability of sediment transport calculation because the sediment transport capacity q_{t*} uses the bed shear stress and flow velocity that are obtained using the flow discharge. To avoid this, the flow velocity is determined from the intercell fluxes as follows:

$$\bar{u}^n_{i,j} = \frac{\mathrm{F}^n_{h,i+1/2,j} + \mathrm{F}^n_{h,i-1/2,j}}{2h^n_{i,j}},\ \bar{v}^n_{i,j} = \frac{G^n_{h,i,j+1/2} + G^n_{h,i,j-1/2}}{2h^n_{i,j}} \tag{7.11}$$

where $\mathrm{F_h}$ and $\mathrm{G_h}$ are the fluxes *uh* and *vh* at cell faces in *x* and *y* directions, respectively. The bed shear stress is then determined from the above flow velocities using the Manning equation, and in turn the sediment transport capacity is determined accordingly. The Manning's *n* for determining the bed shear stress is the same as that used in the momentum equations (7.2) and (7.3). Because the Manning's *n* is related to the bed form development that is not well understood in the case of rapidly varying unsteady flows, it is treated as a calibrated parameter in this study. The sensitivity of model results to the *n* values is assessed in the model test section.

When the bed (lateral and longitudinal) slope exceeds the repose angle, the non-cohesive bed materials slide in particles to the slope toe and form a new slope with the repose angle. This avalanching (sliding) process is simulated using the algorithm presented by Wu (2007, pp. 278–279), which considers the nine-cell cluster shown in Fig. 6.2, checks whether the bed slope between the cell (*i*, *j*) and any of its eight neighboring cells exceeds the repose angle, and determines the bed change due to avalanching if it occurs by setting the slumped bed slope to the repose angle and satisfying the mass conservation. Because the repose angle differs in cases of wet and dry conditions, the avalanching algorithm is enhanced to specify two different repose angles for the submerged (wet) and emergent (dry) materials divided by the water surface. The submerged repose angle is usually about 30°–42° in still water and may be less in flowing water, whereas the repose angle of emergent sediment can be much steeper due to the effects of suction and (apparent) cohesion in the embankment soil.

7.1.2.3 Model Stability

Because the developed solution procedure is explicit, the computational time step should be limited by numerical stability conditions, such as the Courant-Friedrichs-Lewy (CFL) condition for flow computation and additional conditions for sediment transport and bed change computations. By trial and error, it has been found that to obtain a stable solution, the bed change at each time step should be less than about 10% of the local flow depth. Therefore, the time step should satisfy the following condition:

$$\Delta t < \min\left[\frac{\Delta x}{\left(|u|+\sqrt{gh}\right)/\Delta x+\left(|v|+\sqrt{gh}\right)/\Delta y}, \frac{0.1hL\left(1-p'_m\right)}{UhC_t - m_b q_{t*}}\right] \tag{7.12}$$

Note that the last term on the right-hand side of inequality (7.12) was derived by limiting the bed change less than $0.1h$ in Eq. (7.5). The value $0.1h$ is only an empirical estimate through model testing and may vary in different cases.

7.1.3 Model Testing

The present model was tested using two laboratory experiments on dam-break waves over movable beds and two on flow and bed changes around vegetation zones. Considering the dam-break waves in open channels are similar to storm surge and tsunami waves over coastal shelves and beaches, the first two test cases are used to validate the model capability of simulating the morphodynamic processes induced by mixed-regime rapidly-varying transient flows. Due to the scarcity of measurement data of sediment transport and bed changes induced by storm surge and long waves near marsh edges, only two test cases of morphodynamic processes by steady flow near vegetation zones in channels are obtained to validate the present model's vegetation effect module.

Case 1. Dam-break wave over movable bed in a sudden-expanded channel

The first case selected to test the present model was an experiment of dam-break flow over a movable bed in a sudden-expanded flume conducted at the Université catholique de Louvain (UCL), Belgium (Goutiere et al. 2011). The flume was 6 m long, with a non-symmetrical sudden expansion of width from 0.25 to 0.5 m at 4 m downstream of the flume entrance (Fig. 7.1). The breaking of the dam was simulated by rapid downward movement of a thin gate located at 1 m upstream of the sudden expansion. The initial bed of the entire flume was covered by a 0.1 m thick horizontal layer of fully saturated, uniform coarse sand with a median diameter of 1.82 mm, a specific gravity of 2.68, and a deposit porosity of 0.47. The initial water depth was 0.15 m on the upstream side of the gate and 0 m in the downstream side (Palumbo et al. 2008). Considering the sediment layer, the initial upstream and downstream water levels are 0.25 and 0.1 m, respectively, and the initial bed level is 0.1 m above the fixed flume bottom.

The temporal evolution of water level in a period of 12 s was measured by eight ultrasonic gages placed downstream of the gate, as sketched in Fig. 7.1. The gages U1, U3, U5, and U7 were aligned along a line 0.125 m away from the right flume wall (wall at bottom of Fig. 7.1) and located at 0.75, 1.2, 1.45, and 1.95 m downstream of the gate, respectively. The gages U2, U4, U6, and U8 were aligned along a line 0.125 m away from the left wall and located at 1.2, 1.45, 1.95, and 2.45 m downstream of the gate, respectively. The morphological changes generated by the dam-break flow were measured at nine cross-sections (numbered CS1 to CS9)

located every 5 cm from 10 to 50 cm after the sudden expansion, at the end of the experiment by a laser sheet imaging technique.

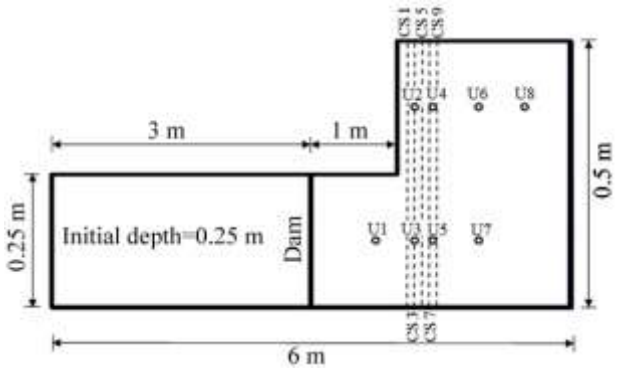

Fig. 7.1. Sketch of the UCL dam-break flow experiment setup (dashed lines: measurement cross-sections; circles: ultrasonic gages) (Palumbo et al. 2008, Goutiere et al. 2011).

The computational domain was represented by a mesh consisting of 600×100 nodes in longitudinal and lateral directions. The longitudinal grid spacing was uniformly set as 0.005 m near the gate, but varied in the regions away from the dam. The lateral grid spacing was uniform at 0.005 m. The sediment adaptation length L was determined by Eq. (7.6), with the suspended-load adaptation coefficient a set as 4.0 and the bed load L_b as 0.025 m. Both values were calibrated by comparing the measured and calculated bed topographies. The a value of 4.0 agrees well with the range of 2.0-4.0 used by Wu and Wang (2007) in a 1-D model. The L_b value of 0.025 m is small, perhaps due to the small scale of sediment transport in this case. The time step length varied with time as determined using inequality (7.12). The Manning's n was given as 0.025 as used by Xia et al. (2010), which is larger than the value of 0.0166 determined with the Manning-Strickler formula corresponding to the grain roughness or a plain bed. However, n was also given different values for model sensitivity assessment as described below. The coefficient β was given a value of 1.0.

Fig. 7.2 shows the calculated water surface at time of 2.8 s. The dam-break wave spread to the left side after it arrived at the channel expansion. It generated a hydraulic jump on the left side downstream of the sudden expansion. Figs. 7.3(a)-(e) compare the measured and calculated water levels at Gages U1, U2, U3, U6 and U7 in a period of 12 s. The simulations used two values of Manning's n: 0.02 and 0.025. Both reproduced well the general trend of the dam-break wave propagation. The Manning's n of 0.02 gave slightly better prediction of water levels on all gages.

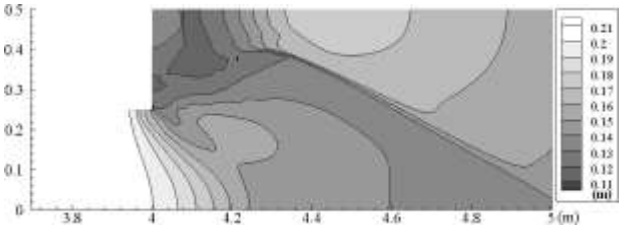

Fig. 7.2. Calculated water level near the sudden expansion at t=2.8 s (Manning's n = 0.025, β = 1.0).

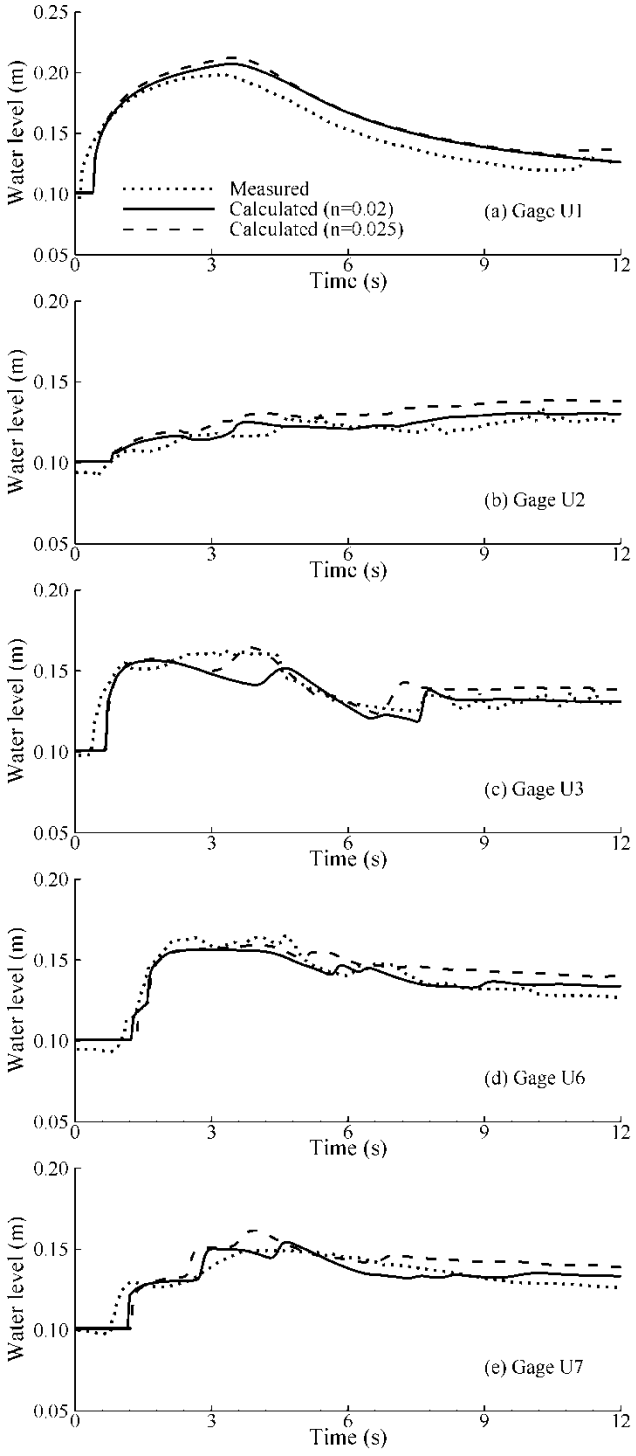

Fig. 7.3. Measured and calculated water levels at Gages U1, U2, U3, U6, and U7 (Calculations using Manning's n = 0.02, 0.025; β =1.0).

Fig. 7.4 shows the calculated total bed changes near the sudden expansion at the end of the experiment. Erosion occurred near the corner of the expansion, and the eroded sediment deposited mostly at the expansion zone. Figs. 7.5(a)-(e) compare the measured and calculated

final bed levels at five cross-sections: CS1, CS3, CS5, CS7 and CS9. At cross-sections CS1 and CS3, both the experiment and simulation present erosion at the center of the flume near the corner of the sudden expansion, but the model underestimated the deposition at the expansion zone along the left flume wall. At cross-sections CS5, CS7 and CS9, the model reproduced well the bed profiles observed in the experiment. The deposition and erosion magnitudes and distributions were predicted with better accuracy when the Manning's n was set as 0.025.

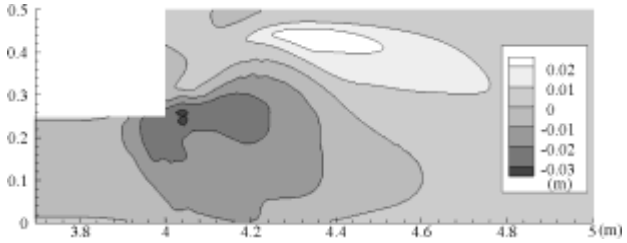

Fig. 7.4. Calculated total bed change near the sudden expansion (Manning's n = 0.025, β = 1.0).

Case 2. Partial dam-break flow on movable bed in a straight channel

The second test case was a benchmark experiment also carried out at UCL-Belgium to investigate the two-dimensional morphological evolution of a movable bed under the action of partial dam-break wave (IAHR Working Group 2011). The flume was 3.6 m wide and about 36 m long, as shown in Fig. 7.6. The partial dam break was represented by rapidly lifting the 1-m wide gate between two impervious blocks. The fixed bed of the flume was covered with an 85 mm thick sand layer extended from 1 m upstream of the dam to 9 m downstream of the gate. The used sand was fully saturated before the experiment and had a median diameter of 1.61 mm, specific gravity of 2.63, and initial bed porosity of 0.42. The downstream end of the flume consisted of a weir and sediment entrapment system, but it did not play any role during the experiment that was stopped after 20 s to avoid the reflection from it. The initial water level in the reservoir was 0.47 m above the fixed flume bed. The experiment considered both wet and dry beds downstream of the dam, but only the dry bed case was selected here, which was assumed to be more difficult to model. Water level evolution in time at 8 gage points was measured by means of ultrasonic probes.

A mesh consisting of 600×140 cells in longitudinal and lateral directions was used to cover the entire flume. The longitudinal and lateral grid spacing was 0.025 m in the movable bed reach near the breach width and increased gradually in the downstream and upstream directions and towards both side walls. The model applied a transmissive condition at the downstream end. The model could use a variable time step, but it used a constant time step of 0.0005 s in this case. The Manning's n in the sand bed was suggested as 0.0165 by the benchmark test (IAHR Working Group 2011). This value was estimated using the Manning-Strickler formula corresponding to a plain bed. Considering that bed forms developed in this experiment, the Manning's n was also set as 0.02 for the sand bed for sensitivity analysis. For the portion of fixed bed the Manning's n was set as 0.01. The suspended-load adaptation coefficient a was set as 4.0 and the bed-load adaptation length L_b was 0.025 m, as used in the previous case. This demonstrates that the present model can be applied to similar cases after a and L_b are calibrated.

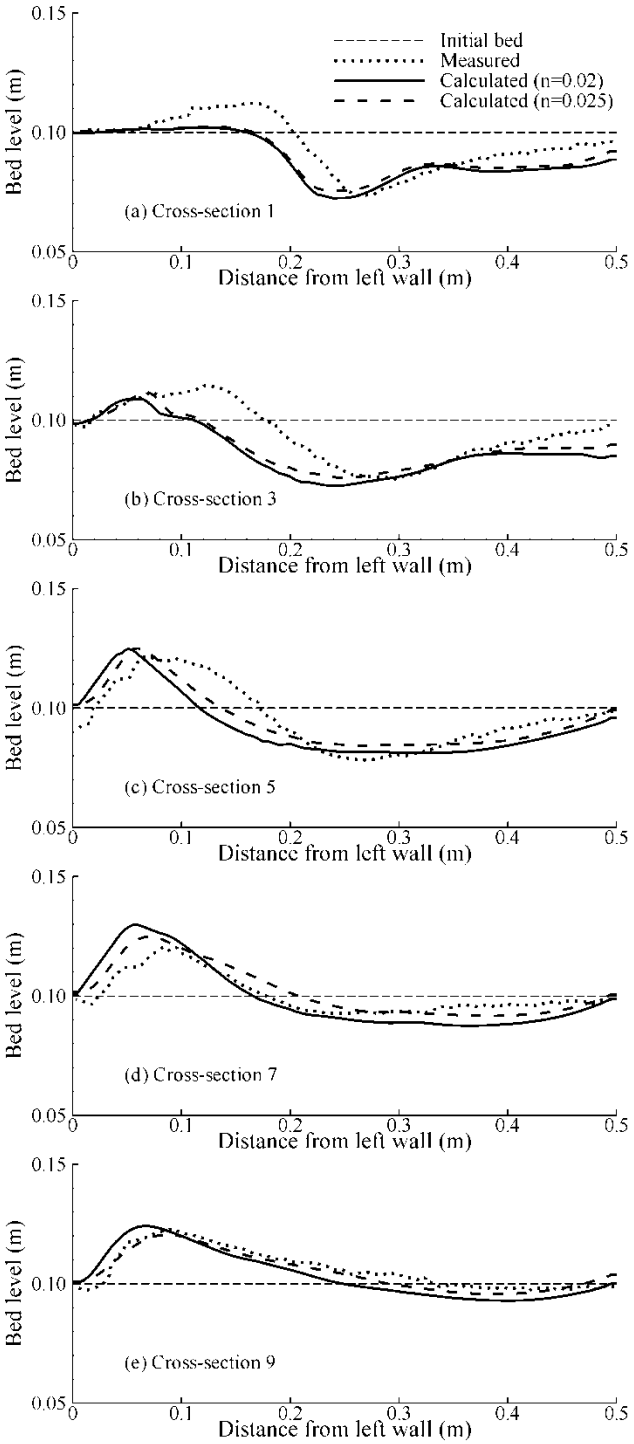

Fig. 7.5. Measured and calculated final bed levels at cross-sections CS1, CS3, CS5, CS7, and CS9 (Calculations using Manning's n = 0.02, 0.025; β=1.0).

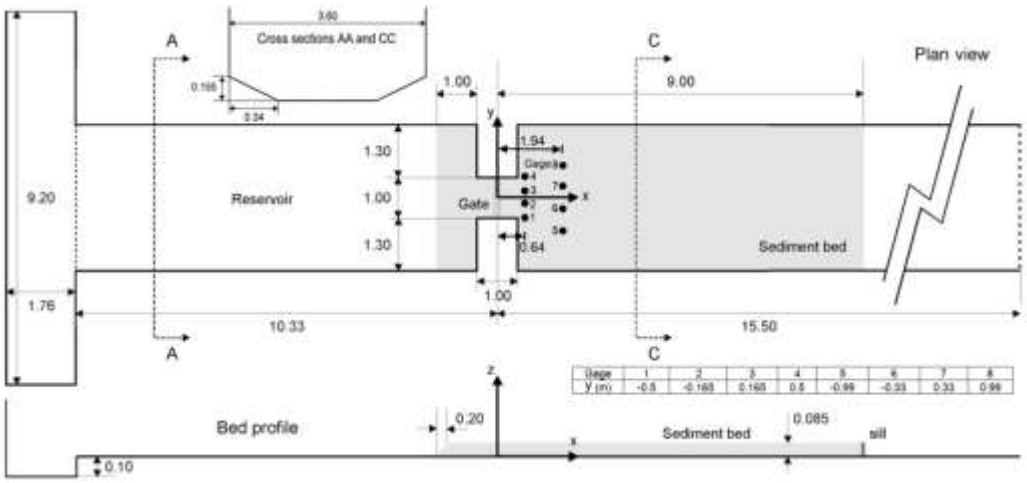

Fig. 7.6. Configurations of the UCL partial dam break experiment (dimension in meters).

Figs. 7.7(a) and (b) compare the calculated and measured bed topographies at the end of the experiment (t=20 s). Both calculation and measurement show that significant erosion led to a large scour hole downstream of the dam. Some of the eroded sediment deposited along the sidewalls where hydraulic jumps appeared and downstream of the scour hole. The deposition pattern was controlled by the cross waves generated by the partial dam break, which spread to the sidewalls of the flume and were then reflected from one side to the other side. The calculated scour hole is deeper than the measured one. Considering the complexity of the problem, the model reproduced generally well the erosion and deposition patterns observed in the experiment.

The measured bed profiles along three longitudinal sections (y=0.2, 0.7 and 1.45 m) at t=20 s are compared with those calculated using different values of Manning's n in Fig. 7.8, and with those calculated using different values of β in the slope limiter (16) in Fig. 7.9. Note that Figs. 7.8 and 7.9 include bed profiles measured in two experimental runs using the same setup, and difference between the two measurements shows the difficulty of repeating such experiments. The calculated erosion depth is between the two measurements along the section of y=0.7 m but is over-predicted in the scour hole along the section of y=0.2 m. The downstream deposition is under-predicted somehow by the model. The erosion was predicted better when the Manning's n was set as 0.02, while the deposition was predicted better when 0.0165 was used. When β was set as 0.5, the model provided smooth bed profiles; however, when β was set as 1 (minmod limiter), the model generated small undulations of high frequency on the bed profile. It was found that β=2 (superbee limiter) also generated similar undulations, but the results are not included here.

Fig. 7.10 shows the measured and simulated time series of water surface elevations (above the fixed flume bottom) at the 8 gage points. The simulation results were obtained using n=0.0165 and β=0.5. The variations of water surface at Gages 1 and 4 have the same trend, due to almost symmetric flow, sediment transport and bed change patterns about the channel centerline observed by the model simulation. Similar trends can also be observed between Gages 2 and 3, between Gages 5 and 8, and between Gages 6 and 7. The calculated water levels at Gages 1 and 4 are lower than the measured ones. This may be due to strong 3-D features of the flow near the two corners of sudden expansion of the flume width, as well as the overpredicted erosion there.

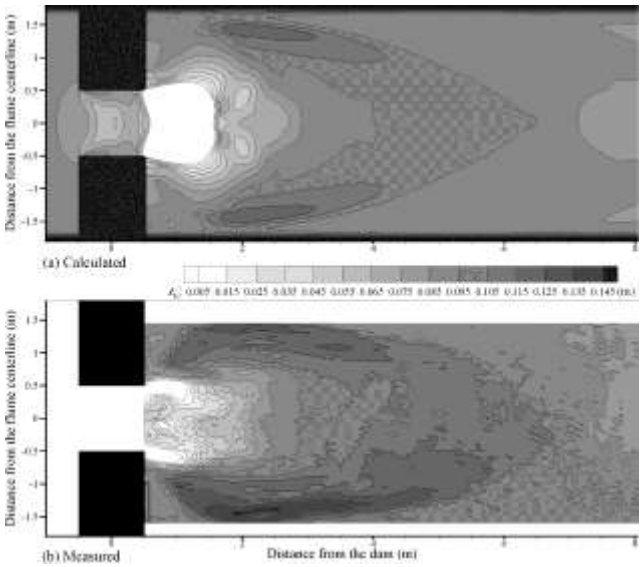

Fig. 7.7. Bed topographies at t=20 s: (a) calculated and (b) measured.

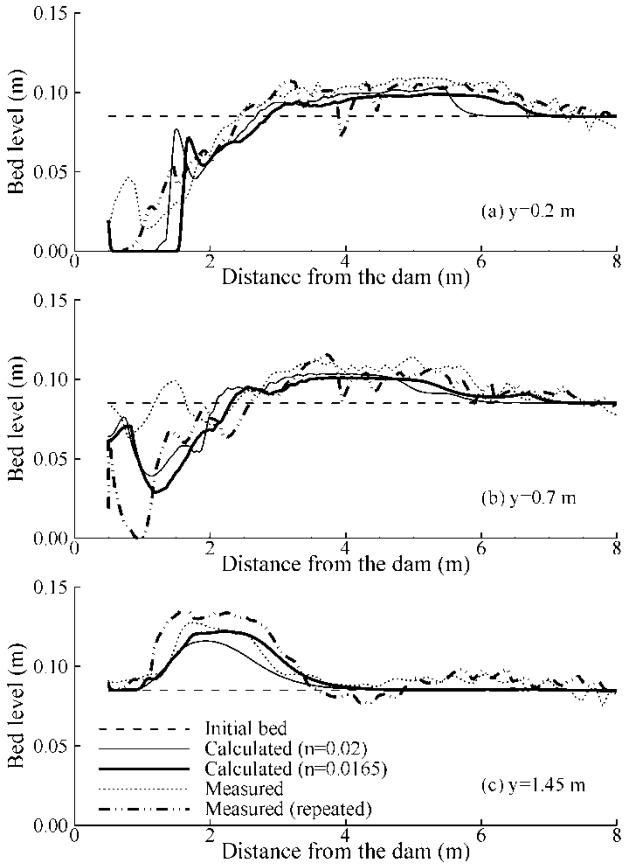

Fig. 7.8. Measured and calculated final bed profiles along three longitudinal sections (Calculations using n = 0.0165, 0.02; β = 0.5).

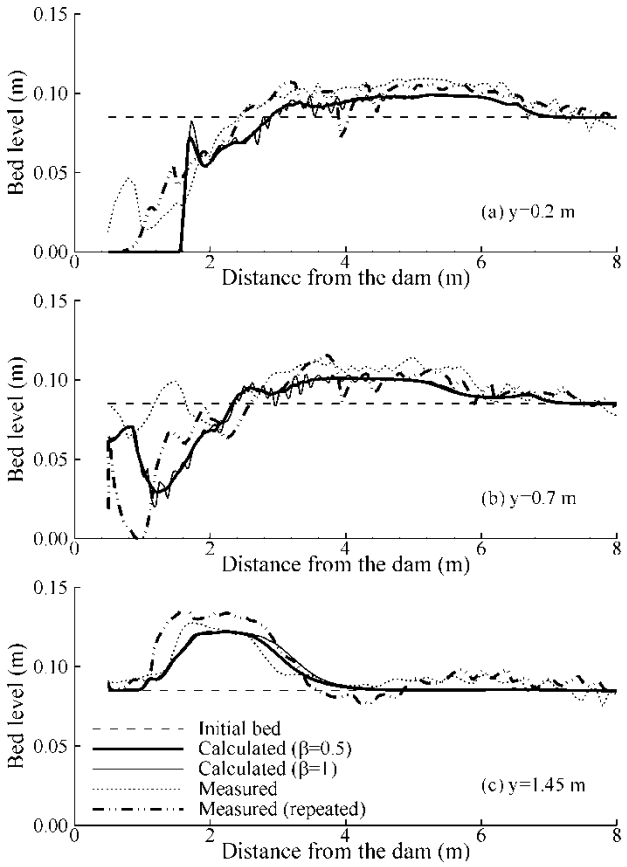

Fig. 7.9. Measured and calculated bed profiles along three longitudinal sections (Calculations using β = 0.5, 1.0; n = 0.0165).

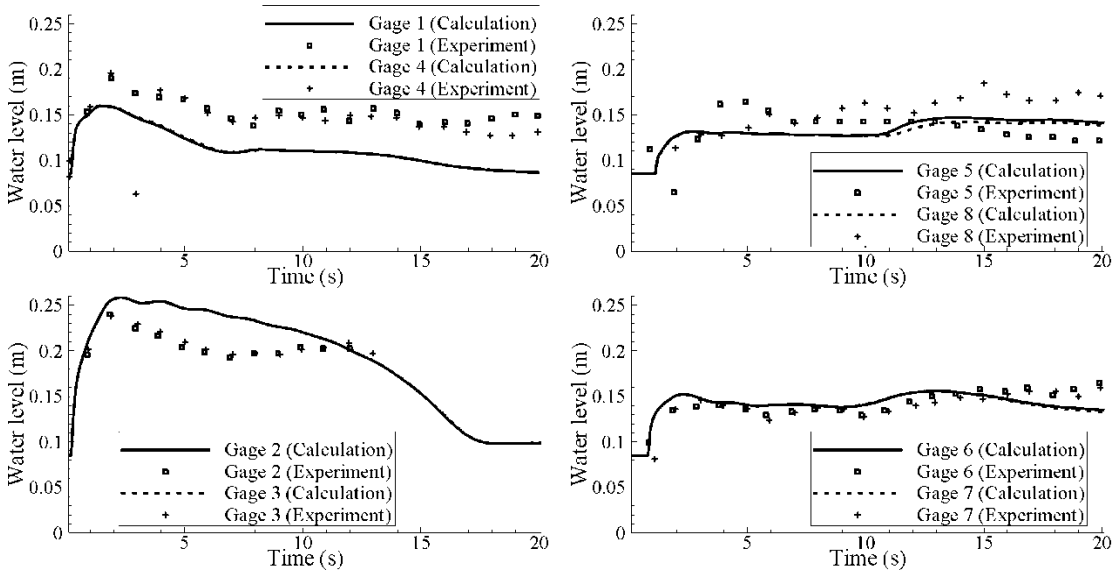

Fig. 7.10. Measured and calculated water surface variations with time at 8 gage points (Calculation using n = 0.0165, β =0.5).

Case 3: Bed morphological changes around a vegetated island

Experiments on bed morphological changes around a vegetated island were conducted by Tsujimoto [1998]. The island was a non-submerged porous body (5 cm wide and 25 cm long), located in the center of a 0.4 m-wide straight flume with a sand bed (d=1.6 mm), as shown in Fig. 7.11. The properties of the model vegetation were not reported, but the projected area $N_v D_v$ was determined as 10 m^{-1} in the experiment. The slope of the flume was 1/100, and the flow discharge was 0.003 m^3/s. The experimental run in which the inflow sediment discharge was at the equilibrium state is simulated here using the present model. The computational mesh consists of 500×160 nodes. The computational time step used is about 0.001 second determined by Eq. (7.12). C_d is set as 3.0. The Manning's bed roughness coefficient is 0.018. The sediment adaptation length is determined using Eq. (7.6) with L_b=0.025 m and a=4.0.

The simulated final flow vectors velocity magnitude and total bed change at t=30 min are shown in Fig. 7.12. Due to the effect of vegetation, the flow velocity is reduced inside, upstream and downstream of the vegetation zone, while the flow velocity is increased along two sides of the island. Fig. 7.13 shows the measured and calculated bed elevation changes near the vegetated island after 30 minutes. The sediment deposits inside and in front of the vegetation island, and erosion occurs on the two sides of the island. The pattern and magnitude of deposition and erosion are well predicted.

Fig. 7.13 also shows the simulated results of Tsujimoto (1998) and Wu and Wang (2004) using different depth-averaged 2-D models. The two models used differ from the present model in numerical methods and sediment transport models. Tsujimoto used the Ashida-Michiue (1971) equation for bed load, whereas Wu and Wang and the present model used the Wu et al. (2000b) formula but different numerical solution algorithms. Tsujimoto (1998) predicted the pattern of deposition and erosion well but the magnitude less accurately. Wu and Wang (2004) and the present model improved the accuracy, primarily due to the use of different sediment transport capacity formula.

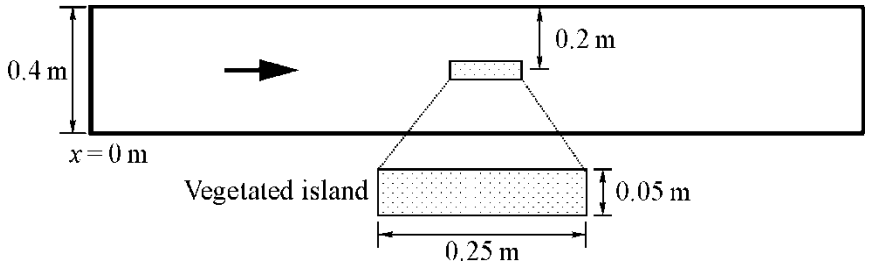

Fig. 7.11. Plan view of Tsujimoto's (1998) experiments.

Case 4. Bed morphological changes around alternate vegetation zones

Bennett and Alonso (2003) performed an experiment in a laboratory flume with movable bed that demonstrated how vegetation might be used to transform a straight, channelized stream into a meandering planform. The initial channel was a preformed trapezoidal cross section with side slopes of 34° (Figs. 7.14 and 7.15). Two vegetation zones were arranged on alternate sides of the channel, separated by a distance of 1.5 m. Two experimental runs with different vegetation zone shapes but the same vegetation density were simulated here. In the first experiment, the vegetation zones were rectangular, 0.49 m long and 0.245 m wide. In the

second experiment, the vegetation zones were semi-cycles with radii of 0.245 m. In both experiments, the vegetation elements were arranged in a staggered pattern. The vegetation elements were rigid, stem diameter was 4.8 mm and density was 2500 units/m^2. The edge of the vegetation zone reached the centerline of the flume, and all vegetation was emergent. The sediment size was 0.8 mm. Digital elevation maps before and after the experiment were obtained at a grid spacing of 2 mm in the cross-sectional direction and 5 mm in the longitudinal direction using an infrared laser microrelief system capable of resolving sub-millimeter changes in bed elevation.

The computational mesh was uniform, with Δx=0.041 m and Δy=0.016 m, as shown in Fig. 7.15. The Manning's roughness coefficient was adjusted to 0.028, which yielded a uniform flow in the absence of vegetation. The drag coefficient C_d is set as 2.0. The sediment adaptation length is determined using Eq. (7.6), with L_b=0.025 m and a=4.0. The computational time step was 0.003 second.

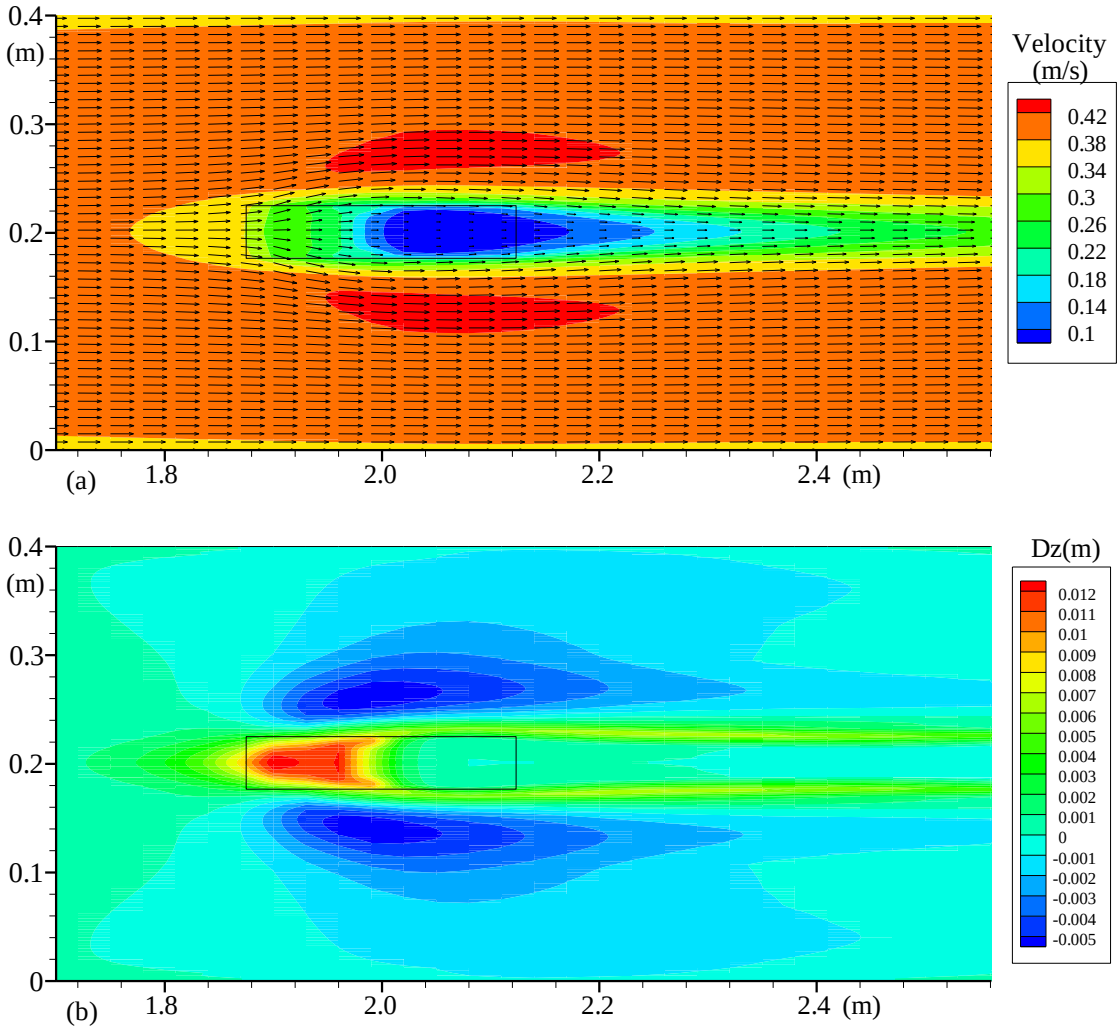

Fig. 7.12. Computed final flow pattern and total bed change around vegetated island at elapsed time of 30 min (Rectangle denotes vegetated island).

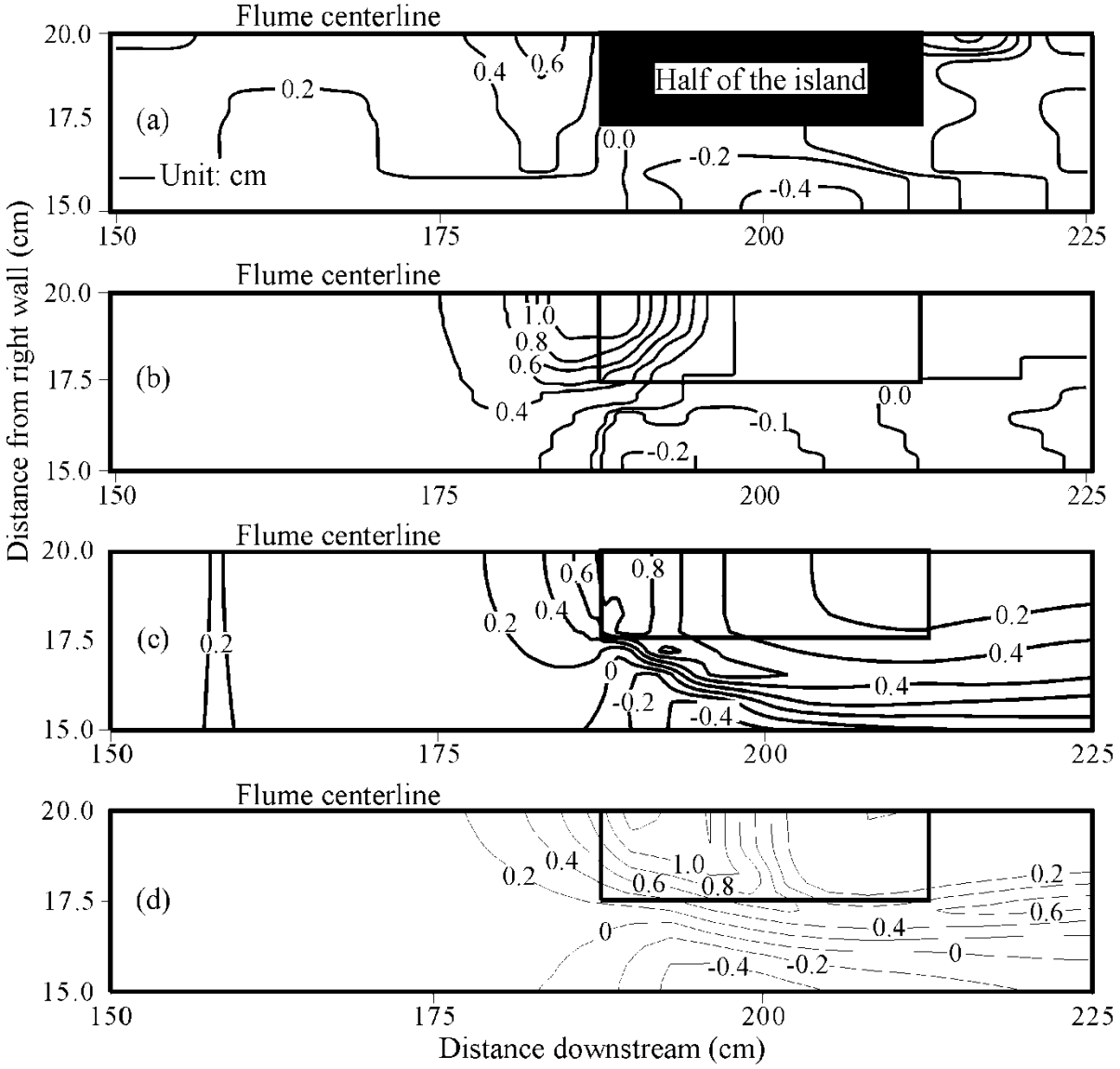

Fig. 7.13. Bed changes around vegetated island: (a) Measured by Tsujimoto (1998); (b) Calculated by Tsujimoto (1998); (c) Calculated by Wu and Wang (2004); and (d) calculated by the present model (contour unit: cm).

In this experiment, the side slope of the bank was close to the angle of repose, and the flow did not reach the bank top. Due to the fluvial erosion at the bed and along the wetted banks, bank failure occurred and the banks retreated. Because the sediment particles were non-cohesive, the model simulated this phenomenon by applying an angle of repose to the bank slope. The wetted and dry repose angles were set as 34° and 50°, respectively. If the bank slope is larger than the angle of repose, the sediment particles would move downslope, forming a new slope at the repose angle. This procedure ensured conservation of sediment mass.

In this test case, the bank slope is very high, close to repose angle. The effect of gravity on bed-load transport on the slope needs to be considered. This is done using the following equation (Watanabe 1985; Struiksma et al. 1985):

Fig. 7.14. Setup of experiments of Bennett and Alonso (2003).

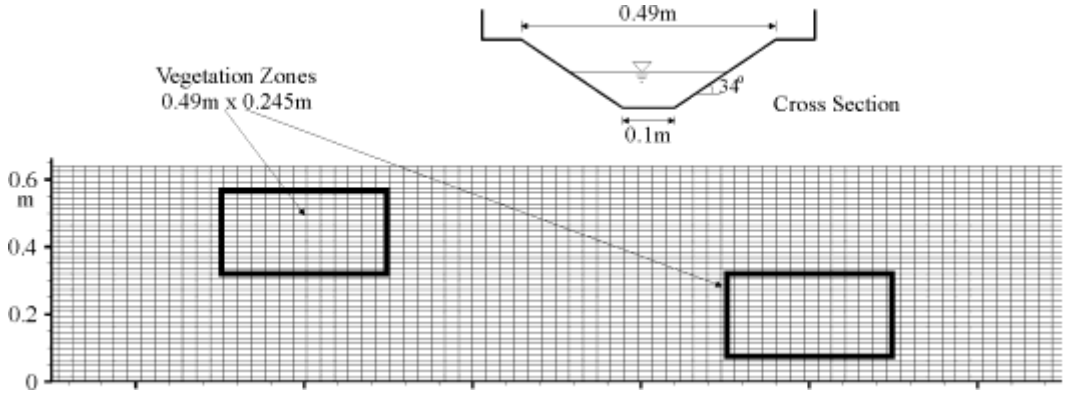

Fig. 7.15. Mesh and sketch of the experiments of Bennett and Alonso (2003).

$$\left(1-p'_m\right)\frac{\partial z_b}{\partial t}=\frac{\partial}{\partial x_i}\left[D_s q\left(1-r_s\right)C_t\frac{\partial z_b}{\partial x_i}\right] \tag{7.13}$$

where D_s is an empirical coefficient, q is the unit flow discharge, and r_s is the ratio of suspended load over the total-load sediment. Watanabe (1985) used D_s = 10 based on a free-body diagram of the grain in a sloping bed. Struiksma et al. (1985) used D_s = 4. Later studies such as Larson et al. (2003) and Karambas (2003) reported good results with D_s = 2. Sanchez and Wu (2011) used a value of about 1 to avoid over-smoothing the morphology change. In practice D_s may be a function of the flow and sediment characteristics and vary from site to site. D_s = 10 is used in the present test case.

Figs. 7.16 and 7.17 show the comparison of the measured and predicted changes in bed and bank topography near the second vegetation zone in an elapsed time of 110 minutes. Deposition occurs in and near the vegetation zone, whereas erosion occurs in the area away from the vegetation zones, resulting in a meandering channel planform. The channel erosion and deposition magnitudes and distribution zones are predicted reasonably well. The erosion and deposition magnitudes near the rectangular vegetation zone are larger than those near the semi-circular vegetation zone.

The same cases were also calculated by Wu et al. (2005) using a depth-averaged 2-D model which uses the standard k-ε turbulence model to close the turbulence stress terms, divides sediment into bed load and suspended load and takes into account the effect of helical flow on main flow and sediment transport and the effect of bed slope on bed load transport in a more sophisticated approach. Their model uses an implicit finite-volume method to solve the governing equations. Compared to the results of Wu et al. (2005) in Fig. 7.16(b), the present model results in Fig. 7.16(c) predict better the bank erosion patterns and the main channel deposition. This is due to that the present model uses two angles of repose for the wet and dry sediments, whereas the model of Wu et al. (2005) used only a single repose angle. The present model gives less erosion and deposition magnitude than the model of Wu et al. (2005), due to that the two models use different approach to accounting for bed slope effect and the present model does not consider the helical flow effect.

7.1.4 Summary

A depth-averaged 2-D finite-volume model has been developed to simulate the flow, sediment transport and morphological changes near marsh edge induced by rapidly-varying transient long waves such as dam-break flow, strong storm surge and tsunami waves. The model uses the generalized shallow water equations that take into account the effects of sediment concentration and bed change on the flow. The sediment transport model simulates the non-equilibrium transport of total load. The governing equations are solved using an explicit finite volume method with the HLL approximate Riemann solver to handle the mixed-regime flows and the wetting-drying problem efficiently. The method has first-order accuracy in time and second-order accuracy in space. A specially designed avalanching algorithm is adopted in this model, to consider different repose angles for the submerged materials and the dry materials above the water surface. The model uses a varying time step that satisfies the CFL stability condition and ensures the bed change at each time step is less than about ten percent of the local flow depth.

The developed model was tested using laboratory experiments of complete dam-break flow over movable bed in a sudden-expanded flume and partial dam-break flow in a straight flume carried out at the Université Catholique de Louvain, Belgium. The model predicted generally well the water surface evolution with time and the final bed profile in both experiments. The developed model was also tested using the laboratory experiment of bed changes around a vegetated island and alternate vegetation zones. The calculated bed changes agree reasonably well with the measurement data. The simulations and experiments show sediment deposition inside and in the front of the vegetation zones but erosion beside the vegetation zones where flow is strengthened. This implies that planting vegetation can stabilize the bed somehow, whereas the nearby erosion has potential to cause loss of planted vegetation.

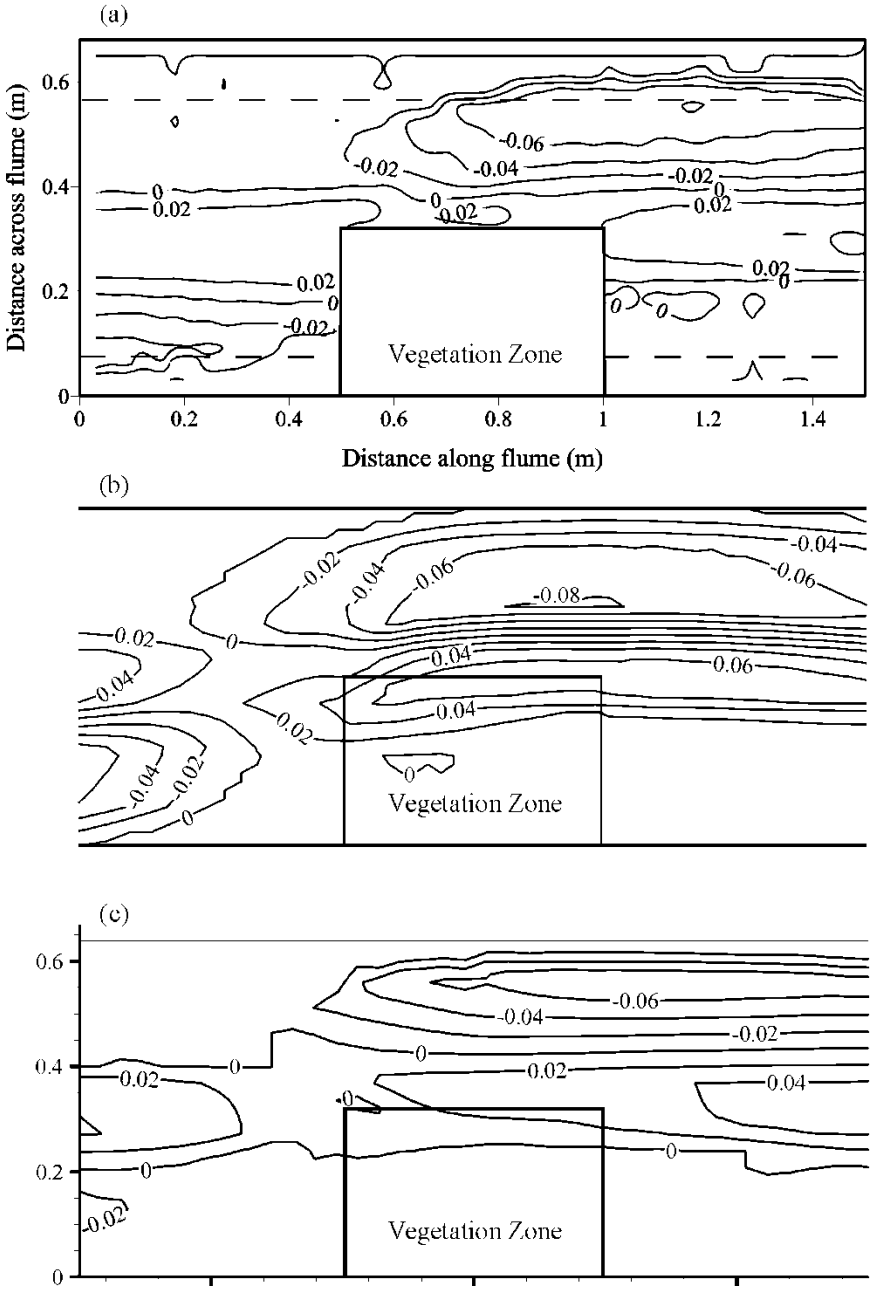

Fig. 7.16. Changes in bed topography due to rectangular vegetation zones: (a) Measured by Bennett and Alonso (2003); (b) Simulated by Wu et al. (2005); (c) Simulated by the present model. Dashed line shows the location of the channel top width, rectangle shows the extent of the vegetation zone, the unit of bed change is m, and the contour interval is 0.02 m. Changes in bed topography in the vegetation zone were not measured in the experiment.

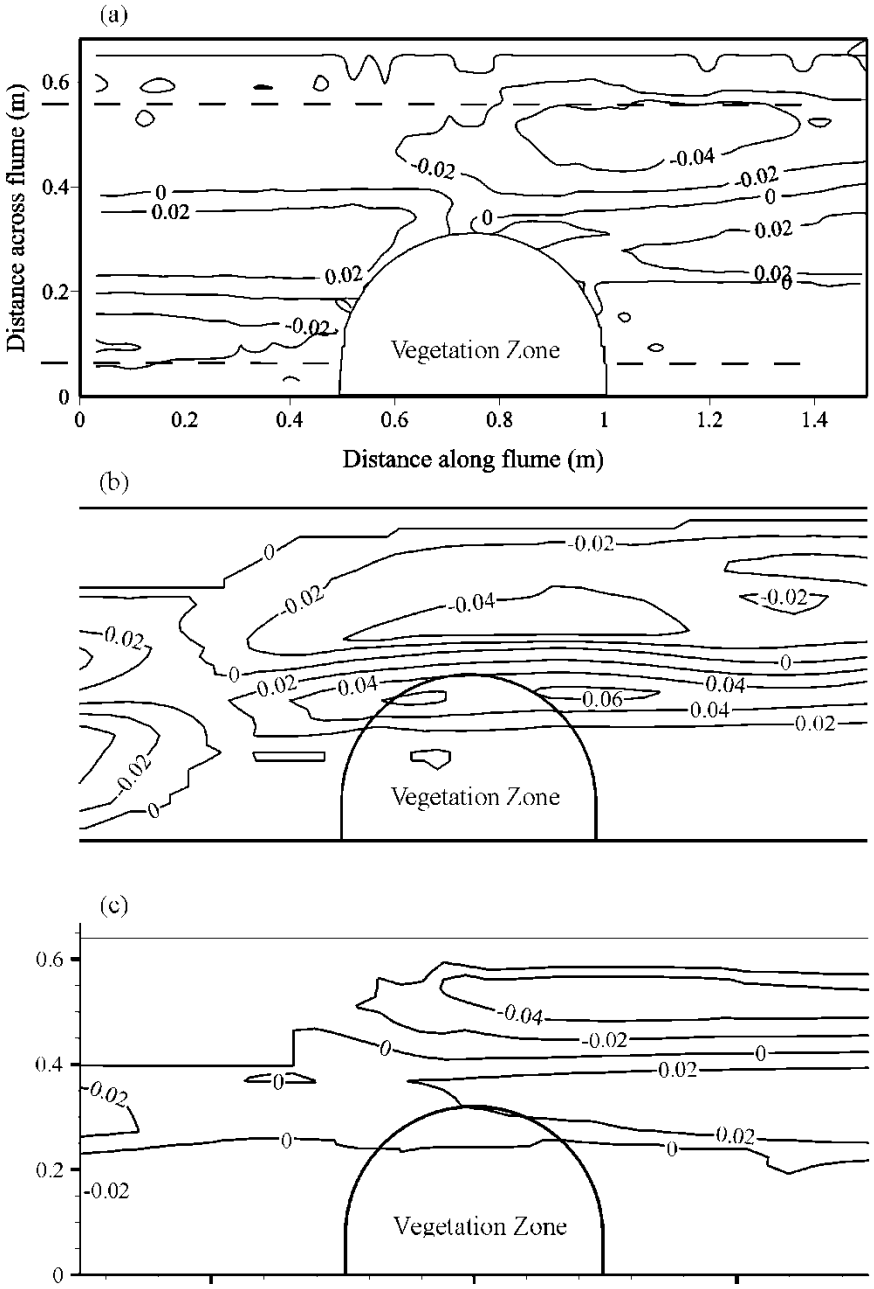

Fig. 7.17. Changes in bed topography due to semi-circular vegetation zones: (a) Measured by Bennett and Alonso (2003); (b) Simulated by Wu et al. (2005); (c) Simulated by the present model. Dashed line shows the location of the channel top width, semi-circle shows the extent of the vegetation zone, the unit of bed change is m, and the contour interval is 0.02 m. Changes in bed topography in the vegetation zone were not measured in the experiment.

The present model is applicable to simulation of marsh edge erosion induced by long waves, such as tsunami waves, storm surges and tidal bores. However, it has the following limitations. First, it does not consider yet that marsh vegetation may be damaged by strong storm surge and waves and thus lose the capability of protecting the bed. Second, the present model is only for long waves and cannot account for the effects of short waves, which often

induce alongshore sediment transport and marsh front slope (beach) erosion. Third, the present model has difficulty in handling the undercutting of marsh edge by waves and surges. The 3-D model based on the RANS equations and the VOF technique developed in the next section is more general and can relax some of these limitations; however, computational cost is significantly increased.

7.2 A 3-D Model for Rapidly-Varying Transient Flow and Sediment Transport over Erodible Beds

A 3-D finite-volume model has been developed to simulate rapidly-varying transient flows and the induced sediment transport and morphology changes. The model solves the RANS equations using a finite-volume method on collocated, unstructured grids. The rapidly-varying water surface is captured using a method introduced by Ubbink and Issa (1999) on arbitrary meshes. The model can be applied to simulate dam-break flow in alluvial channels, as well as storm surge and breaking waves over coastal beaches and marsh edges. The governing equations, numerical solutions, and test results of the 3-D model are presented in this section.

7.2.1 3-D Hydrodynamic Model of Rapidly-Varying Transient Flows

7.2.1.1 Governing Equations

The governing equations are 3-D continuity and RANS equations for incompressible flows, which are written in tensor form as

$$\frac{\partial u_i}{\partial x_i} = 0 \tag{7.14}$$

$$\frac{\partial u_i}{\partial t} + u_j \frac{\partial u_i}{\partial x_j} = \frac{1}{\rho} f_i - \frac{1}{\rho}\frac{\partial p}{\partial x_i} + \frac{1}{\rho}\frac{\partial \tau_{ij}}{\partial x_j} \tag{7.15}$$

where x_i (i=x,y,z) are the components of the coordinate system, u_i are the components of the flow velocity, f_i are the components of the external forces, p is the pressure, ρ is the water density, and τ_{ij} (j=x,y,z) are the shear stresses defined as

$$\tau_{ij} = \mu\left(\frac{\partial u_i}{\partial x_j} + \frac{\partial u_j}{\partial x_i}\right) \tag{7.16}$$

where μ includes molecular and turbulent viscosities. The turbulent viscosity is determined using the Smagorinsky sub-grid model:

$$\mu_t = C_s^2 \Delta^2 \sqrt{2\mathbf{S}_{ij}^2} \tag{7.17}$$

where C_s is a coefficient between 0.1 and 0.2, $S_{ij} = \left(\partial u_i/\partial x_j + \partial u_j/\partial x_i\right)\big/2$ and $\Delta=(dxdydz)^{1/3}$.

For convenience, Eqs. (7.14) and (7.15) can be also written in vector form as

$$\nabla \bullet \mathbf{u} = 0 \tag{7.18}$$

$$\frac{\partial \mathbf{u}}{\partial t} + \nabla \bullet (\mathbf{uu}) = -\frac{1}{\rho}\nabla p + \frac{1}{\rho}\mathbf{f} + \frac{1}{\rho}\nabla \bullet (\mu \nabla \mathbf{u}) \tag{7.19}$$

7.2.1.2 Numerical Solution Methods

Computational grid

The governing equations are discretized using a finite-volume method on collocated and unstructured grids with arbitrary shaped computational cells. The collocated grid, also known as non-staggered grid, allows storing all variables at the center point of each computational cell, which simplifies the computer programming and minimizes the amount of geometrical information required in each computational cell. The attraction of unstructured grids is based on their ability at handling complex geometries.

To preserve the efficiency of the numerical solutions on unstructured grids, the face addressing technique is used in this study. The approach used here was described by Jasak (1996) and applied in the numerical model developed by Ubbink (1997). Fig. 7.18 shows an arbitrary shaped computational cell where point P is the center of the control volume under consideration and point N is the center of a neighbor cell. Vector **A** is the outward-pointing face area vector normal to the face located between cell P and N. The face area vector is determined by the product of the face area and the representative unit vector of face under consideration. A vector called $\mathbf{d} = \overrightarrow{PN}$ can be defined as the vector which connects points P and N (dashed line in Fig. 7.18). The angle between vectors **A** and **d** determines if the mesh is orthogonal or non-orthogonal. The mesh is defined as non-orthogonal if the angle is not zero. The orthogonality and non-orthogonality of faces can be taken into account by introducing vectors **D** and **K** as follows:

$$\mathbf{D} = \frac{\mathbf{d}}{\mathbf{d} \bullet \mathbf{A}} |\mathbf{A}|^2 \tag{7.20}$$

$$\mathbf{K} = \mathbf{A} - \mathbf{D} \tag{7.21}$$

where orthogonality means **K** is equal to zero.

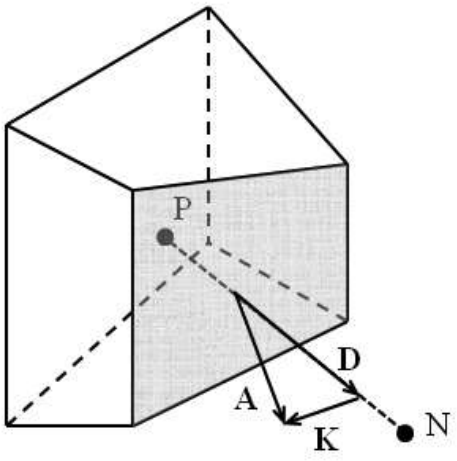

Fig. 7.18. Sketch of an arbitrary shaped computational cell.

Finite-volume discretization of divergence term

In the finite-volume method the governing equations are integrated in each computational cell. The divergence theorem can be used to integrate terms which contain vector divergence and scalar gradient. The divergence theorem, more commonly known especially in older literature as Gauss' theorem, defines the volume integral of the divergence of an arbitrary vector $\boldsymbol{\varphi}$ as

$$\int_V (\nabla \bullet \boldsymbol{\varphi}) dV = \oint_S \boldsymbol{\varphi} \bullet d\mathbf{S} \tag{7.22}$$

where V is the volume of the control volume and S is the surface boundary of the control volume. Eq. (7.22) can be written for a control volume with n faces as

$$\int_V (\nabla \bullet \boldsymbol{\varphi}) dV = \sum_{f=1}^{n} \mathbf{A}_f \bullet \boldsymbol{\varphi}_f \tag{7.23}$$

where subscript f is the face number and variables with index f determine the values on the face. Similarly, for an arbitrary scalar variable φ we have:

$$\int_V (\nabla \varphi) dV = \sum_{f=1}^{n} \mathbf{A}_f \varphi_f \tag{7.24}$$

A second-order accurate approximation of the gradient of flow properties can be calculated based on Eqs. (7.23) and (7.24) as follows:

$$(\nabla \bullet \boldsymbol{\varphi})_P = \frac{1}{V_P} \sum_{f=1}^{n} \mathbf{A}_f \bullet \boldsymbol{\varphi}_f \tag{7.25}$$

$$(\nabla \varphi)_P = \frac{1}{V_P} \sum_{f=1}^{n} A_f \varphi_f \tag{7.26}$$

Discretization of momentum equation

The momentum equation (7.19) can be integrated over the control volume as

$$\int_V \frac{\partial \mathbf{u}}{\partial t} dV + \int_V \nabla \bullet (\mathbf{uu}) dV = -\frac{1}{\rho} \int_V (\nabla p) dV + \frac{1}{\rho} \int_V \mathbf{f}\, dV + \frac{1}{\rho} \int_V \nabla \bullet (\mu \nabla \mathbf{u}) dV \tag{7.27}$$

Integrating the temporal, pressure gradient, and the external force terms over the control volume and also using Eqs. (7.23) and (7.24) leads to:

$$V_P \frac{\partial \mathbf{u}}{\partial t} + \sum_{f=1}^{n} (\mathbf{A}_f \bullet \mathbf{u}_f) \mathbf{u}_f = -\frac{V_P}{\rho} \nabla p + V_P \mathbf{g} + \sum_{f=1}^{n} \mathbf{A}_f \bullet (\upsilon \nabla \mathbf{u})_f \tag{7.28}$$

In Eq. (7.28), the dynamic viscosity μ is replaced with the kinematic viscosity υ, and the only external force that we consider is the gravitational body force, which on unit volume is $\rho \mathbf{g}$, where $\mathbf{g}$ is the vector acceleration of gravity.

The second term on the left-hand side of Eq. (7.28) is the convection term. The dot product of face area vector and velocity vector determines the volumetric flux at the face, thus:

$$\sum_{f=1}^{n}\left(\mathbf{A}_f \bullet \mathbf{u}_f\right)\mathbf{u}_f = \sum_{f=1}^{n} Flux_f \mathbf{u}_f \tag{7.29}$$

To approximate the velocity at the face, the upwind and Hybrid schemes are adopted in this study. The upwind scheme is only first-order accurate with strong numerical diffusion. The hybrid scheme is a combination of upwind scheme, which is first-order accurate, and central scheme, which is second-order accurate. When the Peclet number, the ratio of the strengths of convection and diffusion Pe=ρuΔx/ν, is bigger than 2 the upwind scheme is used otherwise the central scheme. The upwind and central schemes discretize the convection term as follows:

$$\sum_{f=1}^{n} Flux_f \mathbf{u}_f = \sum_{f=1}^{n}\left(\max(Flux_f, 0)\mathbf{u}_P + \min(Flux_f, 0)\mathbf{u}_N\right) \tag{7.30}$$

$$\sum_{f=1}^{n} Flux_f \mathbf{u}_f = \sum_{f=1}^{n} Flux_f \left(\frac{\mathbf{u}_P + \mathbf{u}_N}{2}\right) \tag{7.31}$$

The important feature of the diffusion term in Eq. (7.28) is how to treat the dot product of the face area and the velocity gradient at the face for non-orthogonal meshes. As shown in Fig. 7.18 and Eq. (7.20) the orthogonal and non-orthogonal contributions can be taken into account by introducing vectors **D** and **K**. Therefore, the diffusion term can be written as the following form:

$$\sum_{f=1}^{n} \mathbf{A}_f \bullet \left(\upsilon_f \nabla \mathbf{u}\right)_f = \sum_{f=1}^{n} \upsilon_f \left[\mathbf{D}_f \bullet \left(\nabla \mathbf{u}\right)_f + \mathbf{K}_f \bullet \left(\nabla \mathbf{u}\right)_f\right] \tag{7.32}$$

where the first and second terms in the bracket are the orthogonal and non-orthogonal contributions, respectively. The viscosity at the face is approximated by linear interpolation. Since the angle between vector **D** and vector **d** which connects points P and N is zero, the orthogonal contribution can be computed as

$$\mathbf{D}_f \bullet \left(\nabla \mathbf{u}\right)_f = \left|\mathbf{D}_f\right| \frac{\mathbf{u}_N - \mathbf{u}_P}{\left|\mathbf{d}_f\right|} \tag{7.33}$$

In the term accounting for the non-orthogonal contributions, the velocity gradient at the face is calculated using linear interpolation between the velocity gradient of the cell under consideration (Cell P) and the neighbor cell (Cell N). The velocity gradient of cells can be computed using Eq. (7.25). The non-orthogonal contribution is included in the source term.

The temporal term in Eq. (7.28) is discretized using the first-order Euler scheme as

$$V_P \frac{\partial \mathbf{u}}{\partial t} = V_P \frac{u_P^{t+\Delta t} - u_P^t}{\Delta t} \tag{7.34}$$

The velocity contribution of the previous time step is moved to the right-hand side of Eq. (7.28) and included in the source term.

The discretized terms are inserted into Eq. (7.28) to end up with a general discretization equation. For example, if the upwind scheme is used for convective term, the general discretized equation is written as

$$V_P \frac{\mathbf{u}_P^{t+\Delta t}}{\Delta t} + \sum_{f=1}^{n} \left(\max(Flux_f, 0)\mathbf{u}_P + \min(Flux_f, 0)\mathbf{u}_N \right) = -\frac{V_P}{\rho} \nabla p_P + \sum_{f=1}^{n} \nu_f \left| \mathbf{D}_f \right| \frac{\mathbf{u}_N - \mathbf{u}_P}{\left| \mathbf{d}_f \right|} + S_P \tag{7.35}$$

where the source term is $S_P = V_P \frac{\mathbf{u}_P^t}{\Delta t} + V_P \mathbf{g} + \sum_{f=1}^{n} \upsilon_f \left(\mathbf{K}_f \bullet (\nabla \mathbf{u})_f \right)$.

Putting the velocity terms of cell P on the left-hand side and terms of neighbor cells on the right-hand side yields:

$$a_P^u \mathbf{u}_P = \sum_{N=1}^{nb} a_N^u \mathbf{u}_N - \frac{V_P}{\rho} \nabla p_P + S_P^u \tag{7.36}$$

with $a_N^u = \max(-Flux_f, 0) + \nu_f \frac{\left| \mathbf{D}_f \right|}{\left| \mathbf{d}_f \right|}$, $a_P^u = \sum_{N=1}^{nb} a_N^u - \bar{S}_P^u$, $\bar{S}_P^u = -\sum_{N=1}^{nb} Flux_f - \frac{V_p}{\Delta t}$.

nb denotes the number of neighbor cells or the number of faces. Eq. (7.36) is the general finite-volume discretized form of momentum equation.

Eq. (7.36) shows linear dependence of velocity on pressure and vice versa. Therefore, the RANS equation calculates the correct values of velocity field only when the pressure field in the new time step is given. Since the new time step pressure is unknown, the RANS equation is solved using the guessed pressure which can be the initial or previous time step pressure. The velocity field calculated based on the guessed pressure may not necessarily satisfy the continuity equation. This reveals that a velocity-pressure coupling scheme is required. The PISO (Pressure Implicit solution by Split Operator method) scheme proposed by Issa (1986) is used in this study. To couple velocity and pressure we need to derive a pressure equation which is the subject of next section.

Pressure equation

We shall now derive the pressure equation from the continuity equation. By volume integrating Eq. (7.18) and using the Gauss' theorem we have:

$$\int_V \nabla \bullet \mathbf{u} dV = \sum_{f=1}^{n} \mathbf{A}_f \bullet \mathbf{u}_f = 0 \tag{7.37}$$

For deriving the pressure equation we need to approximate the face velocity values. In the collocated grid, which is adopted in the present study, if we calculate the face velocity by simple linear interpolation it leads to numerical oscillations in the pressure and velocity fields. In order to avoid the decoupling of the pressure and velocity, the momentum interpolation method introduced by Rhie and Chow (1983) is used. This interpolation technique improved the pressure-velocity coupling on the non-staggered grid (Wu 2007).

The discretized momentum equation (7.36) can be rewritten as

$$\mathbf{u}_P = \frac{\mathbf{H}(\mathbf{u})_P}{a_P} - \frac{V_P}{a_P \rho} \nabla p_P \tag{7.38}$$

where $\mathbf{H}(\mathbf{u})_P = \sum_{N=1}^{nb} a_N^u \mathbf{u}_N + S_P^u$.

The face value of the velocity is approximated by

$$\mathbf{u}_f = \left(\frac{\mathbf{H}(\mathbf{u})_P}{a_P^u}\right)_f - \left(\frac{V_P}{a_P^u \rho}\nabla p_P\right)_f \tag{7.39}$$

The face value term $\left(\mathbf{H}(\mathbf{u})_P / a_P^u\right)_f$ is evaluated using the Rhie and Chow's momentum interpolation from those at two neighboring cell centers as follows:

$$\left(\frac{\mathbf{H}(\mathbf{u})}{a_P^u}\right)_f = f_n\left(\frac{\mathbf{H}(\mathbf{u})}{a_P^u}\right)_P + (1-f_n)\left(\frac{\mathbf{H}(\mathbf{u})}{a_P^u}\right)_N \tag{7.40}$$

where f_n is the interpolation function between nodes P and N which is equal to 0.5 for grids with constant grid spacing.

The face value of pressure gradient is calculated by taking into account the orthogonal and non-orthogonal contributions:

$$\sum_{f=1}^{n} \mathbf{A}_f \bullet (\nabla p)_f = \sum_{f=1}^{n} \left(\mathbf{D}_f \bullet (\nabla p)_f + \mathbf{K}_f \bullet (\nabla p)_f\right) \tag{7.41}$$

where $\mathbf{D}_f \bullet (\nabla p)_f = |\mathbf{D}_f| \frac{p_N - p_P}{|\mathbf{d}_f|}$.

In the non-orthogonal term, the face value of pressure gradient is calculated similarly to the face value of velocity gradient in the non-orthogonal diffusion term of the momentum equation described above. The non-orthogonal contribution is considered in the source term of the pressure equation. Substituting Eq. (7.39) into Eq. (7.37), the general form of the pressure equation can be formulated as

$$a_P^p p_P = \sum_{N=1}^{nb} a_N^p p_N + S_P^p \tag{7.42}$$

where $a_N^p = \left(\frac{V_P}{a_P^u \rho}\right)_f \frac{|\mathbf{D}_f|}{|\mathbf{d}_f|}$, $a_P^p = \sum_{N=1}^{nb} a_N^p$, and $S_P^p = \sum_{f=1}^{n} \mathbf{K}_f \bullet (\nabla p)_f - \sum_{f=1}^{n} \mathbf{A}_f \bullet \left(\frac{\mathbf{H}(\mathbf{u})}{a_P^u}\right)_f$.

Pressure-velocity coupling

The most widely-used pressure-velocity coupling schemes include SIMPLE (Semi Implicit Method for Pressure Linked Equations) scheme (Patankar and Spalding, 1972), SIMPLER (SIMPLE Revised) scheme (Patankar, 1980), SIMPLEC (SIMPLE Consistence) scheme (Doormaal and Raithby, 1984), and PISO (Pressure Implicit solution by Split Operator) scheme (Issa, 1986). The PISO scheme is adopted in the present study. The solution steps are summarized as follows:

Step 1: The RANS Eq. (7.36) is solved based on the pressure field of the previous time step. This step calculates the velocity field which does not necessarily satisfy the continuity equation.

Step 2: New values of **H**(**u**) are calculated using Eq. (7.38) and based on the velocity field calculated by the RANS equation in the first step.
Step 3: Using the new values of **H**(**u**) the pressure Eq. (7.42) is solved to obtain a new pressure field.
Step 4: The new flow fluxes $F_f=\mathbf{A}_f \cdot \mathbf{u}_f$ are calculated using the new **H**(**u**) and pressure field. The face value of velocity is computed using Eq. (7.39).
Step 5: Velocity field is corrected using Eq. (7.38) and the new **H**(**u**) and pressure field.
Step 6: If the corrected velocity field satisfies the continuity equation (error less than a small value), the most recent calculated variables are the final values in the current time step, otherwise a new iteration starts using the most recent updated variables.

7.2.1.3 **Boundary Conditions**

The boundary conditions are categorized into inlet, outlet, solid wall, and water surface boundary conditions.

The pressure of the inlet cells are defined using the Neumann condition with constant gradient $\nabla p = \rho \mathbf{g}$. The water surface elevation at inlet needs to be defined in order to specify the F-function boundary condition. Predefined velocity should be assigned to inlet cells.

The Neumann condition with constant gradient $\nabla p = \rho \mathbf{g}$ is used at outlet cells to determine the boundary values of pressure. The velocity is determined with zero gradient condition. The water surface elevation at outlet cells is a copy of adjacent interior cells.

Similar to inlet and outlet boundaries the pressure of solid walls is calculated using the Neumann condition with constant gradient. No-slip condition is used to define the velocity at the boundaries.

Cells which contain the water surface are considered as the water surface boundary. The pressure in a surface cell is calculated by interpolation (or extrapolation) between the pressures at the water surface (the atmospheric pressure) and a neighbor fluid cell as follows:

$$p_{i,j,k} = (1-\eta)\, p_n + \eta\, p_s \tag{7.43}$$

where P_n is the pressure in the neighbor fluid cell, P_s is the water surface pressure and is equal to the atmospheric pressure, and η is a coefficient illustrated in Fig. 7.19. The neighbor cell is chosen using the direction of water surface. The Neumann condition with zero gradient is used to define other flow properties.

The bed and solid wall friction is considered by taking into account the bed shear stress:

$$\boldsymbol{\tau}_{bi} = \rho C_{fb} \mathbf{u}_i \overline{U} \tag{7.44}$$

where C_{fb} is the bed friction coefficient and $\overline{U} = \sqrt{u^2 + v^2 + w^2}$. The bed friction coefficient can be calibrated using measured data. For the test cases presented in this chapter, the friction coefficient C_{fb} is specified equal to 0.001.

7.2.1.4 **Surface Capturing Method**

In the present model the water surface movement is traced using the VOF method. The VOF method treats the water surface by introducing the F-function to be unity at any cell occupied by fluid and zero at empty cells. This implies that a fluid cell (F cell) filled by water has the F-function of a unit value, whereas a zero value indicates an empty cell (E cell) which is filled by

air. Cells with F-function between zero and one contain water surface and are called surface cells (S cell). For an incompressible flow, the VOF algorithm solves the following advection equation to compute the time evolution of the F-function:

$$\frac{\partial F}{\partial t}+\frac{\partial (uF)}{\partial x}+\frac{\partial (vF)}{\partial y}+\frac{\partial (wF)}{\partial z}=0 \tag{7.45}$$

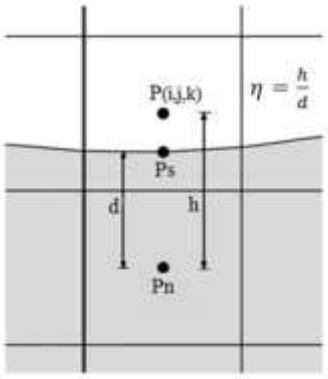

Fig. 7.19. Definition of parameters used in the pressure interpolation of the surface cells.

Ubbink and Issa (1999) developed an interface capturing technique called CICSAM (Compressive Interface Capturing Scheme for Arbitrary Meshes) which is developed in the context of multi-dimensional applications, avoiding the need to use operator splitting and therefore applicable on unstructured meshes.

For convenience, Eq. (7.45) can be rewritten as

$$\frac{\partial F}{\partial t}+\nabla\bullet\left(\mathbf{u}F\right)=0 \tag{7.46}$$

Integrating over control volume gives:

$$\int_V \frac{\partial F}{\partial t}dV+\int_V \nabla\bullet\left(\mathbf{u}F\right)dV=0 \tag{7.47}$$

$$\frac{F_P^{t+\Delta t}-F_P^t}{dt}V_P+\sum_{f=1}^{n}\mathbf{A}_f\bullet\left(\mathbf{u}F\right)_f=0 \tag{7.48}$$

Since F is a scalar variable, Eq. (7.48) can be reformulated as

$$F_P^{t+\Delta t}=F_P^t-\frac{\Delta t}{V_P}\sum_{f=1}^{n}\left(\mathbf{A}_f\bullet\mathbf{u}_f\right)F_f \tag{7.49}$$

F is a step function which changes between zero and one abruptly and special care must be taken into account to estimate the face values of F. In the CICSAM scheme, which was developed on arbitrary meshes, a switching strategy between HYPER-C and ULTIMATE-QUICKEST (UQ) schemes is used to estimate the face values of F. The CICSAM scheme calculates the face value of F as follows:

$$F_f=(1-\beta_f)F_D+\beta_f F_A \tag{7.50}$$

where $\beta_f = \left(F_f - F_D\right)/\left(1 - F_D\right)$. Subscripts *f* stands for cell face, *D* for donor cell, and *A* for acceptor cell. The flow direction must be used to determine the donor and acceptor cells; the donor cell is always upstream and the acceptor cell is always downstream of the face under consideration. For instance, a schematic representation of donor and acceptor cells for a 1-D flow is depicted in Fig. 7.20. The variables with a hat are normalized and defined as

$$F_f = \frac{F_f - F_U}{F_A - F_U} \quad \text{and} \quad F_D = \frac{F_D - F_U}{F_A - F_U} \tag{7.51}$$

in which subscript *U* stands for the cell upstream of the donor cell. The normalized value of *F* at the face, F_f, can be calculated using a blending strategy between HYPER-C and UQ schemes as follows:

$$F_f = \gamma_f F_{f(Hyper-C)} + (1-\gamma_f) F_{f(UQ)} \tag{7.52}$$

where γ_f is the blending function, $F_{f(HYOER-C)}$ and $F_{f(UQ)}$ are face values of F calculated using the HYPER-C and UQ schemes as

$$F_{f(HYPER-C)} = \begin{cases} \min\left(1, \dfrac{F_D}{C_D}\right) & \textit{when } 0 \le F_D \le 1 \\ F_D & \textit{otherwise} \end{cases} \tag{7.53}$$

$$F_{f(UQ)} = \begin{cases} \min\left(F_{f(HYPER-C)}, \dfrac{8C_D F_D + (1-C_D)(6F_D+3)}{8}\right) & \textit{when } 0 \le F_D \le 1 \\ F_D & \textit{otherwise} \end{cases} \tag{7.54}$$

where C_D is the summation of the Courant number for each outflow face of the donor cell:

$$C_D = \sum_{f=1}^{n} \left| C_f^{out} \right| \tag{7.55}$$

The blending function γ_f controls the switching process between the HYPER-C and UQ schemes. The blending function is based on the angle between the interface and the direction of flow motion and takes values between 0 and 1. When the interface orientation is normal to the direction of motion the blending function is equal to one and when the interface is tangential to the motion it equals 0. The blending function is formulated as follows:

$$\gamma_f = \min\left(\frac{\cos(2\theta_f)+1}{2}, 1\right) \tag{7.56}$$

where $\theta_f = \arccos\left|\dfrac{(\nabla F)_D \bullet \mathbf{d}_f}{|(\nabla F)_D||\mathbf{d}_f|}\right|$. Vector $\mathbf{d}_f$ connects the center points of the donor and acceptor cells.

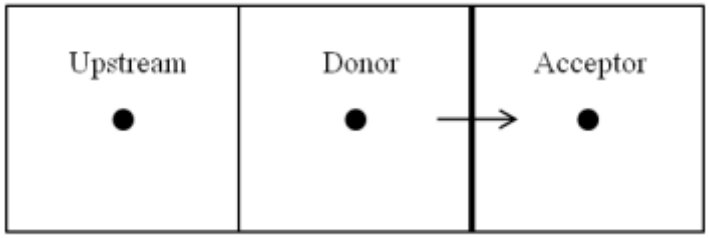

Fig. 7.20. Definition of donor, acceptor, and upstream cells (the arrow shows the flow direction at the face under consideration).

7.2.2 3-D Sediment Transport Model

Sediment transported by the flow can be divided into bed load and suspended load. The bed load consists of sediment particles that roll, crawl, or slide in a thin layer above the river bed shown in Fig. 7.21. It usually accounts for 5-25 percent of the total load for fine particles and more for coarse particles in natural rivers (Wu 2007). The suspended load consists of sediment particles that are suspended in the water column above the bed-load layer. The suspended-load sediments are supported by the flow turbulence. Correspondingly, the water column can be divided into a bed-load zone with a thickness of δ_b above the bed level z_b and a suspended-load zone from $z_b+\delta_b$ to the water surface z_s. The thickness of the bed-load layer is usually assumed to be about twice the sediment particle diameter or half the bed-form height.

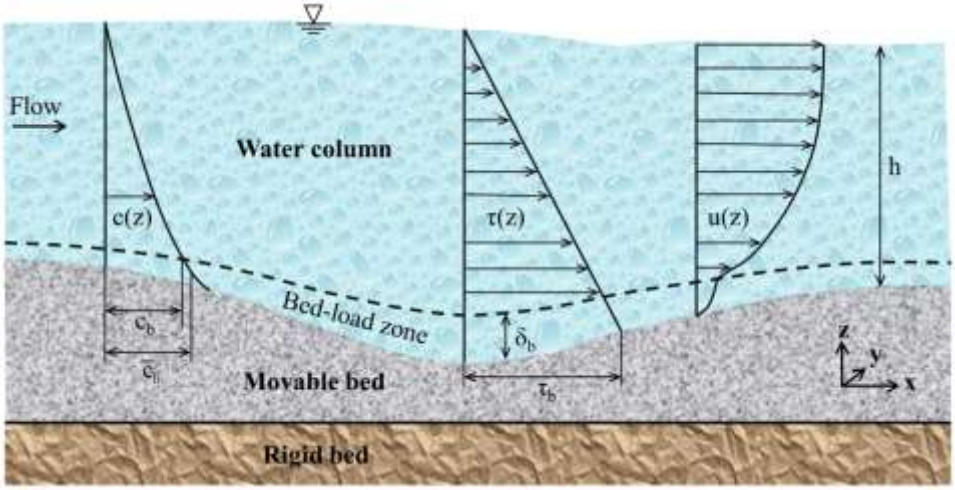

Fig. 7.21. Schematic view of flow and sediment transport (c(z)=sediment concentration, τ(z)= shear stress, u(z)= stream-wise velocity, c_b=near-bed sediment concentration, $\bar{c}_b$ =averaged bed-load concentration, and τ_b=bed shear stress).

Because of variations in flow conditions and channel morphology the sediment transport in natural rivers usually is in non-equilibrium state. Sediment cannot reach new equilibrium states instantaneously due to temporal and spatial lags between flow and sediment transport (Wu 2007). Therefore, the non-equilibrium sediment transport should be taken into account in a model of sediment transport under rapidly-varying flow conditions. In the next section the

governing equations of non-equilibrium sediment transport in suspended-load and bed-load layers are presented.

7.2.2.1 Suspended-Load Transport Equation

The governing equation of single-sized sediment transport in the suspended-load zone with a thickness of h-δ_b is formulated as

$$\frac{\partial c}{\partial t}+\frac{\partial\left[\left(u_j-\omega_s\delta_{j3}\right)c\right]}{\partial x_j}=\frac{\partial}{\partial x_j}\left(\varepsilon_s\frac{\partial c}{\partial x_j}\right) \tag{7.57}$$

where c is the suspended-load concentration, ε_s is the turbulent diffusivity of sediment, ω_s is the settling velocity, and δ_{j3} is the Kronecker delta with "3" indicating the vertical direction. Eq. (7.57) can be written in the following form:

$$\frac{\partial c}{\partial t}+\nabla\bullet\left(\mathbf{u}c\right)=\nabla\bullet\left(\varepsilon_s\nabla c\right)+\frac{\partial\left(\omega_s\delta_{j3}\right)c}{\partial x_j} \tag{7.58}$$

and integrating it over the control volume and using the Gauss' theorem yield

$$V_P\frac{\partial c}{\partial t}+\sum_{f=1}^{n}\mathbf{A}_f\bullet\left(\mathbf{u}c\right)_f=\sum_{f=1}^{n}\mathbf{A}_f\bullet\left(\varepsilon_s\nabla c\right)_f+\int\frac{\partial\left(\omega_s\delta_{j3}\right)c}{\partial x_j}dV \tag{7.59}$$

Similar to Eqs. (7.29) and (7.32), the convection and diffusion terms in Eq. (7.59) can be treated as

$$\sum_{f=1}^{n}\mathbf{A}_f\bullet\left(\mathbf{u}c\right)_f=\sum_{f=1}^{n}Flux_f c_f \tag{7.60}$$

$$\sum_{f=1}^{n}\varepsilon_{sf}\mathbf{A}_f\bullet\left(\nabla c\right)_f=\sum_{f=1}^{n}\varepsilon_{sf}\left[\mathbf{D}_f\bullet\left(\nabla c\right)_f+\mathbf{K}_f\bullet\left(\nabla c\right)_f\right] \tag{7.61}$$

To discretize the last term on the right-hand side of Eq. (7.59) on unstructured meshes, the settling velocity is assumed to be a vector variable $\boldsymbol{\omega}_s$=(0,0, $\omega_{s,z}$), yielding

$$\int\frac{\partial\left(\omega_s\delta_{j3}\right)c}{\partial x_j}dV=\int\nabla\bullet\left(\boldsymbol{\omega}_s c\right)dV=\sum_{f=1}^{n}\mathbf{A}_f\bullet\left(\boldsymbol{\omega}_s c\right)_f \tag{7.62}$$

Eq. (7.62) is included in the source term. The face concentration can be either the concentration of cell under consideration, cell P, or a neighbor cell, cell N, depending on the normal vector of the face. If the z-component of the face area vector $\boldsymbol{A}_f$ is positive the face concentration is equal to the concentration of neighbor cell N. If the z-component of the face area vector is negative the face concentration is equal to the concentration of cell under consideration, cell P.

The temporal term in Eq. (7.59) is discretized using the first-order Euler scheme as

$$V_P\frac{\partial c}{\partial t}=V_P\frac{c_P^{t+\Delta t}-c_P^{t}}{\Delta t} \tag{7.63}$$

Inserting Eqs. (7.60)–(7.63) into Eq. (7.59) leads to the following discretized equation of suspended-load sediment transport:

$$a_P^c c_P = \sum_{N=1}^{nb} a_N^c c_N + S_P^c \tag{7.64}$$

where $a_N^c = \max(-Flux_f, 0) + \varepsilon_{sf} \dfrac{|\mathbf{D}_f|}{|\mathbf{d}_f|}$, $a_P^c = \sum_{N=1}^{nb} a_N^c - \bar{S}_P^c$, $\bar{S}_P^c = -\sum_{N=1}^{nb} Flux_f - \dfrac{V_p}{\Delta t}$, and

$$S_P^c = V_P \frac{c_P^t}{\Delta t} + \sum_{f=1}^{n} \mathbf{A}_f \bullet (\boldsymbol{\omega}_s c)_f + \sum_{f=1}^{n} \varepsilon_{sf} \left(\mathbf{K}_f \bullet (\nabla c)_f \right)$$

If the face value of concentration in the second term of S_P^c takes the value of neighbor cell, it is kept in the source term S_P^c; otherwise, it is included in $\bar{S}_P^c$. Eq. (7.64) is solved explicitly.

7.2.2.2 **Bed-Load Transport Equation**

Because the bed-load layer is very thin, the bed-load transport equation in the 3-D model has the same formulation as the horizontal 2-D model (Wu 2007):

$$\frac{\partial (q_b/u_b)}{\partial t} + \frac{\partial (\alpha_{bx} q_b)}{\partial x} + \frac{\partial (\alpha_{by} q_b)}{\partial y} = \frac{1}{L}(q_{b*} - q_b) \tag{7.65}$$

where q_b and q_{b*} are the actual and equilibrium (capacity) transport rates of bed load, u_b is the bed-load velocity which may be determined using an empirical formula but here is assumed to be equal to the near-bed flow velocity $\bar{U} = (u^2 + v^2)^{0.5}$, $a_{bx}=u/u_b$ and $a_{by}=v/u_b$ are the direction cosines of bed-load movement, and L is the adaptation length of sediment. The equilibrium (capacity) transport rate of bed load is determined using an empirical formula described later.

Eq. (7.65) is valid over the bed-load zone δ_b. In this study the bed load is assumed to occupy the first row of computational cells as shown in Fig 7.22, and the suspended-load zone starts from the second row. Because Eq. (7.65) does not include the bed-load layer thickness, δ_b and the z-grid spacing Δz of the first raw of cells are not necessarily the same. However, to ensure sediment mass balance, it is a good practice to arrange both approximately the same.

To integrate Eq. (7.65) over the control volume for unstructured meshes the direction cosines should be defined as a vector variable $\boldsymbol{a}_b=(a_{bx},a_{by},0)$. Thus, the bed-load transport equation can be written as

$$\frac{\partial (q_b/u_b)}{\partial t} + \nabla \bullet (\boldsymbol{\alpha}_b q_b) = \frac{1}{L}(q_{b*} - q_b) \tag{7.66}$$

Integrating Eq. (7.66) over the control volume and using the Gauss' theorem yields

$$V_P \frac{\partial (q_b/u_b)}{\partial t} + \sum_{f=1}^{n} \mathbf{A}_f \bullet (\boldsymbol{\alpha} q_b)_f = \frac{V_p}{L}(q_{b*} - q_b)_P \tag{7.67}$$

The term on the right-hand side of Eq. (7.67) is included the source term. In addition, the bed-load rate of the previous time step is included in the source term as well. The face values of

bed-load rate in the second term on the left-hand side of Eq. (7.67) are estimated using the first-order upwind scheme. The final discretized equation of bed-load sediment transport can be formulated as follows:

$$a_P^{q_b} q_{b,P} = \sum_{N=1}^{nb} a_N^{q_b} q_{b,N} + S_P^{q_b} \tag{7.68}$$

where $a_N^{q_b} = \phi_{upwinding}\left(\mathbf{A}_f \bullet \boldsymbol{\alpha}_f\right)$, $a_P^{q_b} = \sum_{N=1}^{nb} a_N^{q_b} - \bar{S}_P^{q_b}$, $S_P^{q_b} = \frac{V_P}{u_b \Delta t} q_{b,P}^t + \frac{V_P}{L} q_{b^*,P}$, and $\bar{S}_P^{q_b} = -\sum_{N=1}^{nb}\left(\mathbf{A}_f \bullet \boldsymbol{\alpha}_f\right) - \frac{V_p}{u_b \Delta t} - \frac{V_p}{L}$. $\phi_{upwinding}$ is the upwinding coefficient which depends on the flow direction. When the flux at the face is negative $\phi_{upwinding}$=-1 otherwise $\phi_{upwinding}$=0.

Similar to the suspended-load calculations, Eq. (7.68) is solved explicitly.

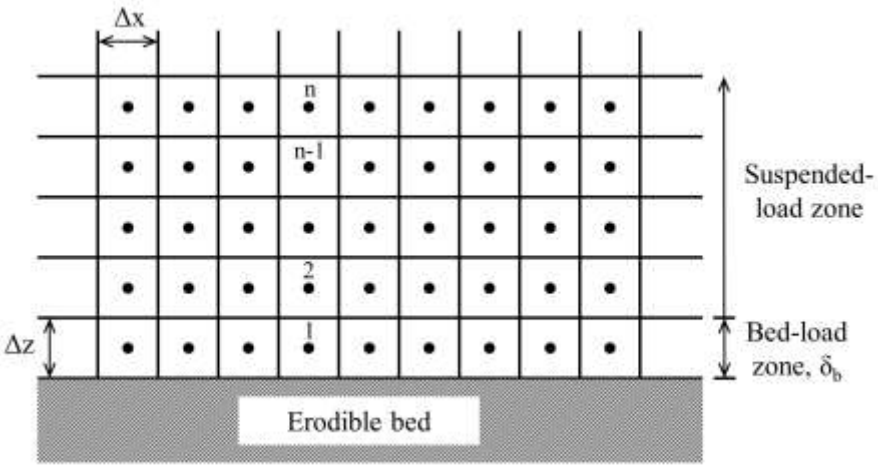

Fig. 7.22. Schematic definition of the bed-load and suspended-load zones in the finite-volume computational mesh

7.2.2.3 **Bed Change Equation**

The bed change due to total load is calculated using the following relation:

$$\left(1 - p'_m\right)\frac{\partial z_b}{\partial t} = D_b - E_b + \frac{1}{L}\left(q_b - q_{b^*}\right) \tag{7.69}$$

where p'_m is the porosity of sediment deposit, and D_b and E_b are the near-bed deposition and entrainment fluxes of sediment, respectively. The near-bed sediment exchange flux, D_b-E_b, is calculated by

$$D_b - E_b = \omega_s\left(c_b - c_{b^*}\right) \tag{7.70}$$

where c_b and c_{b^*} are the actual and equilibrium (capacity) near-bed sediment concentrations, respectively. The equilibrium (capacity) near-bed sediment concentration is calculated using an empirical equation described in a later section.

The bed change equation (7.69) is discretized as

$$\Delta z_{b,P} = \frac{\Delta t}{1-p'_m}\left[D_{b,P}^{t+\Delta t} - E_{b,P}^{t+\Delta t} + \frac{1}{L}\left(q_{b,P}^{t+\Delta t} - q_{b^*,P}^{t+\Delta t} \right) \right] \tag{7.71}$$

The near-bed concentration must be calculated in order to determine the near-bed sediment exchange flux in Eq. (7.70). Wu et al. (2000a) derived the following relation for the near-bed concentration:

$$c_b = c_2 + c_{b^*}\left(1 - e^{-(z_2 - z_b - \delta_b)\omega_s/\varepsilon_s}\right) \tag{7.72}$$

where subscript 2 stands for the cell above the boundary between the bed-load and suspended-load zones as shown in Fig. 7.22. The equilibrium (capacity) near-bed sediment concentration c_{b^*} is explained in the next section.

7.2.2.4 **Model Parameters**

In order to close the developed sediment transport model, several parameters, such as the suspended-load near-bed equilibrium concentration, bed-load transport capacity, sediment turbulent diffusivity, settling velocity, and adaptation length, need to be determined using empirical formulas, as described in this section.

Equilibrium transport rate of bed load

The equilibrium transport rate of single-sized bed load, q_{b^*}, is computed by the Wu et al. (2000b) equation:

$$q_{b^*} = 0.0053\sqrt{\left(\gamma_s/\gamma_w - 1\right) g d^3}\, T^{2.2} \tag{7.73}$$

where q_{b^*} is by volume per unit time and width (m^2/s), γ_s and γ_w are the sediment and water specific weights, d is the sediment diameter, and T is the transport stage number defined as follows:

$$T = k_t \frac{\tau'_b}{\tau_{cr}} - 1 \tag{7.74}$$

where τ'_b is the grain bed shear stress, τ_{cr} is the critical bed shear stress $\tau_{cr} = 0.03\left(\gamma_s - \gamma_w\right) d$, and k_t is a correction factor. The grain bed shear stress is defined as

$$\tau'_b = C'_{fb}\tau_b = \beta C_{fb}\rho\left(u^2 + v^2\right) \tag{7.75}$$

where C_{fb} is the total bed friction coefficient due to the grain and bed form resistances, C'_{fb} is the bed friction coefficient due to the grain resistance, and β is a coefficient between 0 and 1.

The correction factor k_t was introduced by Wu and Wang (2007) to consider very high sediment concentration at the lower layer near the bed under dam-break flow conditions. Therefore, replacing the water density in shear stress formula with the mixture density near the bed leads to the following correction factor:

$$k_t = 1 + \frac{c_b \rho_s}{\left(1 - c_b\right)\rho_w} \tag{7.76}$$

where c_b is the concentration of sediment near the bed, ρ_s is sediment density, and ρ_w is water density. Wu and Wang (2007) found that $k_t \approx 1+1.5\rho_s/\rho_w$ is adequate for two cases tested by their 1-D model.

Near-bed equilibrium concentration of suspended load

The equilibrium (capacity) near-bed concentration of single-sized suspended load, c_{b*}, is often related the bed-load transport rate as

$$c_{b*} = \frac{q_{b*}}{\delta_b u_b} \tag{7.77}$$

where u_b is the bed=load velocity can be determined by the van Rijn's formula or the one modified by Wu (2007). Using this equation with the Wu et al. bed-load transport rate formula (7.73) yields the following near-bed concentration relationship:

$$c_{b*} = \frac{0.0053}{a\delta_b} T^{1.7} d \tag{7.78}$$

where a is an empirical coefficient of about 1.5.

Sediment turbulent diffusivity

The vertical profile of sediment turbulent diffusivity, ε_s, is usually related to the eddy viscosity by $\varepsilon_s=\nu_t/\sigma_c$ with σ_c being the Schmidt number which is between 0.5 and 1. An alternative way is the vertical profile of sediment diffusivity derived by van Rijn (1984), which assumes a parabolic distribution in the lower half of the flow depth and a constant value in the upper half of the flow depth, as expressed below:

$$\varepsilon_s = \begin{cases} \kappa U_* \left(1-\left(z/h\right)\right) z/\sigma_s & z/h < 0.5 \\ 0.25\kappa U_* \, h/\sigma_s & z/h \geq 0.5 \end{cases} \tag{7.79}$$

where κ is the von Karman constant which typically is equal to 0.41 for clear water flow. Van Rijn (1984) applied a damping factor to the von Karman constant in order to account for the effect of sediment concentration on the sediment-laden flow:

$$\kappa = 0.41\left[1+\left(c/c_0\right)^{0.8} - 2\left(c/c_0\right)^{0.4}\right] \tag{7.80}$$

where c is the sediment concentration by volume and c_0 is the maximum sediment concentration (=0.65).

Sediment settling velocity

The settling velocity in clear water is calculated using the following relation proposed by Wu and Wang (2006):

$$\omega_s = \frac{M\nu}{Nd}\left[\sqrt{\frac{1}{4}+\left(\frac{4N}{3M^2}D_*^3\right)^{1/n}} - \frac{1}{2}\right]^n \tag{7.81}$$

where d is the nominal diameter or representative diameter in single-sized sediment transport calculations (in meter), $M=53.5e^{-0.65SP}$, $N=5.65e^{-2.5SP}$, $n=0.7+0.9S_P$ with S_P being the sediment

particle shape factor. The effect of sediment concentration on the settling velocity is taken into account by the Oliver (1961) relation as follows:

$$\omega_{sm} = \left(1 - 2.15c\right)\left(1 - 0.75c^{0.33}\right)\omega_s \tag{7.82}$$

where ω_{sm} is the settling velocity of sediment particles in turbid water.

Sediment adaptation length

The adaptation length is a characteristic distance for sediment to reach the equilibrium transport from the non-equilibrium transport. It is an important parameter in the non-equilibrium sediment transport model. The adaptation length of suspended load is estimated as

$$L_s = \frac{\bar{U}h}{\alpha\omega_s} \tag{7.83}$$

where a is the adaptation coefficient which is determined by calibration.

Since the bed-load movement is closely associated with bed forms, the bed-load adaptation length L_b may differ case by case. L_b is often determined by model calibration based on measured data.

Because bed-material load is a combination of bed load and suspended load the adaptation length of sediment can be given as the larger of L_b and L_s (Wu et al., 2004):

$$L = \max\left(L_b, L_s\right) \tag{7.84}$$

7.2.3 Model Testing

Case 1: Initial stage of dam-break flow over wet and dry flat beds

The developed model is first tested using the experiments of initial stage of dam-break flows over a wet bed and a dry bed. The wet-bed experiment was conducted by Stansby et al. (1998) in a flume 15.24 m long, 0.4 m wide, and 0.4 m high with a horizontal bed. The dam was located 9.76 m downstream of the upper end. The initial water depth in the reservoir, h_0, was 10 cm and the downstream depth was 4.5 cm. To simulate the water surface movement in detail, a fine computational grid spacing equal to 0.75 cm is used. In the experiment, A 7 kg weight attached to a wire rope was used to pull up the dam rapidly. Herein, it is assumed the gate is lifted instantaneously. Fig. 7.23 compares the measured and calculated water surface profiles at several initial instants after dam breaking. Spatial scales are normalized by h_0, and x/h_0=0 corresponds to the dam site. One can see the calculated water surface profiles are generally in a good agreement with the measured data.

The dry-bed experiment was carried out by Kocaman (2007) and the data published by Ozmen-Cagatay and Kocaman (2010). The laboratory flume was 9 m long, 0.3 m wide, and 0.34 m high. The dam was located 4.65 m from the channel entrance. The computational grid spacing is 0.75 cm. Similar to the previous case with a downstream wet bed, the dam break was simulated by instantaneous dam removal. Fig. 7.24 shows a good agreement between the measured and calculated water surface profiles at several instants. The calculated results reveal that the developed 3-D finite-volume model can simulate the initial stage of dam-break flow.

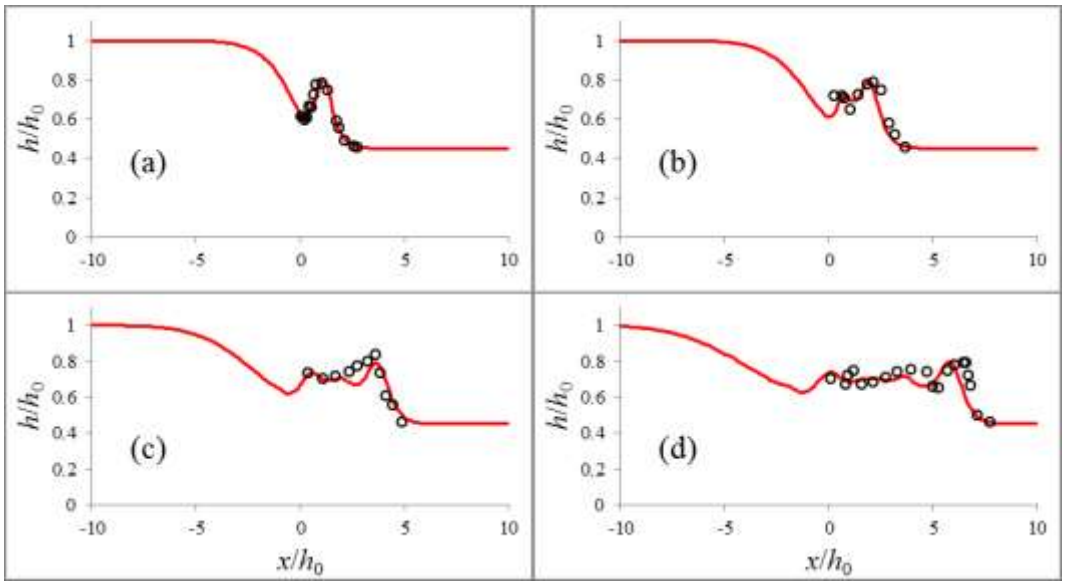

Fig. 7.23. Measured and calculated water surface profiles caused by dam-break flow over wet bed: (a) t=0.22 s, (b) t=0.32 s, (c) t=0.52 s, and (d) t=0.76 s (solid line: calculated, circles: measurements from Stanby et al., 1998).

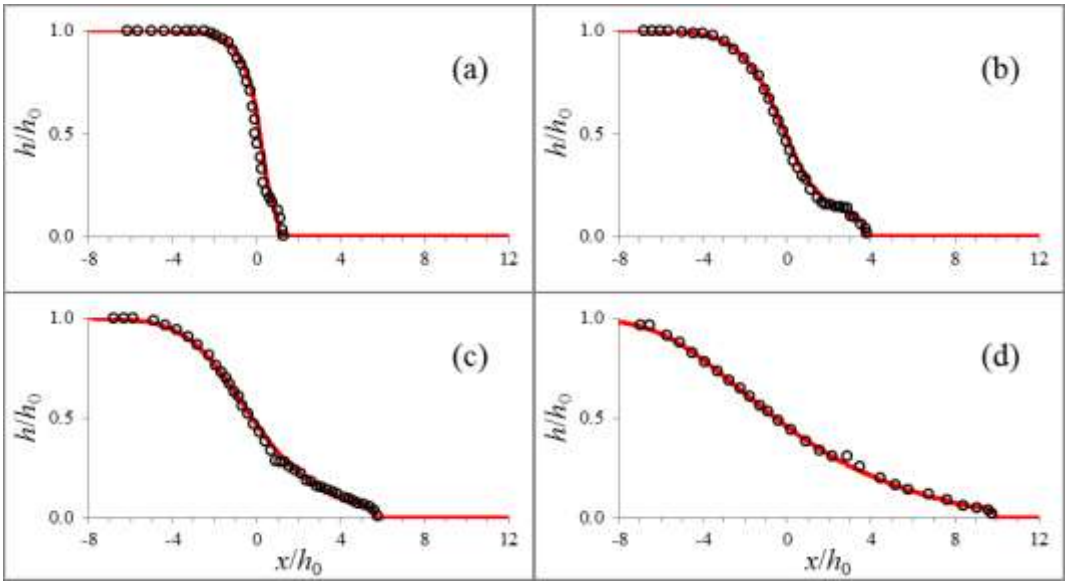

Fig. 7.24. Measured and calculated water surface profiles caused by dam-break flow over dry bed: (a) t=0.18 s, (b) t=0.44 s, (c) t=0.62 s, and (d) t=1.06 s (solid line: calculated, circles: measurements from Ozmen-Cagatay and Kocaman, 2010).

Case 2: Breaking solitary wave on a sloping beach

Synolakis (1986) carried out a series of experiments to investigate runup/rundown and breaking of a solitary wave propagating on a sloping beach. The topography consisted of a plane beach with a slope of 1:19.85 adjacent to a constant depth region, as shown in Fig. 7.25. The initial condition was still water of h=0.2 m in depth. The experimental run with H/h =0.3 is selected here to test the developed model's capability of simulating breaking waves on sloping

beach. The first-order solitary wave theory is used to define the initial surface profile η and longitudinal flow velocity u as follows (Synolakis 1987):

$$\eta = H \sec h^2 \left[\sqrt{\frac{3H}{4h^3}} (x - X) \right], \quad u = -\eta \sqrt{\frac{g}{h}} \tag{7.85}$$

where the initial wave crest is located at x=X. In the experiment, the initial wave crest was located at X=14h (Mahdavi and Talebbeydokhti 2009). The computational domain is represented by a uniform mesh which contains 120000 hexahedral cells. The time step is controlled by the CFL condition. For convenience, the results are reported in non-dimensional forms: $x^* = x/h$, $\eta^* = \eta/h$, and $t^* = t\sqrt{g/h}$.

Figs. 7.26(a)–(l) show the water surface profiles obtained at different times. At t* = 5 and 10 (Figs. 7.26(b) and (c)), the wave shoals and the front face becomes steeper. These two snapshots indicate that the breaking process can be simulated by the numerical model accurately. As can be seen, the wave speed and wave height are well-simulated as well. When the breaking process terminates at t*=15 (Fig. 7.26(d)) the attenuated wave forms a tongue propagating up the sloping beach at t* = 20, 25, and 30 (Fig. 7.26(e) to (g)). After the broken wave reaches the highest point around t* = 35 (Fig. 7.26(h)), rundown takes place in which a thin layer of water accelerates down the beach, and at approximately t* = 40 (Fig. 7.26(i)) the receding supercritical flow impacts the wave tail near the still water shoreline. The model approximates this flow pattern as a hydraulic jump. However, Fig. 7.26(j) exhibits discrepancy in forming hydraulic jump during the receding period.

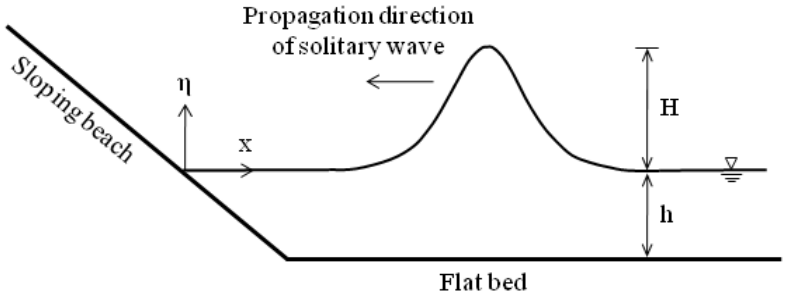

Fig. 7.25. Sketch for solitary wave runup on a sloping beach.

Case 3: Dam-break flow over a rectangular block

A laboratory experiment of dam-break flow carried out at the Maritime Research Institute of the Netherlands (MARIN) (see Kleefsman et al., 2005) is applied to test the model. The laboratory tank was 3.22 m long, 1 m wide, and 1 m high with an open roof. A rectangular block of 0.403×0.161×0.161 m was placed downstream of the reservoir. The initial water surface depth inside the reservoir was 0.55 m and the downstream region was dry. Fig. 7.27 shows the configuration of the tank and the location of measurement gages. The computational domain consists of 161×50×50 cells.

Fig. 7.28 compares the water surface time series at gages H2 and H4. The comparison shows similar patterns in the time evolution of measured and calculated water surface levels. The progressive wave front reaches gage H2 at t=0.4 s and the water surface level increases until t=2.4 s when the reflected wave from the obstacle and the downstream wall moves toward the upstream. This causes a decrease in the water surface level until the second reflected wave

reaches the gage and the water level increases again. At gage H4, the water surface level decreases as the reservoir drains smoothly until t=2.9 s. At this time the first reflected wave reaches and approaches the upstream wall. The reflected wave hits the wall and the second reflected wave shows a peak level around t=3.9 s and propagates toward the downstream.

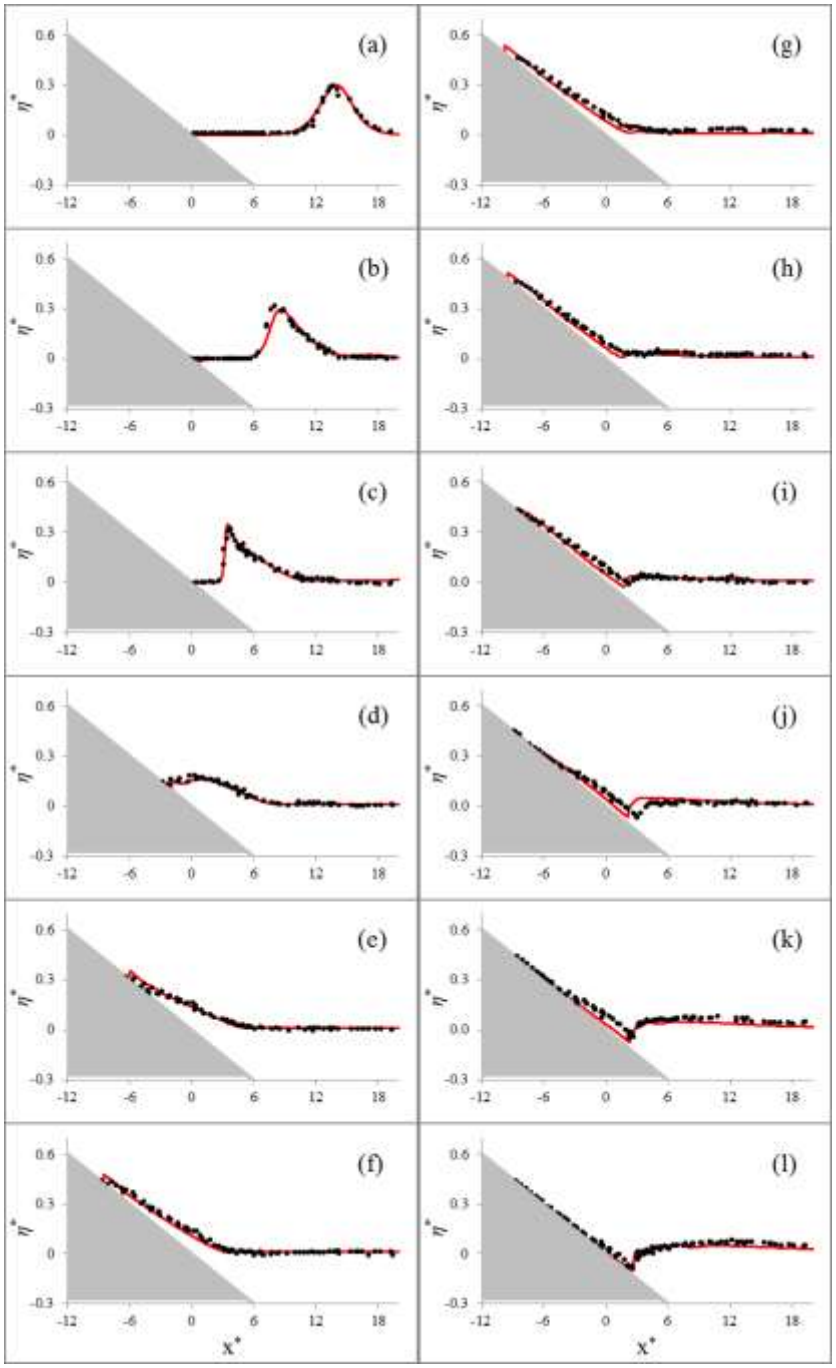

Fig. 7.26. Propagation of breaking solitary wave on a sloping beach: (a) t^*=0, (b) t^*=5, (c) t^*=10, (d) t^*=15, (e) t^*=20, (f) t^*=25, (g) t^*=30, (h) t^*=35, (i) t^*=40, (j) t^*=45, (k) t^*=50, (l) t^*=55 (solid line: calculated, black dots: measurements from Synolakis, 1986).

Fig. 7.29 shows snapshots of the calculated pressure on the bed at different times. The measured and calculated pressure time series at gages P1, P3, P5, and P7 are shown in Fig. 7.30. Both measurement and simulation show sudden increase in pressures at gages P1 and P3 when the wave hits the obstacle. The calculated pressures exhibit spurious spikes, particularly on gages P5 and P7. This is due to the appearance of air bubbles in the water and the model has difficulty in handling an isolated empty cell surrounded by fluid cells. Similar situation occurs in the model results of Kleefsman et al. (2005). Nevertheless, the comparisons in Fig. 7.30 reveal the capability of the developed model to simulate the general pressure changes caused by the progressive and reflected waves.

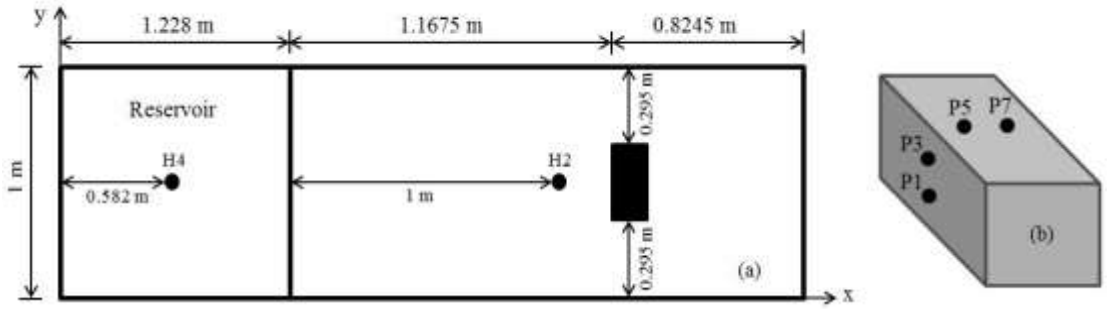

Fig. 7.27. Sketch of the MARIN dam break experiment (H4 and H2: water surface level measurement gages; P1, P3, P5, and P7: pressure measurement gages around the block).

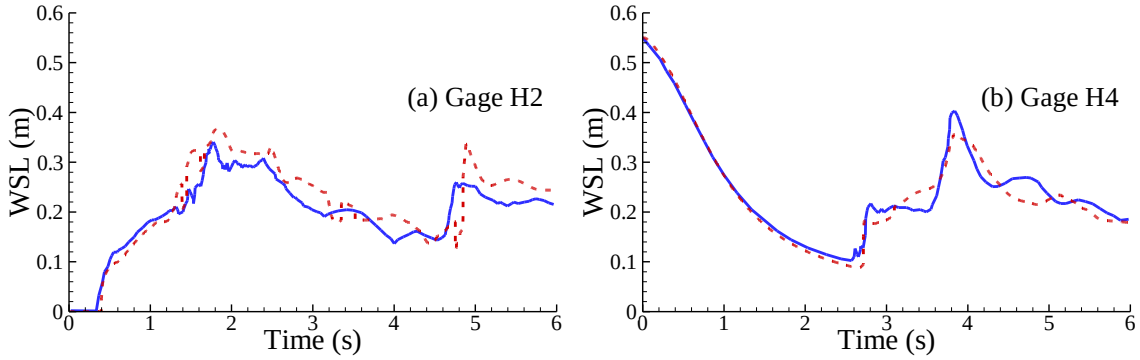

Fig. 7.28. Time evolution of water surface levels (red dashed line: calculated, blue solid line: measurements from Kleefsman et al., 2005).

Case 4: Net sediment entrainment in a straight flume

The model is tested using an experiment reported by van Rijn (1981). The experiment used a flume 30 long, 0.5 m wide and 0.7 m deep. Clear water was initially flowed over the sand bed of the flume and entrained sediment into suspension until the full transport capacity was acquired. The bed material consisted of sand particles with d_{50}=0.23 mm and d_{90}=0.32 mm. the water depth in the flume was 0.25 m and the mean velocity 0.67 m/s. Since the model considers single-sized sediment transport, a representative particle size of 0.2 mm is used, following Wu et al. (2000a). The computational domain is divided to 252000 hexahedral cells. The coefficient α is set equal to 2.0. The model uses the sediment density, shape factor, and porosity equal to 2650 kg/m^3, 0.7, and 0.4, respectively. The Schmidt number is equal to 1. The friction coefficient C_{fb} is

calibrated as 0.01, and the coefficient β is 0.2. The bed-load adaptation length and the suspended load adaptation coefficient α are set as 1 m and 2, respectively.

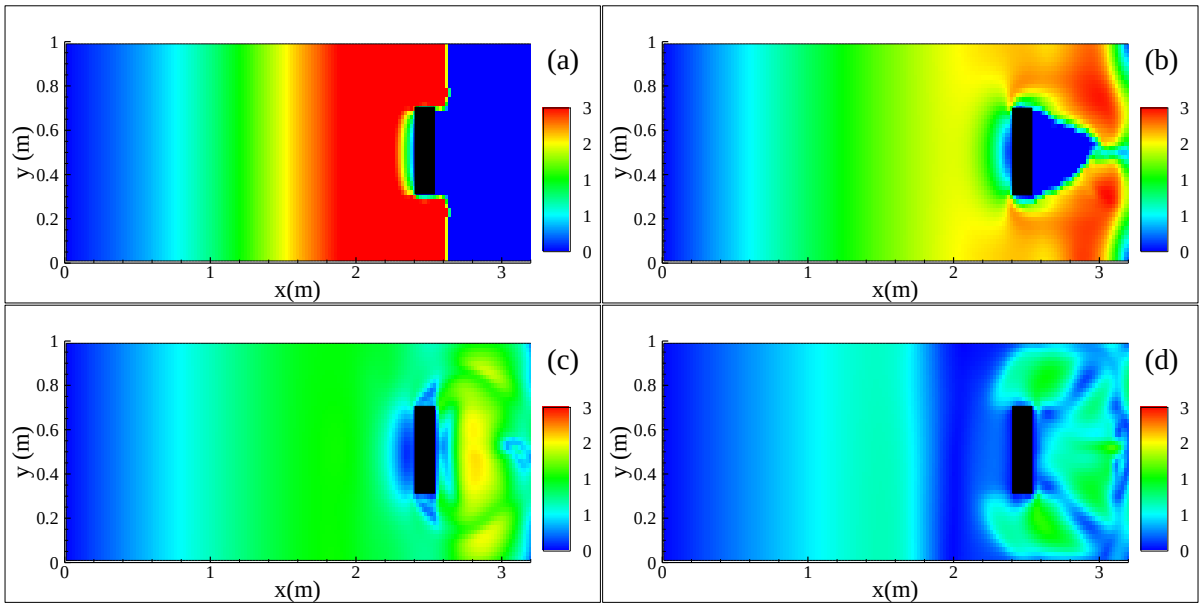

Fig. 7.29. Calculated resultant velocity near the bed: (a) t=0.5 s, (b) t=1.0 s, (c) t=1.5 s, and d) t=2.0 s.

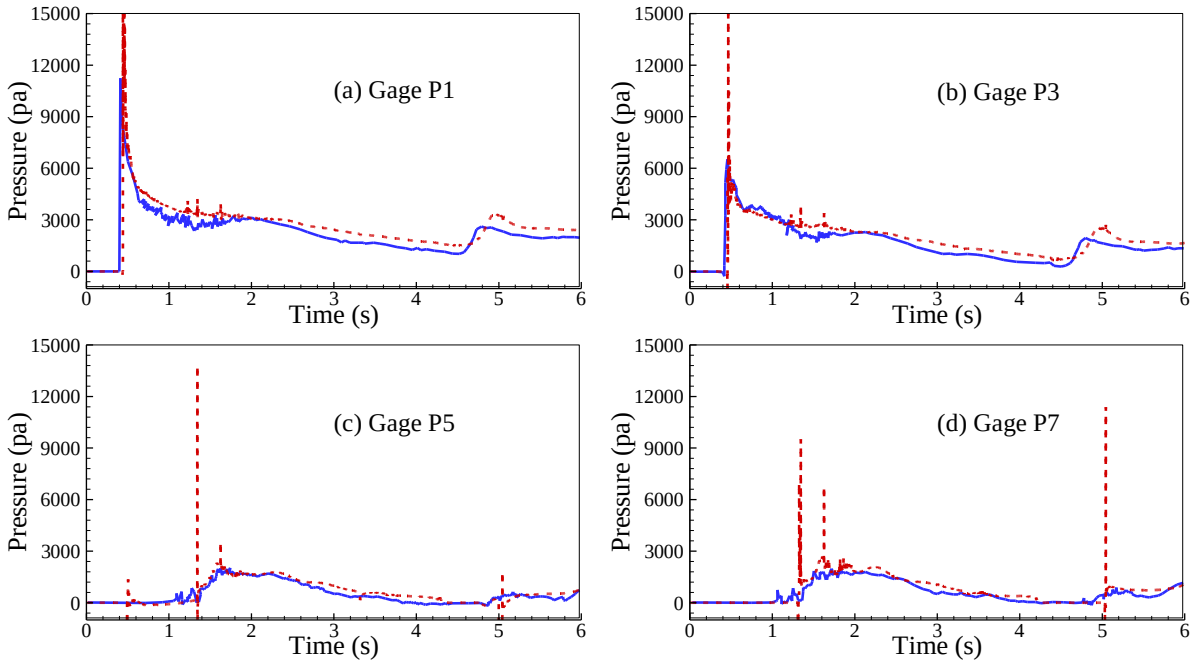

Fig. 7.30. Time evolution of pressures (red dashed line: calculated, blue solid line: measurements from Kleefsman et al., 2005).

Fig. 7.31 compares the calculated and measured vertical profiles of sediment concentration at four different cross sections. It can be seen that the general agreement is fairly good. The

sediment concentration at the boundary between the suspended-load and bed-load zones tends to a high concentration whereas it tends to zero at the water surface.

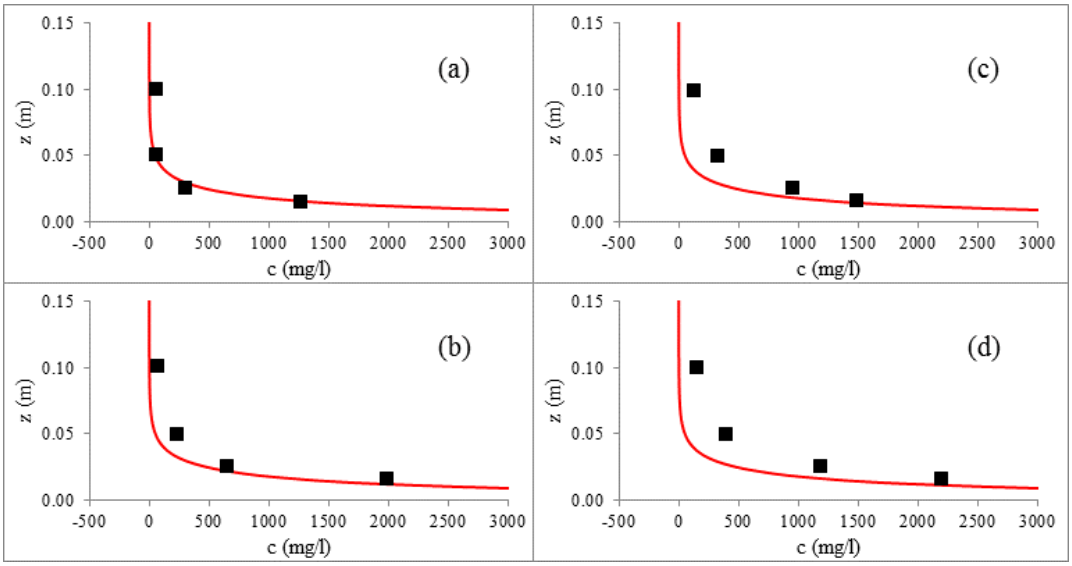

Fig. 7.31. Vertical distribution of sediment concentrations at (a) x/h=4, (b) x/h=10, (c) x/h=20, and (d) x/h=40 (solid line: calculated, squares: measurements from Van Rijn, 1981).

Case 5: Initial stage of dam-break flow over erodible bed

The developed model is also tested by an experimental dam-break flow over erodible bed. The experiment was performed in the University of Taiwan and reported by Capart and Young (1998). The experiment simulated the initial stage of dam-break flow in prismatic channel with movable bed. The flume was 1.2 m long, 0.2 m wide, and 0.7 m deep with a sluice gate placed in the middle of the test reach. The flume bed was covered by a layer of sediment with a thickness of about 5-6 cm. Sediment particles were artificial light spherical pearls covered with a shiny white coating, a diameter of 6.1 mm, density of 1048 kg/m^3, porosity of 0.28, and settling velocity of about 7.6 cm. The computational domain consists of 19800 cells. The total friction coefficient C_{fb} is 0.035 and the coefficient β is 0.5. These coefficients were calibrated based on the measured water surface and bed profiles. The bed-load adaptation length and the coefficient a are set equal to 1 m and 2, respectively.

Fig. 7.32 shows the water and bed surface profiles at different times. The wave front location is well predicted by the model, but the calculated water surface profile does not agree with the calculated one. A hydraulic jump was formed near the dam site, which is not predicted by the model. The hydraulic jump was formed because of the significant changes of bed, whereas the model does not consider the bed changes effects on the flow calculation. The magnitude of bed erosion is well predicted downstream of the dam but the model does not show enough bed erosion upstream of the dam. This might be because of the presence of high hydrodynamic pressure and rapidly varied flow around the dam site in initial stages of dam-break flows while some model parameters such as sediment transport capacity and adaptation length are derived for steady, uniform flow, and under hydrostatic pressure distribution assumptions. Another reason might be the effects of bed change on the flow properties such as near-bed velocity and

consequently the bed shear stress which are very important parameters in sediment transport calculations.

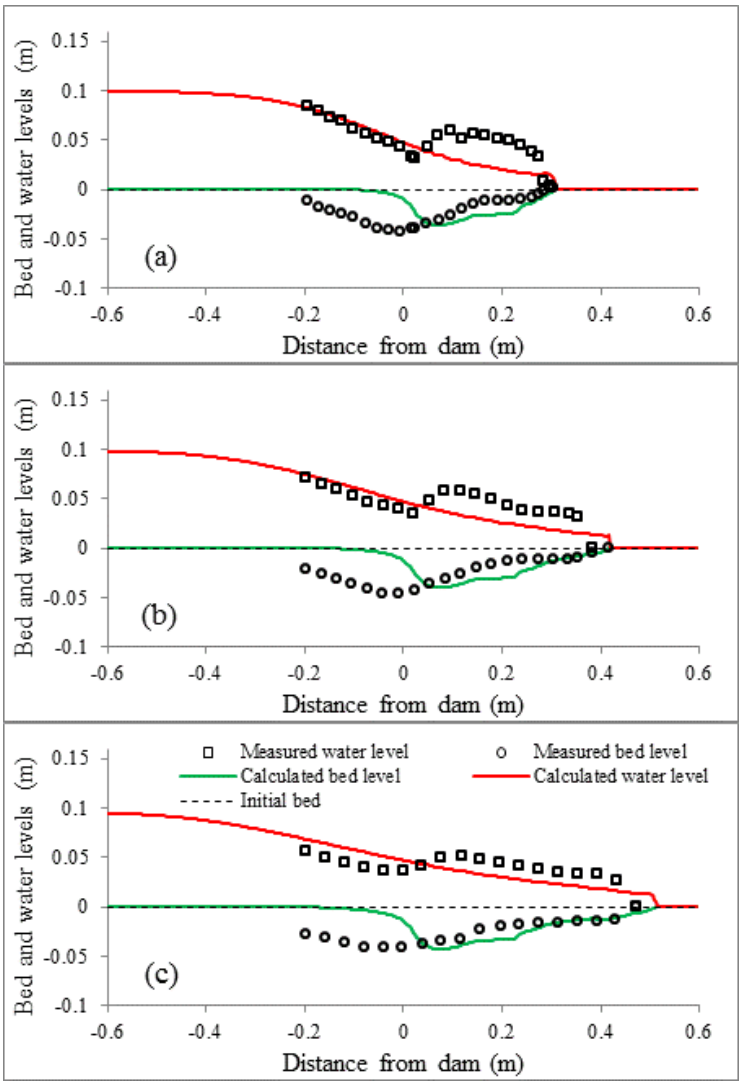

Fig. 7.32. Calculated and measured water levels and bed profiles (a) t=0.3 s, (b) t=0.4 s, and (c) t=0.5 s (measurements from Capart and Young, 1998).

Fig. 7.33 shows the calculated and measured sediment transport rates at different cross sections. Fig 7.33(a) indicates that the model under-predicts the sediment transport rate at upstream of the dam. This is expected from Figs. 7.32 as the predicted bed change shows less erosion at the upstream. At the dam site the peak value is under-predicted too as shown in Fig 7.33(b). At downstream of the dam site shown in Figs. 7.33(c) and (d) the calculated sediment transport rate agrees fairly well with the measured one.

Fig. 7.34 shows the comparison of the longitudinal profiles of sediment concentration by volume at t=0.4 s. The calculated concentration of the present model is compared with results calculated by a model developed by Wu and Wang (2007) which was a depth-averaged 1-D model. The results of the present model and Wu and Wang's model agree with each other. The results show high sediment concentration in the dam-break wave front.

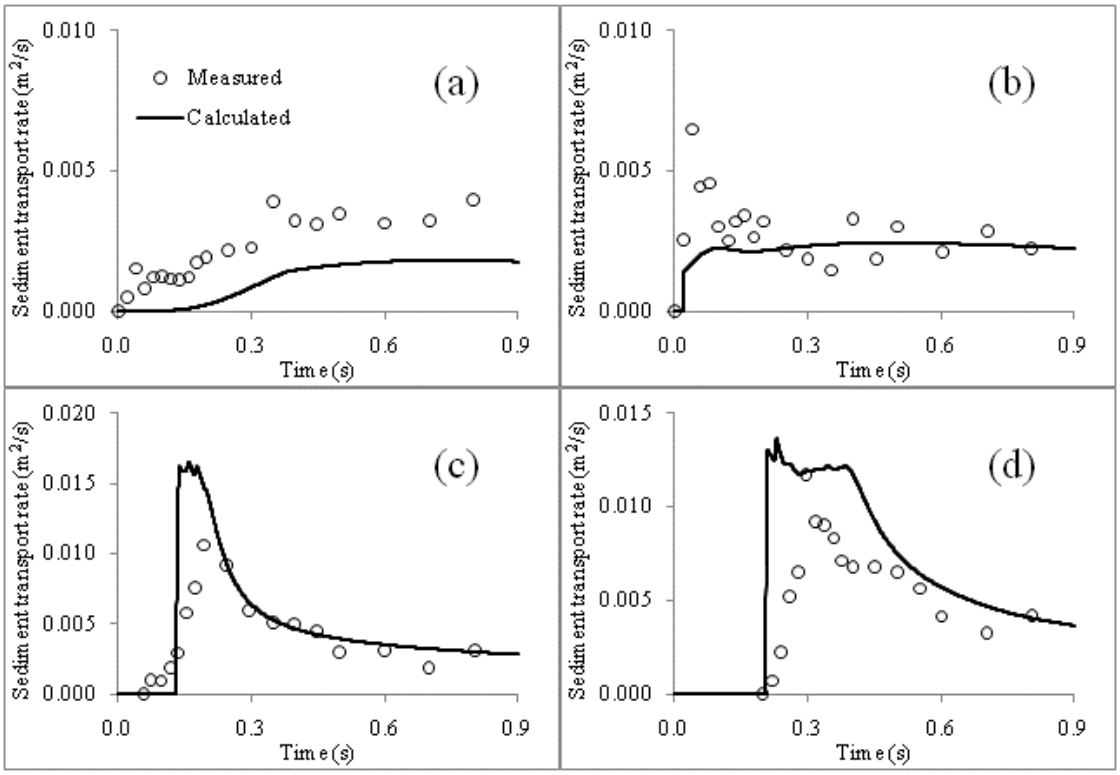

Fig. 7.33. Calculated and measured sediment transport rates at (a) x=-0.1 m, (b) x=0, (c) x=0.1 m, and (d) x=0.2 m (measurements from Capart and Young, 1998).

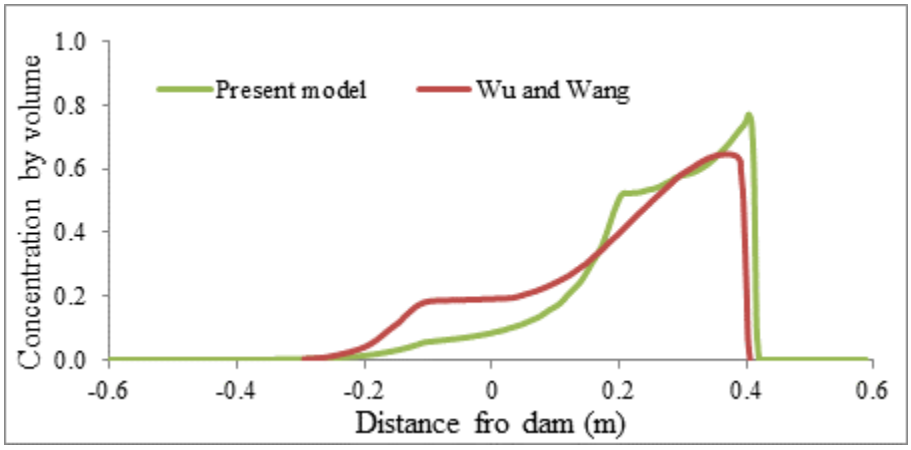

Fig. 7.34. Comparison of sediment concentration profiles at t=0.4 s.

7.2.4 Summary

In this section, a 3-D rapidly-varying transient flow model over erodible beds has been developed. The hydrodynamic model solves the Reynolds-averaged Navier-Stokes equations using a finite volume method on collocated, arbitrary unstructured meshes. The interface fluxes on the collocated cell faces are estimated using the Rhie and Chow's (1983) momentum

interpolation method and the velocity and pressure coupling is achieved by using the PISO iterative method. At the free surface boundary the CICSAM-VOF surface-capturing method is used to trace the changes of water surface due to unsteady behaviors of rapidly-varying transient flows, such as dam-break flow, storm surge, tidal bore, tsunami wave, and breaking short waves. The bed-load and suspended-load transport equations are solved using the same finite-volume method and the calculated hydrodynamic results. In the time being, the model is able to estimate the bed changes based on the calculated bed-load and suspended-load quantities and the near-bed sediment exchange fluxes, but the computational mesh is fixed so that the feedback effects of bed changes to the flow and sediment transport are not taken into account. The model is still under development. It will be enhanced by implementing a moving mesh to tack the bed boundary changes. The developed model has been tested using several sets of classical laboratory experiments, including dam-break flow over dry and wet beds, breaking solitary wave over a slopping beach, dam-break flow over an obstacle, sediment entrainment from an erodible bed, and dam-break flow over an erodible bed. The simulation results are very promising.

The developed 3-D model is more general than the depth-averaged 2-D model presented in Section 7.1. It can simulate both long and short waves and the induced sediment transport morphology changes and has potential to handle undercutting of marsh edge. Even though this SERRI project will end in August 2012, we will continue to enhance this model as part of Mr. Reza Marsooli's PhD dissertation. The model will be further extensively validated in cases of dam-break flows in riverine systems and storm surge and waves in coastal systems.

8. CONCLUSIONS

In order to assess the effectiveness of wetland vegetation in mitigating the impact of hurricane and storm surges, this project studied the attenuation of surge and waves by vegetation through three inter-related research approaches: laboratory experiments, field observations and computational modeling. In Phase I from Jan 2009 to March 2011, the research team collected a large volume of measurement data via laboratory experiments and field campaigns, and developed and validated empirical formulas and numerical models to quantify the reduction of surge and waves by vegetation. In Phase II from April 2011 to August 2012, the team continued and expanded the laboratory experiments, field campaigns and computational modeling of surge and wave attenuation by marshland vegetation, and extended the research scope by including marsh edge erosion.

Phase I of the laboratory work included model and live vegetation experiments at emergent and close to emergent conditions in a flat-bed wave flume and wave setup experiments with rigid model vegetation on a sloping beach. In Phase II, the team extended the experiments by including the interaction of the regular and irregular waves with submerged rigid and flexible artificial vegetation following the same procedures that were used in Phase I. The laboratory experiments were conducted in a 20.6 m long, 0.69 m wide and 1.22 m deep wave flume in the USDA-ARS National Sedimentation Laboratory (NSL), Oxford, Mississippi. Free surface displacement was measured using eight capacitance type wave gauges and a video camera. The gage resolution was increased by adding two wave gages in the vegetation zone and a wave runup gage. Bulk drag coefficients of vegetation were estimated using the measured wave height profiles. The results show a good correlation between bulk drag coefficient (C_D) and both Reynolds number (Re) and Keulegan-Carpenter number (K_c) for rigid and flexible vegetation in regular and irregular wave conditions. The data for rigid model vegetation in the first and second phases of the project follow the same trend when plotted against K_c. There is no apparent dependency of C_D on relative plant height (h_v/h) for both rigid and flexible vegetation. Rigid and flexible vegetation have similar drag coefficients for large values of K_c, although the drag coefficient is always slightly higher for the rigid case. Furthermore, wave setup and runup were measured in a laboratory wave flume on a sloping beach profile for non-vegetated, rigid vegetation, and flexible vegetation for regular and irregular waves. The results show that rigid and flexible vegetation significantly dampened wave height and reduced wave setup, but rigid vegetation generally performed better in reducing wave setup.

The field investigations in Phase I consisted of two campaigns: (1) measurements of waves and surge using rapidly deployed devices on the landing sites of hurricanes and tropical storms, and (2) measurements of waves using devices installed on fixed sites during winter fronts. In Phase II, the team continued and expanded the efforts and performed in-depth analysis on the data. Wave data were collected over a two-day period (September 3-4, 2011) at a salt marsh wetland in Terrebonne Bay on the Louisiana coast of the Gulf of Mexico during Tropical Storm Lee. A field campaign to measure waves and bottom currents near the marsh edge on a vegetated wetland in south Louisiana was successfully conducted from April 12 to April 20, 2012 during a cold front passage. These field campaigns provided very useful data of wave attenuation by vegetation in high-energy wave environments, which fill a knowledge gap in the literature. The datasets revealed the presence of bimodal wave spectra at the study site, consisting of low-frequency ocean swell in addition to the wind sea, providing an opportunity to examine differences in the bulk drag coefficients associated with these two wave systems. The bulk drag coefficient was observed to decrease with increasing stem Reynolds number and

Keulegan-Carpenter number, and to be smaller for the longer-period waves than the shorter-period waves. The data were also used to quantify variation of the drag coefficient across frequency scales and develop a method to determine the frequency-dependent drag coefficient, which can predict energy dissipation with better accuracy than the bulk drag coefficient.

A new plant tension testing device was designed and manufactured to characterize the resistance of coastal wetland vegetation to tensile damage. The device was proved to be capable of quickly and accurately obtaining a plant's resistance to tensile damage on coastal wetlands. A total of eight field visits were made to obtain damage data for *Spartina alterniflora* in two selected sites in Terrebonne Bay and Barataria Bay. During each field visit, a total of 15 plants were tested. The results showed that the tensile damage forces range from 17 to 76 lbs, with an average and standard deviation of 32.41 ± 11.56 lbs. The damage force for plants in the Terrebonne Bay site is only slightly affected by plant dimensions, whereas that for the Barataria Bay site can be reasonably correlated with both plant stem diameter and stem height. The plants show more failures at the stem in winter and early spring, but failure occurs in both stem and root in summer when the plant reaches its maturity and hence maximum strength. In addition, the soil strength is also a key factor influencing the mode of plant failure since soil failure may cause failure of the soil-root system.

An extensive in-situ and laboratory experimental program was designed to determine and understand the critical shear stress of marsh soils. Two sites in Louisiana coastal wetlands were selected: the Terrebonne Bay site and the Barataria Bay site. The critical shear stress at the two sites was measured using a cohesive strength meter (CSM). The surface soil erosion resistance was characterized by in-situ testing, and the soil at depth was tested in the laboratory via examining undisturbed tube samples obtained from the sites. Laboratory testing consisted of CSM, organic matter content, water content, root content, Atterberg limits, and particle size measurements. The results showed that for both sites, the critical shear stress ranges from 0.4 to 1.9 Pa, and the average values are 1.03 to 1.16 Pa. The Terrebonne Bay site has greater surface erosion threshold than the Barataria Bay site, whereas organic matter and root contents in the Barataria Bay site are greater than those in the Terrebonne Bay site. The Terrebonne Bay site is more prone to undercut erosion, most likely due to less root or organic matter content. The Barataria Bay site is characterized by a stronger soil below the ground surface, so that surface erosion is the major cause of its marshland loss. The testing showed that the critical shear stress usually increases with root content, indicating that the roots play an important role in controlling marsh erosion and marshland loss. A certain range of organic matter content was found to have a positive influence on soil stability: 7-10% for the Terrebonne Bay site and 20-30% for the Barataria Bay site. Water content and organic matter content affect soil stability at shallower depths, but at greater depths, root content has a major impact on soil stability.

In Phase II the team continued to investigate the growth forms and productivities of *Spartina alterniflora* and *Juncus roemerianus* and compared the coastal marshes in Louisanna and Mississippi. Two transects were established in Graveline Bayou, MS and three transects in Terrebonne Bay, LA. The soil property data demonstrate that soil moisture, organic matter content, and soil clay percentage at the LA marsh site are significantly higher than those at the MS marsh site, whereas sediment mean grain size and soil sand percentage at the LA marsh site are significantly lower than those at the MS marsh site. There is no significant difference in soil bulk density and silt percentage between the two sites. The plant characteristic data show that live and dead standing shoot heights for *Spartina alterniflora* at the LA site are significantly higher than those at the MS site. *Spartina alterniflora* in the LA site has significantly higher rhizome thickness and bottom stem diameter than those in the MS site. However, there is no

significant difference in the plant stem density, percent cover, top stem diameter, or above- and belowground production between the two sites. In addition, the results based on the combined datasets collected in Phases I and II show that coastal marshes with low elevation have high belowground production. This implies that although native coastal vegetation tends to have lower height and lower density in low marsh zones due to the influence of storm surges and waves, the vegetation can withstand storm waves because of increased belowground primary production. The prolific rhizomes are beneficial for resisting the erosion of sediments that make up the coastal marshlands.

A model marsh edge was constructed in the NSL wave tank using intact marsh edge samples composed of *S. alterniflora* shoots and rhizomes in their native soil that were collected from the Terrebonne Bay area in the second phase of the study. During the experiments, the detailed progression of waves impacting the marsh, as well as erosion of both the marsh material and the underlying substrate, were observed and recorded. Undercutting and exposure of the plant roots were observed, which is consistent with field observations. Marsh edge erosion was also investigated at the LA marshland site. Directional wave measurements were carried out inside a rapidly eroding shallow bay that was partially protected by barrier islands in order to measure the characteristics of the wave field. Potential erosion rates were estimated from the measured wave power using methods in the published literature. The GPS system and aerial photographs were successfully employed to determine the short-term and long-term erosion rates in Terrebonne Bay. The GPS system utilizes the LSU GULFNet Real-Time Network that provides accurate GPS data for rapid short-term surveys, while the aerial photographs provide a long-term database with broad spatial coverage. The erosion rates were found to be comparable with the short term measurements of shoreline retreat obtained from the topographic surveys and long term measurements estimated from the aerial photographs.

In Phase I, four models were selected to demonstrate how to account for the effect of vegetation on surge and waves. The four models include a depth-averaged 2-D shallow water model used for long waves such as tsunami wave propagation, a 1-D Boussinesq-type model primarily used for short waves, a vertical 2-D model based on the Reynolds-averaged Navier-Stokes (RANS) equations with the Volume-of-Fluid (VOF) method which is able to handle both long and short waves, and a wave-action model for wave spectra. In Phase II, a 3-D shallow water flow model coupled with a 2-D wave action model similar to that tested in Phase I was added in the demonstration model list and implemented with vegetation effect modeling capability. The newly added model splits the water motion into current and waves, computes the current by solving the phase-averaged 3-D shallow water equations with wave radiation stresses as the action of waves on current, and determines the wave characteristics such as wave height, period, angle, and radiation stress by solving the 2-D wave action balance equation. The model is able to simulate the 3-D longshore and cross-shore currents induced by waves. The model considers the effects of vegetation on current and waves by including the drag and inertia forces of vegetation in the momentum equations and the wave energy loss due to vegetation resistance in the wave action balance equation. The 3-D model was tested using datasets of tidal flows in two estuaries, undertow flow generated by waves on a sloping beach, and flow and waves through vegetation zones. The calculated tidal levels and velocities, undertow flow velocities induced by waves, and flow velocity and wave properties attenuated by vegetation agree generally well with the measurement data.

The depth-averaged 2-D shallow water model was enhanced in Phase II with several empirical formulas for the vegetation drag coefficient and further tested using three sets of laboratory experiments considered vegetation: steady flow around alternate vegetation zones,

solitary wave through vegetation zone in a flat-bed flume, and long wave on a partially vegetated sloping beach. It was then applied to assess the long wave runup reduction by vegetation on a sloping beach and the possible benefits and drawbacks of vegetation in a riverine system. The results show that it is beneficial to plant vegetation along coastal shoreline to reduce wave runup, whereas planting vegetation in riverine systems reduces the flood level in downstream areas while possibly increasing inundation risk in some upstream areas.

The depth-averaged 2-D shallow water model was further enhanced to simulate sediment transport and morphological changes near marsh edge induced by rapidly-varying transient long waves such as strong storm surge and tsunami waves. The model uses the generalized shallow water equations that take into account the effects of sediment concentration and bed change on the flow. The sediment transport model simulates the non-equilibrium transport of total load. The model was tested using laboratory experiments of dam-break flow over movable bed in a suddenly-expanded flume and a straight flume. The model made generally good predictions of the water surface evolution with time and the final bed profile in both experiments. The model was also tested using data from laboratory experiments on bed changes around a vegetated island and alternate vegetation zones. The calculated bed changes agree reasonably well with the measurement data. The simulations and experiments show sediment deposition inside and in the front of the vegetation zones but erosion beside the vegetation zones where flow is strengthened. This implies that planting vegetation can stabilize the bed, whereas the nearby erosion has potential to cause loss of planted vegetation.

The aforementioned depth-averaged 2-D models are applicable only to long waves. For more general applications, a 3-D rapidly-varying transient flow model over erodible bed was developed to simulate marsh edge erosion induced by both long and short waves. The model solves the Reynolds-averaged Navier-Stokes equations using a finite volume method on collocated, unstructured meshes, and uses the CICSAM-VOF surface-capturing method to trace the changes of water surface due to unsteady behaviors of rapidly-varying transient flows, such as dam-break flow, storm surge, tidal bore, tsunami wave, and breaking short waves. The model computes bed-load and suspended-load transport using a non-equilibrium transport modeling approach, and determines bed change using the near-bed sediment exchange fluxes. The model is still under development, since the computational mesh is fixed so that the feedback effects of bed changes to the flow and sediment transport are not taken into account. It will be enhanced by implementing a moving mesh to track changes in bed elevation. The model has been tested using several sets of classical laboratory experiments, including dam-break flow over dry and wet fixed beds, breaking solitary wave over a slopping beach, dam-break flow over an obstacle, sediment entrainment from an erodible bed, and dam-break flow over an erodible bed. The simulation results are very promising. However, the weakness of the 3-D model is that it incures a much higher computational cost than the 1-D and 2-D models.

During the course of fulfilling the project, the research team sought opportunities to participate in relevant communications, meetings, workshops and conferences organized by homeland security components (e.g., FEMA) and other institutions such as ASCE and IAHR, and published the research findings through journals, conferences and workshops. To confirm and validate the results of this research with key stakeholders and subject matter experts, the team worked closely with stakeholders to confirm the value/merits of the results of this research in helping to mitigate the effects of surge and waves caused by hurricanes and severe storms in coastal areas. As one of such efforts, the team implemented the vegetation effect modeling approaches in the Coastal Modeling System (CMS) of the US Army Corps of Engineers Research and Development Center (ERDC), as described in Section 6.2.

Laboratory and field data obtained in Phase II are included either in the related chapters or as appendices. A number of figures in Chapter 2 present the laboratory experiment results, and tables in Section 4.3 present the vegetation and soil property data collected in LA and MS marshes. Three appendices present the data used in Chapter 3 and Sections 4.1 and 4.2, including the wave and topographic data collected during tropical storms and winter cold fronts, as well as data on the critical shear stress and vegetation damage resistance of marsh soils.

The team has completed all the planned tasks for Phase II and fulfilled the goals of this research project. The collected laboratory and field measurement data are very useful and provide better insight into and understanding of the interactions among hydrodynamics, vegetation and soils in coastal marshlands. The developed empirical formulas for the vegetation drag coefficient and models for vegetation effects on current and waves provide quantitative methods and tools for coastal protection and wetland restoration.

Nevertheless, several related problems need further study. First, the wave tank used in this study included only waves. It is important to conduct more experiments on vegetation effects wherein currents and waves coexist. Second, marsh edge erosion was investigated only preliminarily because it was not the primary goal of this project and the time on this task was limited. Considering the severity of marshland loss along the LA and MS coasts, it would be extremely worthwhile to conduct extensive investigations of marsh edge erosion through laboratory experiments, field observations and computational modeling. Third, sediment transport by waves (and currents coexisted) in vegetated water bodies has not been well investigated via laboratory or field experiments. Such data are sorely needed to validate models of sediment transport and morphology changes near marsh edges.

REFERENCES

Aberle, J., V. Nikora, and R. Walters. 2004. Effects of bed material properties on cohesive sediment erosion. *Marine Geology* **207**(1–4): 83–93.

Amos, C.L., I.G. Droppo, E.A. Gomez, and T. P. Murphy. 2003. The stability of a remediated bed in Hamilton Harbour, Lake Ontario, Canada. *Sedimentology* **50**(1): 149–168.

Anastasiou, C.J., and J.R. Brooks. 2003. Effects of soil pH, redox potential, and elevation on survival of *Spartina patens* planted at a west central Florida salt marsh restoration site. *Wetlands* **23**(4): 845-859.

Anderson, M.E., J.M. Smith, and S.K. McKay. 2011. Wave Dissipation by Vegetation. *Coastal and Hydraulics Engineering Technical Note ERDC/CHL CHETN-I-82*. U.S. Army Engineer Research and Development Center, Vicksburg, MS.

Asano, T., H. Degushi, and N. Kobayashi. 1993. Interaction between water wave and vegetation. *Proceedings of 23rd International Conference on Coastal Engineering* (*ICCE 1993*).

Asano, T., S. Tsutsui, and T. Sakai. 1988. Wave damping characteristics due to seaweed. *Proceedings of the 25th International Coastal Engineering Conference* (ICEC' 88).

Ashida, K., and M. Michiue. 1971. An investigation of river bed degradation downstream of a dam. *Proceeding of 14th Congress of IAHR*: 247–256.

Augustin, L.N., J.L. Irish, and P.L. Lynett. 2009. Laboratory and numerical studies of wave damping by emergent and near-emergent wetland vegetation. *Coastal Engineering* **56**(3): 332-340.

Babanin, A.V., I.R. Young, and M.L. Banner. 2001. Breaking Probabilities for Dominant Surface Waves on Water of Finite Constant Depth. *J. Geophys. Res.* **106**: 11659-11676.

Bannister, P. 1976. *Introduction to physiological plant ecology*. Blackwell Scientific Publications. John Wiley & Sons Inc.: New York. pp. 62-224.

Barbier, E.B., S.D. Hacker, C. Kennedy, E.W. Koch, A.D. Stier, and B.R. Silliman. 2011. The value of estuarine and coastal ecosystem services. *Ecological Monographs* **81**: 169–193.

Barras, J.A. 2005. Land area changes in coastal Louisiana after Hurricanes Katrina and Rita. IN Science and the Storms: the USGS Response to the Hurricanes of 2005. USGS publications circular 1306.

Barras, J., S. Beville, D. Britsch, S. Hartley, S. Hawes, J. Johnston, P. Kemp, Q. Kinler, A. Martucci, J. Porthouse, D. Reed, K. Roy, S. Sapkota, and J. Suhayda. 2003. Historical and projected coastal Louisiana land changes: 1978-2050. *USGS Open File Report 03-334*, (Revised January 2004).

Begnudelli, L., and B.F. Sanders. 2006. Unstructured grid finite volume algorithm for shallow-water flow and transport with wetting and drying. *J. Hydraul. Eng.* **132**(4): 371–84.

Bendat, J.S., and A.G. Piersol. 2000. *Random data: analysis and measurement procedures*, John Wiley and Sons, Inc. New York, NY.

Bennett, S.J., and C.V. Alonso. 2003. Physically modeling stream channel adjustment to woody riparian vegetation. *American Geophysical Union*: abstract #H52A-1171.

Bennett, S.J., T. Pirim, and B.D. Barkdoll. 2002. Using simulated emergent vegetation to alter stream flow direction within a straight experimental channel. *Geomorphology* **44**: 115–126.

Black, C. A. 1965. *Methods of soil analysis: part I physical and mineralogical properties.* American Society of Agronomy, Madison, Wisconsin, USA.

Bokaian, A., and F. Geoola. 1984. Wake-induced galloping of two interfering circular cylinders. *J. Fluid Mechanics* **146**: 383–415.

Booij, N., I.J. Haagsma, L. Holthuijsen, A. Keiftenburg, R. Ris, A. van der Westhuysen, and M. Zijlema. 2004. SWAN Cycle-III version 40.41 User Manual.

Borsje, B.W., B.K. van Wesenbeeck, F. Dekker, P. Paalvast, T.J. Bourma, M.M. van Katwijk, and M.B. de Vries. 2011. How ecological engineering can serve in coastal protection. *Ecol. Eng.* **37** *(2)*: 113–122.

Bradley, K., and C. Houser. 2009. Relative velocity of seagrass blades: Implications for wave attenuation in low energy environments. *J. Geophys. Res.* **114**: F01004, doi:10.1029/ 2007JF000951.

Brady, N. and R. Weil. 2002. *The Nature and Properties of Soils*, 13th Edition. Prentice Hall. Upper Saddle River, New Jersey. 960 p.

Brewer, J.S., and J.B. Grace. 1990. Plant community structure in an oligohaline tidal marsh. *Vegetatio* **90**: 93-107.

Brocchini, M., and N. Nicholas Dodd. 2008. Nonlinear shallow water equation modeling for coastal engineering. *J. Waterway, Port, Coastal, and Ocean Eng*. **134**(2): 104–120.

Brufau, P., M.E.Vázquez-Cendón, and P.A. García-Navarro. 2002. Numerical model for the flooding and drying of irregular domains. *Int. J. Numer. Methods Fluids* **39**: 247–275.

Capart, H., and D.L. Young. 1998. Formation of jump by the dam-break wave over a granular bed. *J. of Fluid Mechanics* **372**: 165-187.

Casulli, V., and R.T. Cheng. 1992. Semi-implicit finite difference methods for three-dimensional shallow water flow. *Int. J. Numer. Methods in Fluids* **15**: 629–648.

Center for Applied Research and Environmental Systems (CARES) Website. 2010. The Cooperative Soil Survey. Soil Bulk Density-Physical Properties. http://soils.missouri.edu/index.asp. accessed on April 20, 2010.

Chakrabarti, A., H.D. Smith, D. Cox, and D.A. Albert. 2011. Investigation of turbulent structures in emergent vegetation under wave forcing. *Proceedings of the Coastal Sediments* (*CS'11*).

Chapman, S.B. 1976. *Methods in plant ecology*. Blackwell Scientific Publications. Halsted Press, a Division of John Wiley & Sons, Inc. New York: 5-400.

Chapman, V.J. 1960. *Salt Marshes and Salt Deserts of the World*, Interscience, New York.

Chen, Q, and H. Zhao. 2012. Theoretical models for wave energy dissipation caused by vegetation. *J. Engineering Mech.* doi:10.1061/(ASCE)EM.1943-7889.0000318.

Chorin, A.J. 1968. Numerical solution of the Navier-Stokes equations. *Math. Comp.* **22**: 745–762.

Coleman, J.M., O.K. Huh, and D. Braud, Jr. 2008. Wetland loss in world deltas. *J. Coastal Res* **24**(1A): 1–14.

Cooper, N.J. 2005. Wave dissipation across intertidal surfaces in the Wash Tidal inlet, Eastern England. *J. Coastal Res.* **21**(1): 28-40.

Costanza R, et al. 1997. The value of the world's ecosystem services and natural capital. *Nature.* **387**: 253–260.

Costanza, R., O. Pe´rez-Maqueo, M.L. Martinez, P. Sutton, S.J. Anderson, and K. Mulder. 2008. The value of coastal wetlands for hurricane protection. *Ambio* **37**: 241–248.

Couvillion, B. R. 2011. Land area change in coastal Louisiana (1932 to 2010). Reston, VA: U.S. Dept. of the Interior, U.S. Geological Survey.

Cox, R., S. Wallace, and R. Thomson. 2003. Wave damping by seagrass meadows, *Proceedings of 6th International COPEDEC Conference*.

CPRA. 2012. Louisiana's Comprehensive Master Plan for a Sustainable Coast. *Coastal Protection and Restoration Authority of Louisiana*. Baton Rouge, LA.

Cronk, J.K., and M.S. Fennessy. 2001. *Wetland Plants: Biology and Ecology.* Lewis Publishers, Boca Raton, Florida: 28-353.

Dalrymple, R.A., J.T. Kirby, and P.A. Hwang. 1984. Wave Diffraction Due to Areas of Energy Dissipation. *J. Waterway, Port, Coastal and Ocean Engineering* **110**(1): 67–79.

Darby, F.A., and R.E. Turner. 2008. Below- and aboveground biomass of *Spartina alterniflora*: response to nutrient addition in a Louisiana salt marsh. *Estuaries and Coasts.* **31**: 326-334.

Day, J.W., D.F. Boesch, E.J. Clairain, G.P. Kemp, S.B. Laska, W.J. Mitsch et al. 2007. Restoration of the Mississippi Delta: Lessons from Hurricanes Katrina and Rita. *Science* **23**: 1679–1684.

Day, J.W., L.D. Britsch, S.R. Hawes, G.P. Shaffer, D.J. Reed, and D. Cahoon. 2000. Pattern and process of land loss in the Mississippi Delta: a spatial and temporal analysis of wetland habitat change. *Estuaries and Coasts* **23**(4): 425-438.

Dean, R.G., and Bender, C.J. 2006. Static wave setup with emphasis on damping effects by vegetation and bottom friction. *Journal of Coastal Engineering* **53**:149-156.

De Baets, J., K. Poesen, B. Wemans, B. Reubens, J. Muys, and S. de Baerdemaeker. 2008. Root tensile strength and root distribution of typical Mediterranean plant species and their contribution to soil shear strength. *Plant and Soil* **305**(1-2): 207-226.

De La Cruz, A.A. 1973. The role of tidal marshes in the productivity of coastal waters. *ASB Bulletin* **20**(4): 147-156.

Defina, A., L. Carniello, S. Fagherazzi, and L. D'Alpaos. 2007. Self organization of shallow basins in tidal flats and salt marshes. *J. Geophys. Res.* **112**: F03001.

Delis, A.I., M. Kazolea, and N.A. Kampanis. 2008. A robust high-resolution finite volume scheme for the simulation of long waves over complex domains. *Int. J. Numer. Methods Fluids* **56**: 419–452.

Dixon, A.M., D.J. Leggett, and R.C. Weight. 1998. Habitat creation opportunities for landward coastal re-alignment: Essex case study. *J. Chartered Institution of Water and Environmental Management* **12**: 107–112.

Dodd, N. 1998. Numerical model of wave run-up, overtopping, and regeneration. *J. Waterway, Port, Coastal and Ocean Eng.* **124**: 73–81.

Dubi, A.M. 1995. Damping of Water Waves by Submerged Vegetation: A Case Study on Laminaria Hyperborea. *PhD thesis*. Norway: University of Trondheim.

Dubi, A., and A. Tørum. 1996. Wave energy dissipation in kelp vegetation. *Proceedings of the 25th International Conference on Coastal Engineering* (*ICCE 1996*).

Eleuterius, L.N. 1972. The marshes of Mississippi. *Southern Appalachian Botanical Society, Castanea* **37**(3): 153-168.

Eleuterius, L.N. 1976. The distribution of *Juncus roemerianus* in the salt marshes of North America. *Chesapeake Science* **17**(4): 289-292.

Eleuterius, L.N. 1990. *Tidal marsh plants.* Pelican Publishing Company, Inc. Gretna, Louisiana: 14-30.

Elwany, M., W. O'Reilly, R. Guza, and R. Flick. 1995. Effects of Southern California kelp beds on waves. *J. Waterw. Port Coastal Ocean Eng.* **121**(2): 143–150.

Fagherazzi S., C. Palermo, M.C. Rulli, L. Carniello, and A. Defina. 2007. Wind waves in shallow microtidal basins and the dynamic equilibrium of tidal flats. *J. Geophys. Res.* **112**(F2): F02024.

Fagherazzi, S., and P.L. Wiberg. 2009. Importance of wind conditions, fetch, and water levels on wave-generated shear stresses in shallow intertidal basins. *J. Geophys. Res.* **114**: F03022.

Feagin, R.A., S.M. Lozada-Bernard, T.M. Ravens, I. Möller, K.M. Yeager, and A.H. Balrd. 2009. Does vegetation prevent wave erosion of salt marsh edges?. *Proceedings of the National Academy of Sciences* (*PNAS)* **106**(25): 10109-10113.

Ferziger, J.H., and M. Peric. 1995. *Computational Methods for Fluid Dynamics*. Springer-Verlag.

Folkard, A.M. 2011. Flow regimes in gaps within stands of flexible vegetation: laboratory flume simulations. *Environ. Fluid Mech.* **11**: 289–306, DOI 10.1007/s10652-010-9197-5.

Gagliano, S. 2003. Neo-tectonic framework of southeast Louisiana and applications to coastal restoration. *Transactions-Gulf Coast Association of Geological Societies* **53**: 262–276.

Gambi, M.C., A.R.M. Nowell, and P.A. Jumars. 1990. Flume observations on flow dynamics in Zostera marina (eelgrass) beds. *Marine Ecology Progress Series* 61: 159– 169.

Gebert, J., H. Kothe, A. Grongroft. 2006. Prognosis of methane formation by river sediments. *Journal of Soils and Sediments* **6**(2): 75–83.

Gedan, K.B., M.L. Kirwan, E. Wolanski, E.B. Barbier, and B.R. Silliman. 2011. The present and future role of coastal wetland vegetation in protecting shorelines: an answering recent challenges to the paradigm. *Climatic Change* **106**: 7-29.

Gerbersdorf, S.U., T. Jancke, and B. Westrich. 2007. Sediment properties for assessing the erosion risk of contaminated riverine sites. *Journal of Soils and Sediments* **7**(1): 25–35.

Ghisalberti, M., and H.M. Nepf. 2002. Mixing layers and coherent structures in vegetated aquatic flow. *J. Geophys. Res.* **107***(C2)*: 3011, doi:10.1029/2001JC000871.

Ghisalberti, M., and H.M. Nepf. 2004. The limited growth of vegetated shear layers. *Water Resources Research* **40**: W07502.

Gillott, J.E. 1987. *Clay in Engineering Geology*. Elsevier, Amsterdam.

Gosseline, J.G. 1984. The ecology of delta marshes of coastal Louisiana- A community profile: Washington, D.C., U. S. Fish and Wildlife Service: FWS/OBS-84/09, 134p.

Goutiere, L., S. Soares-Frazao, and Y. Zech. 2011. Dam-break flow on mobile bed in a channel with sudden widening: experimental data. *J. Hydr. Res.* doi:10.1080/00221686.2010.548969.

Grabowski, R.C., I.G. Droppo, and G. Wharton. 2011. Erodibility of cohesive sediment: The importance of sediment properties. *Earth-Science Reviews* **105**(3–4): 101-120.

Guntenspergen, G.R., D.R. Cahoon, J. Grace, G.D. Steyer, S. Fournet, M.A. Townson, and A.L. Foote. 1995. Disturbance and recovery of the Louisiana coastal marsh landscape from the impacts of Hurricane Andrew. *Journal of Coastal Research Special Issue* **21**: 324-329.

Halpern, B. S., et al. 2008. A global map of human impacts on marine ecosystems. *Science* **319**: 948–952.

Harlow, F.H., and J.E. Welsh. 1965. Numerical calculation of time-dependent viscous incompressible flow with free surface. *Phys. Fluids* **8**: 2182-2189.

Harten, A., P.D. Lax, and B. van Leer. 1983. On upstream differencing and Godunov-type schemes for hyperbolic conservation laws. *SIAM Review* **25**(1): 35–61.

Hasselmann, K., and J. Collins. 1968. Spectral dissipation of finite-depth gravity waves due to turbulent bottom friction. *J. Marine Res.* **26**: 1–12.

Heuscher, S.A., C.C. Brandt, and P.M. Jardine. 2005. Using soil physical and chemical properties to estimate bulk density. *Soil Science Society of America* **69**: 1-7.

Hillel, D. 1982. *Introduction to Soil Physics*. Academic, New York.

Holland, M.M., and C.J. Burk. 1990. The marsh vegetation of three Connecticut River oxbows: a ten-year comparison. *RHODORA* **92**(871): 166-204.

Howes, B.L., J.W. H. Dacey, and D.D. Goehringer. 1986. Factors controlling the growth form of *Spartina alterniflora*: feedbacks between aboveground production, sediment oxidation, nitrogen and salinity. *Journal of Ecology* **74**: 881-898.

Howes, N.C., M.F. Duncan, Z.J. Hughes, I.Y. Georgiou, M.A. Kulp, M.D. Miner, J.M. Smith, and J.A. Barras. 2010. Hurricane-induced failure of low salinity wetlands. PNAS.0914582107/doi/10.1073.

Hu, K, C.G. Mingham, and D.M. Causon. 2000. Numerical simulation of wave overtopping of coastal structures using the non-linear shallow water equations. *Coastal Eng.* **41**: 433–465.

Huang, Z., Y. Yao, S.Y. Sim, and Y. Yao. 2011. Interaction of solitary waves with emergent, rigid vegetation. *Ocean Eng*. **38**: 1080–1088.

Huthoff, F., D.C.M. Augustijn, and S.J.M.H. Hulscher. 2007. Analytical solution of the depth-averaged flow velocity in case of submerged rigid cylindrical vegetation. *Water Resources Research* **43**: W06413, doi:10.1029/2006WR005625.

IAHR Working Group for Dam-Break Flows over Mobile Beds. 2011. Dam-break flows over mobile beds: Experiments and benchmark tests for numerical models. *J. Hydr. Res*., in press.

Irish, J.L., L.N. Augustin, G.E. Balsmeier, and J.M. Kaihatu. 2008. Wave dynamics in coastal wetlands: a state-of-knowledge review with emphasis on wetland functionality for storm damage reduction. *Shore and Beach* **76**: 52–56.

Issa, R.I. 1986. Solution of the implicity discretized fluid flow equations by operator-spliting. *J. Comput. Phys.* **62**(1): 40-65.

Jadhav, R.S., and Q. Chen. 2012. Wave attenuation by salt marsh vegetation during tropical cyclone. *J. Geophys. Res.*: submitted.

Jaramillo, S., A. Sheremet, M.A. Allison, A.H. Reed, and K.T. Holland. 2009. Wave-mud interactions over the muddy Atchafalaya subaqueous clinoform, Louisiana, United States: Wave-supported sediment transport. *J. Geophys. Res.* **114**: C04002.

Jasak, H. 1996. Error analysis and estimation for the Finite Volume method with applications to fluid flows. *PhD thesis*. University of London, UK.

Järvelä, J. 2002. Determination of flow resistance of vegetated channel banks and floodplains. *River Flow 2002*, D. Bousmar and Y. Zech (eds.), Swets & Zeitlinger, Lisse: 311–318.

Karambas, T.V. 2003. Nonlinear wave modeling and sediment transport in the surf and swash zone. *Advances in Coastal Modeling, Elsevier Oceanography Series* **67**: 267-298.

Keddy, P.A. 2010. *Wetland Ecology: principles and conservation*. Cambridge University Press. Cambridge CB2 8RU, UK.: 109-269.

Kineke, G.C., E.E. Higgins, K. Hart, and D. Velasco. 2006. Fine-sediment transport associated with cold front passages on the shallow shelf, Gulf of Mexico. *Cont. Shelf Res.* **26**: 2073–2091.

Kirby, R. 2000. Practical implications of tidal flat shape. *Cont. Shelf Res.* **20**: 1061–1077.

Kleefsman, K.M.T., G. Fekken, A.E.P. Veldman, B. Iwanowski, and B. Buchner. 2005. A volume-of-fluid based simulation method for wave impact problems. *Journal of Computational Physics*. **206**: 363-393.

Knutson, P., R. Brochu, W. Seelig, and M. Inskeep. 1982. Wave Damping in Spartina Alterniflora Marshes. *Wetlands* **2**: 87-104.

Kobayashi, N., A.W. Raichlen, and T. Asano. 1993. Wave attenuation by vegetation. *J. Waterw. Port Coastal Ocean Eng*. **119**: 30–48.

Kocaman, S. 2007. Experimental and theoretical investigation of dam-break problem. *Ph.D. thesis*. University of Cukurova, Turkey [in Turkish].

Koch, D. L., and A.J.C. Ladd. 1997. Moderate Reynolds number flows through periodic and random arrays of aligned cylinders. *J. Fluid Mech.* **349**: 31–66.

Kothyari, U.C., H. Yashimoto, and K. Hayashi. 2009. Effect of tall vegetation on sediment transport by channel flows. *J. Hydr. Res*. **47**(6): 700–710.

Kraus, N.C., and M. Larson. 1991. NMLONG–Numerical model for simulating the longshore current. Report 1: Model development and tests. *Technical Report DRP-91-1*, U.S. Army Engineer Waterways Experiment Station, Vicksburg, MS, USA.

Kuiry, S.N., W. Wu, and Y. Ding. 2011. A hybrid finite-volume finite-difference scheme for one-dimensional Boussinesq equations to simulate wave attenuation due to vegetation. *Proceeding of ASCE World Environmental & Water Resources Congress (EWRI 2011).*

Lai, W. and A.A. Khan. 2012. Discontinuous Galerkin method for 1D shallow water flow in nonrectangular and nonprismatic channels. *J. Hydraulic Eng*. **138**(3): 285–296.

Larson, M., H. Hanson, and N.C. Kraus. 2003. Numerical modeling of beach topography change. *Advances in Coastal Modeling, Elsevier Oceanography Series* **67**: 337-365.

LCWCRTF. 1998. Louisiana Coastal Wetlands Conservation and Restoration Task Force, 1998. Coast 2050: Toward a Sustainable Coastal Louisiana. Louisiana Department of Natural Resources, Baton Rouge, LA. Available online: http://www.coast2050.gov/report.pdf.

Levine, J.M., J.S. Brewer, and M.D. Bertness. 1998. Nutrients, competition and plant zonation in a New England salt marsh. *Jounal of Ecology* **86**: 285-292.

Li, Z.H., K.D. Nguyen, J.C. Brun-Cottan, and J.M. Martin. 1994. Numerical simulation of the turbidity maximum transport in the Gironde Estuary (France). *Oceanologica Acta* **17**(5): 479–500.

Li, R.M. and H.W. Shen. 1973. Effect of tall vegetation on flow and sediment. *J. the Hydraulics Division* **99**(5): 793–814.

Li, C.W., and K. Yan. 2007. Numerical investigation of wave–current–vegetation interaction. *J. Hydraulic Eng*. **133**(7): 794–803.

Liang, Q. and F. Marche. 2009. Numerical resolution of well-balanced shallow water equations with complex source terms. *Adv. Water Resources* **32**: 873–884.

Lick, W., L.J. Jin, and J. Gailani. 2004. Initiation of movement of quartz particles. *Journal of Hydraulic Engineering* **130**(8): 755–761.

Lin, L., Z. Demirbilek, H. Mase, J. Zheng, and F. Yamada. 2008. CMS-Wave: A nearshore spectral wave processes model for coastal inlets and navigation projects, *Technical Report ERDC/CHL TR-08-13*, Coastal and Hydraulics Laboratory, ERDC, US Army Corps of Engineers, Vicksburg, MS, USA.

Lindner, K. 1982. Der Stroemungswiderstand von Pflanzenbestaenden. Mitteilungen 75, Leichtweiss-Institut fuer Wasserbau, TU Braunschweig.

Lopez, J.A. 2009. The Multiple Lines of Defense Strategy to Sustain Coastal Louisiana. *J. Coastal Res.* Special Issue 54 - Geologic and Environmental Dynamics of the Pontchartrain Basin [FitzGerald & Reed]: 186–197.

Lopez, F., and M. Garcia. 1997. Open-Channel Flow through Simulated Vegetation: Turbulence Modeling and Sediment Transport. *Wetlands Research Program Technical Report WRP-CP-10*, Waterways Experiment Station, US Army Corps of Engineers.

Lopez, F., and M. Garcia. 2001. Mean flow and turbulence structure of open-channel flow through non-emergent vegetation. *J. Hydraulic Eng*. **127**(5): 392–402.

Lotze, H.K., H.S.Lenihan, B.J Bourque, R.H. Bradbury, R.G. Cooke, M.C.Kay, S.M. Kidwell, M.X. Kirby, C.H. Peterson, and J.B.C. Jackson. 2006. Depletion, degradation, and recovery potential of estuaries and coastal seas. *Science* **312**: 1806–1809.

Løvås, S.M., and A. Tørum. 2001. Effect of kelp *Laminaria hyperborea* upon sand dune erosion and water particle velocities. *Coastal Eng*. **44**: 37–63.

Lövstedt, C.B., and M. Larson. 2010. Wave damping in reed: Field measurements and mathematical modeling. *J. Hyd. Eng*. **136***(4)*: 222-233.

Lowe, R.J., J.L. Falter, M.D. Bandet, G. Pawlak, M.J. Atkinson, S.G. Monismith, and J.R. Koseff. 2005b. Spectral wave dissipation over a barrier reef. *J. Geophys. Res.* **110**: C04001, doi:10.1029/2004JC002711.

Lowe, R., J. Falter, J. Koseff, S. Monismith, and M. Atkinson. 2007. Spectral wave flow attenuation within submerged canopies: Implications for wave energy dissipation. *J. Geophys. Res.* **112**: C05018, doi:10.1029/2006JC003605.

Lowe, R.J., J.R. Koseff, and S.G. Monismith. 2005a. Oscillatory flow through submerged canopies: 1.Velocity structure. *J. Geophys. Res.* **110**: C10016, doi:10.1029/2004JC002788.

Luhar, M., S. Coutu, E. Infantes, S. Fox, and H. Nepf. 2010. Wave-induced velocities inside a model seagrass bed. *J. Geophys. Res. Oceans.* **115**: C12005, doi:10.1029/ 2010JC006345.

Madsen, O.S. 1994. Spectral wave-current bottom boundary layer flows. *Proceedings of the 24th International Conference on Coastal Engineering* (*ICCE 1994*).

Majumdar, S. 1988. Role of underrelaxation in employing momentum interpolation practice for calculation of flow with non-staggered grids. *Num. Heat Transfer* **13**: 125–132.

Mase, H. 2001. Multi-directional random wave transformation model based on energy balance equation. *Coastal Engineering Journal* **43**(4): 317-337.

Mase, H., K. Oki, T.S. Hedges, and H.J. Li. 2005. Extended energy-balance-equation wave model for multidirectional random wave transformation. *Ocean Engineering* **32**(8-9): 961-985.

Mazda, Y., M. Magi, Y. Ikeda, T. Kurokawa, and T. Asano. 2006. Wave reduction in a mangrove forest dominated by *Sonneratia sp. Wetlands Ecology and Management* **14***:* 365–378.

McKee, K.L., and J.A. Cherry. 2009. Hurricane Katrina sediment slowed elevation loss in subsiding brackish marshes of the Mississippi River Delta. *Wetlands* **29**(1): 2-15.

Mellor, G.L. 2008. The depth-dependent current and wave interaction equations; a revision. *J. Phys. Oceanogr*. **38**: 2587–2596, doi:10.1175/2008JPO3971.1.

Mendez, F.J., and I.J. Losada. 2004. An empirical model to estimate the propagation of random breaking and nonbreaking waves over vegetation fields. *Coastal Eng*. **51**: 103–118.

Mendez, F.J., I.J. Losada, and M.A. Losada. 1999. Hydrodynamics induced by wind waves in a vegetation field. *J. Geophys. Res.* **104**(C8): 18,383–18,396.

Mickovski, S., L. Beek, and F. Salin 2005. Uprooting of vetiver uprooting resistance of vetiver grass (Vetiveria zizanioides). Plant and Soil, **278**(1-2): 33-41.

Mickovski, S., M. Bransby, and A. Bengough. 2010. Resistance of Simple Plant Root Systems to Uplift Load. *Canadian Geotechnical Journal* **47**(1): 78-95.

Moeller, C.C., O.K. Huh, H.H. Roberts, L.E. Gumley and W.P. Menzel. 1993. Response of Louisiana coastal environments to a cold front passage. *J. Coastal Res.* **9** (2): 434-447.

Möller, I. 2006. Quantifying salt marsh vegetation and its effect on wave height dissipation: results from a UK East coast saltmarsh. *Estuarine Coastal Shelf Sci.* **69**: 337–351.

Möller, I., and T. Spencer. 2002. Wave dissipation over macro-tidal salt marshes: effects of marsh edge typology and vegetation change. *J. Coast. Res.* **SI36**: 506–521.

Möller, I., T. Spencer, J.R. French, D. Leggett, and M. Dixon. 1999. Wave transformation over salt marshes: a field and numerical modeling study from North Norfolk, England. *Estuarine Coastal Shelf Sci.* **49**: 411–426.

Morgan, R.P.C. 2005. *Soil Erosion and Conservation*. 3rd Edition. Blackwell Science Ltd. Malder, MA. 316p.

Morison, J.R., M.P. O'Brien, J.W. Johnson, and S.A. Schaaf. 1950. The force exerted by surface waves on piles. *Petroleum Transactions (American Institute of Mining Engineers)* **189**: 149–154.

Morton, R., J. Bernier, and J. Barras. 2006. Evidence of regional subsidence and associated interior wetland loss induced by hydrocarbon production, Gulf coast region, USA. *Environmental Geology* **50**: 261–274.

Mullarney, J.C., and S.M. Henderson. 2010. Wave-forced motion of submerged single-stem vegetation. *J. Geophys. Res.* **115**: C12061, doi:10.1029/2010JC006448.

Myrhaug, D., and L.E. Holmedal. 2011. Drag force on a vegetation field due to long-crested and short-crested nonlinear random waves. *Coastal Eng.* **58**: 562–566.

Nabi, M.A. 2008. A 3D model of detailed hydrodynamics with sediment transport for simulation of subaqueous dunes. *Proceeding of Int. Conf. on Fluvial Hydraulics (River Flow 2008)*.

Naot, D., I. Nezu, and H. Nakagawa. 1996. Hydrodynamic Behavior of partly vegetated open-channels. *J. Hydraulic Eng*. **122**(11): 625–633.

Nepf, H.M. 1999. Drag, turbulence and diffusion in flow through emergent vegetation. *Water Resources Research* **35**: 479–489.

Nepf, H.M., and E.R.Vivoni. 2000. Flow structure in depth-limited, vegetated flow. *J. Geophys. Res.* **105**(C12): 28547–28557.

Neumeier, U., and C.L. Amos. 2006. The influence of vegetation on turbulence and flow velocities in European salt-marshes. *Sedimentology* **53**(2): 259-277.

Niklas, K. 1989. Mechanical Behavior of Plant Tissues as Inferred from the Theory of Pressurized Cellular Solids. *American Journal of Botany* **76**(6): 929-937.

Niklas, K. 1992. *Plant Biomechanics: an engineering approach to form and function*. Chicago: University of Chicago Press.

Nikora, V., I. McEwan, S. McLean, S. Coleman, D. Pokrajac, and R. Walters R. 2007. Double-averaging concept for rough-bed open-channel and overland flows: theoretical background. *J. Hydraulic Eng*. **133**(8): 873–883.

Odum, W.E., E.P. Odum, and H.T. Odum. 1995. Nature's Pulsing Paradigm. *Estuaries* **18**(4): 547-555.

Oliver, D.R. 1961. The sedimentation of suspensions of closely-sized spherical particles. *Chemical Engineering Science* **15**(3-4): 230-242.

Ozmen-Cagatay, H., and S. Kocaman. 2010. Dam-break flows during initial stage using SWE and RANS approaches. *Journal of Hydraulic Research* **48**: 603-611.

Palumbo, A., S. Soares-Frazao, L. Goutiere, D. Pianese, and Y. Zech. 2008. Dam-break flow on mobile bed in a channel with a sudden enlargement. *Proceeding of Int. Conf. on Fluvial Hydraulics (River Flow 2008)*.

Paterson, D.M. 1989. Short-term changes in the erodibility of intertidal cohesive sediments related to the migratory behavior of epipelic diatoms. *Limnology and Oceanography* **34**:223–234.

Pasche, E., and G. Rouve. 1985. Overbank flow with vegetatively roughened flood plains. *J. Hydraulic Eng*. **111**(9): 1262–1278.

Patankar, S.V. 1980. *Numerical Heat Transfer and Fluid Flow*. Hemisphere, New York.

Patankar, S.V., and D.B. Spalding. 1972. A calculation procedure for heat, mass and momentum transfer in three-dimensional parabolic flows. *Int. J. Heat Mass Transfer* **15**: 1787–1806.

Paul, M., and C.L. Amos. 2011. Spatial and seasonal variation in wave attenuation over *Zostera noltii*. *J. Geophys. Res.* **116**: C08019, doi:10.1029/2010JC006797.

Penland, S., L. Wayne, L. Britsch, S. Williams, A. Beall, and V. Butterworth. 2000. Process Classification of Coastal Land Loss between 1932 and 1990 in the Mississippi River Delta Plain, Southeastern Louisiana. U.S. Geological Survey Open File Report 00–418.

Petryk, S., and G. Bosmajan. 1975. Analysis of flow through vegetation. *J. the Hydraulics Division* **101**(HY7): 871–884.

Priestas, A.M., and S. Fagherazzi. 2011. Morphology and hydrodynamics of wave-cut gullies. *Geomorphology* **131**: 1–13.

Quartel, S., A. Kroon, P.G.E.F. Augustinus, P. Van Santen, and N.H. Tri. 2007. Wave attenuation in coastal mangroves in the Red River Delta, Vietnam. *J. Asian Earth Sci.* **29** *(4)*: 576-584.

Raubenheimer, B., R.T. Guza, and S. Elgar. 1996. Wave transformation across the inner surf zone. *J. Geophys. Res.* **101**: 589-597.

Redfield, A.C. 1972. Development of a New England salt marsh. *Ecological Monographs* **42**: 201-237.

Rhie, T.M., and A. Chow. 1983. Numerical study of the turbulent flow past an isolated airfoil with trailing-edge separation. *AIAA J.* **21**: 1525–1532.

Richardson, J.F., and W.N. Zaki. 1954. Sedimentation and fluidisation, part I. *Trans., Inst. Chem. Engrs.* **32**(1): 35–53.

Riffe, K.C., S.M. Henderson, and J.C. Mullarney. 2011. Wave dissipation by flexible vegetation. *Geophys. Res. Lett.* **38**: L18607, 5 pp., doi:10.1029/2011GL048773.

Roberts, J.C. 2009. *Vegetative response to hurricane sedimentation*. Submitted to the Graduate Faculty of the University of New Orleans in partial fulfillment of the requirements for the degree of Master of Science in Earth and Environmental Science. B. S. Colorado State University, August, 2009.

Roe, P.L. 1981. Approximate Riemann solvers, parameter vectors and difference schemes. *J. Computational Physics* **43**: 357–372.

Roland. R.M., and S.L. Douglass. 2005. Wave tolerance of *spartina alterniflora* in coastal Alabama. *J. Coastal Res.* **21**: 453-463.

Saad, Y. 1993. A flexible inner-outer preconditioned GMRES algorithm. *SIAM J. Sci. Comput.* **14**: 461–469.

Saad, Y. 1994. ILUT: a dual threshold incomplete ILU factorization. *Numerical Linear Algebra Appl.* **1**: 387-402

Saad, Y., and M.H. Schultz. 1986. GMRES: A generalized minimal residual algorithm for solving nonsymmetric linear systems. *SIAM J. Sci. Statist. Comput*. **7**: 856-869.

Sanchez, A., and W. Wu. 2011. A non-equilibrium sediment transport model for coastal inlets and navigation channels. *Journal of Coastal Research* **59**(Special Issue): 39–48.

Sánchez-González, J., V. Sánchez-Rojas, and C. Memos. 2011. Wave attenuation due to *Posidonia oceanica* meadows. *J. Hyd. Res.* **49** (4): 503-514.

Sanders, I.A., C.M. Heppell, J.A. Cotton, G. Wharton, A.G. Hildrew, E.J. Flowers, and M. Trimmer. 2007. Emission of methane from chalk streams has potential implications for agricultural practices. *Freshwater Biology* **52**(6): 1176–1186.

Sanford, L.P. 1994. Wave-forced resuspension of upper Chesapeake Bay muds. *Estuaries* **17**(18): 148–165.

Sanford, L.P. 2008. Modeling a dynamically varying mixed sediment bed with erosion, deposition, bioturbation, consolidation, and armoring. *Computers & Geosciences* **34** (10): 1263–1283.

Sarpkaya, T. 1976. Vortex shedding and resistance in harmonic flow about smooth and rough circular cylinders at high Reynolds numbers. *Naval Post Graduate School Technical Report No*: NPS-59L76021, Monterey CA, USA.

Schulgasser, K., and A. Witzum. 1992. On the Strength, Stiffness, and Stability of Tubular Plant Stems and Leaves. *Journal of Theoretical Biology* **155**(4): 497-510.

Schulgasser, K., and A. Witzum. 1997. On the Strength of Herbaceous Vascular Plant Stems. *Annals of Botany* **80**(1): 35-44.

Schwanenberg, D., and M. Harms. 2004. Discontinuous Galerkin finite-element method for transcritical two-dimensional shallow water flows. *J. Hydraulic Eng*. **130**(5): 412–421.

Schwimmer, R.A. 2001. Rates and processes of marsh shoreline erosion in Rehoboth Bay, Delaware, U.S.A. *J. Coastal Res.* **17**(3): 672–683.

Sheremet, A., A.J. Mehta, B. Liu, and G.W. Stone. 2005. Wave-sediment interaction on a muddy inner shelf during Hurricane Claudette. *Estuarine Coastal Shelf Sci.* **63**: 225–233.

Simon, A., N. Pollen, and E. Langendoen. 2006. Influence of two woody riparian species on critical conditions for streambank stability: Upper Truckee River, California. *Journal of the American Water Resources Association* **42**(1): 99–113.

Smith, J.M., R.E. Jensen, A.B. Kennedy, J.C. Dietrich, and J.J. Westerink. 2011. Waves in wetlands: Hurricane Gustav. *Proceedings of the 32nd International Conference on Coastal Engineering* (*ICCE 2011*).

Spalding, D.B. 1972. A novel finite-difference formulation for differential expressions involving both first and second derivatives. *Int. J. Num. Meth. Eng*. **4**: 551–559.

Stansby, P.K., A. Chegini, and T.C.D. Barnes. 1998. The initial stages of dam-break flow. *Journal of Fluid Mechanics* **374**: 407-424.

Stokes, A., A. Lucas, and L. Jouneau. 2007. Plant Biomechanical Strategies to Frequent Disturbance: Uprooting of Phyllostachys Nidularia (Poaceae) Growing on Landslide-Prone Slopes in Sichuan, China. *American Journal of Botany*, **94** (7): 1129-1136.

Stone, B.M., and H.T. Shen. 2002. Hydraulic resistance of flow in channels with cylindrical roughness. *J. Hydraulic Eng*. **128**(5): 500–506.

Stratigaki, V., E. Manca, P. Prinos, I.J. Losada, J.L. Lara, M. Sclavo, C.L. Amos, I. Cáceres, and A. Sánchez-Arcilla. 2011. Large-scale experiments on wave propagation over *Posidonia oceanica. J. Hydraulic Res.* **49**(sup1): 31-43.

Struiksma, N., K.W. Olewesen, C. Flokstra, and H.J. de Vriend. 1985. Bed deformation in curved alluvial channels. *Journal of Hydraulic Research* **23**(1): 57–79.

Struve, J., A. Falconer, and Y. Wu. 2003. Influence of model mangrove trees on the hydrodynamics in a flume. *Estuarine, Coastal and Shelf Science* **58**(1): 163–171.

Sun, D.-L., Z.-G. Qu, Y.-L. He, and W.-Q. Tao. 2009. Performance analysis of IDEAL algorithm for three-dimensional incompressible fluid flow and heat transfer problems. *Int. J. Numerical Methods in Fluids* **61**(10): 1132–1160.

Suzuki, T. 2011. Wave dissipation over vegetation fields. *PhD Thesis*. Delft University of Technology: Delft. ISBN 978-94-91211-44-7. xii, 176 pp.

Suzuki, T., M. Zijlema, B. Burger, M.C. Meijer, and S. Narayan. 2011. Wave dissipation by vegetation with layer schematization in SWAN. *Coastal Eng.* **59**: 64-71.

Synolakis, C.E. 1986. The Run-up of Long Waves. *PhD Thesis*. California Institute of Technology, Pasadena, CA.

Synolakis, C.E. 1987. The Run-up of solitary waves. *Journal of Fluid Mechanics* **185**: 523-545.

Tanino, Y., and H.M. Nepf. 2008. Laboratory investigation of mean drag in a random array of rigid, emergent cylinders. *J. Hydraulic Eng*. **134**(1): 34–41.

Tengbeh, G.T. 1993. The effect of grass roots on shear strength variations with moisture content. *Soil Technology* **6**(3): 287-295.

Teo, F.Y., A. Falconer, and B. Lin. 2009. Modelling effects of mangroves on tsunamis. *Proceeding of the Institution of Civil Engineers*, Water Management **162**: 3–12.

Thornton, E.B., and R.T. Guza. 1982. Energy saturation and phase speeds measured on a natural beach. *J. Geophys. Res.* **87**: 9499–9508.

Thornton, E.B., and R.T. Guza. 1983. Transformation of wave height distribution. *Journal of Geophysical Research* **88**(C10): 5925–5938.

Thuy, N.B., K. Tanimoto, and N. Tanaka. 2010. Flow and potential force due to runup tsunami around a coastal forest with a gap, experiments and numerical simulations. *Science of Tsunami Hazards* **29**(2): 43–69.

Thuy, N.B., K. Tanimoto, N. Tanaka, K. Harada, and K. Iimura. 2009. Effect of open gap in coastal forest on tsunami run-up, investigations by experiment and numerical simulation. *Ocean Eng*. **36**: 1258–1269.

Ting, F.C.K., and J.T. Kirby. 1994. Observation of undertow and turbulence in a laboratory surf zone. *Coastal Eng*. **24**: 51–80, doi:10.1016/0378-3839(94)90026-4.

Tolhurst, T.J., K.S. Black, S.A. Shayler, S. Mather, I. Black, K. Baker, and D.M. Paterson. 1999. Measuring the in situ erosion shear stress of intertidal sediments with the Cohesive Strength Meter (CSM). *Estuarine Coastal and Shelf Science* **49**(2): 281–294.

Tonelli, M., S. Fagherazzi, and M. Petti. 2010. Modeling wave impact on salt marsh boundaries. *J. Geophys. Res.* **115**: C09028.

Toro, E.F. 2001. *Shock-Capturing Methods for Free-Surface Shallow Flows*, Wiley, England.

Tsujimoto, T. 1998. Development of sand island with vegetation in fluvial fan river under degradation. Proceeding of Water Resource Engineering `98, S. R. Abt, J. Young-Pezeshk and C.C. Watson, ASCE (eds.) **1**: 574–579.

Turner, R.E. 2011. Beneath the salt marsh canopy: loss of soil strength with increasing nutrients loads. *Estuaries and Coasts* **34**(5): 1084-1093.

Ubbink, O. 1999. Numerical prediction of two fluid systems with sharp interfaces. *PhD Thesis*. University of London.

Ubbink, O., and R.I. Issa. 1999. A method for capturing sharp fluid interfaces on arbitrary meshes. *Journal of Computational Physics* **153**: 26-50.

USDA-NRCS. 2005. *The PLANTS database*. National Plant Data Center, Baton Rouge, Louisiana.

USGS. 2003. Coastal erosion and wetland change in Louisiana: selected USGS products. USGS Data Series 79.

Valiani, A., V. Caleffi, and A. Zanni. 2002. Case study: Malpasset dam-break simulation using a two-dimensional finite volume method. *J. Hydraulic Eng*. **128**(5): 460–472.

Valiela, I., J. M. Teal and W. J. Sass. 1975. Production and dynamics of salt marsh vegetation and the effects of experimental treatment with sewage sludge. biomass, production and species composition. *Journal of Applied Ecology* **12**(3): 973-981.

Van Doormal, J.P., and G.D. Raithby. 1984. Enhancements of the SIMPLE method for predicting incompressible fluid flows. *Num. Heat Transfer* **7**(2): 147–163.

Van Eerdt, M.M. 1985. Salt marsh cliff stability in the Oosterschelde. *Earth Surface Processes and Landforms* **10**: 95-106.

Van Ledden, M., W.G.M. van Kesteren, and J. C. Winterwerp. 2004. A conceptual framework for the erosion behaviour of sand–mudmixtures. *Continental Shelf Research* **24**(1): 1–11.

Van Leer, B. 1979. Towards the ultimate conservative difference scheme. V. A second order sequel to Godunov's method. *J. Comput. Phys*. **32**(1): 101–136

Van Rijn, L.C. 1981. Entrainment of fine sediment particles; development of concentration profiles in a steady, uniform flow without initial sediment load. *Rep. No M1531, Part II*, Delft Hydraulic Lab, Delft, The Netherlands.

Van Rijn, L.C. 1984. Sediment transport, part II: suspended load transport. *J. Hydraulic Eng*. **110**(11): 1613–1641.

Warren, R.S., and W.A. Niering. 1993. Vegetation change on a northeast tidal marsh: interaction of sea-level rise and marsh accretion. *Ecology* **74**(1): 96-103.

Watanabe, A. 1985. Three-dimensional predictive model of beach evolution around a structure. *Proceeding of International Symposium of Water Wave Research*. University of Hannover, Germany: 121–142.

Wei, Y., X.Z. Mao, and K.F. Cheung. 2006. Well-balanced finite-volume model for longwave run-up. *J. Waterway, Port, Coastal and Ocean Eng*. **132**: 114–124.

Weis, J.S., and C.A. Butler. 2009. *Salt Marshes: A Natural and Unnatural History.* Rutgers University Press: New Brunswick, New Jersey, and London: 3-117.

Whigham, D., and R. Simpson. 1977. Growth, mortality, and biomass partitioning in freshwater tidal wetland populations of wild rice (*Zizania aquatica var. aquatica*). *Bulletin of the Torrey Botanical Club* **104**(4): 347-351.

Williams, J.S. 2001. Coastal Erosion and Land Loss A round the United States : Strategies to Manage and Protect Coastal Resources- Examples from Louisiana. *Coastal Ecosystems and Federal activities Technical Training Symposium Proceedings*.

Wilson, C.A.M.E., J. Hoyt, and I. Schnauder. 2008. The impact of foliage on the drag force of vegetation in aquatic flows. *J. of Hyd. Eng*. **134** (7): 885–891.

Winterwerp, J.C., and W.G.M. van Kesteren. 2004. *Introduction to the Physics of Cohesive Sediment in the Marine Environment*. Elsevier Science, Amsterdam.

Wolanski, E., M. Jones, and J.S. Bunt. 1980. Hydrodynamics of a tidal creek mangrove swamp system. *Australian J. Marine and Freshwater Research* **31**: 431–450.

Worm, B., et al. 2006. Impacts of biodiversity loss on ocean ecosystem services. *Science* **314***:* 787–790.

Wu, W. 2004. Depth-averaged 2-D numerical modeling of unsteady flow and nonuniform sediment transport in open channels. *J. Hydraulic Eng*. **135**(10): 1013–1024.

Wu, W. 2007. *Computational River Dynamics*, Taylor & Francis, UK.

Wu, Y., A. Falconer, and J. Struve. 2001. Mathematical modeling of tidal currents in mangrove fields. *Environmental Modelling and Software* **16**(1): 19–29.

Wu, W., Y. Ozeren, D. Wren, Q. Chen, G. Zhang, M. Holland, Y. Ding, S.N. Kuiry, M. Zhang, R. Jadhav, J. Chatagnier, Y. Chen, and L. Gordji. 2011. Investigation of Surge and Wave Reduction by Vegetation. *Phase I Report for SERRI Project No. 80037*, The University of Mississippi, MS, p. 315. http://www.serri.org/publications/Documents/Ole%20Miss%20Project%2080037%20-%20Final%20Report%20Phase%201%20-31%20March%202011%20%28Wu%29.pdf, accessed in Aug. 10, 2012.

Wu, W., W. Rodi, and T. Wenka. 2000a. 3D numerical modeling of flow and sediment transport in open channels. *J. Hydraulic Eng*. **126**(1): 4–15.

Wu, W., A. Sanchez, and M. Zhang. 2011. An implicit 2-D shallow water flow model on unstructured quadtree rectangular mesh. *J. Coastal Research* **59**(Special Issue): 15–26.

Wu, W., F.D. Jr. Shields, S.J. Bennett, and S.S.Y. Wang. 2005. A depth-averaged 2-D model for flow, sediment transport and bed topography in curved channels with riparian vegetation. *Water Resources Research* **41**: W03015.

Wu, W., D.A. Vieira, and S.S.Y. Wang. 2004. one-dimensional numerical model for nonuniform sediment transport under unsteady flows in channel networks. *Journal of Hydraulic Engineering* **130**(9): 914-923.

Wu, W., and S.S.Y. Wang. 2004. Depth-averaged numerical modeling of flow and sediment transport in open channels with vegetation. *Riparian Vegetation and Fluvial Geomorphology, edited by S. J. Bennett and A. Simon*, AGU: 253–265.

Wu, W., and S.S.Y. Wang. 2006. Formulas for sediment porosity and settling velocity. *Journal of Hydraulic Engineering* **132**(8): 858-862.

Wu, W., and S.S.Y. Wang. 2007. One-dimensional modeling of dam-break flow over movable beds. *J. Hydraulic Eng*. **133**(1): 48-58.

Wu, W., S.S.Y. Wang, and Y. Jia. 2000b. Nonuniform sediment transport in alluvial rivers. *J. Hydr. Res.* **38**(6): 427–434.

Xia, J., B. Lin, R.A. Falconer, and G. Wang. 2010. Modeling dam-break flows over mobile beds using a 2D coupled approach. *Advances in Water Resources* **33**: 171-183.

Ying, X., and S.S.Y. Wang. 2008. Improved implementation of the HLL approximate Riemann solver for one-dimensional open channel flows. *J. Hydr. Res.* **46**(1): 21–34.

Young, I.R., and L.A. Verhagen. 1996. The growth of fetch limited waves in water of finite depth, Part I, Total energy and peak frequency. *Coastal Eng.* **29**(1 and 2): 47-78.

Zar, J.H. 1984. *Biostatistical Analysis*. Prentice-Hall Inc., Englewood Cliffs, New Jersey. 2nd edition: 600-720.

Zhou, J.G., D.M. Causon, C.G. Mingham, and D.M. Ingram. 2001. The surface gradient method for the treatment of source terms in the shallow water equations. *J. Comput. Phy*. **168**(1): 1–25.

Zhu, J. 1991. A low diffusive and oscillation-free convection scheme. *Communication in Applied Numerical Methods* **7**: 225–232.

APPENDIX A. WAVE AND TOPOGRAPHIC DATA

Table A-1. Water depth, zero-moment wave height and peak periods the study area during Tropical Storm Lee (2011).

	Depth, h (m)			H_{mo} (m)			Swell, T_P (s)			Sea, T_P (s)		
Time (UTC)	W0	W1	W4	W0	W1	W4	W0	W1	W4	W0	W1	W4
9/3/2011 0:00	1.396	0.028	0.293	0.329	NaN	NaN	8.5	NaN	NaN	2.5	NaN	NaN
9/3/2011 0:15	1.399	0.027	0.291	0.358	NaN	NaN	8.5	NaN	NaN	2.4	NaN	NaN
9/3/2011 0:30	1.386	0.018	0.281	0.330	NaN	NaN	7.9	NaN	NaN	2.3	NaN	NaN
9/3/2011 0:45	1.412	0.032	0.295	0.303	NaN	NaN	7.9	NaN	NaN	2.4	NaN	NaN
9/3/2011 1:00	1.485	0.114	0.367	0.393	NaN	NaN	8.5	NaN	NaN	2.5	NaN	NaN
9/3/2011 1:15	1.582	0.228	0.475	0.520	0.054	NaN	7.3	7.9	NaN	3.0	NaN	NaN
9/3/2011 1:30	1.653	0.308	0.566	0.561	0.072	0.012	7.9	7.9	NaN	3.3	3.7	3.5
9/3/2011 1:45	1.678	0.332	0.590	0.552	0.086	0.013	9.3	8.5	NaN	3.7	NaN	3.9
9/3/2011 2:00	1.700	0.353	0.611	0.514	0.093	0.014	9.3	8.5	NaN	3.7	3.9	3.9
9/3/2011 2:15	1.705	0.359	0.620	0.512	0.097	0.014	8.5	8.5	NaN	3.8	3.9	3.9
9/3/2011 2:30	1.749	0.399	0.663	0.645	0.113	0.017	7.3	7.9	NaN	3.8	3.9	4.1
9/3/2011 2:45	1.769	0.408	0.678	0.561	0.119	0.018	NaN	7.9	NaN	3.8	3.9	4.1
9/3/2011 3:00	1.826	0.463	0.734	0.614	0.145	0.023	7.3	7.3	NaN	3.8	4.1	3.9
9/3/2011 3:15	1.859	0.496	0.763	0.642	0.180	0.032	7.9	7.9	NaN	3.9	4.1	3.9
9/3/2011 3:30	1.958	0.588	0.858	0.645	0.233	0.065	NaN	7.3	9.3	3.9	4.1	2.1
9/3/2011 3:45	1.987	0.619	0.891	0.774	0.257	0.077	NaN	8.5	10.2	4.1	4.5	2.1
9/3/2011 4:00	1.996	0.629	0.895	0.719	0.261	0.074	NaN	NaN	11.4	4.3	4.7	2.1
9/3/2011 4:15	1.978	0.612	0.879	0.724	0.254	0.070	NaN	7.9	7.3	4.3	4.3	2.6
9/3/2011 4:30	2.029	0.653	0.927	0.713	0.280	0.092	NaN	NaN	10.2	3.9	4.3	2.0
9/3/2011 4:45	2.115	0.735	1.022	0.828	0.338	0.142	NaN	8.5	7.9	3.8	4.1	2.5
9/3/2011 5:00	2.181	0.806	1.072	0.804	0.368	0.167	7.9	NaN	8.5	4.1	4.3	3.2
9/3/2011 5:15	2.117	0.742	1.015	0.769	0.327	0.129	NaN	7.9	8.5	4.3	4.1	4.3
9/3/2011 5:30	2.182	0.802	1.081	0.803	0.389	0.161	7.3	7.9	8.5	3.9	4.3	4.3
9/3/2011 5:45	2.192	0.819	1.092	0.847	0.376	0.148	NaN	NaN	7.9	4.1	4.3	4.3
9/3/2011 6:00	2.169	0.798	1.068	0.789	0.375	0.138	NaN	NaN	9.3	4.5	4.5	4.1
9/3/2011 6:15	2.165	0.795	1.066	0.771	0.380	0.141	NaN	NaN	NaN	4.3	4.5	4.3
9/3/2011 6:30	2.120	0.751	1.019	0.780	0.366	0.116	NaN	9.3	10.2	4.3	4.5	2.6
9/3/2011 6:45	2.086	0.720	0.984	0.722	0.345	0.105	NaN	7.9	9.3	4.3	4.3	4.3
9/3/2011 7:00	2.067	0.698	0.971	0.754	0.337	0.112	7.9	9.3	9.3	4.1	4.1	2.7
9/3/2011 7:15	2.102	0.736	1.008	0.834	0.379	0.135	NaN	8.5	8.5	3.9	3.9	2.8
9/3/2011 7:30	2.099	0.736	1.007	0.852	0.402	0.152	NaN	7.9	7.9	4.1	4.3	2.2
9/3/2011 7:45	2.112	0.745	1.019	0.848	0.420	0.159	NaN	7.9	8.5	4.1	4.1	2.1
9/3/2011 8:00	2.118	0.757	1.020	0.835	0.418	0.157	NaN	NaN	5.1	4.1	4.5	2.2
9/3/2011 8:15	2.076	0.711	0.981	0.721	0.391	0.142	NaN	NaN	10.2	4.3	4.7	2.2
9/3/2011 8:30	2.127	0.758	1.030	0.822	0.375	0.145	NaN	8.5	9.3	3.9	4.1	2.7
9/3/2011 8:45	2.147	0.780	1.052	0.868	0.417	0.160	7.3	7.9	8.5	3.9	3.9	2.6
9/3/2011 9:00	2.134	0.766	1.035	0.758	0.418	0.163	8.5	8.5	8.5	4.1	4.3	2.2
9/3/2011 9:15	2.117	0.749	1.015	0.731	0.396	0.157	NaN	8.5	9.3	3.9	4.3	2.5
9/3/2011 9:30	2.114	0.743	1.016	0.726	0.396	0.157	7.9	7.9	8.5	3.8	4.3	2.1

	Depth, h (m)			H_{mo} (m)			Swell, T_P (s)			Sea, T_P (s)		
Time (UTC)	W0	W1	W4	W0	W1	W4	W0	W1	W4	W0	W1	W4
9/3/2011 9:45	2.104	0.739	1.001	0.752	0.389	0.136	8.5	9.3	9.3	3.9	3.9	4.3
9/3/2011 10:00	2.096	0.728	1.001	0.757	0.380	0.147	8.5	7.9	9.3	3.8	3.9	2.8
9/3/2011 10:15	2.087	0.727	0.991	0.776	0.397	0.163	8.5	9.3	9.3	4.1	4.3	2.2
9/3/2011 10:30	2.085	0.719	0.991	0.856	0.404	0.149	7.9	8.5	9.3	3.9	4.1	2.2
9/3/2011 10:45	2.115	0.752	1.020	0.832	0.413	0.154	NaN	7.9	8.5	4.1	4.1	2.9
9/3/2011 11:00	2.085	0.724	0.989	0.843	0.363	0.161	NaN	8.5	10.2	4.1	4.5	2.6
9/3/2011 11:15	2.059	0.695	0.960	0.697	0.350	0.131	NaN	8.5	9.3	4.3	4.5	2.0
9/3/2011 11:30	2.007	0.648	0.909	0.651	0.326	0.100	9.3	8.5	9.3	4.3	4.3	3.1
9/3/2011 11:45	1.967	0.610	0.872	0.623	0.295	0.088	9.3	8.5	10.2	4.1	4.3	2.0
9/3/2011 12:00	1.925	0.572	0.832	0.645	0.271	0.081	9.3	9.3	10.2	3.9	4.1	1.7
9/3/2011 12:15	1.917	0.564	0.826	0.645	0.266	0.070	8.5	8.5	10.2	3.9	4.1	2.4
9/3/2011 12:30	1.908	0.561	0.817	0.605	0.257	0.060	9.3	10.2	10.2	3.9	4.1	3.7
9/3/2011 12:45	1.862	0.513	0.768	0.603	0.223	0.047	8.5	8.5	10.2	3.9	4.3	4.3
9/3/2011 13:00	1.844	0.495	0.748	0.542	0.206	0.048	8.5	8.5	NaN	4.1	4.1	2.2
9/3/2011 13:15	1.833	0.486	0.738	0.591	0.207	0.053	8.5	9.3	10.2	3.9	4.1	1.7
9/3/2011 13:30	1.818	0.471	0.720	0.609	0.192	0.042	8.5	9.3	NaN	3.9	3.9	3.9
9/3/2011 13:45	1.743	0.400	0.644	0.488	0.150	0.032	8.5	9.3	11.4	3.9	4.1	4.1
9/3/2011 14:00	1.724	0.377	0.625	0.427	0.135	0.025	10.2	9.3	NaN	3.8	3.8	4.5
9/3/2011 14:15	1.677	0.333	0.577	0.425	0.112	0.020	9.3	9.3	NaN	3.7	3.9	4.1
9/3/2011 14:30	1.640	0.303	0.543	0.456	0.098	0.017	10.2	10.2	NaN	3.7	4.1	4.3
9/3/2011 14:45	1.608	0.268	0.507	0.434	0.077	0.014	9.3	8.5	NaN	3.7	3.9	4.1
9/3/2011 15:00	1.620	0.276	0.515	0.449	0.076	0.013	7.3	7.3	NaN	3.7	3.8	3.8
9/3/2011 15:15	1.608	0.266	0.501	0.441	0.069	0.013	10.2	9.3	NaN	3.7	3.8	3.8
9/3/2011 15:30	1.571	0.240	0.470	0.423	0.067	0.011	9.3	7.9	NaN	3.5	3.7	4.1
9/3/2011 15:45	1.530	0.193	0.425	0.400	0.050	NaN	9.3	10.2	NaN	3.7	NaN	NaN
9/3/2011 16:00	1.529	0.191	0.420	0.393	0.046	NaN	7.9	8.5	NaN	3.5	NaN	NaN
9/3/2011 16:15	1.485	0.145	0.379	0.372	NaN	NaN	8.5	NaN	NaN	3.7	NaN	NaN
9/3/2011 16:30	1.459	0.105	0.346	0.302	NaN	NaN	10.2	NaN	NaN	3.4	NaN	NaN
9/3/2011 16:45	1.408	0.055	0.298	0.250	NaN	NaN	10.2	NaN	NaN	3.5	NaN	NaN
9/3/2011 17:00	1.368	0.001	0.251	0.204	NaN	NaN	10.2	NaN	NaN	3.3	NaN	NaN
9/3/2011 17:15	1.346	0.000	0.232	0.225	NaN	NaN	10.2	NaN	NaN	3.2	NaN	NaN
9/3/2011 17:30	1.339	0.000	0.223	0.215	NaN	NaN	8.5	NaN	NaN	3.1	NaN	NaN
9/3/2011 17:45	1.323	0.000	0.208	0.202	NaN	NaN	8.5	NaN	NaN	3.0	NaN	NaN
9/3/2011 18:00	1.311	0.000	0.193	0.222	NaN	NaN	8.5	NaN	NaN	3.1	NaN	NaN
9/3/2011 18:15	1.285	0.000	0.174	0.207	NaN	NaN	11.4	NaN	NaN	3.2	NaN	NaN
9/3/2011 18:30	1.274	0.000	0.156	0.201	NaN	NaN	9.3	NaN	NaN	3.0	NaN	NaN
9/3/2011 18:45	1.282	0.000	0.164	0.230	NaN	NaN	8.5	NaN	NaN	3.1	NaN	NaN
9/3/2011 19:00	1.276	0.000	0.165	0.212	NaN	NaN	9.3	NaN	NaN	2.8	NaN	NaN
9/3/2011 19:15	1.279	0.000	0.163	0.220	NaN	NaN	9.3	NaN	NaN	2.9	NaN	NaN
9/3/2011 19:30	1.287	0.000	0.171	0.226	NaN	NaN	9.3	NaN	NaN	3.0	NaN	NaN
9/3/2011 19:45	1.274	0.000	0.161	0.218	NaN	NaN	9.3	NaN	NaN	2.9	NaN	NaN

	Depth, h (m)			H_{mo} (m)			Swell, T_P (s)			Sea, T_P (s)		
Time (UTC)	W0	W1	W4	W0	W1	W4	W0	W1	W4	W0	W1	W4
9/3/2011 20:00	1.288	0.000	0.167	0.236	NaN	NaN	9.3	NaN	NaN	2.9	NaN	NaN
9/3/2011 20:15	1.300	0.000	0.182	0.266	NaN	NaN	9.3	NaN	NaN	2.9	NaN	NaN
9/3/2011 20:30	1.289	0.000	0.185	0.313	NaN	NaN	10.2	NaN	NaN	3.1	NaN	NaN
9/3/2011 20:45	1.296	0.000	0.181	0.295	NaN	NaN	8.5	NaN	NaN	3.1	NaN	NaN
9/3/2011 21:00	1.298	0.000	0.181	0.268	NaN	NaN	8.5	NaN	NaN	3.1	NaN	NaN
9/3/2011 21:15	1.295	0.000	0.187	0.323	NaN	NaN	8.5	NaN	NaN	3.1	NaN	NaN
9/3/2011 21:30	1.313	0.000	0.205	0.332	NaN	NaN	8.5	NaN	NaN	3.2	NaN	NaN
9/3/2011 21:45	1.321	0.000	0.204	0.317	NaN	NaN	8.5	NaN	NaN	3.1	NaN	NaN
9/3/2011 22:00	1.341	0.000	0.230	0.334	NaN	NaN	7.3	NaN	NaN	3.2	NaN	NaN
9/3/2011 22:15	1.346	0.006	0.241	0.314	NaN	NaN	9.3	NaN	NaN	3.2	NaN	NaN
9/3/2011 22:30	1.340	0.000	0.224	0.323	NaN	NaN	8.5	NaN	NaN	3.2	NaN	NaN
9/3/2011 22:45	1.393	0.040	0.279	0.344	NaN	NaN	7.9	NaN	NaN	3.1	NaN	NaN
9/3/2011 23:00	1.402	0.065	0.295	0.368	NaN	NaN	7.3	NaN	NaN	3.0	NaN	NaN
9/3/2011 23:15	1.419	0.087	0.308	0.424	NaN	NaN	7.9	NaN	NaN	3.1	NaN	NaN
9/3/2011 23:30	1.467	0.149	0.360	0.476	NaN	NaN	7.3	NaN	NaN	3.0	NaN	NaN
9/3/2011 23:45	1.469	0.145	0.361	0.448	NaN	NaN	7.3	NaN	NaN	3.2	NaN	NaN
9/4/2011 0:00	1.463	0.135	0.356	0.440	NaN	NaN	7.3	NaN	NaN	3.2	NaN	NaN
9/4/2011 0:15	1.485	0.159	0.379	0.469	NaN	NaN	NaN	NaN	NaN	3.4	NaN	NaN
9/4/2011 0:30	1.492	0.178	0.392	0.522	NaN	NaN	NaN	NaN	NaN	3.4	NaN	NaN
9/4/2011 0:45	1.505	0.178	0.398	0.460	NaN	NaN	7.3	NaN	NaN	3.4	NaN	NaN
9/4/2011 1:00	1.527	0.186	0.416	0.408	NaN	NaN	NaN	NaN	NaN	3.3	NaN	NaN
9/4/2011 1:15	1.527	0.200	0.421	0.488	0.051	NaN	7.3	8.5	NaN	3.3	3.8	NaN
9/4/2011 1:30	1.533	0.195	0.426	0.437	0.048	NaN	8.5	8.5	NaN	3.4	4.1	NaN
9/4/2011 1:45	1.564	0.226	0.456	0.425	0.061	NaN	7.3	8.5	NaN	3.2	NaN	NaN
9/4/2011 2:00	1.605	0.270	0.501	0.510	0.086	0.014	7.9	8.5	NaN	3.3	NaN	1.9
9/4/2011 2:15	1.627	0.295	0.524	0.507	0.095	0.015	7.9	7.9	NaN	3.3	4.1	3.5
9/4/2011 2:30	1.640	0.308	0.538	0.512	0.103	0.019	7.3	7.9	NaN	3.3	3.5	1.8
9/4/2011 2:45	1.647	0.309	0.543	0.498	0.107	0.020	7.3	7.9	NaN	2.7	NaN	1.6
9/4/2011 3:00	1.655	0.315	0.550	0.476	0.107	0.019	6.8	7.9	NaN	3.2	3.8	2.2
9/4/2011 3:15	1.684	0.342	0.581	0.523	0.113	0.024	7.9	8.5	10.2	3.2	3.8	1.8
9/4/2011 3:30	1.722	0.374	0.617	0.470	0.136	0.028	7.9	7.9	10.2	2.6	4.7	4.1
9/4/2011 3:45	1.749	0.402	0.645	0.547	0.153	0.035	NaN	7.9	8.5	3.3	3.3	1.9
9/4/2011 4:00	1.754	0.415	0.656	0.570	0.152	0.037	NaN	NaN	9.3	3.5	3.8	2.0
9/4/2011 4:15	1.763	0.420	0.663	0.583	0.163	0.040	6.8	7.9	9.3	3.4	3.7	1.9
9/4/2011 4:30	1.813	0.467	0.713	0.675	0.195	0.050	NaN	7.3	8.5	3.5	3.8	2.1
9/4/2011 4:45	1.818	0.474	0.717	0.635	0.196	0.051	NaN	7.9	8.5	3.8	3.9	2.5
9/4/2011 5:00	1.798	0.454	0.696	0.574	0.187	0.046	NaN	NaN	NaN	3.8	3.9	1.9
9/4/2011 5:15	1.786	0.441	0.685	0.595	0.180	0.043	NaN	7.9	10.2	3.8	3.9	1.7
9/4/2011 5:30	1.788	0.445	0.687	0.580	0.183	0.042	NaN	7.3	9.3	3.9	4.3	2.0
9/4/2011 5:45	1.796	0.444	0.691	0.559	0.172	0.044	NaN	7.9	9.3	3.4	4.3	1.9
9/4/2011 6:00	1.811	0.456	0.705	0.571	0.166	0.041	NaN	NaN	NaN	3.4	3.4	3.3

	Depth, h (m)			H_{mo} (m)			Swell, T_P (s)			Sea, T_P (s)		
Time (UTC)	W0	W1	W4	W0	W1	W4	W0	W1	W4	W0	W1	W4
9/4/2011 6:15	1.833	0.483	0.729	0.629	0.193	0.047	6.8	7.3	8.5	3.7	3.8	4.5
9/4/2011 6:30	1.807	0.467	0.709	0.658	0.192	0.045	NaN	7.9	9.3	3.7	3.5	2.1
9/4/2011 6:45	1.823	0.474	0.721	0.609	0.189	0.048	7.3	5.7	10.2	3.4	3.8	4.3
9/4/2011 7:00	1.821	0.476	0.722	0.611	0.204	0.052	NaN	7.9	7.9	3.5	4.1	1.9
9/4/2011 7:15	1.842	0.489	0.741	0.597	0.195	0.054	NaN	6.8	9.3	3.7	4.1	1.9
9/4/2011 7:30	1.857	0.507	0.753	0.620	0.204	0.051	NaN	NaN	11.4	3.7	4.3	2.1
9/4/2011 7:45	1.822	0.474	0.719	0.590	0.190	0.044	7.9	7.3	9.3	3.5	4.1	2.4
9/4/2011 8:00	1.811	0.460	0.707	0.564	0.180	0.039	NaN	7.3	9.3	2.9	3.9	2.3
9/4/2011 8:15	1.836	0.474	0.728	0.493	0.182	0.041	6.8	6.8	8.5	2.7	3.9	2.8
9/4/2011 8:30	1.830	0.477	0.723	0.539	0.172	0.040	8.5	7.9	NaN	3.1	3.7	3.8
9/4/2011 8:45	1.803	0.451	0.697	0.520	0.167	0.037	7.9	7.9	NaN	3.4	3.4	2.0
9/4/2011 9:00	1.793	0.451	0.694	0.562	0.178	0.037	7.3	7.9	NaN	3.2	3.7	3.7
9/4/2011 9:15	1.797	0.444	0.690	0.517	0.167	0.038	NaN	6.8	NaN	2.9	3.8	1.8
9/4/2011 9:30	1.794	0.440	0.687	0.518	0.163	0.038	7.9	8.5	NaN	3.2	3.4	1.7
9/4/2011 9:45	1.837	0.478	0.729	0.506	0.189	0.049	6.8	7.3	8.5	3.3	3.7	1.5
9/4/2011 10:00	1.835	0.486	0.731	0.599	0.198	0.046	NaN	7.3	NaN	3.4	3.7	2.3
9/4/2011 10:15	1.842	0.500	0.743	0.652	0.217	0.054	NaN	7.3	7.9	3.7	3.8	2.1
9/4/2011 10:30	1.805	0.465	0.707	0.643	0.202	0.053	NaN	7.9	9.3	3.8	4.1	1.9
9/4/2011 10:45	1.786	0.451	0.692	0.630	0.187	0.043	NaN	7.3	8.5	3.7	3.9	4.1
9/4/2011 11:00	1.785	0.446	0.687	0.595	0.190	0.045	NaN	7.3	8.5	3.5	4.5	2.7
9/4/2011 11:15	1.736	0.407	0.644	0.618	0.182	0.037	NaN	8.5	9.3	3.9	NaN	2.0
9/4/2011 11:30	1.794	0.456	0.698	0.651	0.205	0.052	NaN	7.9	8.5	3.8	4.5	1.9
9/4/2011 11:45	1.777	0.441	0.679	0.612	0.179	0.047	NaN	8.5	9.3	3.7	4.3	1.9
9/4/2011 12:00	1.759	0.423	0.666	0.657	0.153	0.041	NaN	5.7	9.3	3.2	3.8	1.7
9/4/2011 12:15	1.810	0.466	0.712	0.621	0.192	0.049	NaN	7.9	9.3	3.7	3.8	1.8
9/4/2011 12:30	1.851	0.501	0.751	0.618	0.212	0.053	NaN	6.8	8.5	3.7	3.9	4.3
9/4/2011 12:45	1.839	0.492	0.736	0.611	0.201	0.051	7.9	NaN	11.4	3.7	4.1	2.5
9/4/2011 13:00	1.871	0.520	0.770	0.660	0.216	0.057	NaN	NaN	9.3	2.8	3.7	3.7
9/4/2011 13:15	1.829	0.489	0.733	0.648	0.210	0.047	NaN	7.9	11.4	3.7	4.1	3.5
9/4/2011 13:30	1.797	0.464	0.705	0.639	0.194	0.045	NaN	8.5	9.3	3.8	4.1	1.9
9/4/2011 13:45	1.756	0.416	0.657	0.592	0.161	0.034	7.9	8.5	10.2	3.2	3.4	1.9
9/4/2011 14:00	1.733	0.399	0.637	0.579	0.149	0.027	NaN	7.9	NaN	3.1	4.3	3.9
9/4/2011 14:15	1.723	0.387	0.625	0.594	0.138	0.029	9.3	8.5	NaN	3.2	3.9	3.8
9/4/2011 14:30	1.730	0.398	0.633	0.639	0.150	0.029	7.9	8.5	10.2	3.5	3.9	4.5
9/4/2011 14:45	1.707	0.378	0.612	0.584	0.138	0.025	NaN	8.5	NaN	3.3	3.9	4.3
9/4/2011 15:00	1.659	0.342	0.568	0.616	0.125	0.021	9.3	8.5	11.4	3.1	3.9	1.9
9/4/2011 15:15	1.601	0.287	0.510	0.598	0.089	0.014	NaN	7.9	NaN	3.2	4.1	4.5
9/4/2011 15:30	1.575	0.266	0.483	0.601	0.083	0.012	NaN	7.9	NaN	3.2	4.1	4.3
9/4/2011 15:45	1.519	0.223	0.430	0.610	0.066	0.010	8.5	7.9	NaN	3.3	4.1	2.7
9/4/2011 16:00	1.514	0.206	0.417	0.573	0.053	NaN	NaN	8.5	NaN	3.2	4.1	NaN
9/4/2011 16:15	1.501	0.192	0.403	0.532	0.052	NaN	NaN	7.3	NaN	2.9	3.9	NaN

	Depth, h (m)			H_{mo} (m)			Swell, T_P (s)			Sea, T_P (s)		
Time (UTC)	W0	W1	W4	W0	W1	W4	W0	W1	W4	W0	W1	W4
9/4/2011 16:30	1.479	0.175	0.384	0.526	NaN	NaN	NaN	NaN	NaN	3.7	NaN	NaN
9/4/2011 16:45	1.483	0.188	0.390	0.538	0.050	NaN	NaN	8.5	NaN	3.3	4.3	NaN
9/4/2011 17:00	1.424	0.131	0.339	0.530	NaN	NaN	NaN	NaN	NaN	3.2	NaN	NaN
9/4/2011 17:15	1.415	0.106	0.317	0.497	NaN	NaN	NaN	NaN	NaN	2.5	NaN	NaN
9/4/2011 17:30	1.390	0.095	0.299	0.510	NaN	NaN	7.3	NaN	NaN	2.9	NaN	NaN
9/4/2011 17:45	1.379	0.077	0.282	0.470	NaN	NaN	NaN	NaN	NaN	2.9	NaN	NaN
9/4/2011 18:00	1.378	0.074	0.280	0.475	NaN	NaN	NaN	NaN	NaN	2.9	NaN	NaN
9/4/2011 18:15	1.386	0.092	0.290	0.526	NaN	NaN	8.5	NaN	NaN	3.1	NaN	NaN
9/4/2011 18:30	1.374	0.082	0.281	0.494	NaN	NaN	NaN	NaN	NaN	3.0	NaN	NaN
9/4/2011 18:45	1.371	0.073	0.275	0.480	NaN	NaN	NaN	NaN	NaN	2.9	NaN	NaN
9/4/2011 19:00	1.359	0.059	0.263	0.451	NaN	NaN	9.3	NaN	NaN	2.9	NaN	NaN
9/4/2011 19:15	1.333	0.032	0.235	0.437	NaN	NaN	NaN	NaN	NaN	3.1	NaN	NaN
9/4/2011 19:30	1.310	0.000	0.210	0.385	NaN	NaN	11.4	NaN	NaN	2.7	NaN	NaN
9/4/2011 19:45	1.302	0.000	0.196	0.341	NaN	NaN	8.5	NaN	NaN	2.8	NaN	NaN
9/4/2011 20:00	1.267	0.000	0.167	0.333	NaN	NaN	NaN	NaN	NaN	2.8	NaN	NaN
9/4/2011 20:15	1.225	0.000	0.120	0.327	NaN	NaN	NaN	NaN	NaN	2.6	NaN	NaN
9/4/2011 20:30	1.218	0.000	0.094	0.279	NaN	NaN	NaN	NaN	NaN	2.6	NaN	NaN
9/4/2011 20:45	1.209	0.000	0.095	0.259	NaN	NaN	NaN	NaN	NaN	2.4	NaN	NaN
9/4/2011 21:00	1.204	0.000	0.081	0.272	NaN	NaN	NaN	NaN	NaN	2.5	NaN	NaN
9/4/2011 21:15	1.209	0.000	0.088	0.268	NaN	NaN	10.2	NaN	NaN	2.6	NaN	NaN
9/4/2011 21:30	1.203	0.000	0.081	0.291	NaN	NaN	9.3	NaN	NaN	2.3	NaN	NaN
9/4/2011 21:45	1.168	0.000	0.055	0.286	NaN	NaN	11.4	NaN	NaN	2.3	NaN	NaN
9/4/2011 22:00	1.141	0.000	0.026	0.243	NaN	NaN	10.2	NaN	NaN	2.5	NaN	NaN
9/4/2011 22:15	1.126	0.000	0.011	0.247	NaN	NaN	10.2	NaN	NaN	2.4	NaN	NaN
9/4/2011 22:30	1.150	0.000	0.018	0.288	NaN	NaN	11.4	NaN	NaN	2.4	NaN	NaN
9/4/2011 22:45	1.131	0.000	0.020	0.300	NaN	NaN	NaN	NaN	NaN	2.4	NaN	NaN
9/4/2011 23:00	1.126	0.000	0.004	0.285	NaN	NaN	NaN	NaN	NaN	2.4	NaN	NaN
9/4/2011 23:15	1.135	0.000	0.002	0.280	NaN	NaN	9.3	NaN	NaN	2.3	NaN	NaN
9/4/2011 23:30	1.146	0.000	0.020	0.263	NaN	NaN	9.3	NaN	NaN	2.3	NaN	NaN
9/4/2011 23:45	1.133	0.000	0.011	0.249	NaN	NaN	9.3	NaN	NaN	2.2	NaN	NaN

Table A-2. Relative wave height, relative water depth, spectral width, and Ursell number for the wave conditions in the study area during Tropical Storm Lee (2011).

	H_{mo}/h			h/L_z			Spectral width			Ursell no.		
Time (UTC)	W0	W1	W4	W0	W1	W4	W0	W1	W4	W0	W1	W4
9/3/2011 0:00	0.24	NaN	NaN	0.18	NaN	NaN	0.47	NaN	NaN	7.1	NaN	NaN
9/3/2011 0:15	0.26	NaN	NaN	0.20	NaN	NaN	0.41	NaN	NaN	6.5	NaN	NaN
9/3/2011 0:30	0.24	NaN	NaN	0.20	NaN	NaN	0.44	NaN	NaN	5.8	NaN	NaN
9/3/2011 0:45	0.21	NaN	NaN	0.20	NaN	NaN	0.46	NaN	NaN	5.5	NaN	NaN
9/3/2011 1:00	0.26	NaN	NaN	0.20	NaN	NaN	0.45	NaN	NaN	6.7	NaN	NaN
9/3/2011 1:15	0.33	0.24	NaN	0.21	0.05	NaN	0.47	0.79	NaN	7.7	83.3	NaN
9/3/2011 1:30	0.34	0.23	0.02	0.22	0.06	0.03	0.49	0.68	1.15	7.3	68.6	19.3
9/3/2011 1:45	0.33	0.26	0.02	0.22	0.09	0.04	0.51	0.71	1.16	7.1	34.0	18.1
9/3/2011 2:00	0.30	0.26	0.02	0.22	0.09	0.04	0.51	0.69	1.16	6.2	30.7	15.0
9/3/2011 2:15	0.30	0.27	0.02	0.22	0.10	0.05	0.50	0.64	1.22	6.1	26.8	9.1
9/3/2011 2:30	0.37	0.28	0.03	0.19	0.11	0.06	0.46	0.61	1.13	10.0	24.8	7.1
9/3/2011 2:45	0.32	0.29	0.03	0.20	0.11	0.07	0.48	0.65	1.05	7.8	24.6	6.2
9/3/2011 3:00	0.34	0.31	0.03	0.23	0.12	0.08	0.49	0.59	0.93	6.3	22.0	4.8
9/3/2011 3:15	0.35	0.36	0.04	0.23	0.13	0.11	0.50	0.58	0.76	6.3	22.3	3.9
9/3/2011 3:30	0.33	0.40	0.08	0.20	0.12	0.15	0.49	0.57	0.58	7.9	26.3	3.6
9/3/2011 3:45	0.39	0.42	0.09	0.24	0.14	0.15	0.52	0.59	0.56	6.8	21.6	3.9
9/3/2011 4:00	0.36	0.41	0.08	0.21	0.15	0.15	0.48	0.56	0.55	8.5	18.5	3.6
9/3/2011 4:15	0.37	0.41	0.08	0.22	0.14	0.15	0.51	0.56	0.57	7.7	20.0	3.7
9/3/2011 4:30	0.35	0.43	0.10	0.22	0.15	0.16	0.48	0.54	0.54	7.5	19.4	3.9
9/3/2011 4:45	0.39	0.46	0.14	0.28	0.15	0.17	0.50	0.56	0.51	5.1	20.5	5.0
9/3/2011 5:00	0.37	0.46	0.16	0.23	0.16	0.20	0.48	0.55	0.51	6.9	17.6	3.8
9/3/2011 5:15	0.36	0.44	0.13	0.23	0.16	0.19	0.49	0.53	0.51	6.6	17.5	3.7
9/3/2011 5:30	0.37	0.49	0.15	0.26	0.18	0.20	0.49	0.54	0.50	5.5	15.6	3.8
9/3/2011 5:45	0.39	0.46	0.14	0.26	0.15	0.15	0.50	0.53	0.53	5.7	19.4	5.9
9/3/2011 6:00	0.36	0.47	0.13	0.24	0.16	0.18	0.52	0.54	0.50	6.2	19.2	4.2
9/3/2011 6:15	0.36	0.48	0.13	0.28	0.14	0.16	0.51	0.52	0.50	4.7	24.2	5.0
9/3/2011 6:30	0.37	0.49	0.11	0.23	0.15	0.16	0.50	0.54	0.55	7.2	21.1	4.6
9/3/2011 6:45	0.35	0.48	0.11	0.19	0.16	0.15	0.45	0.56	0.56	9.8	19.8	4.8
9/3/2011 7:00	0.36	0.48	0.12	0.22	0.14	0.15	0.51	0.57	0.57	7.4	25.6	5.3
9/3/2011 7:15	0.40	0.51	0.13	0.21	0.15	0.16	0.48	0.57	0.55	9.1	22.2	5.5
9/3/2011 7:30	0.41	0.55	0.15	0.22	0.15	0.19	0.52	0.59	0.52	8.1	23.7	4.3
9/3/2011 7:45	0.40	0.56	0.16	0.22	0.15	0.17	0.51	0.60	0.57	8.1	24.1	5.5
9/3/2011 8:00	0.39	0.55	0.15	0.25	0.15	0.17	0.54	0.58	0.53	6.5	24.8	5.5
9/3/2011 8:15	0.35	0.55	0.14	0.21	0.15	0.17	0.53	0.60	0.57	7.6	25.6	4.9
9/3/2011 8:30	0.39	0.50	0.14	0.25	0.13	0.16	0.51	0.58	0.58	6.4	28.3	5.7
9/3/2011 8:45	0.40	0.53	0.15	0.25	0.16	0.17	0.51	0.58	0.53	6.7	21.9	5.5
9/3/2011 9:00	0.36	0.55	0.16	0.22	0.16	0.19	0.53	0.57	0.53	7.2	20.4	4.3
9/3/2011 9:15	0.35	0.53	0.15	0.23	0.16	0.20	0.53	0.59	0.54	6.4	20.7	3.7
9/3/2011 9:30	0.34	0.53	0.15	0.23	0.15	0.19	0.51	0.59	0.56	6.6	23.6	4.1

	H_{mo}/h			h/L_z			Spectral width			Ursell no.		
Time (UTC)	W0	W1	W4	W0	W1	W4	W0	W1	W4	W0	W1	W4
9/3/2011 9:45	0.36	0.53	0.14	0.23	0.16	0.18	0.51	0.57	0.57	7.0	21.0	4.1
9/3/2011 10:00	0.36	0.52	0.15	0.25	0.16	0.18	0.50	0.54	0.50	6.0	20.5	4.7
9/3/2011 10:15	0.37	0.55	0.16	0.22	0.14	0.19	0.51	0.60	0.55	7.8	27.4	4.6
9/3/2011 10:30	0.41	0.56	0.15	0.25	0.15	0.17	0.52	0.58	0.54	6.7	24.2	5.1
9/3/2011 10:45	0.39	0.55	0.15	0.23	0.15	0.18	0.49	0.56	0.54	7.3	25.1	4.9
9/3/2011 11:00	0.40	0.50	0.16	0.20	0.13	0.20	0.49	0.57	0.53	10.1	28.9	3.9
9/3/2011 11:15	0.34	0.50	0.14	0.22	0.14	0.19	0.55	0.59	0.56	7.1	24.1	3.7
9/3/2011 11:30	0.32	0.50	0.11	0.20	0.14	0.16	0.52	0.59	0.59	8.1	27.5	4.2
9/3/2011 11:45	0.32	0.48	0.10	0.20	0.13	0.17	0.49	0.59	0.57	7.6	26.7	3.4
9/3/2011 12:00	0.34	0.47	0.10	0.21	0.12	0.17	0.50	0.59	0.59	7.6	33.4	3.5
9/3/2011 12:15	0.34	0.47	0.09	0.21	0.13	0.15	0.52	0.60	0.60	7.7	28.1	4.0
9/3/2011 12:30	0.32	0.46	0.07	0.20	0.13	0.13	0.50	0.59	0.63	7.8	26.6	4.5
9/3/2011 12:45	0.32	0.44	0.06	0.20	0.13	0.12	0.49	0.56	0.64	7.8	27.8	4.4
9/3/2011 13:00	0.29	0.42	0.06	0.18	0.12	0.13	0.44	0.55	0.60	8.7	26.9	3.9
9/3/2011 13:15	0.32	0.43	0.07	0.21	0.12	0.16	0.49	0.57	0.59	7.5	27.8	2.9
9/3/2011 13:30	0.33	0.41	0.06	0.21	0.12	0.13	0.48	0.54	0.64	7.3	29.7	3.2
9/3/2011 13:45	0.28	0.37	0.05	0.20	0.11	0.13	0.50	0.58	0.73	7.0	31.2	3.1
9/3/2011 14:00	0.25	0.36	0.04	0.21	0.11	0.11	0.48	0.55	0.78	5.4	29.2	3.5
9/3/2011 14:15	0.25	0.34	0.04	0.21	0.10	0.10	0.47	0.57	0.90	5.8	32.0	3.3
9/3/2011 14:30	0.28	0.32	0.03	0.20	0.10	0.09	0.47	0.59	1.01	7.3	34.3	3.9
9/3/2011 14:45	0.27	0.29	0.03	0.22	0.08	0.06	0.49	0.57	1.11	5.8	43.9	7.1
9/3/2011 15:00	0.28	0.27	0.03	0.20	0.08	0.07	0.47	0.53	1.10	6.8	48.5	4.9
9/3/2011 15:15	0.27	0.26	0.03	0.22	0.07	0.05	0.47	0.58	1.24	5.7	50.0	8.4
9/3/2011 15:30	0.27	0.28	0.02	0.19	0.06	0.04	0.48	0.70	1.22	7.5	67.6	19.8
9/3/2011 15:45	0.26	0.26	NaN	0.19	0.06	NaN	0.48	0.77	NaN	7.1	66.0	NaN
9/3/2011 16:00	0.26	0.24	NaN	0.21	0.05	NaN	0.48	0.72	NaN	6.0	102.1	NaN
9/3/2011 16:15	0.25	NaN	NaN	0.23	NaN	NaN	0.52	NaN	NaN	4.9	NaN	NaN
9/3/2011 16:30	0.21	NaN	NaN	0.26	NaN	NaN	0.48	NaN	NaN	3.0	NaN	NaN
9/3/2011 16:45	0.18	NaN	NaN	0.25	NaN	NaN	0.47	NaN	NaN	2.9	NaN	NaN
9/3/2011 17:00	0.15	NaN	NaN	0.30	NaN	NaN	0.46	NaN	NaN	1.7	NaN	NaN
9/3/2011 17:15	0.17	NaN	NaN	0.29	NaN	NaN	0.40	NaN	NaN	2.0	NaN	NaN
9/3/2011 17:30	0.16	NaN	NaN	0.30	NaN	NaN	0.40	NaN	NaN	1.8	NaN	NaN
9/3/2011 17:45	0.15	NaN	NaN	0.26	NaN	NaN	0.41	NaN	NaN	2.2	NaN	NaN
9/3/2011 18:00	0.17	NaN	NaN	0.28	NaN	NaN	0.42	NaN	NaN	2.2	NaN	NaN
9/3/2011 18:15	0.16	NaN	NaN	0.27	NaN	NaN	0.43	NaN	NaN	2.3	NaN	NaN
9/3/2011 18:30	0.16	NaN	NaN	0.26	NaN	NaN	0.40	NaN	NaN	2.3	NaN	NaN
9/3/2011 18:45	0.18	NaN	NaN	0.28	NaN	NaN	0.42	NaN	NaN	2.4	NaN	NaN
9/3/2011 19:00	0.17	NaN	NaN	0.23	NaN	NaN	0.40	NaN	NaN	3.2	NaN	NaN
9/3/2011 19:15	0.17	NaN	NaN	0.25	NaN	NaN	0.43	NaN	NaN	2.7	NaN	NaN
9/3/2011 19:30	0.18	NaN	NaN	0.27	NaN	NaN	0.41	NaN	NaN	2.5	NaN	NaN
9/3/2011 19:45	0.17	NaN	NaN	0.23	NaN	NaN	0.39	NaN	NaN	3.1	NaN	NaN

	H_{mo}/h			h/L_z			Spectral width			Ursell no.		
Time (UTC)	W0	W1	W4	W0	W1	W4	W0	W1	W4	W0	W1	W4
9/3/2011 20:00	0.18	NaN	NaN	0.25	NaN	NaN	0.40	NaN	NaN	2.9	NaN	NaN
9/3/2011 20:15	0.20	NaN	NaN	0.26	NaN	NaN	0.43	NaN	NaN	3.0	NaN	NaN
9/3/2011 20:30	0.24	NaN	NaN	0.23	NaN	NaN	0.44	NaN	NaN	4.7	NaN	NaN
9/3/2011 20:45	0.23	NaN	NaN	0.22	NaN	NaN	0.42	NaN	NaN	4.7	NaN	NaN
9/3/2011 21:00	0.21	NaN	NaN	0.25	NaN	NaN	0.43	NaN	NaN	3.3	NaN	NaN
9/3/2011 21:15	0.25	NaN	NaN	0.23	NaN	NaN	0.39	NaN	NaN	4.6	NaN	NaN
9/3/2011 21:30	0.25	NaN	NaN	0.21	NaN	NaN	0.42	NaN	NaN	5.8	NaN	NaN
9/3/2011 21:45	0.24	NaN	NaN	0.22	NaN	NaN	0.43	NaN	NaN	5.0	NaN	NaN
9/3/2011 22:00	0.25	NaN	NaN	0.23	NaN	NaN	0.41	NaN	NaN	4.6	NaN	NaN
9/3/2011 22:15	0.23	NaN	NaN	0.24	NaN	NaN	0.42	NaN	NaN	4.2	NaN	NaN
9/3/2011 22:30	0.24	NaN	NaN	0.24	NaN	NaN	0.40	NaN	NaN	4.2	NaN	NaN
9/3/2011 22:45	0.25	NaN	NaN	0.25	NaN	NaN	0.42	NaN	NaN	3.8	NaN	NaN
9/3/2011 23:00	0.26	NaN	NaN	0.25	NaN	NaN	0.41	NaN	NaN	4.2	NaN	NaN
9/3/2011 23:15	0.30	NaN	NaN	0.23	NaN	NaN	0.43	NaN	NaN	5.7	NaN	NaN
9/3/2011 23:30	0.32	NaN	NaN	0.20	NaN	NaN	0.38	NaN	NaN	8.1	NaN	NaN
9/3/2011 23:45	0.30	NaN	NaN	0.23	NaN	NaN	0.44	NaN	NaN	5.6	NaN	NaN
9/4/2011 0:00	0.30	NaN	NaN	0.24	NaN	NaN	0.44	NaN	NaN	5.2	NaN	NaN
9/4/2011 0:15	0.32	NaN	NaN	0.24	NaN	NaN	0.43	NaN	NaN	5.6	NaN	NaN
9/4/2011 0:30	0.35	NaN	NaN	0.24	NaN	NaN	0.48	NaN	NaN	6.1	NaN	NaN
9/4/2011 0:45	0.31	NaN	NaN	0.21	NaN	NaN	0.44	NaN	NaN	6.7	NaN	NaN
9/4/2011 1:00	0.27	NaN	NaN	0.22	NaN	NaN	0.43	NaN	NaN	5.7	NaN	NaN
9/4/2011 1:15	0.32	0.25	NaN	0.23	0.05	NaN	0.44	0.68	NaN	5.8	94.1	NaN
9/4/2011 1:30	0.29	0.25	NaN	0.25	0.07	NaN	0.43	0.68	NaN	4.5	57.9	NaN
9/4/2011 1:45	0.27	0.27	NaN	0.24	0.05	NaN	0.42	0.68	NaN	4.8	91.0	NaN
9/4/2011 2:00	0.32	0.32	0.03	0.25	0.08	0.08	0.44	0.67	1.09	5.1	45.1	4.5
9/4/2011 2:15	0.31	0.32	0.03	0.26	0.08	0.06	0.46	0.65	1.03	4.5	48.2	8.9
9/4/2011 2:30	0.31	0.33	0.03	0.22	0.08	0.09	0.45	0.65	0.97	6.3	54.2	3.9
9/4/2011 2:45	0.30	0.35	0.04	0.25	0.09	0.11	0.45	0.67	0.96	4.9	40.5	3.2
9/4/2011 3:00	0.29	0.34	0.03	0.24	0.10	0.09	0.46	0.64	0.96	4.8	35.9	4.1
9/4/2011 3:15	0.31	0.33	0.04	0.27	0.08	0.10	0.46	0.64	0.83	4.2	55.0	3.9
9/4/2011 3:30	0.27	0.36	0.04	0.26	0.10	0.10	0.43	0.59	0.77	4.2	34.6	4.8
9/4/2011 3:45	0.31	0.38	0.05	0.25	0.11	0.12	0.44	0.59	0.69	5.1	32.1	4.0
9/4/2011 4:00	0.33	0.36	0.06	0.24	0.09	0.11	0.45	0.57	0.71	5.9	48.3	4.8
9/4/2011 4:15	0.33	0.39	0.06	0.23	0.11	0.13	0.45	0.57	0.64	6.3	34.4	3.5
9/4/2011 4:30	0.37	0.42	0.07	0.25	0.11	0.12	0.46	0.58	0.63	6.0	32.7	5.2
9/4/2011 4:45	0.35	0.41	0.07	0.23	0.10	0.12	0.47	0.58	0.64	6.5	38.3	5.1
9/4/2011 5:00	0.32	0.41	0.07	0.21	0.12	0.13	0.45	0.57	0.63	7.3	29.4	3.8
9/4/2011 5:15	0.33	0.41	0.06	0.25	0.12	0.14	0.47	0.60	0.65	5.2	29.0	3.4
9/4/2011 5:30	0.32	0.41	0.06	0.26	0.12	0.12	0.46	0.60	0.69	4.7	29.5	4.3
9/4/2011 5:45	0.31	0.39	0.06	0.25	0.12	0.14	0.41	0.57	0.62	5.0	28.4	3.1
9/4/2011 6:00	0.32	0.36	0.06	0.28	0.11	0.12	0.44	0.52	0.65	3.9	32.6	3.8

	H_{mo}/h			h/L_z			Spectral width			Ursell no.		
Time (UTC)	W0	W1	W4	W0	W1	W4	W0	W1	W4	W0	W1	W4
9/4/2011 6:15	0.34	0.40	0.06	0.27	0.12	0.12	0.44	0.55	0.65	4.8	27.1	4.5
9/4/2011 6:30	0.36	0.41	0.06	0.27	0.11	0.12	0.49	0.58	0.67	5.2	32.3	4.6
9/4/2011 6:45	0.33	0.40	0.07	0.26	0.12	0.13	0.47	0.54	0.63	4.9	27.8	3.8
9/4/2011 7:00	0.34	0.43	0.07	0.23	0.12	0.13	0.43	0.60	0.64	6.4	28.2	4.3
9/4/2011 7:15	0.32	0.40	0.07	0.27	0.12	0.14	0.44	0.54	0.60	4.3	26.7	3.8
9/4/2011 7:30	0.33	0.40	0.07	0.27	0.13	0.13	0.43	0.53	0.59	4.7	22.8	3.9
9/4/2011 7:45	0.32	0.40	0.06	0.27	0.12	0.12	0.48	0.56	0.65	4.5	29.2	4.1
9/4/2011 8:00	0.31	0.39	0.06	0.30	0.13	0.13	0.44	0.54	0.67	3.6	23.7	3.4
9/4/2011 8:15	0.27	0.38	0.06	0.26	0.13	0.12	0.39	0.50	0.65	4.0	21.8	3.8
9/4/2011 8:30	0.29	0.36	0.05	0.27	0.13	0.12	0.43	0.49	0.65	4.1	23.0	3.7
9/4/2011 8:45	0.29	0.37	0.05	0.27	0.13	0.13	0.42	0.50	0.65	4.1	22.7	3.3
9/4/2011 9:00	0.31	0.39	0.05	0.24	0.13	0.11	0.42	0.50	0.64	5.6	23.3	4.3
9/4/2011 9:15	0.29	0.38	0.05	0.22	0.12	0.13	0.38	0.53	0.65	5.9	24.6	3.1
9/4/2011 9:30	0.29	0.37	0.05	0.24	0.13	0.14	0.38	0.47	0.61	4.9	22.6	2.8
9/4/2011 9:45	0.28	0.39	0.07	0.27	0.13	0.16	0.41	0.51	0.58	3.8	22.5	2.7
9/4/2011 10:00	0.33	0.41	0.06	0.26	0.13	0.12	0.43	0.52	0.61	4.9	24.8	4.1
9/4/2011 10:15	0.35	0.43	0.07	0.23	0.13	0.14	0.46	0.55	0.59	6.4	26.5	4.0
9/4/2011 10:30	0.36	0.43	0.08	0.25	0.12	0.14	0.49	0.60	0.62	5.6	31.9	4.1
9/4/2011 10:45	0.35	0.41	0.06	0.21	0.11	0.12	0.44	0.58	0.65	8.1	36.2	4.6
9/4/2011 11:00	0.33	0.43	0.07	0.24	0.12	0.13	0.49	0.61	0.65	5.9	31.1	3.8
9/4/2011 11:15	0.36	0.45	0.06	0.20	0.10	0.10	0.46	0.66	0.76	8.5	41.7	5.5
9/4/2011 11:30	0.36	0.45	0.07	0.24	0.11	0.13	0.46	0.64	0.63	6.3	35.6	4.6
9/4/2011 11:45	0.34	0.41	0.07	0.24	0.11	0.13	0.47	0.62	0.66	5.9	35.8	4.1
9/4/2011 12:00	0.37	0.36	0.06	0.25	0.08	0.13	0.47	0.57	0.65	5.8	50.5	3.4
9/4/2011 12:15	0.34	0.41	0.07	0.23	0.13	0.14	0.42	0.56	0.59	6.6	26.0	3.4
9/4/2011 12:30	0.33	0.42	0.07	0.25	0.13	0.13	0.43	0.54	0.61	5.3	24.8	4.4
9/4/2011 12:45	0.33	0.41	0.07	0.25	0.13	0.14	0.45	0.54	0.59	5.2	25.3	3.5
9/4/2011 13:00	0.35	0.41	0.07	0.28	0.12	0.13	0.44	0.51	0.56	4.3	27.4	4.3
9/4/2011 13:15	0.35	0.43	0.06	0.26	0.12	0.11	0.47	0.56	0.64	5.2	28.9	4.9
9/4/2011 13:30	0.36	0.42	0.06	0.24	0.12	0.13	0.46	0.57	0.64	6.0	28.0	3.6
9/4/2011 13:45	0.34	0.39	0.05	0.24	0.11	0.12	0.43	0.57	0.71	5.8	29.5	3.7
9/4/2011 14:00	0.33	0.37	0.04	0.21	0.11	0.10	0.39	0.56	0.76	7.3	28.5	4.7
9/4/2011 14:15	0.34	0.36	0.05	0.24	0.11	0.12	0.44	0.56	0.72	5.9	30.4	3.1
9/4/2011 14:30	0.37	0.38	0.05	0.25	0.10	0.10	0.46	0.57	0.74	5.7	35.1	4.5
9/4/2011 14:45	0.34	0.36	0.04	0.21	0.10	0.10	0.42	0.58	0.79	7.6	33.6	4.6
9/4/2011 15:00	0.37	0.36	0.04	0.22	0.10	0.08	0.45	0.62	0.95	8.0	37.5	5.0
9/4/2011 15:15	0.37	0.31	0.03	0.25	0.08	0.07	0.45	0.60	1.20	6.2	45.8	6.4
9/4/2011 15:30	0.38	0.31	0.02	0.23	0.09	0.06	0.44	0.59	1.31	7.5	39.3	6.9
9/4/2011 15:45	0.40	0.30	0.02	0.21	0.07	0.03	0.47	0.63	1.40	8.7	54.8	25.1
9/4/2011 16:00	0.38	0.26	NaN	0.23	0.05	NaN	0.46	0.61	NaN	7.1	88.6	NaN
9/4/2011 16:15	0.35	0.27	NaN	0.21	0.07	NaN	0.43	0.67	NaN	7.7	60.0	NaN

	H_{mo}/h			h/L_z			Spectral width			Ursell no.		
Time (UTC)	W0	W1	W4	W0	W1	W4	W0	W1	W4	W0	W1	W4
9/4/2011 16:30	0.36	NaN	NaN	0.23	NaN	NaN	0.44	NaN	NaN	6.9	NaN	NaN
9/4/2011 16:45	0.36	0.26	NaN	0.18	0.06	NaN	0.41	0.65	NaN	10.7	81.7	NaN
9/4/2011 17:00	0.37	NaN	NaN	0.26	NaN	NaN	0.47	NaN	NaN	5.5	NaN	NaN
9/4/2011 17:15	0.35	NaN	NaN	0.25	NaN	NaN	0.42	NaN	NaN	5.6	NaN	NaN
9/4/2011 17:30	0.37	NaN	NaN	0.22	NaN	NaN	0.44	NaN	NaN	7.6	NaN	NaN
9/4/2011 17:45	0.34	NaN	NaN	0.23	NaN	NaN	0.46	NaN	NaN	6.3	NaN	NaN
9/4/2011 18:00	0.34	NaN	NaN	0.22	NaN	NaN	0.42	NaN	NaN	7.0	NaN	NaN
9/4/2011 18:15	0.38	NaN	NaN	0.21	NaN	NaN	0.44	NaN	NaN	8.5	NaN	NaN
9/4/2011 18:30	0.36	NaN	NaN	0.21	NaN	NaN	0.43	NaN	NaN	8.5	NaN	NaN
9/4/2011 18:45	0.35	NaN	NaN	0.22	NaN	NaN	0.43	NaN	NaN	7.4	NaN	NaN
9/4/2011 19:00	0.33	NaN	NaN	0.23	NaN	NaN	0.43	NaN	NaN	6.3	NaN	NaN
9/4/2011 19:15	0.33	NaN	NaN	0.22	NaN	NaN	0.43	NaN	NaN	6.8	NaN	NaN
9/4/2011 19:30	0.29	NaN	NaN	0.23	NaN	NaN	0.42	NaN	NaN	5.4	NaN	NaN
9/4/2011 19:45	0.26	NaN	NaN	0.20	NaN	NaN	0.37	NaN	NaN	6.6	NaN	NaN
9/4/2011 20:00	0.26	NaN	NaN	0.24	NaN	NaN	0.39	NaN	NaN	4.5	NaN	NaN
9/4/2011 20:15	0.27	NaN	NaN	0.27	NaN	NaN	0.36	NaN	NaN	3.6	NaN	NaN
9/4/2011 20:30	0.23	NaN	NaN	0.28	NaN	NaN	0.34	NaN	NaN	2.9	NaN	NaN
9/4/2011 20:45	0.21	NaN	NaN	0.28	NaN	NaN	0.34	NaN	NaN	2.8	NaN	NaN
9/4/2011 21:00	0.23	NaN	NaN	0.28	NaN	NaN	0.35	NaN	NaN	2.9	NaN	NaN
9/4/2011 21:15	0.22	NaN	NaN	0.29	NaN	NaN	0.36	NaN	NaN	2.5	NaN	NaN
9/4/2011 21:30	0.24	NaN	NaN	0.30	NaN	NaN	0.35	NaN	NaN	2.7	NaN	NaN
9/4/2011 21:45	0.24	NaN	NaN	0.29	NaN	NaN	0.36	NaN	NaN	2.9	NaN	NaN
9/4/2011 22:00	0.21	NaN	NaN	0.24	NaN	NaN	0.36	NaN	NaN	3.6	NaN	NaN
9/4/2011 22:15	0.22	NaN	NaN	0.25	NaN	NaN	0.35	NaN	NaN	3.5	NaN	NaN
9/4/2011 22:30	0.25	NaN	NaN	0.25	NaN	NaN	0.34	NaN	NaN	4.0	NaN	NaN
9/4/2011 22:45	0.27	NaN	NaN	0.25	NaN	NaN	0.36	NaN	NaN	4.3	NaN	NaN
9/4/2011 23:00	0.25	NaN	NaN	0.24	NaN	NaN	0.32	NaN	NaN	4.4	NaN	NaN
9/4/2011 23:15	0.25	NaN	NaN	0.25	NaN	NaN	0.33	NaN	NaN	3.9	NaN	NaN
9/4/2011 23:30	0.23	NaN	NaN	0.25	NaN	NaN	0.34	NaN	NaN	3.7	NaN	NaN
9/4/2011 23:45	0.22	NaN	NaN	0.25	NaN	NaN	0.33	NaN	NaN	3.4	NaN	NaN

Table A-3. Wave energy density spectra recorded at four marsh gages on September 3, 2011 at 6:45 UTC during Tropical Storm Lee (2011).

f (Hz)	E1 (m^2/Hz)	E2 (m^2/Hz)	E3 (m^2/Hz)	E4 (m^2/Hz)
0.009766	0.000246	0.000296	0.000262	0.000251
0.019531	0.000366	0.000354	0.000321	0.000284
0.029297	0.000571	0.000444	0.000405	0.00034
0.039063	0.000877	0.000575	0.000509	0.00042
0.048828	0.001333	0.000775	0.000636	0.000529
0.058594	0.002018	0.001078	0.000802	0.000668
0.068359	0.00301	0.001495	0.001019	0.000828
0.078125	0.00433	0.001992	0.001277	0.000986
0.087891	0.005878	0.002497	0.001534	0.001113
0.097656	0.007423	0.002922	0.001735	0.001188
0.107422	0.008677	0.003203	0.001836	0.001205
0.117188	0.009405	0.003316	0.001829	0.001172
0.126953	0.009534	0.003283	0.001746	0.001103
0.136719	0.009182	0.003153	0.001637	0.001011
0.146484	0.008621	0.002996	0.001546	0.000908
0.15625	0.008183	0.002891	0.001502	0.000807
0.166016	0.008189	0.002917	0.001515	0.000735
0.175781	0.008884	0.00313	0.001592	0.000725
0.185547	0.010391	0.003544	0.001735	0.000799
0.195313	0.012661	0.004117	0.001939	0.000951
0.205078	0.015435	0.004754	0.002181	0.001144
0.214844	0.018251	0.005315	0.00242	0.001323
0.224609	0.020537	0.005653	0.002598	0.001443
0.234375	0.021779	0.005654	0.002667	0.001485
0.244141	0.021702	0.005291	0.002604	0.001454
0.253906	0.02037	0.004649	0.002427	0.001374
0.263672	0.018169	0.003899	0.002189	0.001274
0.273438	0.015658	0.003228	0.001955	0.00118
0.283203	0.013378	0.002757	0.001779	0.001111
0.292969	0.011698	0.002508	0.001685	0.001079
0.302734	0.010737	0.002424	0.001671	0.00108
0.3125	0.010374	0.002429	0.001723	0.001101
0.322266	0.010322	0.002481	0.00182	0.001125
0.332031	0.010247	0.002574	0.001944	0.001142
0.341797	0.009904	0.002717	0.002075	0.001153
0.351563	0.009248	0.002896	0.002192	0.001167
0.361328	0.008451	0.003074	0.002283	0.001193
0.371094	0.007808	0.003211	0.002343	0.001234
0.380859	0.007555	0.0033	0.002383	0.001284
0.390625	0.007728	0.00338	0.002413	0.00133

f (Hz)	E1 (m^2/Hz)	E2 (m^2/Hz)	E3 (m^2/Hz)	E4 (m^2/Hz)
0.400391	0.008144	0.003505	0.002443	0.001358
0.410156	0.008529	0.00371	0.002468	0.00136
0.419922	0.008691	0.00398	0.002474	0.001338
0.429688	0.008618	0.004259	0.002445	0.001298
0.439453	0.008435	0.004482	0.002376	0.001253
0.449219	0.008276	0.004609	0.002276	0.001211
0.458984	0.008186	0.004631	0.002169	0.001175
0.46875	0.00811	0.004565	0.002074	0.001145
0.478516	0.007962	0.004447	0.002002	0.001119
0.488281	0.007696	0.004318	0.001947	0.001098
0.498047	0.007325	0.004219	0.001904	0.001093
0.507813	0.006901	0.004179	0.001882	0.001013
0.517578	0.006496	0.004193	0.001898	0.00094
0.527344	0.006197	0.004225	0.001966	0.000874
0.537109	0.006103	0.004215	0.002075	0.000813
0.546875	0.006296	0.004117	0.002181	0.000757
0.556641	0.00678	0.003915	0.002235	0.000706
0.566406	0.007441	0.003641	0.002201	0.00066
0.576172	0.008074	0.00336	0.002086	0.000617
0.585938	0.008467	0.003143	0.001927	0.000577
0.595703	0.008506	0.003037	0.001772	0.000541
0.605469	0.008219	0.003043	0.001661	0.000508
0.615234	0.007744	0.003118	0.001605	0.000477
0.625	0.00724	0.003203	0.001592	0.000448
0.634766	0.006807	0.003262	0.001597	0.000421
0.644531	0.006461	0.003297	0.001595	0.000397
0.654297	0.006174	0.003326	0.001575	0.000374
0.664063	0.005925	0.003363	0.001545	0.000353
0.673828	0.00573	0.003394	0.001526	0.000333
0.683594	0.005637	0.003394	0.001536	0.000315
0.693359	0.005673	0.003352	0.001577	0.000298
0.703125	0.005811	0.003276	0.001627	0.000282
0.712891	0.005959	0.003185	0.001654	0.000267
0.722656	0.006001	0.003087	0.001635	0.000253
0.732422	0.005852	0.002974	0.001573	0.00024
0.742188	0.005519	0.002839	0.001499	0.000227
0.751953	0.005097	0.002689	0.001449	0.000216
0.761719	0.004739	0.002555	0.001447	0.000205
0.771484	0.004586	0.002468	0.001486	0.000195
0.78125	0.004709	0.00244	0.001538	0.000186
0.791016	0.005085	0.002455	0.001568	0.000177
0.800781	0.0056	0.002476	0.001563	0.000168

f (Hz)	E1 (m^2/Hz)	E2 (m^2/Hz)	E3 (m^2/Hz)	E4 (m^2/Hz)
0.810547	0.006088	0.002466	0.001532	0.000161
0.820313	0.006387	0.002403	0.001497	0.000153
0.830078	0.006397	0.002292	0.001477	0.000146
0.839844	0.006114	0.002152	0.00147	0.00014
0.849609	0.005621	0.002014	0.001464	0.000133
0.859375	0.005057	0.001905	0.001442	0.000127
0.869141	0.004563	0.00184	0.0014	0.000122
0.878906	0.004189	0.00176	0.001347	0.000117
0.888672	0.00401	0.001685	0.001275	0.000112
0.898438	0.00384	0.001613	0.001221	0.000107
0.908203	0.00368	0.001546	0.00117	0.000102
0.917969	0.003527	0.001482	0.001122	9.82E-05
0.927734	0.003382	0.001421	0.001076	9.41E-05
0.9375	0.003245	0.001363	0.001032	9.03E-05
0.947266	0.003115	0.001309	0.000991	8.67E-05
0.957031	0.002991	0.001256	0.000951	8.32E-05
0.966797	0.002873	0.001207	0.000914	8.00E-05
0.976563	0.002761	0.00116	0.000878	7.68E-05
0.986328	0.002654	0.001115	0.000844	7.39E-05
0.996094	0.002552	0.001072	0.000812	7.10E-05
1.005859	0.002456	0.001032	0.000781	6.83E-05

Table A-4. Spatial variation of measured mean RMS wave heights at four marsh gages for selected ranges of vegetation submergence ratio, $s=h_v/h$, at gage W1 during Tropical Storm Lee (2011).

s	Mean H_{rms} at W1 (m)	Mean H_{rms} at W2 (m)	Mean H_{rms} at W3 (m)	Mean H_{rms} at W4 (m)
0.2-0.3	0.240	0.155	0.117	0.093
0.3-0.4	0.164	0.087	0.061	0.047
0.4-0.5	0.118	0.058	0.038	0.030
0.5-1.0	0.087	0.036	0.022	0.018

Table A-5. Variation of exponential wave height decay rate with RMS wave height, Reynolds number, and Keulegan-Carpenter number during Tropical Storm Lee (2011).

Deacy rate, k_H (/m)	H_{rms} at W1 (m)	Swell H_{rms} at W1 (m)	Sea H_{rms} at W1 (m)	Reynolds number, R_e	Keulegan-Carpenter number, K_c
-0.041	0.155	0.070	0.137	2374	85
-0.037	0.165	0.067	0.149	2446	88
-0.035	0.164	0.052	0.154	2383	83
-0.039	0.161	0.059	0.149	2383	83
-0.032	0.179	0.058	0.168	2524	87
-0.025	0.239	0.078	0.224	2942	104
-0.028	0.210	0.066	0.198	2721	94
-0.025	0.245	0.072	0.233	3006	104
-0.022	0.251	0.073	0.238	3030	105
-0.025	0.257	0.070	0.246	3215	114
-0.029	0.239	0.070	0.227	3085	108
-0.028	0.220	0.075	0.206	2943	104
-0.027	0.224	0.085	0.205	3056	109
-0.026	0.259	0.110	0.231	3441	126
-0.026	0.253	0.107	0.227	3300	118
-0.024	0.257	0.120	0.224	3379	123
-0.028	0.227	0.099	0.202	3128	114
-0.033	0.212	0.088	0.191	3073	113
-0.035	0.191	0.080	0.172	2861	104
-0.035	0.181	0.081	0.161	2820	101
-0.037	0.171	0.081	0.149	2695	97
-0.037	0.164	0.065	0.150	2607	96
-0.043	0.143	0.049	0.133	2382	85
-0.042	0.131	0.043	0.123	2225	78
-0.042	0.131	0.048	0.121	2263	81
-0.044	0.125	0.041	0.117	2172	75
-0.051	0.095	0.040	0.086	1844	66
-0.044	0.097	0.046	0.085	1882	68
-0.042	0.104	0.043	0.093	1991	77
-0.043	0.106	0.043	0.096	1993	71
-0.037	0.127	0.058	0.111	2241	81
-0.038	0.131	0.057	0.117	2308	85
-0.040	0.119	0.042	0.110	2137	77
-0.041	0.113	0.058	0.096	2072	75
-0.042	0.116	0.056	0.100	2109	76
-0.042	0.109	0.045	0.098	1976	70
-0.041	0.112	0.038	0.104	1983	69

Deacy rate, k_H (/m)	H_{rms} at W1 (m)	Swell H_{rms} at W1 (m)	Sea H_{rms} at W1 (m)	Reynolds number, R_e	Keulegan-Carpenter number, K_c
-0.039	0.123	0.051	0.111	2121	74
-0.041	0.126	0.052	0.113	2214	79
-0.040	0.122	0.042	0.113	2112	73
-0.040	0.128	0.065	0.109	2243	82
-0.037	0.126	0.053	0.113	2132	73
-0.037	0.128	0.040	0.121	2120	72
-0.042	0.124	0.055	0.109	2145	75
-0.045	0.112	0.051	0.098	1965	66
-0.041	0.113	0.043	0.104	1937	63
-0.042	0.111	0.038	0.103	1882	61
-0.047	0.104	0.035	0.097	1839	60
-0.045	0.110	0.036	0.104	1949	64
-0.046	0.105	0.042	0.095	1883	64
-0.046	0.102	0.030	0.097	1813	57
-0.041	0.118	0.047	0.107	2004	66
-0.040	0.125	0.039	0.118	2127	73
-0.038	0.137	0.046	0.128	2306	81
-0.039	0.129	0.063	0.111	2293	84
-0.042	0.123	0.053	0.109	2221	81
-0.045	0.120	0.058	0.104	2196	82
-0.048	0.117	0.071	0.091	2271	89
-0.038	0.132	0.067	0.112	2388	92
-0.041	0.117	0.061	0.098	2151	80
-0.043	0.105	0.055	0.088	2001	79
-0.039	0.121	0.043	0.112	2119	73
-0.039	0.133	0.050	0.122	2235	77
-0.040	0.128	0.041	0.120	2160	74
-0.036	0.142	0.043	0.134	2307	78
-0.040	0.135	0.047	0.125	2299	81
-0.041	0.123	0.042	0.114	2167	77
-0.045	0.101	0.041	0.092	1911	67
-0.050	0.098	0.041	0.088	1896	67

Table A-6. Variation of bulk drag coefficient estimated by the Chen and Zhao (2012) (C_D-CZ) and Mendez and Losada (2004) (C_D-ML) models, with Reynolds number (R_e) during Tropical Storm Lee (2011).

R_e	Cd-CZ	Cd-ML	R_e	Cd-CZ	Cd-ML	R_e	Cd-CZ	Cd-ML
2232	1.9	1.7	1985	1.4	1.3	1233	2.7	2.6
2298	1.8	1.6	2108	1.4	1.2	1092	2.8	2.7
2238	1.8	1.6	2004	1.4	1.3	1079	2.9	2.8
2240	1.9	1.7	1993	1.5	1.3	1013	3.0	2.8
2372	1.6	1.5	1884	1.6	1.5	978	3.3	3.1
2766	1.4	1.4	2000	1.5	1.4	791	4.2	3.9
2558	1.5	1.4	2168	1.4	1.2	766	4.0	3.7
2826	1.4	1.4	2155	1.3	1.1	771	4.0	3.7
2849	1.2	1.1	2087	1.4	1.2	711	4.0	3.7
3023	1.3	1.2	2064	1.5	1.3	615	4.0	3.7
2901	1.4	1.4	2133	1.3	1.2	677	4.1	3.8
2766	1.4	1.3	2245	1.1	1.0	666	3.8	3.4
2872	1.3	1.2	2022	1.3	1.2	833	3.3	3.1
3235	1.2	1.1	1880	1.4	1.2	843	3.3	3.1
3102	1.2	1.1	1991	1.4	1.3	768	3.9	3.6
3176	1.1	1.0	2101	1.5	1.3	712	3.8	3.5
2941	1.2	1.1	2031	1.5	1.4	715	4.0	3.7
2888	1.3	1.2	2168	1.4	1.3	665	4.0	3.6
2689	1.4	1.3	2161	1.3	1.2	681	3.9	3.6
2649	1.3	1.2	2036	1.4	1.3	811	4.2	3.9
2533	1.4	1.3	1796	1.5	1.3	772	3.7	3.5
2450	1.4	1.3	803	3.9	3.8	756	3.8	3.5
2238	1.6	1.4	908	3.6	3.5	798	3.4	3.1
2091	1.5	1.4	925	3.3	3.2	797	3.3	3.1
2126	1.5	1.3	850	3.5	3.3	807	3.5	3.2
2041	1.5	1.4	1048	3.0	2.9	697	4.1	3.8
1768	1.4	1.3	1414	2.4	2.4	758	4.0	3.7
1870	1.3	1.2	1247	2.6	2.5	845	3.3	3.1
1873	1.4	1.2	1421	2.5	2.5	830	3.3	3.1
2107	1.2	1.1	1549	2.4	2.4	741	3.5	3.2
2170	1.3	1.1	1533	2.5	2.6	690	3.0	2.8
2008	1.3	1.2	1361	2.6	2.6	661	2.6	2.5
1947	1.4	1.2	1309	2.6	2.5	874	3.3	3.1
1981	1.4	1.2	1341	2.3	2.3	739	3.7	3.4
1857	1.5	1.4	1557	2.0	2.0	663	4.2	3.9
1864	1.5	1.4	1535	2.0	2.0	748	3.2	3.0
1994	1.3	1.2	1601	1.9	2.0	810	3.7	3.4
2080	1.4	1.2	1388	2.3	2.3	777	3.8	3.5

Table A-7. Variation of bulk drag coefficient estimated by the Chen and Zhao (2012) (C_D-CZ) model with Keulegan-Carpenter (K_C) number during Tropical Storm Lee (2011).

K_C	Cd-CZ	K_C	Cd-CZ	K_C	Cd-CZ	K_C	Cd-CZ
90	1.9	90	1.3	36	3.6	30	3.9
94	1.8	81	1.3	37	3.3	29	3.8
88	1.8	80	1.4	35	3.5	29	4.0
88	1.9	81	1.4	42	3.0	27	4.0
92	1.6	74	1.5	60	2.4	27	3.9
110	1.4	73	1.5	53	2.6	33	4.2
100	1.5	78	1.3	59	2.5	31	3.7
110	1.4	84	1.4	64	2.4	30	3.8
111	1.2	77	1.4	61	2.5	33	3.4
121	1.3	87	1.4	56	2.6	32	3.3
115	1.4	77	1.4	54	2.6	33	3.5
111	1.4	76	1.5	54	2.3	27	4.1
115	1.3	70	1.6	63	2.0	30	4.0
134	1.2	77	1.5	65	2.0	33	3.3
126	1.2	85	1.4	66	1.9	34	3.3
130	1.1	89	1.3	57	2.3	30	3.5
121	1.2	86	1.4	52	2.7	34	3.0
120	1.3	86	1.5	45	2.8	34	2.6
110	1.4	94	1.3	44	2.9	35	3.3
107	1.3	97	1.1	43	3.0	30	3.7
103	1.4	85	1.3	40	3.3	27	4.2
102	1.4	84	1.4	32	4.2	30	3.2
91	1.6	78	1.4	31	4.0	32	3.7
82	1.5	82	1.5	31	4.0	32	3.8
86	1.5	79	1.5	29	4.0	35	3.4
80	1.5	82	1.4	25	4.0	34	3.7
72	1.4	86	1.3	28	4.1	31	3.6
82	1.3	82	1.4	27	3.8	25	4.2
75	1.4	71	1.5	33	3.3		
86	1.2	32	3.9	34	3.3		

Table A-8. Estimated drag coefficients estimated by the Chen and Zhao (2012) model for the long-period (swell) and short-period (wind-sea) waves during Tropical Storm Lee (2011). Each spectrum is represented by a single Keulegan-Carpenter number (K_C).

	Swell	Sea		Swell	Sea		Swell	Sea		Swell	Sea
K_C	Cd	Cd	K_C	Cd	Cd	K_C	Cd	Cd	K_C	Cd	Cd
86	1.5	2.0	85	1.1	1.3	33	3.4	3.8	27	2.3	4.4
89	1.5	1.8	78	1.1	1.3	34	3.0	3.5	26	2.6	4.4
84	1.4	1.8	76	1.3	1.4	32	2.7	3.8	26	3.0	4.4
84	1.5	2.0	77	1.2	1.4	39	2.4	3.2	24	2.8	4.4
88	1.2	1.7	71	1.4	1.5	55	2.1	2.6	25	2.8	4.2
106	1.0	1.5	69	1.2	1.6	49	2.1	2.8	30	2.7	4.8
96	1.2	1.6	75	1.2	1.4	54	2.2	2.7	28	2.6	4.3
106	0.9	1.5	80	1.1	1.4	59	2.2	2.6	27	2.6	4.2
107	1.0	1.2	73	1.1	1.5	56	2.0	2.8	30	2.9	3.7
116	0.9	1.3	83	1.2	1.4	51	2.1	2.9	29	2.7	3.6
110	0.9	1.5	74	1.1	1.5	49	2.1	2.8	30	2.6	3.7
106	1.1	1.4	72	1.2	1.5	50	2.1	2.5	25	2.7	4.6
111	1.0	1.4	67	1.3	1.7	58	1.8	2.1	27	2.9	4.3
128	1.0	1.2	73	1.1	1.5	59	1.7	2.2	30	2.2	3.7
120	1.0	1.2	81	1.1	1.4	61	1.8	2.1	31	2.7	3.7
125	0.9	1.1	85	1.0	1.3	52	1.9	2.7	27	2.6	3.9
115	1.0	1.3	82	1.1	1.4	47	2.4	2.9	31	3.0	3.2
115	1.1	1.4	82	1.2	1.6	41	2.1	3.3	31	2.4	3.0
105	1.2	1.5	90	1.1	1.4	40	2.6	3.1	32	2.7	3.6
103	1.0	1.4	93	1.1	1.1	39	2.5	3.4	27	2.9	4.1
98	1.1	1.5	81	1.2	1.3	36	2.6	3.7	25	2.8	4.8
97	1.2	1.4	80	1.2	1.4	29	3.0	4.5	27	2.5	3.5
86	1.3	1.6	74	1.1	1.5	28	2.9	4.4	29	2.8	4.0
79	1.2	1.6	78	1.2	1.5	28	2.9	4.4	29	2.6	4.1
82	1.2	1.5	75	1.2	1.5	26	2.3	4.5	32	2.3	3.7
76	1.2	1.6	79	1.1	1.4	23	2.9	4.5	31	2.3	4.2
69	1.2	1.4	82	1.2	1.4	25	3.1	4.5	28	2.6	3.9
78	1.1	1.4	78	1.1	1.5	25	3.1	4.0	23	3.3	4.6
72	1.1	1.4	68	1.2	1.6	30	2.4	3.7			
82	1.1	1.3	29	3.9	4.1	31	2.6	3.6			

Table A-9. Mean of all normalized energy density and energy dissipation spectra in reach W1-W2 and reach W2-W3 during Tropical Storm Lee (2011). Spectra normalized by the zero-th moment (m_0) of the energy spectrum measured at the windward gage of the pair of gages.

f (Hz)	(E/m_0) (/Hz) W1	(E/m_0) (/Hz) W2	(S_{ds}/m_0) W1-W2	(E/m_0) (/Hz) W2	(E/m_0) (/Hz) W3	(S_{ds}/m_0) W2-W3
0.0098	0.0480	0.0571	0.0005	0.2139	0.1951	0.0061
0.0195	0.0711	0.0678	0.0011	0.2528	0.2220	0.0086
0.0293	0.1147	0.0864	0.0026	0.3198	0.2655	0.0143
0.0391	0.1867	0.1140	0.0080	0.4183	0.3243	0.0224
0.0488	0.2978	0.1522	0.0168	0.5535	0.3977	0.0358
0.0586	0.4590	0.2019	0.0310	0.7287	0.4844	0.0553
0.0684	0.6751	0.2624	0.0510	0.9406	0.5812	0.0813
0.0781	0.9381	0.3294	0.0763	1.1749	0.6810	0.1115
0.0879	1.2224	0.3953	0.1045	1.4054	0.7725	0.1425
0.0977	1.4884	0.4510	0.1316	1.5997	0.8422	0.1699
0.1074	1.6952	0.4883	0.1534	1.7293	0.8788	0.1900
0.1172	1.8157	0.5032	0.1668	1.7800	0.8779	0.2008
0.1270	1.8485	0.4971	0.1717	1.7567	0.8436	0.2024
0.1367	1.8171	0.4762	0.1703	1.6810	0.7880	0.1973
0.1465	1.7593	0.4489	0.1664	1.5823	0.7266	0.1883
0.1563	1.7138	0.4232	0.1641	1.4884	0.6737	0.1787
0.1660	1.7096	0.4053	0.1663	1.4196	0.6390	0.1707
0.1758	1.7637	0.3984	0.1749	1.3869	0.6267	0.1659
0.1855	1.8817	0.4035	0.1903	1.3929	0.6356	0.1649
0.1953	2.0578	0.4189	0.2118	1.4333	0.6611	0.1677
0.2051	2.2727	0.4410	0.2372	1.4973	0.6953	0.1736
0.2148	2.4934	0.4643	0.2626	1.5681	0.7289	0.1809
0.2246	2.6788	0.4828	0.2833	1.6264	0.7534	0.1870
0.2344	2.7911	0.4911	0.2951	1.6548	0.7628	0.1897
0.2441	2.8090	0.4867	0.2958	1.6436	0.7565	0.1871
0.2539	2.7339	0.4703	0.2859	1.5941	0.7382	0.1789
0.2637	2.5879	0.4462	0.2679	1.5181	0.7140	0.1664
0.2734	2.4036	0.4200	0.2457	1.4330	0.6893	0.1524
0.2832	2.2126	0.3968	0.2228	1.3554	0.6675	0.1397
0.2930	2.0375	0.3798	0.2015	1.2960	0.6497	0.1301
0.3027	1.8900	0.3695	0.1833	1.2582	0.6367	0.1241
0.3125	1.7723	0.3650	0.1684	1.2395	0.6296	0.1208
0.3223	1.6812	0.3644	0.1565	1.2354	0.6293	0.1189
0.3320	1.6105	0.3663	0.1469	1.2414	0.6357	0.1177
0.3418	1.5539	0.3699	0.1389	1.2540	0.6470	0.1167
0.3516	1.5069	0.3746	0.1320	1.2708	0.6602	0.1162
0.3613	1.4675	0.3801	0.1259	1.2899	0.6730	0.1162

f (Hz)	(E/m_0) (/Hz) W1	(E/m_0) (/Hz) W2	(S_{ds}/m_0) W1-W2	(E/m_0) (/Hz) W2	(E/m_0) (/Hz) W3	(S_{ds}/m_0) W2-W3
0.3711	1.4358	0.3860	0.1207	1.3103	0.6839	0.1167
0.3809	1.4122	0.3924	0.1163	1.3322	0.6930	0.1179
0.3906	1.3957	0.3992	0.1127	1.3562	0.7012	0.1194
0.4004	1.3834	0.4064	0.1095	1.3827	0.7094	0.1214
0.4102	1.3717	0.4141	0.1063	1.4110	0.7182	0.1234
0.4199	1.3577	0.4219	0.1028	1.4396	0.7275	0.1254
0.4297	1.3410	0.4297	0.0991	1.4671	0.7364	0.1272
0.4395	1.3231	0.4374	0.0954	1.4932	0.7438	0.1288
0.4492	1.3061	0.4453	0.0918	1.5191	0.7491	0.1307
0.4590	1.2911	0.4541	0.0884	1.5467	0.7529	0.1331
0.4688	1.2781	0.4636	0.0851	1.5769	0.7559	0.1358
0.4785	1.2662	0.4732	0.0820	1.6080	0.7593	0.1386
0.4883	1.2550	0.4816	0.0792	1.6368	0.7630	0.1407
0.4980	1.2447	0.4879	0.0768	1.6608	0.7668	0.1419
0.5078	1.2357	0.4910	0.0748	1.6740	0.7684	0.1417
0.5176	1.2282	0.4927	0.0732	1.6826	0.7687	0.1409
0.5273	1.2218	0.4941	0.0718	1.6902	0.7681	0.1401
0.5371	1.2165	0.4959	0.0704	1.6993	0.7671	0.1395
0.5469	1.2123	0.4980	0.0692	1.7092	0.7659	0.1390
0.5566	1.2089	0.4991	0.0681	1.7168	0.7632	0.1383
0.5664	1.2047	0.4983	0.0671	1.7184	0.7575	0.1396
0.5762	1.1979	0.4955	0.0661	1.7125	0.7476	0.1407
0.5859	1.1864	0.4913	0.0647	1.6998	0.7329	0.1390
0.5957	1.1700	0.4867	0.0630	1.6834	0.7151	0.1371
0.6055	1.1499	0.4824	0.0609	1.6668	0.6944	0.1356
0.6152	1.1292	0.4788	0.0587	1.6528	0.6749	0.1342
0.6250	1.1089	0.4758	0.0565	1.6421	0.6581	0.1330
0.6348	1.0889	0.4729	0.0544	1.6337	0.6454	0.1316
0.6445	1.0685	0.4696	0.0523	1.6249	0.6344	0.1298
0.6543	1.0478	0.4652	0.0503	1.6123	0.6240	0.1274
0.6641	1.0275	0.4588	0.0494	1.5925	0.6116	0.1243
0.6738	1.0095	0.4501	0.0472	1.5635	0.5972	0.1203
0.6836	0.9956	0.4392	0.0472	1.5258	0.5810	0.1155
0.6934	0.9857	0.4271	0.0477	1.4834	0.5658	0.1103
0.7031	0.9775	0.4152	0.0475	1.4413	0.5509	0.1052

Table A-10. Wave energy reduction in the swell and sea band (0.03-0.36 Hz) as a percentage of the total (0.03-0.7 Hz) energy reduction during Tropical Storm Lee (2011).

Kc at W1	Percentage Swell+Sea wave energy reduction in W1-W2	Kc at W2	Percentage Swell+Sea wave energy reduction in W2-W3	Kc at W1	Percentage Swell+Sea wave energy reduction in W1-W2	Kc at W2	Percentage Swell+Sea wave energy reduction in W2-W3
85	58.9	29	52.5	85	60.9	29	44.2
88	62.4	33	48.7	78	58.6	28	43.4
83	58.9	33	52.0	81	61.2	28	45.1
83	59.9	31	51.4	75	58.9	26	41.5
87	58.0	38	49.2	66	56.7	20	49.7
102	66.4	48	49.9	58	54.9	17	42.7
104	62.8	54	48.7	66	65.2	18	49.8
94	58.5	48	46.1	63	57.5	19	45.6
104	63.8	52	46.0	68	58.9	23	44.4
105	63.5	57	55.2	77	65.2	25	43.8
107	62.6	50	45.0	71	58.2	25	45.7
114	66.1	54	44.9	81	65.0	29	40.8
108	61.8	50	49.6	85	63.9	30	44.9
104	64.5	48	50.2	77	64.0	27	38.2
109	63.1	48	54.2	75	64.2	26	44.0
114	61.7	57	56.6	76	60.3	26	43.8
126	67.6	56	53.4	70	58.4	24	41.3
128	66.6	63	58.6	69	50.9	24	42.2
128	69.4	61	56.1	74	56.2	29	40.1
128	68.9	57	52.9	79	61.0	28	44.3
122	69.7	58	52.7	73	55.2	27	39.4
123	70.4	63	51.2	82	61.0	30	49.6
123	69.3	59	48.9	73	52.8	29	44.5
118	66.7	58	50.1	72	55.9	29	45.6
123	63.0	59	53.3	75	55.8	28	40.3
117	58.0	54	48.9	66	50.4	24	45.1
110	62.7	51	44.5	73	54.6	27	38.8
128	67.7	60	56.2	81	60.4	30	40.3
126	68.0	60	51.6	84	65.0	30	49.5
121	69.8	53	45.8	81	64.2	27	43.6
114	64.6	51	48.8	92	69.3	31	49.5
113	64.1	46	54.5	80	64.3	27	48.5
104	60.7	40	50.1	79	65.3	24	41.9
101	61.9	39	50.2	73	56.4	27	42.0
97	60.9	38	49.6	77	56.3	29	42.9
96	63.2	35	41.8	74	57.3	29	40.0

Kc at W1	Percentage Swell+Sea wave energy reduction in W1-W2	Kc at W2	Percentage Swell+Sea wave energy reduction in W2-W3
78	51.3	31	39.5
81	58.1	30	39.7
77	61.9	28	45.9
67	56.8	23	45.9

Kc at W1	Percentage Swell+Sea wave energy reduction in W1-W2	Kc at W2	Percentage Swell+Sea wave energy reduction in W2-W3
63	55.8	21	51.3
61	55.7	19	46.3
67	56.9	21	44.9

Table A-11. Frequency distribution of the mean normalized dissipation rate for three ranges of Keulegan-Carpenter number during Tropical Storm Lee (2011).

	S_{ds}/E (Hz)		
f (Hz)	KC<47	47<KC<83	KC>83
0.0098	0.00026	0.00031	0.00010
0.0195	0.00030	0.00030	0.00015
0.0293	0.00041	0.00024	0.00024
0.0391	0.00049	0.00042	0.00043
0.0488	0.00060	0.00055	0.00056
0.0586	0.00071	0.00067	0.00067
0.0684	0.00082	0.00076	0.00074
0.0781	0.00091	0.00083	0.00080
0.0879	0.00098	0.00087	0.00084
0.0977	0.00104	0.00090	0.00086
0.1074	0.00108	0.00092	0.00088
0.1172	0.00111	0.00094	0.00089
0.1270	0.00114	0.00095	0.00090
0.1367	0.00116	0.00096	0.00091
0.1465	0.00117	0.00097	0.00092
0.1563	0.00119	0.00097	0.00094
0.1660	0.00119	0.00097	0.00097
0.1758	0.00118	0.00098	0.00100
0.1855	0.00116	0.00099	0.00102
0.1953	0.00114	0.00100	0.00104
0.2051	0.00113	0.00101	0.00106
0.2148	0.00112	0.00101	0.00107
0.2246	0.00113	0.00101	0.00107
0.2344	0.00113	0.00101	0.00107
0.2441	0.00113	0.00100	0.00106
0.2539	0.00112	0.00099	0.00105
0.2637	0.00110	0.00098	0.00103
0.2734	0.00107	0.00096	0.00101
0.2832	0.00105	0.00095	0.00099
0.2930	0.00102	0.00093	0.00096
0.3027	0.00100	0.00091	0.00093
0.3125	0.00099	0.00090	0.00091
0.3223	0.00098	0.00088	0.00088
0.3320	0.00097	0.00086	0.00087
0.3418	0.00096	0.00084	0.00085
0.3516	0.00094	0.00082	0.00084
0.3613	0.00093	0.00080	0.00083
0.3711	0.00092	0.00078	0.00082
0.3809	0.00091	0.00076	0.00080
0.3906	0.00091	0.00075	0.00078
0.4004	0.00090	0.00074	0.00076
0.4102	0.00090	0.00073	0.00075
0.4199	0.00089	0.00073	0.00072
0.4297	0.00089	0.00072	0.00070
0.4395	0.00088	0.00071	0.00068
0.4492	0.00087	0.00071	0.00065
0.4590	0.00087	0.00070	0.00063
0.4688	0.00087	0.00069	0.00060
0.4785	0.00087	0.00069	0.00058
0.4883	0.00087	0.00068	0.00056
0.4980	0.00086	0.00067	0.00054
0.5078	0.00085	0.00066	0.00053
0.5176	0.00085	0.00064	0.00052
0.5273	0.00084	0.00063	0.00051
0.5371	0.00083	0.00062	0.00051
0.5469	0.00082	0.00060	0.00051
0.5566	0.00081	0.00059	0.00051
0.5664	0.00082	0.00058	0.00051
0.5762	0.00083	0.00057	0.00051
0.5859	0.00082	0.00056	0.00050
0.5957	0.00082	0.00056	0.00049
0.6055	0.00081	0.00056	0.00047
0.6152	0.00081	0.00056	0.00045
0.6250	0.00081	0.00055	0.00043
0.6348	0.00081	0.00053	0.00042
0.6445	0.00080	0.00052	0.00041
0.6543	0.00079	0.00050	0.00041
0.6641	0.00079	0.00049	0.00042
0.6738	0.00078	0.00048	0.00040
0.6836	0.00076	0.00049	0.00040
0.6934	0.00075	0.00049	0.00041
0.7031	0.00073	0.00048	0.00041

Table A-12. Frequency exponent for individual spectra (data points with R^2>0.8 only) during Tropical Storm Lee (2011).

Kc	Exponent
85	-0.94
88	-1.04
83	-0.86
83	-0.74
87	-0.94
94	-0.60
108	-1.00
104	-1.14
109	-1.31
126	-1.52
123	-1.67
114	-1.31
113	-1.00
104	-0.98
101	-1.02
97	-0.81
96	-1.17
85	-0.78

Kc	Exponent
78	-0.61
81	-0.84
75	-0.66
68	-0.85
71	-0.71
85	-1.16
77	-1.05
75	-0.79
76	-0.79
70	-0.70
69	-0.96
79	-1.04
73	-0.80
82	-0.85
73	-0.71
72	-0.64
66	-0.67
73	-0.85

Kc	Exponent
81	-0.90
84	-0.96
81	-0.91
80	-0.87
73	-0.77
77	-0.81
78	-0.91
81	-0.75
77	-0.66
67	-0.64
48	-0.74
28	-0.28
26	-0.42
23	-0.46
25	-0.44
24	-0.50
27	-0.47

Table A-13. Probability of occurrence of exponent b with respect to ranges of Keulegan-Carpenter number during Tropical Storm Lee (2011).

Exponent	KC<47			47<KC<83			KC>83		
b	Swell	Sea	High f.	Swell	Sea	High f.	Swell	Sea	High f.
0.0-0.5	0	1	2	0	1	1	0	0	0
0.5-1.0	0	2	7	0	0	0	0	0	0
1.0-1.5	1	20	29	1	33	2	0	17	0
1.5-2.0	23	18	6	36	7	8	25	9	2
2.0-2.5	16	4	1	7	2	21	1	0	6
2.5-3.0	5	1	0	1	1	10	0	0	9
3.0-3.5	0	0	1	0	0	2	0	0	6
3.5-4.0	1	0	0	0	1	1	0	0	2
4.0-4.5	0	0	0	0	0	0	0	0	0
4.5-5.0	0	0	0	0	0	0	0	0	0
5.0-5.5	0	0	0	0	0	0	0	0	0
5.5-6.0	0	0	0	0	0	0	0	0	0
>6.0	0	0	0	0	0	0	0	0	1

Table A-14. Spectral variation of bulk drag coefficient estimated during Tropical Storm Lee (2011). All individual spectral distributions ensemble-averaged based on the ranges of Keulegan-Carpenter number.

	Mean Cd		
f (Hz)	KC<47	47<KC<83	KC>83
0.0391	1.12	0.64	0.45
0.0488	1.42	0.83	0.63
0.0586	1.73	1.04	0.79
0.0684	2.07	1.22	0.92
0.0781	2.38	1.35	1.01
0.0879	2.65	1.45	1.09
0.0977	2.87	1.52	1.14
0.1074	3.04	1.57	1.18
0.1172	3.18	1.61	1.21
0.1270	3.29	1.65	1.23
0.1367	3.39	1.69	1.25
0.1465	3.48	1.72	1.28
0.1563	3.55	1.74	1.32
0.1660	3.58	1.77	1.37
0.1758	3.57	1.80	1.43
0.1855	3.52	1.83	1.49
0.1953	3.47	1.87	1.55
0.2051	3.44	1.91	1.60
0.2148	3.44	1.93	1.64
0.2246	3.48	1.95	1.67
0.2344	3.53	1.96	1.69
0.2441	3.56	1.96	1.70
0.2539	3.55	1.95	1.70
0.2637	3.51	1.92	1.69
0.2734	3.45	1.88	1.67
0.2832	3.39	1.83	1.64
0.2930	3.34	1.80	1.60
0.3027	3.32	1.78	1.57
0.3125	3.31	1.76	1.53
0.3223	3.31	1.74	1.51
0.3320	3.32	1.71	1.49
0.3418	3.32	1.66	1.47
0.3516	3.32	1.62	1.46
0.3613	3.32	1.58	1.45
0.3711	3.32	1.55	1.43
0.3809	3.35	1.55	1.42
0.3906	3.38	1.55	1.41
0.4004	3.43	1.57	1.39
0.4102	3.47	1.59	1.37
0.4199	3.50	1.63	1.34
0.4297	3.53	1.67	1.31
0.4395	3.55	1.71	1.28
0.4492	3.59	1.75	1.25
0.4590	3.66	1.79	1.22
0.4688	3.74	1.83	1.19
0.4785	3.82	1.87	1.17
0.4883	3.90	1.90	1.15
0.4980	3.97	1.93	1.13
0.5078	4.03	1.94	1.13
0.5176	4.08	1.96	1.14
0.5273	4.15	1.97	1.15
0.5371	4.22	2.00	1.16
0.5469	4.29	2.02	1.18
0.5566	4.37	2.04	1.21
0.5664	4.55	2.06	1.23
0.5762	4.77	2.09	1.26
0.5859	4.90	2.13	1.29
0.5957	5.04	2.19	1.30
0.6055	5.20	2.29	1.29
0.6152	5.38	2.38	1.29
0.6250	5.57	2.46	1.29
0.6348	5.76	2.51	1.30
0.6445	5.94	2.52	1.32
0.6543	6.12	2.54	1.34
0.6641	6.29	2.57	1.41
0.6738	6.46	2.63	1.41
0.6836	6.61	2.72	1.50
0.6934	6.75	2.83	1.62
0.7031	6.88	2.95	1.70

Table A-15. Spectral variation of ensemble-averaged α_n with ±1 standard deviation based on all data measured during Tropical Storm Lee (2011).

f	α_n	α_n+1 Stdev	α_n-1 Stdev
0.0391	0.56	0.69	0.42
0.0488	0.65	0.77	0.53
0.0586	0.73	0.83	0.63
0.0684	0.79	0.88	0.71
0.0781	0.84	0.91	0.77
0.0879	0.88	0.94	0.82
0.0977	0.91	0.96	0.86
0.1074	0.93	0.98	0.88
0.1172	0.94	0.99	0.89
0.1270	0.96	1.01	0.90
0.1367	0.97	1.02	0.91
0.1465	0.98	1.03	0.92
0.1563	0.99	1.05	0.93
0.1660	1.00	1.06	0.94
0.1758	1.01	1.07	0.94
0.1855	1.02	1.08	0.95
0.1953	1.02	1.09	0.96
0.2051	1.03	1.10	0.96
0.2148	1.04	1.10	0.97
0.2246	1.04	1.11	0.98
0.2344	1.05	1.12	0.98
0.2441	1.05	1.12	0.98
0.2539	1.05	1.12	0.98
0.2637	1.04	1.12	0.97
0.2734	1.04	1.12	0.96
0.2832	1.03	1.11	0.94
0.2930	1.02	1.10	0.93
0.3027	1.01	1.10	0.92
0.3125	1.00	1.10	0.91
0.3223	1.00	1.09	0.91
0.3320	0.99	1.09	0.90
0.3418	0.99	1.08	0.90
0.3516	0.98	1.07	0.90
0.3613	0.98	1.06	0.89
0.3711	0.98	1.06	0.89
0.3809	0.97	1.06	0.88
0.3906	0.97	1.07	0.88
0.4004	0.97	1.07	0.88
0.4102	0.98	1.07	0.88
0.4199	0.98	1.07	0.89
0.4297	0.98	1.06	0.90
0.4395	0.98	1.06	0.90
0.4492	0.98	1.06	0.90
0.4590	0.98	1.07	0.89
0.4688	0.99	1.08	0.89
0.4785	0.99	1.09	0.89
0.4883	0.99	1.10	0.89
0.4980	1.00	1.11	0.88
0.5078	1.00	1.12	0.88
0.5176	1.00	1.12	0.88
0.5273	1.01	1.13	0.88
0.5371	1.01	1.15	0.88
0.5469	1.02	1.17	0.87
0.5566	1.02	1.19	0.86
0.5664	1.04	1.21	0.87
0.5762	1.05	1.21	0.90
0.5859	1.06	1.23	0.90
0.5957	1.08	1.25	0.90
0.6055	1.09	1.27	0.90
0.6152	1.10	1.30	0.90
0.6250	1.11	1.33	0.90
0.6348	1.12	1.35	0.89
0.6445	1.13	1.37	0.89
0.6543	1.14	1.40	0.88
0.6641	1.16	1.41	0.90
0.6738	1.16	1.45	0.88
0.6836	1.19	1.47	0.91
0.6934	1.21	1.49	0.94
0.7031	1.23	1.52	0.94

Table A-16. Comparison of observed and predicted spectral energy dissipation using average and spectral drag coefficients for a sample wave record on September 3, 2011 at 12:30 UTC during Tropical Storm Lee (2011).

	W12					W23				
	Cd		Dissipation using			Cd		Dissipation using		
f (Hz)	Obs. Cd	$\alpha_n{*}\overline{Cd}$	Obs. Cd	$\overline{Cd}$=1.4	$\alpha_n{*}\overline{Cd}$	Obs. Cd	$\alpha_n{*}\overline{Cd}$	Obs. Cd	$\overline{Cd}$=3.0	$\alpha_n{*}\overline{Cd}$
0.0391	0.37	0.43	2.9E-7	1.1E-6	3.4E-7	1.71	0.94	4.0E-7	6.9E-7	2.1E-7
0.0488	0.55	0.58	6.9E-7	1.7E-6	7.4E-7	1.97	1.27	6.5E-7	9.7E-7	4.1E-7
0.0586	0.71	0.73	1.4E-6	2.7E-6	1.4E-6	2.14	1.60	9.7E-7	1.3E-6	7.1E-7
0.0684	0.85	0.87	2.5E-6	4.0E-6	2.5E-6	2.25	1.90	1.4E-6	1.8E-6	1.1E-6
0.0781	0.96	0.98	3.9E-6	5.6E-6	4.0E-6	2.32	2.14	1.8E-6	2.3E-6	1.6E-6
0.0879	1.04	1.07	5.4E-6	7.2E-6	5.6E-6	2.37	2.33	2.2E-6	2.7E-6	2.1E-6
0.0977	1.10	1.13	6.9E-6	8.6E-6	7.1E-6	2.44	2.47	2.6E-6	3.1E-6	2.5E-6
0.1074	1.15	1.18	7.9E-6	9.5E-6	8.2E-6	2.52	2.58	2.8E-6	3.3E-6	2.8E-6
0.1172	1.19	1.22	8.5E-6	9.8E-6	8.7E-6	2.63	2.67	2.9E-6	3.2E-6	2.9E-6
0.1270	1.24	1.26	8.6E-6	9.6E-6	8.7E-6	2.75	2.75	2.8E-6	3.0E-6	2.7E-6
0.1367	1.29	1.29	8.3E-6	8.9E-6	8.3E-6	2.90	2.81	2.5E-6	2.6E-6	2.4E-6
0.1465	1.35	1.32	7.8E-6	8.0E-6	7.7E-6	3.07	2.88	2.3E-6	2.2E-6	2.1E-6
0.1563	1.39	1.35	7.2E-6	7.2E-6	7.0E-6	3.23	2.94	2.0E-6	1.8E-6	1.8E-6
0.1660	1.42	1.37	6.7E-6	6.5E-6	6.5E-6	3.29	3.00	1.8E-6	1.6E-6	1.6E-6
0.1758	1.45	1.40	6.4E-6	6.1E-6	6.2E-6	3.21	3.05	1.6E-6	1.5E-6	1.5E-6
0.1855	1.49	1.42	6.5E-6	6.1E-6	6.2E-6	2.98	3.10	1.4E-6	1.4E-6	1.5E-6
0.1953	1.55	1.44	7.0E-6	6.2E-6	6.5E-6	2.71	3.14	1.3E-6	1.4E-6	1.5E-6
0.2051	1.62	1.46	7.8E-6	6.6E-6	7.0E-6	2.54	3.18	1.2E-6	1.4E-6	1.5E-6
0.2148	1.67	1.48	8.7E-6	7.2E-6	7.7E-6	2.57	3.22	1.2E-6	1.4E-6	1.5E-6
0.2246	1.70	1.50	9.6E-6	7.8E-6	8.4E-6	2.82	3.27	1.4E-6	1.4E-6	1.5E-6
0.2344	1.70	1.51	1.0E-5	8.2E-6	9.0E-6	3.17	3.30	1.6E-6	1.5E-6	1.6E-6
0.2441	1.68	1.52	1.0E-5	8.3E-6	9.2E-6	3.43	3.32	1.7E-6	1.5E-6	1.6E-6
0.2539	1.66	1.52	9.7E-6	8.1E-6	8.9E-6	3.47	3.31	1.8E-6	1.5E-6	1.7E-6
0.2637	1.64	1.50	8.9E-6	7.5E-6	8.2E-6	3.28	3.28	1.6E-6	1.5E-6	1.6E-6
0.2734	1.62	1.48	7.9E-6	6.7E-6	7.2E-6	2.93	3.23	1.4E-6	1.4E-6	1.5E-6
0.2832	1.60	1.45	6.8E-6	5.9E-6	6.2E-6	2.54	3.17	1.2E-6	1.3E-6	1.4E-6
0.2930	1.56	1.43	5.9E-6	5.2E-6	5.4E-6	2.27	3.11	9.8E-7	1.3E-6	1.3E-6
0.3027	1.51	1.41	5.2E-6	4.7E-6	4.8E-6	2.17	3.07	9.1E-7	1.2E-6	1.3E-6
0.3125	1.47	1.39	4.7E-6	4.4E-6	4.5E-6	2.22	3.03	9.2E-7	1.2E-6	1.2E-6
0.3223	1.45	1.38	4.6E-6	4.4E-6	4.4E-6	2.34	3.00	9.7E-7	1.2E-6	1.2E-6
0.3320	1.45	1.36	4.7E-6	4.4E-6	4.4E-6	2.48	2.98	1.1E-6	1.2E-6	1.2E-6
0.3418	1.45	1.35	4.8E-6	4.6E-6	4.5E-6	2.64	2.94	1.1E-6	1.3E-6	1.3E-6
0.3516	1.44	1.33	4.9E-6	4.7E-6	4.6E-6	2.80	2.91	1.2E-6	1.3E-6	1.3E-6
0.3613	1.42	1.32	4.9E-6	4.7E-6	4.5E-6	2.95	2.88	1.3E-6	1.3E-6	1.3E-6
0.3711	1.40	1.31	4.7E-6	4.6E-6	4.4E-6	3.07	2.86	1.4E-6	1.3E-6	1.3E-6
0.3809	1.39	1.30	4.5E-6	4.5E-6	4.3E-6	3.16	2.85	1.4E-6	1.3E-6	1.2E-6
0.3906	1.39	1.30	4.4E-6	4.3E-6	4.1E-6	3.20	2.85	1.4E-6	1.3E-6	1.2E-6

	W12					W23				
	Cd		Dissipation using			Cd		Dissipation using		
f (Hz)	Obs. Cd	α_n*$\overline{Cd}$	Obs. Cd	$\overline{Cd}$=1.4	α_n*$\overline{Cd}$	Obs. Cd	α_n*$\overline{Cd}$	Obs. Cd	$\overline{Cd}$=3.0	α_n*$\overline{Cd}$
0.4004	1.40	1.31	4.3E-6	4.2E-6	4.0E-6	3.23	2.85	1.3E-6	1.2E-6	1.1E-6
0.4102	1.41	1.31	4.1E-6	4.0E-6	3.8E-6	3.25	2.86	1.3E-6	1.2E-6	1.1E-6
0.4199	1.41	1.31	4.0E-6	3.9E-6	3.7E-6	3.27	2.87	1.3E-6	1.1E-6	1.1E-6
0.4297	1.39	1.32	3.7E-6	3.7E-6	3.5E-6	3.22	2.87	1.2E-6	1.1E-6	1.1E-6
0.4395	1.35	1.32	3.4E-6	3.5E-6	3.3E-6	3.07	2.88	1.2E-6	1.1E-6	1.1E-6
0.4492	1.30	1.32	3.2E-6	3.3E-6	3.2E-6	2.85	2.88	1.1E-6	1.1E-6	1.1E-6
0.4590	1.25	1.33	2.9E-6	3.2E-6	3.1E-6	2.65	2.90	1.1E-6	1.2E-6	1.1E-6
0.4688	1.19	1.34	2.8E-6	3.2E-6	3.1E-6	2.58	2.92	1.1E-6	1.2E-6	1.2E-6
0.4785	1.15	1.35	2.7E-6	3.2E-6	3.2E-6	2.69	2.94	1.2E-6	1.3E-6	1.2E-6
0.4883	1.13	1.36	2.7E-6	3.3E-6	3.3E-6	2.95	2.96	1.3E-6	1.3E-6	1.3E-6
0.4980	1.12	1.36	2.8E-6	3.4E-6	3.4E-6	3.32	2.98	1.5E-6	1.3E-6	1.3E-6
0.5078	1.12	1.37	2.7E-6	3.4E-6	3.4E-6	3.69	3.00	1.6E-6	1.3E-6	1.3E-6
0.5176	1.10	1.38	2.6E-6	3.3E-6	3.3E-6	4.01	3.02	1.7E-6	1.2E-6	1.2E-6
0.5273	1.07	1.40	2.4E-6	3.1E-6	3.1E-6	4.20	3.05	1.7E-6	1.2E-6	1.2E-6
0.5371	1.03	1.41	2.2E-6	2.9E-6	2.9E-6	4.23	3.08	1.6E-6	1.1E-6	1.1E-6
0.5469	1.04	1.43	2.0E-6	2.7E-6	2.8E-6	4.13	3.11	1.5E-6	1.0E-6	1.1E-6
0.5566	1.13	1.44	2.1E-6	2.5E-6	2.7E-6	3.97	3.14	1.3E-6	9.7E-7	1.0E-6
0.5664	1.28	1.48	2.3E-6	2.5E-6	2.7E-6	3.86	3.22	1.2E-6	8.9E-7	9.5E-7
0.5762	1.45	1.53	2.7E-6	2.5E-6	2.8E-6	3.93	3.34	1.1E-6	8.2E-7	9.1E-7
0.5859	1.56	1.56	3.0E-6	2.6E-6	3.0E-6	4.23	3.41	1.1E-6	7.8E-7	8.8E-7
0.5957	1.61	1.60	3.2E-6	2.7E-6	3.2E-6	4.64	3.48	1.2E-6	7.7E-7	8.9E-7
0.6055	1.61	1.63	3.2E-6	2.7E-6	3.3E-6	4.96	3.57	1.3E-6	7.7E-7	9.2E-7
0.6152	1.58	1.67	3.1E-6	2.7E-6	3.2E-6	5.03	3.65	1.3E-6	7.8E-7	9.4E-7
0.6250	1.55	1.70	2.9E-6	2.5E-6	3.1E-6	4.86	3.72	1.3E-6	7.6E-7	9.4E-7
0.6348	1.54	1.73	2.6E-6	2.3E-6	2.9E-6	4.55	3.78	1.1E-6	7.2E-7	9.1E-7
0.6445	1.54	1.76	2.3E-6	2.0E-6	2.6E-6	4.26	3.84	9.8E-7	6.6E-7	8.5E-7
0.6543	1.52	1.78	2.0E-6	1.8E-6	2.3E-6	4.19	3.89	8.8E-7	6.1E-7	7.8E-7
0.6641	1.48	1.85	1.7E-6	1.6E-6	2.2E-6	4.43	4.03	8.5E-7	5.6E-7	7.5E-7
0.6738	1.42	1.86	1.5E-6	1.5E-6	2.0E-6	4.88	4.05	8.7E-7	5.2E-7	7.0E-7
0.6836	1.40	1.94	1.4E-6	1.4E-6	2.0E-6	5.28	4.24	8.9E-7	4.9E-7	6.9E-7
0.6934	1.45	2.03	1.4E-6	1.3E-6	2.0E-6	5.39	4.43	8.7E-7	4.6E-7	6.8E-7
0.7031	1.56	2.09	1.5E-6	1.3E-6	2.0E-6	5.19	4.56	8.0E-7	4.4E-7	6.7E-7

Table A-17. Comparison of percentage error between the observed and estimated spectral energy dissipation using average and spectral drag coefficients during Tropical Storm Lee (2011).

f (Hz)	Using $\overline{Cd}$	Using $\alpha_n * \overline{Cd}$
0.1074	17.3	0.8
0.1172	13.5	0.9
0.1270	10.5	0.9
0.1367	7.8	0.9
0.1465	5.3	0.9
0.1563	3.2	1.0
0.1660	1.5	1.3
0.1758	0.0	1.5
0.1855	-1.6	1.4
0.1953	-3.0	1.4
0.2051	-4.3	1.3
0.2148	-5.5	1.3
0.2246	-6.8	1.3
0.2344	-7.7	1.3
0.2441	-8.1	1.4
0.2539	-7.8	1.5
0.2637	-6.8	1.7
0.2734	-5.1	1.9
0.2832	-3.1	2.2
0.2930	-1.0	2.6
0.3027	1.0	3.1
0.3125	2.3	3.3
0.3223	3.3	3.3
0.3320	4.2	3.1
0.3418	5.1	2.9
0.3516	6.0	2.6

Table A-18. Comparison of predicted and observed total energy dissipation (S_v) during Tropical Storm Lee (2011).

Obs. S_v (m^2/s)	Pred. S_v (m^2/s)	Obs. S_v (m^2/s)	Pred. S_v (m^2/s)	Obs. S_v (m^2/s)	Pred. S_v (m^2/s)	Obs. S_v (m^2/s)	Pred. S_v (m^2/s)
2.8E-4	2.8E-4	1.7E-4	1.8E-4	8.1E-5	7.8E-5	4.8E-5	4.7E-5
3.1E-4	3.1E-4	1.4E-4	1.4E-4	8.1E-5	8.0E-5	3.8E-5	3.8E-5
2.9E-4	3.0E-4	1.3E-4	1.3E-4	6.5E-5	6.4E-5	4.0E-5	3.9E-5
3.0E-4	3.0E-4	1.4E-4	1.4E-4	1.1E-4	1.1E-4	3.3E-5	3.2E-5
3.3E-4	3.3E-4	1.2E-4	1.2E-4	2.3E-4	2.2E-4	3.5E-5	3.4E-5
5.4E-4	5.5E-4	1.3E-4	1.3E-4	1.6E-4	1.6E-4	6.0E-5	5.8E-5
4.3E-4	4.4E-4	1.5E-4	1.5E-4	2.4E-4	2.4E-4	4.8E-5	4.7E-5
5.7E-4	5.8E-4	1.6E-4	1.7E-4	3.0E-4	3.0E-4	4.6E-5	4.5E-5
5.3E-4	5.4E-4	1.5E-4	1.5E-4	3.0E-4	3.0E-4	4.9E-5	4.8E-5
6.1E-4	6.3E-4	1.7E-4	1.7E-4	2.2E-4	2.1E-4	4.9E-5	4.9E-5
5.8E-4	5.9E-4	1.6E-4	1.6E-4	1.9E-4	1.8E-4	5.3E-5	5.3E-5
4.8E-4	4.9E-4	1.6E-4	1.7E-4	1.9E-4	1.8E-4	3.9E-5	3.9E-5
4.9E-4	5.0E-4	1.4E-4	1.4E-4	2.5E-4	2.5E-4	4.8E-5	4.8E-5
6.6E-4	6.6E-4	1.6E-4	1.6E-4	2.5E-4	2.4E-4	5.9E-5	5.8E-5
6.1E-4	6.1E-4	1.9E-4	2.0E-4	2.7E-4	2.6E-4	5.4E-5	5.2E-5
6.0E-4	6.0E-4	1.7E-4	1.7E-4	2.1E-4	2.0E-4	4.0E-5	4.0E-5
5.1E-4	5.1E-4	1.6E-4	1.6E-4	1.5E-4	1.5E-4	2.9E-5	2.8E-5
4.9E-4	4.9E-4	1.6E-4	1.6E-4	1.1E-4	1.1E-4	2.3E-5	2.1E-5
4.0E-4	4.0E-4	1.5E-4	1.5E-4	1.1E-4	1.1E-4	6.1E-5	6.0E-5
3.4E-4	3.4E-4	1.7E-4	1.8E-4	9.3E-5	8.9E-5	4.2E-5	4.1E-5
3.1E-4	3.1E-4	1.4E-4	1.4E-4	9.1E-5	8.8E-5	3.3E-5	3.2E-5
2.9E-4	2.9E-4	1.2E-4	1.2E-4	5.7E-5	5.6E-5	4.0E-5	4.0E-5
2.3E-4	2.3E-4	1.5E-4	1.5E-4	5.0E-5	5.0E-5	5.6E-5	5.5E-5
1.8E-4	1.9E-4	1.8E-4	1.9E-4	5.1E-5	5.0E-5	5.0E-5	4.9E-5
1.8E-4	1.9E-4	1.7E-4	1.7E-4	4.0E-5	4.0E-5	6.8E-5	6.7E-5
1.7E-4	1.7E-4	2.0E-4	2.0E-4	2.6E-5	2.5E-5	6.1E-5	6.0E-5
9.5E-5	9.6E-5	1.8E-4	1.9E-4	3.4E-5	3.3E-5	4.4E-5	4.3E-5
1.1E-4	1.1E-4	1.6E-4	1.6E-4	3.1E-5	3.0E-5	2.6E-5	2.5E-5
1.1E-4	1.2E-4	1.1E-4	1.1E-4	5.5E-5	5.4E-5		
1.6E-4	1.6E-4	6.0E-5	5.8E-5	5.6E-5	5.5E-5		

Table A-19. Observed mean water depth inside wetland, at a station 1 m from the shoreline.

Time (UTC)	Depth (m)	Time (UTC)	Depth (m)	Time (UTC)	Depth (m)	Time (UTC)	Depth (m)
4/13/2012 4:00	0.000	4/13/2012 23:30	0.167	4/14/2012 19:00	0.247	4/15/2012 14:30	0.211
4/13/2012 4:30	0.000	4/14/2012 0:00	0.154	4/14/2012 19:30	0.256	4/15/2012 15:00	0.231
4/13/2012 5:00	0.000	4/14/2012 0:30	0.143	4/14/2012 20:00	0.259	4/15/2012 15:30	0.270
4/13/2012 5:30	0.000	4/14/2012 1:00	0.127	4/14/2012 20:30	0.259	4/15/2012 16:00	0.300
4/13/2012 6:00	0.000	4/14/2012 1:30	0.118	4/14/2012 21:00	0.245	4/15/2012 16:30	0.317
4/13/2012 6:30	0.000	4/14/2012 2:00	0.108	4/14/2012 21:30	0.231	4/15/2012 17:00	0.328
4/13/2012 7:00	0.000	4/14/2012 2:30	0.106	4/14/2012 22:00	0.216	4/15/2012 17:30	0.312
4/13/2012 7:30	0.000	4/14/2012 3:00	0.103	4/14/2012 22:30	0.208	4/15/2012 18:00	0.288
4/13/2012 8:00	0.000	4/14/2012 3:30	0.097	4/14/2012 23:00	0.196	4/15/2012 18:30	0.258
4/13/2012 8:30	0.000	4/14/2012 4:00	0.091	4/14/2012 23:30	0.188	4/15/2012 19:00	0.236
4/13/2012 9:00	0.000	4/14/2012 4:30	0.080	4/15/2012 0:00	0.181	4/15/2012 19:30	0.235
4/13/2012 9:30	0.000	4/14/2012 5:00	0.070	4/15/2012 0:30	0.178	4/15/2012 20:00	0.249
4/13/2012 10:00	0.000	4/14/2012 5:30	0.062	4/15/2012 1:00	0.178	4/15/2012 20:30	0.260
4/13/2012 10:30	0.000	4/14/2012 6:00	0.000	4/15/2012 1:30	0.172	4/15/2012 21:00	0.255
4/13/2012 11:00	0.000	4/14/2012 6:30	0.000	4/15/2012 2:00	0.169	4/15/2012 21:30	0.255
4/13/2012 11:30	0.000	4/14/2012 7:00	0.000	4/15/2012 2:30	0.165	4/15/2012 22:00	0.248
4/13/2012 12:00	0.000	4/14/2012 7:30	0.000	4/15/2012 3:00	0.163	4/15/2012 22:30	0.246
4/13/2012 12:30	0.049	4/14/2012 8:00	0.000	4/15/2012 3:30	0.156	4/15/2012 23:00	0.237
4/13/2012 13:00	0.073	4/14/2012 8:30	0.000	4/15/2012 4:00	0.160	4/15/2012 23:30	0.235
4/13/2012 13:30	0.086	4/14/2012 9:00	0.000	4/15/2012 4:30	0.162	4/16/2012 0:00	0.243
4/13/2012 14:00	0.104	4/14/2012 9:30	0.000	4/15/2012 5:00	0.165	4/16/2012 0:30	0.232
4/13/2012 14:30	0.121	4/14/2012 10:00	0.000	4/15/2012 5:30	0.160	4/16/2012 1:00	0.230
4/13/2012 15:00	0.136	4/14/2012 10:30	0.000	4/15/2012 6:00	0.153	4/16/2012 1:30	0.230
4/13/2012 15:30	0.153	4/14/2012 11:00	0.000	4/15/2012 6:30	0.148	4/16/2012 2:00	0.229
4/13/2012 16:00	0.173	4/14/2012 11:30	0.000	4/15/2012 7:00	0.144	4/16/2012 2:30	0.217
4/13/2012 16:30	0.191	4/14/2012 12:00	0.000	4/15/2012 7:30	0.139	4/16/2012 3:00	0.211
4/13/2012 17:00	0.205	4/14/2012 12:30	0.000	4/15/2012 8:00	0.141	4/16/2012 3:30	0.201
4/13/2012 17:30	0.209	4/14/2012 13:00	0.068	4/15/2012 8:30	0.144	4/16/2012 4:00	0.201
4/13/2012 18:00	0.218	4/14/2012 13:30	0.084	4/15/2012 9:00	0.142	4/16/2012 4:30	0.216
4/13/2012 18:30	0.228	4/14/2012 14:00	0.100	4/15/2012 9:30	0.137	4/16/2012 5:00	0.223
4/13/2012 19:00	0.231	4/14/2012 14:30	0.118	4/15/2012 10:00	0.132	4/16/2012 5:30	0.210
4/13/2012 19:30	0.236	4/14/2012 15:00	0.132	4/15/2012 10:30	0.125	4/16/2012 6:00	0.198
4/13/2012 20:00	0.233	4/14/2012 15:30	0.151	4/15/2012 11:00	0.129	4/16/2012 6:30	0.192
4/13/2012 20:30	0.232	4/14/2012 16:00	0.166	4/15/2012 11:30	0.133	4/16/2012 7:00	0.185
4/13/2012 21:00	0.210	4/14/2012 16:30	0.185	4/15/2012 12:00	0.144	4/16/2012 7:30	0.183
4/13/2012 21:30	0.213	4/14/2012 17:00	0.204	4/15/2012 12:30	0.159	4/16/2012 8:00	0.173
4/13/2012 22:00	0.201	4/14/2012 17:30	0.223	4/15/2012 13:00	0.168	4/16/2012 8:30	0.166
4/13/2012 22:30	0.186	4/14/2012 18:00	0.236	4/15/2012 13:30	0.181	4/16/2012 9:00	0.158
4/13/2012 23:00	0.175	4/14/2012 18:30	0.243	4/15/2012 14:00	0.199	4/16/2012 9:30	0.150

Time (UTC)	Depth (m)
4/16/2012 10:00	0.147
4/16/2012 10:30	0.135
4/16/2012 11:00	0.125
4/16/2012 11:30	0.118
4/16/2012 12:00	0.111
4/16/2012 12:30	0.114
4/16/2012 13:00	0.101
4/16/2012 13:30	0.098
4/16/2012 14:00	0.095
4/16/2012 14:30	0.097
4/16/2012 15:00	0.095
4/16/2012 15:30	0.097
4/16/2012 16:00	0.102
4/16/2012 16:30	0.111
4/16/2012 17:00	0.101
4/16/2012 17:30	0.104
4/16/2012 18:00	0.112
4/16/2012 18:30	0.111
4/16/2012 19:00	0.120
4/16/2012 19:30	0.116

Time (UTC)	Depth (m)
4/16/2012 20:00	0.113
4/16/2012 20:30	0.120
4/16/2012 21:00	0.112
4/16/2012 21:30	0.109
4/16/2012 22:00	0.108
4/16/2012 22:30	0.107
4/16/2012 23:00	0.104
4/16/2012 23:30	0.091
4/17/2012 0:00	0.102
4/17/2012 0:30	0.094
4/17/2012 1:00	0.094
4/17/2012 1:30	0.096
4/17/2012 2:00	0.104
4/17/2012 2:30	0.103
4/17/2012 3:00	0.115
4/17/2012 3:30	0.111
4/17/2012 4:00	0.125
4/17/2012 4:30	0.107
4/17/2012 5:00	0.108
4/17/2012 5:30	0.116

Time (UTC)	Depth (m)
4/17/2012 6:00	0.107
4/17/2012 6:30	0.116
4/17/2012 7:00	0.127
4/17/2012 7:30	0.146
4/17/2012 8:00	0.141
4/17/2012 8:30	0.143
4/17/2012 9:00	0.181
4/17/2012 9:30	0.179
4/17/2012 10:00	0.159
4/17/2012 10:30	0.138
4/17/2012 11:00	0.164
4/17/2012 11:30	0.118
4/17/2012 12:00	0.072
4/17/2012 12:30	0.055
4/17/2012 13:00	0.050
4/17/2012 13:30	0.061
4/17/2012 14:00	0.080
4/17/2012 14:30	0.089
4/17/2012 15:00	0.104
4/17/2012 15:30	0.106

Time (UTC)	Depth (m)
4/17/2012 16:00	0.103
4/17/2012 16:30	0.093
4/17/2012 17:00	0.093
4/17/2012 17:30	0.073
4/17/2012 18:00	0.063
4/17/2012 18:30	0.052
4/17/2012 19:00	0.047
4/17/2012 19:30	0.043
4/17/2012 20:00	0.041
4/17/2012 20:30	0.041
4/17/2012 21:00	0.000
4/17/2012 21:30	0.000
4/17/2012 22:00	0.000
4/17/2012 22:30	0.000
4/17/2012 23:00	0.000
4/17/2012 23:30	0.000
4/18/2012 0:00	0.000

Table A-20. Observed mean water depth, significant wave height, and peak wave period at the offshore wave gauge.

Time (UTC)	Depth (m)	H_{mo} (m)	T_p (s)
4/14/2012 14:30	1.00	0.32	2.83
4/14/2012 15:00	1.03	0.34	2.84
4/14/2012 15:30	1.06	0.36	2.86
4/14/2012 16:00	1.08	0.36	2.95
4/14/2012 16:30	1.10	0.37	2.96
4/14/2012 17:00	1.12	0.40	2.91
4/14/2012 17:30	1.14	0.39	2.89
4/14/2012 18:00	1.15	0.39	2.97
4/14/2012 18:30	1.16	0.40	2.98
4/14/2012 19:00	1.17	0.39	2.96
4/14/2012 19:30	1.17	0.40	2.98
4/14/2012 20:00	1.17	0.36	2.86
4/14/2012 20:30	1.17	0.35	2.98
4/14/2012 21:00	1.16	0.33	2.92
4/14/2012 21:30	1.14	0.32	2.86
4/14/2012 22:00	1.12	0.31	2.81
4/14/2012 22:30	1.11	0.30	2.77
4/14/2012 23:00	1.10	0.30	2.75
4/14/2012 23:30	1.09	0.30	2.72
4/15/2012 0:00	1.08	0.30	2.65
4/15/2012 0:30	1.08	0.31	2.76
4/15/2012 1:00	1.08	0.30	2.77
4/15/2012 1:30	1.07	0.30	2.81
4/15/2012 2:00	1.06	0.31	2.81
4/15/2012 2:30	1.05	0.31	2.77
4/15/2012 3:00	1.05	0.31	2.79
4/15/2012 3:30	1.04	0.33	2.86
4/15/2012 4:00	1.04	0.34	2.93
4/15/2012 4:30	1.04	0.38	2.92
4/15/2012 5:00	1.04	0.38	2.97
4/15/2012 5:30	1.03	0.39	2.91
4/15/2012 6:00	1.02	0.40	3.03
4/15/2012 6:30	1.00	0.40	3.05
4/15/2012 7:00	1.00	0.40	3.05
4/15/2012 7:30	0.99	0.37	2.98
4/15/2012 8:00	0.99	0.40	3.02
4/15/2012 8:30	0.99	0.41	2.98
4/15/2012 9:00	0.99	0.41	3.09
4/15/2012 9:30	0.98	0.39	3.04
4/15/2012 10:00	0.98	0.40	3.08
4/15/2012 10:30	0.97	0.37	3.06
4/15/2012 11:00	0.98	0.37	2.99
4/15/2012 11:30	0.99	0.38	2.94
4/15/2012 12:00	1.00	0.37	2.92
4/15/2012 12:30	1.02	0.41	2.91
4/15/2012 13:00	1.04	0.40	2.87
4/15/2012 13:30	1.05	0.40	2.96
4/15/2012 14:00	1.07	0.41	2.89
4/15/2012 14:30	1.09	0.41	2.86
4/15/2012 15:00	1.11	0.42	2.95
4/15/2012 15:30	1.15	0.44	2.84
4/15/2012 16:00	1.17	0.42	2.91
4/15/2012 16:30	1.18	0.42	2.87
4/15/2012 17:00	1.19	0.43	2.84
4/15/2012 17:30	1.18	0.39	2.89
4/15/2012 18:00	1.16	0.34	2.91
4/15/2012 18:30	1.13	0.34	2.71
4/15/2012 19:00	1.11	0.29	2.81
4/15/2012 19:30	1.11	0.32	2.78
4/15/2012 20:00	1.12	0.32	2.69
4/15/2012 20:30	1.12	0.34	2.73
4/15/2012 21:00	1.11	0.33	2.74
4/15/2012 21:30	1.11	0.37	2.81
4/15/2012 22:00	1.10	0.34	2.89
4/15/2012 22:30	1.09	0.37	2.85
4/15/2012 23:00	1.09	0.33	2.90
4/15/2012 23:30	1.09	0.33	2.87
4/16/2012 0:00	1.10	0.34	2.74
4/16/2012 0:30	1.09	0.33	2.82
4/16/2012 1:00	1.10	0.32	2.78
4/16/2012 1:30	1.09	0.34	2.79
4/16/2012 2:00	1.09	0.33	2.83
4/16/2012 2:30	1.09	0.32	2.81
4/16/2012 3:00	1.09	0.31	2.84
4/16/2012 3:30	1.08	0.31	2.80
4/16/2012 4:00	1.07	0.32	2.73
4/16/2012 4:30	1.08	0.34	2.76
4/16/2012 5:00	1.08	0.37	2.82
4/16/2012 5:30	1.07	0.37	2.88
4/16/2012 6:00	1.05	0.37	2.93
4/16/2012 6:30	1.04	0.34	2.89
4/16/2012 7:00	1.03	0.34	2.78
4/16/2012 7:30	1.03	0.34	2.84
4/16/2012 8:00	1.02	0.33	2.81
4/16/2012 8:30	1.01	0.34	2.76
4/16/2012 9:00	1.00	0.32	2.82
4/16/2012 9:30	0.99	0.30	2.77
4/16/2012 10:00	1.00	0.29	2.81
4/16/2012 10:30	0.99	0.26	2.75
4/16/2012 11:00	0.98	0.27	2.71

Table A-21. Observed mean water depth, significant wave height, and mean wave period at a station 1m inside wetland.

Time (UTC)	Depth (m)	H_{mo} (m)	T_z (s)	Time (UTC)	Depth (m)	H_{mo} (m)	T_z (s)	Time (UTC)	Depth (m)	H_{mo} (m)	T_z (s)
4/14/2012 14:30	0.118	0.037	2.76	4/15/2012 6:00	0.153	0.054	2.72	4/15/2012 21:30	0.255	0.086	2.41
4/14/2012 15:00	0.132	0.044	2.60	4/15/2012 6:30	0.148	0.053	2.79	4/15/2012 22:00	0.248	0.083	2.50
4/14/2012 15:30	0.151	0.051	2.65	4/15/2012 7:00	0.144	0.050	2.64	4/15/2012 22:30	0.246	0.082	2.46
4/14/2012 16:00	0.166	0.057	2.44	4/15/2012 7:30	0.139	0.049	2.68	4/15/2012 23:00	0.237	0.080	2.58
4/14/2012 16:30	0.185	0.064	2.51	4/15/2012 8:00	0.141	0.050	2.61	4/15/2012 23:30	0.235	0.078	2.39
4/14/2012 17:00	0.204	0.072	2.60	4/15/2012 8:30	0.144	0.050	2.72	4/16/2012 0:00	0.243	0.080	2.41
4/14/2012 17:30	0.223	0.077	2.65	4/15/2012 9:00	0.142	0.049	2.81	4/16/2012 0:30	0.232	0.076	2.41
4/14/2012 18:00	0.236	0.080	2.57	4/15/2012 9:30	0.137	0.047	2.76	4/16/2012 1:00	0.230	0.074	2.40
4/14/2012 18:30	0.243	0.084	2.53	4/15/2012 10:00	0.132	0.045	2.82	4/16/2012 1:30	0.230	0.074	2.33
4/14/2012 19:00	0.247	0.081	2.55	4/15/2012 10:30	0.125	0.042	2.78	4/16/2012 2:00	0.229	0.077	2.36
4/14/2012 19:30	0.256	0.089	2.57	4/15/2012 11:00	0.129	0.044	2.88	4/16/2012 2:30	0.217	0.070	2.35
4/14/2012 20:00	0.259	0.093	2.65	4/15/2012 11:30	0.133	0.048	2.75	4/16/2012 3:00	0.211	0.068	2.39
4/14/2012 20:30	0.259	0.092	2.44	4/15/2012 12:00	0.144	0.052	2.72	4/16/2012 3:30	0.201	0.064	2.29
4/14/2012 21:00	0.245	0.082	2.38	4/15/2012 12:30	0.159	0.059	2.69	4/16/2012 4:00	0.201	0.063	2.38
4/14/2012 21:30	0.231	0.073	2.33	4/15/2012 13:00	0.168	0.060	2.57	4/16/2012 4:30	0.216	0.071	2.30
4/14/2012 22:00	0.216	0.071	2.49	4/15/2012 13:30	0.181	0.067	2.55	4/16/2012 5:00	0.223	0.079	2.46
4/14/2012 22:30	0.208	0.064	2.29	4/15/2012 14:00	0.199	0.074	2.57	4/16/2012 5:30	0.210	0.069	2.52
4/14/2012 23:00	0.196	0.060	2.24	4/15/2012 14:30	0.211	0.081	2.67	4/16/2012 6:00	0.198	0.068	2.54
4/14/2012 23:30	0.188	0.058	2.30	4/15/2012 15:00	0.231	0.089	2.75	4/16/2012 6:30	0.192	0.065	2.55
4/15/2012 0:00	0.181	0.056	2.27	4/15/2012 15:30	0.270	0.101	2.59	4/16/2012 7:00	0.185	0.061	2.58
4/15/2012 0:30	0.178	0.057	2.40	4/15/2012 16:00	0.300	0.106	2.68	4/16/2012 7:30	0.183	0.061	2.46
4/15/2012 1:00	0.178	0.057	2.29	4/15/2012 16:30	0.317	0.112	2.71	4/16/2012 8:00	0.173	0.055	2.54
4/15/2012 1:30	0.172	0.055	2.30	4/15/2012 17:00	0.328	0.114	2.64	4/16/2012 8:30	0.166	0.053	2.47
4/15/2012 2:00	0.169	0.057	2.33	4/15/2012 17:30	0.312	0.107	2.58	4/16/2012 9:00	0.158	0.049	2.46
4/15/2012 2:30	0.165	0.054	2.35	4/15/2012 18:00	0.288	0.108	2.64	4/16/2012 9:30	0.150	0.046	2.55
4/15/2012 3:00	0.163	0.055	2.42	4/15/2012 18:30	0.258	0.089	2.50	4/16/2012 10:00	0.147	0.043	2.52
4/15/2012 3:30	0.156	0.053	2.54	4/15/2012 19:00	0.236	0.078	2.37	4/16/2012 10:30	0.135	0.037	2.39
4/15/2012 4:00	0.160	0.054	2.39	4/15/2012 19:30	0.235	0.074	2.41	4/16/2012 11:00	0.125	0.032	2.59
4/15/2012 4:30	0.162	0.058	2.59	4/15/2012 20:00	0.249	0.082	2.31				
4/15/2012 5:00	0.165	0.059	2.62	4/15/2012 20:30	0.260	0.090	2.33				
4/15/2012 5:30	0.160	0.057	2.65	4/15/2012 21:00	0.255	0.086	2.40				

Table A-22. Observed near-bottom velocity and direction at a station 1 m inside wetland.

Time (UTC)	Velocity (m/s)	Dir. (degree)	Time (UTC)	Velocity (m/s)	Dir. (degree)	Time (UTC)	Velocity (m/s)	Dir. (degree)
4/14/2012 14:30	0.033	131.3	4/15/2012 5:30	0.141	149.1	4/15/2012 21:00	0.088	187.6
4/14/2012 15:00	0.033	124.6	4/15/2012 6:00	0.106	148.0	4/15/2012 21:30	0.095	188.4
4/14/2012 15:30	0.107	124.0	4/15/2012 6:30	0.083	154.7	4/15/2012 22:00	0.088	188.3
4/14/2012 16:00	0.143	141.2	4/15/2012 7:00	0.075	148.2	4/15/2012 22:30	0.107	184.0
4/14/2012 16:30	0.159	141.9	4/15/2012 7:30	0.059	158.3	4/15/2012 23:00	0.107	175.6
4/14/2012 17:00	0.123	154.8	4/15/2012 8:00	0.143	140.1	4/15/2012 23:30	0.092	189.3
4/14/2012 17:30	0.112	167.4	4/15/2012 8:30	0.106	153.7	4/16/2012 0:00	0.111	184.0
4/14/2012 18:00	0.124	175.6	4/15/2012 9:00	0.077	144.7	4/16/2012 0:30	0.110	172.7
4/14/2012 18:30	0.082	192.5	4/15/2012 9:30	0.091	140.7	4/16/2012 1:00	0.107	168.5
4/14/2012 19:00	0.106	178.9	4/15/2012 10:00	0.110	142.7	4/16/2012 1:30	0.100	175.9
4/14/2012 19:30	0.068	194.2	4/15/2012 10:30	0.075	131.1	4/16/2012 2:00	0.091	172.5
4/14/2012 20:00	0.085	185.6	4/15/2012 11:00	0.119	164.3	4/16/2012 2:30	0.086	166.4
4/14/2012 20:30	0.092	176.9	4/15/2012 11:30	0.130	139.1	4/16/2012 3:00	0.111	159.6
4/14/2012 21:00	0.076	177.8	4/15/2012 12:00	0.053	151.8	4/16/2012 3:30	0.103	144.6
4/14/2012 21:30	0.089	169.4	4/15/2012 13:00	0.112	156.5	4/16/2012 4:00	0.113	149.1
4/14/2012 22:00	0.107	150.5	4/15/2012 13:30	0.137	163.6	4/16/2012 4:30	0.112	159.7
4/14/2012 22:30	0.113	150.9	4/15/2012 14:00	0.141	175.1	4/16/2012 5:00	0.101	165.3
4/14/2012 23:00	0.130	146.2	4/15/2012 14:30	0.133	178.0	4/16/2012 5:30	0.130	162.8
4/14/2012 23:30	0.138	138.6	4/15/2012 15:00	0.144	186.8	4/16/2012 6:00	0.115	154.2
4/15/2012 0:00	0.152	137.3	4/15/2012 15:30	0.115	203.9	4/16/2012 6:30	0.100	160.5
4/15/2012 0:30	0.135	137.0	4/15/2012 16:00	0.133	200.4	4/16/2012 7:00	0.088	153.2
4/15/2012 1:00	0.138	134.5	4/15/2012 16:30	0.143	201.7	4/16/2012 7:30	0.084	164.8
4/15/2012 1:30	0.127	137.9	4/15/2012 17:00	0.135	214.2	4/16/2012 8:00	0.067	157.0
4/15/2012 2:00	0.137	141.6	4/15/2012 17:30	0.114	206.0	4/16/2012 8:30	0.079	163.9
4/15/2012 2:30	0.129	129.9	4/15/2012 18:00	0.109	201.4	4/16/2012 9:00	0.080	145.1
4/15/2012 3:00	0.125	141.8	4/15/2012 18:30	0.104	201.2	4/16/2012 9:30	0.085	132.9
4/15/2012 3:30	0.135	138.4	4/15/2012 19:00	0.095	187.8	4/16/2012 10:00	0.090	134.8
4/15/2012 4:00	0.124	138.9	4/15/2012 19:30	0.092	184.8	4/16/2012 10:30	0.033	159.6
4/15/2012 4:30	0.119	150.8	4/15/2012 20:00	0.105	201.5			
4/15/2012 5:00	0.105	152.4	4/15/2012 20:30	0.085	204.1			

Table A-23. Observed near-bottom velocity and direction at a station 2 m inside wetland.

Time (UTC)	Velocity (m/s)	Dir. (degree)	Time (UTC)	Velocity (m/s)	Dir. (degree)	Time (UTC)	Velocity (m/s)	Dir. (degree)
4/14/2012 14:30	0.020	141.6	4/15/2012 5:30	0.121	161.0	4/15/2012 21:00	0.091	180.8
4/14/2012 15:00	0.040	147.8	4/15/2012 6:00	0.089	160.1	4/15/2012 21:30	0.104	183.4
4/14/2012 15:30	0.095	154.8	4/15/2012 6:30	0.091	160.1	4/15/2012 22:00	0.104	182.2
4/14/2012 16:00	0.141	159.9	4/15/2012 7:00	0.077	160.0	4/15/2012 22:30	0.121	174.8
4/14/2012 16:30	0.122	159.6	4/15/2012 7:30	0.056	159.6	4/15/2012 23:00	0.136	179.0
4/14/2012 17:00	0.158	160.2	4/15/2012 8:00	0.070	154.6	4/15/2012 23:30	0.104	183.7
4/14/2012 17:30	0.118	162.8	4/15/2012 8:30	0.082	157.2	4/16/2012 0:00	0.123	182.4
4/14/2012 18:00	0.112	175.1	4/15/2012 9:00	0.073	151.8	4/16/2012 0:30	0.134	175.9
4/14/2012 18:30	0.076	175.6	4/15/2012 9:30	0.049	166.0	4/16/2012 1:00	0.119	179.0
4/14/2012 19:00	0.087	179.6	4/15/2012 10:00	0.046	150.9	4/16/2012 1:30	0.111	178.9
4/14/2012 19:30	0.075	185.6	4/15/2012 10:30	0.026	160.2	4/16/2012 2:00	0.125	176.9
4/14/2012 20:00	0.059	179.4	4/15/2012 11:00	0.041	159.9	4/16/2012 2:30	0.118	171.4
4/14/2012 20:30	0.062	182.9	4/15/2012 11:30	0.056	149.4	4/16/2012 3:00	0.119	168.7
4/14/2012 21:00	0.072	173.6	4/15/2012 12:00	0.076	156.3	4/16/2012 3:30	0.120	167.5
4/14/2012 21:30	0.091	173.8	4/15/2012 13:00	0.130	168.0	4/16/2012 4:00	0.111	166.1
4/14/2012 22:00	0.111	160.8	4/15/2012 13:30	0.146	173.9	4/16/2012 4:30	0.136	174.6
4/14/2012 22:30	0.118	157.7	4/15/2012 14:00	0.153	177.4	4/16/2012 5:00	0.145	172.4
4/14/2012 23:00	0.125	162.0	4/15/2012 14:30	0.150	177.2	4/16/2012 5:30	0.141	170.9
4/14/2012 23:30	0.143	157.2	4/15/2012 15:00	0.133	186.2	4/16/2012 6:00	0.133	167.4
4/15/2012 0:00	0.134	158.2	4/15/2012 15:30	0.078	208.5	4/16/2012 6:30	0.136	166.4
4/15/2012 0:30	0.129	153.3	4/15/2012 16:00	0.090	219.8	4/16/2012 7:00	0.119	162.8
4/15/2012 1:00	0.116	156.3	4/15/2012 16:30	0.100	223.4	4/16/2012 7:30	0.118	169.2
4/15/2012 1:30	0.123	153.9	4/15/2012 17:00	0.079	241.3	4/16/2012 8:00	0.101	170.6
4/15/2012 2:00	0.129	160.3	4/15/2012 17:30	0.068	230.7	4/16/2012 8:30	0.096	164.7
4/15/2012 2:30	0.138	160.6	4/15/2012 18:00	0.078	213.6	4/16/2012 9:00	0.050	168.5
4/15/2012 3:00	0.102	156.1	4/15/2012 18:30	0.078	205.1	4/16/2012 9:30	0.046	154.5
4/15/2012 3:30	0.121	157.1	4/15/2012 19:00	0.127	189.9	4/16/2012 10:00	0.037	153.9
4/15/2012 4:00	0.128	158.5	4/15/2012 19:30	0.097	183.5	4/16/2012 10:30	0.034	159.8
4/15/2012 4:30	0.124	163.0	4/15/2012 20:00	0.105	191.0			
4/15/2012 5:00	0.126	164.9	4/15/2012 20:30	0.095	189.3			

Table A-24. Topographic survey of the study area shoreline performed on June 8, 2011. Coordinates with respect to N 29°13.411', W 090°36.347'.

E	N	E	N	E	N	E	N	E	N	E	N
25.92	0.893	37.44	-20.6	-11.33	-19.77	-14.62	17.75	-8.568	64.84	-43.39	114.3
25.4	0.631	37.11	-21.1	-10.77	-17.04	-14.15	19.99	-11.34	65.59	-44.36	114.5
25.79	-1.189	37.56	-22.35	-11.56	-17.08	-11.2	25.12	-10.88	68.27	-44.56	117
27.8	-3.338	36.92	-24.83	-11.76	-16.21	-11.78	27.45	-9.421	71.11	-49.16	115.3
27.05	-3.658	35.96	-26.9	-10.35	-11.85	-10.96	30.41	-10.38	71.1	-48.48	118.9
27.73	-7.205	35.43	-27.42	-13	-12.2	-11.16	30.91	-10.5	73.27	-49.22	119.5
28.31	-10.07	34.53	-29.32	-12.37	-8.08	-10.37	32.56	-9.659	76.01	-50.84	118.2
29.57	-10.51	31.23	-32	-12.63	-7.291	-10.89	33.44	-11.76	75.56	-51.04	120.1
29.72	-11.23	26.97	-33.32	-12.11	-6.867	-9.446	37.25	-11.95	78.57	-51.8	119.2
30.23	-11.52	24.16	-33.15	-12.1	-6.87	-10.34	38.18	-10.07	83.43	-54.31	120.1
30.96	-11.43	19.93	-29.78	-12.57	-6.325	-8.891	41.93	-10.58	84.1	-54.67	121
30.56	-11.83	13.98	-31.81	-14.48	-6.715	-9.394	42.53	-9.659	87.91	-55.63	120.7
31.21	-12.94	4.017	-31.09	-13.93	-2.585	-9.037	43.87	-11.41	87.66	-58.19	122.1
32.44	-13.36	3.402	-30.19	-14.47	-1.951	-9.744	45.17	-12.18	92.12	-61.12	123.1
31.92	-13.67	2.414	-30.85	-13.86	0.6	-9.025	48.29	-13.08	94.02	-63.57	123.3
32.06	-14.62	1.576	-30.03	-13.07	2.777	-6.76	49.72	-12.51	97.15	-65.21	125
32.56	-14.82	1.244	-29.23	-13.24	3.844	-6.334	51.29	-17.84	101.3	-67.03	129.7
32.94	-15.58	0.351	-30.63	-12.35	5.886	-8.37	54.21	-20.62	101.9	-69.43	128.9
33.96	-16.09	-0.271	-29.54	-13.07	5.995	-9.473	55.05	-25.89	104.8	-70.35	132.3
34.14	-16.71	-1.286	-29.77	-13.12	6.666	-9.488	56.66	-27.83	106.7	-72.05	132.5
34.55	-17.21	-4.258	-28.72	-12.25	8.641	-9.086	57.48	-29.02	107.4	-73.14	134.1
34.74	-17.69	-7.516	-26.94	-12.62	10.5	-9.988	57.45	-34.22	111.3	-74.45	132.9
36.22	-18.53	-9.47	-24.52	-12.4	11.23	-10.47	58.47	-36.88	110.7	-76.16	133.3
36.48	-19.23	-9.653	-22.64	-13.04	11.39	-9.016	60.14	-39.79	111.9	-77.71	135.5
36.88	-19.58	-10.62	-21.76	-12.97	13.63	-10.58	60.83	-41.32	111.8	-81.34	135.6
36.84	-20.03	-9.827	-19.89	-12.59	14.83	-10.3	62.82	-42.92	112.9		

Table A-25. Topographic survey of the study area shoreline performed on September 9, 2011. Coordinates with respect to N 29°13.411', W 090°36.347'.

E	N	E	N	E	N
-76.96	136	-65.06	127.1	-50.43	119.1
-75.13	134.5	-65.13	125.5	-48.31	120.7
-73.39	134.3	-64.4	125	-48.1	119.1
-72.42	133.7	-63.27	124.6	-48.72	116.4
-71.02	133	-62.44	123.7	-48.18	116
-70.1	132.9	-60.73	123.6	-45.92	116.7
-69.74	132.1	-59.62	123	-43.95	119.1
-69.21	131.2	-58.35	122.8	-41.79	119.6
-68.83	130	-56.38	122.1	-42.87	116.3
-67.72	130	-54.65	121.5	-42.54	114
-66.79	130	-52.57	120.1	-39.95	112.5
-65.09	129	-50.89	120.9	-36.48	111.3

Table A-26. Topographic survey of the study area shoreline performed on December 13, 2011. Coordinates with respect to N 29°13.411', W 090°36.347'.

E	N	E	N	E	N	E	N
-93.06	143.2	-63.14	125.8	-33.12	112.5	-9.078	70.63
-92.24	143	-61.85	125	-32.23	112.6	-9.832	69.08
-91.68	142.5	-60.35	124.3	-32.1	111.2	-10.36	67.76
-90.68	141.8	-58.72	123.3	-30.91	110.3	-10.33	66.63
-89.89	141.6	-56.69	123	-29.37	109.3	-10.44	65.63
-89.48	141	-55.63	122.3	-27.81	109.3	-9.393	65.7
-89.21	140.7	-53.61	121.4	-26.41	109.9	-7.921	65.86
-88.4	140.8	-51.66	120.9	-25	108.7	-6.938	65.2
-87.98	140.4	-50.88	121.3	-23.18	108.3	-6.198	64.85
-87.06	140.5	-50.29	119.9	-22.21	106.7	-7.517	63.99
-86.11	139.6	-49.54	120	-21.21	105	-8.648	63.74
-85.41	139.3	-48.52	121.1	-19.54	103.2	-9.705	62.86
-83.85	138.3	-47.93	121.1	-17.72	102.5	-9.938	61.71
-82.17	137.6	-47.88	120.1	-15.97	101.7	-9.744	60.86
-81.53	138.2	-48.02	119.3	-13.95	100.4	-9.194	61.16
-80.83	137.7	-48.37	118.2	-12.23	97.8	-8.58	61.87
-80.12	137.2	-48.63	116.9	-12.21	95.58	-8.588	60.47
-79.42	136.8	-48.41	116.5	-12.05	93.78	-9.425	59.37
-78.86	136.5	-48.05	116.6	-10.89	92.28	-9.841	58.62
-77.93	136.5	-47.63	117.5	-10.93	90.72	-9.835	58.14
-76.37	136.5	-47.06	116.8	-10.64	89.05	-8.951	58.43
-75.81	135.6	-46.22	117	-9.66	88.66	-8.434	58.23
-74.45	134.8	-44.66	118.6	-8.795	87.43	-8.766	57.2
-73.18	134.8	-43.43	118.7	-8.664	85.94	-9.086	56.58
-72.21	134.2	-42.02	118.3	-8.905	85.2	-8.924	55.56
-70.99	133.4	-40.68	117.1	-8.906	83.9	-8.45	54.99
-70	133.3	-40.9	116.4	-9.587	83.19	-7.718	54.61
-69.4	132.7	-41.91	116.1	-9.978	81.75	-7.656	53.67
-68.76	131.4	-42.18	115.4	-10.4	80.41	-6.726	52.37
-68.15	130.6	-41.9	114.9	-11.02	79.06	-6.494	51.95
-66.51	130.3	-41.3	114.6	-11.47	77.63	-4.905	51.63
-65.75	130.3	-40.65	113.9	-10.88	76.69	-6.164	50.34
-64.93	129.9	-38.75	112.9	-9.712	76.38	-7.298	49.22
-64.35	128.9	-37.4	112.8	-9.136	74.78	-8.552	48.45
-64.85	128	-36.75	112.3	-9.844	73.18	-9.109	47.14
-64.8	127.3	-35.92	113.9	-9.593	72.47	-9.052	45.11
-64.62	126.3	-35.13	114.5	-8.463	72.24	-8.472	43.96
-64.34	125.5	-33.95	113.5	-8.389	71.07	-8.803	42.42

E	N
-8.381	41.55
-8.552	40.75
-9.137	40.08
-9.6	38.74
-8.776	37.96
-9.398	36.5
-9.73	35.04
-10.28	33.7
-10.27	32
-10.43	30.53
-11.03	29.61
-11.26	28.19
-11.21	26.89
-10.88	24.79
-11.79	23.69
-12.8	21.84
-13.77	20.09
-13.98	18.81
-13.7	17.44
-12.35	15.31
-12.47	13.46
-12.65	11.8
-11.56	12.13
-11.32	11.76
-12.44	10.59
-12.19	9.586
-11.42	9.108
-12.35	7.585
-12.56	6.796
-11.83	6.248
-12.13	5.534
-12.83	4.156
-12.86	3.427
-13.29	1.301
-13.79	-1.37
-13.38	-2.62
-13.77	-4.597
-14.03	-6.355
-12.48	-5.82
-11.78	-6.334

E	N
-12.01	-7.534
-12.08	-8.744
-12.6	-10.97
-12.07	-11.53
-10.71	-11.44
-9.98	-11.76
-10.35	-12.48
-10.26	-13.63
-10.58	-14.36
-11.05	-15.64
-10.68	-16.15
-10.78	-17.85
-10.25	-18.26
-10.49	-18.93
-10.3	-19.34
-9.459	-18.98
-9.443	-19.99
-9.959	-21.34
-8.887	-21.64
-8.69	-22.89
-7.843	-24.21
-7.182	-25.09
-5.666	-26.34
-3.945	-27.3
-2.55	-27.39
-1.713	-27.85
-0.342	-28.22
0.999	-28.49
2.602	-29.25
3.709	-28.86
3.953	-29.5
6.129	-30.18
8.057	-30.14
10.32	-30.33
12.28	-30.8
14.12	-30.8
15.81	-30.22
16.84	-29.7
19.13	-29.36
21.32	-29.58

E	N
23.08	-30.52
24.42	-31.65
27.02	-31.53
29.59	-31.22
31.96	-29.77
33.69	-27.89
34.89	-26.05
35.39	-23.99
36.03	-21.65
35.89	-19.9
34.55	-18.35
33.34	-16.96
31.43	-16.45
29.41	-15.13
28.06	-13.11
26.61	-10.68
25.03	-8.333
24.14	-5.668
23.17	-2.887
22.69	-0.78
21.34	2.291
21.95	3.793
20.32	5.738
20.1	8.54
21.84	10.75
22.05	12.69
20.92	15.18
19.9	17.18
19.17	19.56
16.92	22.25
15.58	25.06
14.6	28.17
14.22	30.61
10.51	30.66
8.855	32.65
8.347	33.24
7.603	32.97
6.607	33.25
6.326	33.87
7.446	35.76

E	N
6.253	39.03
4.751	41.89
3.03	43.45
0.575	44.12
0.106	46.66
0.205	49.29
0.685	51.04
3.013	49.78
6.15	48.01
9.435	45.56
12.14	46.27
14.92	46.77
18.72	49.53
17.13	52.52
13.85	54.39
13.52	58.54
11.62	60.39
11.37	63.81
11.19	65.18
14.07	66.31
8.158	66.39
14.56	65.04
16.55	65.24
18.74	67.26
18.06	69.98
18.89	72.94
20.18	75.28
21.32	76.2
23.28	75.83
23.94	73.25
25.13	70.46
28.95	68.02
33.54	65.2
34.35	65.21
34.89	67.73
36.73	71.81

Table A-27. Topographic survey of the study area shoreline performed on March 5, 2012. Coordinates with respect to N 29°13.411', W 090°36.347'.

E	N	E	N	E	N	E	N	E	N
-102.1	149.9	-65.74	130.3	-32.16	111.6	-9.221	72.46	-11.41	23.66
-101.1	148.8	-64.52	129.4	-31.32	110.8	-7.721	72.62	-12.17	22.49
-100.2	147.8	-64.45	128.1	-30.32	110.4	-8.03	71.57	-12.73	21.55
-98.88	147.3	-64.41	126.7	-28.88	109.4	-9.259	69.4	-13.06	20.73
-97.85	146.8	-64.01	125.6	-28.01	110.1	-9.84	67.82	-10.68	24.69
-96.81	146	-63.38	125.9	-26.84	110.1	-9.982	65.96	-11.76	23.04
-96.17	145.1	-61.9	125	-25.78	109.4	-8.886	65.74	-12.95	21.04
-95.07	144.3	-60.76	124.6	-24.85	110.4	-7.318	65.44	-13.41	18.97
-93.59	143.8	-59.33	124.1	-23.22	110.8	-5.615	64.57	-13.25	17.5
-92.7	143.3	-57.71	123.4	-21.82	110.2	-5.267	63.95	-11.96	14.88
-91.67	142.4	-56.51	123.7	-20.73	109.8	-6.721	63.55	-12.13	12.77
-90.41	141.9	-55.03	123.2	-20.95	108.6	-8.536	63.38	-12.19	12.09
-89.5	141.2	-53.76	122.2	-21.67	107.5	-9.518	62.05	-10.97	12.14
-88.74	140.8	-52.41	121.1	-21.71	106.6	-8.008	61.47	-12.16	10.27
-87.72	140.4	-51.07	121.3	-21.07	105.3	-9.057	59.41	-11.82	9.534
-86.81	140.5	-49.8	120.4	-20.47	104.5	-9.517	58.5	-11.11	8.955
-86.13	139.7	-49.07	120.6	-19.02	103.7	-7.925	58.45	-11.8	7.597
-85.55	139.5	-48.29	121.4	-17.64	102.6	-8.872	56.44	-12.27	6.726
-84.8	139.5	-47.85	121	-16.41	102	-8.277	55.02	-11.41	6.315
-84.08	140.1	-47.79	119.5	-14.79	102.1	-6.989	53.17	-12.14	4.655
-82.69	140.2	-48.08	117.8	-13.35	100.2	-5.793	51.85	-12.4	3.632
-81.69	139.4	-47.33	118.4	-12.43	98.39	-6.052	50.3	-12.13	2.869
-81.91	138.3	-46.84	116.8	-12.26	96.4	-7.386	48.83	-12.94	1.259
-80.66	137.4	-46.3	117	-12.1	94.59	-8.758	47.07	-13.17	-0.3
-79.71	136.8	-45.33	118	-11.36	92.88	-8.727	45.46	-13.32	-1.505
-78.78	136.6	-45.31	118	-10.74	91.38	-8.042	44.45	-12.93	-2.516
-77.49	136.4	-43.8	118.3	-10.54	89.68	-8.396	42.77	-13.38	-4.259
-76.22	136.5	-43.71	118.2	-9.274	88.3	-8.053	41.27	-13.66	-5.582
-75.92	135.6	-43.02	116.6	-8.371	87.46	-9.143	38.9	-13.43	-6.078
-74.55	134.8	-41.9	115.8	-8.474	85.74	-8.666	37.94	-11.96	-5.81
-73.32	134.9	-40.98	115.1	-8.721	83.91	-9.125	36.51	-11.51	-7.353
-72.23	134.4	-40.05	113.9	-9.763	82.24	-10.01	34	-11.49	-8.387
-70.86	133.3	-38.61	113.5	-10.23	80.61	-9.842	32.42	-12.04	-9.892
-70.43	133.5	-37.2	112.8	-11.02	78.22	-10.05	30.58	-12.23	-10.91
-69.57	133	-36.21	112.7	-10.38	76.87	-10.7	29.18	-11.97	-11.39
-68.88	132	-35.81	113.9	-9.14	76.94	-10.96	27.76	-10.59	-11.45
-68.04	131.3	-34.12	114.1	-9.092	76.05	-10.95	26.44	-9.596	-11.59
-66.96	130.5	-32.52	112.9	-9.224	74.29	-10.6	24.85	-10.05	-13.09

E	N
-9.792	-14.03
-10.5	-15.37
-10.53	-16.15
-9.885	-16.48
-10.25	-17.55
-9.804	-18.14
-9.875	-19.04
-8.777	-18.87
-9.209	-20.4
-9.382	-21.27
-8.223	-21.81
-7.924	-23.29
-7.128	-24.04
-6.418	-24.9
-5.465	-25.74
-3.93	-26.61
-2.661	-26.98
-1.408	-27.45
-0.487	-27.79
0.587	-28.31
1.857	-28.21
3	-28.98
4.321	-28.67
5.046	-29.51
5.954	-29.82
7.16	-29.71
9.19	-30.12
10.33	-30.29
11.05	-29.62
12.03	-30.7
13.83	-30.5
15.47	-30.45
16.56	-29.46
18.76	-29.51
21.27	-29.62
22.86	-30.51
25.03	-31.5
27.29	-31.52
29.68	-31.07

E	N
31.54	-29.91
32.79	-28.48
34.03	-26.81
34.7	-24.88
35.32	-23.02
34.95	-22.31
35.83	-21.9
36.09	-21.36
35.6	-19.85
34.8	-18.87
33.26	-17.93
32.49	-16.72
31.48	-16.65
30.24	-16.92
30.49	-16.94
29.44	-15.51
28.49	-13.97
27.7	-12.75
27.58	-11.49
26.84	-11.18
26.16	-9.578
25.35	-8.333
24.41	-6.738
24.66	-5.299
23.43	-3.664
22.53	-1.924
22.4	-0.428
21.76	1.45
22.18	3.203
21.21	5.056
20.48	6.815
19.89	8.034
21.06	9.05
22.24	10.18
22.77	10.7
22.08	11.95
21.53	13.54
20.59	15.07
19.85	16.36

E	N
19.65	17.64
18.87	19.25
17.7	20.24
17.02	21.36
16.22	22.98
15.44	24.7
14.52	26.77
13.78	28.91
13.71	30.6
11.21	30.68
9.49	31.8
8.407	32.86
7.076	32.75
6.598	33.53
6.3	34.4
7.215	35.77
6.563	37.08
6.197	38.89
5.826	40.49
4.976	41.75
4.314	43.19
3.68	44.75
3.449	45.39
2.373	46.23
2.981	48.53
4.365	48.98
6.165	48.01
7.7	46.63
9.428	45.66
11.04	46.55
14.36	47.08
14.85	47.95
15.89	47.87
17.09	49.16
18.1	49.64
17.13	50.95
16.38	52.01
15.48	52.33
13.89	53.61

E	N
13.5	55.63
13.94	56.35
13.76	57.69
13.05	58.77
11.87	59.52
11.35	60.87
11.32	62.56
11.22	64.2
10.43	65.06
9.061	65.6
7.226	67.07
6.239	68.92
5.681	70.41
4.467	70.33
2.951	69.05
1.27	67.66
-0.712	66.82
-2.36	65.79
-3.969	64.82
-5.13	63.91
-5.774	62.97
-6.719	63.47
-7.922	63.3
-8.576	63.34
-9.361	62.59
-9.424	62.04
-9.696	66.84
-10.08	66.05
-9.053	65.88
-7.248	65.45
-5.564	64.7
-4.221	65.89
-2.788	67.12
-0.648	68.19
1.715	69.65
3.951	71.48
4.462	72.42
4.128	74.8
4.294	77.45

E	N
4.897	80.54
5.542	83.44
6.276	86.39
7.292	88.85
8.824	90.93
10.25	92.94
11.21	94.65
11.75	94.73
11.77	93.55
10.37	91.38
9.013	89.42
7.932	87.29
7.378	85.09
6.978	82.5
6.706	79.93
6.384	77.19
6.316	73.88
7.191	71.76
8.663	69.58
10.2	67.85
11.2	67.98
13	68.69
14.63	69.14
15.64	68.56
15.39	67.24
14.33	66.29
14.04	65.77
14.4	65.24
15.94	65.24
17.15	65.4
18.14	66.4
18.21	67.51
17.61	69.82
18.28	71.22
18.9	73.63
19.81	74.93
21.15	76.2

Table A-28. Topographic survey of the study area shoreline performed on July 6, 2012. Coordinates with respect to N 29°13.411', W 090°36.347'.

E	N	E	N	E	N	E	N	E	N
-85.86	140.35	-55.50	124.99	-18.51	104.55	-9.39	66.44	8.90	69.27
-84.95	140.23	-53.97	124.63	-17.20	103.74	-8.32	66.24	10.07	68.42
-84.02	140.20	-52.65	123.60	-15.80	103.25	-7.07	66.06	11.22	68.89
-83.01	140.17	-51.53	122.92	-14.34	102.71	-6.76	65.72	12.68	69.03
-82.18	139.50	-50.44	122.17	-13.79	101.48	-5.50	66.33	14.05	69.55
-81.51	138.77	-49.62	121.41	-13.10	100.19	-4.44	66.11	15.11	69.64
-80.30	138.03	-48.90	121.66	-12.15	98.67	-3.68	67.18	4.62	70.58
-79.34	137.52	-47.96	122.88	-11.62	96.94	-2.69	67.44	3.28	69.62
-78.57	137.71	-47.64	121.65	-11.81	95.24	-1.48	68.22	1.82	68.35
-78.05	137.24	-47.29	120.82	-11.11	93.73	-0.53	68.35	0.18	67.32
-77.64	137.57	-46.65	120.62	-10.49	92.34	0.39	68.89	-1.41	66.47
-77.17	137.39	-46.34	119.77	-9.82	90.72	1.81	69.79	-2.45	65.93
-76.98	137.03	-45.73	119.54	-8.77	90.15	2.96	70.97	-3.27	65.23
-76.09	137.17	-44.47	120.02	-8.69	88.78	4.02	71.85	-4.49	63.91
-75.49	137.35	-43.12	120.48	-7.45	88.69	4.08	73.03	-5.13	62.86
-74.68	136.66	-41.59	120.93	-7.82	87.00	3.94	74.55	-5.78	62.00
-73.68	135.95	-40.13	120.22	-7.80	85.74	4.05	76.49	-6.56	60.83
-73.02	135.79	-38.84	119.00	-8.12	84.72	4.28	78.34	-7.21	60.41
-72.03	136.20	-36.96	118.87	-8.44	83.28	4.35	79.47	-7.98	59.97
-71.15	135.51	-35.09	117.60	-9.20	82.42	4.58	80.97	-8.35	59.70
-70.49	134.37	-35.49	115.91	-9.51	81.23	5.11	82.30	-8.59	59.17
-69.57	134.30	-35.44	114.94	-10.07	80.18	5.48	83.91	-7.20	59.29
-68.99	134.15	-34.07	114.81	-10.07	78.59	5.90	84.98	-7.75	58.16
-68.54	133.21	-33.22	113.56	-10.18	77.47	6.49	86.67	-8.31	57.00
-67.48	132.35	-31.84	112.43	-9.33	77.40	7.20	87.56	-7.31	56.21
-67.09	131.69	-31.15	111.29	-8.63	77.69	7.54	86.17	-7.82	55.40
-66.50	131.34	-29.58	111.10	-8.71	76.22	7.04	84.58	-7.21	54.93
-65.57	131.10	-28.55	110.52	-8.51	74.90	6.86	82.71	-6.07	54.90
-64.89	130.87	-26.73	110.32	-7.90	74.25	6.64	81.26	-6.35	54.18
-64.03	130.05	-25.90	109.68	-8.33	73.65	6.56	79.93	-6.95	53.97
-63.52	128.14	-24.67	109.60	-8.00	73.14	6.40	78.93	-6.21	53.40
-62.37	128.01	-23.18	110.38	-7.22	73.20	6.42	77.21	-5.23	53.44
-61.89	127.51	-22.29	109.92	-7.06	72.40	6.44	75.91	-4.06	54.13
-61.84	126.08	-21.26	109.16	-7.68	71.59	6.45	74.95	-3.15	53.19
-61.07	125.43	-21.35	107.99	-7.72	70.33	6.26	73.90	-2.71	51.36
-59.66	125.74	-21.40	106.82	-7.58	68.68	6.91	72.46	-4.30	50.46
-58.35	126.01	-20.68	105.86	-7.93	67.40	7.68	71.34	-5.47	49.22
-57.02	125.56	-20.03	105.29	-8.85	67.05	8.31	70.35	-6.87	47.83

E	N
-8.28	45.64
-7.24	44.76
-7.83	43.72
-7.88	42.77
-7.30	41.76
-8.02	40.29
-8.52	39.40
-8.31	38.42
-8.68	36.75
-9.01	35.13
-9.48	34.06
-9.61	32.10
-10.02	29.92
-10.51	27.79
-10.45	26.63
-10.08	25.07
-10.94	23.47
-12.06	22.02
-12.56	20.85
-12.93	19.66
-12.81	18.09
-12.27	16.66
-11.43	15.23
-11.78	13.42
-11.70	12.61
-10.37	12.44
-10.94	11.60
-11.48	11.14
-11.10	9.69
-10.46	9.18
-11.43	7.64
-11.23	6.90
-11.12	5.69
-11.56	5.12
-11.66	3.72
-12.28	2.11
-12.63	0.48
-12.72	-0.97
-12.30	-1.31
-12.58	-2.47

E	N
-12.68	-4.02
-12.54	-4.63
-11.11	-4.58
-10.44	-5.75
-10.64	-7.15
-11.01	-8.38
-11.66	-9.80
-11.71	-10.72
-10.58	-10.78
-9.29	-11.27
-9.56	-12.49
-9.63	-13.02
-8.94	-13.49
-9.41	-14.03
-9.58	-15.51
-9.42	-17.08
-8.42	-18.36
-8.56	-19.49
-8.54	-20.42
-7.61	-20.62
-7.73	-21.67
-6.57	-22.75
-6.23	-23.80
-5.33	-24.02
-5.09	-24.44
-3.83	-24.79
-2.89	-25.84
-1.60	-25.50
-1.10	-25.02
-0.59	-25.96
0.31	-25.88
0.93	-26.67
2.05	-27.06
3.41	-27.38
4.89	-27.78
6.29	-27.92
8.17	-27.10
9.58	-27.27
11.26	-27.32
13.09	-26.86

E	N
13.94	-27.88
15.07	-28.03
16.19	-28.13
16.99	-27.20
19.08	-27.22
20.62	-27.19
22.12	-27.65
23.43	-28.36
24.52	-29.03
25.98	-29.27
27.93	-28.81
30.29	-27.94
31.50	-27.13
32.49	-26.62
33.40	-25.41
33.67	-24.20
34.47	-23.12
34.41	-22.17
35.14	-21.01
34.92	-19.49
33.56	-18.57
32.37	-17.47
31.60	-17.35
30.74	-17.68
29.05	-16.57
28.35	-15.21
28.48	-14.70
28.16	-13.47
27.43	-12.16
26.94	-11.42
26.13	-10.08
25.81	-8.99
25.41	-7.96
24.32	-7.15
24.36	-5.77
24.49	-4.88
23.36	-3.86
22.18	-3.11
22.05	-1.39
21.97	0.07

E	N
21.74	1.76
22.06	3.06
21.71	4.31
20.64	5.36
19.90	6.67
19.63	7.83
19.97	8.90
20.65	9.66
21.38	10.25
21.80	11.13
21.20	12.45
21.03	13.51
19.86	14.69
19.44	15.94
18.56	17.10
18.35	18.21
17.34	19.78
16.57	21.14
15.69	23.13
14.85	24.75
14.13	26.43
14.02	27.18
13.56	27.57
13.68	28.38
12.56	29.05
12.72	30.12
11.76	30.36
10.56	30.27
9.62	31.06
9.27	31.76
8.31	32.30
7.02	32.22
5.98	31.96
4.00	32.70
3.88	33.97
4.66	35.24
5.60	35.16
6.64	35.38
6.96	36.01
6.15	37.35

E	N
5.84	38.48
5.27	40.05
4.33	41.85
3.61	43.52
3.01	45.33
1.74	46.84
0.48	47.78
0.67	49.56
1.73	50.62
2.98	49.76
4.04	48.99
5.39	48.34
6.60	47.72
7.74	47.03
8.99	46.42
10.17	46.70
11.35	47.39
12.66	47.52
14.10	48.24
15.31	48.35
15.82	49.71
16.50	50.41
15.95	51.63
14.58	52.13
13.47	53.41
12.76	54.89
13.00	56.51
12.94	58.19
11.66	59.27
10.74	60.53
10.58	62.39
10.53	63.84
9.68	65.09
8.29	65.92
7.16	67.41

Table A-29. Shoreline profile of the main beach with respect to an arbitrary origin (June 8, 2011).

X	Y	X	Y	X	Y
110.25	4.58	73.99	5.59	55.17	5.60
103.61	5.88	72.67	7.73	52.89	4.69
100.88	5.10	69.35	4.11	50.63	5.50
94.88	5.29	68.33	7.62	46.88	8.85
92.25	6.16	67.38	7.86	45.14	6.99
90.87	6.27	66.52	5.97	42.75	9.65
84.47	7.37	65.47	7.58	41.16	9.02
82.38	5.61	65.21	6.43	39.43	10.02
79.27	5.30	62.57	6.08	38.81	8.35
77.93	4.56	61.85	6.70	37.14	7.87
76.02	4.79	61.12	6.02	34.75	9.15
74.94	5.85	58.21	6.09	31.45	7.62

Table A-30. Shoreline profile of the main beach with respect to an arbitrary origin (Sept. 9, 2011).

X	Y	X	Y	X	Y
35.19	9.94	49.84	7.40	66.51	6.91
37.48	9.47	50.51	5.93	67.68	9.27
39.12	10.08	51.37	5.84	68.57	7.99
40.30	9.91	52.57	5.98	69.24	5.31
41.83	9.99	53.70	5.58	69.92	5.17
42.70	10.29	55.25	6.30	71.58	6.86
43.38	9.76	56.54	6.22	72.27	9.86
44.29	9.15	57.74	6.66	73.97	11.30
45.14	8.31	59.84	6.88	74.51	7.85
46.15	8.79	61.64	7.17	75.83	5.99
46.95	9.25	64.14	6.84	78.83	5.81
48.95	9.05	65.27	8.33	82.45	6.34

Table A-31. Shoreline profile of the main beach with respect to an arbitrary origin (Dec. 13, 2011).

X	Y
17.58	9.02
18.38	9.28
19.14	9.01
20.31	8.91
21.11	9.09
21.75	8.73
22.12	8.60
22.82	9.01
23.35	8.89
24.13	9.41
25.41	8.97
26.18	9.01
28.01	8.86
29.81	9.03
30.13	9.79
30.98	9.68
31.81	9.60
32.64	9.52
33.27	9.51
34.08	9.99
35.48	10.66
36.42	10.07
37.94	10.05
39.11	10.56
40.22	10.52
41.69	10.33
42.61	10.70
43.42	10.44
44.56	9.60
45.47	9.17
47.06	9.65
47.78	9.92
48.65	10.00
49.63	9.36
49.60	8.33
49.96	7.71
50.57	6.92
51.20	6.31
52.12	7.15
53.63	7.01
55.29	7.08
57.20	6.91
59.14	7.57
60.40	7.44
62.60	7.57
64.60	7.93
65.11	8.64
66.25	7.71
66.87	8.16
67.28	9.60
67.80	9.87
68.32	8.96
68.54	8.22
68.76	7.03
69.10	5.78
69.48	5.52
69.73	5.82
69.70	6.81
70.53	6.44
71.23	6.92
71.87	9.07
72.91	9.76
74.35	10.03
76.10	9.54
76.19	8.88
75.44	8.15
75.53	7.38
76.02	7.03
76.68	7.04
77.58	6.73
79.70	6.74
80.96	7.23
81.78	7.05
81.79	8.88
82.20	9.80
83.72	9.43
84.91	8.93
85.66	9.42
86.42	8.21
87.89	7.94
89.70	7.78
91.10	8.45
92.09	9.61
93.87	9.22
95.70	9.64
97.25	8.73
98.95	7.60
101.25	6.77
103.19	6.95
105.11	7.03
107.48	6.86
110.20	5.29

Table A-32. Shoreline profile of the main beach with respect to an arbitrary origin (March 5, 2012).

X	Y
6.45	10.86
7.88	10.43
9.15	9.96
10.53	10.04
11.68	10.06
12.94	9.86
13.93	9.34
15.30	9.08
16.84	9.32
17.86	9.26
19.16	8.99
20.53	9.08
21.63	8.92
22.52	8.86
23.58	9.02
24.35	9.50
25.35	9.05
25.92	9.19
26.60	9.52
26.98	10.38
28.15	11.12
29.45	10.80
29.74	9.72
31.24	9.53
32.35	9.45
33.27	9.68
34.53	10.05
35.62	10.73
36.32	10.01
37.87	9.98
38.94	10.59
40.13	10.64
41.86	10.27
42.14	10.68
43.13	10.62
44.21	10.02
45.25	9.84
46.58	9.61
47.79	9.93
49.29	9.67
49.93	8.56
50.60	7.32
51.44	6.56
51.89	7.06
53.60	6.96
54.82	7.11
56.30	7.34
58.04	7.49
59.00	8.23
60.53	8.49
62.10	8.20
63.85	7.77
64.95	8.56
66.49	8.33
67.01	8.92
67.34	9.97
67.95	9.76
68.67	8.47
69.17	6.86
69.56	7.75
70.74	6.51
71.12	6.96
71.51	8.30
71.56	8.27
72.79	9.19
72.90	9.17
74.22	8.10
75.61	7.83
76.76	7.61
78.12	6.99
79.58	7.29
81.14	7.34
82.08	7.67
81.87	8.96
83.30	9.88
85.29	9.49
86.17	8.54
87.28	8.21
88.38	8.28
90.10	8.07
90.56	9.09
91.59	9.63
92.87	9.46
93.22	10.81
94.49	11.91
96.02	12.01
97.19	12.11
97.54	10.94
97.40	9.61
97.76	8.84
98.90	7.98
99.83	7.48
101.48	7.46
103.18	7.15
104.60	7.09
105.97	7.95
108.11	6.94
109.75	5.72

Table A-33. Shoreline profile of the main beach with respect to an arbitrary origin (July 6, 2012).

X	Y
25.28	9.78
26.14	10.08
26.99	10.48
27.91	10.91
28.94	10.69
29.87	10.34
31.28	10.23
32.37	10.21
32.97	10.74
33.65	10.55
33.86	11.03
34.37	11.08
34.70	10.85
35.43	11.37
35.88	11.81
36.92	11.56
38.13	11.39
38.79	11.54
39.49	12.36
40.59	12.14
41.69	11.42
42.54	11.78
43.13	11.91
43.96	11.28
45.29	10.99
45.94	10.58
46.62	10.54
47.55	10.75
48.27	10.85
49.41	10.51
50.72	9.04
51.81	9.45
52.47	9.22
53.16	7.97
54.14	7.73
55.26	8.65
56.31	9.48
57.69	9.69
59.31	9.88
60.83	10.25
62.48	9.92
63.78	9.83
65.10	9.66
66.17	9.35
66.69	9.90
66.98	11.41
67.82	10.46
68.51	9.88
69.17	10.00
69.83	9.38
70.48	9.45
71.39	10.45
72.39	11.47
73.54	12.57
75.17	12.60
76.87	12.10
78.60	12.84
80.85	12.55
81.26	10.87
81.74	10.02
83.03	10.53
84.35	9.80
86.09	9.42
87.22	8.72
88.71	9.26
89.89	9.22
91.60	9.86
92.63	9.67
93.76	10.16
94.73	11.53
95.73	11.52
97.00	11.32
97.45	10.23
97.94	9.17
99.01	8.64
99.85	8.42
101.54	8.45
103.08	8.33
104.55	8.52
106.10	8.71
107.14	7.85
108.34	7.02
109.88	6.10

APPENDIX B. DATA ON MARSH SOIL'S CRITICAL SHEAR STRESS AND OTHER INDEX PROPERTIES

Date: 9/23/2011
Site: Barataria Bay
Core sample tests

Layer (inch)	Average critical shear stress (N/m^2)	Water content (%)	Organic matter content (%)	Root content (%)	D_{50} (mm)	LL (%)	PL (%)	PI (%)	Specific gravity
0-3	0.74	123.60	20.89	3.60	0.12	66.50	46.82	19.68	2.27
3-6	1.19	176.03	25.00	2.90					
6-9	1.60	190.66	17.25	6.30					
9-12	1.56	220.49	21.57	2.60					
12-15	1.81	279.42	25.49	5.80					
15-18	1.45	222.16	17.61	6.90					

Date: 12/13/2011
Site: Terrebonne Bay
In situ tests

Spot	Critical shear stress (N/m^2)
1	0.95
2	1.9
3	Test error

Core sample tests

Layer (inch)	Average critical shear stress (N/m^2)	Water content (%)	Organic matter content (%)	Root content (%)	D_{50} (mm)	LL (%)	PL (%)	PI (%)	Specific gravity
0-3	0.90	146.80	12.06	2.13	0.09	63.60	36.37	27.23	2.55
3-6	1.03	120.74	7.66	0.77					
6-9	1.11	162.86	7.33	1.92					
9-12	1.08	196.56	11.62	1.88					
12-15	1.20	151.13	9.22	2.77					
15-18	1.18	144.42	8.51	2.74					
18-21	0.61	151.38	10.74	2.08					
21-24	0.29	155.52	12.51	1.42					

Date: 3/5/2012
Site: Terrebonne Bay
In situ tests

Depth (m)	Critical shear stress test 1 (N/m^2)	Critical shear stress test 2 (N/m^2)	Average critical shear stress (N/m^2)
0.00	0.45	0.75	0.60
0.15	1.00	1.04	1.02
0.23	0.40	0.92	0.66

Core sample tests

Layer (inch)	Average critical shear stress (N/m^2)	Water content (%)	Organic matter content (%)	Root content (%)	D_{50} (mm)	LL (%)	PL (%)	PI (%)	Specific gravity
0-3	0.90	100.64	6.76	2.26	0.095	45.20	23.14	22.06	2.53
3-6	0.83	170.00	10.63	2.52					
6-9	1.09	110.82	8.78	1.19					
9-12	0.23	119.28	8.17	1.32					
12-15	0.28	122.10	9.94	3.24					
15-18	1.05	171.35	10.22	2.60					
18-21	0.35	140.59	9.05	2.01					
21-24	0.97	149.20	9.83	2.03					

Date: 3/26/2012
Site: Barataria Bay
In situ tests

Spot	Critical shear stress test 1 (N/m^2)	Critical shear stress test 2 (N/m^2)	Average critical shear stress (N/m^2)
1	0.40	0.52	0.46

Core sample tests

Layer (inch)	Average critical shear stress (N/m^2)	Water content (%)	Organic matter content (%)	Root content (%)	D_{50} (mm)	LL (%)	PL (%)	PI (%)	Specific gravity
0-3	1.20	28.46	22.83	10.67	0.098	65.00	43.09	21.91	2.31
3-6	1.68	219.26	54.65	5.69					
6-9	1.55	214.22	18.90	1.95					
9-12	0.97	226.75	21.22	2.46					
12-15	1.40	210.30	16.46	3.09					
15-18	1.12	242.37	18.56	3.97					
18-21	1.66	300.07	22.52	6.03					
21-24	1.42	364.90	27.09	3.43					

Date: 4/18/2012
Site: Barataria Bay
In situ tests

Spot	Critical shear stress test 1 (N/m^2)	Critical shear stress test 2 (N/m^2)	Average critical shear stress (N/m^2)	Organic matter content (%)
1	0.80	0.47	0.64	39.18
2	1.57	1.60	1.59	33.38
3	1.38	1.52	1.45	30.59

Core sample tests

Layer (inch)	Average critical shear stress (N/m^2)	Water content (%)	Organic matter content (%)	Root content (%)	D_{50} (mm)	LL (%)	PL (%)	PI (%)	Specific gravity
0-3	0.37	351.69	20.00	3.38					
3-6	1.20	280.53	19.64	2.34					
6-9	0.93	271.84	15.53	1.78					
9-12	1.74	188.51	12.21	5.65	0.12	73.00	46.77	26.23	2.22
12-15	1.10	387.13	26.00	0.98					
15-18	1.05	276.86	17.80	1.88					
18-22	1.23	322.31	22.48	2.47					

Date: 7/6/2012
Site: Terrebonne Bay
In situ tests

Spot	Distance from shore line (N/m^2)	Critical shear stress test 1 (N/m^2)	Critical shear stress test 2 (N/m^2)	Average critical shear stress (N/m^2)	Organic matter content (%)	Root content (%)
1	1.70	0.60	0.95	0.78	7.30	0.78
2	3.00	1.68	1.92	1.80	9.01	0.92
3	8.00	1.10	1.70	1.40	9.39	1.15
4	9.00	0.74		0.74	10.64	0.89

Date: 7/23/2012
Site: Terrebonne Bay
In situ tests

Spot	Critical shear stress (N/m^2)	Organic matter content (%)	Water content (%)
1	0.80	3.43	55.12
2	1.00	4.09	58.93

APPENDIX C. DATA ON VEGETATION DAMAGE RESISTANCE

Date: 12/13/2011
Site: Terrebonne Bay

Plant	Height (in)	Root depth (in)	Diam.(mm)	Force(lb)	D (in)
1	3	3.5	5.67	42	0.22322835
2	5.5	3.5	6.23	34	0.24527559
3	6.5	3	7.52	28	0.29606299
4	21	4	7.62	26	0.3
5	19.5	4	6.63	42	0.26102362
6	29	5	6.67	38	0.26259843
7	6.5	7.5	8.13	25	0.32007874
8	16.5	7.5	11.41	27	0.4492126
9	9.5	5	9.77	38	0.38464567
10	5	2	9.04	31	0.35590551

Date: 3/5/2012
Site: Terrebonne Bay

Number	Force (lb)	Break type	H (in)	D (in)
1	27	r	17	0.39
2	29	r	13	0.3
3	22	j	7	0.28
4	28	j	23	0.17
5	24	j	15	0.32
6	21	r	17	0.2
7	25	r	24	0.38
8	26	r	25	0.33
9	29	r	28	0.43
10	23	r	14	0.27
11	24	r	11	0.26
12	25	r	16	0.26
13	28	r	25	0.35
14	36	r	22	0.49
15	19	j	8	0.14

Date: 3/26/2012
Site: Barataria Bay

Number	Force (lb)	Break type	H (in)	D (in)
1	31	r	31	0.32
2	22	j	33	0.41
3	24	j	19	0.32
4	29	j	22	0.34
5	27	r	15	0.24
6	25	r	34	0.27
7	34	r	19	0.43
8	33	r	29	0.44
9	18	j	11	0.15
10	28	r	21	0.26
11	19	r	7	0.12
12	17	j	13	0.19
13	28	j	25	0.29
14	26	r	17	0.21
15	25	r	23	0.28

Date: 4/27/2012
Site: Barataria Bay

Number	Force (lb)	Break type	H (in)	D (in)
1	23	j	22	0.29
2	35	j	25	0.31
3	32	r	23	0.34
4	34	r	27	0.26
5	27	r	21	0.34
6	29	j	32	0.3
7	39	r	34	0.45
8	42	r	29	0.49
9	25	j	26	0.23
10	24	j	23	0.27

Date: 7/6/2012
Site: Terrebonne Bay

Plant #	Force (lb)	D (in)	H (in)	Break type
1	26	0.16	1.3	j
2	22	0.16	2	j
3	28	0.26	5.9	j
4	33	0.16	4.9	j
5	25	0.25	4.4	j
6	36	0.26	8.7	j
7	33	0.28	5.5	j
8	45	0.1	4.5	r
9	55	0.38	7.8	r
10	44	0.36	6.1	j
11	49	0.29	4.7	j
12	56	0.25	5.3	j
13	27	0.48	5.1	r
14	26	0.21	4.2	j
15	59	0.36	10.2	r

Date: 7/23/2012
Site: Terrebonne Bay

Plant #	Force (lb)	D (in)	H (in)	Break type
1	27	0.21	11.1	r
2	21	0.22	5.6	j
3	30	0.23	7.9	j
4	42	0.25	4.5	j
5	17	0.29	12.4	r
6	28	0.26	12.3	r
7	22	0.28	11.4	r
8	52	0.38	11.8	r
9	55	0.36	15.6	r
10	61	0.49	8.9	r
11	76	0.33	15.5	r
12	38	0.31	5.3	j
13	45	0.27	11.5	j
14	46	0.3	13.3	r
15	56	0.38	15.7	r

Southeast Region Research Initiative
National Security Directorate
P.O. Box 6242
Oak Ridge National Laboratory
Oak Ridge, TN 37831-6252

www.serri.org